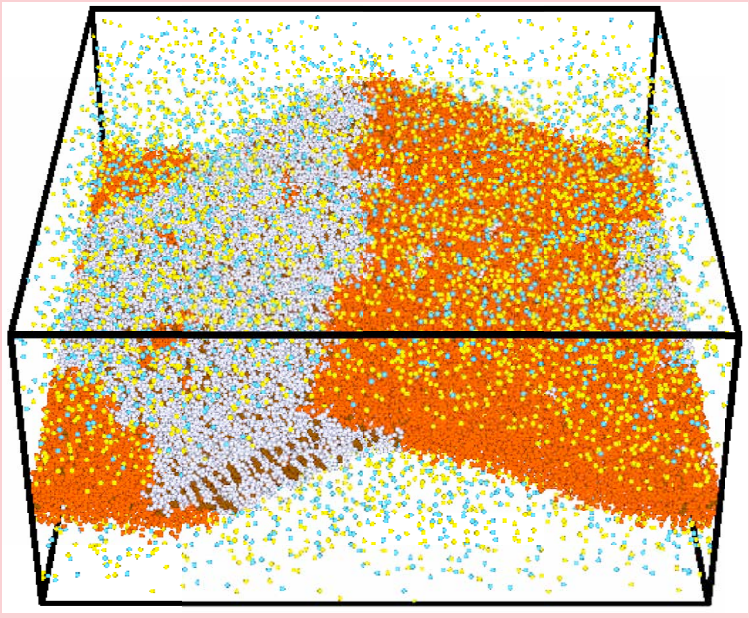
ISSN 2188-5001



MATERIALS DESIGN AND
CHARACTERIZATION LABORATORY

SUPERCOMPUTER CENTER

ACTIVITY REPORT 2025



THE UNIVERSITY OF TOKYO

Materials Design and Characterization Laboratory (MDCL)

The MDCL was established as the third research facility of the Institute for Solid State Physics (ISSP) when the latter was reorganized in May 1996. Its aim is to promote material science with an emphasis on the "DSC cycle", where DSC stands for design, synthesis and characterization, three processes for developing new materials.

The MDCL consists of two sections, Materials Design (MD) section and Materials Synthesis and Characterization (MSC) section. The Supercomputer Center of the ISSP (SCC-ISSP) is placed in the MD section, while in the MSC section there are seven laboratories for joint use; Materials Synthesis Laboratory, Chemical Analysis Laboratory, X-ray Diffraction Laboratory, Electron Microscope Laboratory, Electromagnetic Measurement Laboratory, Spectroscopy Laboratory, and High-Pressure Synthesis Laboratory.

Almost all the facilities of the MDCL are open to scientists in Japan through the User Programs conducted by two steering committees of the MDCL. One is the steering committee of the SCC-ISSP, under which the Supercomputer Project Advisory Committee is placed for reviewing proposals. The other is the steering committee of the MSC facilities. More than half of the members of these committees are from the outside of ISSP.

COVER FIGURE

Phase separation of a lipid membrane in NaCl solution.
See Page 32–38, Y. Higuchi et al. "Ion Distribution near Phase Separated Charged Phospholipid Membranes".
Reproduced from Y. Higuchi et al. J. Mol. Liq., 444, 129168 (2026). Licensed under CC BY 4.0.

PREFACE

The Supercomputer Center (SCC) is a part of the Materials Design and Characterization Laboratory (MDCL) of Institute for Solid State Physics (ISSP). Its mission is to serve the whole community of computational condensed-matter physics of Japan providing it with high performance computing environment. In particular, the SCC selectively promotes and supports large-scale computations. For this purpose, the SCC invites proposals for supercomputer-aided research projects and hosts the Steering Committee, as mentioned below, that evaluates the proposals.

The ISSP supercomputer system consists of two subsystems: System B, which was last replaced in Oct. 2020, is intended for larger total computational power and has more nodes with relatively loose connections, whereas System C is intended for higher communication speed among nodes. System B (ohtaka) consists of 1680 CPU nodes of AMD EPYC 7702 (64 cores) and 8 FAT nodes of Intel Xeon Platinum 8280 (28 cores) with total theoretical performance of 6.881 PFlops. System C was replaced in June 2022 and the current system (kugui) consists of 128 CPU nodes of AMD EPYC 7763 (64 cores) and 8 ACC nodes of AMD EPYC 7763 (64 cores) NVIDIA A100 40GB for HGX with total theoretical performance of 0.973 PFLOPS.

In addition to the hardware administration, the SCC puts increasing effort on the software support. Since 2015, the SCC has been conducting “Project for advancement of software usability in materials science (PASUMS).”In this project, for enhancing the usability of the ISSP supercomputer system, we conduct several software-advancement activities: developing new application software that runs efficiently on the ISSP supercomputer system, adding new functions to existing codes, help releasing private codes for public use, creating/improving manuals for public codes, etc. Two target programs were selected for fiscal year 2025: (1) PHYSBO (proposal made by R. Tamura (NIMS)), and (2) TurboRVB (proposal made by K. Nakano (NIMS)). In addition, since 2021, we have been maintaining the data repository service for secure storage and enhanced usability of results of numerical calculation.

All staff members of university faculties or public research institutes in Japan are invited to propose research projects (called User Program). The proposals are evaluated by the Steering Committee of SCC. Peer-reviewing is done by the Supercomputer Project Advisory Committee. In fiscal year 2025, totally 382 projects were approved including the ones under the framework of Supercomputing Consortium for Computational Materials Science (SCCMS), which specially supports major projects in computational materials science.

The research projects are roughly classified into the following three (the number of projects approved):

First-Principles Calculation of Materials Properties (202)
Strongly Correlated Quantum Systems (40)
Cooperative Phenomena in Complex, Macroscopic Systems (132)
SCCMS projects (8)

In all four categories, most proposals involve both methodology and applications. The results of the projects are reported in 'Activity Report 2025' of the SCC. Every year 3-4 projects are selected for “invited papers” and published at the beginning of the Activity Report. In the Activity Report 2025, the following three invited papers are included:

“First-Principles Calculations on Attosecond Transient Absorption Spectroscopy for Bulk Nickel”,
Shunsuke A. SATO (Tohoku Univ.)

“Many-body wavefunction approach to topological quantum magnets”
Kota IDO (ISSP)

“Ion Distribution near Phase Separated Charged Phospholipid Membranes”
Yuji HIGUCHI (Kyushu Univ.), Hiroaki ITO (Chiba Univ.), Naofumi SHIMOKAWA (JAIST), Jurij REŠČIČ (University of Ljubljana), and Klemen BOHINC (University of Ljubljana)

On April 1, 2026, ISSP reorganized the divisions. Computational physics groups and SCC at MDCL and the Center for Computational Materials Science (CCMS) were reorganized into Numerical Materials Research Laboratory (NML). SCC continues to provide computational resources and support large-scale computations for the computational condensed-matter physics community in Japan as the center at NML.

June 10, 2026

Naoki Kawashima
(Chairman of the steering committee 2025, SCC, ISSP)

CONTENTS

PREFACE

1 OUTLINE **1**

1.1 Supercomputer System 1
1.2 Project Proposals 1
1.3 Committees 3
1.4 Staff 7

2 STATISTICS (SCHOOL YEAR 2025) **7**

2.1 System and User Statistics 7
2.2 Queue and Job Statistics 8
2.3 Project for Advancement of Software Usability in Materials Science 13
2.4 ISSP Data Repository 13

3 RESEARCH REPORTS **14**

3.1 Invited Articles 14
3.2 First-Principles Calculation of Material Properties 39
3.3 Strongly Correlated Quantum Systems 216
3.4 Cooperative Phenomena in Complex Macroscopic Systems 257
3.5 SCCMS Projects 380
3.6 Software Advancement Projects and Workshop Support 387

4 PUBLICATION LIST **393**

ISSP Joint Research Projects 394
SCCMS Projects 454

5 THESES **456**

Doctor Theses 457
Master Theses 459

1 OUTLINE

1.1 Supercomputer System

In School year 2025(SY 2025), the ISSP supercomputer center provided users with System B - Dell PowerEdge C6525/R940 system named "ohtaka" and System C - HPE Apollo 2000 Gen10 Plus/HPE Apollo 6500 Gen10 Plus system named "kugui". System B is a massively-parallel supercomputer with two types of compute nodes: 8 "Fat" nodes and 1680 "CPU" nodes. "Fat" nodes are each comprised of four Intel Xeon Platinum 8280 CPUs (28 cores/CPU) and 3 TB of memory per node. "CPU" nodes have two AMD EPYC 7702 CPUs (64 cores/CPU) and 256 GB of memory per node. System B achieves about 6.881 PFLOPS in theoretical peak performance with high power efficiency. The subsystem comprised of only CPU nodes ranks 87th in the Nov. 2020 Top 500 List, which is a ranking based on total performance measured by the HPL benchmark. The compute nodes communicate to each other through HDR100 Infiniband and are connected in fat tree topology. SY 2025 was the sixth year of the operation of the current System B. System C is a massively-parallel supercomputer with two types of compute nodes: 128 "CPU" nodes and 8 "ACC" nodes. "CPU" nodes are each comprised of two AMD EPYC 7763 CPUs (64 cores/CPU) and 256 GB of memory. The compute nodes communicate to each other through HDR200 Infiniband and are connected in fat tree topology. "ACC" nodes are each comprised of one AMD EPYC 7763 CPUs (64 cores/CPU), four NVIDIA A100 40GB for HGX GPUs and 256 GB of memory. System C achieves 973 TFLOPS in theoretical peak performance. SY 2025 was the fourth year of the operation of the current System C. As shown in Fig. 1, users can access both systems via the Internet using SSH public key authentication. For further details, please contact ISSP Supercomputer Center (SCC-ISSP).

[Correspondence: center@issp.u-tokyo.ac.jp]

1.2 Project Proposals

The ISSP supercomputer system provides computation resources for scientists working on condensed matter sciences in Japan. All scientific staff members (including post-docs) at universities or public research institutes in Japan can submit proposals for projects related to research activities on materials and condensed matter sciences. These proposals are peer-reviewed by the Advisory Committee members (see Sec. 1.3), and then the computation resources are allocated based on the review reports. The leader of an approved project can set up user accounts for collaborators. Other types of scientists, including graduate students, may also be added. Proposal submissions, peer-review processes, and user registration are all managed via a web system.

The computation resources are distributed in a unit called "point", determined as a function of available CPU utilization time and consumed disk resources. There

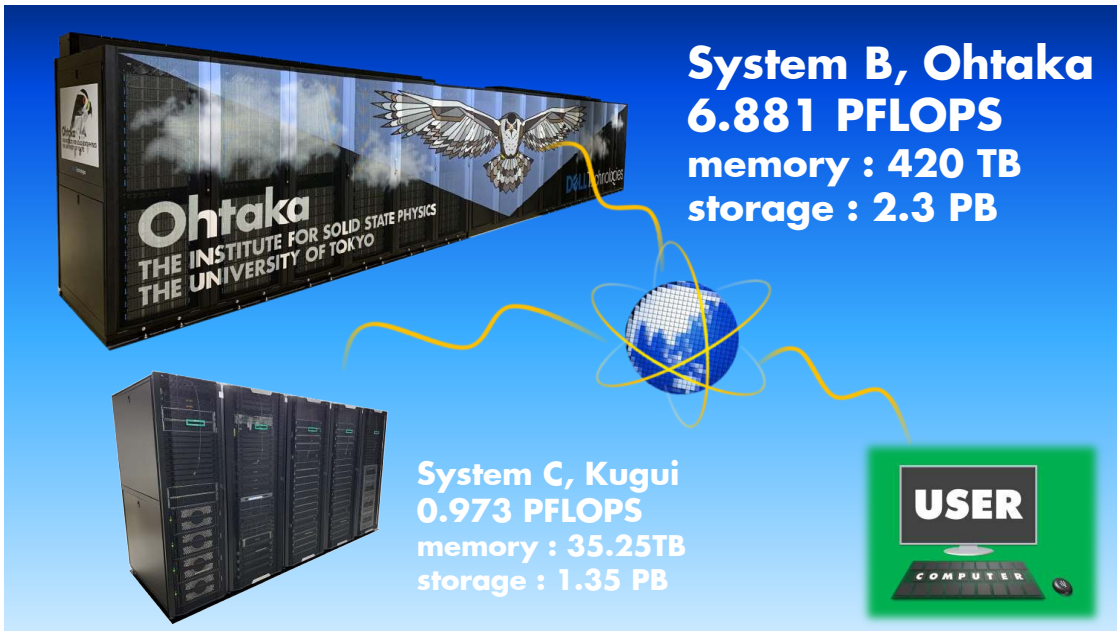


Figure 1: Supercomputer System at the SCC-ISSP

were calls for six classes of research projects in SY 2025. The number of projects and the total number of points that were applied for and approved in this school year are listed in Table 1.

- Class A is for trial use by new users; proposals for Class A projects are accepted throughout the year.
- Proposals for projects in Classes B (small), C (mid-size), E (large-scale), and S (exceptional) can be submitted twice a year. Approved projects in Classes A, B, C, and E continue to the end of the school year.
- In Class D, projects can be proposed on rapidly-developing studies that need to perform urgent and relatively large calculations. An approved project continues for 6 months from its approval.
- Class S is for projects that are considered extremely important for the field of condensed matter physics and requires extremely large-scale computation. The project may be carried out either by one research group or cooperatively by several investigators at different institutions. A project of this class should be applied with at least 10,000 points; there is no maximum. We require group leaders applying for Class S to give a presentation on the proposal to the Steering Committee of the SCC-ISSP. Class S projects are carried out within one year from its approval.
- Project leaders can apply for points so that the points for each system do not exceed the maximum point shown in this table.

Table 1: Classes of research projects in SY 2025. Total points listed in this table are rounded. In Class D, we collect information about the projects ended in each semester.

Class	Maximum Points		Application	# of Proj.	Total points			
					Applied		Approved	
	Sys–B	Sys–C			Sys–B	Sys–C	Sys–B	Sys–C
A	100	50	any time	30	3.0k	1.5k	3.0k	1.5k
B	650	100	twice a year	112	66.7k	7.8k	42.0k	6.0k
C	6.5k	500	twice a year	201	1042.4k	60.5k	553.5k	40.7k
D	10k	500	any time	8	57.3k	1.5k	35.7k	2.1k
E	20k	1.5k	twice a year	23	416.3k	34.0k	203.5k	19.6k
S	–	–	twice a year	0	0	0	0	0
SCCMS				8	19.0k	1.6k	19.0k	1.6k
Total				382	1604.7k	106.9k	856.7k	71.4k

In addition, from SY 2016, ISSP Supercomputer has been providing 20% of its computational resources for Supercomputing Consortium for Computational Materials Science (SCCMS), which aims at advancing parallel computations in condensed matter, molecular, and materials sciences on the 10-PFlops K Computer and the exascale post-K project. From SY 2020, up to 10% of the computational resources have been provided for SCCMS. Computational resources have also been allotted to Computational Materials Design (CMD) workshops, as well as CCMS hands-on workshops.

1.3 Committees

In order to fairly manage the projects and to smoothly determine the system operation policies, the Materials Design and Characterization Laboratory (MDCL) of the ISSP has organized the Steering Committee of the MDCL and the Steering Committee of the SCC-ISSP, under which the Supercomputer Project Advisory Committee (SPAC) is formed to review proposals. The members of the committees in SY 2025 were as follows:

Steering Committee of the MDCL

OKAMOTO, Yoshihiko	ISSP (Chairperson)
KAWASHIMA, Naoki	ISSP
YAMAURA, Jun-ichi	ISSP
OZAKI, Taisuke	ISSP
NOGUCHI, Hiroshi	ISSP
KITAGAWA, Kentaro	ISSP
SUGINO, Osamu	ISSP
KUBO, Momoji	Tohoku Univ.

HUKUSHIMA, Koji	Univ. of Tokyo
OHGUSHI, Kenya	Tohoku Univ.
NUNOURA, Teppei	Univ. of Tokyo
OTSUKI, Junya	Okayama Univ.
OBA, Fumiyasu	Science Tokyo
KAGI, Hiroyuki	Univ. of Tokyo
MATSUHIRA, Kazuyuki	Kyushu Inst. Tech.

Steering Committee of the SCC-ISSP

KAWASHIMA, Naoki	ISSP (Chairperson)
NOGUCHI, Hiroshi	ISSP
OZAKI, Taisuke	ISSP
SUGINO, Osamu	ISSP
TSUNETSUGU, Hirokazu	ISSP
KATO, Takeo	ISSP
NAKAJIMA, Taro	ISSP
FUKUDA, Masahiro	ISSP
IDO, Kota	ISSP
NAKANO, Hiroyoshi	ISSP
TAKAHASHI, Jun	ISSP
NAKAJIMA, Kengo	Univ. of Tokyo
OTSUKI, Junya	Okayama Univ.
YAMAJI, Youhei	NIMS
KASAMATSU, Shusuke	Yamagata Univ.
HUKUSHIMA, Koji	Univ. of Tokyo
KITAO, Akio	Science Tokyo
HAMADA, Ikutaro	Osaka Univ.
TODO, Synge	Univ. of Tokyo
KUBO, Momoji	Tohoku Univ.
OBA, Fumiyasu	Science Tokyo
WATANABE, Hiroshi	Keio Univ.
YOSHIMI, Kazuyoshi	ISSP
YATA, Hiroyuki	ISSP
FUKUDA, Takaki	ISSP
MOTOYAMA, Yuichi	ISSP

Supercomputer Project Advisory Committee

KAWASHIMA, Naoki	ISSP (Chairperson)
OZAKI, Taisuke	ISSP
NOGUCHI, Hiroshi	ISSP
SUGINO, Osamu	ISSP
TSUNETSUGU, Hirokazu	ISSP
NAKAJIMA, Taro	ISSP

KATO, Takeo	ISSP
FUKUDA, Masahiro	ISSP
IDO, Kota	ISSP
NAKANO, Hiroyoshi	ISSP
TAKAHASHI, Jun	ISSP
NAKAJIMA, Kengo	Univ. of Tokyo
TODO, Synge	Univ. of Tokyo
KUBO, Momoji	Tohoku Univ.
OBA, Fumiyasu	Science Tokyo
WATANABE, Hiroshi	Keio Univ.
HUKUSHIMA, Koji	Univ. of Tokyo
OTSUKI, Junya	Okayama Univ.
KITAO, Akio	Science Tokyo
HAMADA, Ikutaro	Osaka Univ.
KASAMATSU, Shusuke	Yamagata Univ.
YAMAJI, Youhei	NIMS
SHIBATA, Naokazu	Tohoku Univ.
AKAGI, Kazuto	Tohoku Univ.
YANASE, Yoichi	Kyoto Univ.
HATSUGAI, Yasuhiro	Univ. of Tsukuba
OKADA, Susumu	Univ. of Tsukuba
KOBAYASHI, Nobuhiko	Univ. of Tsukuba
HOTTA, Takashi	Tokyo Metropolitan Univ.
MATSUKAWA, Hiroshi	Aoyama Gakuin Univ.
YAMAUCHI, Jun	Keio Univ.
HAGITA, Katsumi	National Defense Academy
KONTANI, Hiroshi	Nagoya Univ.
YUKAWA, Satoshi	Osaka Univ.
SUGA, Seiichiro	Univ. of Hyogo
YASUDA, Chitoshi	Univ. of the Ryukyus
KIM, Kang	Osaka Univ.
MORIKAWA, Yoshitada	Osaka Univ.
KOGA, Akihisa	Science Tokyo
SHIMOJO, Fuyuki	Kumamoto Univ.
TAKETSUGU, Tetsuya	Hokkaido Univ.
TSURUTA, Kenji	Okayama Univ.
HAMAGUCHI, Satoshi	Osaka Univ.
NISHIDATE, Kazume	Iwate Univ.
KAGESHIMA, Hiroyuki	Shimane Univ.
ISHII, Fumiyuki	Kanazawa Univ.
TATETSU, Yasutomi	Meio Univ.
YANAGISAWA, Susumu	Univ. of the Ryukyus
SHUDO, Ken-ichi	Yokohama Natl. Univ.
OHMURA, Satoshi	Hiroshima Inst. Tech.
NOGUCHI, Yoshifumi	Shizuoka Univ.

NAKAMURA, Kazuma	Kyushu Inst. Tech.
GOHDA, Yoshihiro	Science Tokyo
RAEBIGER, Hannes	Yokohama Natl. Univ.
KAWARABAYASHI, Tohru	Toho Univ.
KATO, Yusuke	Univ. of Tokyo
NASU, Joji	Tohoku Univ.
HOTTA, Chisa	Univ. of Tokyo
ISOBE, Masaharu	Nagoya Inst. Tech.
TANAKA, Shu	Keio Univ.
HIGUCHI, Yuji	Kyushu Univ.
KAWAMURA, Mitsuaki	Yokohama National Univ.
TATEYAMA, Yoshitaka	Science Tokyo
KOBAYASHI, Kazuaki	NIMS
TAMURA, Ryo	NIMS
MOTOME, Yukitoshi	Univ. of Tokyo
ONO, Tomoya	Kobe Univ.
TADA, Tomofumi	Kyushu Univ.
HATANO, Naomichi	Univ. of Tokyo
YOSHINO, Hajime	Osaka Univ.
OKUMURA, Hisashi	NINS-ExCELLS
HOSHI, Takeo	NIFS-PQP
TSUNEYUKI, Shinji	Univ. of Tokyo
SUZUKI, Takafumi	Univ. of Hyogo
YOSHIMOTO, Yoshihide	Univ. of Tokyo
TOHYAMA, Takami	Tokyo Univ. of Sci.
ARITA, Ryotaro	Univ. of Tokyo
OGATA, Masao	Univ. of Tokyo
WATANABE, Satoshi	Univ. of Tokyo
YABANA, Kazuhiro	Univ. of Tsukuba
FURUKAWA, Nobuo	Aoyama Gakuin Univ.
KUROKI, Kazuhiko	Osaka Univ.
TANAKA, Yukio	Nagoya Univ.
KUSAKABE, Koichi	Univ. of Hyogo
SAKAI, Toru	Univ. of Hyogo
ISHIBASHI, Shoji	AIST
OTANI, Minoru	Univ. of Tsukuba
TOMITA, Yusuke	Shibaura Inst. Tech.
SHIRAISHI, Kenji	Nagoya Univ.
OGUCHI, Tamio	Osaka Univ.
KAWAKATSU, Toshihiro	Tohoku Univ.
OTSUKI, Tomi	Sophia Univ.
ODA, Tatsuki	Kanazawa Univ.
ARAI, Noriyoshi	Keio Univ.
UNEYAMA, Takashi	Nagoya Univ.
MORITA, Satoshi	Keio Univ.

FUKUSHIMA, Tetsuya	AIST
HAYAMI, Satoru	Hokkaido Univ.
NOMURA, Yusuke	Tohoku Univ.
TSUJI, Yuta	Kyushu Univ.
NOZAWA, Kazuki	Kagoshima Univ.
TEN-NO, Seiichiro	Kobe Univ.
SEINO, Kaori	Kyushu Inst. Tech.
OHNISHI, Masato	ISM
SHINODA, Wataru	Oakayama Univ.

1.4 Staff

The following staff members of the SCC-ISSP usually administrate the ISSP Supercomputer.

KAWASHIMA, Naoki	Professor (Chairperson)
NOGUCHI, Hiroshi	Associate Professor
OZAKI, Taisuke	Professor
SUGINO, Osamu	Professor
IDO, Kota	Research Associate
FUKUDA, Masahiro	Research Associate
NAKANO, Hiroyoshi	Research Associate
TAKAHASHI, Jun	Research Associate
YOSHIMI, Kazuyoshi	Project Researcher
AOYAMA, Tatsumi	Project Researcher
YATA, Hiroyuki	Senior Technical Specialist
FUKUDA, Takaki	Technical Specialist
MOTOYAMA, Yuichi	Technical Specialist
ARAKI, Shigeyuki	Project Academic Specialist

2 STATISTICS (SCHOOL YEAR 2025)

2.1 System and User Statistics

In the following, we present statistics for operation time taken in the period from April 1st 2025 to March 31th 2026 (SY 2025). In Table 2, we show general statistics of the supercomputer system in SY 2025. The total numbers of compute nodes in System B "ohtaka" and System C "kugui" are 1688 and 136, respectively. Consumed disk points amount to about a few percent of the total consumed points in both System B and System C.

In Fig. 2, availabilities, utilization rates, and consumed points in Systems B and C are plotted for each month. Throughout the school year, the availability and the utilization rates were very high: the availability and the utilization rates exceed about 80% and 80% throughout most of the year, respectively. In this SY,

Table 2: Overall statistics of SY 2025

	System B ohtaka	System C kugui
total service time ($\times 10^3$ node·hours)	13134	1168
number of executed jobs	409501	241157
total consumed points ($\times 10^3$ point)	464	29
CPU points ($\times 10^3$ point)	442	28
disk points ($\times 10^3$ point)	22	1
total exec. time ($\times 10^3$ node·hours)	11934	942
availability	88.80%	98.02%
utilization rate	90.80%	80.47%

we stopped the operation of System B for 10 days in August for power saving. This affects the availability of System B in August below 80%, as shown in Fig. 2. Similarly, due to power-saving measures, the compute nodes were shut down for four days each month from November through March. As a result, the utilization rate after November decreased by 15% compared with the period before July. Note that the decline of the availabilities on Sep. is due to a planned power outage at ISSP.

The user statistics are shown in Fig. 3. The horizontal axis shows the rank of the user/group arranged in the descending order of the execution time (hour×nodes). The execution time of the user/group of the first rank is the longest. The vertical axis shows the sum of the execution time up to the rank. From the saturation points of the graphs, the numbers of "active" users of Systems B and C are around 500 and 100, respectively. The maximum ranks in the graphs correspond to the number of the users/groups that submitted at least one job.

2.2 Queue and Job Statistics

Queue structures of Systems B and C in SY 2025 are shown in Tables 3 and 4, respectively. In System B "ohtaka", users can choose from two types of compute nodes; jobs submitted to queues with "cpu" and "fat" at the end of their queue names are submitted to CPU and Fat nodes, respectively. In System C, there are two types of compute nodes: CPU and ACC nodes. Jobs submitted to queues with "cpu" and "acc" at the end of their queue names are submitted to CPU and ACC nodes, respectively, If users submit a job to queues with "accs" at the end of their queue names, the job runs in the ACC node shared by other jobs of "accs" queues. See Sec. 1.1 for a description of each type of compute node. The user then has to choose the queue according to the number of nodes to use and the duration of their calculation jobs. Queue names starting with "F" are for jobs taking 24 hours or less, while those starting with "L" can run much longer up to 120 hours. More nodes are allotted to "F" queues in order to maximize the turnaround time of user

Table 3: Queue structures of System B in SY 2025

System B, ohtaka

queue name	Elapsed time limit (hr)	# of nodes /job	# of nodes /queue	Memory limit (GB)	job points /(node·day)
F1cpu	24	1	600	230/node	1
L1cpu	120	1	300	230/node	1
F4cpu	24	2–4	216	230/node	1
L4cpu	120	2–4	108	230/node	1
F16cpu	24	5–16	288	230/node	1
L16cpu	120	5–16	144	230/node	1
F36cpu	24	17–36	72	230/node	1
L36cpu	120	17–36	36	230/node	1
F72cpu	24	72	576	230/node	1
L72cpu	120	72	288	230/node	1
F144cpu	24	144	432	230/node	1
L144cpu	120	144	144	230/node	1
i8cpu	0.5	1–8	72	230/node	1
F2fat	24	1–2	7	2900/node	4
L2fat	120	1–2	3	2900/node	4
i1fat	0.5	1	1	2900/node	4

jobs. The queue names starting with “i” are used for interactive debugging of user programs and the elapsed time limit is 30 minutes. The number following “F”, “L”, or “i” correspond to the number of nodes that can be used by one user job. Although we do not mention here in detail, to promote utilization of the massively parallel supercomputer, background queues (queue name starting with “B”) for Systems B and C which charge no points for the jobs have also been open.

To prevent overuse of the storage, points are charged also for usage of disk quota in the systems, as shown in Table 5. Disk points are revised often for optimal usage of the resources by examining usage tendencies.

The number of jobs, average waiting time, and total execution time in each queue are shown in Tables 6 and 7. In Systems B and C, a large portion of jobs have been executed in “F” queues. The largest amount of the execution time has been consumed in “F72cpu” and “F1cpu” queues for Systems B and C, respectively. However, substantial number of jobs were run in every queue, suggesting that a wide variety of user needs are met by this queuing scheme. In most of these queues, the queue settings meet the user’s tendencies in that the waiting times are on the order of the elapsed-time limit.

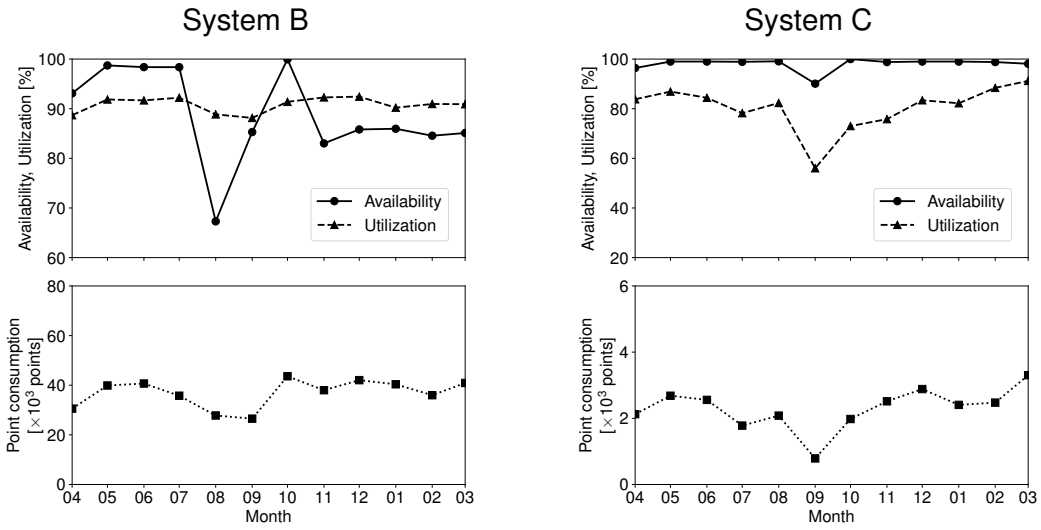


Figure 2: Availabilities, utilization rates and point consumptions of each month during SY 2025.

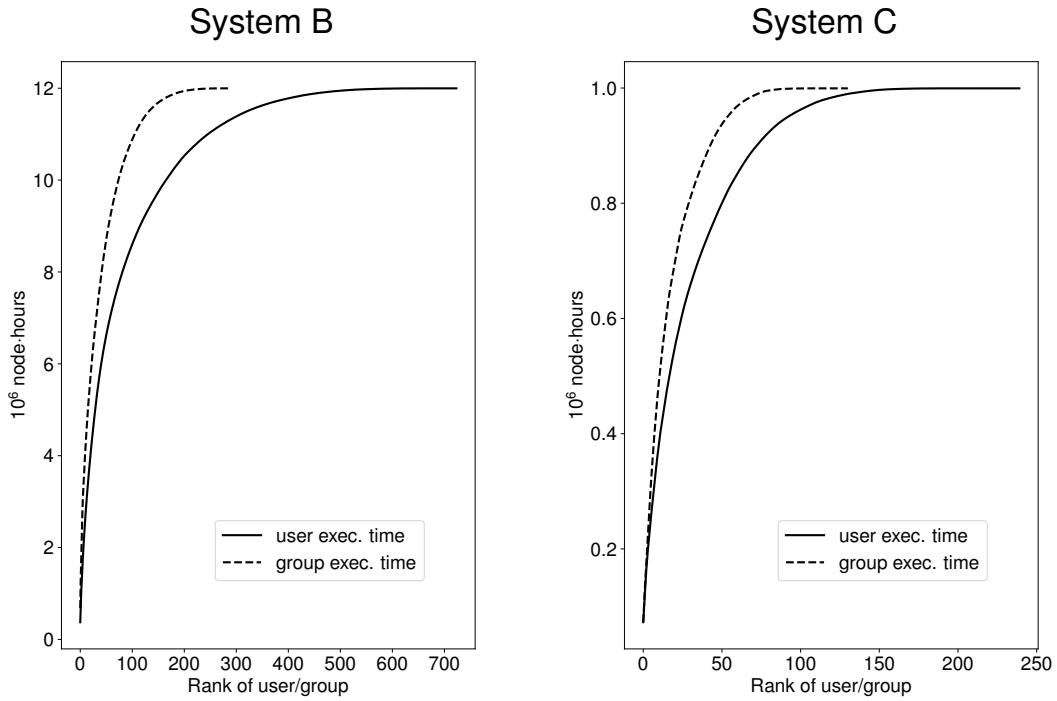


Figure 3: User statistics. The horizontal axis shows the rank of the user/group arranged in the descending order of the execution time (hour×nodes). The vertical axis shows the sum of the execution time up to the rank.

Table 4: Queue structures of System C in SY 2025

System C, kugui

queue name	Elapsed time limit (hr)	# of nodes /job	# of nodes /queue	Memory limit (GB)	job points /(node·day)
i2cpu	0.5	1–2	8	240/node	1
F1cpu	24	1	120	240/node	1
L1cpu	120	1	60	240/node	1
F4cpu	24	2–4	32	240/node	1
L4cpu	120	2–4	16	240/node	1
F16cpu	24	5–16	64	240/node	1
L16cpu	120	5–16	32	240/node	1
F1accs	24	1	3	$60\times N_{\mathrm{GPU}}$	1
L1accs	120	1	1	$60\times N_{\mathrm{GPU}}$	1
i1accs	0.5	1	1	$60\times N_{\mathrm{GPU}}$	1
F2acc	24	1–2	4	240/node	1
L2acc	120	1–2	2	240/node	1

* N_{GPU} in ACC queues denotes the number of occupied GPUs.

Table 5: Disk points of Systems B and C

		point/day
System B ohtaka	`/home`	$0.001 \times \theta(q - 300)$
	`/work`	$0.0001 \times \theta(q - 6000)$
System C kugui	`/home`	$0.001 \times \theta(q - 150)$
	`/work`	$0.0001 \times \theta(q - 1500)$

* q is denoted in unit of GB.
* $\theta(x)$ is equal to the Heaviside step function $H(x)$ multiplied by x, i.e., $xH(x)$.

Table 6: Number of jobs, average waiting time, total execution time, and average number of used nodes per job in each queue of System B.

System B, ohtaka

queue	# of Jobs	Waiting Time (hour)	Exec. Time ($\times 10^3$ node·hour)	# of nodes
F1cpu	83056	22.23	137.05	1.00
L1cpu	4011	76.57	122.86	1.00
F4cpu	94315	30.69	1191.36	2.85
L4cpu	6210	96.59	457.67	3.62
F16cpu	24626	20.34	1495.23	9.57
L16cpu	1324	79.53	594.45	11.49
F36cpu	1246	31.49	327.67	31.11
L36cpu	107	84.53	112.62	31.27
F72cpu	8038	54.94	3252.00	72.00
L72cpu	98	84.83	318.88	72.00
F144cpu	3012	15.39	1907.83	144.00
L144cpu	73	67.29	476.88	144.00
i8cpu	164792	0.19	115.06	4.15
F2fat	4391	138.61	29.22	1.13
L2fat	347	143.14	17.63	1.05
i1fat	2628	0.11	0.41	1.00

Table 7: Number of jobs, average waiting time, total execution time, and average number of used nodes per job in each queue of System C.

System C, kugui

queue	# of Jobs	Waiting Time (hour)	Exec. Time ($\times 10^3$ node·hour)	# of nodes
i2cpu	39624	0.04	2.40	1.15
F1cpu	55486	2.20	188.59	1.00
L1cpu	3225	4.74	70.82	1.00
F4cpu	17549	8.95	95.13	3.59
L4cpu	742	25.01	44.71	3.48
F16cpu	1397	22.02	122.77	11.99
L16cpu	140	7.82	31.05	8.86
i1accs	22534	0.02	4.23	1.00
F1accs	9270	42.48	62.07	1.00
L1accs	933	10.70	10.18	1.00
F2acc	2378	22.47	24.24	1.08
L2acc	229	87.56	5.89	1.07

2.3 Project for Advancement of Software Usability in Materials Science

From School Year 2015, the supercomputer center (SCC) has started "Project for advancement of software usability in materials science". In this project, for enhancing the usability of the supercomputer system in ISSP, we perform some software-advancement activity such as implementing a new function to an existing code, releasing a private code on Web, writing manuals. Target programs are publicly offered in December and selected in the review by the Steering Committee of SCC. The projects are carried out by the software development team composed of three members in ISSP. In SY 2025, two projects were selected as listed in Table 8.

Table 8: List of Project for advancement of software usability in materials science for SY 2025.

Project Proposer	Project Name
Ryo TAMURA NIMS	Bayesian optimization library PHYSBO
Kousuke NAKANO NIMS	Enhancement of ab initio Quantum Monte Carlo Package

2.4 ISSP Data Repository

From School Year 2021, the supercomputer center (SCC) has started to operate ISSP Data Repository (ISSP-DR) for accumulating and utilizing research data in materials science. GitLab is used as the data management system, and a portal site is provided as a data registration and search system for the registered data. By using ISSP-DR, it is possible to store and publish research data used in papers and datasets useful in the field of condensed matter science. Users of ISSP Supercomputer are welcome to apply for and use ISSP-DR.

3 RESEARCH REPORTS

3.1 Invited Articles

First-Principles Calculations on Attosecond Transient Absorption Spectroscopy for Bulk Nickel 15

Shunsuke A. SATO

Many-body wavefunction approach to topological quantum magnets 23

Kota IDO

Ion Distribution near Phase Separated Charged Phospholipid Membranes 32

Yuji HIGUCHI, Hiroaki ITO, Naofumi SHIMOKAWA,
Jurij REŠČIČ, and Klemen BOHINC

First-Principles Calculations on Attosecond Transient Absorption Spectroscopy for Bulk Nickel

Shunsuke A. Sato
Department of Physics, Tohoku University
Sendai 980-8578, Japan

1 Introduction

Light-driven electron dynamics in solids is a central subject in ultrafast condensed-matter physics. Intense and ultrashort optical fields can drive electrons far from equilibrium and modify the optical and magnetic properties of materials on femtosecond and attosecond time scales. Recent progress in attosecond spectroscopy has made it possible to probe such electronic motion directly in the time domain, including light-induced spin dynamics in magnetic materials through attosecond circular dichroism [1]. These developments require microscopic theories that connect the electron dynamics induced by a pump pulse to the transient optical response measured by an attosecond probe.

Attosecond transient absorption spectroscopy (ATAS) is a useful approach for investigating ultrafast electron dynamics in solids because it measures pump-induced changes in the absorption spectrum with attosecond temporal resolution. In magnetic transition metals, the absorption around the $M_{2,3}$ edge is especially informative, since it involves optical transitions from $3p$ semicore states to unoccupied states with substantial $3d$ character. The spectral response in this region is sensitive to the exchange splitting of the semicore states and to the microscopic screening associated with localized $3p$–$3d$ electronic response. Therefore, ATAS with linearly polarized probe pulses can provide a complementary route to magnetic dynamics, although the measured transient spectrum is not a direct magnetic observable.

The interpretation of ATAS spectra in solids is generally difficult because the macroscopic optical response reflects several microscopic processes at the same time. Previous first-principles studies of magnetic transition metals have shown that transient absorption spectra around the $M_{2,3}$ edge contain both magnetic and nonmagnetic electronic contributions [2, 3]. A reduction of the local spin polarization and of the associated exchange splitting of the $3p$ semicore states can produce a narrow absorption decrease near the edge. In contrast, pump-induced charge redistribution and the modification of microscopic screening and local-field effects can generate a broader absorption increase. Thus, even near a magnetic semicore edge, the transient absorption spectrum must be interpreted as a combined response of spin-dependent electronic structure and charge-screening dynamics. While this two-component picture has been examined in finite-electron-temperature calculations for magnetic materials and in explicit nonequilibrium pump–probe simulations for bulk Co, its applicability to laser-driven ferromagnetic Ni in a fully real-time nonequilibrium calculation remains to be clarified.

First-principles real-time time-dependent density functional theory (TDDFT) provides a direct way to address this problem [5]. By solving the time-dependent Kohn–Sham equation in the presence of pump and probe fields, one

can simulate the pump–probe process and evaluate the transient optical response from the induced current [4, 3]. This approach is useful for connecting microscopic electronic motion in a driven solid to experimentally relevant optical quantities such as the transient dielectric function and absorption coefficient. In addition, comparison with finite-electron-temperature calculations provides a reference for quasi-equilibrium hot-electron states and helps distinguish thermalized electronic effects from coherent nonequilibrium dynamics during and shortly after pump irradiation.

In this work, we study ATAS of bulk ferromagnetic Ni using first-principles real-time TDDFT. Ni is a prototypical itinerant ferromagnet with a relatively small magnetic moment and a clear $M_{2,3}$ absorption edge originating from $3p$ semicore states. It therefore provides a useful test case for examining how the magnetic sensitivity of the $M_{2,3}$ edge appears in a nonequilibrium optical response. We first analyze the equilibrium electronic structure and optical response of Ni, then introduce finite-electron-temperature calculations as quasi-equilibrium references, and finally perform explicit pump–probe simulations around the Ni $M_{2,3}$ edge. The aim of the present study is to clarify how the ultrafast electron dynamics of laser-driven ferromagnetic Ni are reflected in the transient absorption spectrum, and to examine to what extent the two-component interpretation established in earlier studies of magnetic transition metals applies to Ni in a real-time nonequilibrium calculation.

2 Methods

2.1 First-principles electron dynamics calculations

We investigate the transient optical response of bulk ferromagnetic Ni using real-time TDDFT for periodic solids. The first-principles electron dynamics method is summarized here; further details are given elsewhere [3, 6]. Unless otherwise stated, atomic units are used. The ions are fixed at their equilibrium positions, which is appropriate for the electronic time scale considered in this work.

In the collinear spin-polarized formulation, the electron dynamics is described by the time-dependent Kohn–Sham equation for the periodic part of the Bloch orbital,

$$i\frac{\partial}{\partial t}u_{bs\boldsymbol{k}}(\boldsymbol{r},t) = \hat{h}_{s\boldsymbol{k}}(t)u_{bs\boldsymbol{k}}(\boldsymbol{r},t), \tag{1}$$

where b is the band index, $s = \uparrow, \downarrow$ is the spin index, and $\boldsymbol{k}$ is the Bloch wave vector. The time-dependent Kohn–Sham Hamiltonian is

$$\begin{aligned}\hat{h}_{s\boldsymbol{k}}(t) &= \frac{1}{2}\left[\boldsymbol{p}+\boldsymbol{k}+\boldsymbol{A}(t)\right]^2 \\ &+ \hat{v}_{\mathrm{ion}} + v_{\mathrm{Hxc},s}[\rho_\uparrow(\boldsymbol{r},t),\rho_\downarrow(\boldsymbol{r},t)]\end{aligned} \tag{2}$$

where $\hat{v}_{\mathrm{ion}}$ is the ionic pseudopotential and $v_{\mathrm{Hxc},s}$ is the spin-dependent Hartree–exchange–correlation potential. Here, $\rho_\uparrow(\boldsymbol{r},t)$ and $\rho_\downarrow(\boldsymbol{r},t)$ are the electron densities for the respective spin channels. The Hartree–exchange–correlation potential is evaluated within the adiabatic approximation, and exchange–correlation contributions to the vector potential are neglected. The applied electromagnetic field is treated in the long-wavelength approximation by a spatially uniform vector potential $\boldsymbol{A}(t)$, and the corresponding electric field is $\boldsymbol{E}(t) = -d\boldsymbol{A}(t)/dt$. Because the present study focuses on the Ni $M_{2,3}$ edge, the Ni $3p$ semicore states are explicitly included in the valence space of the pseudopotential calculation.

The initial orbitals are obtained from the self-consistent spin-polarized Kohn–Sham equation for ferromagnetic Ni. The occupation factors are given by the Fermi–Dirac distribution, $f_{bs\boldsymbol{k}} = \left[\exp\left[(\epsilon_{bs\boldsymbol{k}}-\mu)/(k_{\mathrm{B}}T_e)\right]+1\right]^{-1}$, where $\epsilon_{bs\boldsymbol{k}}$ is the Kohn–Sham eigenvalue, μ is the chemical potential, and T_e is the electron temperature. For the equilibrium and explicit pump–probe calculations, $T_e = 300$ K is used unless otherwise stated. The chemical potential is determined from charge neutrality, and

the occupation factors are kept fixed during the real-time propagation.

Spin–orbit coupling is not included. The spin quantization axis is therefore chosen as the z axis, and the time propagation remains diagonal in the spin index. Consequently, the number of electrons in each spin channel is conserved in the explicit pump–probe dynamics. The magnetic changes discussed below should therefore be understood as changes in the local spin polarization and in the associated spin-dependent electronic structure, rather than as spin-flip demagnetization. The notation $M_{2,3}$ denotes the Ni $3p$ semicore absorption region, without resolving the spin–orbit splitting between the M_2 and M_3 edges.

The macroscopic current density is evaluated as

$$\boldsymbol{J}(t) = -\frac{1}{\Omega_{\mathrm{cell}}} \sum_{b,s} \frac{1}{\Omega_{\mathrm{BZ}}} \int_{\mathrm{BZ}} d\boldsymbol{k}\, f_{bs\boldsymbol{k}} \times \int_{\mathrm{cell}} d\boldsymbol{r}\, u^*_{bs\boldsymbol{k}}(\boldsymbol{r},t) \hat{\boldsymbol{v}}_{s\boldsymbol{k}}(t) u_{bs\boldsymbol{k}}(\boldsymbol{r},t), \quad (3)$$

where Ω_{cell} and Ω_{BZ} are the volumes of the unit cell and Brillouin zone, respectively. The velocity operator is $\hat{\boldsymbol{v}}_{s\boldsymbol{k}}(t) = \left[\boldsymbol{r}, \hat{h}_{s\boldsymbol{k}}(t)\right]/i$.

2.2 Computational details

All calculations are performed with the Octopus code in a real-space, real-time framework [7]. Bulk Ni is modeled by the fcc crystal structure with lattice constant $a = 3.52$ Å. The fcc unit cell is discretized into 28^3 real-space grid points, and the Brillouin zone is sampled with 24^3 k-points. Norm-conserving pseudopotentials are employed, and the Ni $3s$, $3p$, $3d$, and $4s$ electrons are treated explicitly as valence electrons. The exchange–correlation functional is the adiabatic local spin-density approximation [8].

3 Results

3.1 Electronic structure and equilibrium optical response

We first examine the equilibrium electronic structure and optical response of bulk Ni, which serve as references for the transient spectra discussed below. Figure 1 shows the spin-resolved band structure in a wide energy window, with the Fermi level set to zero. The bands near the Fermi level show the metallic character expected for elemental Ni. In addition, nearly dispersionless semicore bands appear around 60 eV below the Fermi level and are assigned to the Ni $3p$ states. Both the valence and semicore states are spin split in the ferromagnetic ground state. The exchange splitting of the Ni $3p$ semicore bands is about 1 eV, which provides an important microscopic energy scale for the $M_{2,3}$-edge response.

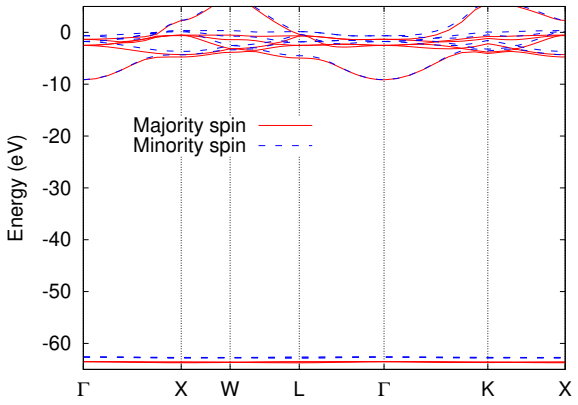


Figure 1: Spin-resolved band structure of ferromagnetic bulk Ni in a wide energy window. The Fermi level is set to 0 eV. Majority- and minority-spin bands are shown separately.

The $M_{2,3}$-edge absorption considered here mainly originates from optical transitions from the $3p$ semicore states to unoccupied states with substantial $3d$ character near the Fermi level. The spectrum is therefore sensitive not only to the spin-dependent positions of the semicore levels but also to the microscopic

screening associated with the localized $3p$–$3d$ electronic response. This point is important for interpreting the transient spectra, because the edge region contains magnetic information through the exchange splitting of the semicore states and nonmagnetic electronic information through charge redistribution and local-field effects.

The equilibrium optical response is obtained from a real-time linear-response calculation. A weak impulsive distortion is applied along a Cartesian direction β through

$$\boldsymbol{A}_{\mathrm{imp}}^{(\beta)}(t) = -k_0 \boldsymbol{e}_\beta \Theta(t), \tag{4}$$

where k_0 is sufficiently small to remain in the linear-response regime, $\boldsymbol{e}_\beta$ is a unit vector along the β direction, and $\Theta(t)$ is the Heaviside step function. From the induced current, the optical conductivity tensor is evaluated as

$$\sigma_{\alpha\beta}(\omega) = \frac{1}{k_0} \int_0^\infty dt\, J_\alpha^{(\beta)}(t) e^{i\omega t - \gamma t}, \tag{5}$$

where γ is a damping parameter introduced to suppress finite-time artifacts. We use $\gamma = 0.5$ eV in the Fourier analysis. The dielectric tensor and absorption coefficient are then obtained as

$$\varepsilon_{\alpha\beta}(\omega) = \delta_{\alpha\beta} + \frac{4\pi i}{\omega} \sigma_{\alpha\beta}(\omega), \tag{6}$$

and

$$\mu_\alpha(\omega) = \frac{2\omega}{c} \mathrm{Im}\left[\sqrt{\varepsilon_{\alpha\alpha}(\omega)}\right]. \tag{7}$$

The equilibrium absorption spectrum in the Ni $M_{2,3}$-edge region is used as the reference for the transient absorption spectra.

Figure 2 (a) shows the current induced by the weak impulsive distortion at $t = 0$. The current is generated immediately after the perturbation and subsequently exhibits dephasing among electronic transitions. In the Fourier analysis, the exponential damping factor further suppresses finite-time artifacts. The dielectric function is obtained from this current according to the procedure described above.

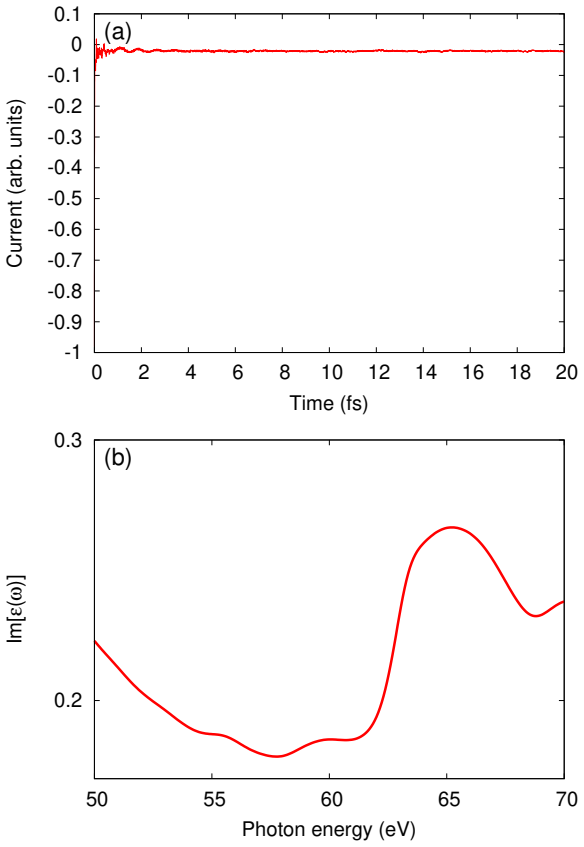


Figure 2: Equilibrium linear response of bulk Ni. (a) Current induced by a weak impulsive perturbation. (b) Imaginary part of the dielectric function around the Ni $M_{2,3}$ edge.

Figure 2 (b) shows the imaginary part of the dielectric function around the Ni $M_{2,3}$ edge. The calculated spectrum exhibits a sharp increase in the absorption-related response near the edge. Because the spectral weight changes rapidly in this energy region, a small pump-induced modification of the edge position or line shape can produce a localized structure in the differential spectrum. The spin splitting of the Ni $3p$ states is therefore expected to affect the transient signal through the edge position. In particular, a reduction of the local exchange splitting can shift the edge-related spectral weight and lead to a narrow absorption decrease in the differential response, as discussed below.

3.2 Finite-electron-temperature reference for the Ni $M_{2,3}$ edge

Before analyzing the explicit pump–probe response, we introduce a finite-T_e linear-response calculation as a quasi-equilibrium reference for a hot-electron state of Ni [9]. This reference is useful for separating spectral changes that can be attributed to electronic redistribution and the self-consistent modification of the electronic structure from those specific to the coherent nonequilibrium dynamics generated by the pump pulse. For a given electron temperature T_e, the occupation factors are replaced by the corresponding Fermi–Dirac distribution, and the static Kohn–Sham potential is recomputed self-consistently under the charge-neutrality condition. The optical response is then evaluated by the same impulsive-distortion procedure as in the equilibrium calculation. Thus, the finite-T_e calculation does not simulate the pump–probe dynamics itself, but provides the optical response of a quasi-equilibrium electronic state with a cold lattice.

The finite-T_e changes in the dielectric function and absorption coefficient are defined relative to the 300 K ferromagnetic state as

$$\Delta\varepsilon_{\alpha\alpha}(\omega;T_e) = \varepsilon_{\alpha\alpha}(\omega;T_e) - \varepsilon_{\alpha\alpha}(\omega;300\ \mathrm{K}), \quad (8)$$

and

$$\Delta\mu_{\alpha}(\omega;T_e) = \mu_{\alpha}(\omega;T_e) - \mu_{\alpha}(\omega;300\ \mathrm{K}). \quad (9)$$

The finite-T_e response includes the effect of state filling through the Fermi–Dirac occupations, the self-consistent change in the spin-dependent Kohn–Sham potential, and the modification of microscopic screening and local-field effects through the time-dependent Hartree–exchange–correlation potential.

Figure 3 shows the change in $\mathrm{Im}[\varepsilon(\omega)]$ for several electron temperatures, measured relative to the 300 K ferromagnetic state. The labels in the figure denote the electron temperature in energy units. The calculated response is not a uniform increase or decrease of the equilibrium spectrum. Instead, positive and negative components appear in the photon-energy region of the Ni $M_{2,3}$ edge, showing that the finite-T_e modification changes both the spectral weight and the line shape near the edge.

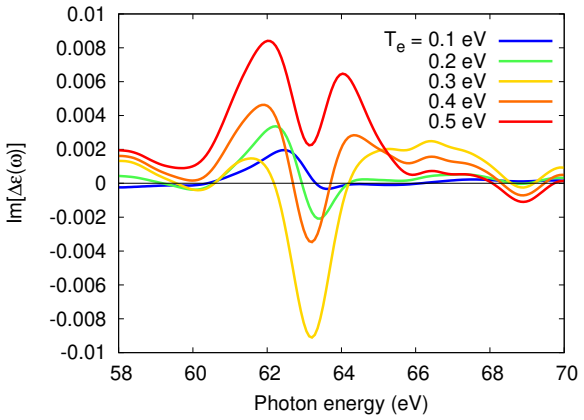


Figure 3: Change in the imaginary part of the dielectric function of Ni obtained from finite-electron-temperature reference calculations. The change is measured relative to the 300 K ferromagnetic state.

The spectral features in Fig. 3 can be understood as the combination of two main contributions [2]. One is a relatively narrow edge-related change associated with the reduction of the local spin polarization and the corresponding exchange splitting of the Ni $3p$ semicore states. The other extends over a broader photon-energy range and is associated with changes in charge redistribution, state filling, and microscopic screening. The localized character and large spatial overlap of the $3p$ and $3d$ states make the response particularly sensitive to local-field effects, as already indicated by the equilibrium optical response.

The finite-electron-temperature analysis therefore provides a useful quasi-equilibrium reference for the electronic state after thermalization. However, it cannot describe coherent subcycle modulations during pump–probe overlap, nor does it represent the nonthermal occupation pattern produced immediately

by the pump pulse. To analyze the optical response in the nonequilibrium phase more directly, we next perform real-time pump–probe TDDFT simulations.

3.3 Attosecond transient absorption

We next evaluate the transient optical response by explicit pump–probe TDDFT simulations [4]. The electron dynamics are calculated in the presence of the pump and probe vector potentials,

$$\boldsymbol{A}(t;\tau) = \boldsymbol{A}_{\mathrm{pump}}(t) + \boldsymbol{A}_{\mathrm{probe}}(t-\tau), \quad (10)$$

where τ is the delay between the centers of the pump and probe pulses. The pump pulse drives the electronic system of Ni out of equilibrium, whereas the probe pulse is kept sufficiently weak so that the probe-induced response can be treated as linear on top of the pump-driven state.

In the present study, the pump pulse is given by

$$\boldsymbol{A}_{\mathrm{pump}}(t) = -\frac{E_{\mathrm{pump}}}{\omega_{\mathrm{pump}}}\boldsymbol{e}_{\mathrm{pump}} \times \cos^2\left(\frac{\pi t}{T_{\mathrm{pump}}}\right)\sin(\omega_{\mathrm{pump}}t) \quad (11)$$

for $|t| < \frac{T_{\mathrm{pump}}}{2}$, and is zero otherwise. The probe pulse is given by

$$\boldsymbol{A}_{\mathrm{probe}}(t-\tau) = -\frac{E_{\mathrm{probe}}}{\omega_{\mathrm{probe}}}\boldsymbol{e}_{\mathrm{probe}} \times \cos^4\left[\frac{\pi(t-\tau)}{T_{\mathrm{probe}}}\right]\sin\left[\omega_{\mathrm{probe}}(t-\tau)\right] \quad (12)$$

for $|t-\tau| < \frac{T_{\mathrm{probe}}}{2}$, and is zero otherwise. The pump parameters are $\hbar\omega_{\mathrm{pump}} = 1.55$ eV, $T_{\mathrm{pump}} = 20$ fs, $E_{\mathrm{pump}} = 2.7$ MV/cm. The pump and probe polarizations are taken to be parallel. The probe duration is $T_{\mathrm{probe}} = 1$ fs, and the central photon energy is chosen so that the probe spectrum covers the Ni $M_{2,3}$-edge region. The probe field strength is sufficiently small compared with the pump field.

For each delay τ, two real-time calculations are performed. The pump-only calculation gives the current $\boldsymbol{J}_{\mathrm{pump}}(t)$, whereas the pump–probe calculation gives the current $\boldsymbol{J}_{\mathrm{pump+probe}}(t;\tau)$. The current induced by the probe pulse in the pump-driven state is then extracted as

$$\Delta\boldsymbol{J}_{\mathrm{probe}}(t;\tau) = \boldsymbol{J}_{\mathrm{pump+probe}}(t;\tau) - \boldsymbol{J}_{\mathrm{pump}}(t). \quad (13)$$

This subtraction removes the nonlinear current generated solely by the pump pulse and isolates the response to the weak probe field. The transient optical conductivity is obtained by comparing the Fourier component of this probe-induced current with that of the probe electric field,

$$\sigma^{\mathrm{tr}}_{\alpha\beta}(\omega,\tau) = \frac{\int dt\, \Delta J_{\mathrm{probe},\alpha}(t;\tau)e^{i\omega t-\gamma t}}{\int dt\, E_{\mathrm{probe},\beta}(t-\tau)e^{i\omega t-\gamma t}}. \quad (14)$$

The same damping parameter as in the equilibrium linear-response calculation is used in the Fourier analysis. The transient dielectric tensor and absorption coefficient are then evaluated as

$$\varepsilon^{\mathrm{tr}}_{\alpha\beta}(\omega,\tau) = \delta_{\alpha\beta} + \frac{4\pi i}{\omega}\sigma^{\mathrm{tr}}_{\alpha\beta}(\omega,\tau), \quad (15)$$

and

$$\mu^{\mathrm{tr}}_{\alpha}(\omega,\tau) = \frac{2\omega}{c}\mathrm{Im}\left[\sqrt{\varepsilon^{\mathrm{tr}}_{\alpha\alpha}(\omega,\tau)}\right]. \quad (16)$$

The theoretical ATAS signal is defined as the differential absorption relative to the equilibrium response, $\Delta\mu_\alpha(\omega,\tau) = \mu^{\mathrm{tr}}_\alpha(\omega,\tau) - \mu_\alpha(\omega)$.

Figure 4 (a) shows the calculated differential absorption $\Delta\mu(\omega,\tau)$ around the Ni $M_{2,3}$ edge, and Fig. 4 (b) shows the pump electric field. During the temporal overlap of the pump and probe pulses, the spectrum exhibits rapidly varying structures. These structures reflect the coherent electron dynamics driven by the pump field and are therefore distinct from the quasi-equilibrium response discussed in the finite-T_{e} calculation.

After the main part of the pump pulse has passed, the spectrum becomes simpler and more persistent. The post-pump response is not described by a rigid shift or by a uniform

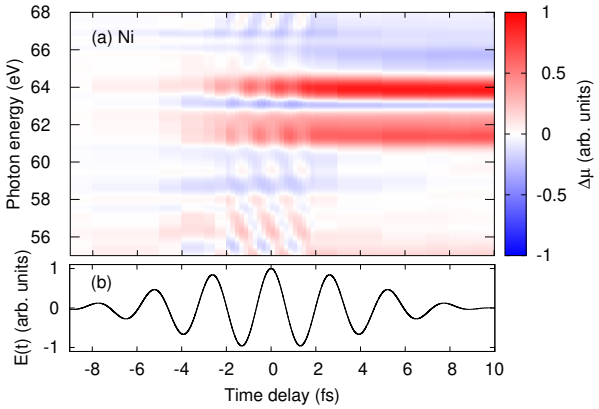


Figure 4: Attosecond transient absorption of bulk Ni from the real-time pump–probe TDDFT simulation. (a) Differential absorption $\Delta\mu(\omega, \tau)$ around the Ni $M_{2,3}$ edge. (b) Pump electric field as a function of delay.

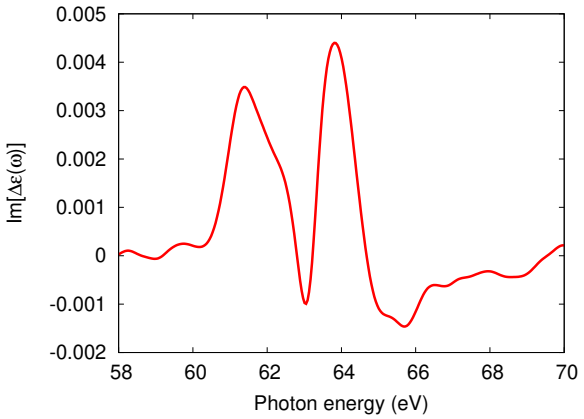


Figure 5: Change in the imaginary part of the dielectric function due to the pump field at the delay of 10 fs. The change is evaluated relative to the equilibrium response.

amplitude change of the equilibrium spectrum. Instead, it contains positive spectral weight over a relatively broad photon-energy range, together with a narrower negative component near the steep edge structure around the Ni $M_{2,3}$ edge. This form already indicates that the transient absorption contains more than one microscopic contribution.

To compare the pump–probe result with the finite-electron-temperature reference more directly, Fig. 5 shows the change in the imaginary part of the dielectric function at the delay of 10 fs. The spectrum contains positive peaks in the lower part of the edge region and negative components near and above the edge. This line shape is qualitatively consistent with the two-component structure found in the finite-electron-temperature calculation in Fig. 3. The detailed profile is different, however, because the explicit pump–probe calculation describes a coherent nonthermal electronic state, not a self-consistent hot-electron distribution.

The narrow negative component around the edge can be interpreted as a consequence of a pump-induced reduction of the local exchange splitting of the Ni $3p$ semicore states. Because the $M_{2,3}$-edge absorption involves transitions from the $3p$ semicore states to unoccupied states with substantial $3d$ character, a change in the $3p$ exchange splitting modifies the effective edge position. This produces an edge-localized decrease in the differential spectrum, similar to the behavior discussed in the finite-electron-temperature reference calculation [2]. Since spin–orbit coupling is not included here, the total number of electrons in each spin channel is conserved during the propagation. Therefore, this effect should not be described as spin-flip demagnetization. Within the present approximation, it reflects changes in the local spin polarization and in the associated spin-dependent electronic structure.

The broader positive contribution has a different origin. Following the interpretation established for transition-metal $M_{2,3}$-edge transient absorption [2, 3], this component is naturally associated with pump-induced changes in microscopic screening and local-field effects. It is linked to the redistribution of electronic charge around the Ni atoms and is not specific to ferromagnetic order. Thus, the Ni $M_{2,3}$-edge ATAS signal should not be interpreted as a direct measure of the magnetization alone. Even near a magnetic semicore

edge, the macroscopic optical response contains both magnetic information and nonmagnetic charge-screening dynamics.

4 Summary

We have investigated attosecond transient absorption spectroscopy of bulk ferromagnetic Ni using first-principles real-time TDDFT. The calculation explicitly treats the Ni $3p$ semicore states and evaluates the transient optical response around the $M_{2,3}$ edge. The purpose of the study was to clarify how the microscopic electron dynamics induced by an ultrashort pump pulse are reflected in the macroscopic absorption spectrum of a magnetic transition metal.

The finite-electron-temperature calculations provided a quasi-equilibrium reference and showed that the change in $\mathrm{Im}[\varepsilon(\omega)]$ near the $M_{2,3}$ edge is not a simple uniform increase or decrease of the equilibrium spectrum. Instead, positive and negative spectral components appear in the edge region, indicating that the transient response contains contributions from both spin-dependent electronic-structure changes and charge-screening dynamics.

The explicit pump–probe TDDFT simulations showed that the calculated differential absorption $\Delta\mu(\omega, \tau)$ exhibits rapidly varying structures during the temporal overlap of the pump and probe pulses, reflecting coherent nonequilibrium electron dynamics. After the main part of the pump pulse has passed, the response becomes more persistent and contains a broad positive contribution together with a narrower negative component near the $M_{2,3}$ edge. The line shape of the corresponding change in $\mathrm{Im}[\varepsilon(\omega)]$ is qualitatively consistent with the two-component structure found in the finite-T_e reference calculation.

The narrow edge-related negative component is attributed to a reduction of the local spin polarization and of the associated exchange splitting of the Ni $3p$ semicore states. In contrast, the broader positive contribution is associated with pump-induced charge redistribution and the modification of microscopic screening and local-field effects. Because spin–orbit coupling is not included in the present calculation, the magnetic change discussed here should be understood as a change in local spin polarization and spin-dependent electronic structure, rather than spin-flip demagnetization. These results show that the Ni $M_{2,3}$-edge ATAS signal encodes both magnetic and nonmagnetic electronic dynamics, and that a direct real-time TDDFT pump–probe simulation provides a useful microscopic basis for interpreting the macroscopic transient optical response of laser-driven ferromagnetic Ni.

References

[1] F. Siegrist *et* al.: Nature **571**, 240 (2019).

[2] S. A. Sato: Electron. Struct. **4**, 014007 (2022).

[3] S. A. Sato, H. Hübener, U. De Giovannini, A. Rubio: npj Computational Materials **11**, 233 (2025).

[4] S. A. Sato, K. Yabana, Y. Shinohara, T. Otobe, G. F. Bertsch Phys. Rev. B **89**, 064304 (2014).

[5] E. Runge, E. K. U. Gross: Phys. Rev. Lett. **52**, 997 (1984).

[6] S. A. Sato: Comput. Mater. Sci. **194**, 110274 (2021).

[7] N. Tancogne-Dejean *et* al.: J. Chem. Phys. **152**, 124119 (2020).

[8] J. P. Perdew, Y. Wang: Phys. Rev. B **45**, 13244 (1992).

[9] S. A. Sato, Y. Shinohara, T. Otobe, K. Yabana: Phys. Rev. B **90**, 174303 (2014).

Many-body wavefunction approach to topological quantum magnets

Kota IDO

Graduate School of Sciences and Technology for Innovation, Yamaguchi University
Tokiwadai, Ube, Yamaguchi 755-8611

I. INTRODUCTION

Strongly correlated quantum materials have long attracted attention as a class of materials that not only are of fundamental scientific interest, exhibiting intriguing phenomena such as high-temperature superconductivity, quantum spin liquids, and topological transport, but also hold potential for applications in advanced technologies [1–17]. To search for novel candidate materials with new functionalities or high performance, it is important to elucidate the microscopic mechanisms underlying these phenomena. This requires accurate methods for analyzing quantum many-body problems. Therefore, the development of high-accuracy methods, and of software implementing such methods, is progressing rapidly worldwide.

The variational Monte Carlo (VMC) method is a numerical method for analyzing such quantum many-body systems [18]. As its name suggests, VMC optimizes a trial wavefunction parameterized by variational parameters based on the variational principle, and then evaluates the expectation values of physical quantities via Monte Carlo sampling using the optimized trial wavefunction. Starting from many-body problems in liquid helium [19, 20], VMC has been applied to a wide range of many-body systems, including quantum lattice models such as the Hubbard model [21–23]. Although VMC has long been used for ground-state analysis, in recent years it has also been extended to nonequilibrium states [24–27], finite-temperature states [28, 29], open quantum systems [30–33], and excitation spectra [34–38], and its scope of application continues to expand.

The enhanced flexibility of VMC has been driven by improvements in computational resources, development and extension of methods and algorithms, and refinement of trial wavefunctions. An example of a VMC trial wavefunction capable of treating strongly correlated quantum materials is the pair-product wavefunction equipped with many-body correlation factors [39–41]. By introducing a large number of variational parameters not only into the many-body correlation factors but also into the pair-product wavefunction, one can represent a variety of quantum states including unconventional superconducting states, quantum spin liquids, magnetic states, and correlated metals. Furthermore, one can systematically improve the accuracy by employing tensor-network or neural-network representations of many-body correlation factors, thereby enabling high-accuracy analyses [42, 43]. Indeed, this type of wavefunction has been applied to strongly correlated quantum materials such as cuprate high-temperature superconductors, iron-based superconductors, and molecular solids, and its usefulness has been demonstrated [44–50].

In this report, we present our recent VMC analyses of quantum many-body systems that exhibit topological states, using the pair-product wavefunction. In Sec. II, we summarize the methods we employed, namely the VMC method and the pair-product wavefunction. Section III presents the VMC results for a frustrated Kondo lattice model [51] and the Kitaev-Kondo model. Finally, we devote Sec. IV to a summary of the results and discuss future prospects related to this topic, including the implementation of developed methods into open source software.

II. METHOD

A. Variational Monte Carlo method

In VMC, the expectation value of an operator $\mathcal{A}$ is evaluated by Monte Carlo sampling using a trial wavefunction $|\psi_{\boldsymbol{\alpha}}\rangle$ parameterized by variational parameters $\boldsymbol{\alpha}$ as follows:

$$\begin{aligned}\langle\mathcal{A}\rangle &= \frac{\langle\psi_{\boldsymbol{\alpha}}|\mathcal{A}|\psi_{\boldsymbol{\alpha}}\rangle}{\langle\psi_{\boldsymbol{\alpha}}|\psi_{\boldsymbol{\alpha}}\rangle} \\ &= \sum_x \rho(x)A(x) \approx \frac{1}{N_{\mathrm{MC}}}\sum_{i=1}^{N_{\mathrm{MC}}} A(x_i), \quad (1)\end{aligned}$$

$$\rho(x) = \frac{|\langle x|\psi_{\boldsymbol{\alpha}}\rangle|^2}{\langle\psi_{\boldsymbol{\alpha}}|\psi_{\boldsymbol{\alpha}}\rangle}, \quad A(x) = \frac{\langle x|\mathcal{A}|\psi_{\boldsymbol{\alpha}}\rangle}{\langle x|\psi_{\boldsymbol{\alpha}}\rangle}. \quad (2)$$

Here, N_{MC} is the number of Monte Carlo samples, and $|x\rangle$ denotes a real-space configuration of electrons or spins. Since $\rho(x)$ satisfies $\sum_x \rho(x) = 1$ and $\rho(x) \geq 0$, it can be regarded as a probability distribution. Provided that the inner product between the trial wavefunction and a real-space configuration is evaluable, real-space samples can be generated according to the probability distribution $\rho(x)$ using a Monte Carlo method such as the Metropolis-Hastings algorithm [52, 53]. Since Monte Carlo sampling can be parallelized over multiple independent Markov chains, it can be performed efficiently on supercomputers.

When the operator $\mathcal{A}$ is a physical observable such as an order parameter or an equal-time correlation function, $\mathcal{A}|x\rangle$ can be expressed as a linear combination of real-space configurations. Thus, $A(x)$ can be computed if the overlap integrals between the trial wavefunction and real-space configurations are evaluable. On the other hand, dynamical correlation functions involve a resolvent operator and thus cannot be expressed straightforwardly in terms of real-space configurations. To compute excitation spectra such as the optical conductivity and dynamical structure factors, one has to utilize methods such as Fourier-transforming a physical quantity obtained by real-time evolution, and evaluating the Lehmann representation on the subspace spanned by trial excited states [34–38].

The variational parameters $\boldsymbol{\alpha}$ can be optimized efficiently by the stochastic reconfiguration (SR) method [54], which is essentially equivalent to the natural gradient method, an optimization method in the field of machine learning [55].

B. Pair-product wavefunction with correlation factors

The pair-product wavefunction with many-body correlation factors is a trial wavefunction that can be flexibly applied to a wide range of quantum many-body systems [39–41]. The form of the wavefunction is defined as

$$|\psi_{\boldsymbol{\alpha}}\rangle = \mathcal{P}\,|\phi\rangle\,. \quad (3)$$

Here, $\mathcal{P}$ denotes a many-body correlation factor, and $|\phi\rangle$ is the pair-product wavefunction represented as

$$|\phi\rangle = \left(\sum_{i,j}\sum_{\sigma_i,\sigma_j} f_{i\sigma_i j\sigma_j} c^\dagger_{i\sigma_i} c^\dagger_{j\sigma_j}\right)^{N/2} |0\rangle\,, \quad (4)$$

where N is the number of fermions, i and j are site indices, σ_i and σ_j are spin indices, and $c^\dagger_{i\sigma_i}$ is the creation operator with spin index σ_i at site i. The pairing amplitude $f_{i\sigma_i j\sigma_j}$ contained in the pair-product wavefunction is treated as a variational parameter. The many-body correlation factor $\mathcal{P}$ is often constructed as a product of several correlation factors. The most conventional one is the Gutzwiller-Jastrow correlation factor [56, 57]:

$$\mathcal{P} = \mathcal{P}_{\mathrm{G}}\mathcal{P}_{\mathrm{J}}, \quad (5)$$

$$\mathcal{P}_{\mathrm{G}} = \exp\left(g\sum_i n_{i\uparrow}n_{i\downarrow}\right), \quad (6)$$

$$\mathcal{P}_{\mathrm{J}} = \exp\left(\frac{1}{2}\sum_{i\neq j} v_{ij}n_i n_j\right). \quad (7)$$

Here, $n_{i\sigma} = c^\dagger_{i\sigma}c_{i\sigma}$, $n_i = n_{i\uparrow} + n_{i\downarrow}$, and g and v_{ij} are variational parameters. Although these

many-body correlation factors contain operators in their exponents, most of them are diagonal with respect to real-space configurations, so their inner products with real-space configurations are easily computed. The inner product between the pair-product wavefunction and a real-space configuration can also be evaluated using the Pfaffian, a standard operation in linear algebra on skew-symmetric matrices, by exploiting the fact that $f_{i\sigma_i j\sigma_j} - f_{j\sigma_j i\sigma_i}$ forms a skew-symmetric matrix as a consequence of the fermion anticommutation relations. The trial wavefunction described above can therefore be handled within the VMC method.

III. APPLICATION TO TOPOLOGICAL MAGNETS

A. Kondo lattice model on the triangular lattice

We first present the VMC study of a magnetic topological state that emerges in the Kondo lattice model on the triangular lattice [51]. The Kondo lattice model is defined as a model in which localized spins and conduction electrons are coupled through the Kondo coupling, as follows:

$$\mathcal{H}_{\text{Kondo}} = -t \sum_{\langle i,j\rangle,\sigma} \left(c^{\dagger}_{i\sigma \text{c}} c_{j\sigma \text{c}} + \text{h.c.} \right) + J \sum_{i} \boldsymbol{S}_{i\text{c}} \cdot \boldsymbol{S}_{i\text{s}}, \tag{8}$$

$$\boldsymbol{S}_{i\lambda} = \frac{1}{2} \sum_{\sigma,\sigma'} c^{\dagger}_{i\sigma\lambda} \boldsymbol{\sigma}_{\sigma\sigma'} c_{i\sigma'\lambda} \tag{9}$$

Here, λ is an index distinguishing the conduction electrons (c) and the localized spins (s), $c^{\dagger}_{i\sigma\lambda}/c_{i\sigma\lambda}$ are the fermion creation/annihilation operators with spin index σ at site i in λ layer, $\boldsymbol{S}_{i\lambda}$ is the spin operator at site i in λ layer, and $\boldsymbol{\sigma}$ denotes the Pauli matrices. The fermion operators $c^{\dagger}_{i\sigma\text{s}}/c_{i\sigma\text{s}}$ representing the localized spins are called Abrikosov fermions [58]. Note that the Hilbert space of the localized spins under the Abrikosov fermion representation is enlarged compared to the original one. The ground state in the physical Hilbert space can be obtained by applying the Gutzwiller projection to exclude unphysical states, i.e., double occupancy and vacancy of the Abrikosov fermions at each site. $\langle i,j\rangle$ denotes a pair of neighboring sites. In addition, t is the hopping amplitude of the conduction electrons, and J is the Kondo coupling [59]. The Kondo coupling in the Kondo lattice model gives rise to the Ruderman-Kittel-Kasuya-Yosida (RKKY) interaction [60–62], a long-range effective magnetic interaction, and to the formation of Kondo singlets between the conduction electrons and the localized spins. The competition between these two effects has been shown to realize various intriguing quantum states, such as nonmagnetic Kondo insulators, magnetic phases accompanied by charge order, and unconventional superconductivity [63–72].

The Kondo lattice model has long been regarded as a representative effective model for heavy-fermion systems [68–72], but in recent years it has also attracted attention as a platform on which topological states such as topological insulators emerge [73–81]. It has been proposed theoretically that topological states are realized when the localized spins form a noncoplanar magnetic structure [73], and it has been pointed out that such states are indeed realized in Kondo lattice models with geometrical frustration, as represented by the triangular lattice [74–77]. However, most of these studies treat the localized spins in the classical limit, and it has been unclear whether such topological states remain stable when the localized spins are treated as quantum spins.

Using the variational Monte Carlo method, we analyze the Kondo lattice model on the triangular lattice at quarter filling up to a system size of $L = 16$, where L is the linear dimension of the system [51]. Preparing various magnetic states as initial states of the trial wavefunction and optimizing them, we find that a state with a noncoplanar triple-Q magnetic structure is

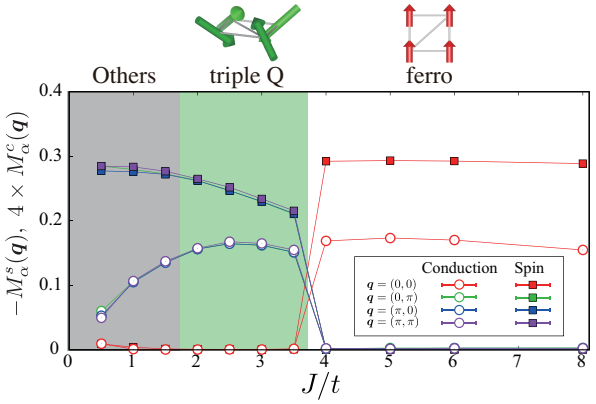


FIG. 1. J dependence of the magnetic order parameters of the localized spins and the conduction electrons for $L = 16$. Open and filled symbols represent the results for the conduction electrons and the localized spins, respectively. Shaded areas are guides to the eye for visualizing regions where the triple-Q state, the ferromagnetic state, and other magnetic states are stabilized. On top of the figure, the ground state in each region is labeled, and the schematic pictures of the spin configurations in the triple-Q state and the ferromagnetic state are also shown. Adapted from Ref. [51] with modifications for the present report.

most stable for $2 \lesssim J/t \lesssim 3.5$, a ferromagnetic state for $3.5 \lesssim J/t$, and other magnetic states for $J/t \lesssim 2$. Figure 1 shows the J dependence of the magnetic order parameters of the localized spins and the conduction electrons. The results for the ferromagnetic state are plotted where it is most stable, and those for the triple-Q state for the other values of J/t. We can see typical behavior in the Kondo lattice model: the formation of conduction-electron spin order due to the RKKY interaction, and the reduction of the localized spin moments due to Kondo screening. We also confirm that the triple-Q state is an insulator from the doping dependence of the chemical potential.

Previous studies in the classical limit have shown that the noncoplanar triple-Q magnetic insulator is a Chern insulator [76, 77], which is a type of topological insulator characterized by a nonzero Chern number. Because the triple-Q state we obtain is represented by the many-body wavefunction defined by Eq. (3), which goes beyond a mean-field treatment, it is desirable to directly compute a many-body topological number to determine whether it is a topological insulator or not. To address this, we extend to the VMC method a numerical approach for computing the many-body Chern number C using the twist operator [82, 83]. In previous studies, it has been pointed out that, by introducing a flux θ_x into the hopping terms along the x direction, the slope, with respect to the flux θ_x, of the argument of the expectation value of the twist operator along the y direction defined below corresponds to the many-body Chern number C:

$$T_y = \exp\left(i\frac{2\pi}{L}\sum_j y_j n_{jc}\right) \tag{10}$$

Here, y_j is the y-coordinate of site j, and n_{jc} is the number operator for the conduction electrons at site j. Although the twist operator is an exponential operator containing the electron-number operator, it is diagonal with respect to real-space configurations and can therefore be measured easily in VMC.

Figure 2 shows the flux dependence of the argument for the triple-Q insulator and for a nonmagnetic Kondo insulator on the square lattice at half filling. For the Kondo insulator, the argument does not change with the flux, indicating that it is topologically trivial. In contrast, for the triple-Q insulator the argument increases linearly with the flux, which indicates that it is indeed a topologically nontrivial many-body Chern insulator with $C = 1$.

B. Kitaev-Kondo model

Next, we present results on the Kitaev-Kondo model, where the Kitaev model on the honeycomb lattice is coupled to a conduction-electron layer via the Kondo coupling [84–87]. The Kitaev model is a system whose ground state is a topological quantum spin liquid, the Kitaev spin liquid, in which Majorana fermions relevant to topological quantum computation

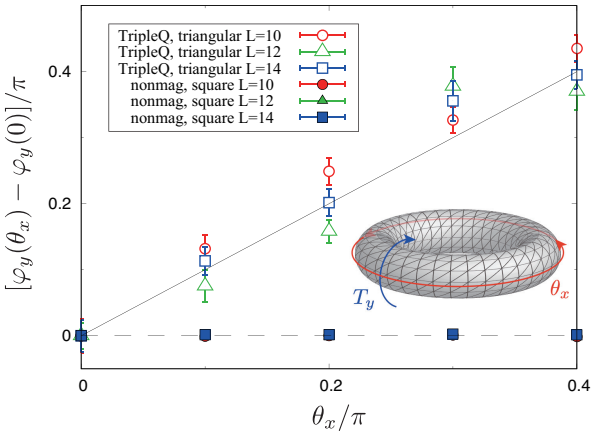


FIG. 2. Flux dependence of the argument of the expectation value of the twist operator. Open and filled symbols represent the results for the triple-Q insulator on the triangular lattice at quarter filling and the Kondo insulator on the square lattice at half filling, respectively. Shapes of the symbols represent different system sizes. Black lines are guides to the eye. Inset shows a schematic picture of the flux insertion θ_x and the twist operator T_y. Adapted from Ref. [51] with modifications for the present report.

emerge [88]. Its Hamiltonian is defined as follows:

$$\mathcal{H}_{\text{Kitaev}} = K \sum_{\gamma=x,y,z} \sum_{\langle i,j\rangle_\gamma} S_i^\gamma S_j^\gamma \qquad (11)$$

Here, S_i^γ is the γ component of the spin operator at site i, and $\langle i,j\rangle_\gamma$ indicates that sites i and j are on a γ bond. K denotes the strength of the Kitaev interaction.

Although the Kitaev model is a many-body problem when viewed in terms of the spin degrees of freedom, it is known to be exactly solvable by expressing the spin degrees of freedom in an alternative representation and exploiting the existence of conserved quantities such as the flux operator, as explained later. For instance, in Kitaev's original paper, a spin with a two-dimensional local Hilbert space is represented by four Majorana fermions [88]. Although the introduction of Majorana fermions enlarges the Hilbert space beyond the original one, it was shown that the true ground state can be expressed as the ground state of the free Majorana fermions with a projection onto the original Hilbert space. The model can also be solved using a representation based on the Jordan-Wigner transformation [89, 90].

In fact, it has been pointed out that the Abrikosov fermion representation introduced in the previous section and the Kitaev Majorana representation can be connected by a simple transformation matrix [91–94]. Using this, one can construct a Gutzwiller-projected wavefunction in the Abrikosov fermion representation corresponding to the exact Kitaev spin liquid state because the Gutzwiller factor used in VMC projects onto the physical Hilbert space.

Building on this, we use VMC to analyze the Kitaev-Kondo model on the honeycomb lattice at half filling, namely the model in which the conduction layer and the Kitaev model as the localized spin layer are coupled through the Kondo coupling,

$$\mathcal{H}_{\text{Kitaev-Kondo}} = \mathcal{H}_{\text{Kondo}} + \mathcal{H}_{\text{Kitaev}}. \qquad (12)$$

To clarify physical properties of the Kitaev-Kondo model, we measure the magnetic order parameter and the site-averaged on-site Kondo-singlet correlation $\langle \boldsymbol{S}_{\text{c}} \cdot \boldsymbol{S}_{\text{s}} \rangle$, which are typical physical quantities characterizing the ground state of the Kondo lattice model. We also compute the expectation value of the flux operator defined on each hexagonal plaquette of the honeycomb lattice, $W_p = \prod_{i\in p} 2S_i^{\gamma_i}$, where the subscripts of S represent the six sites around the hexagonal plaquette and γ_i denotes the bond type of the link at site i that points outside the plaquette p. This is a conserved quantity in the Kitaev model, and $\langle W_p \rangle = 1$ in the Kitaev spin liquid.

We first analyze the honeycomb Kondo lattice model with the Kitaev interaction set to zero, as shown in Fig. 3. As J/t is increased, the magnetic moment of the conduction electrons $|\boldsymbol{S}_{\text{c}}|$ forms while that of the localized spins $|\boldsymbol{S}_{\text{s}}|$ decreases. This behavior is attributed to the magnetically ordered state generated by the RKKY interaction and the

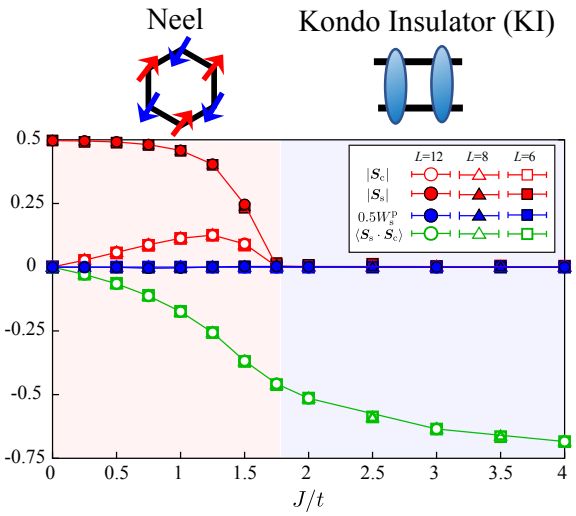


FIG. 3. J dependence of physical quantities for the honeycomb Kondo lattice model. Red open and filled symbols represent the magnetic order parameters of the conduction electrons and the localized spins, respectively. Blue filled symbols represent the expectation values of the flux operator on the localized spin layer. Green open symbols represent the Kondo-singlet correlation. Shapes of the symbols represent different system sizes. Schematic pictures of the Néel state and the Kondo insulator (KI) are shown on top of the figure. Thin lines and shaded areas are guides to the eye.

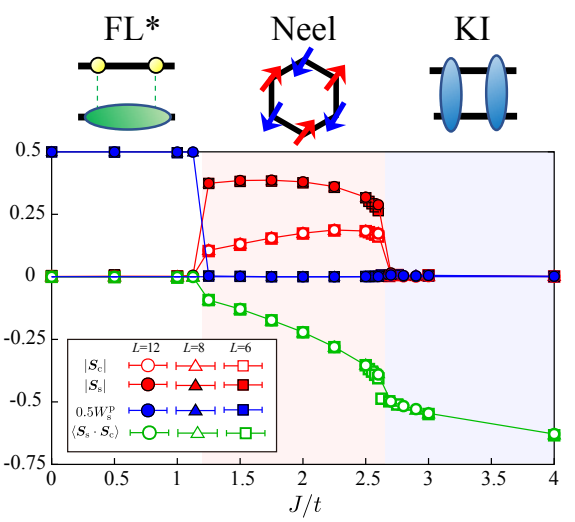


FIG. 4. J dependence of various physical quantities for the Kitaev-Kondo model for $K/t = 4$. Schematic pictures of the fractionalized Fermi liquid (FL*) state, the Néel state, and the Kondo insulator (KI) are shown on top of the figure. Notations are the same as in Fig. 3.

reduction of $|\boldsymbol{S}_{\rm s}|$ due to Kondo screening. Because the RKKY interaction on the honeycomb lattice produces an antiferromagnetic effective spin interaction, the spin configuration is of Néel type [95]. As J/t is increased further, not only the localized-spin order but also the conduction-electron spin order is suppressed, and the system undergoes a continuous transition to a nonmagnetic Kondo insulator around $J/t \sim 1.75$. This is qualitatively consistent with the results of the same model analyzed by the quantum Monte Carlo method [96].

Figure 4 shows the J dependence of various physical quantities at $K/t = 4$. For $J/t < 1.2$, both the magnetic order parameter and the Kondo-singlet correlation are numerically nearly zero, and the expectation value of the flux operator, plotted as the blue filled symbols and characteristic of the Kitaev spin liquid, takes $\langle W_p \rangle = 1$. This result suggests that the conduction layer and the Kitaev layer are decoupled, which is interpreted as a fractionalized Fermi liquid (FL*), as pointed out in previous studies using mean-field theory [84, 85]. As J/t is increased, the Kondo-singlet correlation eventually forms and $\langle W_p \rangle$ drops to nearly zero. For $1.2 < J/t < 2.7$, the magnetic order parameter, plotted as the red open and filled symbols, remains finite. As in the $K/t = 0$ result, the antiferromagnetic state with a Néel pattern is realized, which is naturally interpreted as a result of the RKKY interaction. Increasing J/t further suppresses the spin order through Kondo screening, and the system transitions into a nonmagnetic Kondo insulator. An interesting point is that the transition between the magnetic phase and the Kondo insulator is first-order-like. Since the Kondo lattice model exhibits a continuous transition, this suggests the existence of a quantum tricritical point in the K-J phase diagram.

IV. SUMMARY

In summary, we have presented two analyses of topological magnetic states performed with the variational Monte Carlo method. In the first part, we investigate the stability of the magnetic topological insulator in the Kondo lattice model on the triangular lattice and propose the efficient approach to compute the many-body Chern number in VMC. In the second part, we report the VMC analysis of the ground state in the Kitaev-Kondo model on the honeycomb lattice.

In the study on the magnetic topological insulator, we compute the many-body Chern number from the expectation value of the twist operator, which is well suited to VMC measurements. As in the present case, the twist operator can be applied to the measurement of other topological numbers in addition to the many-body Chern number. For example, in Ref. [97], VMC measurement of the twist operator is used to compute the many-body Zak phase. We have recently implemented the twist operator measurement functionality in mVMC [41, 98], open-source software developed under the Project for advancement of software usability in materials science (PASUMS) [99]. Since the twist operator has also attracted attention as a quantity capable of detecting other topological phase transitions [100–102], such applications of twist operator measurement to topological states are expected to further promote the use of mVMC.

As shown in the second study, VMC can analyze topological quantum spin liquids together with many-body effects of charge degrees of freedom. How topological properties are affected by the inclusion of charge degrees of freedom, and whether new exotic states emerge, are research directions to pursue as future work.

ACKNOWLEDGMENTS

We acknowledge Takahiro Misawa for collaboration on these studies. We also thank the Supercomputer Center, the Institute for Solid State Physics, the University of Tokyo and the Information Technology Center, the University of Tokyo for their facilities. This work was supported by Grant-in-Aid for Scientific Research (Nos. JP16H06345, JP19K03739, JP19K14645, JP23H03818, and JP23K13055) from Ministry of Education, Culture, Sports, Science and Technology, Japan.

[1] M. Imada, A. Fujimori, and Y. Tokura, Rev. Mod. Phys. **70**, 1039 (1998).
[2] B. Keimer, S. A. Kivelson, M. R. Norman, S. Uchida, and J. Zaanen, Nature **518**, 179 (2015).
[3] G. Stewart, Rev. Mod. Phys. **83**, 1589 (2011).
[4] H. Hosono and K. Kuroki, Physica C **514**, 399 (2015).
[5] Q. Si, R. Yu, and E. Abrahams, Nat. Rev. Mater. **1**, 16017 (2016).
[6] Y. Nomura and R. Arita, Rep. Prog. Phys. **85**, 052501 (2022).
[7] P. Puphal, T. Schäfer, B. Keimer, and M. Hepting, Nat. Rev. Phys. **8**, 70 (2026).
[8] S. Paschen and Q. Si, Nat. Rev. Phys. **3**, 9 (2021).
[9] L. Balents, Nature **464**, 199 (2010).
[10] C. Broholm, R. J. Cava, S. Kivelson, D. Nocera, M. Norman, and T. Senthil, Science **367**, eaay0668 (2020).
[11] H. Takagi, T. Takayama, G. Jackeli, G. Khaliullin, and S. E. Nagler, Nat. Rev. Phys. **1**, 264 (2019).
[12] S. Trebst and C. Hickey, Phys. Rep. **950**, 1 (2022).
[13] N. Nagaosa, J. Sinova, S. Onoda, A. H. MacDonald, and N. P. Ong, Rev. Mod. Phys. **82**, 1539 (2010).
[14] M. Z. Hasan and C. L. Kane, Rev. Mod. Phys. **82**, 3045 (2010).
[15] Y. Tokura, K. Yasuda, and A. Tsukazaki, Nat. Rev. Phys. **1**, 126 (2019).

[16] C.-X. Liu, S.-C. Zhang, and X.-L. Qi, Annu. Rev. Condens. Matter Phys. **7**, 301 (2016).
[17] B. A. Bernevig, C. Felser, and H. Beidenkopf, Nature **603**, 41 (2022).
[18] F. Becca and S. Sorella, *Quantum Monte Carlo approaches for correlated systems* (Cambridge University Press, 2017).
[19] W. L. McMillan, Phys. Rev. **138**, A442 (1965).
[20] D. Ceperley, G. V. Chester, and M. H. Kalos, Phys. Rev. B **16**, 3081 (1977).
[21] C. Gros, R. Joynt, and T. M. Rice, Phys. Rev. B **36**, 381 (1987).
[22] H. Yokoyama and H. Shiba, J. Phys. Soc. Jpn. **56**, 1490 (1987).
[23] T. Giamarchi and C. Lhuillier, Phys. Rev. B **43**, 12943 (1991).
[24] G. Carleo, F. Becca, M. Schiró, and M. Fabrizio, Sci. Rep. **2**, 243 (2012).
[25] G. Carleo, F. Becca, L. Sanchez-Palencia, S. Sorella, and M. Fabrizio, Phys. Rev. A **89**, 031602 (2014).
[26] L. Cevolani, G. Carleo, and L. Sanchez-Palencia, Phys. Rev. A **92**, 041603 (2015).
[27] K. Ido, T. Ohgoe, and M. Imada, Phys. Rev. B **92**, 245106 (2015).
[28] K. Takai, K. Ido, T. Misawa, Y. Yamaji, and M. Imada, J. Phys. Soc. Jpn. **85**, 034601 (2016).
[29] Y. Nomura, N. Yoshioka, and F. Nori, Phys. Rev. Lett. **127**, 060601 (2021).
[30] N. Yoshioka and R. Hamazaki, Phys. Rev. B **99**, 214306 (2019).
[31] A. Nagy and V. Savona, Phys. Rev. Lett. **122**, 250501 (2019).
[32] M. J. Hartmann and G. Carleo, Phys. Rev. Lett. **122**, 250502 (2019).
[33] F. Vicentini, A. Biella, N. Regnault, and C. Ciuti, Phys. Rev. Lett. **122**, 250503 (2019).
[34] T. Li and F. Yang, Phys. Rev. B **81**, 214509 (2010).
[35] K. Ido, T. Ohgoe, and M. Imada, Sci. Adv. **3**, e1700718 (2017).
[36] K. Ido, M. Imada, and T. Misawa, Phys. Rev. B **101**, 075124 (2020).
[37] M. Charlebois and M. Imada, Phys. Rev. X **10**, 041023 (2020).
[38] A. Mahajan, P. J. Robinson, J. Lee, and D. R. Reichman, Phys. Rev. B **112**, 184310 (2025).
[39] D. Tahara and M. Imada, J. Phys. Soc. Jpn. **77**, 114701 (2008).
[40] M. Kurita, Y. Yamaji, S. Morita, and M. Imada, Phys. Rev. B **92**, 035122 (2015).
[41] T. Misawa, S. Morita, K. Yoshimi, M. Kawamura, Y. Motoyama, K. Ido, T. Ohgoe, M. Imada, and T. Kato, Comput. Phys. Commun. **235**, 447 (2019).
[42] H.-H. Zhao, K. Ido, S. Morita, and M. Imada, Phys. Rev. B **96**, 085103 (2017).
[43] Y. Nomura, A. S. Darmawan, Y. Yamaji, and M. Imada, Phys. Rev. B **96**, 205152 (2017).
[44] T. Ohgoe, M. Hirayama, T. Misawa, K. Ido, Y. Yamaji, and M. Imada, Phys. Rev. B **101**, 045124 (2020).
[45] M. T. Schmid, J.-B. Morée, R. Kaneko, Y. Yamaji, and M. Imada, Phys. Rev. X **13**, 041036 (2023).
[46] T. Misawa, K. Nakamura, and M. Imada, J. Phys. Soc. Jpn. **80**, 023704 (2011).
[47] T. Misawa, K. Nakamura, and M. Imada, Phys. Rev. Lett. **108**, 177007 (2012).
[48] T. Misawa and M. Imada, Nat. Commun. **5**, 5738 (2014).
[49] K. Ido, K. Yoshimi, T. Misawa, and M. Imada, npj Quantum Mater. **7**, 48 (2022).
[50] K. Yoshimi, T. Misawa, T. Tsumuraya, and H. Seo, Phys. Rev. Lett. **131**, 036401 (2023).
[51] K. Ido and T. Misawa, Phys. Rev. B **109**, 245114 (2024).
[52] N. Metropolis, A. W. Rosenbluth, M. N. Rosenbluth, A. H. Teller, and E. Teller, J. Chem. Phys. **21**, 1087 (1953).
[53] W. K. Hastings, Biometrika **57**, 97 (1970).
[54] S. Sorella, Phys. Rev. B **64**, 024512 (2001).
[55] S.-I. Amari, Neural Comput. **10**, 251 (1998).
[56] M. C. Gutzwiller, Phys. Rev. Lett. **10**, 159 (1963).
[57] R. Jastrow, Phys. Rev. **98**, 1479 (1955).
[58] A. A. Abrikosov, Physics Physique Fizika **2**, 5 (1965).
[59] J. Kondo, Prog. Theor. Phys. **32**, 37 (1964).
[60] M. A. Ruderman and C. Kittel, Phys. Rev. **96**, 99 (1954).
[61] T. Kasuya, Prog. Theor. Phys. **16**, 45 (1956).
[62] K. Yosida, Phys. Rev. **106**, 893 (1957).
[63] S. Doniach, Physica B+C **91**, 231 (1977).
[64] Y. Motome, K. Nakamikawa, Y. Yamaji, and M. Udagawa, Phys. Rev. Lett. **105**, 036403 (2010).

[65] J. Otsuki, H. Kusunose, and Y. Kuramoto, J. Phys. Soc. Jpn. **78**, 034719 (2009).
[66] R. Peters, S. Hoshino, N. Kawakami, J. Otsuki, and Y. Kuramoto, Phys. Rev. B **87**, 165133 (2013).
[67] T. Misawa, J. Yoshitake, and Y. Motome, Phys. Rev. Lett. **110**, 246401 (2013).
[68] H. Tsunetsugu, M. Sigrist, and K. Ueda, Rev. Mod. Phys. **69**, 809 (1997).
[69] G. R. Stewart, Rev. Mod. Phys. **73**, 797 (2001).
[70] H. v. Löhneysen, A. Rosch, M. Vojta, and P. Wölfle, Rev. Mod. Phys. **79**, 1015 (2007).
[71] P. Gegenwart, Q. Si, and F. Steglich, Nat. Phys. **4**, 186 (2008).
[72] Q. Si and F. Steglich, Science **329**, 1161 (2010).
[73] K. Ohgushi, S. Murakami, and N. Nagaosa, Phys. Rev. B **62**, R6065 (2000).
[74] I. Martin and C. D. Batista, Phys. Rev. Lett. **101**, 156402 (2008).
[75] S. Kumar and J. van den Brink, Phys. Rev. Lett. **105**, 216405 (2010).
[76] Y. Akagi and Y. Motome, J. Phys. Soc. Jpn. **79**, 083711 (2010).
[77] Y. Akagi, M. Udagawa, and Y. Motome, Phys. Rev. Lett. **108**, 096401 (2012).
[78] Y. Akagi, M. Udagawa, and Y. Motome, J. Phys. Soc. Jpn. **82**, 123709 (2013).
[79] R. Takagi, J. S. White, S. Hayami, R. Arita, D. Honecker, H. M. Rønnow, Y. Tokura, and S. Seki, Sci. Adv. **4**, eaau3402 (2018).
[80] P. Park, W. Cho, C. Kim, Y. An, Y.-G. Kang, M. Avdeev, R. Sibille, K. Iida, R. Kajimoto, K. H. Lee, *et al.*, Nat. Commun. **14**, 8346 (2023).
[81] H. Takagi, R. Takagi, S. Minami, T. Nomoto, K. Ohishi, M.-T. Suzuki, Y. Yanagi, M. Hirayama, N. Khanh, K. Karube, *et al.*, Nat. Phys. **19**, 961 (2023).
[82] R. Resta, Phys. Rev. Lett. **80**, 1800 (1998).
[83] H. Dehghani, Z.-P. Cian, M. Hafezi, and M. Barkeshli, Phys. Rev. B **103**, 075102 (2021).
[84] U. F. Seifert, T. Meng, and M. Vojta, Phys. Rev. B **97**, 085118 (2018).
[85] W. Choi, P. W. Klein, A. Rosch, and Y. B. Kim, Phys. Rev. B **98**, 155123 (2018).
[86] V. S. de Carvalho, R. M. Teixeira, H. Freire, and E. Miranda, Phys. Rev. B **103**, 174512 (2021).
[87] A. M. Tsvelik and P. Coleman, Phys. Rev. B **106**, 125144 (2022).
[88] A. Kitaev, Annals of Physics **321**, 2 (2006), january Special Issue.
[89] X.-Y. Feng, G.-M. Zhang, and T. Xiang, Phys. Rev. Lett. **98**, 087204 (2007).
[90] H.-D. Chen and Z. Nussinov, J. Phys. A **41**, 075001 (2008).
[91] F. J. Burnell and C. Nayak, Phys. Rev. B **84**, 125125 (2011).
[92] R. Schaffer, S. Bhattacharjee, and Y. B. Kim, Phys. Rev. B **86**, 224417 (2012).
[93] J. Fu, J. Knolle, and N. B. Perkins, Phys. Rev. B **97**, 115142 (2018).
[94] M. Udagawa, J. Phys. Condens. Matter. **33**, 254001 (2021).
[95] M. Sherafati and S. Satpathy, Phys. Rev. B **83**, 165425 (2011).
[96] M. Raczkowski, B. Danu, and F. F. Assaad, Phys. Rev. B **106**, L161115 (2022).
[97] T. Misawa and M. Naka, Phys. Rev. B **108**, L081120 (2023).
[98] https://www.pasums.issp.u-tokyo.ac.jp/mvmc/en/.
[99] https://www.pasums.issp.u-tokyo.ac.jp/en/.
[100] M. Oshikawa, Phys. Rev. Lett. **84**, 3370 (2000).
[101] M. Nakamura and J. Voit, Phys. Rev. B **65**, 153110 (2002).
[102] M. Nakamura and S. Todo, Phys. Rev. Lett. **89**, 077204 (2002).

Ion Distribution near Phase Separated Charged Phospholipid Membranes

Yuji HIGUCHI[1], Hiroaki ITO[2], Naofumi SHIMOKAWA[3], Jurij REŠČIČ[4], and Klemen BOHINC[5]

[1]*Research Institute for Information Technology, Kyushu University, 744 Motooka, Nishi-ku, Fukuoka 819-0395, Japan*

[2]*Department of Physics, Graduate School of Science, Chiba University, Chiba 263-8522, Japan*

[3]*School of Materials Science, Japan Advanced Institute of Science and Technology, Ishikawa 923-1292, Japan*

[4]*Faculty of Chemistry and Chemical Technology, University of Ljubljana, Večna pot 113, Ljubljana, Slovenia*

[5]*Faculty of Health Sciences, University of Ljubljana, Zdravstvena 5, SI-1000 Ljubljana, Slovenia*

1. Introduction

Phospholipids, the main components of cell membranes, spontaneously form bilayer structures in aqueous solution. Phospholipid bilayers as a model for biological membranes have been studied to elucidate their structures and physical properties. In multicomponent lipid bilayers, heterogeneous lipid distributions and phase separation arise depending on the lipid composition and temperature [1]. This membrane heterogeneity has attracted broad interest because it resembles lipid raft domains observed in biological membranes [2], which are thought to play pivotal roles in intracellular signal transduction and membrane trafficking.

Charged lipids are abundant in biological membranes [3] and participate in a wide range of biological functions, including protein adsorption [4] and ion channel activity [5]. Experimental investigations of phospholipid membranes containing charged lipids have demonstrated that long-range electrostatic interactions influence phase separation behavior [6, 7, 8, 9, 10]. For example, Shimokawa et al. used fluorescence microscopy to show that the phase diagram of charged–neutral lipid mixtures shifts with salt concentration [9]. Himeno et al. observed large-scale deformation of charged lipid liposomes accompanying phase separation [10]. Collectively, these experimental studies establish that the ionic environment in solution plays a critical role in phase separation involving charged lipids. However, the spatial distribution of ions near the heterogeneous membrane is difficult to observe experimentally, and the molecular-scale picture of ion distributions remains incompletely understood.

Molecular simulation is a powerful tool for resolving membrane structure and dynamics at the molecular level [11]. All-atom molecular dynamics (MD) simulations have shed light on how headgroup charges influence hydration states and membrane physicochemical properties [12, 13]. However, all-atom simulations long enough to capture phase separation are computationally prohibitive. Coarse-

grained MD simulations can instead target longer-timescale, larger-scale phenomena such as phase separation [14] and bilayer deformation [15]. Using a coarse-grained model with a Debye–Hückel electrostatic potential, our group has previously elucidated characteristic deformation processes of phospholipid membranes driven by long-range electrostatic interactions [10, 16, 17, 18]. However, in our own earlier coarse-grained simulations using a Debye–Hückel potential, ions were not treated explicitly, making it difficult to directly observe the relationship between ion distributions and phase separation at the molecular scale. The MARTINI model [19] explicitly includes coarse-grained ions, lipid molecules, and water molecules, enabling simultaneous treatment of charged membranes and ions. Previous MARTINI studies have revealed the Ca^{2+}-mediated fusion of charged lipid membranes [20] and elucidated phase separation dynamics and lipid molecular orientation at the molecular level [21, 22]. Nevertheless, the correlation between lipid phase separation and ion distributions in the surrounding aqueous solution has remained unresolved.

The ion distribution perpendicular to charged lipid membranes is classically described by Poisson–Boltzmann (PB) theory [23], which has also been applied to phase-separated membranes [9]. By contrast, the lateral ion distribution parallel to the membrane—particularly near the boundary between charged and uncharged lipid domains—has been a difficult problem to elucidate. Clarifying the spatiotemporal correlation between lipid phase separation and ion distributions at the molecular scale therefore represents the central challenge addressed in this report.

Here we summarize two studies that take up this challenge. The first one employed coarse-grained MD simulations with the MARTINI model to investigate the spatiotemporal correlation between phase separation and ion distributions in charged phospholipid bilayers [24]. The second one extended this work to a larger system and compared the results with Monte Carlo (MC) simulations and modified PB theory to quantitatively characterize how ion distributions change near the phase-separation interface [25].

2. Models and Methods

Coarse-grained MD simulations were performed using the MARTINI model (version 2.0) [19], which explicitly incorporates ions, lipid molecules, and water molecules and is well suited to simulating long-timescale, large-scale phenomena such as phase separation. A polarizable water model (version 2.2) [26] was adopted for the solvent. The lipid components were the zwitterionic saturated phospholipid DPPC (dipalmitoylphosphocholine), the negatively charged monounsaturated phospholipid DOPG (dioleoylphosphoglycerol), and the negatively charged, tetraunsaturated phospholipid DAPG (diarachidonoylphosphoglycerol). NaCl was chosen as a representative monovalent salt, and simulations were carried out at several salt concentrations.

In Section 3, each lipid bilayer system consisted of 2,048 lipid molecules. In Section 4, the system size was expanded approximately fivefold relative to the earlier work—to 3,500 DPPC, 3,500 DAPG, and 3,000 cholesterol molecules—to obtain a sharper phase-separation interface and improved statistical precision. This inclusion of 30% cholesterol was motivated by findings from prior MARTINI MD studies [21].

Initial structures were built with CHARMM-GUI [27]. MD calculations were performed using GROMACS [28] under isothermal–isobaric (NpT) conditions at 303 K and 1 bar.

The degree of phase separation was quantified by the local order parameter ϕ_i, defined as the fraction of neighboring lipids of the same

species around each lipid molecule. Ion distributions in the aqueous phase near the membrane were analyzed both perpendicular and parallel to the bilayer plane.

3. Correlation between Phase Separation and Ion Distribution

Coarse-grained MD simulations with the MARTINI model revealed the spatiotemporal correlation between phase separation dynamics and ion distributions in charged phospholipid bilayers [24]. In a DPPC:DAPG = 1:1 mixture at 100 mM NaCl, phase separation began within 0.1 µs, and DPPC-rich and DAPG-rich domains became fully segregated after approximately 1.0 µs. Figure 1 shows a representative snapshot at 2.0 µs with a NaCl concentration of 100 mM (left) and the corresponding cation density map just above the membrane surface (right). The cation concentration is elevated above the negatively charged lipid regions, demonstrating a clear spatial correlation between charged lipid distribution and cation localization.

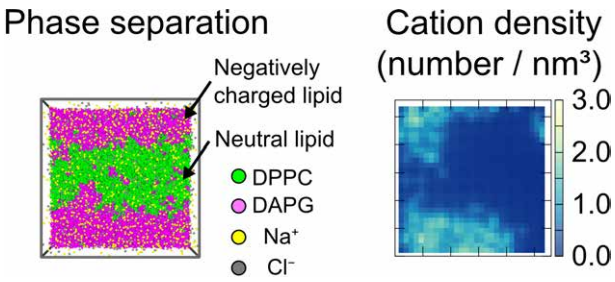


Figure 1: Phase separation and cation distribution in the charged–neutral lipid mixture at 2.0 µs with a NaCl concentration of 100 mM. Left: top-view snapshot of the membrane. Right: cation density (number/nm^3) near the membrane surface.

Two-dimensional mapping of phase separation and ion distribution showed that the Na^+ density profile closely tracked the DAPG distribution throughout the phase separation process. A clear correlation persisted up to 0.5 nm above the surface. Beyond 0.5–1.0 nm, the correlation decayed rapidly. Quantitative analysis using the time correlation function confirmed that cations follow the motion of negatively charged lipids on a microsecond timescale. Analysis of the perpendicular ion distribution further showed that the peak Na^+ concentration above DAPG increased with the local phase-separation order parameter ϕ_i, i.e., with the local area fraction of charged lipids.

This behavior can be understood from the large difference in diffusivity: lipid molecules diffuse on the membrane with a coefficient of approximately 10^0 µm^2/s [29], roughly three orders of magnitude slower than ions in aqueous solution ($\sim 10^3$ µm^2/s). Since the collective diffusion of phase-separated domains is even slower, ions can equilibrate their distribution on the timescale of phase separation. This rapid ionic redistribution screens the electrostatic repulsion between charged lipids and is expected to facilitate domain formation. Analysis of the Coulomb energy as a function of time further supported this picture: the energy decreased more substantially in the phase-separated DPPC:DAPG = 1:1 system than in the DPPC:DOPG = 1:1 system without phase separation, indicating that the screening of negatively charged headgroups by Na^+ is particularly pronounced when phase separation occurs.

Comparison of the simulation results of the ion distribution just above the charged lipids with classical PB theory [23] revealed that the classical theory significantly overestimates the cation concentration near the membrane surface. This discrepancy arises because classical PB theory treats ions as point charges, thereby neglecting the steric repulsion between ions crowded near the membrane surface. Applying a modified PB theory that incorporates the finite ion size through a lattice model [30, 31] showed that accounting for the hydrated sodium ion diameter ($\sim$0.6 nm) brought

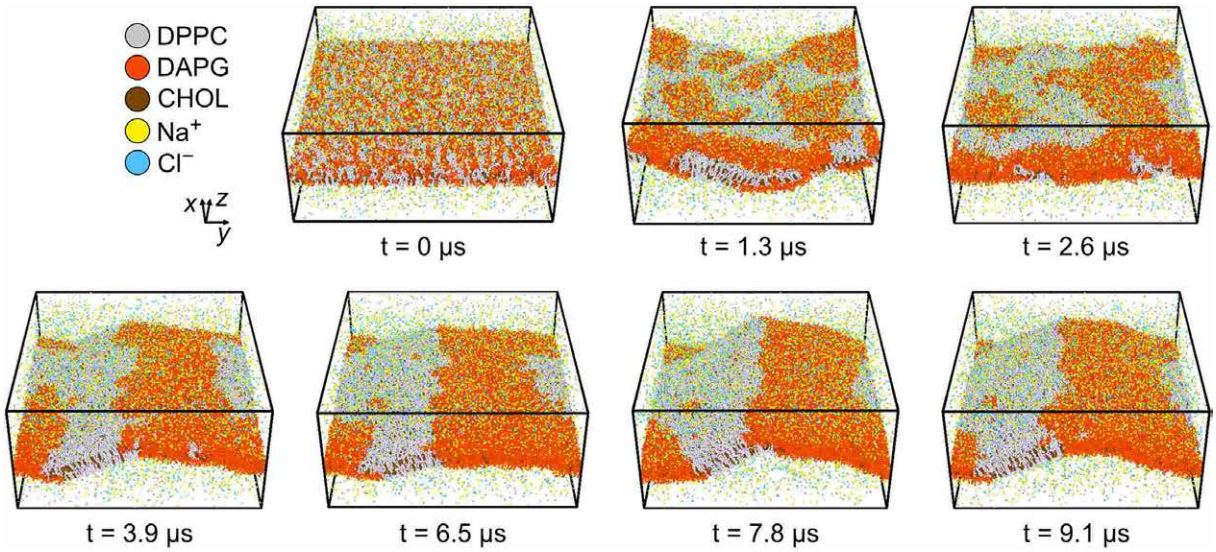


Figure 2: Time evolution of the phase separation process in a lipid bilayer membrane composed of 3,500 DPPC, 3,500 DAPG, and 3,000 cholesterol molecules at a NaCl concentration of 100 mM, obtained from coarse-grained MD simulations using the MARTINI model. Each panel shows a snapshot at the indicated simulation time. Reprinted from Higuchi Y., Ito H., Shimokawa N., Reščič J., Maset S., Bohinc K., *J. Mol. Liq.*, **444**, 129168 (2026), `https://doi.org/10.1016/j.molliq.2025.129168`, under CC BY 4.0.

the theoretical predictions into quantitative agreement with the simulation results. This ion size was independently supported by analysis of the radial distribution function of water molecules around Na^+ obtained from all-atom MD simulations based on the third-order density functional tight-binding (DFTB3) method [32]: the first hydration shell has a radius of 0.29 nm (diameter 0.58 nm), consistent with the value used in the modified PB model.

4. Ion Distribution near the Phase-Separation Interface

Although the previous study [24] characterized the ion distribution on the membrane surface, the ion distribution at the phase-separation interface was not resolved. The relatively small system size caused the lipid distribution at the interface to be blurred. To overcome this limitation, we performed larger-scale coarse-grained MD simulations [25]. The system was expanded approximately fivefold to ∼10,000 molecules (3,500 DPPC, 3,500 DAPG, and 3,000 cholesterol), and 30% cholesterol was included to produce a sharper, well-defined phase-separation interface. Figure 2 shows simulation snapshots during the phase separation. Starting from a homogeneously mixed initial configuration, small domains formed by 1.3 μs, grew progressively from 2.6 to 7.8 μs, and eventually produced two separated phases within the simulation cell. The system reached a steady state between 7.8 and 9.1 μs, and the results from this period were used for analysis.

The concentration profiles of DAPG and Na^+ across the phase-separation interface were fitted with sigmoid functions (Figure 3). The correlation coefficient between the sigmoid center positions of Na^+ and DAPG was 0.973, providing quantitative evidence for the strong colocalization of cations with the charged lipid domain. A positive correlation was also observed for the sigmoid width parameter, which characterizes the thickness of the transition

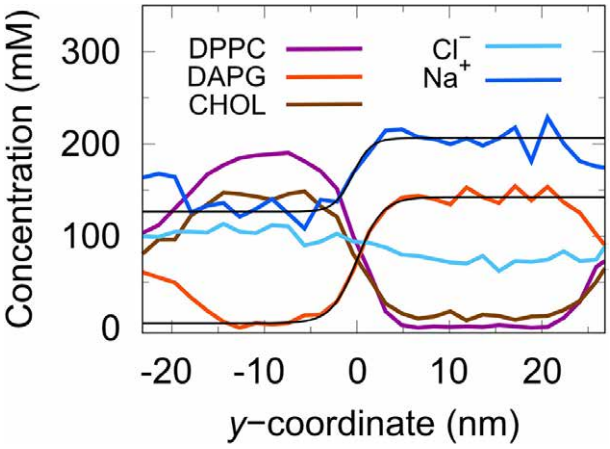


Figure 3: Lateral concentration profiles of DPPC, DAPG, cholesterol, Na^+, and Cl^- as a function of the y-coordinate at 9.1 µs, obtained by averaging over the x- and z-directions. The sigmoid fits to the DAPG and Na^+ profiles are shown as black lines. Reprinted from Higuchi Y., Ito H., Shimokawa N., Reščič J., Maset S., Bohinc K., *J. Mol. Liq.*, **444**, 129168 (2026), `https://doi.org/10.1016/j.molliq.2025.129168`, under CC BY 4.0.

zone across the interface. The width of the Na^+ concentration change tended to be narrower than that of the DAPG lipids, suggesting that fluctuations of the lipid distribution at the interface are larger than those of the ion distribution. Analysis of the perpendicular concentration profiles further showed that Na^+ concentration is high near the surface of the DAPG domain and converges to the bulk value within approximately 2 nm of the membrane.

As a more idealized model, the ion distribution at a planar surface that is half charged and half neutral was also investigated using MC simulations and modified PB theory. Both approaches yielded a continuous, sigmoid-shaped transition in counterion concentration from the uncharged to the charged region. This sigmoid-shaped transition is consistent with the MD results. Interestingly, the ion distribution can be well represented by a sigmoid function, even though the boundary between the charged and neutral surfaces is ideally sharp and discontinuous. The mean counterion concentration near the charged domain was approximately 150 mM in the MC simulations and 200 mM in the MD simulations, showing reasonable overall agreement.

Regarding the width of the ion concentration transition at the interface, the MC simulations predict a sharper change than the MD simulations. This is because the interface in the MC model is defined by discrete, fixed charges and has no positional fluctuation, whereas the phase-separation interface in the MD simulations undergoes continuous thermal motion, which broadens the effective width of the ion distribution. On the other hand, MD simulations indicated that, at domain boundaries, the distribution width for Na^+ ions tends to be narrower than that for DAPG lipids, and the reason remains an unresolved challenge.

The decay length of the perpendicular ion distribution (∼2 nm) agreed well between the MD simulations and the theoretical calculations, validating the theoretical model. Together, these results demonstrate the overall consistency of the three approaches and establish a quantitative foundation for understanding the electric double-layer structure at phase-separation interfaces in charged lipid membranes.

5. Summary and Outlook

We have summarized a series of studies on the correlation between phase separation and ion distributions in charged phospholipid bilayers. Coarse-grained MD simulations demonstrated that cations follow the dynamics of charged lipids on a microsecond timescale during phase separation, and that incorporating ion-size effects through modified PB theory is essential for a quantitative understanding of the ion distribution [24]. Analysis of a larger system and comparison with MC simulations and theory

showed that the lateral change in ion concentration near the phase-separation interface can be described by a sigmoid function, and quantified the correlation between charged lipid and cation distributions [25]. These findings substantially advance the molecular-level understanding of the interplay between charged lipid membranes and electrolyte solutions.

Beyond ion distributions, the behavior of water molecules near the membrane is also an important subject. Recent studies have begun to reveal that the charge state of phospholipid membranes significantly affects water dynamics near the interface [13, 33, 34]. Specifically, neutron scattering experiments and all-atom MD simulations have shown that the orientational order of water molecules and the hydration structure at the membrane interface are strongly sensitive to lipid charge [33, 34]. Since water–lipid interactions influence everything from membrane hydration to the stability of supramolecular assemblies, an integrated understanding of ionic environments and water dynamics represents an important future challenge.

Acknowledgments

This research was supported by JSPS and MESS Japan-Slovenia Research Cooperative Program Grant Numbers JPJSBP120215001 and JPJSBP120265002, and by JSPS KAKENHI Grant Numbers JP21K13891 and JP24K06972 (H.I.) and JP19H05718 and JP25K07244 (Y.H.). The authors thank the Supercomputer Center at the Institute for Solid State Physics, the University of Tokyo, for the use of their facilities. The computation was partly carried out using the computer facilities at the Research Institute for Information Technology, Kyushu University, Japan.

References

[1] S. L. Veatch, S. L. Keller: *Phys. Rev. Lett.* **89**, 268101 (2002).

[2] K. Simons, J. L. Sampaio: *Cold Spring Harbor Perspect. Biol.* **3**, a004697 (2011).

[3] T. Yeung, G. E. Gilbert, J. Shi, J. Silvius, A. Kapus, S. Grinstein: *Science* **319**, 210 (2008).

[4] N. Ben-Tal, B. Honig, C. Miller, S. McLaughlin: *Biophys. J.* **73**, 1717 (1997).

[5] B. Hille, E. J. Dickson, M. Kruse, O. Vivas, B.-C. Suh: *Biochim. Biophys. Acta, Mol. Cell Biol. Lipids* **1851**, 844 (2015).

[6] C. C. Vequi-Suplicy, K. A. Riske, R. L. Knorr, R. Dimova: *Biochim. Biophys. Acta, Biomembr.* **1798**, 1338 (2010).

[7] S. Pataraia, Y. Liu, R. Lipowsky, R. Dimova: *Biochim. Biophys. Acta, Biomembr.* **1838**, 2036 (2014).

[8] B. Kubsch, T. Robinson, R. Lipowsky, R. Dimova: *Biophys. J.* **110**, 2581 (2016).

[9] N. Shimokawa, M. Hishida, H. Seto, K. Yoshikawa: *Chem. Phys. Lett.* **496**, 59 (2010).

[10] H. Himeno, H. Ito, Y. Higuchi, T. Hamada, N. Shimokawa, M. Takagi: *Phys. Rev. E* **92**, 062713 (2015).

[11] S. J. Marrink, V. Corradi, P. C. Souza, H. I. Ingólfsson, D. P. Tieleman, M. S. Sansom: *Chem. Rev.* **119**, 6184 (2019).

[12] T. Ishiyama, D. Terada, A. Morita: *J. Phys. Chem. Lett.* **7**, 216 (2016).

[13] Y. Higuchi, Y. Asano, T. Kuwahara, M. Hishida: *Langmuir* **37**, 5329 (2021).

[14] I. R. Cooke, K. Kremer, M. Deserno: *Phys. Rev. E* **72**, 011506 (2005).

[15] H. Noguchi: *J. Phys. Soc. Jpn.* **78**, 041007 (2009).

[16] H. Ito, Y. Higuchi, N. Shimokawa: *Phys. Rev. E* **94**, 042611 (2016).

[17] J. Guo, H. Ito, Y. Higuchi, K. Bohinc, N. Shimokawa, M. Takagi: *Langmuir* **37**, 9683 (2021).

[18] N. Shimokawa, H. Ito, Y. Higuchi: *Phys. Rev. E* **100**, 012407 (2019).

[19] S. J. Marrink, H. J. Risselada, S. Yefimov, D. P. Tieleman, A. H. de Vries: *J. Phys. Chem. B* **111**, 7812 (2007).

[20] M. Pannuzzo, D. H. De Jong, A. Raudino, S. J. Marrink: *J. Chem. Phys.* **140**, 124905 (2014).

[21] G. A. Pantelopulos, J. E. Straub: *Biophys. J.* **115**, 2167 (2018).

[22] S. Thallmair, H. I. Ingólfsson, S. J. Marrink: *J. Phys. Chem. Lett.* **9**, 5527 (2018).

[23] J. Israelachvili: *Intermolecular and Surface Forces*, Academic Press (2011).

[24] Y. Higuchi, K. Bohinc, J. Reščič, N. Shimokawa, H. Ito: *Soft Matter* **19**, 3640 (2023).

[25] Y. Higuchi, H. Ito, N. Shimokawa, J. Reščič, S. Maset, K. Bohinc: *J. Mol. Liq.* **444**, 129168 (2026).

[26] S. O. Yesylevskyy, L. V. Schäfer, D. Sengupta, S. J. Marrink: *PLoS Comput. Biol.* **6**, 1 (2010).

[27] S. Jo, T. Kim, V. G. Iyer, W. Im: *J. Comput. Chem.* **29**, 1859 (2008).

[28] M. J. Abraham, T. Murtola, R. Schulz, S. Páll, J. C. Smith, B. Hess, E. Lindahl: *SoftwareX* **1–2**, 19 (2015).

[29] R. Machán, M. Hof: *Biochim. Biophys. Acta, Biomembr.* **1798**, 1377 (2010).

[30] I. Borukhov, D. Andelman, H. Orland: *Electrochim. Acta* **46**, 221 (2000).

[31] K. Bohinc, V. Kralj-Iglič, A. Iglič: *Electrochim. Acta* **46**, 3033 (2001).

[32] B. Hourahine et al.: *J. Chem. Phys.* **152**, 124101 (2020).

[33] Md. K. Rahman, T. Yamada, N. L. Yamada, M. Hishida, Y. Higuchi, H. Seto: *Struct. Dyn.* **10**, 044701 (2023).

[34] Md. K. Rahman, T. Yamada, N. L. Yamada, Y. Higuchi, H. Seto: *J. Phys. Chem. B* **129**, 3998 (2025).

3.2 First-Principles Calculation of Material Properties

Construction of anharmonic phonon property database using first-principles calculations

Masato OHNISHI

Institute of Statistical Mathematics,

Research Organization of Information and Systems, Tachikawa, Tokyo 190-8562

Introduction

Phonons, arising from collective atomic vibrations, play a key role in thermal transport and influence electronic, optical, and magnetic properties. While materials informatics (MI) has accelerated materials discovery, existing databases mainly focus on electronic properties, and datasets for anharmonic phonon properties remain limited.

First-principles calculations of these properties are computationally demanding due to large supercells and extensive force evaluations, making supercomputing resources essential. In this study, we construct a first-principles database of anharmonic phonon properties and develop machine learning models for thermal property prediction (Fig. 1) [1].

Methods

We developed an automated workflow (auto-kappa: https://github.com/phonix-db/auto-kappa) integrating first-principles calculations with VASP and phonon analysis with ALAMODE. It includes structural optimization, evaluation of harmonic and anharmonic force constants, and calculation of lattice thermal conductivity by solving the phonon Boltzmann transport equation.

The workflow enables high-throughput calculations and automatically handles unstable structures through additional optimization or larger supercells. Graph neural network (GNN)-based models were also developed for thermal property prediction.

High-throughput calculations were performed using the bulk job scheme on system B (Ohtaka), enabling massively parallel execution across many materials and improving efficiency. System C (Kugui) was used for machine learning tasks, including model training and large-scale screening.

Results and Discussion

Using supercomputing resources, we calculated anharmonic phonon properties for over 6,800 materials and constructed the Phonix database (https://phonix-db.org). The dataset provides comprehensive phonon transport information, including thermal conductivity and lifetimes.

Machine learning models trained on this dataset achieved high accuracy and revealed a scaling law, where prediction improves with increasing training data size. The models were further applied to screen approximately 380,000

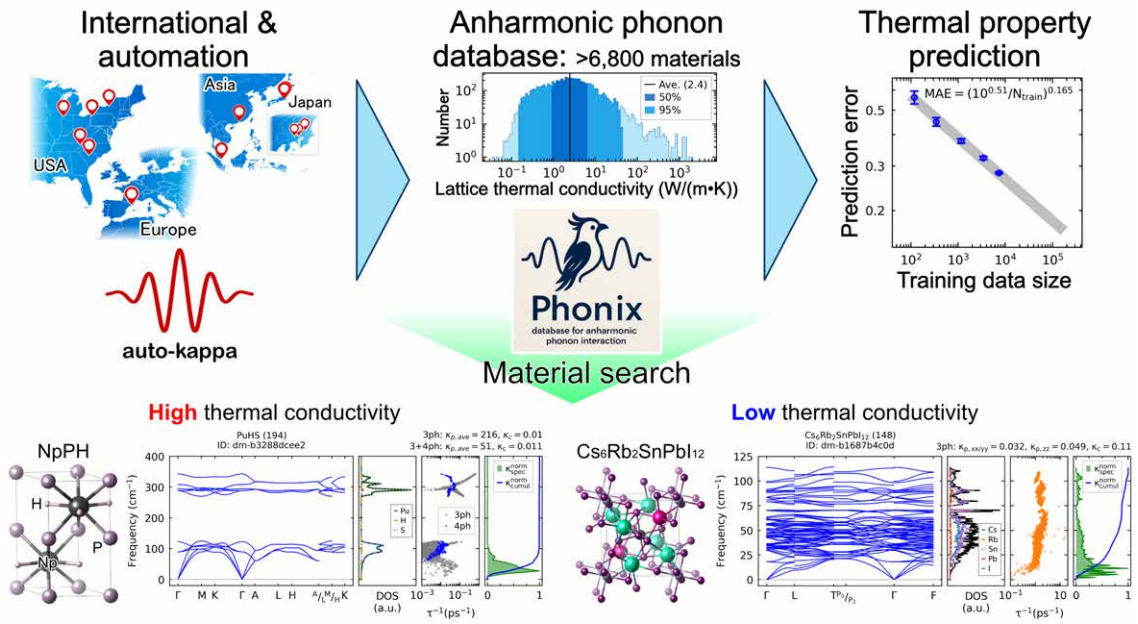


Fig. 1: Project overview. High-throughput calculations were conducted using automation software for anharmonic phonon properties (auto-kappa) through international collaboration. Anharmonic phonon properties, including lattice thermal conductivity, were calculated for over 6,800 crystal compounds and released as the Phonix database. Using the developed database and graph neural networks (GNNs), machine learning models for thermal property prediction were constructed, and a deep-learning scaling law—showing improved prediction accuracy with increasing training data size—was demonstrated. Finally, the prediction model was applied to screen high- and low-thermal-conductivity materials from approximately 380,000 candidates.

materials, identifying candidates with high and low thermal conductivity. These results demonstrate the effectiveness of combining first-principles calculations and machine learning.

Conclusion

We developed an automated high-throughput framework for anharmonic phonon calculations (auto-kappa) and constructed a large-scale database (Phonix) using supercomputing resources. The integration of first-principles calculations and machine learning enables efficient prediction and screening of thermal properties, providing a foundation for data-driven materials design.

References

[1] M. Ohnishi, npj Comp. Mater. (2026) accepted.

Theoretical study on chemical reaction processes at surfaces and interfaces using density functional theory and machine learning methods

Meliton R. Chiong III, Muhammad Fadhlan ANSHOR, Beatriz A. C. TAN, Samuel E. M. P. PUTRA, Harry Handoko HALIM, and Yoshitada MORIKAWA
Department of Precision Engineering, The University of Osaka
Yamada-oka 2-1, Suita, Osaka 565-0871

First-principles electronic structure methods offer high predictive accuracy and have been widely employed to elucidate a variety of reaction processes. However, their application has traditionally been constrained to spatial scales of a few nanometers and time scales on the order of hundreds of picoseconds due to their substantial computational cost. Recently, the integration of machine learning techniques has made it possible to overcome these limitations.

By combining first-principles electronic structure calculations with machine learning, kinetic Monte Carlo methods, and microkinetic modeling within a multiscale simulation framework, we aim to elucidate heterogeneous catalytic reaction processes. In particular, this approach enables long-timescale simulations at surfaces and interfaces that were previously inaccessible.

By comparing our simulation results with the latest experimental data, we seek to identify the key factors governing catalytic reactivity and to establish guiding principles for the rational design of more efficient catalysts.

In this fiscal year, using Supercomputer Systems at the SCC-ISSP, we have investigated 1) photodetachment in Al_{13}^- anions and photoionization in Al_{13} neutrals[1], 2) reactive graphene edge-adsorbed Pt single-atom catalyst structures for oxygen reduction reactions[2], 3) the effect of hydrogen gas pressure in hydrogenation of CO_2 to Formate on Cu(100)[3] and 4) improvement of global structural optimization method, "The Scaled-LCB"[4]. In this report, we focus on the first topic.

The Al_{13} anion has attracted particular attention due to its remarkable stability arising from its high symmetry and closed-shell electronic structure. Consequently, Al_{13} neutral behaves as a "superhalogen", characterized by a notably high electron affinity. Experimentally, the Al_{13}^- anion exhibits an adiabatic detachment energy (ADE) of 3.62 $\pm$0.06 eV and a vertical detachment energy (VDE) of 3.75 $\pm$0.1 eV. Within the jellium model, its 40 valence electrons complete the superatomic orbitals $(1S)^2(1P)^6(1D)^{10}(2S)^2(2P)^6(1F)^{14}$ into a closed shell. The ground-state structure of Al_{13}^- is icosahedral, where symmetry splits the closely spaced 2P and 1F superatomic states into overlapping hybrid PF states. In contrast, the ground state Al_{13}^+ cation adopts a low-symmetry cap-like structure consisting of $1-5-1-6$ layers of Al atoms.

In this study, we employ diffusion Monte Carlo (DMC) to compute the vertical and adiabatic detachment energies (VDE, ADE) of Al_{13}^- anion and the corresponding ionization energies (VIE, AIE) of Al_{13} neutral. We assess the effects of basis set choice and multideterminant expansions on the trial wave function, and simulate the vibronic transitions to enable direct comparison with experimental photoelectron spectra. Finally, we use these results to clarify

the photodetachment of Al_{13}^- anions and the photoionization of Al_{13} neutrals and to provide benchmark-quality values for future theoretical and experimental work.

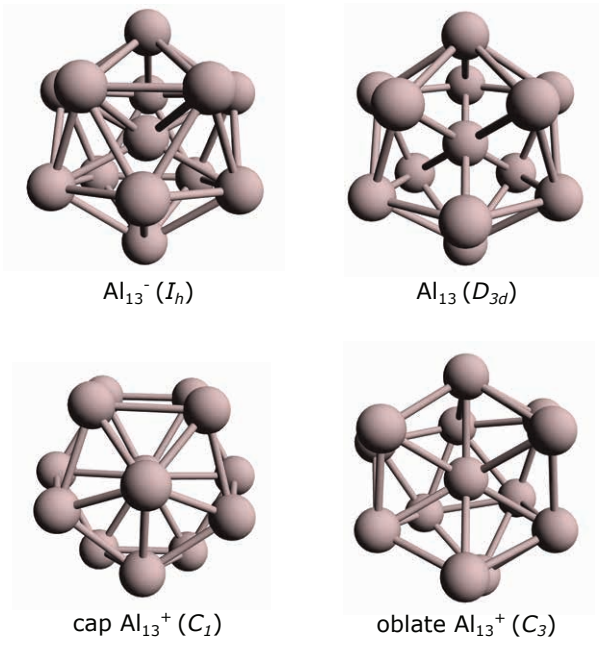


Figure 1: Isomers of Al_{13}^-, Al_{13}, and Al_{13}^+ optimized at the PBE0/6−311+G(d,p) level. The anionic Al_{13}^- has an icosahedral geometry (Ih), the neutral Al_{13} undergoes a Jahn-Teller distortion to a distorted icosahedron (D3d), and the cationic Al_{13}^+ has two low-symmetry isomers: a cap-like structure (C1) and an oblate structure (C3). The cap isomer is 0.51 eV lower in energy than the oblate.

We have employed diffusion Monte Carlo to clarify the photodetachment and photoionization processes of the prototypical superatom Al_{13}. For the anion, DMC combined with vibronic analysis accurately reproduces both adiabatic and vertical detachment energies, highlighting the need to account for finite-temperature effects when comparing with experiment. For the Al_{13} neutral cluster, we resolve a long-standing controversy by revealing that the experimental ionization energy corresponds to the adiabatic ionization into a metastable oblate cation, not into the cap-like ground state. This structural assignment is supported by laser photoionization mass spectra and reconciles prior theoretical inconsistencies.

References

[1] M. R. Chiong III, A. Nakajima, and Y. Morikawa: J. Phys. Chem. A **130**, 1851-1860 (2026).

[2] B. A. C. Tan, N. A. Sofi, P. N. Thanh, K. I. M. Rojas, S. E. P. P. Masan, Y. Hamamoto, I. Hamada, and Y. Morikawa: Phil. Trans. R. Soc. A, **384**, 20240555 (2026).

[3] W. O. N. F. Rajaelo †, H. H. Halim †, M. F. Anshor, Y. Yamada, S. Ramadhani, F. A. Mubarok, S. E. M. Putra, A. L. Ivansyah, T. D. K. Wungu, Suprijadi, Y. Morikawa*, and F. Muttaqien*, † These authors contributed equally: ACS Catal., **16**, 5068-5079 (2026).

[4] S. E. P. P. Masan, T. N. Pham, K. I. M. Rojas, B. A. C. Tan, F. Rusydi, Y. Hamamoto, and Y. Morikawa: J. Ceram. Soc. Jpn., **133**, 602-609 (2025).

Identification of Semiconductor Donor Structures Using First-Principles Calculations and Development of Quantum Algorithms

Yu-ichiro MATSUSHITA

Department of Physics,

The University of Tokyo, Hongo, Bunkyo-ku, Tokyo 113-8654

This research project leveraged the high-performance computing (HPC) resources of the Institute for Solid State Physics and other centers to address two of the most significant frontiers in computational materials science: the advancement of quantum algorithms for spectroscopy and the microscopic elucidation of semiconductor defect physics. Throughout this fiscal year, the utilization of large-scale parallel processing has enabled us to achieve major scientific milestones that provide a new blueprint for both future material simulations and next-generation device optimization.

The first major achievement is the advancement of quantum computing methodologies for materials science, specifically the implementation of a logical Quantum Phase Estimation (QPE) framework for spectroscopic analysis[1]. Calculating the X-ray absorption spectra (XAS) of strongly correlated systems, such as transition metal oxides, is notoriously difficult for classical computers. We focused on the iron $L_{2,3}$-edge of $FePO_4$, initially utilizing HPC resources to define a chemically relevant active space through the Automated Valence Active Space (AVAS) method. To address the inherent noise of current quantum hardware, we integrated the [k+2, k, 2] Iceberg code for quantum error detection (QED). Validation on a trapped-ion quantum computer demonstrated that the application of QED effectively reduced the spectral ℓ^2 error, marking a critical step toward high-fidelity material diagnostics in the era of fault-tolerant quantum computing. This achievement establishes a robust framework for integrating classical supercomputing with quantum processors to solve complex multi-body problems in materials science.

The second major achievement is the definitive identification of the microscopic origin of "hydrogen-related donors" (HDs) in silicon, a phenomenon that has remained an enigma in semiconductor physics for over fifty years[2]. By performing large-scale first-principles calculations based on the HSE06 hybrid functional, we identified the core of the HD defect as a cluster of four silicon self-interstitials (I_4). Our analysis revealed a unique synergistic mechanism where the I_4 cluster generates empty defect levels just below the

conduction band edge, which then capture an electron from an incorporated hydrogen atom to function as a shallow donor. This discovery represents a paradigm shift from traditional substitutional doping, where an impurity atom is expected to take the place of a host atom. Furthermore, our results suggest that this HD mechanism is transferable to other covalently bonded wide-bandgap semiconductors like diamond, offering a novel strategy for achieving efficient n-type doping in power electronics and potentially overcoming long-standing material constraints in high-performance device fabrication. In summary, the computational achievements of this year have yielded significant dividends in both fundamental quantum research and practical semiconductor applications. These results, published in prestigious journals such as Physical Review Applied and Communications Materials, underscore the vital role of supercomputing in driving the future of material science and industrial technology.

References

[1] H. Nishi, T. Kosugi, S. Hirose, T. Okayama, and Y. Matsushita, Phys. Rev. Applied **25**, 034026 (2026).

[2] A. Kiyoi, Y. Nishiya, Y. Matsushita, and T. Umeda, Comm. Materials **7**, 8 (2026).

First-principles study on functionality of electronic devices

Tomoya ONO
Graduate School of Engineering, Kobe University
Rokkodai-cho, Nada, Kobe 657-8501

Tunneling magnetoresistance plays an important role in spintronics in magnetic tunnel junctions (MTJs), which consist of two ferromagnetic electrodes divided by an extremely thin tunnel barrier with controllable magnetization directions. Tunnel barrier is the key element of an MTJ, which is traditionally composed of MgO or Al_2O_3. Recently, two-dimensional (2D) materials with atomic-layer thickness have gained significant interest as useful nonmagnetic materials for tunnel barriers in MTJs.

We performed the density functional theory calculations to investigate the atomic and electronic structures of the graphene/NiFe alloy interface[1] using the DFT-based code Vienna Ab initio Simulation Package.[2] FM metal is deposited on the graphene in some experiments while the graphene is transferred to the FM metal substrate in many cases. We assume that Ni is adsorbed with (111) face because (111) face is the most stable face for a fcc crystal and the lattice constant mismatch between Ni(111) and graphene is less than 1%. In our computational model, the bare metal substrate consists of nine atomic layers, in which the topmost and bottommost layers are referred to as the surface layers and the remaining layer is defined as the bulk layer. The surface layers consist of a binary alloy $Ni_\alpha Fe_{1-\alpha}$ (α=0.00, 0.25, 0.50, 0.75, and 1.00), whereas the bulk layer is composed of $Ni_\beta Fe_{1-\beta}$ with β=0.50, 0.75, and 1.00. In the bulk layer of Ni_3Fe, Fe atoms lie on a $(\bar{1}10)$ plane, while the atomic configuration is $L1_0$ in the bulk layer for NiFe. The atomic configurations of Ni and Fe atoms in the surface layers are defined so as to keep the stacking sequence of $Ni_\beta Fe_{1-\beta}$ when $\alpha = \beta$. Monolayer graphenes are adsorbed on both the edges of the substrate. Four possible adsorption geometries are examined, with C atoms located at the hcp-fcc, top-fcc, top-hcp, and bridge-top sites. The Perdew–Burke–Ernzerhof generalized gradient approximation are used for electronic exchange and correlation interactions and The projector-augmented wave method is employed for the electron–ion interactions. The supercell size is $\sqrt{2}a_b \times \sqrt{6}a_b/2 \times 36.34$ Å^3 with a_b (=3.524 Å) being the experimental lattice constant of the Ni fcc bulk. A 19 × 19 × 1 Monkhorst–Pack mesh of k points is used for the Brillouin-zone integration. Structural optimization for the atoms in the surface layers and graphenes is performed until all the force components decrease to below 0.02 eV/Å.

The formation energy of surface layer $E_{\rm form}^{\rm surf}$ is defined as follows:

$$E_{\rm form}^{\rm surf} = \frac{-E_{\rm NiFe}^{(9)} + E_{\rm NiFe}^{(7)}}{N} + \alpha\mu_{\rm Ni} + (1-\alpha)\mu_{\rm Fe}, \quad (1)$$

where $E_{\rm NiFe}^{(n)}$ is the total energy of n layers of $Ni_\beta Fe_{1-\beta}$, $N(=8)$ is the number of metal atoms in the surface layers, and $\mu_{\rm Ni}$ ($\mu_{\rm Fe}$) is the chemical potential of the Ni (Fe) atom, which is taken from an fcc (bcc) bulk. Equation (1) implies that the surface with higher formation energies are preferred. The formation energy of the bare NiFe alloy substrate is shown in Fig. 1. The surface layer with $\alpha = 0.75$ ex-

hibits the largest formation energies. In addition, the substrates with the Fe-rich surface layer ($\alpha < 0.50$) are less preferable than those with the Ni-rich surface layer for all the binary compounds of the bulk layer, which can be explained by the formation energy of the bulk.

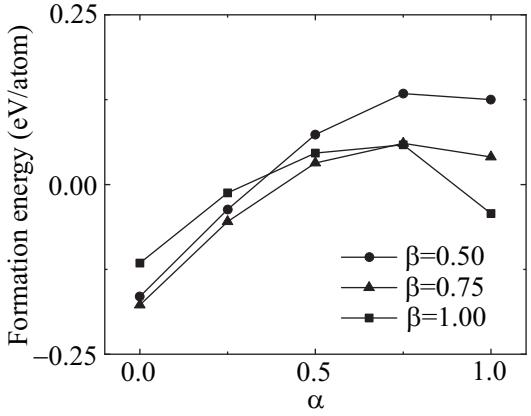


Figure 1: Formation energy of surface layer. Reprinted from Ref. 1.

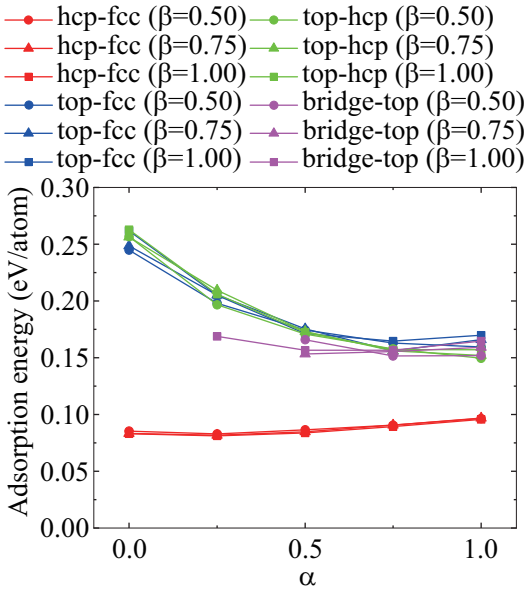


Figure 2: Adsorption energy of graphene on NiFe alloy substrate. Reprinted from Ref. 1.

The adsorption energy of graphene on the NiFe alloy substrate E_{ads} is defined as follows:

$$E_{\mathrm{ads}} = \frac{-E_{\mathrm{Gr/NiFe}} + E_{\mathrm{NiFe}} + 2E_{\mathrm{Gr}}}{N_C}, \qquad (2)$$

where E_{NiFe} is the total energy of nine layers of the NiFe alloy substrate, E_{Gr} is the total energy of the graphene monolayer, $E_{\mathrm{Gr/NiFe}}$ is the total energy of the NiFe alloy substrate with the graphene monolayer at both ends, and $N_C(= 16)$ is the number of C atoms in the supercell. Equation (2) indicates that the interface with large adsorption energy is preferable. Figure 2 shows the adsorption energy. In the case of the Fe-rich surface, the graphene adsorbed at the bridge-top site shifts to the top-fcc or top-hcp site after the structural optimization. When graphene is adsorbed on the Fe-rich surface at the top-hcp site, the adsorption energy is the largest. In contrast, for Ni-rich surfaces, the graphene adsorption at the top-fcc or bridge-top site is favorable, and the difference in the adsorption energy among top-hcp, top-fcc and bridge-top sites is small. It is found that the distance d between the atoms in the surface layer and graphene is *ca* 2.1 Å. The interfaces with the surface layer of α=0.00 are the most stable regardless of the adsorption sites and binary compounds of the bulk layer. These results do not agree with the stability of the bare NiFe alloy substrate with respect to the composition ratio of the surface layer. Our results imply that the composition ratio of the interface of graphene/NiFe alloy substrate is affected by the fabrication process.

References

[1] N. Matsumoto, R. Endo, M. Uemoto, and T. Ono, J. Appl. Phys. **138** 104305 (2025).

[2] G. Kresse and J. Hafner, Phys. Rev. B **47**, 558 (1993).

Density functional theory study of adsorption, reaction, and manipulation of molecules on solid surfaces

Ikutaro Hamada

Department of Precision Engineering, Graduate School of Engineering,

The University of Osaka, 2-1 Yamadaoka, Suita, Osaka 565-0871

Understanding molecular adsorption and reactions at solid surfaces is crucial for a wide range of phenomena, from everyday processes such as wetting and corrosion to technologically important applications including heterogeneous and electrochemical catalysis. Despite their importance, the atomic-scale mechanisms governing surface adsorption and reactions remain incompletely understood, hindering the rational design of efficient materials and energy conversion devices.

In this project, we performed density functional theory (DFT)-based simulations to investigate adsorption states and reaction mechanisms of molecules relevant to heterogeneous catalysis and energy conversion. In addition, extending beyond static descriptions of surface adsorption, we aim to elucidate the microscopic mechanisms of adsorbate manipulation induced by scanning probe microscopy (SPM) tips.

Our DFT simulations cover a wide range of systems, including:

- organic molecules on semiconductor surfaces [1],
- molecular adsorption on terraces and edges of hexagonal boron (HB) sheets [2,3],
- H_2 formation from bilayers of HB sheets [4],
- intermolecular complexes such as C_6H_6–H_2 and H_2–H_2 [5], and
- oxygen reduction reactions on OH-functionalized Fe- and Co-based single-atom catalysts [6].

These simulations were carried out using several DFT codes, including STATE [7], Quantum ESPRESSO [8], VASP [9], and MOLGW [10]. Below, we describe selected results obtained mainly using System B of the ISSP supercomputer facility.

We investigated the adsorption states of PTCDA and its derivatives on Si(111)-(7×7) surfaces [1], successfully determining their adsorption sites and adsorption energies, as well as characterizing their vibrational modes.

For HB sheets, we predicted that H_2 adsorption can be enhanced by introducing boron vacancies, and clarified the origin of this enhancement [2]. We also investigated water adsorption and the reaction of H_2O at the edges of HB sheets. We found that H_2O is adsorbed

near the edges, rather than directly at edge sites. Furthermore, the activation energy for H_2O dissociation to form OH near the edge is lower than that on the terrace. This result indicates that H_2O dissociation—considered the onset of the hydrolysis reaction observed experimentally—preferentially occurs in the near-edge region of HB sheets [3].

Finally, we investigated H_2 formation from bilayers composed of HB sheets. We found that the H–H distance is a key factor governing H_2 formation on HB sheets [4].

References

[1] Y. Park, I. Hamada, M. Wolf, and A. Shiotari, Angew. Chem. Int. Ed. e202514215 (2025).

[2] S. Naka, K. I. M. Rojas, and I. Hamada, e-J. Surf. Sci. Nanotechnol **23**, 339-345 (2025).

[3] K. I. M. Rojas,L. T. Ta, S. Naka, Y. Morikawa, and Ikutaro Hamada, J. Chem. Phys. **163**, 124702-1-11 (2025).

[4] Y. Yasuda, O. Ok, K. Goto, N. Noguchi, S. Ito, M. Hikichi, R. Tsuji, Y. Nakahira, R. Utsumi, H. Saitoh, S. Nakano, S. Naka, I. Hamada, S. Orimo, and T. Kondo, ACS Nano **20**, 9951-9960 (2026).

[5] Y. Kataoka and I. Hamada, Phys. Rev. B **113**, 085143 (2026).

[6] A. F. Z. Abidin and I. Hamada, Phil. Trans. R. Soc. A **384**, 2318 (2026).

[7] STATE documentation, https://state-doc.readthedocs.io/

[8] P. Giannozzi et al., J. Phys. Condens. Matter **21**, 395502 (2009).

[9] G. Kresse and J. Furthmüller, Comput. Mat. Sci. **6**, 15 (1996); G. Kresse and J. Furthmüller, Phys. Rev. B **54**, 11 169 (1996).

[10] F. Bruneval, et al., Comput. Phys. Commun. **208**, 149 (2016)

Theoretical Studies on the Electron Traps in a-SiN for Flash Memory Application

Kenji SHIRAISHI

Center for Innovative Integrated Electronic Systems, Tohoku University,

468-1 Aramaki Aza Aoba, Aoba-ku, Sendai, Miyagi 980-8572

The a-SiN known as a useful hard material is now indispensable in current semiconductor technology: It is placed near the interface of Si-based metal-oxide-semiconductor structures and utilized as a nonvolatile flash memory which sustains our current data-driven society [1]. We focused on the charge-trap properties of amorphous silicon nitride (a-SiN) acting as charge-trap layer in 3D NAND flash memories. The scope is to improve the device performance by tuning the relevant microscopic properties. The electron trapping mechanism in silicon-rich a-SiN is primarily facilitated by the presence of the peculiar LFS, associated with tetracoordinated Si atoms. As the amount of Si increases, the a-SiN displays deeper trap levels, a higher density of electron traps, and improved programming/erase (P/E) endurance, which can all be ascribed to the characteristics of LFS as shown in Fig.1. By considering the influence of shallow trap levels, we identified an optimal nitrogen-to-silicon (N/Si) ratio is approximately 1.13. Furthermore, by accurate tuning of the H concentration, mainly passivating undercoordinated N, we have shown how the device performance can improve, since H atoms affect indirectly (i.e. upon N–H bond formation) the percentage of Si–Si bonds in the material, where LFS can form. By carefully adjusting both the N/Si ratio and the H content, the performance of charge-trap silicon nitride (CT-SiN) can be maximized.

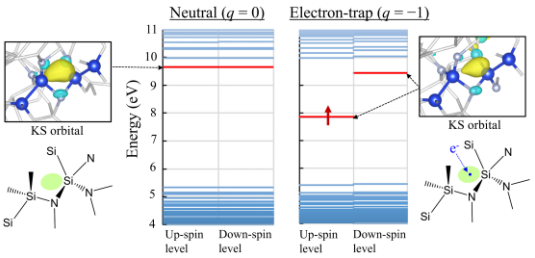


Fig.1. Kohn–Sham (KS) energy levels (central panels) and their corresponding orbitals along with the local schematic structures (side panels), in the neutral (q = 0) and charged electron-trap state (q = −1) for the $Si_{48}N_{63}H_3$ model. KS orbitals are shown by yellow (+) and blue (−) isosurfaces at a value of 50 % of the maximum. In the schematic structures, the light green areas indicate the LFS where electrons are trapped.

References

[1] M Boero, K Shiraishi, T Nagahashi, F Nanataki, and A Oshiyama, Physical Review Materials **9**, 084601 (2025).

Clarification of Atomic Level Operation Mechanism of New Vibration-Powered Generator Using Si/SiO_2 Interfaces

Kenji SHIRAISHI

Center for Innovative Integrated Electronic Systems, Tohoku University,

468-1 Aramaki Aza Aoba, Aoba-ku, Sendai, Miyagi 980-8572

A potassium-ion electret, which is a key element of vibration-powered micro-electromechanical generators, can store negative charge almost permanently. However, the mechanism by which this negative charge is stored is still unclear. We theoretically study the atomic and electronic structures of amorphous silica (a-SiO_2) with and without potassium atoms using first-principles molecular-dynamics calculations. Our calculations show that a fivefold-coordinated Si atom with five Si–O bonds (an SiO_5 structure) is the characteristic local structure of a-SiO_2 with potassium atoms, which becomes negatively charged and remains so even after removal of the potassium atoms. These results indicate that this SiO5 structure is the physical origin of the robust negative charge observed in potassium-ion electrets. Here we identify pentacoordinate silicon in potassium-ion-processed amorphous silica by XPS and first-principles calculations. The XPS spectra is consistent with the predicted electronic fingerprint of SiO_5. These results establish pentacoordinate silicon as the microscopic origin of long-lived negative charge retention in silica electrets.

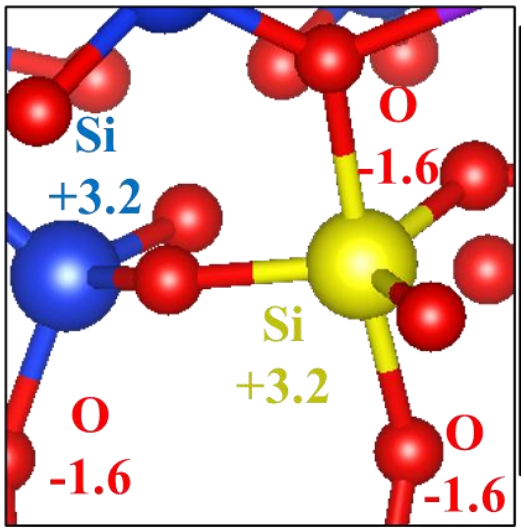


Fig.1. Structure around a fivefold-coordinated Si atom in a-SiO2.

References

[1] T. Nakanishi, T. Miyajima, K. Chokawa, M. Araidai, H. Toshiyoshi, T. Sugiyama, G. Hashiguchi, and K. Shiraishi, Appl. Phys. Lett., 117, 193902 (2020).

[2] Y. Ohata, T. Nakanishi, K. Chokawa, M. Araidai, T. Ishiguro, H. Mitsuya, H. Toshiyoshi, Y. Shibata, G. Hashiguchi, and K. Shiraishi, Appl. Phys. Lett., 121, 243903 (2022).

First-Principles Methods for Spin Conversion and Real-Space Transport Analysis

Fumiyuki ISHII, Naoya YAMAGUCHI, Hana Pratiwi KADARISMAN, Shohei MIURA, Rifky SYARIATI, Yaotang ZHANG, Yedija Yusua Sibuea TEWENG, Jin INOUE, Sota YAMATE, Shota SASAJIMA, Jingwen YANG, Zohan Syah FATOMI, Ahmad SOHIB, Syifa Fauzia Hariyanti PUTRI, Ahmad Al GHIFFARI, Salsabila Amanda PUTRI, Nadia Maharani CHADIZA, Shigetomo YANASE

Nanomaterials Research Institute, Kanazawa University

Kanazawa, 920-1192, Japan

This report summarizes the results obtained in the ISSP projects 2025-Ca-0091 and 2025-Cb-0054. The common objective was to extend first-principles methods for spin conversion phenomena and to analyze transport coefficients in layer- and real-space-resolved forms. We used OpenMX-based density-functional calculations, local Berry phase methods, hybrid Wannier functions, effective-screening-medium calculations, and Green's-function transport calculations on the ISSP supercomputer systems.

1. *First-principles method for spin Hall conductivity*

We developed a first-principles method for spin Hall conductivity (SHC), a key quantity for spin-current generation in spin-orbit-coupled materials. Conventional SHC calculations often rely on maximally localized Wannier functions and a spin-current operator. In contrast, our approach uses Bloch wave functions and the Fukui–Hatsugai–Suzuki Berry-phase formalism, enabling SHC calculations without Wannierization and without explicitly introducing a spin-current operator. Benchmark calculations for Pt showed qualitative agreement with conventional Kubo-formula results.

The method was further extended to slab geometries by constructing spin-resolved hybrid Wannier functions localized along the surface normal. This allowed the spin Hall conductivity to be decomposed into layer contributions. Applications to $MnBi_2Te_4$ and Bi_2Se_3 thin films showed surface-localized contributions associated with topological surface states and surface spin responses. This extension uses the same uniaxial-Wannier framework as layer anomalous Hall conductivity [1]. Dense Brillouin-zone sampling on the ISSP systems was essential for checking convergence of surface and bulk contributions in topological thin films.

2. *Real-space topological indices in skyrmion systems*[2]

We investigated how topological transport responses can be visualized in real space for finite magnetic textures. As a first step toward first-principles real-space Chern-marker calculations, we studied a tight-binding model of finite skyrmion lattices under open boundary conditions. The local Chern marker $C(\mathbf{r})$ was evaluated from the projector onto occupied states and was used to map the spatial distribution of the Chern-number contribution. The resulting maps showed a clear correlation between the skyrmion spin texture and the local topological response, while edge regions carried compensating contributions as expected for finite samples.

We also calculated the Bott index as a real-space topological invariant. By varying the number of occupied states and the skyrmion supercell size, we confirmed that the Bott index converges to the Chern number obtained

under periodic boundary conditions in the large-system limit. This benchmark clarifies the numerical requirements for applying real-space topological markers to more realistic systems, including skyrmion crystals, magnetic thin films, and disordered or inhomogeneous topological materials.

3. *Thermoelectric transport in atomically thin materials*[3]
We applied first-principles Green's-function transport calculations to few-layer SnSe in order to clarify the thickness dependence of its thermoelectric performance. The transport coefficients were evaluated within the Landauer formalism using density-functional Hamiltonians. The monolayer showed the largest thermoelectric figure of merit along the zigzag direction, with calculated values reaching $ZT = 4.08$ for n-type doping and $ZT = 3.41$ for p-type doping at 723 K. The enhancement is attributed to the suppression of interlayer electronic coupling, an enlarged band gap, and reduced lattice thermal conductivity caused by phonon-boundary scattering.

These results demonstrate that atomic-scale thickness engineering is an effective strategy for controlling thermoelectric properties in layered materials and provide useful test cases for real-space decomposition of longitudinal conductivity based on closest Wannier functions.

4. *Spin conversion and polarization-driven functional materials*
Several applications were carried out to connect the method development with materials design. For Janus WSSe, first-principles calculations showed that the broken mirror symmetry produces an out-of-plane electric dipole moment. Born effective charge analysis clarified the microscopic origin of the dipole, and the internal electric field was found to induce Rashba-type spin splitting near the Γ point. This result shows that Janus transition-metal dichalcogenides can realize spin-split electronic states without an external electric field, making them promising spin-conversion materials[4].

We also investigated the capacitance profile of graphene electrodes using the effective-screening-medium method[5]. This calculation provided a reference model for separating electrode and dielectric contributions in nanoscale capacitors. Together with multilayer h-BN polarization and strain-induced shift-current responses in $CsPbI_3$[6], these applications show the usefulness of ISSP supercomputers for designing spin, charge, thermal, and optical energy-conversion materials.

References

[1] Y. Morishima, F. Ishii, and N. Yamaguchi, arXiv:2506.01160 (2025).

[2] J. Yang, N. Yamaguchi, and F. Ishii, submitted.

[3] Z. S. Fatomi, R. Syariati, N. Yamaguchi, and F. Ishii, submitted.

[4] S. A. Putri, M. A. U. Absor, N. Yamaguchi, and F. Ishii, Jpn. J. Appl. Phys. **64**, 10SP21 (2025).

[5] A. Sohib, N. Yamaguchi, and F. Ishii, Jpn. J. Appl. Phys. **64**, 11SP11 (2025).

[6] Y. Y. S. Teweng, N. Yamaguchi, and F. Ishii, Appl. Phys. Express **18**, 121001 (2025).

Analyses on correlation between material properties and atomic structures in complex structures via ab-initio-based methods

Satoshi WATANABE
Department of Materials Engineering, the University of Tokyo
7-3-1 Hongo, Bunkyo-ku, Tokyo, 113-8656

Understanding the relationship between atomic structure and physical properties in complex materials systems–such as surfaces, interfaces, defects, and amorphous phases–has become increasingly important for the development of next-generation information devices and energy-related technologies. In particular, phenomena involving dynamics, including ion transport, phonons, and thermal conduction, are often governed by structural features that extend beyond nearest-neighbor atomic configurations. Elucidating such structure–property correlations, especially those involving medium-range order in structurally disordered systems, remains a major scientific challenge. At the same time, these problems are computationally demanding and constitute important targets for large-scale simulations utilizing modern supercomputing resources.

To address these challenges, our research aims to achieve a microscopic and quantitative understanding of such phenomena through first-principles calculations based on density functional theory (DFT), as well as large-scale atomistic simulations employing machine-learning interatomic potentials (MLIPs) constructed from first-principles datasets. In fiscal year 2025, building upon our previous efforts, we have carried out computational and methodological studies on a variety of systems, including defects in layered materials, metal–solid electrolyte interfaces, ceramics, metallic and oxide glasses, and alloy nanoparticle catalysts. In the following, we highlight our recent results on grain boundaries in ceramic materials as a representative example.

Grain boundaries (GBs) in ceramics play a crucial role in ionic transport and are central to processes such as sintering, flash sintering, and electrochemical functionality. However, the microscopic mechanisms governing ion behavior at GBs, particularly under applied electric fields, remain insufficiently understood. To address this issue, we performed DFT and density functional perturbation theory (DFPT) calculations for the $\Sigma5(310)/[001]$ grain boundary in cubic ZrO_2 [1].

The calculations were carried out using VASP, employing a GGA with the PBE functional and the grain boundary supercell containing 120 atoms. The DFPT calculations were conducted to evaluate Born effective charges (BECs), which quantify the response of atomic forces to external electric fields.

The calculated electronic structure reveals the emergence of acceptor-like states just above the valence band maximum localized near the grain boundary region, indicating a distinct electronic environment compared to the bulk. Furthermore, we found significant deviations in the BECs of both Zr and O ions near the GB as seen in Fig. 1. Especially, some of the off-diagonal components of BECs took finite values.

These anomalous BEC characteristics imply that, under applied electric fields, ions near

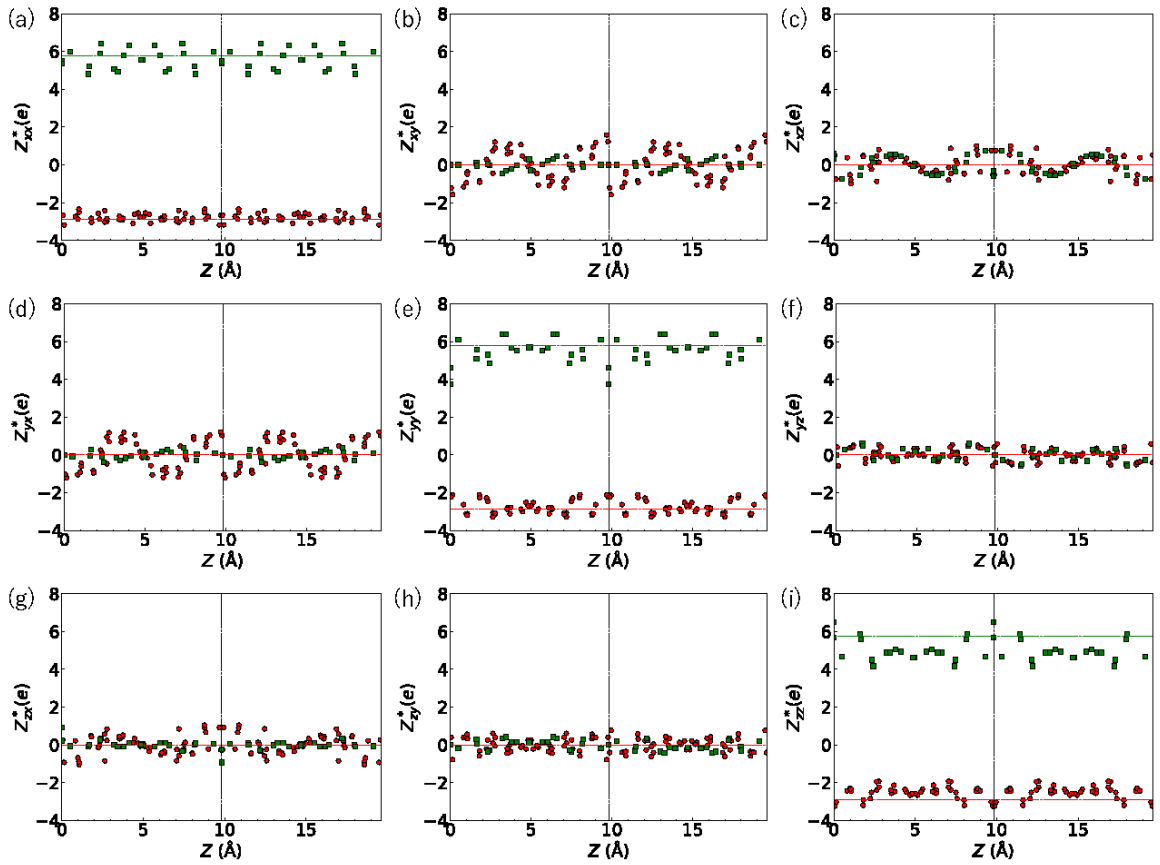


Figure 1: Calculated BECs Z^* for each ion. Each tensor component is depicted along the Z-direction (perpendicular to the GB plain). Green and red circles denote values of Zr and O, respectively. The vertical dotted lines indicate the boundary between two grains, while the horizontal dotted lines represent the Z^* values of bulk cubic-ZrO_2. Reprinted from Ref. [1].

the grain boundary experience enhanced and anisotropic forces, including components perpendicular to the field direction. Such effects are expected to play a crucial role in enhancing ionic mobility and may provide a microscopic basis for phenomena such as flash sintering, where rapid densification occurs under strong electric fields at relatively low temperatures. Importantly, these findings highlight that polarization effects and environment-dependent charge responses must be explicitly considered in modeling ion transport in structurally complex systems.

References

[1] S. Arai, K. Shimizu, A. K. A. Lu, H. Masuda, H. Yoshida, and S. Watanabe: e-J. Surf. Sci. Nanotechnol. **23** (2025) 323.

Analysis of atomic and ionic behavior in complex structures using first-principles calculations and machine learning

Koji SHIMIZU

Materials DX Research Center, National Institute of Advanced Industrial Science and Technology, Umezono, Tsukuba, Ibaraki 305-8568

Understanding physical properties emerging from complex atomic environments, such as amorphous phases, defects, and interfaces, is increasingly important for advanced electronic and ionic devices. Although recent advances in computational techniques have enabled the study of more complex structural models, first-principles calculations based on density functional theory (DFT) remain restricted in system size and time scale due to their high computational cost.

Machine-learning interatomic potentials (MLPs) trained on first-principles datasets offer an effective solution by achieving near-DFT accuracy with substantially reduced computational cost, enabling large-scale and long-time simulations beyond the limits of conventional first-principles approaches.

The author has studied lithium-ion conduction mechanisms in solid electrolytes using MLP-based simulations, focusing on property changes induced by additive incorporation. Applications to metal/solid-electrolyte interfacial systems were also explored using an equivariant neural network potential based on graph representations, trained on extensive DFT datasets and applied to molecular dynamics simulations.

High-entropy alloys (HEAs), solid-solution materials composed of five or more elements, were examined with a focus on catalytic applications. CO adsorption, a key elementary step in the CO_2 conversion, was investigated on CoCuFeMnNi HEA surfaces. A machine-learning approach based on local surface descriptors enabled accurate prediction of adsorption energies and revealed the influence of local surface structures on adsorption strength and the electronic states of surface atoms [1].

Furthermore, reaction-energy analyses provided theoretical support for experimentally identified synthesis pathways of solid electrolytes [2]. Additional studies included analyses of Born effective charges at zirconia grain boundaries [3].

References

[1] E.R. Beronio et al., Surf. Interfaces 82, 108457 (2026).

[2] K. Onoue et al., submitted.

[3] S. Arai et al., e-J. Surf. Sci. Nanotechnol. 23, 323 (2025).

Development of First-Principles Self-Interaction-Corrected GWΓ Method

Yoshifumi NOGUCHI

Department of Applied Chemistry and Biochemical Engineering, Graduate School of Engineering, Shizuoka University, Johoku 3-5-1, Hamamatsu, Shizuoka 432-8561, Japan

We have developed a first-principles self-interaction-corrected GWΓ method and implemented it into our original all-electron mixed basis program. To completely remove self-interaction contributions from the GWΓ one-electron self-energy operator, we have also developed a self-screening-corrected GW (SSC-GW) method [1]. Figure 1 shows the Γ terms for (a) self-interaction-included and (b) self-interaction-corrected cases. It should be noted that the $\nu = \mu$ matrix elements in the Γ terms correspond to the self-interaction contributions. We applied our methods to simulate the first ionization potentials of 97 atoms and molecules.

For all systems, the self-interaction contributions in the GW one-electron self-energy operator range within ± 0.5 eV. Consequently, there is no significant difference in computational accuracy between the conventional GW and SSC-GW methods, with both yielding a mean absolute error (MAE) of approximately 0.4 eV. In contrast to the GW methods, significant self-interaction contributions were observed in the GWΓ method. The MAE of the self-interaction-included GWΓ method is approximately twice as large as that of the GW method. However, by applying self-interaction corrections to the Γ term, this error is reduced by approximately half [2]. Indeed, the self-interaction contributions in the GWΓ one-electron self-energy operator correlate clearly with the errors found in uncorrected method; that is, systems with more pronounced self-interaction contributions exhibit larger errors. These results demonstrate that the self-interaction corrections are essential for the GWΓ method.

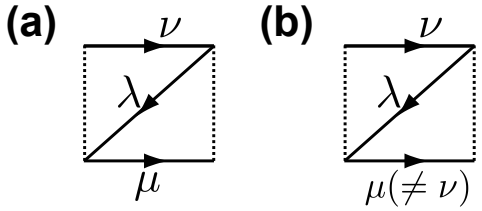


Fig. 1 Feynman diagrams of (a) self-interaction-included and (b) self-interaction-corrected Γ terms.

References

[1] F. Aryasetiawan, R. Sakuma, and K. Karlsson, Phys. Rev. B, **85**, 035106 (2012).

[2] T. Isago, Y. Noguchi, and K. Ohno, Phys. Rev. B, **111**, 195146 (2025).

Study of unconventional multi-orbital and multi-layer superconductors in first-principles

Hirofumi Sakakibara

Faculty of Engineering, Tottori University, Tottori, Tottori 680-8552

Cuprate superconductor is one of the hottest scientific topic throughout this decade. One of the standard models of cuprates is single orbital square lattice Hubbard model, which incorporates only one degrees of orbital/site freedom. Lately this single orbital physics, some theorists proposed bilayer Hubbard model in which the interlayer coupling is crusial to superconductivity. Cooper pair is formed in such models between faced layers and relatively high Tc compared to single orbital square lattice model is realized. However, no material in which such "ideal" bilayer model manifest was discovered until 2023.

The recent discovery of the Ruddlesden-popper type bilayer nickelate superconductor $La_3Ni_2O_7$ in 2023 [1] have stimulated a ton of works, where one reason is it have high T_c as cuprates. Only pressurized sample exhibits superconductivity in bulk system, on the contrary, thin-film samples with compressive strain from substrates exhibits superconductivity even in ambient pressure [2]. In our previous report [3], the essence of high- T_c superconductivity is the bilayer Hubbard model originated from the Ni-$d_{3z^2-r^2}$ orbitals coupled between layers. In this project, we have investigated the possibility of new superconductors in which bilayer Hubbard model manifests.

First, here we report our investigation of thin-film sample in Ref. [4]. In bulk samples, it is believed, although another possible symmetries are under debate, that the space group changes from *Amam* (*Cmcm*) to *I*4/*mmm* and this transition can be a trigger to the superconducting transition. In Ref. [4], we have shown that $La_3Ni_2O_7$ on the substrate of $SrLaAlO_4$(SLAO), is close to the critical point between Amam and I4/mmm. This may be consistent with experimental report that I4/mmm phase probably realizes even in ambient pressure [5]. Another remarkable point is that the γ Fermi surface, which is regarded to be important for pairing especially along the traditional low energy theories, is about to be vanished. By adopting fluctuation-exchange approximation (FLEX), we have found that the (nearly) vanished γ Fermi surface is still effective, especially for finite energy spin-fluctuation and superconductivity mediated by it. This implies that the robustness of superconductivity.

Second, we report our advanced studies of

effective bilayer models. As described in Refs. [6,7], two-band Hubbard model is identical to the bilayer Hubbard model in a special condition that $U=U'=J=J'$, where these denote intra-orbital repulsion, inter-orbital repulsion, Hund's coupling, and pair hopping parameters, respectively. Even there may be some quantitative ambiguity, Kitamine *et al*. have demonstrated that $s\pm$wave superconductivity similar to that of bilayer Hubbard model can be realized through some numerical calculations [6]. Recently we have named this effective model as an orbital space bilayer model (OSBM). As described in Ref. [6], band insulator can be a parent compound of OSBM, this aspect is very contrasting to cuprates superconductors, a doped Mott insulator. In Ref. [8], we have investigated an infinite layer nickelate as a candidate of OSBM. We have performed first-principles calculation to obtain parameters of an effective Hubbard model not only the hopping integrals but also interaction parameter using RESPACK code [9] in which constrained random phase approximation method is implemented. By adopting FLEX approximation to the derived model, we have found that $s\pm$wave can be realized in heavily hole doped region [8].

This design concept can be adopted to several candidates. In Ref. [9], we have investigated T'- and T- structure of $La_3Ni_2O_6$, in which oxygen bonding the faced Ni-O layer does not exist unlike $La_3Ni_2O_7$. Based on an analysis using FLEX and rigid band approximation, we have found that $s\pm$wave can be realized in hole fewer doped region compared to that of infinite layer nickelate. This material design is very promising strategy because stochiometric $La_3Ni_2O_6$ has already synthesized, although it is an insulator. We will show the further studies, where the calculations are partially done but paper is now under preparation, related to OSBM in the next forum of activity report.

References

[1] H. Sun *et al*., Nature (London) **621**, 493 (2023).

[2] E. K. Ko *et al*., Nature (London) **638**, 935 (2025).

[3] H. Sakakibara, N. Kitamine, M. Ohi, and K. Kuroki, Phys. Rev. Lett. **132**, 106002 (2024).

[4] K. Ushio *et al*., arXiv: 2506.20497.

[5] C. Yue *et al*., Natl. Sci. Rev. **12**, nwaf253 (2025).

[6] N. Kitamine *et al*.., Phys. Rev. Res. 2, 042032 (2020).

[7] H. Shinaoka *et al*., Phys. Rev. B 92, 1951256 (2015).

[8] H. Sakakibara *et al*., Phys. Rev. B **111**, 224511 (2025)

[9] K. Nakamura *et al*., Comput. Phys. Commun 261, 107781 (2021).

[10] S. Kamiyama, H. Sakakibara *et al*., arXiv: 2603.11771 (2026).

Analyses on electronic structure and magnetic anisotropy in high-performance spintronics magnetic materials and development/application in quasi-particle self-consistent GW code

Tatsuki ODA, Takumi KATSUTA, Haruya NIWA, Hikaru YAMAGUCHI, Itsuki NAKANISHI, Puke Lajaladita Litle MECCI, Masao OBATA,

Graduate School of Natural Science and Technology, Kanazawa University, Kakuma, Kanazawa, Ishikawa 920-1192

We have studied several systems in high-performance spintronics and magnetic materials on electronic structure and magnetic anisotropy. In these investigations, we have checked physical accuracy in the materials of spintronics application. We have also studied electronic structures in some systems using a quasi-particle self-consistent GW code. Here, we report (A) developments of a refined version of grand canonical force theorem approach (reGCFT) on the estimation of magnetic anisotropy energy (MAE) and (B) applications of the computational code for the quasi-particle self-consistent GW method (QSGW).

(A) The method of reGCFT

This method, based on the total energy associated with density functional theory including the magnetic dipole contribution, improves the numerical accuracy of MAEs. The original approaches of conventional GCFT or simple FT frequently fail to reproduce the resulting value obtained from the method of total energy difference (TET), in which the heavy element is included, such as Pt element, expecting a large spin-orbit coupling (SOC). We have demonstrated the properties mentioned above in the interface PtCoO/ZnO and some systems [1]. Its demonstration indicated the agreement between reGCFT and TET within only a few percents.

(B) The method of QSGW

The computational code of QSGW has been optimized to obtain efficient computation. The computational demonstrations, such as magnetic shape memory alloy Ni_2MnGa [2], some transition mental oxides, etc., were performed. QSGW provides narrowing of band manifolds to the electronic structure of *d*-orbitals, indicating the property of electron correlation .

References

[1] T. Katsuta, M. Obata, et al., submitted.

[2] J. Luštinec, M. Obata, et al., J. Phys.: Condens. Matter **38**, 015502 (2026).

Development/application in quasi-particle self-consistent GW and analyses on magnetic anisotropy in spintronics magnetic materials

Tatsuki ODA, Haruya NIWA, Hikaru YAMAGUCHI, Takumi KATSUTA, Itsuki NAKANISHI, Puke Lajaladita Litle MECCI, Masao OBATA,

Graduate School of Natural Science and Technology, Kanazawa University, Kakuma, Kanazawa, Ishikawa 920-1192

We have studied first-principles electronic structures in several materials using a quasi-particle self-consistent GW code (QSGW). QSGW provides narrowing of band manifolds to the electronic structure of *d*-orbitals and reasonable crystal field splitting on the transition metal atoms induced by the anion atoms. The former indicates the property of large electron correlation, compared with the results obtained with the conventional first-principles approach based on the density functional theory (DFT).

Here, we briefly report achievements on the transparent transition metal oxides $LiTi_2O_4$ [1], which has a normal spinel-type crystal structure. This structure belongs to a cubic space-group symmetry as same as diamond and, but has 14 atoms in the unit cell, requiring a large amount of computational resources. The current supercomputer in ISSP fortunately allows us to investigate electronic structures within GW approximation, and optical properties through the microscopically calculated dielectric function with independent particle approximation. This approach demonstrates the transparent property in the visible range to the light. Such transparency cannot be explained in the electronic structure obtained with the DFT approach. This is because the DFT does not provide narrow band manifolds to Ti 3d t_{2g}- and e_g-bands and the small separation between the oxygen band manifolds and t_{2g}-band manifolds. In QSGW, the self-energies of single particle are evaluated, and thus one-particle electronic spectra also evaluated. In this work, the cumulant approach (CA) was applied to investigate their improved spectra (QSGW+CA), so that the plasmon satellites are included in the resulting spectra. These spectra were compared with those observed in experimental photoemission measurement. In QSGW, renormalization factors can be calculated at each state in the Brillouin zone. In the current calculation, these are around 0.5 at the Fermi level.

References

[1] H. Niwa, M. Obata, et al., Phys. Rev. B **113**, 155114 (2026).

Reduction of Rare Metals in Fuel Cell and Formic Acid Decomposition Catalysts

Norihito Sakaguchi

Center for Advanced Research of Energy and Materials, Faculty of Engineering, Hokkaido University, Sapporo, Hokkaido 060-8628

We investigated the effects of light irradiation on the stability of single Pt atoms on light-element-doped graphene using first-principles calculations based on density functional theory (DFT) and time-dependent DFT (TDDFT).[1] Furthermore, we evaluated the catalytic selectivity of single Pt and Cu atoms supported on light-element-doped graphene for formic acid decomposition reactions. Additionally, we examined the adsorption and magnetic states of an O_2 monolayer on Ag(111) surfaces.[2]

Regarding the effects of light irradiation, we focused on the diffusion barriers of single Pt atoms on light-element-doped graphene. Total energy and electronic structure calculations were performed using the Vienna Ab initio Simulation Package (VASP) and the Scalable Ab-initio Light-Matter simulator for Optics and Nanoscience (SALMON). The VASP code was parallelized using the Intel® MPI and Math Kernel Libraries. The influence of electron temperature on the diffusion barriers was approximated via Fermi-Dirac smearing. The results demonstrated that while the diffusion barrier decreased with increasing electron temperature, the change remained within a few percent, indicating that the overall impact was not significant.

In the analysis of catalytic selectivity for formic acid decomposition, we compared single Pt and Cu atoms on light-element-doped graphene. It was found that single Cu atoms, when supported on suitable supports, exhibit higher catalytic activity and selectivity than single Pt atoms.

Finally, we also investigated the adsorption of an O_2 monolayer on Ag(111) surfaces.[2] The calculated adsorption structures and magnetic states revealed that the lattice distortion observed via atomic force microscopy (AFM) is attributable to a reduction in the O_2 magnetic moment. This finding suggests that measuring lattice distortion can serve as a means of determining local magnetic structures.

References

[1] Y. Kunisada, K. Sato, N. Sakaguchi, Vacuum and Surface Science 69 (2026) 135.

[2] M. Kimura, Y. Kunisada, Y. Sugimoto, ACS Nano 20 (2026) 263.

Hydrogen Ion Doping and Property Modulation Focused on Acid–Base Sites in Solids

Soshi IIMURA

National Institute for Materials Science (NIMS), Tsukuba, Ibaraki 305-0044

Hydrogen in materials plays a crucial role as an active site that determines functionality in energy and environmental materials such as amorphous silicon, zeolites, and next-generation fuel cell electrolytes. In these materials, hydrogen typically loses an electron and is incorporated as a proton. On the other hand, hydrogen is also known to accept an electron from the host material and form a hydride anion [1,2]. In molecular systems, hydrides exhibit strong hydrogenation and reduction ability toward positively polarized carbon atoms, such as those in carbonyl groups.

Recently, we have found that oxides capable of incorporating protons and intermetallic compounds capable of incorporating both protons and hydrides can act as active sites in photocatalysts and electrocatalysts, enabling the activation of carbon dioxide. In this study, we investigated the electronic states of hydrogen and the conditions under which hydrogen can be incorporated into materials, using first-principles calculation software such as VASP and pydefect, which is used to calculate defect formation energies in semiconductors.

First, structural models of materials were obtained from the Materials Project database. Next, interstitial sites capable of accommodating hydrogen were systematically searched, and hydrogen atoms were introduced into these sites. By evaluating the total energy differences before and after hydrogen incorporation, we successfully identified a large number of intermetallic compounds capable of incorporating hydrogen.

Subsequently, we analyzed the electronic structures prior to hydrogen incorporation, as well as the charge densities and wave functions at hydrogen incorporation sites. The results revealed that empty s and p orbitals of transition metals—whose d orbitals are fully occupied due to electron donation from electropositive metals—act as Lewis acid sites, thereby stabilizing hydrogen within the material. In future work, we will establish computational methods to quantify the acidity and basicity of metals and apply them to the discovery of new catalysts.

References

[1] S. Iimura et al., Nat. Commun., **3**, 943-1-6, (2012).

[7] K. Fukui, S. Iimura et al., J. Am. Chem. Soc., **144**, 1523-1527, (2022).

First-principles study on the control of valley transport properties in two-dimensional honeycomb structured materials

Yoshiyuki EGAMI
Division of Applied Physics, Faculty of Engineering, Hokkaido University
Kita 13, Nishi 8, Kita-ku, Sapporo, Hokkaido 060-8628

Recently, the valley degree of freedom has attracted considerable attention as a unique electronic property of graphene, promoting intensive research on valleytronics. One of the major challenges in realizing valleytronic devices is the establishment of a valley filter function that enables the selective generation and detection of electrons from a specific valley. Recent studies have revealed a strong correlation between the geometric symmetry of defect structures with respect to the electron-transport axis and valley-dependent transport properties. For instance, in graphene systems incorporating Stone–Wales defects or blister defects, it has been reported that mirror symmetry of defect with respect to the transport axis facilitates both the generation of valley polarization and the suppression of its relaxation. Beyond graphene, other 2D materials known as Xenes also possess similar valley degrees of freedom, suggesting that analogous transport properties may emerge in these systems.

In this study, we focused on arsenene, a 2D material composed of arsenic atoms. Although pristine arsenene typically exhibits a buckled honeycomb structure with a band gap, the adsorption of atoms such as hydrogen or fluorine induces a transition to a planar honeycomb structure. This transition results in a band structure with linear dispersion near the Fermi level, similar to graphene. However, unlike graphene, where electronic states are dominated by π orbitals, the bands in this system are derived from σ orbitals. To clarify how this difference in orbital character influences valley-dependent transport properties, we theoretically evaluated fluorinated arsenene using first-principles electron-transport calculations[1, 2].

Our results for arsenene systems incorporating 5-8-5 type defects confirm that electron transport occurs without hybridization between the two valley states. Furthermore, a valley filtering function was observed, in which electrons from a specific valley exhibit nearly unity transmission. We also evaluated the hybridization of valley states caused by the structural symmetry breaking, which acts as "noise" in valley information. While this noise increases exponentially with atomic displacements from the ideal symmetric structure, we found that the hybridization remains sufficiently suppressed under lattice vibrations at room temperature.

This work has been performed on System B of the Supercomputer Center, the Institute for Solid State Physics, the University of Tokyo.

References

[1] K. Hirose *et al.*: First-principles calculations in real-space formalism (Imperial College Press, 2005).

[2] Y. Egami, S. Tsukamoto and T. Ono: Phys. Rev. Res. **3**, 013038 (2021).

First-principles calculations of electronic structures in molecular spintronic devices

Hideo KAIJU, Mizuki MATSUZAKA, Chika HASHIMOTO, and Koki TERAI

Faculty of Science and Technology, Keio University

Yokohama, Kanagawa 223-8522, Japan

Molecular spintronics has been attracted attention because of the unique possibilities. Molecular spintronic devices exhibit magnetoresistance (MR) effect, in which the resistance changes with magnetic field [1, 2]. A large MR effect was observed in molecular spintronic devices at low temperature because of the high spin polarization, which is attributed to the effective orbital hybridization between molecules and magnetic materials. Recently, we have observed MR effect in $Ni_{78}Fe_{22}$/tris-(8-hydroxyquinoline) erbium (Erq_3)/FeCo organic spin valves [3]. In this study, we calculate the density of states (DOS) at each atom in FeCo/Erq_3/FeCo and Ni_3Fe/Erq_3/Ni_3Fe systems, and estimate the spin polarization of the magnetic atoms.

We used Quantum ESPRESSO for first-principles calculations. The calculations were performed using density functional theory, plane wave approximation, and pseudopotential model. We prepared the supercells of FeCo/Erq_3/FeCo and Ni_3Fe/Erq_3/Ni_3Fe, as shown in Fig. 1. The size of the supercells is 14.305 × 14.305 × 25.489 Å^3 in Fig. 1(a) and 14.156 × 14.156 × 28.201 Å^3 in Fig. 1(b), respectively. The energy

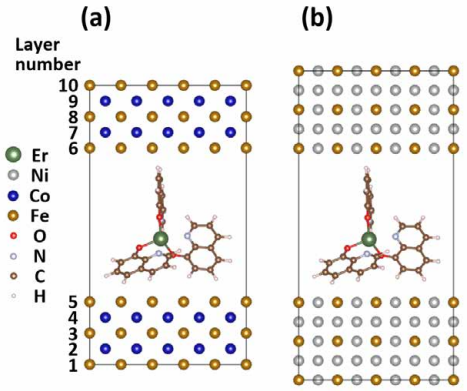


Figure 1: Supercells of (a) FeCo/Erq_3/FeCo and (b) Ni_3Fe/Erq_3/Ni_3Fe.

cutoff for the plane wave basis were 60 Ry for wave function and 480 Ry for charge density and the convergence criterion for energy estimation was set to 1×10^{-6} Ry in all calculations. The *k*-point mesh was set to 3 × 3 × 1 for the self-consistent field calculations and 5 × 5 × 1 for calculating the DOS.

Figure 2 shows the calculated DOS of Fe atom at the 1st and 5th layers in the FeCo/Erq_3/FeCo, and Ni atom at the 1st and 5th layers and Fe atom at the 1st and 5th layers in Ni_3Fe/Erq_3/Ni_3Fe. The Fermi level is at 0 eV in each DOS. The DOS of Fe and Ni atoms at the 5th layer is different from that at the 1st layer. We have confirmed that the DOS of Fe and Ni

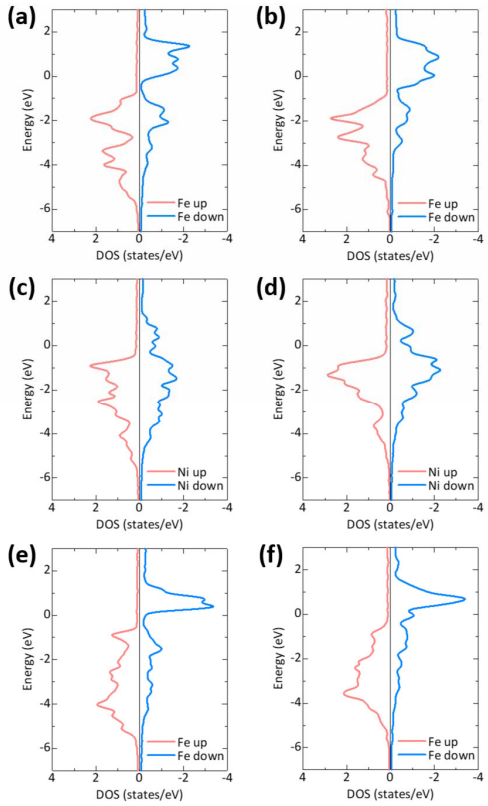


Figure 2: Calculated DOS of Fe atom at (a) 1st and (b) 5th layers in FeCo/Erq$_3$/FeCo, and Ni atom at (c) 1st and (d) 5th layers and Fe atom at (e) 1st and (f) 5th layers in Ni$_3$Fe/Erq$_3$/Ni$_3$Fe.

atoms in bulk FeCo and Ni$_3$Fe is almost the same as that at the 1st layers in the FeCo/Erq$_3$/FeCo and Ni$_3$Fe/Erq$_3$/Ni$_3$Fe. This result suggests that our calculations are reasonably reliable. Then, the DOS at the Fermi energy for each atom was summed up at each layer. Figure 3 shows the spin polarization at each layer number in the FeCo/Erq$_3$/FeCo and Ni$_3$Fe/Erq$_3$/Ni$_3$Fe supercells. The spin polarization of Fe atom at the interface of FeCo/Erq$_3$ is higher than that in

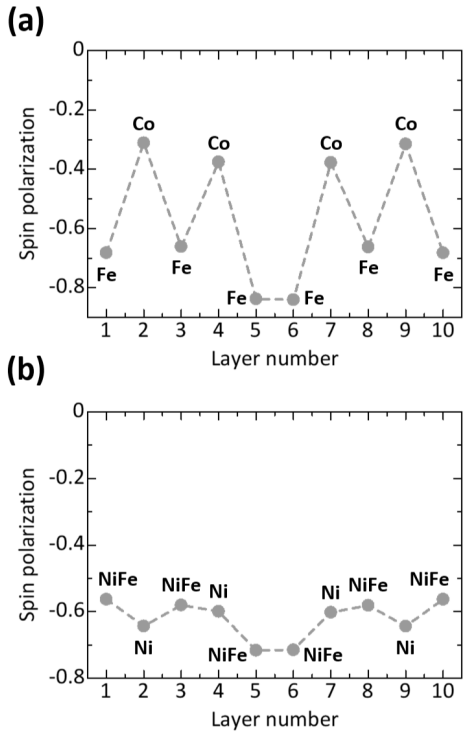


Figure 3: Spin polarization at each layer number in (a) FeCo/Erq$_3$/FeCo and (b) Ni$_3$Fe/Erq$_3$/Ni$_3$Fe supercells.

Fe and Co atoms in the inner site of FeCo. The same tendency is also found in Ni$_3$Fe/Erq$_3$/Ni$_3$Fe. Additionally, the spin polarization of the Fe atom at the FeCo/Erq$_3$ interface is slightly higher than that of Ni and Fe atoms at the Ni$_3$Fe/Erq$_3$. The findings of this study may contribute to the development of molecular spintronics.

References

[1] Z. H. Xiong et al., *Nature* **427**, 821 (2004).

[2] C. Barraud et al., *Nat. Phys.* **6**, 615 (2010).

[3] M. Matsuzaka et al., *J. Magn. Magn. Mater.* **630**, 173465 (2025).

Simulation of Metal Nitriding by Ammonia Flame

Peijie FENG, Minhyeok LEE, and Yuji SUZUKI
Department of Mechanical Engineering, School of Engineering,
The University of Tokyo, 7-3-1 Hongo, Bunkyo-ku, Tokyo 113-8656

As the energy sector transitions from fossil fuel to green ammonia, the "unwanted" nitriding of iron-based materials in ammonia-fueled combustion systems [1] has become a major concern. Our previous work [1,2] revealed a mutual interaction between ammonia and iron-based materials: ammonia molecules are thermally decomposed on an iron-based material, and the nitrogen atoms diffuse into the material forming iron nitrides. To understand the dynamics of ammonia decomposition when the iron-based material is nitrided, we incorporated density functional theory (DFT) calculations using VASP. The primary objective is to elucidate the reaction mechanisms governing "unwanted nitriding" in high-temperature environments and to derive reliable kinetic data for the iron nitrides (γ'-Fe_4N and ε'-Fe_2N).

To investigate the reaction energetics and microkinetics on iron nitrides, two representative phases are selected: γ'-Fe_4N and ε'-Fe_3N. These phases correspond to experimentally observed layers in the bilayer structures formed during typical gas nitriding processes [3].

First, we used the method proposed by Tian et al [4] and Yalcin et al. [5] to identify the stable surface. The stable surface corresponds to the energetically most favorable configuration; hence, when polycrystalline metals form, surfaces with low surface energy tend to be exposed, contributing to the macroscopic surface morphology. Therefore, macroscopic surface reactions are most likely to occur on facets with low surface energy. The results shows that the γ'-Fe_4N (001) and ε'-Fe_3N (101) termination exhibit low surface energies, indicating that these facets are likely to dominate the macroscopic surface

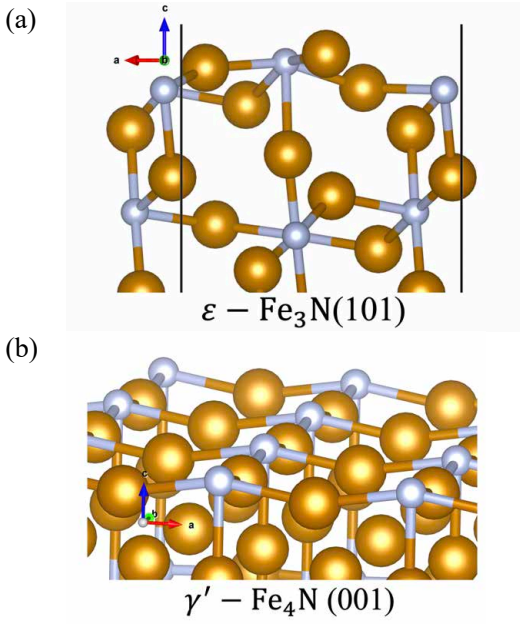


Fig 1: (a) ε'-Fe_3N (101) termination, (b) γ'-Fe_4N (001) termination.

morphology, the atomic model is shown in Fig. 1.

Then it is necessary to identify the adsorption sites for reactional species, e.g. NH_3, NH_2, NH, N, and H. Therefore, a Python code using Delaunay triangulation is developed to exhaustively identify the symmetry-reduced set of possible adsorption sites. The results are shown in Fig. 2.

Finally, we investigated the barrier of the key N–N recombination step to quantify how strongly the surface binds nitrogen atoms derived from ammonia decomposition. This step is the rate-limiting reaction on pure iron surfaces [5].

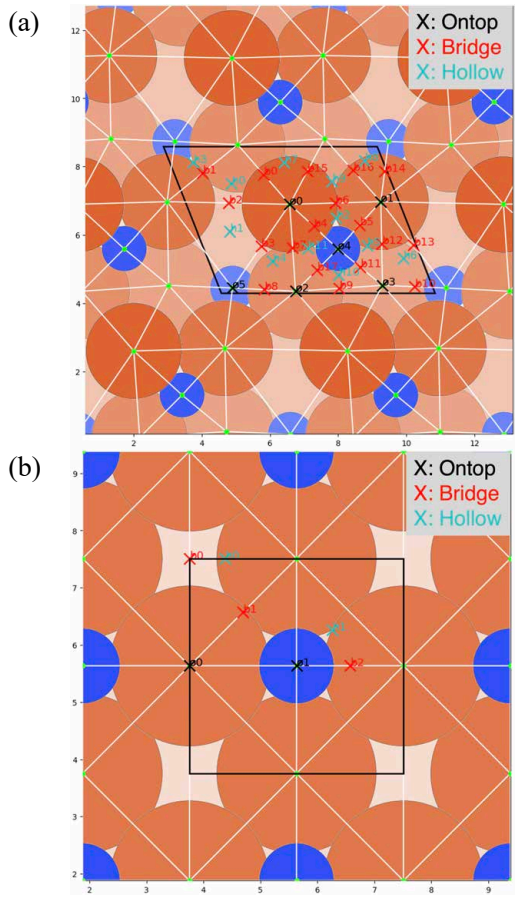


Fig. 2: Possible adsorption sites identified on (a) ε'-Fe_3N (101), and (b) γ'-Fe_4N (001).

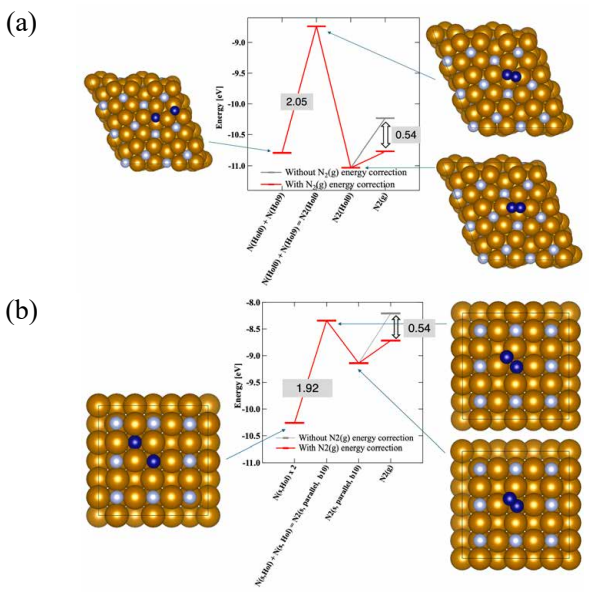


Fig. 3: DFT computed reactional energetics of N-N recombination reaction on (a)ε'-Fe_3N (101), and (b) γ'-Fe_4N (001).

We used the dimer method to locate the transition states. As shown in Fig. 3, iron nitride has a lower barrier than pure iron (2.38 eV [5]) for the same step, indicating higher reactivity, consistent with our experimental observation [2]. In total, approximately 1,000 node-days of CPU computation is used on ISSP System B.

References

[1] Wang, D., Lee, M., and Suzuki, Y., Proc. Combust. Inst., 40, 105562 (2024).

[2] Feng, P., Lee, M., Wang, D., and Suzuki, Y., Int. J. Hydrog. Energy 48, 75 (2023).

[3] Middendorf, C., and Mader, W., Int. J. Mater. Res. 94, 3 (2003).

[4] Tian, X., et al., Appl. Surf. Sci. 427,357 (2018).

[5] Yalcin, F. and Wolloch, M., Comput. Mater. Sci. 234 (2024)

[6] Weiss, M. et al., Appl. Surf. Sci. 2, 4 (1979).

Development of Ceramic Protective Coating to Suppress Corrosion and Hydrogen Embrittlement of Metallic Materials

Yuji Kunisada

Center for Advanced Research of Energy and Materials, Faculty of Engineering, Hokkaido University, Sapporo, Hokkaido 060-8628

To develop efficient hydrogen-permeation barriers, we investigated the formation energies of hydrogen impurities at the interface between ceramic and metallic materials using first-principles calculations based on density functional theory (DFT). We also investigated the behaviors of hydrogen impurities at the grain boundaries of FeCrAl alloys.

In addition to our previous investigations into the behavior of hydrogen impurities at interfaces between different ceramics,[1] we also investigated the behaviors of hydrogen impurities at the interface between ceramic and metallic materials using the Vienna Ab initio Simulation Package (VASP). We installed a parallelized version of VASP using the Intel® MPI Library and the Intel® Math Kernel Library. We considered α-Al_2O_3/Fe interfaces. Previously, it was clarified that the stability of hydrogen impurities varies significantly across impurity sites due to the incoherent nature of the α-Al_2O_3/Fe interface. Therefore, in the current fiscal year, we have performed systematic analyses by calculating the formation energies of hydrogen impurities at all interfacial sites within the supercell. As a result, the interfacial sites were found to be classified into four categories. Furthermore, the results revealed that the stability of hydrogen impurities strongly depends on the size of the interstitial voids at the interfacial sites. It was also clarified that an increase in the concentration of hydrogen impurities significantly promotes the delamination of the α-Al_2O_3 film.

We also investigated the formation energies of hydrogen impurities at the grain boundaries of FeCrAl alloys. The results indicated that hydrogen impurities are more stable at the grain boundaries than in the bulk regions of the FeCrAl alloy. Furthermore, it was found that the presence of alloying elements, such as Al and Cr, reduces the stability of hydrogen impurities. This observed tendency is consistent with previously reported behavior on FeCrAl alloy surfaces.[2]

References

[1] Y. Kunisada, R. Sano, N. Sakaguchi, Int. J. Hydrog. Energy 97 (2025) 1327.

[2] X. Li, Y. Ma, W. Zhou, Z. Liu, Appl. Surf. Sci. 581 (2022) 152273.

Advancement and application of methods for predicting dielectric properties and structure exploration of materials

Shinji TSUNEYUKI

Department of Physics, The University of Tokyo

Hongo, Bunkyo-ku, Tokyo 113-0033

The dielectric properties of polymer materials in the sub-terahertz to terahertz range—which are critical for the development of electronic and communication devices in the 6G and beyond-5G eras—are difficult to understand because they are influenced by various physical phenomena, including anharmonic lattice vibrations, molecular rotation, intra- and inter-molecular polarization, and structural relaxation. Furthermore, due to strong anharmonic effects and slow relaxation, computational simulations are extremely challenging to date. We have been developing dielectric property calculation methods and data-assimilation-based crystal structure search methods for the development of these dielectric materials.

By FY2024, we proposed a versatile machine learning model for organic molecular dipoles and demonstrated that it can calculate the complex dielectric constants of alcohols in the terahertz and lower frequency ranges at relatively low cost. We also developed a method for crystal structure exploration using low-quality powder X-ray diffraction experimental data and succeeded in distinguishing and reproducing multiple crystal structures mixed in the diffraction data; furthermore, we have demonstrated that highly reliable structural models can be obtained using experimental data from amorphous materials. In fiscal year 2025, we further developed these methods.

Calculation of the THz dielectric properties

The dielectric constant of liquids and polymers is calculated from the autocorrelation function of the system's dipole moment. Therefore, to quantitatively predict the molecular dipole moment, we proposed a machine learning model that predicts the position of the Wannier centers of electrons for each chemical bond based on atomic configurations. This fiscal year, using this chemical-bond-based machine learning model for dipole moments, we performed first-principles calculations on the dielectric properties of liquid propylene glycol (PG) and liquid polypropylene glycol (PPG), demonstrating that the frequency and temperature dependencies of the dielectric properties can be accurately calculated even at

frequencies below the terahertz range. We also identified the rebranding peak at 600 cm^{-1} and the intermolecular mode at 100 cm^{-1}, which had been experimentally reported. A key finding was that the model trained using data from propylene glycol dimers can also be applied to PPG with longer chains not included in the training data [1]. This research demonstrates the potential to predict the dielectric properties of polymer materials with various chain lengths and compositions using models trained with inexpensive first-principles calculations of low-molecular-weight oligomers.

On the other hand, it was also found that attempting to calculate the dielectric constants of π-conjugated systems with a Kekulé structure using this method is difficult because the representation of the double bond is ambiguous, making it hard to improve the model's accuracy. Therefore, we developed a new type of machine learning model that accurately predicts the dipole moment of π-conjugated systems by distributing the dipole moment calculated from the Wannier center to each atom [2].

Structure Search Using Experimental Data

We performed a structure search for yttrium under ultra-high pressure using a data-assimilation structure search method.

It is known that yttrium exhibits a phase transition characterized by a change in the stacking order of atomic layers upon compression. However, details regarding the high-pressure phase remain unclear, and no widely accepted consensus has yet been reached regarding the distorted face-centered cubic (dfcc) structure that appears at 45 GPa. Therefore, in this study, we combined machine learning potentials with data assimilation crystal structure search methods to expand the search range to structures containing up to 128 atoms per unit cell and conducted a search for the dfcc structure. As a result, we discovered the *Ibam* and *R*-3 structures, which differ from the previously known *R*-3*m* and $I4_1/a$ structures. First-principles calculations revealed that, among these structures, the *R*-3*m* structure—which had previously been the most widely accepted—is the least stable, and that the enthalpy differences between the other structures are very small. Furthermore, Rietveld analysis showed that, among these, the $I4_1/a$ and *Ibam* structures agree well with experimental diffraction data [3].

References

[1] T. Amano, T. Yamazaki, N. Matsumura, Y. Yoshimoto and S. Tsuneyuki, Phys. Rev. B 111, 165148 (2025).

[2] Y. Zhao, T. Yamazaki, R. Hosoya, Y. Matsushita and S. Tsuneyuki, to be submitted.

[3] Y. Kubo, T. Ishikawa, Y. Tanaka, Y. Nakamoto, M. Sakata and S. Tsuneyuki, submitted.

Polaronic Nature of Impurity Doping in Two-Dimensional Transition-Metal Dichalcogenides from First-Principles Calculations

Soungmin Bae

Institute for Materials Research, Tohoku University, 2-1-1 Katahira, Aoba-ku, Sendai, 980-8577, Japan

Introduction

Two-dimensional transition-metal dichalcogenides (TMDs), such as MoS_2, WS_2, and $MoSe_2$, have attracted considerable attention as promising channel materials for next-generation electronic devices. Owing to their atomically thin layered structures and semiconducting electronic properties, TMDs offer a potential route toward device architectures beyond the scaling limit of conventional silicon-based technology. However, reliable control of carrier concentration and contact properties remains a major challenge for practical device applications. Impurity doping is therefore a key strategy for tuning the electronic properties of TMDs.

In conventional bulk semiconductors, dopants are often understood within the shallow donor/acceptor picture, where introduced carriers are spatially extended and contribute to band-like conduction. In contrast, our previous first-principles study on monolayer MoS_2 revealed that doped carriers can be strongly localized around impurity atoms, forming dopant-bound polaron states.[1] This finding indicates that impurity doping in two-dimensional TMDs cannot be fully described by the conventional shallow-dopant model.

In this project, we extend this perspective from monolayer MoS_2 to representative two-dimensional TMD materials, including MoS_2, WS_2, and $MoSe_2$. We focus on Re and Nb as representative n-type and p-type dopants, respectively, and investigate their electronic structures using PBE0 hybrid-functional calculations. By comparing the impurity-induced carrier distributions across different TMD hosts, we aim to clarify whether dopant-bound polaron formation is a general feature of impurity doping in two-dimensional TMD materials.

Computational Methods

First-principles calculations were performed within the framework of density functional theory using the projector-augmented-wave method as implemented in the Vienna Ab initio Simulation Package (VASP). Representative monolayer transition-metal dichalcogenides, MoS_2, WS_2, and $MoSe_2$, were considered as host materials. Re and Nb atoms were introduced as substitutional dopants at the transition-metal

sites, corresponding to representative n-type and p-type dopants, respectively.

To properly describe impurity-induced carrier localization, electronic-structure calculations were carried out using the PBE0 hybrid functional. For each doped system, atomic structures were relaxed, and the resulting charge-density distributions were analyzed to examine the spatial localization of doped electrons and holes around the impurity sites. These calculations allow us to distinguish localized dopant-bound polaron states from spatially extended shallow donor or acceptor states.

Defect-related quantities, including formation energies and charge-state stability, were analyzed using our pydefect-based workflow where appropriate. The use of the ISSP supercomputer enabled systematic PBE0 calculations for multiple doped TMD supercells, which are computationally demanding due to the large supercell sizes and the high cost of hybrid-functional calculations.

Discussion

The PBE0 hybrid-functional calculations reveal a clear tendency toward carrier localization in Re- and Nb-doped monolayer TMDs. Re and Nb are widely regarded as representative n-type and p-type dopants in TMD materials, respectively. In a conventional shallow donor/acceptor picture, Re doping is expected to donate an electron to the conduction band, while Nb doping is expected to introduce a hole near the valence-band maximum. In such a case, the doped carriers would be spatially extended over the host lattice and could contribute to band-like electrical conduction. However, the present calculations show a qualitatively different behavior.

For Re-doped MoS_2, WS_2, and $MoSe_2$, the additional electron introduced by Re substitution does not spread uniformly over the TMD layer. Instead, the electron density is strongly concentrated around the Re dopant and its neighboring transition-metal and chalcogen atoms. This indicates that the donor electron is trapped near the impurity site rather than forming a shallow, delocalized conduction-band state. Similarly, in Nb-doped MoS_2, WS_2, and $MoSe_2$, the hole introduced by Nb substitution is localized around the Nb dopant. The localized hole state is accompanied by a modification of the electronic structure near the valence-band edge, suggesting that Nb does not simply act as a conventional shallow acceptor.

Importantly, this localization behavior is consistently observed in all three host materials considered in this study: MoS_2, WS_2, and $MoSe_2$. The result indicates that dopant-induced carrier localization is not an exceptional feature of a particular material, such as MoS_2, but rather a

general characteristic of impurity doping in monolayer TMD systems. The common behavior found for both Re-donor and Nb-acceptor cases suggests that the reduced dimensionality of TMDs, together with local lattice relaxation and electron-lattice coupling, plays an essential role in stabilizing dopant-bound carrier states.

These localized impurity-induced states can be interpreted as dopant-bound polaron states. In this picture, the carrier introduced by the dopant becomes trapped near the impurity and is stabilized by local lattice relaxation. This is fundamentally different from the standard shallow donor/acceptor model used for conventional three-dimensional semiconductors, where doped carriers are often assumed to be weakly bound and spatially extended. The present results therefore suggest that electrical doping in two-dimensional TMDs should be understood in terms of carrier localization and polaron formation, rather than only in terms of simple carrier donation or acceptance.

The present study also highlights the importance of using hybrid-functional calculations for describing impurity doping in TMDs. Conventional semi-local exchange-correlation functionals tend to over-delocalize impurity-induced carriers because of self-interaction errors, and they may therefore fail to capture the polaronic nature of doped states. In contrast, the PBE0 hybrid functional stabilizes localized carrier states and provides a more appropriate description of the electronic structure around dopants. This difference is particularly important for evaluating whether a dopant can generate mobile carriers or instead forms localized impurity states.

Overall, these results extend our previous MoS_2-based study to a broader class of two-dimensional TMD materials. The consistent localization of doped electrons and holes in MoS_2, WS_2, and $MoSe_2$ demonstrates that dopant-bound polaron formation is a general feature that must be considered when designing impurity doping strategies for TMD-based electronic devices.

References

[1] Universal Polaronic Behavior in Elemental Doping of MoS_2 from First-Principles,
Soungmin Bae, Ibuki Miyamoto, Shin Kiyohara, Yu Kumagai, ***ACS Nano*** 8, 33988–33997(2024).

[2] Koopmans-compliant density functional framework for polaron self-trapping in titanate oxides Soungmin Bae*, Yu Kumagai
npj Computational Materials (accepted, date: 2026.03.19)

Hydrogen–Vacancy Interactions in bcc Iron: Effects of Mo, C, and N

Naoki UEMURA

Department of Physics, Kansai Medical University,

2-5-1 Shin-machi, Hirakata, Osaka 573-1010

This study investigates the interactions among hydrogen (H), vacancies, and alloying elements (Mo, C, and N) in body-centered cubic (bcc) iron using density functional theory calculations performed with the VASP code [1]. Both bulk lattice and grain boundary (GB) models (Σ3 and Σ5) were considered to evaluate trapping behavior and interaction energies.

In the bulk lattice, hydrogen is strongly trapped at vacancies, indicating that vacancies act as dominant trapping sites. In contrast, solute atoms repel hydrogen, with stronger repulsion observed for C and N than for Mo. Although Mo exhibits weaker interaction with hydrogen, its higher solubility suggests that it may reduce hydrogen diffusivity by limiting available diffusion pathways.

The interaction between vacancies and solute atoms shows differences among elements. C and N exhibit relatively strong interactions with vacancies and stabilize H–vacancy complexes, which may influence vacancy behavior and reduce vacancy diffusion. In contrast, Mo shows weaker interaction with vacancies and has limited influence on vacancy formation.

At grain boundaries, solute atoms segregate to the GB plane, while vacancies are stabilized in adjacent layers. Hydrogen is also trapped at GBs. C and N exhibit stronger repulsion with hydrogen at the GB compared to Mo, which may reduce hydrogen segregation at these sites in the absence of vacancies, although this effect is diminished in the presence of vacancies. Mo shows weaker repulsion and has a smaller direct effect on hydrogen distribution at GBs. When a vacancy is present near the GB, hydrogen trapping becomes dominant regardless of the solute species.

These results suggest that C and N suppress hydrogen locally while influencing vacancy-related behavior, whereas Mo has limited influence on vacancy formation and may reduce hydrogen mobility, although hydrogen trapping is primarily governed by vacancies.

References

[1] S. Kato, N. Uemura, M. Vijendran, and R. Matsumoto, ISIJ Int. **66**, 702 (2026).

Development of the optimization method for the long-range correlation factor in the first-principles wave-function theory

Masayuki OCHI
Department of Physics, The University of Osaka
1-1 Machikaneyama-cho, Toyonaka, Osaka 560-0043

We have developed a first-principles electronic structure calculation software using the transcorrelated (TC) method [1, 2]. The TC method is a many-body wave function theory, where Hamiltonian is similarity-transformed with the Jastrow correlation factor. By this transformation, electron correlation effects are efficiently considered. In particular, one-electron orbitals in the Jastrow-Slater-type wave function can be optimized in the same manner as the Hartree–Fock (HF) method, to say, by solving a one-body self-consistent-field (SCF) equation. It is advantageous that the computational cost for this process is the same order as that for the HF method [3].

We have developed our computational code TC++, which was published on github [4, 5]. One can perform TC calculations using TC++ by reading some output files dumped by DFT calculation using the Quantum-Espresso package [6]. TC++ supports the following functionalities: HF, TC, and biorthogonal TC (BITC) calculations, SCF and band calculations, solids and homogeneous electron gas, a plane-wave-basis set, and norm-conserving pseudopotentials. MPI+OpenMP parallelization is supported.

In this year, we have developed the optimization method of the Jastrow factor with the variational quantum Monte Carlo (VMC) method using the CASINO [7] code. In particular, we have tried to construct the long-range correlation factor as required in TC++ calculation from the short-range polynomial Jastrow factor obtained by VMC calculations. An RPA long-range asymptotic form, which is often used in metallic calculations, was fixed through optimization. We have performed test calculations for Na metal. We achieved stable optimization of the short-range part of the Jastrow factor using VMC. On the other hand, an efficient convergence with respect to the number of k points is one of the ongoing problems.

We have also calculated the total energy and the band gap of narrow-gap semiconductors using the TC+VMC method. The accuracy of the lattice constants seem to be improved while the Jastrow factor is at present short-ranged as is usually adopted in quantum Monte Carlo calculations.

References

[1] S. F. Boys and N. C. Handy, Proc. R. Soc. London Ser. A **309**, 209 (1969); *ibid.* **310**, 43 (1969); *ibid.* **310**, 63 (1969); *ibid.* **311**, 309 (1969).

[2] N. C. Handy, Mol. Phys. **21**, 817 (1971).

[3] M. Ochi, K. Sodeyama, R. Sakuma, and S. Tsuneyuki, J. Chem. Phys. **136**, 094108 (2012).

[4] https://github.com/masaochi/TC

[5] M. Ochi, Comput. Phys. Commun. **287**, 108687 (2023).

[6] https://www.quantum-espresso.org/

[7] https://vallico.net/casinoqmc/

Implementation of Self-Consistent *GWΓ* in TOMBO

Kaoru OHNO

Yokohama National University, Tokiwadai, Hodogaya-ku, Yokohama 240-8501

So far, we have applied a self-consistent *GWΓ* method, which incorporates a vertex correction to the first order in the bare Coulomb interaction or the screened Coulomb interaction, to small molecules using a different version of TOMBO [1,2]. TOMBO is the all-electron mixed basis code, in which both plane waves and numerical atomic orbitals are used as a basis set [3]. The code is highly parallelized using MPI and OpenMP. Recently, we have ported the self-consistent *GWΓ* routine from the different version to the latest version of TOMBO. We modified the routine to save the memory usage by extensively using a distributed memory for each process. We also modified the code to be able to handle all applications including Hartree-Fock, one-shot *GW*, and Bethe-Salpeter equation approaches just by changing a flag in an input file. The self-consistent *GWΓ* method can use three different plasmon-pole models by von der Linden and Horsch [4], Engel and Farid [5], and Hybertsen and Louie [6], as well as the full ω integration [7]. To treat the ω dependence of the self-energy, we introduced the linearized *GW* technique [8], in which the self-energy is expanded linearly around a reference energy, which is usually set at the middle point between the HOMO and LUMO levels of the target molecule. We have checked that all the results in our test calculations fully coincide with the ones that calculated by the old, separate version of TOMBO. Independ to these studies, we have also performed extensive one-shot *GWΓ* calculations for variety of molecules [9,10].

References

[1] R. Kuwahara, Y. Noguchi, and K. Ohno, Phys. Rev. B **94**, 121116(R) (2016).

[2] T. Isobe, R. Kuwahara, and K. Ohno, Phys. Rev. A **97**, 060502(R) (2018).

[3] S. Ono, Y. Noguchi, R. Sahara, Y. Kawazoe, and K. Ohno, Comp. Phys. Comm. **189**, 20-30 (2015).

[4] W. von der Linden and P. Horsch, Phys. Rev. B **37**, 8351-8362 (1988).

[5] E. Engel and Behnam Farid, Phys. Rev. B **47**, 15931-15934 (1993).

[6] M. S. Hybertsen and S. G. Louie, Phys. Rev. B **34**, 5390-5413 (1986).

[7] Z. Ming, S. Ono, N. Nagatsuka, and K. Ohno, Phys. Rev. B **93**, 155116 (2016).

[8] R. Kuwahara and K. Ohno, Phys. Rev. A **90**, 032506 (2014).

[9] T. Isago, Y. Noguchi, and K. Ohno, Phys. Rev. B **111**, 195146 (2025).

[10] T. Isago, Y. Noguchi, and K. Ohno, J. Chem. Phys. **164**, 144110 (2026).

Ab Initio Study of Finite-Temperature Magnetic Properties in Transition Metal Systems

Ryoya HIRAMATSU, Takashi MIYAKE, and Tetsuya FUKUSHIMA
Materials DX Research Center
National Institute of Advanced Industrial Science and Technology
1-1-1 Umezono, Tsukuba, Ibaraki 305-8568

Recent advances in magnetic devices have rapidly accelerated their role as a key enabling technology in modern information society. Achieving further performance improvements requires not only understanding the intrinsic properties of magnetic materials but also accurately predicting their behavior under realistic device operating conditions. Traditional device-design workflows typically combine microscopic electronic-structure analysis with macroscopic device-level simulations in a sequential manner. However, this multistage approach often loses detailed information about the underlying electronic states, which has become a bottleneck in exploring and designing next-generation magnetic materials.

To address this challenge, the present project has developed and applied a first-principles evaluation framework capable of incorporating operational environment effects—specifically temperature and external magnetic fields—into electronic-structure calculations. In this fiscal year, our primary goal was to validate the effectiveness of the proposed scheme through quantitative evaluation of a representative magnetic material, $L1_0$-FePt.

Electronic structures are calculated using the tight-binding linear muffin-tin orbital method based on density functional theory within the local spin-density approximation. Finite-temperature magnetic behavior is modeled using the disordered local moment (DLM) picture, while external magnetic-field effects are incorporated via a spin-Zeeman Hamiltonian. The effective medium required in the DLM framework is computed using the coherent potential approximation. Because the evaluation requires electronic-structure calculations for each temperature and magnetic-field condition, the simulations involve large-scale computations. To this end, OpenMP parallelization is employed to improve computational efficiency.

Figure 1 shows the calculated magnetization curves along the hard-magnetization axis. The magnetization initially increases linearly with increasing field and then gradually saturates. As temperature increases, the linear regime systematically decreases and eventually disappears near the Curie temperature (820 K). These behaviors are characteristic of experimentally observed magnetization curves, and our results demonstrate—for the first time—quantitative reproduction of magnetization-curve profiles of real materials using a fully first-principles approach. This accomplishment not only confirms the validity of our evaluation framework but also establishes a computational technique capable of directly providing magnetization-curve data suitable for practical materials design.

In summary, the project has successfully developed and validated a first-principles methodology capable of predicting finite-temperature magnetic properties under external magnetic fields. The quantitative repro-

duction of the magnetization curve of $L1_0$-FePt confirms the potential of the method as a powerful tool for magnetic-material design. Future work will extend this framework to a broader range of materials.

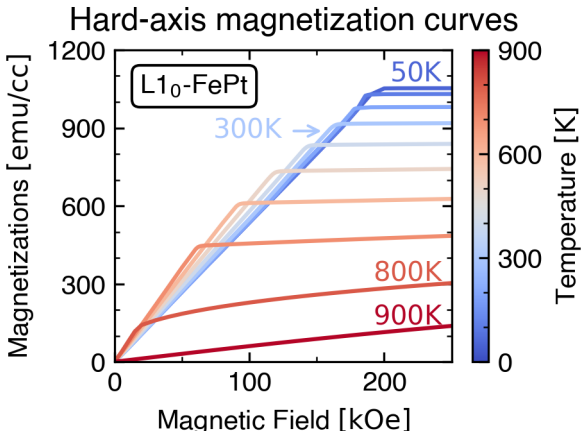


Figure 1: Magnetization curves of $L1_0$-FePt along the hard axis obtained from first-principles calculations.

Weak electronic interaction at the pentacene/graphene interface

Susumu Yanagisawa
University of the Ryukyus
Senbaru 1, Nishihara, Okinawa 903-0213

Understanding the molecule−substrate interactions and formation mechanism of interfacial level alignment at organic molecular semiconductor/metal interface is a critical issue. It may contribute to the advancement of organic electronic materials, while it addresses fundamental academic interests. In this study, to gain insight into the electronic properties of the system, the electronic states of pentacene molecular films adsorbed on graphene were investigated using first-principles calculations.

Electronic states at the pentacene/graphene interface were theoretically examined using the Vienna Ab-initio Simulation Package (VASP). A periodic slab model was constructed based on the experimentally determined adsorption configuration (Structure A), with lattice parameters $a = b = 16.16$ Å and $\beta = 60°$ [1]. The unit cell contained two pentacene molecules. Electron wave functions were expanded in a plane-wave basis set, and the projector augmented wave (PAW) potential was employed to describe the ionic cores. A 2×2 **k**–point mesh was used for sampling the two-dimensional Brillouin zone. A vacuum layer of 2 nm was inserted normal to the substrate to eliminate artificial interactions between slabs. Lattice constants and adsorption geometries were optimized using the van der Waals density functional (vdW-DF) [2]. Numerical calculations were performed using up to 1,024 cores on System B.

It was found that the molecular plane of pentacene is slightly tilted relative to the graphene substrate. The result suggests that the physisorption structure is determined by subtle interplay between intermolecular and molecule-substrate interactions. In the calculated band structure, the HOMO- and LUMO-derived bands of pentacene exhibit almost no dispersion, indicating that they retain the characteristics of the single molecule. Furthermore, energy levels above the conduction band show non-negligible dispersion, and it was found that those bands involve contributions from the wave functions of both the graphene and the pentacene molecules. In contrast, for an adsorption configuration with larger intermolecular distances (Structure D) compared to Structure A, the dispersion of the energy bands near the conduction band was weaker than that of Structure A. This reveals that the band dispersion in the high-energy region originates from the intermolecular interactions. The nature of the intermolecular and molecule-substrate interactions contributing to high-energy band dispersion was found to be consistent with experimental measurements of Fano resonance [1].

References

[1] Y. Hasegawa, T. Yamaguchi, M. Meissner, T. Ueba, F. Bussolotti, S. Ideta, K. Tanaka, S. Yanagisawa and S. Kera: Phys. Rev. B **112**, 085301 (2025).

[2] I. Hamada: Phys. Rev. B **89**, 121103(R) (2014).

Materials Design Through Defect Analysis and First-Principles Calculations

Tomoki YAMASHITA
Department of Electrical, Electronics and Information Engineering,
Nagaoka University of Technology
Kamitomioka-machi, Nagaoka, Niigata, 940-2188

$Li_{2(1-x)}Mg_{1+x}Cl_4$ is attracting attention as a solid electrolyte material in which vacancies are introduced depending on x [1]. Prior to performing large-scale molecular dynamics (MD) simulations using a universal machine learning potential (UMLP), we validated the agreement between density functional theory (DFT) and the UMLP for small-cell calculations. Specifically, DFT-MD was carried out for 56-atom Li_2MgCl_4, as shown in Fig. 1, under NVT conditions at 700 K for 10 ps using the VASP code within the PAW framework and the PBE exchange-correlation functional on System B of the ISSP supercomputer. To evaluate the force accuracy of the UMLP, 50 structures were extracted from the trajectory at 0.2 ps intervals. Force evaluations using MatterSim [2] for these structures showed a mean absolute error of 30 meV/Å relative to DFT, indicating that the UMLP is sufficiently accurate for MD simulations of this system.

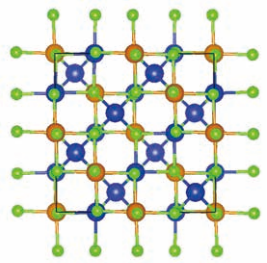


Figure 1: Computational model used for the DFT-MD simulation. Blue, orange, and green spheres represent Li, Mg, and Cl, respectively.

Another research topic addressed in this study was the investigation of defect formation in the semiconductor materials Cu_2SnS_3 (CTS) and Cu_2GeS_3 (CGS). Formation energies of native and Cd-related defects in CTS and CGS were calculated using VASP on System B of the ISSP supercomputer. The HSE06 hybrid functional, which provides a good reproduction of the band gap, was employed for the exchange-correlation treatment. The eFNV correction scheme by Kumagai and Oba [3] was applied to account for defect formation energy corrections, as implemented in the pydefect code [4]. Although calculations for all defect species have not yet been completed, the results obtained so far indicate that Cd substitutional defects at cation sites are likely to form preferentially. In particular, Cd substituting for Cu was found to have the potential to act as a shallow donor.

References

[1] J. Pan et al., Inorg. Chem. **63**, 3418 (2024).

[2] H. Yan et al., arXiv:2405.04967 (2024).

[3] Y. Kumagai and F. Oba, Phys. Rev. B **89**, 195205 (2014).

[4] Y. Kumagai, N. Tsunoda, A. Takahashi, and F. Oba, Phys. Rev. Mater. **5**, 123803 (2021).

Material design of perovskite photocatalysts using first-principle calculations

Seiichiro L. TEN-NO
Graduate School of System Informatics, Kobe University
Rokkodai-Cho, Nada-Ku, Kobe 657-8501

Photocatalytic water splitting under solar irradiation is a promising route to sustainable hydrogen production. Semiconductor photocatalysts are attractive because in principle they can drive the reaction without external bias. [1]

First-principles analysis of layered perovskite $\mathbf{Sr}_{n+1}\mathbf{Ti}_n\mathbf{O}_{3n+1}$ ($n = 1, 2, 3$)

Ruddlesden–Popper (RP) compounds have attracted considerable attention as photocatalysts. In particular, $Sr_{n+1}Ti_nO_{3n+1}$ ($n = 1, 2, 3$) has been regarded as a model system for water-splitting because of its chemical stability and tunable band structure. [2] The electronic properties of the layered RP titanate series Sr_2TiO_4 (**214**), $Sr_3Ti_2O_7$ (**327**), and $Sr_4Ti_3O_{10}$ (**4310**) were systematically investigated using first-principles calculations based on density functional theory (DFT).

From the band calculations, we have identified the conduction band minimum (CBM) and valence band maximum (VBM) of the RP titanates and STO and estimated their effective masses (Figure 1). The anisotropy of the effective masses at the CBM and VBM indicates that RP titanates exhibit a higher degree of two-dimensionality than STO, particularly in **214**. Moreover, the pronounced difference between the in-plane and out-of-plane effective masses leads to anisotropic carrier transport: electron carriers preferentially move in the in-plane direction, whereas hole carriers move out of plane. In addition, the chemical-potential phase diagram indicates that **214** has the widest stability region among the RP titanates (Figure 2). Finally, the analysis of the formation energies suggests that **214** is the least likely to form oxygen defects among the RP titanates and STO, and is therefore less susceptible to photocatalytic degradation associated with defect states.

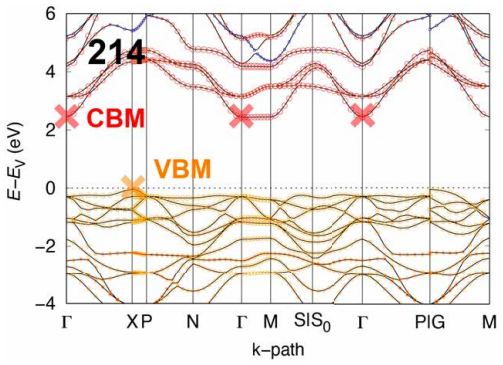


Figure 1: Band structure and CBM/VBM position of **214**. The orbital components are represented by colored circles: Sr 4*d* in blue, Ti 3*d* in red, and O 2*p* in yellow.

Band edge positions for preovskeite oxynitrides $A\mathbf{TaO_2N}$ (*A* = Ba, Sr, Ca)

The design of photocatalysts for visible-light-driven water splitting requires both appropriate band-edge alignment and a sufficiently narrow band gap. Oxynitrides are promising candidates because partial substitution of oxygen by nitrogen raises the valence band maximum (VBM) via N-2*p* states while retaining the chemical stability of oxide frameworks. [3] Here, we examine the band edge positions of $ATaO_2N$ (A=BaSrCa) by DFT calculations and compare them with experimental data.

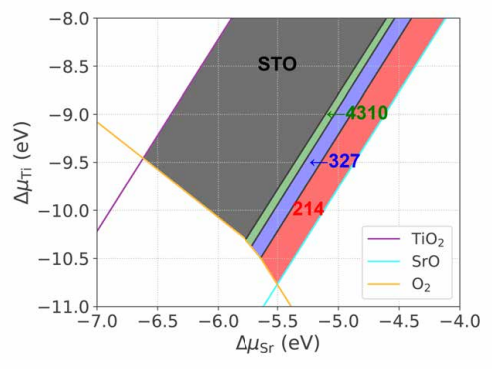


Figure 2: Ternary phase diagram of the chemical potentials. The stable regions for STO and the **214**, **327**, and **4310** phases are highlighted in gray, red, blue, and green, respectively. The purple, cyan, and yellow lines represent the phase boundaries of TiO_2, SrO, and O_2 molecule, respectively.

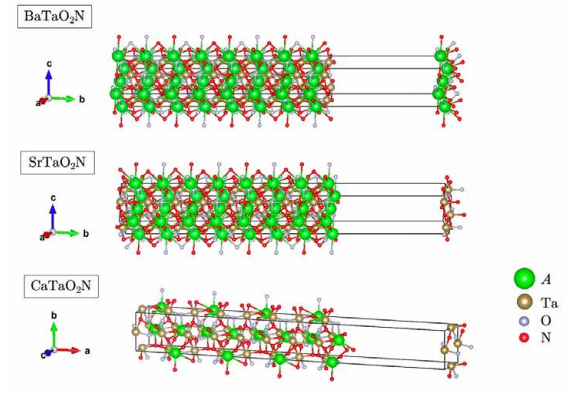


Figure 3: Slab models of *A*TaO2N (*A* = Ba, Sr, Ca).

For the bulk electronic structures of $ATaO_2N$, PBE systematically underestimates the band gaps, whereas HSE06 reproduces both the experimental values and their trend with the A-site cation. The CBM is mainly composed of Ta 5*d* states, while the VBM arises from hybridized O/N 2*p* states, explaining the band-gap narrowing upon nitrogen incorporation. Slab calculations (Figure 3) further show that the VBM and CBM positions depend on the A-site cation through changes in lattice parameters and local bonding. After uniform energy shift correction based on HSE06 by potential alignment, all $ATaO_2N$ compounds satisfy the energetic requirements for visible-light-driven water splitting, although their CBM positions and thus reduction abilities differ appreciably. A direct empirical correction was also tested by aligning the calculated VBM of $BaTaO_2N$ to the experimental value of −6.03 eV reported in Ref. [3], confirming the validity of the relative band-edge trends obtained under identical computational conditions (Figure 4).

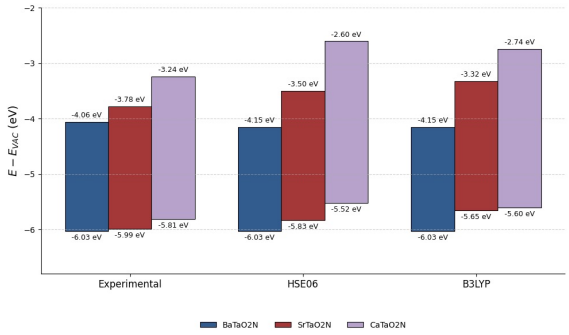


Figure 4: CBM and VBM values for $ATaO_2N$ using uniform energy shift in comparison with experiments.

Calculation conditions

We have performed hybrid (MPI+OpenMP) parallel computing using, where the parallelization over bands and k-points is used by VASP version 6.4.2. [4]

References

[1] K. Nishiguchi, T. Takayama, S. Takasuka, Y. Harashima, M. Fujii, and S. L. Ten-no: J. Phys. Chem. Lett. 2025, 16, 11, 2823–2830.

[2] P. Wang *et. al.*: Nanomaterials **2013**, 15, 20.

[3] S. Balaz *et. al.*: Chem. Mater. 2013, 25, 16, 3337–3343.

[4] G. Kresse *et. al.*: Phys. Rev. B **47**, 558 (1993); Phys. Rev. B **49**, 14251 (1994); Computational Materials Science **6** (1996) 15–50; Phys. Rev. B **54**, 11169 (1996).

Materials discovery for quantum materials: MAX phase and haeckelite systems

Hannes RAEBIGER[1], Mitsuaki KAWAMURA[1], Soungmin BAE[2], Mohammad KHAZAEI[3]

[1)]*Department of Physics,*

Yokohama National University, Hodogaya-ku, Yokohama, Kanagawa 250-8501

[2)] *Institute of Materials Research,*

Tohoku University, Aoba-ku, Sendai, Miyagi 980-0812

[3)] *Department of Physics,*

University of Tehran, North Kargar Avenue, Tehran 14395547, Iran

The discovery of novel quantum materials, including superconductors and systems with emergent electronic properties, is a central objective in condensed matter physics and materials science. A widely adopted computational approach is high-throughput screening, in which large numbers of candidate compounds are generated or collected, and their energetic and mechanical stability is evaluated. Only those systems that are both energetically favorable and mechanically stable are retained for further investigation of their electronic and quantum properties.

This conventional framework has proven highly successful and forms the basis of part of our work. Using first-principles calculations within this approach, we identify new superconducting materials in both MAX phase–derived systems and haeckelite-based compounds. In particular, superconductivity is predicted in o-MAX phase systems and in three-dimensional metallic haeckelite structures, demonstrating that both classes of materials provide fertile ground for quantum materials discovery within the space of energetically and mechanically stable compounds [1,2].

At the same time, conventional screening inherently excludes a large class of materials—those that are mechanically unstable—from consideration. To overcome this limitation, we develop a complementary materials design paradigm, first introduced in Ref. [3], that instead utilizes these unstable systems as starting points. The key idea is to exploit imaginary phonon modes as directional guides in the energy landscape. By following these unstable vibrational modes and relaxing the resulting distorted structures, we obtain new configurations corresponding to local or global energy minima. This instability-driven framework enables access to a previously unexplored region of the materials space and

represents a conceptual shift in materials discovery [3,4].

Applying this approach to MAX phase systems, we discover a series of reconstructed structures that significantly expand their structural landscape. In particular, we identify MAX phase variants with expanded A-layer periodicity, leading to enlarged unit cells and new stacking sequences. These reconstructed phases demonstrate that MAX phases possess a much richer structural diversity than previously recognized, providing additional degrees of freedom for tuning electronic and quantum properties [3,4].

In addition to bulk reconstructions, we identify a wide range of surface reconstructions in MAX phase systems. The predicted surface structures exhibit significant complexity, comparable to that observed in semiconductor surfaces, and arise from the interplay between bulk instability and surface energetics. This is especially relevant for MXene-related materials, where surface structure plays a central role in determining functional properties [4].

Taken together, these results demonstrate that the conventional high-throughput approach and the instability-driven design paradigm are highly complementary. While conventional screening identifies superconducting materials within the stable region of the materials space, the instability-driven approach expands this space by uncovering new reconstructed phases that may serve as future platforms for quantum materials.

References

[1] K. Hamidi et al., Prediction of superconductivity in haeckelite compounds using first-principles calculations, iScience **28**, 113219 (2025).

[2] M. Keivanloo et al., Superconductivity in o-MAX phases, Nanoscale **17**, 5341 (2025).

[3] M. Khazaei et al., Superlattice MAX phases with A-layers reconstructed into 0D-clusters, 1D-chains, and 2D-lattices, J. Phys. Chem. C **127**, 14906 (2023).

[4] M. Khazaei et al., Diverse surface reconstructions in MAX phases, Nanoscale **17**, 24184 (2025).

Hydrogen Atoms Diffusion on Ru(001) Surface

Yiping Chen[1], Kotaro Matsuda[1], Takehiko Sasaki[1],
Bo Thomsen[2], Motoyuki Shiga[2]

1 Department of Complexity Science and Engineering, Graduate School of Frontier Sciences, The University of Tokyo, Kashiwa-no-ha, Kashiwa, Chiba 277-8561

2 Center for Computational Science and e-Systems, Japan Atomic Energy Agency, 178-4-4, Wakashiba, Kashiwa, Chiba , 277-0871

The hydrogen adsorption state on Ru(001) has been extensively studied from the perspectives of surface physics and chemistry. Detailed studies on the diffusion of adsorbed hydrogen atoms by laser-induced thermal desorption (LITD) have been reported by S.M. George et al.[1]. Ru nanoparticles are known to be active in ammonia synthesis, and the behavior of adsorbed hydrogen is important in the ammonia production process. In addition, LITD measurement results have been shown for Ru step surfaces Ru(S)-[15(001)x2(100)], and the diffusion coefficient is smaller than that on Ru(001) surfaces [2]. It is expected that surface diffusion is anisotropic on such step surfaces. Hydrogen diffusion on Ru(001) is a benchmark problem for nuclear quantum effects in surface kinetics. DFT was used to identify stable adsorption sites and representative migration paths, and a neural-network potential (NNP) was trained to reproduce the DFT potential-energy surface (Fig. 1) . Using the NNP, diffusion coefficients were evaluated over a wide temperature range by (i) classical molecular dynamics with mean-squared-displacement analysis and (ii) path-integral approaches combining quantum transition state theory (QTST) and ring-polymer dynamics. The resulting D(T) was compared with laser-induced thermal desorption measurements on Ru(001) and stepped Ru surfaces. Ongoing H/D/T calculations will quantify isotope effects and the sensitivity to the underlying exchange–correlation functional.

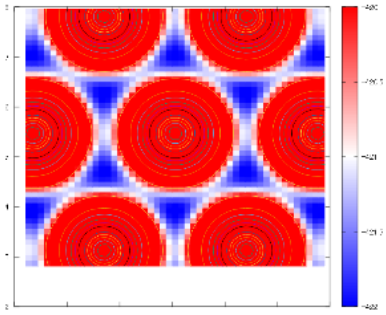


Fig. 1 Contour map of DFT total energy for H/Ru(001).

References

[1] C. H. Mak *et al.*, J. Chem. Phys. **1986**, 85, 1676.

[2] M. V. Arena *et al.*, Surf. Sci. **1995**, 325, 151.

Structures and Stability of Adsorbed Oxygen Species on Pt Nanoparticles

Takehiko SASAKI

Department of Complexity Science and Engineering, Graduate School of Frontier Sciences, The University of Tokyo, Kashiwa-no-ha, Kashiwa, Chiba 277-8561

For the purpose of high-energy resolution fluorescence detected Xray absorption near-edge structure (HERFD-XANES) simulations, structural models for oxygen atoms and hydroxyl groups adsorbed on a platinum truncated octahedron NP, which consists of 586 Pt atoms (corresponding to 2.62 nm diameter close to 2.70 nm particle size (averaged) estimated by TEM) with (111) facets and (100) facets, were obtained by DFT calculations. We used a Pt_{586} truncated octahedron NP as a model structure closest to spheric Pt NPs in MEA Pt/C. In the truncated octahedron model structure the fraction of (111) facets involving edges and corners at the boundary of (111) facets is 91.2 % as shown in Figure 1. The stabilized energies of adsorbed oxygen species on the (100) facets were smaller than those on the (111) facets of Pt truncated octahedron NPs. Hence, in this study we have discussed on the behavior of oxygen species on the (111) facets, edges, and corners.

In order to reduce computational costs for calculating the system consisted of adsorbed oxygen species

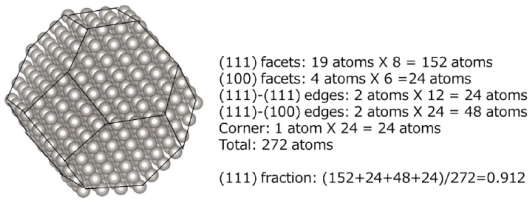


Fig. 1: Pt_{586} truncated octahedron model structure and the numbers of surface atoms at various surface sites.

and Pt_{586} cluster, small Pt clusters consisted of 3-layers, 6-layers and 8-layers, which can reproduce Pt_{586} truncated octahedron NP by applying symmetry operations, were prepared. The adsorption models on the corners, edges and facets of the small Pt clusters were built. Nearest neighbor and second nearest neighbor Pt atoms around adsorbed species were allowed to relax and other Pt atoms were fixed as the bulk Pt crystal. After the structural optimization, symmetry operations were achieved to obtain the 586 Pt truncated octahedron NP with adsorbed oxygen species, namely adsorbed oxygen adatoms and adsorbed hydroxyl groups on edge, corner and terrace sites on Pt NP surfaces as shown in Fig. 2.

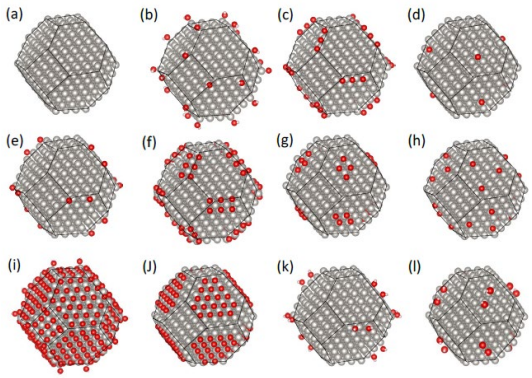


Fig. 2: Model truncated octahedron structures with oxygen-species employed for DFT calculations.

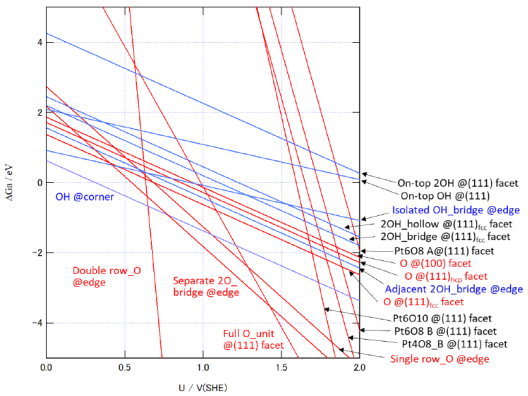


Fig. 3: Potential-dependent stability of adsorbed oxygen species at the corners, edges and facets on Pt NPs calculated by DFT.

DFT calculations were performed using the Vienna ab initio Simulation Package (VASP version 5.4.4). The generalized gradient approximation (GGA) with the exchange correlation functional of Perdew-Burke-Ernzerhof (PBE) was adopted. The projector-augmented wave pseudopotentials (PAW) were used to describe interaction between cores and valence electrons. Cut-off energy for the plane wave basis sets was taken as 400 eV. The unit cells containing Pt cluster and adsorbed species were prepared as mentioned above. The Monkhorst-Pack k-mesh of 3x2x2 was used for the structural optimization calculation. Vibrational frequency calculations were achieved for the Gibbs free energy calculations assuming that all Pt atoms are fixed. Reaction Gibbs free energies of electrochemical processes at 353 K were calculated in the similar way to the previous reports [1,2] to obtain the potential dependence of adsorbed species as shown in Fig. 3. Structural models were used to compute FDMNES simulation for XANES analysis. The potential dependent Pt L_{III} edge XANES data could be successfully reproduced by the linear curve fit on the basis of the potential-dependent stability data (Fig. 3). The whole results were published in 2025 [3].

References

[1] J.K. Norskov et al. , J. Phys. Chem. B **108**, 17886 (2004).

[2] R. Jinnouchi et al., Catal. Today **262**, 100 (2016).

[3] H. Ariga-Miwa et al., ACS Catal. 15, 9856 (2025).

Dopant segregation behavior at grain boundaries in oxide material

Kazutoshi INOUE
Advanced Institute for Materials Research, Tohoku University
Katahira 2-1-1, Aoba, Sendai, Miyagi 980-8577

Wide-bandgap oxides are important materials for insulating and electronic applications. However, their local electronic properties can be significantly affected by lattice defects such as grain boundaries (GBs). MgO, a representative wide-bandgap oxide with a simple rock-salt structure, provides a suitable model system for clarifying how GB atomic structures and dopant segregation modify local electronic states. In particular, rare-earth dopants are expected to interact strongly with MgO GBs because of their large ionic size and different valence states compared to Mg.

In this study, we investigate the atomic and electronic structures of high-angle tilt and twist GBs in MgO using atomistic simulations and first-principles calculations. Possible pristine GB core structures were first explored by molecular dynamics (MD) simulations with a Buckingham-type force field. Simulated annealing was repeatedly performed to identify stable and metastable GB configurations corresponding to local energy minima. For the high-angle tilt GB, two representative low-energy core structures were identified, whereas further analysis is required for the twist GB. First-principles calculations were then carried out for the high-angle tilt GB structures obtained from the MD simulations. We applied the the plane-wave basis projector-augmented wave method included in VASP to screen and determine the stable atomic structure by using the CPU nodes in System B. The generalized gradient approximation was used for the exchange-correlation potentials in the Perdew-Burke-Ernzerhof form, employing an ultrasoft pseudopotential. The GB energy is the interfacial excess free energy calculated by

$$\Delta E = \frac{1}{2A}\left(E_{\mathrm{total}} - N\sigma_i\right),$$

where E_{total} is the total energy of the system including GBs, σ_i is the energy of the unit cell of the bulk crystal, N is the number of unit cells contained in the supercell, and A is the area of the GB. The substitution energies of rare-earth dopants at different GB sites were then evaluated to determine their preferred segregation sites. In addition, the density of states near the GB was calculated to assess the effects of GB structure and dopant incorporation on the electronic properties.

The results indicate that dopant atoms preferentially segregate at specific GB core sites. Dopant substitution can also induce a structural transformation between the two representative GB configurations, suggesting that dopant segregation not only decorates the GB but actively modifies its local structural units. Furthermore, the calculated density of states shows that both the presence of the GB and dopant incorporation reduce the bandgap of MgO [1].

References

[1] Q. Chen, M. Saito, K. Kawahara, A. Nakamura, K. Inoue, Y. Ikuhara, to be submitted (2026).

First-principles study of surface and defect systems for power electronics materials II

Kaori SEINO
Department of Materials Science and Engineering, Kyushu Institute of Technology
1-1 Sensui-cho, Tobata, Kitakyushu, Fukuoka 804-8550

In the field of power electronics, SiC and GaN are considered promising materials of the future beyond silicon, while diamond is expected to surpass both. To date, experiments and computational approaches have been employed to elucidate the mechanisms of surface reconstructions and defect control in crystals, with a view to deepening the fundamental understanding of Si-based semiconductors. However, since SiC, GaN, and diamond exhibit surface reconstructions and crystal structures that differ from those of silicon, research findings and experience obtained from silicon cannot be directly transferred to these materials. In this project, therefore, we investigated (i) defect complexes of Mg impurities in GaN, and (ii) surface structure and properties of wide-bandgap power semiconductor materials. This report is dedicated to an investigation of the former.

Selective doping in GaN by ion implantation is a key technique for GaN power devices, particularly those with a vertical structure. Understanding the atomic diffusion of Mg acceptors as a thermally activated process governed by an energy barrier provides important insights into the device performance. We performed spin-polarized density functional theory (DFT) calculations using the Vienna *Ab initio* Simulation Package (VASP) to investigate Mg diffusion in GaN [1]. Energy barriers were obtained using the climbing-image nudged elastic band (CINEB) method. Our calculations clarify microscopic atomic processes of Mg migration in GaN via the vacancy-mediated mechanism. We identified the microscopic processes involving not only the Mg hopping into a Ga vacancy (V_{Ga}) site but also the subsequent Ga hopping process to the nearby vacant site.

In the CINEB method, the intermediate points along the reaction pathways are treated as a series of *images*, and the atomic structure corresponding to each image must be optimised. In the system B (ohtaka), each of the seven images, based on using a 360-atom supercell, can be assigned to a separate node, enabling parallel CINEB calculations.

We also focused on the fundamental properties of the pair of a substitutional Mg and a Ga vacancy ($\mathrm{Mg_{Ga}}$-V_{Ga}) in GaN, which are the key structures for the vacancy-mediated mechanism of Mg diffusion in GaN. The structural and electronic properties were studied using the Heyd-Scuseria-Ernzerhof (HSE) hybrid functional for $\mathrm{Mg_{Ga}}$-V_{Ga} defect pair as well as an isolated $\mathrm{Mg_{Ga}}$ and an isolated V_{Ga} [2]. A competition between the spin polarization due to localized nitrogen orbitals and the crystal-field splitting of tetrahedral semiconductors is revealed by the present calculations.

References

[1] K. Seino, K. Shiraishi, and A. Oshiyama, Phys. Rev. B **113**, 045201 (2026).

[2] K. Seino, K. Shiraishi, and A. Oshiyama, Jpn. J. Appl. Phys. **64**, 121004 (2025).

First-principles electron theory of strain-induced magnetic switching

Yoshihiro GOHDA

Department of Materials Science and Engineering, Institute of Science Tokyo
J2-22, Nagatsuta-cho 4259, Midori-ku, Yokohama 226-8501, Japan

Switching of magnetic states, in the sense of both the magnetic coupling and the magnetization direction, is of importance in the operation of magnetic devices. One of the promising route for such control is the application of strain [1]. The strain can be imposed by, for example, ferroelectric substrates under applied electric fields [2].

In this project, we demonstrated that the chromium diiodide (CrI_2) monolayer exhibits a strong coupling between lattice geometry and magnetism, allowing for tunable magnetic order as shown in Fig. 1. The in-plane tensile strain drives the phase transition from antiferromagnetic (AFM)-stripe to ferromagnetic (FM) states. In this magnetic phase transition, tensile strain increases the FM $d-p-d$ superexchange mediated by Iodine p-orbitals relative to direct AFM Cr-Cr $d-d$ interaction [3]. In addition, we investigated Janus CrICl and CrIBr monolayers as multiferroic platforms, where broken structural inversion symmetry activates the Dzyaloshinskii-Moriya Interaction (DMI). We found that the DMI in these Janus structures can be tuned by an external electric field.

Similar to CrI_2, an switching of FM-AFM couplings has also been demonstrated for Co/Ru/Co synthetic antiferromagnets, where the experimental behavior of the interlayer exchange coupling was consistent with the first-principles one [4].

Furthermore, magnetocrystalline-anisotropy (MCA) energy dependent on strain has been investigated from first principles: The behavior of the MCA energy of Co_2FeSi depends significantly on the Miller indices of the plane of applied strains [5]. The origin of the MCA modulation can be attributed to energy-band shifts [1].

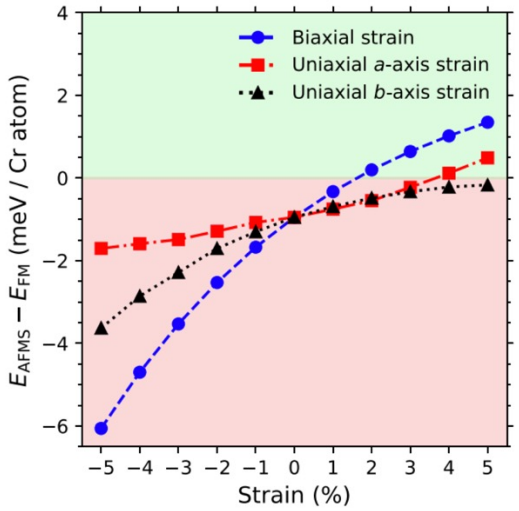


Figure 1: Energy difference between collinear antiferromagnetic-stripe (AFMS) and ferromagnetic (FM) CrI_2 under strain. Reproduced from Ref. [3] ©The Authors.

[1] A.M. Yatmeidhy and Y. Gohda, Sci. Technol. Adv. Mater. **25**, 2391268 (2024).

[2] T. Taniyama, Y. Gohda, K. Hamaya, and T. Kimura, Sci. Technol. Adv. Mater. **25**, 2412970 (2024).

[3] H. Y. Widyandaru and Y. Gohda, npj Spintronics **3**, 34 (2025).

[4] Y. Hisada, S. Komori, K. Imura, C. Shen, Y. Gohda, C.C.I. Ang, W.S. Lew, and T. Taniyama, Adv. Sci. **13**, e17798 (2026).

[5] R. Watarai and Y. Gohda, npj Spintronics **3**, 50 (2025).

Electrochemical reaction analysis using density functional calculation + implicit solvation model 7

Jun Haruyama

Pioneering Research Institute,

RIKEN, 2-1 Hirosawa, Wako, Saitama 351-0198

The Li-ion battery (LIB) has been attracted attention for use in mobile batteries and electric vehicles due to its high energy density. Currently, Li-excess positive electrodes and high-capacity negative electrodes are necessary to overcome the conventional LIB performance. However, the conventional organic electrolytes easily decompose and cannot be used with such electrodes. Recently reported high-concentration electrolytes are promising due to their high durability at both high and low potentials. [1, 2]

In this study, we aim to determine the theoretical electrochemical windows (ECWs) and candidate redox species of the high-concentration electrolytes using FPMD (first principles: FP, molecular dynamics: MD) simulations. A previous study by Ong et al. suggested that the electronic (HOMO and LUMO) levels during FPMD simulations can be used as the approximated values of ECW. [3] The vacuum level outside the solution was used as the reference to align the electronic levels, however, a solution surface cannot be formed for a volatile solvent unlike ionic liquids. Instead of the vacuum level, we introduce a ferrocene molecule (Fc, $FeC_{10}H_{10}$) into the solution and used its time-averaged molecular level as the reference, see Fig. 1 (a). Then, we calculated various kind of electrolyte solutions: 1 M $LiPF_6$ ethylene carbonate (EC): dimethyl carbonate (DMC), LiTFSI and LiFSI salts with acetonitrile (AN) and DMC solvents at low and high concentrations, and some ionic liquids. The calculation cell size was set to adjust the solution density equal to experimental values, and typical cell included about 40–50 molecules as shown in Fig. 1 (a). VASP was used for FPMD simulations. [4]

We obtained the ECWs of ionic liquids referenced by Fc level and compared them with those obtained by the previous study. The results suggest that the Fc reference level works well in these electrolytes.

We obtained the radial pair distribution functions of the mixed solution of 1 M $LiPF_6$ EC/DMC as shown in Fig. 1 (c). The coordination numbers of Li^+ ions were good agreement with previous MD results based on quantum-chemical calculation. [5] Then, we found that the LUMOs during FPMD simulation can be attributed to EC molecules,

which suggests the main component of solid electrolyte interphase (SEI) at a negative electrode comes from the EC decomposition.

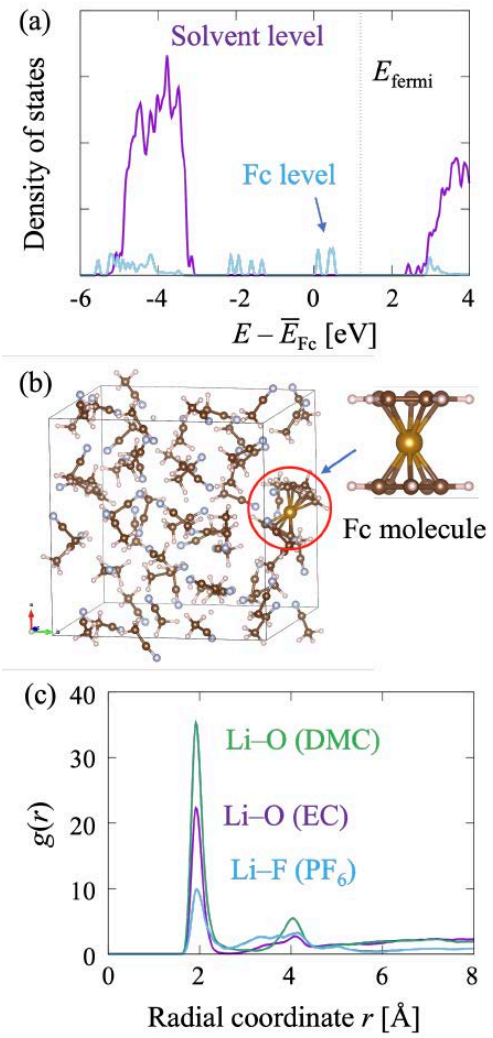


Fig. 1: (a) The density of states of Fc included AN solution. (b) FPMD simulation cell. (c) Radial distribution function $g(r)$.

For the LiFSI DMC solutions, the low-concentrate solution showed a similar ECW compared with that of 1 M $LiPF_6$ EC/DMC. However, the ECW of high-concentrate solution showed an approximately 0.3 V shift to the higher potential side, and the possible oxidation (HOMO) state can be attributed to anion species.

For the AN solution, the pure solvent showed a wide ECW, but the introduction of electrolyte ions shifted the oxidation potential to the lower potential side. The reduction potential of high-concentrate solution was slightly shifted to the higher potential side, which suggests that the high reduction durability for the high-concentrate AN solution [1] cannot be explained by the ECW. In that case, we need to discuss kinetic reasons such as the sacrificial decomposition of anion species. [6] Finally, we need to discuss that the reference Fc level can be used for many kind of solutions in future.

References

[1] Y. Yamada, K. Furukawa, K. Sodeyama, K. Kikuchi, M. Yaegashi, Y. Tateyama, A. Yamada, J. Am. Chem. Soc. **136**, 5039 (2014).

[2] J. Wang, Y. Yamada, K. Sodeyama, C. H. Chiang, Y. Tateyama, and A. Yamada, Nat. Commun. **7**, 12032 (2016).

[3] S. P. Ong, O. Andreussi, Y. Wu, N. Marzari, and G. Ceder, Chem. Mater. **23**, 2979 (2011).

[4] G. Kresse and J. Furthmüller, Phys. Rev. B **54**, 11169 (1996).

[5] O. Borodin and G. D. Smith, J. Phys. Chem. B **113**, 1763 (2009).

[6] K. Sodeyama, Y. Yamada, K. Aikawa, A. Yamada, and Y. Tateyama, J. Phys. Chem. C **118**, 14091 (2014).

Development of an electrolyte database based on automated molecular dynamics simulations

Atsuo YAMADA

Department of Chemical System Engineering,

The University of Tokyo, Bunkyo-ku, Hongo, Tokyo 113-8656

With the expanding application of rechargeable batteries, electrolytes must simultaneously achieve high ionic conductivity, wide electrochemical stability windows, and chemical/thermal stability. As these properties often conflict, efficient exploration of the vast compositional space requires a data-driven approach. However, existing databases provide physicochemical properties of isolated molecules and lack structural/thermodynamic information for electrolyte solutions.

To address this challenge, we systematically generated large-scale structural and physicochemical data for electrolyte solutions using automated high-throughput molecular dynamics simulations (Fig. 1). Specifically, a total of 5,616 compositions were investigated, consisting of combinations of three cations (Li^+, Na^+, K^+), nine anions, twenty-six solvents, and concentrations ranging from 0.5 to 4.0 mol kg^{-1}. For each system, structural and transport properties, including coordination numbers, ionic conductivity, diffusion coefficients, viscosity, and density, were evaluated.

The resulting dataset was organized into the Open Electrolyte Database for Batteries (OEDB, https://oedb.jp). Furthermore, integration with a large language model enables natural language queries to suggest candidate electrolyte compositions and summarize property trends based on user-defined requirements.

References

[1] K. Nakamura, et al., A. Yamada, *npj Comp. Mater.* Accepted, DOI: 10.1038/s41524-026-02093-y (2026).

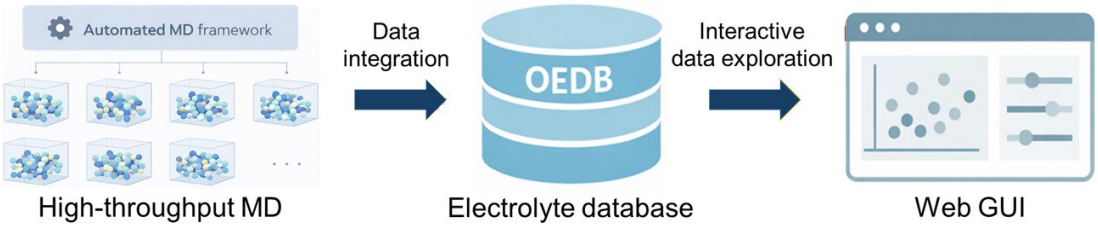


Figure 1 Overview of the workflow employed in this study, including high-throughput molecular dynamics (MD) simulations, construction of the Open Electrolyte Database for Batteries (OEDB), interactive data exploration using a web-based graphical user interface, and use of the database by LLM-based agents.

First-Principles Study of the OER Catalytic Performance of a High-Entropy Oxide with a Stable Atomic Configuration

Haolun LI, Yuta TSUJI

Department of Advanced Analytical Science for Materials and Devices, Faculty of Engineering Sciences,

Kyushu University, Kasuga-koen 6-1, Kasuga, Fukuoka 816-8580

High-entropy oxides (HEOs) have attracted considerable attention because of their promising catalytic activity. In our previous work [1], a stable atomic configuration of a rock-salt type HEO structure, (NiMgCuCoZn)O, was obtained through Bayesian optimization. In this study, the oxygen evolution reaction (OER) catalytic performance of this stable HEO structure was investigated by density functional theory (DFT) calculations using the Vienna Ab initio Simulation Package (VASP).

For many rock-salt transition-metal oxides, the AFM-II configuration is generally considered to be the energetically preferred magnetic ordering. However, because of the complex atomic configurations in HEOs, the most stable spin configuration of the rock-salt type HEOs at room temperature remains unclear. Thus, in this study, two representative spin configurations, ferromagnetic (FM) and type-II antiferromagnetic (AFM-II), were considered for comparison. To investigate the catalytic performance, after optimization of the initial bulk structure, a series of slab models were constructed to identify the most stable surfaces. Then, the most active sites on these surfaces were determined, and the Gibbs free energies of the OER intermediates were calculated.

The most active sites were found to be either Co or Cu atoms in both spin configurations. In all cases, the potential-determining step in the OER was the *OH → *O step, with the largest ΔG among all reaction steps. The average ΔG_{max} of the Co sites was lower than that of the Cu sites, indicating that the Co sites are more favorable for OER catalysis. In addition, the ΔG_{max} values of the Co sites in the FM configuration were lower than those in the AFM-II configuration, suggesting that the FM-ordered HEO structure exhibits better catalytic activity.

References

[1] T. Ueno, and Y. Tsuji, J. Chem. Theory Comput. **21**, 11697 (2025).

Quantum transport theory based on large-scale first-principles electron transport calculations

NOBUHIKO KOBAYASHI
Department of Applied Physics, University of Tsukuba
1-1-1 Tennodai Tsukuba Ibaraki 305-8573

Quantum transport theory based on large-scale first-principles electron transport calculations is important from the viewpoint of materials science and technology. We have developed the nonequilibrium Green's function (NEGF) method and the O(N) time dependent wave-packet diffusion (TD-WPD) method on the basis of the density functional theory (DFT) as techniques for analyzing electronic structure and transport properties. We have also developed methods to predict the crystal structures of organic materials, and have applied the methods to the design of organic semiconductors.

Organic semiconductors have attracted much attention for their applications to flexible, printable, lightweight, and low-cost electronic devices. The organic crystals are assemblies of π-conjugated molecules weakly bonded by van der Waals interactions, and it is difficult to predict the crystal structures. We have developed an efficient method based on DFT to predict the crystal structures of organic semiconductors from molecular structural formulas without using experimental data. We successfully obtained organic crystal structures from the molecular structural formulas. The predicted stable structures agree well with the experimentally observed structures,[1] Furthermore, we developed a method to rapidly predict structures by combining with machine learning.

We investigated charge or spin ordering instabilities in organic semiconductors induced by hole doping via EDLT in low temperature. We calculated phase diagrams against the off-site Coulomb repulsion energy and hole concentration. We elucidated a sufficiently large off-site Coulomb repulsion energy could induce charge ordering instability in the system, which aligns with the experimentally observed unusual temperature dependence of the Hall coefficient as the hole concentration increases.[2]

We calculated the field emission from vertically aligned graphene edges at the apex of the pencil lead. The pencil lead emitter exhibits characteristic emission patterns of the graphene edge, suggesting the presence of the sparsely distributed, vertically aligned graphene edges at the apex of the pencil lead. We showed that the energy spectrum of the emitted electrons exhibits the characteristic lineshape due to the characteristic electronic states of π-bands of graphene [3]

References

[1] S. Hakata, H. Ishii, H. Takaki, T. Okamoto, J. Takeya, N. Kobayashi,
Appl. Phys. Express 17 101001 (2024)

[2] N. Kasuya, T. Furukawa, H. Ishii, N. Kobayashi, K. Hirose, H. Takayanagi, T. Okamoto, S. Watanabe, J. Takeya,
*Nat. Commun.*16, 3214 (2025)

[3] T. Igari, R. Tsuruta, Y. Nishiyama, M. Adachi, T. Myojin, K. Asanagi, M. Sasaki, N. Kobayashi, Y. Yamada
Sci. Rep. 15, 27456 (2025)

Ab initio molecular-dynamics study on self-healing in cement-based hydrated minerals

Ikumi KANEMASU and Satoshi OHMURA

Graduate School of Science and Engineering,

Division of Informatics and Computation, Premier Institute for Advanced Studies,

Ehime University, Matsuyama, Ehime 790-8577, JAPAN

Concrete is one of the most widely used construction materials and plays a central role in sustainable development and carbon neutrality. To improve the mechanical properties of concrete, it is essential to understand the properties of cement hydration products. In particular, the mechanical response of calcium silicate hydrates (C–S–H) is a key factor governing the stability of cementitious materials. Tobermorite, a crystalline analog of the C–S–H phase, serves as an ideal model system for investigating pressure-dependent mechanical properties at the atomic and molecular scales. In this study, we investigated the deformation behavior of tobermorite under tensile and compressive loading using molecular dynamics simulations based on density functional theory and a machine-learning interatomic potential.

The results of the tensile simulations indicate that stretching tobermorite along the stacking direction causes the CaO layers to break, resulting in delamination of layers. On the other hand, the stress-strain curve obtained from the compression simulation indicates that the stress initially increased linearly, followed by a sudden decrease and subsequent increase with the application of further strain. This behavior indicates the occurrence of a stress recovery phenomenon.

To understand the atomic origin of the stress recovery under compression, we investigated the time evolution of the atomic configuration during the compression. Before compression, the interlayer oxygen atoms aligned parallel to the direction of compression. Consequently, compressive deformation induced resistance owing to repulsive interactions between the oxygen atoms in the upper and lower layers. Under the influence of this repulsive force, the Si–O chains slipped, leading to the rearrangement of the silicon and oxygen atoms. Under further compression, new Si–O bonds that penetrated and bridged the Ca–O layers were formed. This is the origin of stress recovery of tobermorite.

References

[1] I Kanemasu and S. Ohmura, *High Pressure Research*, 1–9 (2026)

Ab Initio Molecular Dynamics Study of the Structural Instability of Ettringite under Dehydration and Rehydration Conditions

Tomohiro SASAOKA, Ikumi KANEMASU and Satoshi OHMURA

1) Department of Civil and Environmental Engineering Hiroshima Institute of Technology, Hiroshima, Hiroshima 731-5193

2) Graduate School of Science and Engineering, Ehime University, Matsuyama, 790-8577,

3) Division of Informatics and Computation, Premier Institute for Advanced Studies, Ehime University, Matsuyama, Ehime 790-8577,

Ettringite, a hydration product of Portland cement, is known to play an important role in the development of early strength in cement paste. It has a hexagonal structure and forms needle-like crystals. Ettringite undergoes dehydration upon heating and rehydrates upon cooling in the presence of water. This dehydration–rehydration reaction is reversible and enables the material to absorb and release thermal energy. For this reason, ettringite has attracted attention as a thermochemical energy storage material. To evaluate its instability at high temperatures, we performed *ab initio* molecular dynamics simulations.

The simulation results indicate that sulfate ions are linked through hydrogen bonds mediated by water molecules, and that the S–S correlation becomes weaker with increasing temperature. We also investigated dehydrated ettringite by means of machine-learning molecular dynamics simulations. The simulations show that the S–O distance in the dehydrated system is shorter than that in the hydrated system. This result is consistent with experimental observations.

.

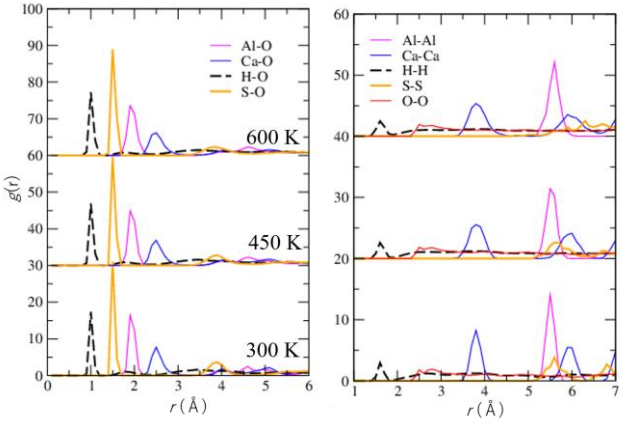


Fig. 1. Temperature dependence of $g(r)$ of ettringite.

References

[1] K. Nomura, *et al.*, The Journal of Physical Chemistry Letters **16**, 6637-6644 (2025).

Thermodynamics of disordered crystalline systems considering charge and spin ordering

Shusuke KASAMATSU

Academic Assembly (Faculty of Science),

Yamagata University, Kojirakawa, Yamagata-shi, Yamagata 990-8560

When first-principles calculations based on the DFT+U method are applied to transition-metal oxides, the electronic state is often trapped in local minima corresponding to various charge and spin configurations, preventing convergence to the true ground-state solution. This can often lead to qualitatively wrong energies, which, in turn, would lead to completely wrong understanding of the thermodynamics of the material. To address this issue, we implemented in the abICS framework [1] a *local perturbation* + *relaxation* scheme, in which transition-metal ions in the structure are randomly selected, locally distorted, and the electronic structure is subsequently re-optimized in an iterative manner. VASP code was used for the DFT+U calculation part. We validated the effectiveness of this approach using benchmark tests with known "correct" solutions: (i) the antiferromagnetic ordering in NiO, (ii) the Mn^{3+}/Mn^{4+} charge ordering in $LiMn_2O_4$, and (iii) the optimization of polaron configurations in oxygen-deficient TiO_2, obtaining physically reasonable results in all cases (the $LiMn_2O_4$ example is given in Fig. 1). Furthermore, applying the present method to the lithium-ion battery cathode material $LiNi_{1/3}Mn_{1/3}Co_{1/3}O_2$, we obtained an electronic configuration whose energy is lower by as much as 1 eV compared to that obtained via conventional structural optimization based on standard first-principles calculations.

These results clearly demonstrate that, for transition-metal complex oxides with disordered elemental distributions or defects, conventional structural optimization alone is insufficient for accurate thermodynamic calculations, and explicit optimization of electronic configurations, as performed in this study, is essential.

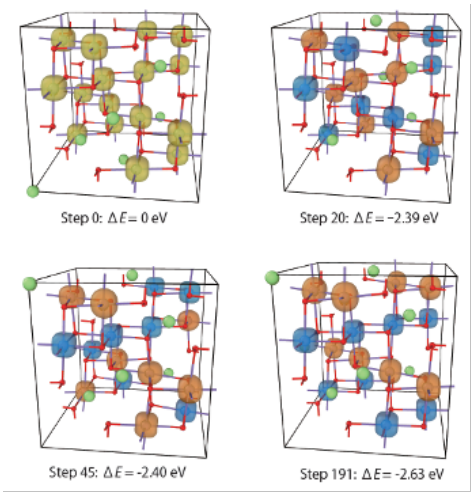


Fig. 1: Optimization of charge ordering in $LiMn_2O_4$.

References

[1] https://www.pasums.issp.u-tokyo.ac.jp/abics

First-Principles Molecular-Dynamics Study of Structural and Electronic Properties of Disordered Materials under Extreme Conditions

Fuyuki SHIMOJO

Institute for Solid State Physics,

Department of Physics, Kumamoto University, Kumamoto 860-8555

Computer simulations are essential for studying the structural and dynamic properties of disordered materials, which lack the long-range order found in crystals. Using first-principles molecular dynamics (FPMD) simulations, we have investigated pressure-induced structural transformation in glassy covalent materials [1], and the intermolecular correlations in molecular liquids [2].

While FPMD simulations are sufficiently accurate to reproduce a wide range of material properties, they are computationally expensive. In contrast, machine-learning interatomic potentials (MLIPs) based on artificial neural networks offer much higher efficiency with FPMD accuracy. In this study, we have applied robust MLIPs developed for highly covalent materials [3] to silica glass and liquid lactic acid.

To elucidate the microscopic mechanism of permanent densification in silica glass, we have investigated the decompression process from 60 to 0 GPa at room temperature using MLIPs for a system containing about 250,000 atoms. We confirmed that the transformation from sixfold- to fourfold-coordinated structures occurs most significantly at 14 GPa, consistent with the result obtained for the 30,000-atom system. A remarkable finding is that a peak in the static structure factor appears at a small wave number of about k = 0.1 Å^{-1}, which has never been reported in either experimental or theoretical studies. This result indicates the existence of density fluctuations on length scales exceeding 60 Å.

To clarify the intermediate-range intermolecular correlations in liquid lactic acid, we have employed MLIPs for systems containing about 24,000 atoms. We found that the number of molecular dimers differs between liquid racemic lactic acid and liquid L-lactic acid, which may be related to the difference in their melting temperatures.

References

[1] E. Ryuo, D. Wakabayashi, A. Koura, and F. Shimojo, Phys. Rev. B **96**, 054206 (2017).

[2] K. Ito, H. Shimakura, S. Tahara, K. Ohara *et al*., J. Phys. Soc. Jpn. **94**, 044604 (2025).

[3] D. Wakabayashi, K. Shimamura, A. Koura, F. Shimojo, J. Phys. Soc. Jpn. **92**, 074002 (2023).

HPC-based fusion of simulation, experiment analysis and data driven science

Takeo Hoshi[1,2]

[1] *National Institute for Fusion Science,*

322-6 Oroshi-cho, Toki city, Gifu Prefecture, 509-5292, Japan.

[2]*Interfaculty Initiative in Information Studies, The University of Tokyo, 7-3-1 Hongo, Bunkyo-ku, Tokyo 113-8654, Japan*

The HPC-based integration of simulation, experiment analysis and data driven science was performed among material science and fusion science. The research was carried out mainly using our open-source software Open Data Analysis Tool for Science and Engineering (ODAT-SE), which was developed by the PASUMS project in FY2024 as a major upgrade of 2DMAT [1]. ODAT-SE (2DMAT) was developed for the data analysis of advanced experimental measurements and offers five analysis methods: (i) grid search, (ii) Nelder-Mead optimization, (iii) Bayesian optimization, (iv) replica exchange Monte Carlo method, and (v) population-annealing Monte Carlo method. The parallel computation with ODAT-SE was carried out on the ISSP supercomputers and other supercomputers such as Fugaku.

At this year, we have improved the ODAT-SE for general applicability to measurement informatics by separating codes of forward models (emulation or simulation of experimental measurement) from the ODAT-SE code.

As an application study, we used the improved ODAT-SE code to calculate incoherent Thomson scattering spectra in high temperature plasmas. [3] The basic idea is to treat the entire scattering process as the superposition of individual photon-electron interactions. We introduce macro-particles, referred from particle-in-cell simulations, to reduce the computational cost, and obtain scattered spectra within a reasonable computational time. The simulated spectra show good agreement with both analytical and numerical results, demonstrating that the present analysis method can reliably reproduce incoherent Thomson scattering spectra.

[1] Y. Motoyama *et al*., Comput. Phys. Commun. 280, 108465 (2022).

[2] https://www.pasums.issp.u-tokyo.ac.jp/odat-se/

[3] K. Sakai *et al.*, JINST 21, C01002 (2026).

Electron excitation induced phase transformation of quantum materials

Koichi KUSAKABE
Graduate School of Science, University of Hyogo
Kouto, Kamigori-cho, Ako-gun, Hyogo 678-1297

We analyzed the photo-induced phase transition phenomenon in quantum materials using density functional theory calculations based on the variational principle for excited states. Wannier orbital analysis was performed on the stable crystal structure of (EDO-TTF)$_2$PF$_6$, revealing that the electron occupation of antibonding orbitals appearing in the molecular pair forming the CDW ground state is the origin of local strain generation.[1] We derived a picture in which reducing the number of electrons occupying this antibonding orbital through photoexcitation leads to strain relaxation in the insulating CDW structure, ultimately resulting in metallization.

Based on phenalenyl tesselation molecules (PTMs) designed by our group, we have developed a design method for poly-PTMs, which form a super-honeycomb structure of the zero modes. By controlling the connection order between adjacent PTMs, it became possible to design Dirac electron systems with systematically altered Fermi velocities.[2] We then expanded our research to the design of electronic devices based on this material structure.

The deaggregation mechanism of amyloid-β may involve the formation of a reaction pathway that stabilizes degradation reaction intermediates due to a unique steric hindrance effect. We set up a parallel stacking model of two molecules and estimated the activation barrier of the molecular dissociation pathway triggered by structural deformation to a twisted molecular structure.[3] Based on this reaction pathway, we discussed the deaggregation from the quasi-one-dimensional microcrystal end faces.

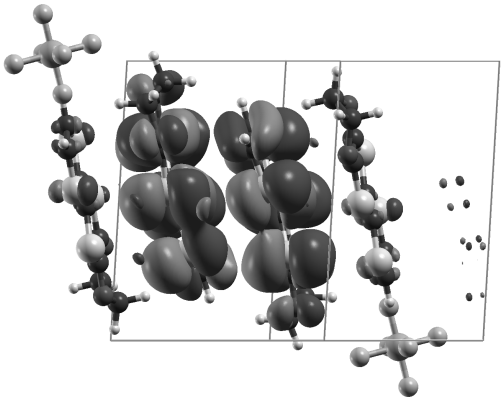


Figure 1: The intermolecular anti-bonding Wannier orbital appearing in the valence band of (EDO-TTF)$_2$PF$_6$.

References

[1] K. Fukumoto, K. Onda, T. Tanaka, K. Kusakabe, E. Pyatenko, H. Yamochi, S. Adachi, S. Koshihara, preprint, submitted to Phys. Rev. Res.

[2] N. Morishita, K. Komatsu, M. Kitatani, and K. Kusakabe, Physical Review B **111**, 235117 (2025).

[3] Y. Oishi, M. Kitatani, K. Nakajima, H. Ogi, and K. Kusakabe, RSC Advances, **15**, 42395 (2025).

Study on physical properties of structural elementary excitations at solid surfaces and interfaces

Hiroyuki KAGESHIMA
Graduate School of Natural Science and Technology, Shimane University
1060 Nishi-Kawatsucho, Matsue, Shimane 690-8504

In this project, we have been focused on physical properties of structural elementary excitations, such as point defects and precursors, of semiconductor surfaces and interfaces. In this year, we have focused on the physical properties of excess Si transport in Si oxide growing on Si(100) [1, 2, 3, 4]. The calculations were performed based on the first-principles calculation. Program package PHASE/0 was employed [5].

In the Si thermal oxidation process, structural elementary excitations, namely 'excess Si's', released from the interface toward the Si oxide film play a significant role. Although the generation of this released Si's originates from compressive stress at the interface, it is essential for providing a consistent explanation of phenomena such as the initial enhanced oxidation and PADOX.

We have used a quartz interface model up to now because quartz can be formed by oxidizing Si and then releasing the Si appropriately to relieve strain. Roughly speaking, oxidizing Si simply involves inserting O into the Si-Si bonds; however, this results in the formation of an extremely dense cristobalite-like structure that requires a 2.25-times volume expansion to relieve strain. The quartz interface model was developed to account for the Si release required to alleviate this high density.

We have also shown that we must use the quartz interfacial model to reproduce the barrier heights of interfacial reactions observed in experiments. Since quartz is expected to maintain a stable structure even at high temperatures and under pressure, it is reasonable to assume that such layers exist at the interface during the process of structural relaxation.

On the other hand, we have shown that we must use the cristobalite model to reproduce the experimental values for the barrier height of O_2 diffusion in the oxide film. This differs from the quartz-like interfacial layer. Although β-cristobalite has a lower density of 2.21 g/cm^3 compared to β-quartz's 2.54 g/cm^3, this is consistent with the idea that cristobalite forms in regions slightly removed from the interface due to further structural relaxation from quartz. In fact, the Deal-Grove theory cannot be reproduced unless the quartz layer at the interface has a constant thickness, regardless of the thickness of the oxide film. In other words, it can be assumed that the Si thermal oxide film consists of at least two layers: a quartz-like high-density interface layer and a cristobalite-like upper oxide layer.

Just as removing excess Si from cristobalite produces quartz, removing excess Si from quartz causes it to transform into cristobalite. Based on various experiments, the density of the upper oxide layer is estimated to be 2.2 g/cm^3, which indeed matches the density of cristobalite. Therefore, it is consistent to assume that further Si is released from the quartz-like high-density interfacial layer, resulting in strain relaxation and the formation of a cristobalite-like upper oxide layer. Incidentally, the thickness of the high-density in-

terfacial layer is reported to be approximately 1 nm, and the Si oxide layer is reported to exhibit cristobalite-like order on average.

Based on these observations, we have successfully developed a model of the Si thermal oxide film interface consisting of two layers: a quartz-like interfacial high-density layer and a cristobalite-like upper relaxed oxide layer (Fig. 1). Since there are no dangling bonds anywhere and the structure consists of a seamless network of only Si-Si and Si-O-Si bonds, there are no interface defects. This contrasts with the situation where Si dangling bonds invariably appear at the interface when structurally relaxed cristobalite is directly bonded to Si.

Next, using this two-layer oxide film model, we investigated the transport pathways of excess Si within the oxide film and the associated energy changes via first-principles calculations. In the upper cristobalite layer, as in quartz, both the tetrahedral and dihedral Si structures become metastable. Furthermore, unlike in quartz, the kick-out mechanism – where Si atoms are transported via a domino effect – does not operate in cristobalite; instead, the deformation step of the dihedral Si plays a crucial role, resulting in the characteristic continuous transport of the same Si atom.

The barrier height in the upper cristobalite layer was 5.38 eV, which agreed well with the experimental value of 5.13 eV. The barrier height in the quartz layer was 5.61 eV, which is higher than that in the cristobalite layer. This difference is thought to be due to the fact that the kick-out mechanism does not operate in cristobalite. Furthermore, the cristobalite surface is approximately 1.92 eV more stable than the initial structure, indicating that Si emission toward the oxide film is indeed energetically favorable. Furthermore, the boundary between cristobalite and quartz is also stable by about 1.44 eV; this implies that Si released at the interface precipitates at the boundary, suggesting that the $L_1 \sim 1$ nm reported by Massoud et al. for the initial enhanced oxidation phenomenon is closely related to the thickness of the high-density layer at the interface within the thermally oxidized film.

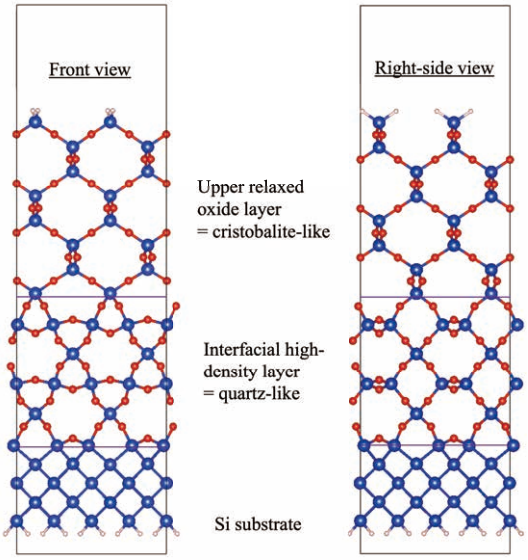


Figure 1: Schematic picture of the atomic model of the Si thermal oxide film interface consisting of two layers with a quartz-like interfacial high-density layer and a cristobalite-like upper relaxed oxide layer.

References

[1] H. Kageshima, T. Akiyama, and K. Shiraishi, J. Phys. Soc. Jpn. 94 (2025) 074707 (4 pages).

[2] H. Kageshima, T. Akiyama, and K. Shiraishi, e-J. Surf. Sci. Nanotechnol. 23 (2025) 306 (8 pages).

[3] H. Kageshima, I. Seo, T. Akiyama, and K. Shiraishi, Jpn. J. Appl. Phys. 65 (2026) 03SP18 (10 pages).

[4] H. Kageshima, I. Seo, T. Akiyama, K. Shiraishi, Mater. Sci. Semicond. Process. 209 (2026) 110582 (8 pages).

[5] https://azuma.nims.go.jp

Effects of anomalous chemical bonding and local structures on thermal transport and thermoelectric properties

Naoki SATO

Research Center for Materials Nanoarchitectonics (MANA),

National Institute for Materials Science (NIMS), 1-1 Namiki, Tsukuba, Ibaraki 305-0044

For the development of high-performance thermoelectric power generation and cooling materials, it is essential to explore classes of materials with low lattice thermal conductivity and to elucidate their microscopic heat transport mechanisms. The factors governing lattice thermal conductivity can be broadly classified into two categories: intrinsic factors, such as chemical composition and crystal structure, and extrinsic factors, such as lattice defects and grain boundaries. Establishing methods to control both types of factors is highly beneficial for the systematic discovery and design of low lattice thermal conductivity materials. In this study, we focused on chemical bonding and local structural motifs in materials, which are closely related to both intrinsic and extrinsic factors. By clarifying specific forms of bonding and local structure that can strongly influence thermal transport and thermoelectric properties, we aimed to establish useful design principles for realizing high-performance thermoelectric materials.

We developed a script to define cation-centered coordination polyhedra in crystal structures and to automatically calculate the distortion index (DI) proposed by Baur [1]. Using this script, we ranked materials in the Materials Project database according to their DI values. For the top 30 compounds in this ranking, we performed phonon calculations and calculations of thermal transport properties based on density functional theory (DFT). The DFT calculations were carried out using VASP [2], while the calculations of harmonic and anharmonic interatomic force constants, as well as lattice thermal conductivity, were performed using ALAMODE [3]. Chemical bonding analyses were conducted using LOBSTER [4].

Most of the materials containing markedly distorted coordination polyhedra with DI > 0.20 exhibited anisotropic crystal structures, and pronounced anisotropy was also observed in their lattice thermal conductivity. Among them, several mixed-anion compounds with complex layered structures, such as Sillén–Aurivillius-type layered perovskites, were predicted to exhibit extremely low lattice thermal conductivities below 0.10 W m^{-1} K^{-1}. The microscopic origins of these ultralow lattice thermal conductivities were identified as rattling-like anharmonic vibrations of off-

centered cations at the centers of highly distorted coordination polyhedra, highly localized phonon modes, and a large scattering phase space arising from bonding heterogeneity. These results demonstrate that focusing on the distortion index enables efficient screening of materials with low lattice thermal conductivity and provides useful guidelines for the discovery of novel thermoelectric and thermal-insulation materials.

References

[1] W.H. Baur, Acta Crystallogr. B **30**, 1195–1215 (1974).

[2] G. Kresse and J. Hafner, Phys. Rev. B **48**, 13115 (1993).

[3] T. Tadano et al., J. Phys.: Condens. Matter **26**, 225402 (2014).

[4] S. Maintz et al., J. Comput. Chem. **37**, 1030–1035 (2016).

Structure and properties of Fe-Pd-In and Pt-based nanoalloys from Ab-initio research

Yasutomi TATETSU

Meio University, Biimata, Nago, Okinawa 905-8585

The development of novel ordered alloy nanoparticles relies on controlling atomic arrangements at the nanoscale. In this project, we investigated the formation mechanisms and structural properties of ternary alloy systems, specifically focusing on $Z3$-type Fe–Pd–In and $L1_0$-type Pt-based alloys. We explored how inter-element miscibility and chemical ordering can be manipulated to stabilize unexplored crystal phases. All first-principles calculations were performed using the OpenMX code [1].

We first explored the kinetic aspects of $Z3$-type phase formation in the Fe–Pd–In system by calculating atomic diffusion barriers [2]. Experimental results indicated that the formation temperature of the $Z3$ structure depends significantly on the initial precursor (e.g., $FePd_3$:In vs. $PdIn_x$:Fe). Our calculation results using Matlantis [3] and DFT clarified that this difference originates from the varying activation energy barriers of atomic diffusion, which are governed by the inter-element miscibility between Fe, Pd, and In. Specifically, the repulsion between Fe and In atoms creates high energy barriers along certain diffusion paths, dictating the non-equilibrium process of phase transition. These findings suggest that diffusion pathway design is essential for the synthesis of complex intermetallic nanoparticles.

Next, we investigated the effect of Zinc (Zn) addition on the ordering and catalytic performance of $L1_0$-type Pt-based alloys for the oxygen reduction reaction (ORR) [4]. The calculations demonstrated that Zn effectively lowers the disorder-to-order transition temperature, allowing for the formation of highly ordered $L1_0$ phases at lower temperatures. This mechanism is crucial for maintaining a small particle size while achieving a high degree of chemical order. Furthermore, we showed that the surface strain induced by Zn–Pt coordination optimizes the adsorption energy of oxygen-containing species, thereby enhancing the ORR activity and durability.

References

[1] T. Ozaki, *Phys. Rev. B*, **67**, 155108 (2003); http://www.openmx-square.org

[2] K. Matsumoto, *et. al.*, *Chem. Sci.*, **16**, 18705-18712 (2025).

[3] S. Takamoto, *et al*., Nat Commun 13, 2991 (2022); https://matlantis.com/

[4] W. Tian, *et. al.*, *J. Mater. Chem. A*, **14**, 7552-7562 (2026).

Materials design for interfacial spin-orbitronics

Kohji NAKAMURA

Graduate School of Engineering, Mie University, Tsu Mie 5148507

Search of materials with desired magnetic properties is an important issue in the field of spintronics. Two examples are presented related this proposal by using full-potential linearized augmented plane-wave (FLAPW) method.[1]

Rashba effect at magnetic tunnel junction interface Fe/MgO: At the Fe/MgO interface in magnetic tunnel junctions (MTJs), a sharp electrostatic potential gradient results in the breaking of inversion symmetry of the system and gives rise to the Rashba-type spin–orbit coupling. Based on FLAPW method, this coupling is found to govern voltage-controlled magnetic anisotropy (VCMA) of MgO-based MTJs. The Rashba splitting, arising from the asymmetric character of wavefunction along the out-of-plane direction, is driven by orbital admixture between the intra-atomic *d* and *p* orbitals at the interfacial Fe near the Fermi energy, together with hybridization with O *p* orbitals. The study further predicts that interfacial modification by AlN/MgO and LiF/MgO, enhancing the VCMA coefficient by 60% for the former, while reducing 15% for the latter than that of the pristine Fe/MgO model.

Magnon in antiferromagnetic insulator NiO: Magnetic interactions in an antiferromagnet govern the spin moment carried by magnons and the strength of multimagnon interactions that lead to magnetization relaxation. A numerical method to generate a four-magnon interactions Hamiltonian by fourth-rank tensor was here developed, and applied to an antiferromagnetic insulator NiO where magnetic dipolar interactions (MDIs) have non-negligible effects on the magnon states. First, we confirmed the suppressed magnon spin moment of two magnon modes, α and β modes, owing to non-spin-conserving interactions of the MDIs. Second, by expressing the four-magnon scattering probability in the fourth-rank tensor form, we found that the low magnon decay rates of both magnon modes are mainly caused by the suppressed magnon spin moment.

References

[1] K. Nakamura et.al., Phys. Rev. B **67**, 014420 (2003).

Theoretical Study Aiming at Novel Renewable Energy Materials Using First-Principles Calculations

Azusa MURAOKA

Department of Mathematics, Physics and Computer Science,

Japan Women's University, 2-8-1, Mejirodai, Bunkyo-ku, Tokyo 112-8681

Perovskite solar cells are promising next-generation photovoltaic materials because of their high-power conversion efficiency and low-cost fabrication [1]. However, Pb-based perovskites raise toxicity concerns [2]. Sn-based perovskites are attractive Pb-free alternatives, but their performance and stability are limited by Sn(II) oxidation to Sn(IV), self-p-doping, and defects such as Sn vacancies [3]. In this study, DFT calculations were used to investigate Sn single perovskites, $FASnI_3$ and $MASnI_3$, and Sn/Ge double perovskites, FA_2SnGeI_6 and MA_2SnGeI_6.

The ISSP Supercomputer System was used mainly for parallel first-principles calculations with VASP at the PBE-D3 level [4,5]. The computational resources were used to perform structural optimizations, electronic-structure calculations, and a large number of defect calculations using 2×2×2 supercells for the four target perovskite systems.

The calculated band gaps of $FASnI_3$, $MASnI_3$, FA_2SnGeI_6, and MA_2SnGeI_6 were 0.60, 0.70, 0.57, and 0.89 eV, respectively, and all were direct-gap semiconductors. The valence-band edge was mainly composed of iodine p orbitals, while Ge contributions became important at the conduction-band edge in the double perovskites, especially in FA_2SnGeI_6. The effective-mass analysis showed that FA-based systems have more favorable carrier transport than MA-based systems. In addition, partial substitution of Sn with Ge balanced the electron and hole effective masses while maintaining strong optical absorption, suggesting improved carrier transport without loss of light-harvesting ability. Chemical-potential analysis showed that iodine-rich conditions promote formation of SnI_4, corresponding to oxidation from Sn(II) to Sn(IV). This explains the intrinsic instability of Sn-based perovskites under iodine-rich or oxidative environments. $FASnI_3$ showed a narrower stability region than $MASnI_3$, indicating that FA-based tin perovskites require careful control of growth conditions. For the Sn/Ge double perovskites, the chemical-potential ranges were estimated from overlapping Sn and Ge single-perovskite stability regions.

As shown in Figure 1, defect formation strongly depends on growth conditions. Under Sn-poor/I-rich conditions, acceptor-type defects

such as I_{Sn} and V_{Sn} show low formation energies. These defects are related to tin loss and Sn oxidation and can promote self-p-doping and carrier trapping. In contrast, Sn-rich/I-poor conditions increase their formation energies, reducing stable in-gap trap levels. Thus, chemical-environment control is essential for improving defect tolerance.

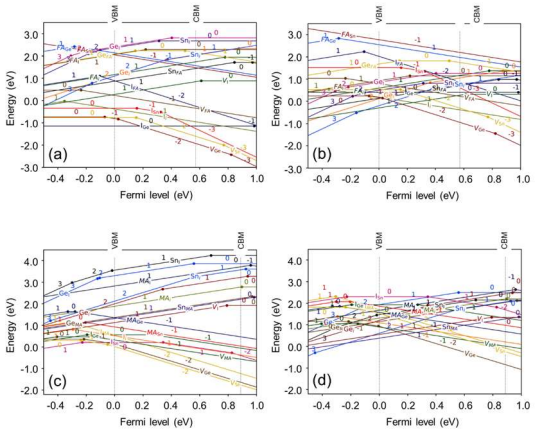


Fig 1: Defect formation energies of Sn/Ge double perovskites calculated using the PBE-D3 level: FA_2SnGeI_6 under (a) Sn-poor/I-rich and (b) Sn-rich/I-poor conditions, and MA_2SnGeI_6 under (c) Sn-poor/I-rich and (d) Sn-rich/I-poor conditions.

Across all four compositions, I_{Sn} and V_{Sn} were the dominant low-energy defects. In $FASnI_3$, stable in-gap defect levels appeared under Sn-poor/I-rich conditions, whereas $MASnI_3$ showed no thermodynamically stable in-gap levels within the examined limits. The Sn/Ge double perovskites also showed Sn-related defect levels under Sn-poor/I-rich conditions. HSE06 calculations confirmed the same qualitative trend as PBE-D3: I_{Sn} remained the lowest-energy defect, followed by V_{Sn}.

Overall, by using the ISSP Supercomputer System to complete many independent supercell defect calculations and selected hybrid-functional calculations, this study showed that low-energy tin-loss defects, especially I_{Sn} and V_{Sn}, are the microscopic origin of poor stability in Sn-based perovskites. Ge alloying improves carrier-transport balance while maintaining strong absorption, but Sn-related defects remain important. Therefore, combining Sn/Ge alloying with Sn-rich and I-poor growth conditions is a promising strategy to suppress deep traps, mitigate Sn oxidation, and improve the defect tolerance of Pb-free perovskite solar-cell absorbers.

References

[1] A. K. Jena, A. Kulkarni and T. Miyasaka, Chem. Rev. **119**, 3036 (2019).

[2] J. Li, H. L. Cao, H. L, W. B. Jiao, Q. Wang, M. Wei, I. Cantone, J. Lü and A. Abate, Nat. Commun. **11**, 310 (2020)

[3] D. Meggiolaro, D. Ricciarelli, and A. A. Alasmari, J. Phys. Chem. Lett. **11**, 3546 (2020).

[4] Kresse, G.; Furthmüller, J. Phys. Rev. B. **54**, 11169 (1996).

[5] J. P. Perdew, K. Burke, M. Ernzerhof, Phys. Rev. Lett. **77**, 3865 (1996).

Microscopic Structure and Proton Dynamics at Methanol/CeO_2 Interfaces

Akira NAKAYAMA
Department of Chemical System Engineering,
The University of Tokyo, Tokyo 113-8656, JAPAN

1. Introduction

Interfaces between metal oxides and alcohols are central to heterogeneous catalysis, including CO_2 conversion reactions over CeO_2. At such interfaces, alcohol molecules can undergo molecular and dissociative adsorption, and the resulting methoxy and hydroxyl species participate in proton-transfer processes. Because these reactions involve bond breaking and formation in a fluctuating liquid environment, conventional force fields are not sufficient. In this study, we constructed neural network potentials (NNPs) trained on density functional theory (DFT) data and performed nanosecond-scale molecular dynamics (NNP-MD) simulations of liquid methanol on CeO_2(111) and CeO_2(110) surfaces.

2. Results and Discussion

The NNPs were trained using DFT-MD data generated with CP2K and DeePMD-kit, and production NNP-MD simulations were carried out with LAMMPS at 300 K for 5 ns using large *p*(8×8) surface models. The simulations revealed clear facet-dependent adsorption equilibria. On CeO_2(111), methanol formed a well-ordered interfacial monolayer. Approximately 79% of the surface Ce sites were coordinated by methanol-derived species, while only 24% were coordinated by dissociated methoxy species, even though single-molecule DFT adsorption energies favor dissociation. This indicates that collective hydrogen-bonding interactions in the dense adlayer stabilize molecular adsorption. In contrast, CeO_2(110) showed weaker interfacial ordering and a larger degree of dissociation, with about 60% of surface Ce sites coordinated by methoxy species and 47% by molecular methanol.

Frequent proton hopping events were observed at both interfaces. The dominant pathway was direct adlayer proton transfer between adsorbed methanol and methoxy species, whereas solvent-assisted pathways involving additional methanol molecules were much less frequent. On CeO_2(110), proton hopping exhibited strong directional anisotropy reflecting the surface geometry. These results demonstrate that the surface facet and the collective structure of the adsorbed methanol layer jointly control dissociation equilibria and proton mobility at alcohol/CeO_2 interfaces. This work provides microscopic insight relevant to CeO_2-catalyzed alcohol activation and CO_2 conversion reactions.

Software used

CP2K was used for DFT and DFT-MD calculations, DeePMD-kit was used to construct neural network potentials, PLUMED was used to apply wall potentials during training-data generation, and LAMMPS was used for production NNP-MD simulations.

References

[1] Sakaguchi, C.; Ikeda, T.; Nakayama, (in revision).

Challenge of *in-silico* design for negative-thermal-expansion materials: $KNbSi_2O_7$

Yasuhide MOCHIZUKI

Department of Materials Science and Engineering,

Institute of Science Tokyo, Ookayama, Meguro-ku, Tokyo 152-8550

Negative thermal expansion (NTE) materials, whose lattice constant or volume shrinks upon heating, are essential for applications such as heat-resistant fillers, microdevices in light-emitting diodes (LEDs), large-scale integration (LSI), power semiconductors, and micropositioners in telescopes [1]. Despite over a century of intensive study, the rational design of NTE materials remains a challenging research topic. How can we design an NTE material?

In the previous reports, it has been empirically shown that larger average atomic volume (AAV) tends to yield NTE behavior, indicating that the framework structure with large AAV is expected to possess an NTE behavior. Alkali-metal ions have a large ionic radius compared to other cations. Particularly, inserting K and Rb into the framework structure is expected to increase the AAV (Figure 1a), consisting of corner-sharing octahedral and tetrahedral coordination structures. A material that has these characteristics is NASICON (Na Super Ionic CONductor) family: $AZr_2(PO_4)_3$ (*A* = Li, Na, K, and Rb), in which ZrO_6 octahedra and PO_4 tetrahedra are corner-sharing, and as the *A*-site atoms become larger, the volumetric thermal expansion switches from positive to negative. Note that $KZr_2(PO_4)_3$ has negative volumetric coefficient of thermal expansion (CTE), whereas $NaZr_2(PO_4)_3$ has the positive volumetric CTE. Based on the aforementioned perspective, we have selected Nb, generally forming octahedral coordination, and Si, usually forming tetrahedral coordination. Given that inserting K into the crystal structure (Figure 1b),

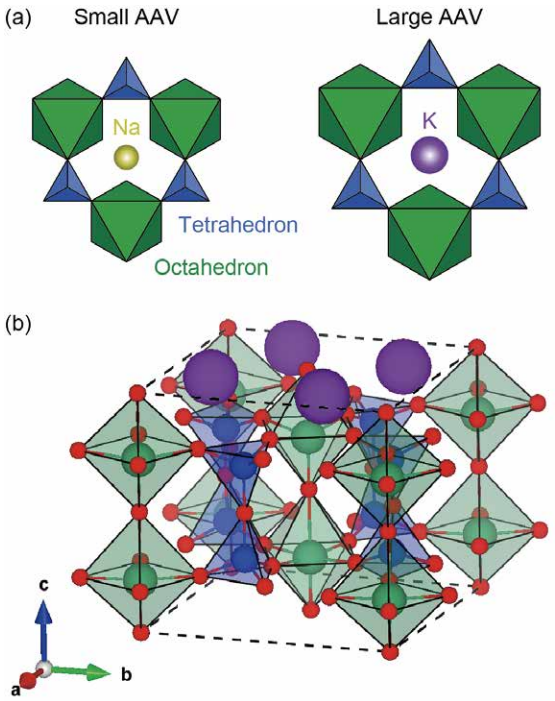


FIG. 1. (a) Perspective to design an NTE material. (b) Crystal structure of $KNbSi_2O_7$.

we have extracted $KNbSi_2O_7$ (KNSO), which we expect to show NTE, from Materials Project by searching for K-Nb-Si-O composition.

We have calculated the equilibrium lattice constants of KNSO from the molecular-dynamics (MD) calculations using the machine-learning force field (MLFF) in the range 100–800 K, indicating its biaxial NTE behavior. Then, we have prepared polycrystalline KNSO by a solid-state reaction method, and experimentally observed the temperature-dependent XRD patterns, which indicate the biaxial NTE behavior of KNSO.

As a result of the MD calculations, KNSO has been predicted to exhibit the NTE behavior in the *a*- and *b*-axes (Figure 2a), whereas the PTE behaviors are predicted in the *c*-axis (Figure 2b) and volume (Figure 2c). The calculated CTE from the MD calculations were found to be –2.3 ppm/K in the *a*-axis, 20.0 ppm/K in the *c*-axis, and 11.4 ppm/K in the volume at room temperature (300 K). Then, we also prepared a polycrystalline sample of KNSO by the solid-state reaction method using Nb_2O_5, KNO_3, and SiO_2 powders as starting materials. From the temperature-dependent XRD patterns, we have also derived the lattice constants of KNSO over the temperature range 303 K to 673 K, as shown in Figure 2d–2f [2]. The experimentally observed linear CTEs of *a*- and *c*-axis at 300 K are –2.3 ppm/K and 20.0 ppm/K, respectively. The experimentally observed

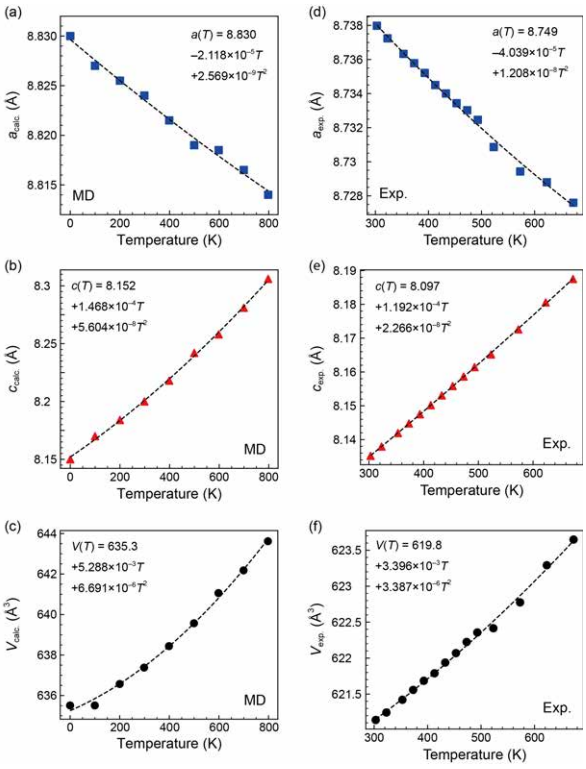


FIG. 1. (a–c) Calculated temperature dependences of (a) *a*- and (b) *c*-lattice constants, and that of (c) unit cell volume of $KNbSi_2O_7$ at equilibrium states in the relevant temperature using the MD calculations. (d–f) Experimentally observed temperature dependences of (a) *a*- and (b) *c*-lattice constants, and that of (c) unit cell volume. in the relevant temperature for KNSO.

volumetric CTE at 300 K is 11.4 ppm/K. We can see that the computationally predicted CTEs are well compatible with the experimental values.

References

[1] Y. Mochizuki et al., J. Phys. Chem. C **128**, 525 (2024).

[2] H. Koiso and Y. Mochizuki et al., J. Phys. Chem. C **129**, 9509 (2025).

Design and Understanding of the Activity and Stability of Promising CO_2 Reduction Electrocatalysts via Precise Catalysis Theory and AI
Precise Catalysis Theory and AI

HAO LI

Advanced Institute for Materials Research (WPI-AIMR),

Tohoku University, Sendai, 980-8577

We have studied the development of new catalytic theories and AI-assisted models, as well as the design of effective catalysts for CO_2 reduction reactions, by integrating precise theoretical models, high-level computations, machine learning (ML), and experimental validation.

This year, we utilized supercomputing resources to perform high-throughput density functional theory (DFT) calculations and ab initio molecular dynamics (AIMD) simulations to provide predictive insights into the activity, selectivity, and stability of CO2 reduction electrocatalysts. This integrated computational framework enables us to understand how magnetic properties affect catalytic behavior in two-dimensional transition-metal-based catalysts, making it possible to identify promising materials with improved CO2RR performance efficiently. Beyond this, high-throughput screening and data-driven analysis were employed to establish quantitative correlations between magnetic features and catalytic activity, thereby accelerating the discovery of advanced catalysts. Leveraging the synergy between physics-based insights and data-driven methods, we aim to develop catalysts that are not only highly active and selective but also robust for long-term operation. Through this integrated approach, the work presented here outlines a path toward optimizing CO_2 electro-reduction catalysts and demonstrates the broader potential of combining fundamental theory with cutting-edge computational strategies.

During the project period, **76 papers** were published in leading journals, including JACS, Angew. Chem., Nature Commun., etc., under this ISSP supercomputer support. Some notable works will be discussed in the following:

1. Closed-Loop Framework for Discovering Stable and Low-Cost Bifunctional Metal Oxide Catalysts for Efficient Electrocatalytic Water Splitting in Acid (JACS; Hao Li as the Last and Corresponding Author)

In this work, we developed a closed-loop framework integrating catalyst exploration, synthesis and electrochemical testing, and advanced characterization to identify stable and

low-cost metal oxide catalysts for acidic water splitting. By combining data mining, surface state analysis, microkinetic modeling, and proof-of-concept experiments, we identified RbSbWO6 as a promising bifunctional catalyst for acidic OER and HER. Experimental results confirmed its excellent stability and performance, surpassing many reported non-noble stoichiometric metal oxides without major modification. This study highlights the effectiveness of our DigCat-based data-driven workflow as a powerful strategy for accelerating electrocatalyst discovery.

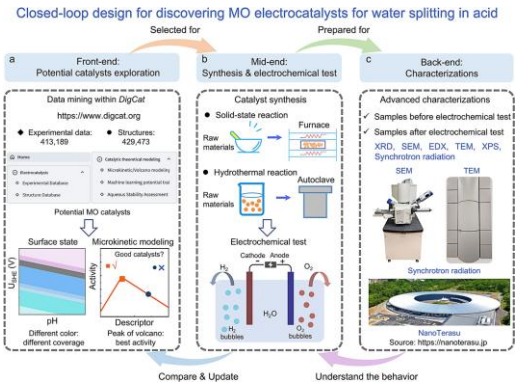


Fig. 1. Closed-loop design for discovering non-noble MO electrocatalysts for water splitting.

2. C60 Fullerene as the Active Site for CO2 Electroreduction (Angewandte Chemie; Hao Li as the Last and Corresponding Author)

we integrate large-scale data mining (with >2,300 CO2RR catalysts from available experimental literature during the past decade), ab initio computations, ML force field accelerated molecular dynamic simulations, and pH-field coupled modelling to unravel their pH dependence. We reveal a fascinating contrast: the electric field response of the binding strength of *OCHO on Sn−N4−C and polyatomic Sn exhibits opposite behaviors due to their differing dipole moment changes upon *OCHO formation. Such response leads to an intriguing opposite pH-dependent volcano evolution for Sn−N4−C and polyatomic Sn.

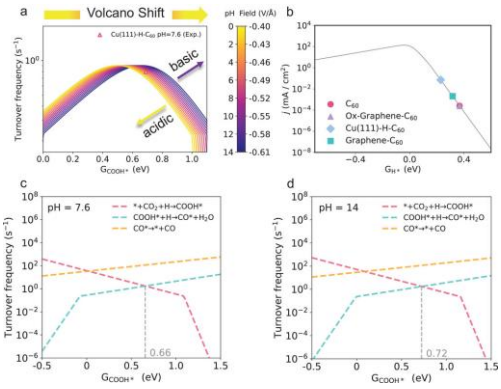


Figure 2. pH-dependent microkinetic CO2RR volcano models at the RHE scale and rate-determining analysis of C60-based catalysts

References

[1] X. Jia, Z. Zhou, F. Liu, T. Wang, Y. Wang, D. Zhang, H. Liu, Y. Wang, S. Ye, K. Amezawa*, L. Wei*, and H. Li*, Journal of the American Chemical Society, 2025, 147, 22642–22654.

[2] S.-W. Ying, Y. Wang, P. Du, Q. Wang*, C. Yue, D. Zhang, Z.-C. Chen, J.-W. Zheng*, S.-Y. Xie*, and H. Li*, Angewandte Chemie International Edition, 2025, 64, e202511924.

Investigation of polarization switching in Li_2GeO_3

Sou YASUHARA

School of Materials and Chemical Technology,

Institute of Science Tokyo, Ookayama, Meguroku, Tokyo 152-8550

Since the discovery of ferroelectricity in Sc-doped AlN in 2019,[1] wurtzite-type materials have attracted significant attention. Exploring new wurtzite-type structures is essential for understanding the mechanisms of polarization switching. In the previous fiscal year, we focused on $LiGaO_2$[2, 3] and evaluated the energy changes associated with single-ion motions.

In this year, we extended our research to Li_2GeO_3, which possesses a similar crystal structure. Our objective was to investigate the polarization switching pathways and energy barriers more accurately using the Nudged Elastic Band (NEB) method and to examine the effects of various element substitutions on the switching characteristics.

First-principles calculations were performed using the projector augmented wave (PAW) method as implemented in the VASP. The PBEsol-type generalized gradient approximation (GGA) was utilized as the exchange-correlation functional. The k-point mesh was 8×8×8. The cutoff energy and convergence energy were 550 eV and 1.0×10^{-7} eV, respectively. The NEB method was employed to identify the minimum energy path and calculate the activation energy for polarization switching in Li_2GeO_3.

Calculations result of the NEB method for Li_2GeO_3 polarization switching was shown in Fig. 1. The activation energy of Li_2GeO_3 is lower than that of $LiGaO_2$, suggesting that Li_2GeO_3 is more favorable for polarization switching. Additionally, the effects of elemental substitution about 20 patterns were investigated, revealing that and (Mn, Y) co-substitution is the most effective for achieving the switching.

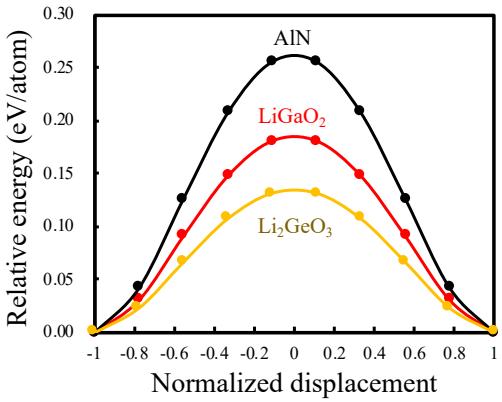


Fig. 1 Relative energy during polarization switching of AlN (black), $LiGaO_2$ (red) and Li_2GeO_3 (yellow).

References

[1] S. Fichtner *et al.*, J. Appl. Phys. **125**, 114103 (2019). [2] S. Yasuhara *et al.*, RSC adv. **14**, 13900 (2024). [3] S. Yasuhara *et al.*, J. J. Appl. Phys. **64**, 08SO02 (2026).

Topological surface state in RuO_2

Kunihiko YAMAUCHI

Center for Spintronics Research Network, Osaka University, Toyonaka, Osaka 560-8531, Japan

We have studied the electronic structure of RuO_2, a candidate altermagnetic material, by means of first-principles calculations, focusing on the origin of surface-dependent states observed in recent ARPES measurements. The calculations were performed within density functional theory as implemented in VASP, adopting the generalized gradient approximation.

The calculated bulk band structure is dominated by Ru-*4d* states near the Fermi level and shows good agreement with ARPES results, supporting a nonmagnetic description without clear spin splitting. In particular, the absence of sizable band splitting is consistent with a spin-degenerate picture of the bulk states.

To investigate the surface electronic structure, we constructed Wannier-based tight-binding models using Wannier90 and computed surface spectral functions for different crystallographic terminations. The calculations reveal surface-dependent states whose dispersion and intensity vary depending on the surface orientation.

These surface states are found to originate from bulk Dirac nodal lines inherent to the rutile crystal structure of RuO_2. The nodal-line topology leads to spin-polarized nontrivial surface states appearing near the Fermi level, providing a natural explanation for the surface-dependent features observed in ARPES as shown in Figure.[1]

We are also pursuing several research directions aimed at potential spintronics applications.[2, 3]

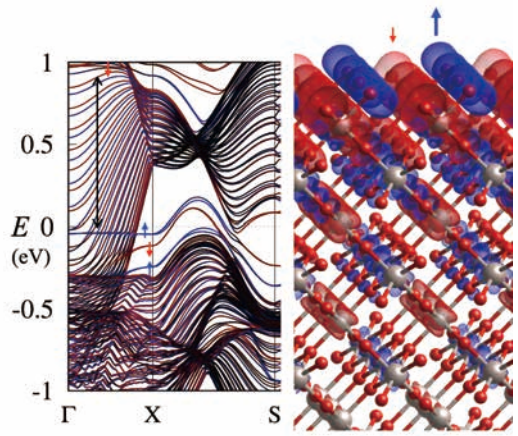


Figure: Topological surface bands (left) and the spin density (right) in nonmagnetic RuO_2.

References

[1] T. Osumi, K. Yamauchi, S. Souma, *et al.*, Phys. Rev. B **113**, 085116/1-18 (2026).

[2] T. P. T. Nguyen and K. Yamauchi, arXiv: 2603.29202 (2026).

[3] K. Yamauchi and T. Oguchi, arXiv: 2604.04557 (2026).

Mechanism of fast ion conductivity

Osamu SUGINO

Institute for Solid State Physics,

The University of Tokyo, Kashiwa-no-ha, Kashiwa, Chiba 277-8581

We have studied the hydride-ion (H^-) conduction mechanism in a K_2NiF_4-type Ba–Li oxyhydride, $Ba_{1.75}LiH_{2.7}O_{0.9}$ (BLHO), using the System B of the ISSP supercomputer. Density functional calculations and first-principles molecular dynamics (FPMD) simulations were conducted using Quantum ESPRESSO and VASP, respectively. BLHO had been synthesized by some of the collaborators as the first H^--based conducting material whose conduction mechanism had not been elucidated.

We modeled the disordered phases of BLHO using supercells $Ba_{56}Li_{32}H_{88}O_{28}$, $Ba_{57}Li_{32}H_{90}O_{28}$, and $Ba_{58}Li_{32}H_{90}O_{29}$, which successfully reproduced experimental data on electronic structures and diffusion coefficients. The Lindemann index of H atoms exceeds the threshold (0.1) for a solid–liquid transition at temperatures above 700 K, which provides theoretical evidence for sublattice melting of the H^- equatorial sites.

Fast conducting behavior of H^- was analyzed using the descriptor called rearrangement indicator (RI), which allows us to distinguish slow atomic motion from fast vibrational motions. The analysis revealed a highly cooperative diffusion mechanism, typical of supercooled liquids.

H^- ions transiently form a string-like cluster consisting of several ions. The tendency to form clusters is suggested to reduce the activation energy of ion diffusion, as was found for superionic conductors like PbF_2, but the tendency looks stronger for BLHO presumably due to densely populated Ba and H vacancies contained in this material.

Fast diffusion is known generally related to glass property of materials. The elucidation of diffusion from the perspective of glassy properties is a key target for our future studies, which we plan to pursue using machine learning potentials.

O. Sugino, "Statistical Mechanics of Atomic Diffusion via Machine Learning Potentials," Project Proposal 2025-Ca-0064 (2025).

References

[1] J. Haruyama, F. Takeiri, G. Kobayashi, and O. Sugino, "Elucidation of superionic conduction in K_2NiF_4-type Ba–Li oxyhydride from a first-principles molecular dynamics study," J. Mater. Chem. A, 14, 8332 (2026).

First principles study of germanene superstructures on Ag(111)

Yuji Hamamoto

Department of Communication Engineering,

Okayama Prefectural University, Kuboki, Soja, Okayama 719-1197

Germanene, a germanium analog of graphene, is important not only as a potential two-dimensional topological insulator but also for applications due to its higher compatibility with existing semiconductor technology. Recently, Ge atoms segregated through an Ag(111) thin film on Ge(111) were shown to form a two-dimensional Ge sheet [1]. Unlike freestanding germanene with an alternating buckled structure, this sheet exhibits a nontrivial $7\sqrt{7} \times 7\sqrt{7}$ superstructure on Ag(111), making structure determination by first-principles calculations computationally demanding.

To investigate the geometrical and electronic structures of germanene on Ag(111), we here performed first-principles calculations of the $7\sqrt{7} \times 7\sqrt{7}$ superstructure based on the recently proposed structural model [2], which consists of 332 Ge atoms and 1029 Ag atoms. Large-scale parallel computing enabled us to obtain the relaxed structure of the system, as shown in Fig. 1, which includes five- and seven-membered rings in the Ge sheet, unlike the naïve honeycomb model suggested in Ref. [1]. We also analyzed the electronic structure, especially derived from the Ge layer, by performing band structure unfolding [3] and projection onto the region where the Ge layer exists.

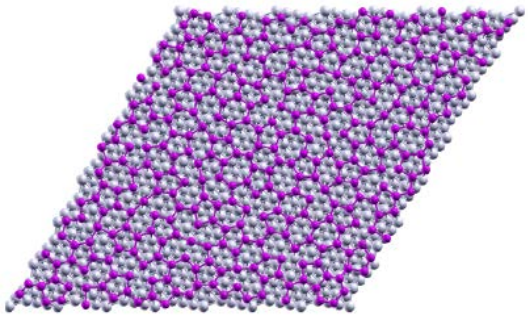


Fig. 1: Relaxed structure of the $7\sqrt{7} \times 7\sqrt{7}$ superstructure of germanene on Ag(111). Pink and gray balls represent Ge and Ag atoms, respectively.

References

[1] J. Yuhara et al., ACS Nano **12**, 11632 (2018).

[2] K. Zhang et al., ACS Nano **17**, 15687 (2023).

[3] V. Popescu and A. Zunger, Phys. Rev. B **85**, 085201 (2012).

Structure search for planar silicene on Au(111) thin films based on Gaussian process regression

Yuji Hamamoto

Department of Communication Engineering,

Okayama Prefectural University, Kuboki, Soja, Okayama 719-1197

Silicene, a silicon analog of graphene, is important not only as a potential two-dimensional topological insulator but also for applications due to its higher compatibility with existing semiconductor technology. Recently, Si atoms segregated through an Au(111) thin film on Si(111) were shown to form a two-dimensional Si sheet [1]. Intriguingly, scanning tunneling microscopy revealed a planar honeycomb pattern, unlike the theoretically predicted buckled structure of freestanding silicene. Although angle-resolved photoemission spectroscopy suggested a Dirac-cone-like linear dispersion at the Γ point, its origin remains unclear due to the unresolved structure of the Si sheet.

Expanding the machine-learned structure search for silicene on the Ag(111) surface [2], we here searched for stable structures of Si sheets formed on Au thin films using GOFEE [3], which accelerates structure search by leveraging the energy landscape predicted by a Gaussian process trained on the fly during the search. Our results revealed that silicene formed on a pristine Au thin film is not rotated with respect to Si(111), whereas that on an Au thin film doped with an Si atom is rotated by 21.8 degrees, in good agreement with low-energy electron diffraction measurements. This suggests that the Au thin film underlying silicene is slightly silicified by segregation of Si atoms, consistent with the fact that Au forms a silicide more easily than Ag. Although silicene formed on such a doped Au thin film is significantly buckled, it has also been found that a more planar structure can be obtained by introducing lattice vacancies into the honeycomb lattice, as shown in Fig. 1.

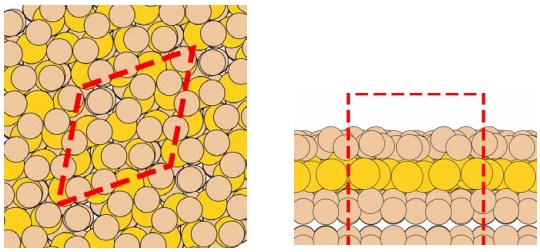


Fig 1: Stable structure of Si sheet on a Au thin film obtained by the structure search.

References

[1] A. Stępniak-Dybal et al., Adv. Funct. Mater. **29**, 1906053 (2019).

[2] Y. Hamamoto et al., Phys. Rev. Materials 7, 124002 (2023).

[3] M. Bisbo and B. Hammer, Phys. Rev. Lett. **124**, 086102 (2020).

Investigating the Role of Oxidation in Amorphous TeO_2 Properties from First Principles

Rafael COSTA-AMARAL

Institute for Materials Research, Tohoku University, 2-1-1 Katahira, Aoba-ku, Sendai, 980-8577, Japan

Introduction

Amorphous oxide semiconductors are attractive for large-area and low-temperature electronics, but high-mobility p-type counterparts remain rare because O-2p-derived valence states are usually deep and localized. Motivated by recent experimental reports of unusually high hole mobilities in oxygen-deficient amorphous tellurium oxides (*a*-TeO_x), this study [1] aimed to clarify how oxygen deficiency reorganizes the amorphous network, which defects supply holes, and how network connectivity controls transport. These questions require atomistic modeling of disordered structures across multiple compositions together with accurate defect and electronic-structure calculations, making large-scale use of the ISSP supercomputer essential.

Computational Methods

First-principles calculations were performed with the Vienna Ab initio Simulation Package (VASP) within density functional theory using the projector augmented-wave method. Models of *a*-TeO_x spanning x = 0.0-2.0, including the experimentally relevant x = 1.2 composition, were generated by melt-quench molecular dynamics. To make large-cell sampling tractable, the quench simulations were accelerated by an on-the-fly machine-learning force-field workflow in VASP. The resulting structures were relaxed and Hybrid-functional calculations were then used to evaluate electronic structure. Bader charge analysis was used to distinguish tellurium atoms between oxidized Te^{4+} and reduced Te^{0}.

Results and Discussion

The calculations show that oxygen deficiency in *a*-TeO_x drives spontaneous nanoscale segregation into interpenetrating Te-rich and oxide-rich amorphous domains, which play distinct and complementary roles in transport. Te vacancies located in oxide-like or interfacial environments act as the dominant source of holes, whereas hole transport itself is mediated by connected Te-5p states within the Te-rich subnetwork. Thus, carrier generation and carrier transport originate from different structural motifs.

Further lowering the oxygen content expands

the Te-rich network and improves the connectivity of transport-supporting pathways. This compositional trend strengthens the link between oxygen deficiency, nanoscale phase segregation, and hole transport, and shows that control of oxygen content provides a practical route to tuning the electronic functionality of *a*-TeO_x.

Our results demonstrate the value of combining machine-learning-accelerated molecular dynamics with hybrid-functional electronic-structure calculations for disordered materials. In addition, we provide a physically consistent explanation for the high hole mobility reported experimentally in oxygen-deficient *a*-TeO_x films, establishing a basis for the rational design of defect-engineered amorphous semiconductors.

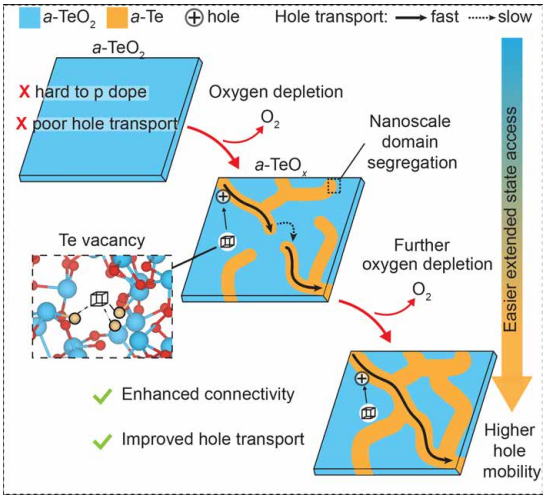


Figure 1. Oxygen deficiency modify nanoscale connectivity and transport pathways for holes in amorphous tellurium oxide.

References

[1] R. Costa-Amaral and Y. Kumagai, "Oxygen-deficiency-driven phase segregation enables enhanced hole transport in amorphous tellurium oxides," submitted to ***Chemistry of Materials***; preprint available as arXiv:2510.00473.

Understanding the Super High-Pressure Synthesis of Superhydride by Machine-Learning Potential MD Simulations

Ryuhei Sato

Department of Materials Engineering,

The University of Tokyo, 7-3-1 Hongo, Bunkyo-ku, Tokyo 113-8656, Japan

The realization of room-temperature superconductivity is considered one of the holy grails in physics. Polyhydrides with high hydrogen-to-metal (H/M) ratios are among the most promising candidates in terms of superconducting transition temperature (Tc). For instance, CaH_6 exhibits an exceptionally high Tc of 210 K at 160 GPa [1], suggesting that room-temperature superconductivity may be achievable through the exploration of ternary or quaternary compounds within this material class. However, the synthesis of such materials remains a significant challenge. As an example, although CaH_6 was theoretically predicted in 2010 [2], its experimental synthesis was not realized until nearly a decade later [1]. Thus, in addition to predicting stable structures and T_c values, it is crucial to identify feasible synthetic pathways and gain a fundamental understanding of the underlying reaction mechanisms.

In previous our study, machine learning potential molecular dynamics (MLP-MD) simulations successfully reproduced the synthesis of CaH_4 polyhydride [3]. Based on the observation, we constructed the thermodynamic model to explain how the superhydride synthesis is promoted under high pressure [3]. However, this thermodynamic model only shows the synthesis guideline of stable superhydride and there is no clear guideline to synthesize metastable superhydride phase. In this study, we conducted MLP-MD simulations of the $CaHx/H_2$ interface to seek for the synthesis route of metastable CaH_6 [4]. Note that the DFT training dataset (with over 0.15 million structures) calculations and all the MLP-MD simulations were performed in system B in ISSP supercomputer center.

MLP–MD simulations of the CaH_x/H_2 interface revealed two competing hydrogenation pathways [4]. One is the formation of the $CaH_{5.75}$ observed at high temperature (~1500 K; Fig. 1). Above ~100 GPa, hydrogen-rich phases such as CaH_{12}, in which Ca is incorporated into molecular hydrogen, become stable. Accordingly, Ca first dissolves into the H_2 phase. Upon supersaturation, heterogeneous nucleation occurs near the CaH_4/H_2 interface, leading to the formation of $CaH_{5.75}$. This phase grows

with time and becomes dominant after ~1 ns.

The second pathway is the formation of CaH_6 at the CaH_2/H_2 interface under 1000 K and 150 GPa (Fig. 2). Here, the less stable CaH_2 is used as a precursor under high pressure. Here, due to the relatively low temperature, significant Ca rearrangement is suppressed. As a result, a diffusionless, martensitic-like transformation occurs, resulting in the formation of CaH_6.

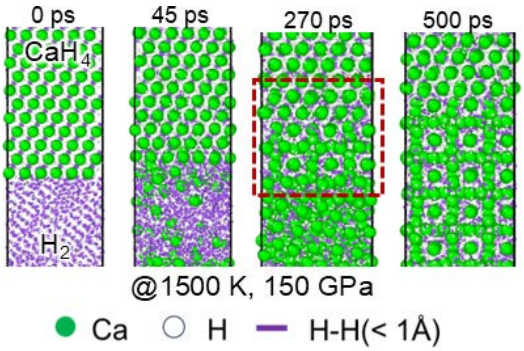


Fig. 1 $CaH_{5.75}$ synthesis at 1500K and 150GPa during MLP-MD for CaH_4/H_2 interface.

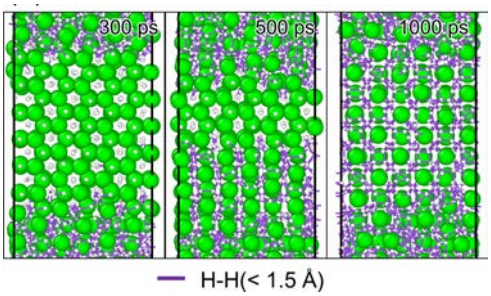


Fig. 2 CaH_6 synthesis at 1000 K and 150 GPa during MLP-MD for CaH_2/H_2 interface.

The competition between these pathways can be understood in terms of hydrogenation enthalpy and lattice similarity between precursors and products. Figure 3 shows the hydrogenation enthalpies of the superhydrides. $CaH_{5.75}$ is thermodynamically stable above 100 GPa, whereas CaH_6 is metastable over the entire pressure range. However, $CaH_{5.75}$ has a complex crystal structure, requiring substantial Ca diffusion and rearrangement from precursors such as Ca, CaH_2, and CaH_4 with hcp/fcc-like Ca lattices. Therefore, its formation is only observed at high temperature. In contrast, although CaH_6 is metastable, it possesses a bcc-like Ca lattice similar to these precursors, enabling formation via diffusionless transformation at lower temperatures.

These results demonstrate that MLP–MD simulations can capture competing hydrogenation pathways of superhydrides under extreme conditions, and that metastable phases can be selectively synthesized by controlling temperature and lattice compatibility between precursors and target structures.

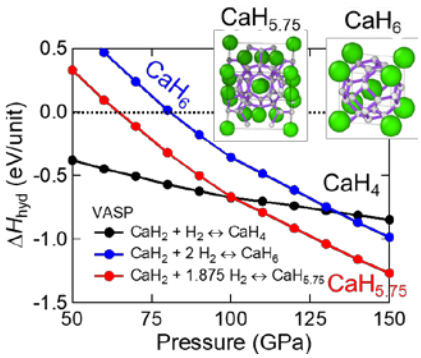


Fig. 3 Hydrogenation enthalpy of CaH_4, $CaH_{5.75}$, and CaH_6 obtained from DFT calculation as a function of pressure.

References

[1] H. Wang et. al. PNAS 109 (2012) 6463.
[2] L. Ma et. al. PRL 128 (2022) 167001.
[3] R. Sato et. al. PNAS 122 (2025) e2413480122.
[4] R. Sato et. al. arXiv (2026). DOI: 10.48550/arXiv.2603.08950

Improving Stability of Molecular Dynamics Simulation using Machine-Learning Interatomic Potentials II

Kohei Shimamura

Department of Physics,

Kumamoto University, 2-39-1 Kurokami, Chuo-ku, Kumamoto 860-8555

The development of machine-learning interatomic potentials (MLIPs) has enabled molecular dynamics (MD) simulations that retain the accuracy of first-principles molecular dynamics (FPMD) while significantly extending accessible time and length scales. In our previous work, we proposed the Potential Averaging (PA) method [1], an ensemble-learning-based approach in which multiple MLIPs are combined by averaging the predicted atomic forces. This approach improves robustness and provides a natural framework for uncertainty estimation through the variance of predicted forces. However, the stability of MD simulations using MLIPs, particularly for systems outside the training domain, remains an important challenge. In the present study, we continued our efforts to improve the stability of MD simulations by extending the PA method to a graph neural network (GNN)-based MLIP, namely the Allegro model [2].

A major focus of this year's work was the implementation of the PA method within the Allegro framework. Since Allegro is implemented in Python using PyTorch, whereas MD codes typically interface through C++ (e.g., via libtorch), careful modification of the interface layer was required. We successfully implemented the use of multiple Allegro models within the MD framework and confirmed that the PA method can be applied without altering the core structure of the Allegro model. This achievement ensures the portability of the approach across different MD codes.

The developed framework was tested using silver chalcogenide systems. We evaluated the stability of MD simulations as well as the accuracy of thermal conductivity calculated via the Green–Kubo method. The results demonstrate that the PA method improves the stability of simulations.

Overall, the project in FY2025 progressed steadily. The successful implementation of the PA method for the Allegro model and the initial development of computational optimization strategies represent important steps toward practical large-scale MD simulations using MLIPs.

References

[1] D. Wakabayashi, *et al.*: J. Phys. Soc. Jpn., **92**, 074002 (2023).

[2] A. Musaelian, *et al.*: Nat. Commun. **14**, 579 (2023).

Active Sites Evolution in Cu Catalysts: Insights from Machine Learning Molecular Dynamics

Harry H. Halim, M. Fadhlan Anshor, Syahrul Ramadhani, Asahi Morita, and Yoshitada Morikawa
Graduate School of Engineering, The University of Osaka

Results Report

We performed large-scale atomistic simulations to investigate Cu-based catalysts for CO_2 hydrogenation and the water–gas shift reaction (WGSR), using a combination of density functional theory (DFT), machine learning interatomic potentials (MLIPs), and multi-scale modeling techniques. The main objective was to elucidate dynamic catalytic behavior under realistic reaction conditions and to resolve the inconsistency between theory and experiment by bridging the pressure and materials gap.

Use of Supercomputer Resources

The supercomputer (ISSP system B and system C) was utilized for (i) first-principles DFT calculations, (ii) training of MLIPs via active learning, and (iii) large-scale molecular dynamics (MD) simulations.

DFT calculations were carried out to generate high-quality training datasets covering diverse surface configurations, adsorbate states, and reaction intermediates. These calculations were computationally demanding due to the need to sample high-coverage adsorbate configurations and reconstructed surface structures.

To overcome the limitations of DFT in terms of system size and simulation time, we employed MLIPs trained on the DFT dataset. The training process involved iterative active learning cycles, where new configurations were generated from MD simulations and selectively added to the dataset.

The MLIPs were trained using two machine learning frameworks: Gaussian Process regression within the Gaussian Approximation Potential (GAP) formalism (for the Water Gas Shift Reaction project), and Graph Neural Network (GNN) architectures (for H-induced surface reconstruction project) as implemented in Allegro. The training workflows were executed on high-performance computing systems, where DFT-generated datasets were iteratively refined via active learning, and model optimization was parallelized to handle diverse configurational spaces. Molecular dynamics simulations were performed using LAMMPS, while post-processing and analysis of atomic structures and trajectories were conducted using the Atomic Simulation Environment (ASE). This integrated workflow enables both high accuracy and computational efficiency in modeling complex catalytic systems.

Algorithmic Improvements and Efficiency

We neither developed nor improved the algorithms of the methods in this project. However, we implemented active learning strategy to build the MLIPs with more compact database while keeping the high accuracy. In particular, we applied committee method and further point sampling to select the most unique and relevant atomic structures to be included in the database.

Scientific Results

Figure 1 shows the time evolution of the lateral coordination number (LCN) of Cu atoms in Cu(100) at $T = 300$ K under different hydrogen coverages. As the coverage increases, the average coordination number shifts toward higher values, approaching LCN ~ 6. This indicates that hydrogen induces significant restructuring of the Cu surface, leading to the formation of three-fold hollow sites [1]. Such structural evolution is not accessible within static surface models and highlights the importance of capturing dynamic surface states under realistic conditions.

In the second project, we evaluated the impact of the formation of Cu clusters on the catalytic performance of the water gas shift reaction [2]. The turnover frequency (TOF) of the water–gas shift reaction (WGSR) is significantly enhanced for the surface with Cu clusters (Cu_n) compared to the flat Cu(111) surface. The calculated temperature dependence of TOF shows good agreement with experimental trends, confirming that dynamically formed clusters act as highly active catalytic sites.

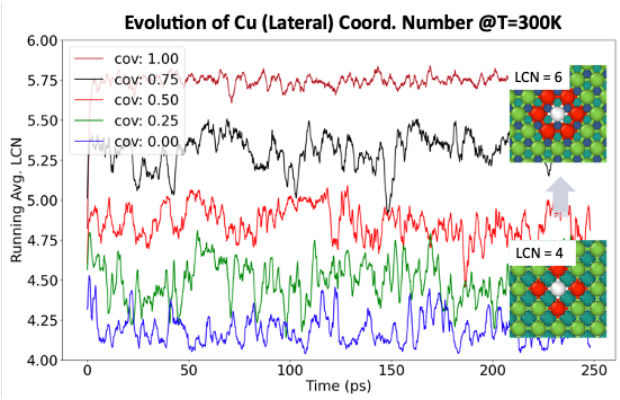


Figure 1: Time evolution of the lateral coordination number (LCN) of Cu atoms at $T = 300$ K under different adsorbate coverages. Increasing coverage leads to higher average coordination (LCN ~ 6), indicating adsorbate-induced surface restructuring and the formation of three-fold hollow sites.

Summary and Future Work

This project shows that MLIP-based simulations, combined with HPC resources, provide a framework for investigating complex catalytic systems beyond the limitations of conventional approaches. We will continue expanding the training dataset, incorporating kinetic Monte Carlo simulations for higher-scale modeling, and developing the inverse catalyst design.

List of Publications and Related Outputs

International Journal Publications:

- W. O. N. F. Rajaelo, H. H. Halim, M. F. Anshor, Y. Yamada, S. Ramadhani, F. A. Mubarok, S. E. M. Putra, A. L. Ivansyah, T. D. K. Wungu, Suprijadi, Y. Morikawa, and F. Muttaqien, "Bridging the Pressure Gap in Hydrogenation of CO_2 to Formate on Cu(100) by Machine Learning Molecular Dynamics and First-Principles Microkinetic Modeling," *ACS Catalysis* **16**, 5068–5079 (2026).
- M. F. Anshor, H. H. Halim, and Y. Morikawa, "CO Coadsorption Effects on Water–Gas Shift Reaction over Cu Clusters on Cu(111): Insights from Machine Learning Force Field and Microkinetic Modeling," *Phys. Chem. Chem. Phys.* (2026). In press.

Software Used:

- **First-principles calculations:** STATE, Quantum ESPRESSO
- **Machine learning potentials:** GAP, Allegro
- **MD simulations:** LAMMPS
- **Data analysis:** ASE (Atomic Simulation Environment)

Machine-Learning Molecular Dynamics for High-Pressure Hydride Synthesis and Superionic Transport

Kartik Sau

Advanced Institute for Materials Research (WPI- AIMR), Tohoku University, Sendai 980-8577, Japan

Two recent papers I worked on, both powered by AI-assisted atomic-scale simulations, ask very different questions but share the same trick: let a machine learn the rules of how atoms talk to each other, then watch what happens. One paper [1] catches hydrogen sneaking into a crystal at crushing pressures — a clue for the long hunt for room-temperature superconductors. The other [2] draws a kind of subway map of how ions go through next-generation battery materials.

Squeeze hydrogen hard enough and it slips inside metals to form "superhydrides" — exotic compounds that may one day carry electricity without losing a watt. The trouble is, even when theorists predict a winner, the lab can take a decade to actually make it. Why is the hydrogen so slow to get in? Our simulations caught the surface of a calcium hydride crystal doing something unexpected: instead of slowly soaking up hydrogen like a sponge, it briefly melts, swallows the gas as a liquid, then snaps back into a new crystal. Pressure doesn't just make the reaction possible — it greases the slide by stabilizing that fleeting liquid step. The takeaway is a simple rulebook for picking which materials are worth the effort: look for ones with a low melting point and a thermodynamic appetite for hydrogen under pressure.

The best solid battery materials don't move one ion at a time — their ions travel in packs, like commuters pushing through a crowded train. Spotting those coordinated dashes in a flood of simulation data has always been part science, part guesswork. We turned the problem into a network: every ion hop is an arrow, and arrows that land close together in space and time get linked, sketching a map of who pushed whom. The cutoffs aren't fudged — they fall out of the physics of the material itself. Tested on three very different battery candidates — a lithium sulfide, a sodium oxide, and an old silver iodide — the same map reveals the same kind of crowd dynamics, giving battery designers a clean way to ask: does this material's traffic actually flow?

References

[1] R. Sato, L. J. Conway, D. Zhang, C. J. Pickard, K. Akagi, K. Sau, H. Li, S. Orimo, Proc. Natl. Acad. Sci. U.S.A. 122 (22), e2413480122 (2025).

[2] R. Sato, Y. Ando, K. Sau, Y. Shibuta, Chem. Mater. 38 (1), 287–295 (2026).

Exploration of hydride superconductors

Takahiro ISHIKAWA
Department of Physics, The University of Tokyo
7-3-1 Hongo, Bunkyo-ku, Tokyo 113-0033

Lanthanum hydride (La-H) shows superconductivity at 260 K under 170 GPa [1, 2]. Recently, it has been suggested that the superconducting critical temperature (T_c) may further increase through repeated cooling and heating of the sample [3]. This enhancement has been speculated to originate from reactions between La-H and other materials present in the diamond anvil cell, such as nitrogen (N) and boron (B) from the hydrogen source (NH_3BH_3), and platinum (Pt), gold (Au), and gallium (Ga) from electrodes.

Assuming a reaction between La-H and Pt, we searched for thermodynamically stable phases in the La-Pt-H system at 20 GPa using a structure-search framework combining evolutionary algorithms (EA), density functional theory (DFT), and neural network potentials (NNPs) [4]. At each generation, a few thousand EA-generated structures were rapidly optimized using pre-trained NNPs calculations implemented in Matlantis [5], and several dozen low-enthalpy structures near the convex hull (CH) were further refined using DFT calculations with the Quantum ESPRESSO (QE) code [6] on the ISSP supercomputer. For the stable compounds, we estimated T_c using the Allen–Dynes formula [7]. Our results show that thermodynamically stable $LaPtH_6$ exhibits the highest T_c of 18.7 K at 20 GPa [8].

We also explored superconducting phases in another candidate system, La–N–B–H, at 20 GPa using a similar approach, and predicted ternary $LaBH_5$ (T_c = 29.0 K) and quaternary La_2NBH (T_c = 6.3 K). In addition, because the accuracy of pre-trained NNPs implemented in Matlantis may be limited in hydrogen-containing systems at pressures above 100 GPa, we are developing machine-learning potentials specifically for this quaternary system using an active learning scheme implemented in the GeNNIP4MD code [9] on the ISSP supercomputer.

References

[1] M. Somayazulu *et al.*: Phys. Rev. Lett. **122**, 027001 (2019).

[2] A. P. Drozdov *et al.*: Nature **569**, 528 (2019).

[3] A. D. Grockowiak *et al.*: Front. Electron. Mater. **2**, 837651 (2022).

[4] T. Ishikawa *et al.*: Phys. Rev. B **109**, 094106 (2024).

[5] Matlantis (https://matlantis.com/), software as a service style material discovery tool.

[6] P. Giannozzi *et al.*: J. Phys.: Condens. Matter **21**, 395502 (2009).

[7] P. B. Allen and R. C. Dynes: Phys. Rev. B **12**, 905 (1975).

[8] T. Ishikawa *et al.*: Phys. Scr. **101**, 105903 (2026).

[9] N. Matsumura *et al.*: J. Chem. Theory Comput. **21**, 3832 (2025).

Prediction of properties of organic ferroelectrics and piezoelectrics by first-principles calculation

Shoji ISHIBASHI
National Institute of Advanced Industrial Science and Technology (AIST)
Tsukuba, Ibaraki 305-8565

We have been searching for dielectric crystals composed of relatively small organic molecules that can be expected to exhibit multiple dipole moment arrangements due to proton displacement [1]. Here, two of the most recent examples 1,2-phenylenedipropiolic acid (PDPLA) and α,α'-dihydroxy-1,3-diisopyopylbenzene (DHIB), which have been discovered by data mining the Cambridge Structural Database, are shown.

The previously reported crystal structure of PDPLA assumed hydrogen disorder on the carboxyl group, but our re-examination reveals that PDPLA has a ferroelectric (FE) crystal structure where the hydrogen atoms are ordered (Fig. 1) [1]. To confirm the validity of the assignment, its relative stability against a few hypothetical antiferroelectric (AFM) forms is investigated by means of DFT calculations. As shown in Fig. 1, the FE form is the most stable. The calculated polarization value of 8.8 μC/cm^2 closely matches the measured value of 9 μC/cm^2.

As for DHIB, our reassessment reveals that the hydrogen atoms in the intermolecular hydrogen bonding are disordered (Fig. 2) [1]. We calculate and compare relative energies of one FE and two AFE forms (Fig. 2) and find that they are almost degenerate within 0.12 meV/molecule. The calculated polarization for the FE form (4.6 μC/cm^2) agrees well with the saturated polarization observed in the polarization-electric field (P-E) curve. Thus, the experimental and computational findings are consistent with each other.

All the calculations have been performed using the QMAS code.

References

[1] S. Horiuchi, H. Minemawari, J. Tsutsumi, and S. Ishibashi, Crystals **15**, 736 (2025).

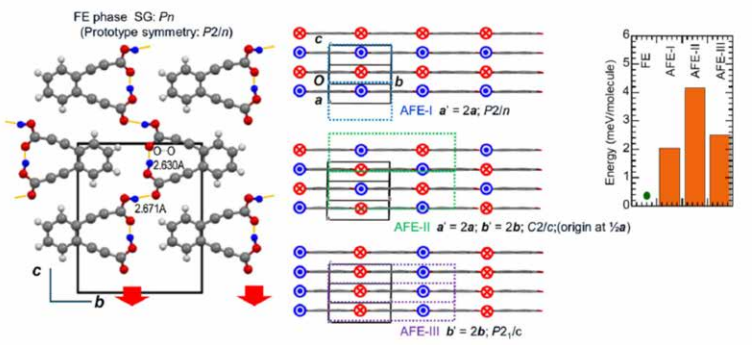


Figure 1: Crystal structure of PDPLA (left), arrangements of dipole moments in hypothetical AFE forms (middle), and relative energy comparison (right) (S. Horiuchi, H. Minemawari, J. Tsutsumi, and S. Ishibashi, Crystals **15**, 736 (2025), DOI: 10.3390/cryst15080736).

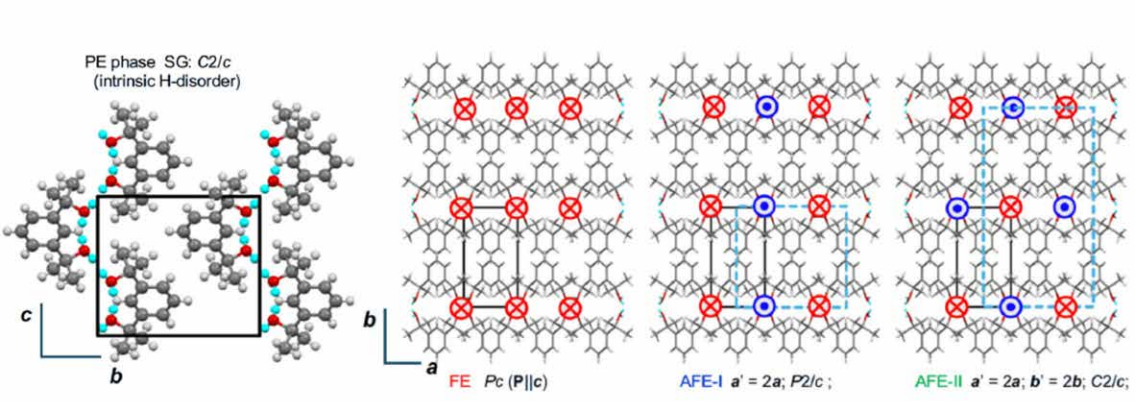


Figure 2: Crystal structure of DHIB (left) and arrangements of dipole moments in candidate FE and AFE forms (right) (S. Horiuchi, H. Minemawari, J. Tsutsumi, and S. Ishibashi, Crystals **15**, 736 (2025), DOI: 10.3390/cryst15080736).

First-principles study of surface atomic structure and chemical properties of intermetallic compounds

Kazuki Nozawa

Department of Physics and Astronomy, Kagoshima University,

1-21-35, Korimoto, Kagoshima 890-0065

In this fiscal year, we performed first-principles density functional theory (DFT) calculations to study the atomic-scale origin of the catalytic activity in the quasicrystal-related intermetallic compound $Al_{13}Fe_4$ and the applicability of cluster-based methods for molecular adsorption calculations on quasicrystal surfaces.

For $Al_{13}Fe_4$, we focused on the site-selective occupation behavior of trace transition metal additives [1]. Using the VASP code, we examined the substitution behavior of Rh and Ru atoms introduced into the monoclinic and orthorhombic phases of $Al_{13}Fe_4$. Calculations were performed for systems in which Rh or Ru was added at concentrations of approximately 1 at. % and 4 at. %, and the formation energies were evaluated by systematically substituting the additive elements into the crystallographically non-equivalent atomic sites. For the monoclinic phase, periodic bulk models consisting of 102 atoms were employed and calculated mainly on System B using flat MPI parallelization with 6 nodes (768 cores), while for the orthorhombic phase, 204 atom bulk models were used and calculated on System C with 2 nodes (256 cores). All calculations were performed using the VASP code within the generalized gradient approximation, and structural optimizations were performed to evaluate the relative stability of the substituted structures.

In addition, we studied the applicability of cluster-based DFT calculations for molecular adsorption on a quasicrystalline surface by comparing the slab model calculations [2]. Although the slab model is a well-established method for periodic crystal surfaces, it cannot be applied to quasicrystal surfaces that lack translational periodicity, even in the surface-parallel directions. Therefore, using both slab and disk-shaped cluster models, we investigated the adsorption of pentacene molecule on a periodic Cu(111) surface. By comparing the potential energy surfaces obtained using these two approaches, we examined the accuracy and limitations of the cluster approximation. Although small clusters produce artificial corrugation in the potential energy surface near unstable regions, we confirmed that the most stable adsorption positions were correctly reproduced even with moderately sized clusters, and that the potential energy surface smoothly converged toward the slab-model results with

increasing cluster radius. In these calculations, large cluster models containing approximately 700–1100 atoms were employed, and flat MPI-parallelized calculations were mainly performed on System B using 1 to 4 nodes (128–512 cores) with the VASP code.

References

[1] M. Hanaoka, S. Iwado, K. Nozawa, M. Aoyama, S. Ohhashi, N. Fujita, S. Kameoka, Appl. Mater. Today, 46, 102878 (2025).

[2] M. Sato and K. Nozawa, Mat. Trans. (in press).

Adsorption Reactions at the Solid Electrode/Aqueous Solution Interfaces

Satoshi Hagiwara
Center for Computational Sciences, University of Tsukuba
1-1-1 Tennodai, Tsukuba, Ibaraki 305-8577

An interface between the electrode and aqueous solution (electrochemical interface) is known as one of the important reaction fields in electrochemistry. To compute electrochemical interface problems, the effective screening medium (ESM) method [1] combined with the three-dimensional reference interaction site model (3D-RISM) method [2], termed ESM-RISM, has been developed by Nishihara and Otani [3]. Since the ESM-RISM method treats the electronic structure of the target electrode with reactant and solvation environment by density functional theory and the classical solution theory, respectively, we can simulate the electrochemical interface with relatively lower computational costs. However, the original implementation of ESM-RISM includes an unphysical approximation, which serves to broaden the molecular structure in the solution and deviated results from the original 3D-RISM ones and requires the higher computational costs for solving Laue-represented RISM equation (order $N^{4/3}$) compared to the 3D-RISM method (order $N \log N$).

For a sufficient simulation of the electrochemical interface, we have reconsidered the formulation of ESM-RISM and implemented it into the QMAS (Quantum MAterials Simulator) code [4]. Our reformulation successfully removes the unphysical approximation. We numerically confirmed that the calculated hydration free energy by ESM-RISM converges to that by 3D-RISM. In addition, the reformulation enables us to reduce the computational complexity, which scales on the order $N \log N$. Subsequently, we have applied the current version of the ESM-RISM method to the Pt(111)/HCl aqueous solution interface. The results of the potential of zero charges (PZC) of the Pt electrode, interfacial capacitance, and standard hydrogen electrode (SHE) potential reasonably reproduced the original ESM-RISM ones. Then, we have computed the hydrogen adsorption energy at the electrified interface. The results of the adsorption energy demonstrated that the stable hydrogen adsorption site depends on the applied bias voltage measured from the SHE potential [5]. We will apply the reformulated ESM-RISM method to understand the details of adsorption phenomena at the electrochemical interfaces in near future.

References

[1] M. Otani, and O. Sugino, Phys. Rev. B **73**, 115407 (2006).

[2] A. Kovalenko, and F. Hirata, J. Chem. Phys. **110**, 10095 (1999).

[3] S. Nishihara and M. Otani, Phys. Rev. B **96**, 115429 (2017).

[4] QMAS website: https://www.qmas.jp

[5] S. Hagiwara, and M. Otani, J. Chem. Theory Comput. **22**, 3633 (2026).

First-Principles and Data-Driven Design of Electrocatalysts for CO_2 Reduction, Water Splitting, and H_2O_2 Synthesis

Di ZHANG

Frontier Research Institute for Interdisciplinary Sciences (FRIS),

Tohoku University, Sendai 980-8577, Japan

We have studied electrocatalytic materials for sustainable energy conversion using massive parallel first-principles simulations on the Supercomputer System at ISSP. This year, we focused on the computational design and mechanistic understanding of advanced catalysts for several important electrochemical reactions, including CO2 electroreduction, oxygen evolution reaction, alkaline hydrogen evolution reaction, and electrochemical hydrogen peroxide synthesis [1–6]. Large-scale density functional theory calculations were performed to construct realistic catalyst surface models, evaluate adsorption free energies of key reaction intermediates, analyze electronic structures, and identify activity descriptors under electrochemical conditions.

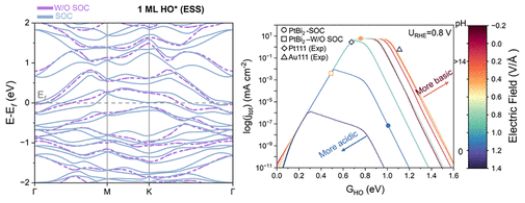


Fig. 1 2D Topological Electrocatalysts with Spin–Orbit Coupling

For CO2 electroreduction, we investigated both extended solid surfaces and molecular carbon-based active sites. In two-dimensional topological electrocatalysts, monolayer PtBi2 was used as a representative platform to clarify how electrochemical surface states induced by adsorbates can interact with spin-orbit-coupling-enabled topological surface states (Fig. 1). The calculations showed that reconstructed surface electronic states under reaction conditions can strongly influence the adsorption energetics of oxygen intermediates and thereby regulate oxygen reduction activity [1]. In another study, C60 fullerene was examined as a molecular active site for CO2-to-CO conversion. By combining first-principles calculations with pH- and electric-field-dependent microkinetic analysis, we revealed that the curved molecular surface of C60 can stabilize COOH* intermediates through large dipole moment changes, providing a mechanism beyond its conventional role as an electronic promoter [2] (Fig. 2).

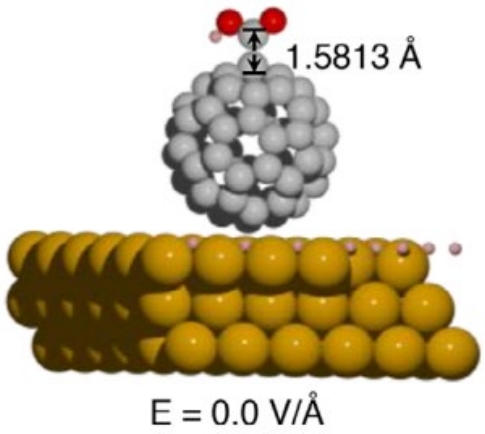


Fig. 2 Electric field effects on the adsorption energies of CO2RR adsorbates

We also studied pyridinic-N incorporated cobalt phthalocyanine catalysts, where

electronic-structure calculations demonstrated that molecular backbone modification optimizes the adsorption of key CO2 reduction intermediates such as *COOH and *CO, explaining the enhanced intrinsic activity and high CO selectivity [3].

For oxygen evolution catalysis, we investigated high-density tungsten single atoms anchored in two-dimensional spinel oxide matrices. The first-principles simulations clarified how W single atoms modify the local coordination environment of Co sites, strengthen OH adsorption, promote surface reconstruction into active oxyhydroxide species, and optimize the adsorption energetics of OER intermediates [4]. For alkaline hydrogen evolution, we studied Ru/VO2-based catalysts and identified a stepwise acceleration mechanism involving both water dissociation and hydrogen spillover. The simulations showed that interfacial V–O–Ru bonding dynamically modulates the electronic structure around Ru active sites, facilitates Volmer-step water dissociation, and optimizes hydrogen adsorption through reversible spillover, thereby improving the overall alkaline HER kinetics [5]. In addition, for electrochemical hydrogen peroxide synthesis through the two-electron water oxidation reaction, we developed a data-driven catalyst design framework by integrating density functional theory, weighted atom-centered symmetry function descriptors, machine learning, and microkinetic modeling. This framework enabled efficient prediction of adsorption free energies and high-throughput screening of catalyst candidates across different material families [6].

Overall, these studies demonstrate how atomic-scale simulations can connect catalyst structure, electronic properties, adsorbate-induced surface reconstruction, and reaction kinetics. The obtained insights provide theoretical guidance for the rational design of efficient electrocatalysts for sustainable energy conversion. The density functional calculations and microkinetic/data-driven simulations were conducted using VASP and in-house Python scripts, respectively.

References

[1] H. Liu et al., J. Phys. Chem. Lett. 16, 12892 (2025).

[2] T. Liu et al., Small 21, e202507824 (2025).

[3] S.-W. Ying et al., Angew. Chem. Int. Ed. 64, e202511924 (2025).

[4] Y. Wang et al., J. Am. Chem. Soc. 147, 32249 (2025).

[5] T. Lu et al., ACS Catal. 16, 2827 (2026).

[6] Z. Liu et al., Angew. Chem. Int. Ed. 65, e202518027 (2026).

Molecular Dynamics Analysis for Water Molecule Dynamics Under Local-Electric-Field Exited by Microstructures

Ayumu TAKAHASHI[1], Kiyoto KAWAI[1], Hiroki GONOME[1]

[1]*Graduate School of Science and Engineering,*

Yamagata University, Jonan, Yonezawa, Yamagata 992-8510

Mitigating global warming requires the development of highly efficient, low-energy energy conversion processes. Controlling water-mediated processes is essential for many energy technologies. While these processes traditionally rely on thermal processes, the photomolecular effect, which is the non-thermal excitation of water molecules by light, offers a promising alternative [1]. Because light is an electromagnetic wave, we hypothesize that electric fields can similarly activate polar water molecules.

In this study, we evaluated the dynamics of water molecules under exited electric field when light was irradiated into microstructures. The electric fields exited by microstructures were pre-calculated by COMSOL Multiphysics and applied to the MD analysis. Figure 1 shows that temperature distribution at no electric field and with electric field. It shows that the thermal diffusivity during transient response varies depending on presence or absence of an exited electric field. Table 1 shows that thermal reach distance over the same elapsed time. It shows that thermal propagation proceeded more rapidly under conditions where an electric field was applied. In these results, it has been suggested that applying an electric field may improve the thermal diffusivity of water.

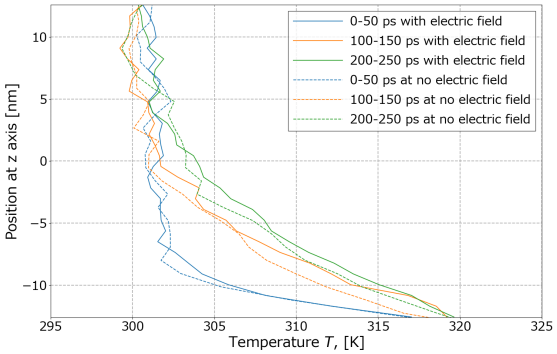


Fig.1: Temperature distribution at no electric field and with electric field.

Table 1: Thermal reach position over the same elapsed time

	With EF [nm]	Without EF [nm]
0-50 ps	-9.4	-9.6
100-150 ps	-2.7	-3.8
200-250 ps	0.2	-1.3

References

[1] Yaodong Tu, Jiawel Zhou, Shaoting Lin, and Gang Chen, Proceedings of the National Academy of Science, 120, e2312751120 (2023).

Electronic state calculations under photoinduced reactions

Kaori Niki

Graduate school of science

Chiba University, Yayoi-cho, Inage-ku, Chiba 263-8522

Introduction

In recent years, understanding the dynamics of hot carriers generated by photoexcitation and their spin-dependent electronic states has become a crucial issue in photocatalytic reactions and spintronic material design. However, a unified understanding of electronic transitions and relaxation processes after photoirradiation, as well as interactions with the substrate and coupling with phonons, is still insufficient. This research performed hot carrier relaxation process in CuPc/$TiSe_2$ systems by combining electronic states obtained by Vienna *Ab initio* Simulation Package (VASP) with non-adiabatic molecular dynamics (NAMD) calculations.

Method

We performed density functional theory (DFT) calculations using VASP version 6.4.3 [1,2]. Exchange–correlation effects were treated within the spin-polarized generalized gradient approximation (GGA) using the Perdew–Burke–Ernzerhof (PBE) functional [3]. The $TiSe_2$ slab model (8×8×1) was constructed with lattice constants. The projector augmented wave (PAW) method was employed with a plane-wave cutoff energy of 380 eV.

NAMDk simulations were carried out [4], which operates directly in momentum space. In this framework, the time-dependent carrier wave function is expanded in the basis of Kohn–Sham eigenstates. Nonadiabatic transitions between electronic states are described using the fewest switches surface hopping (FSSH) algorithm [5], hopping probabilities are determined from the time evolution of the density matrix. Electron–phonon coupling matrix elements were computed using the Perturbo code [6] The Ti 3d and Se 4p orbitals were used as initial projections for constructing Wannier functions [7]. Phonon properties were calculated using density functional perturbation theory (DFPT) [8] on q-point grids of 4×4×4 for the bulk and 16×16×1 for the single-layer system.

Results

This study tracked the hot carrier relaxation process in the CuPc/$TiSe_2$ system. By using a model with an increased number of substrate layers, relaxation times consistent with experimental results, suggesting the important contribution of substrate phonons to electron relaxation. Filtering the calculation results by specific momentum (M point) and energy to correspond to the tr-ARPES experimental conditions revealed that intra-band relaxation

proceeds as an energy-dependent multi-step (cascade) process.

Conclusion

In summary, NAMDk demonstrates that it is a powerful theoretical analysis method that complements tr-ARPES experiments for a wide range of systems, including charge density wave materials.

References

[1] G. Kresse and J. Hafner, Phys. Rev. B **47**, 558 (1993).

[2] G. Kresse and D. Joubert, Phys. Rev. B **59**, 1758 (1999).

[3] J. P. Perdew, K. Burke, and M. Ernzerhof, Phys. Rev. Lett. **77**, 3865 (1996).

[4] Z. Zheng, Y. Shi, J.-J. Zhou, O.V. Prezhdo, Q. Zheng, and J. Zhao, Sci. **3**, 532 (2023).

[5] J.C. Tully, J. Chem. Phys. **93**, 1061 (1990).

[6] J.-J. Zhou, J. Park, I.-T. Lu, I. Maliyov, X. Tong, and M. Bernardi, Comput. Phys. Commun. **264**, 107970 (2021).

[7] G. Pizzi, V. Vitale, R. Arita, S. Bl¨ugel, F. Freimuth, G. G´eranton, M. Gibertini, D. Gresch, C. Johnson et al., Condens. Matter **32**, 165902 (2020).

[8] S. Baroni, S. de Gironcoli, A. Dal Corso, and P. Giannozzi, Rev. Mod. Phys. **73**, 515 (2001).

Prediction of materials properties and exploration of materials with materials informatics

Yosuke HARASHIMA
Graduate School of Science and Technology, Nara Institute of Science and Technology
Takayama-cho, Ikoma, Nara 630-0192

1 Background

Machine learning for materials discovery requires large datasets, yet experimental data on materials properties are scarce. First-principles simulations supply more data but carry systematic errors (e.g. GGA-PBE underestimates band gaps). We developed **CLAUDE** (**C**ovariance **L**inkage **A**ssimilation method for **U**nobserved **D**ata **E**xploration), which integrates experimental and simulation data via data assimilation and couples the resulting model with Bayesian optimization for efficient materials search. As a practical application, the band gap of the perovskite solid solution $(\mathrm{Sr}_{1-x_1-x_2}\mathrm{La}_{x_1}\mathrm{Na}_{x_2})(\mathrm{Ti}_{1-x_1-x_2}\mathrm{Ga}_{x_1}\mathrm{Ta}_{x_2})\mathrm{O}_3$ was modeled for photocatalytic water splitting.

2 Data Assimilation Methodology

Descriptors x and $y = (y_{\mathrm{sim}}, y_{\mathrm{exp}})^\top$ are concatenated into $z = (x^\top, y^\top)^\top$, assumed to follow a multivariate Gaussian distribution with precision matrix Λ: $p(z \mid \Lambda) \propto \exp(-\frac{1}{2} z^\top \Lambda z)$. The off-diagonal block Λ_{yx} encodes the simulation–experiment correlation. The conditional mean $\mu = -(\Lambda_{yy})^{-1}\Lambda_{yx}x$ gives the assimilated prediction of y_{exp}. Λ is estimated via MAP estimation using the sufficient statistic $C^N_{\gamma_1\gamma_2} = \sum_i z_{i\gamma_1} z_{i\gamma_2}$, enabling sequential updates without retaining raw data.

Mismatched composition grids between datasets produce missing values. These are treated via the *direct likelihood*: missing variables are integrated out analytically, and the integration result in the Schur complement $\bar{\Lambda} = \Lambda_{\alpha\alpha} - \Lambda_{\alpha\bar{\alpha}}\Lambda^{-1}_{\bar{\alpha}\bar{\alpha}}\Lambda_{\bar{\alpha}\alpha}$. Each data point thereby contributes to Λ regardless of whether its counterpart in the other dataset exists.

3 Bayesian Optimization with Assimilation

M=500 models are sampled from the posterior of Λ to capture uncertainty without a Gaussian process. Each iteration:

- Retrain the assimilation model with added data.
- Propose one experimental candidate maximising $\alpha_{\mathrm{EI}} = \langle \max(\mu_k - y^*, 0) \rangle_k$.
- Propose ξ simulation candidates maximising the variance $\alpha_{\mathrm{Var}} = \langle (\mu_k - \mu)^2 \rangle_k$.

Because the two models share components of Λ, simulation data (Step 3) narrows the posterior of the experimental model (Step 2) even before new experiments are performed.

4 Computations at ISSP Supercomputer Center

The KKR-CPA band gap calculations using AkaiKKR were conducted primarily

on the ISSP supercomputer. AkaiKKR (`http://kkr.issp.u-tokyo.ac.jp/`) is a first-principles code based on the Korringa–Kohn–Rostoker (KKR) Green's function method. Coupled with the Coherent Potential Approximation (CPA), the code treats chemical substitutional disorder self-consistently without explicit supercells, enabling band gap evaluation across a continuous (x_1, x_2) composition space. A uniform mesh of 54 compositions of $(Sr_{1-x_1-x_2}La_{x_1}Na_{x_2})(Ti_{1-x_1-x_2}Ga_{x_1}Ta_{x_2})O_3$ was computed with GGA-PBE ($l_{\max}$=4 for cations, 3 for O; `bzqlty` = 8). These 54 simulation points, combined with 24 experimental values from master's theses of the Kudo group (Tokyo Univ. of Science), form the complete training set for CLAUDE (simulation RMSE: 0.13 eV; experimental RMSE: 0.17 eV).

5 First-Principles Calculations

Four types of first-principles calculations were performed. First, band gap training data for the assimilation model were generated using AkaiKKR with the KKR-CPA method and the GGA-PBE functional, covering 54 compositions on a uniform grid. Second, the lattice constants of the end-member compounds $SrTiO_3$, $LaGaO_3$, and $NaTaO_3$ were optimised with VASP using the projector augmented-wave (PAW) method and GGA-PBE (energy cutoff: 400 eV; k-mesh: 8^3); these values served as the basis for Vegard's law interpolation across the solid-solution composition space. Third, total energies of all 867 symmetry-inequivalent substitutional configurations in a 2×2×2 supercell were evaluated with VASP at the GGA-PBE level to identify the most stable atomic arrangement. Finally, the band gap of the most stable configuration was calculated at a higher level of theory using the hybrid functional HSE06 in VASP, providing an accurate verification of the convex-downward E_g trend predicted by the assimilation model.

The HSE06 calculations confirmed the convex-downward E_g at $(0.375, 0.375)$: 2.87 eV vs. $SrTiO_3$ (3.02), $LaGaO_3$ (4.67), $NaTaO_3$ (3.73 eV). The assimilation model predicted test compositions in data-sparse regions with errors of -0.05, -0.22, -0.13 eV at (x_1, x_2)=$(0.25, 0.50)$, $(0.50, 0.25)$, $(1/3, 1/3)$, respectively, reproducing the atomic cocktail effect (enhanced visible-light absorption) consistent with both experiment and HSE06 calculations.

References

[1] Y. Harashima, *et al.*: Phys. Rev. Materials **9**, 093803 (2025); `https://github.com/yy-harashima/CLAUDE`.

Closed-Loop Framework for Discovering Stable and Low-Cost Bifunctional Metal Oxide Catalysts for Efficient Electrocatalytic Water Splitting in Acid

XUE JIA

Advanced Institute for Materials Research (WPI-AIMR),

Tohoku University, Sendai, 980-8577

We develop a loop-based design framework comprising front-end exploration of potential catalysts, mid-end synthesis and electrochemical testing, and back-end characterizations to identify promising non-noble MO catalysts for acidic water splitting.

This year, we utilized supercomputing resources to perform density functional theory (DFT) calculations to accurately evaluate the theoretical activity for a promising MO electrocatalyst, $RbSbWO_6$, which was determined by data mining. First, we calculated the surface energy (γ) among various surface structures, and two surface structures with a Miller index of (011) were identified as the most thermodynamically favorable surfaces. Therefore, these two $RbSbWO_6$ surfaces were selected as potential exposed surfaces for subsequent surface state analysis. Based on adsorption energy calculations across the adsorption sites, 2D surface Pourbaix diagrams are displayed. Based on these altered surface structures, theoretical activities were analyzed using microkinetic modeling. For the OER, structure A, with 1/6 ML of O* coverage and adsorption of O* or OH* on the W site, is positioned near the peak of the volcano model, indicating a promising OER activity at this site. For HER, Structure B, with 11 Ov, which is almost at the top of the volcano model, indicating a promising HER activity. Therefore, both sides of the $RbSbWO_6$(011) surface can provide active sites for catalyzing the OER and HER, suggesting that this could be a bifunctional catalyst for water splitting.

Experimental validations successfully synthesized $RbSbWO_6$ and demonstrated its robust performance and stability in acidic OER and HER environments. As summarized from the DigCat platform, $RbSbWO_6$ stands out as one of the most effective bifunctional MO catalysts for acidic water splitting compared with other reported stoichiometric non-noble MO catalysts without significant engineering or modification. This demonstrates the effectiveness of our comprehensive strategy.

References

[1] **X. Jia**, Z. Zhou, F. Liu, T. Wang, Y. Wang, D. Zhang, H. Liu, Y. Wang, S. Ye, K. Amezawa*, L. Wei*, and H. Li*, Journal of the American Chemical Society, 2025, 147, 226

Development of First-principles Berry Phase Calculation codes for Application to Large Systems

Naoya YAMAGUCHI
Nanomaterials Research Institute (NanoMaRi), Kanazawa University
Kakuma-machi, Kanazawa, Ishikawa 920-1192

This year, we focused particularly on refining computational methods and applying them to complex systems, conducting calculations based on first-principles electronic structure calculations.

First, we further advanced the computational methods and code development for intrinsic anomalous Hall conductivity (AHC), and improved algorithms to overcome computational difficulties arising in complex material systems containing defects, impurities, layered materials, and artificial superlattices. In such systems, numerous degenerate points may appear due to the folding of the electronic band structure, requiring high-density k-point sampling and increasing computational costs. In this study, we further developed the minor determinant method based on the local Berry phase (LBP) method [1] developed in the previous year, implementing an algorithm capable of efficiently evaluating AHC while suppressing numerical instability. This year, we additionally implemented a tetrahedron method and confirmed that it suppresses numerical oscillations in AHC associated with changes in chemical potential. This has enabled stable and high-precision calculations of chemical potential-dependent AHC. Furthermore, by adding a checkpoint function to the computational code for the LBP method, we enabled the resumption of calculations even if they were interrupted midway, thereby making it possible to handle long-duration computations exceeding one day.

In addition, we advanced the development of a method that combines the LBP method with the hybrid Wannier function method to analyze the contribution of each AHC layer (layer anomalous Hall conductivity) [2]. We performed computational studies applying this method to magnetic topological insulators and magnetic metal thin films, and released the computational code as `layerAHC` [3].

Furthermore, we developed the giant molecule band unfolding (GMBU) procedure as a method for analyzing electronic states in non-periodic nanostructures [4]. In this procedure, in a finite-size giant molecular model, we first calculate the eigenvalues and eigenvectors for the molecular orbitals. We then introduce relative position vectors of atoms in place of lattice parameters in periodic systems and evaluate spectral weights by assigning effective wave number parameters, thereby enabling the depiction of band-like structures corresponding to band structures even in non-periodic or finite systems. We applied this procedure to various nanoflakes, confirming that it can reproduce clear band-like structures even in finite-size systems. We have released the computational code for this procedure as `GMBU.jl` [5]. As described above, we have continued to develop and release computational methods for electron transport based on the Berry phase and for analyzing electronic states in non-periodic systems. Furthermore, by utilizing computational resources, we have achieved the analysis of electronic states and Berry phase-related physical properties in complex material systems.

References

[1] H. Sawahata, N. Yamaguchi, S. Minami, F. Ishii, Phys. Rev. B **107**, 024404 (2023).

[2] Y. Morishima, F. Ishii, N. Yamaguchi, arXiv:2506.01160.

[3] https://isspns-gitlab.issp.u-tokyo.ac.jp/n-yamaguchi/layerAHC.

[4] N. Yamaguchi, S. Yunitasari, W. Amalia, C.-C. Lee, T. Ozaki, F. Ishii, Nano Lett. **25**, 17725 (2025).

[5] https://isspns-gitlab.issp.u-tokyo.ac.jp/n-yamaguchi/GMBU.jl; https://doi.org/10.5281/zenodo.17815785.

A novel framework for predicting non-van der Waals two-dimensional materials

Shota ONO
Muroran Institute of Technology, Muroran, Hokkaido 050-8585, Japan

Many two-dimensional (2D) materials are categorized as van der Waals (vdW) type-systems, in which the parent 3D crystals have layered structures. However, there also exists non-vdW 2D materials whose 3D counterparts exhibit no geometrical anisotropy. To date, no physically transparent descriptors for predicting non-vdW 2D materials have been proposed.

In this project, we developed a framework for identifying non-vdW 2D materials [1]. This is achieved by calculating the thickness dependence of total energy of thin films truncated from a specific surface. Non-vdW materials in the monolayer limit exhibit a downward deviation from the law of finite-thickness excess energy (FTEE) inverse to the number of layers:

$$\Delta E \propto N^{-1}, \tag{1}$$

where ΔE is the total energy of N layered thin film relative to the bulk energy. The total energies of thin films in single-component systems were calculated using Quantum Espresso (QE). The thin film geometries derived from bulk surfaces were constructed using Atomic Simulation Environment (ASE).

Figure 1(a) shows a breakdown of N^{-1} law below $N \leq 2$ for IV and V group systems. Noble metals including Au also exhibit a deviation from the N^{-1} law, as shown in Fig. 1(b). Such deviations indicate that these systems prefer 2D structures in the monolayer limit and can thus be regarded as 2D materials. This is consistent with experimental realization of non-vdW 2D materials such as silicene (Si), germanene (Ge), and goldene (Au). Figure 1(c) lists $p = d\ln\Delta E/d\ln N$ at $N = 1$ for single-component systems in the periodic table. Elements having small negative values of p can adopt 2D structures. This may be useful for comparisons with future experiments.

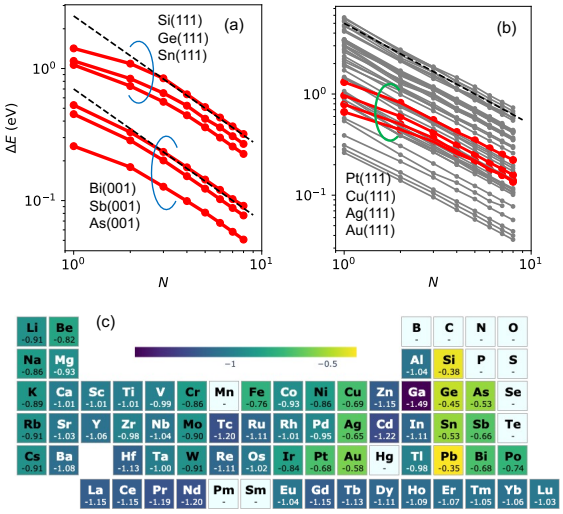


Figure 1: ΔE versus N for (a) IV and V group and (b) metallic elements. The dashed line indicates $\Delta E \propto N^{-1}$. (c) $p = d\ln\Delta E/d\ln N$ at $N = 1$ for elements in the periodic table. p at $N = 2$ is shown for Pb. Data reproduced from Ref. [1].

References

[1] S. Ono: Phys. Rev. B **112**, 075403 (2025).

Anomalous electron-phonon coupling in Cu-Ni alloys

Shota ONO
Muroran Institute of Technology, Muroran, Hokkaido 050-8585, Japan

Ultrafast relaxation following excitation by a femtosecond laser pulse enables the investigation of electron-phonon (e-ph) coupling in metals. The ultrafast luminescence dynamics have been studied in various elements [1]. The decay rate of luminescence has been successfully described by a modified two-temperature model (TTM), in which the e-ph coupling parameters are determined using first-principles calculations. In this project, we extend this framework to the luminescence of Cu-Ni solid solutions, and demonstrate an anomalous dependence of the e-ph coupling strength on Ni concentration [2].

According to the modified TTM, the decay rate Γ of non-equilibrium electrons in metals is proportional to the e-ph coupling constant $\lambda\langle\omega^2\rangle$. This is expressed as

$$\Gamma = \frac{3\hbar\lambda\langle\omega^2\rangle}{2\pi k_{\mathrm{B}} T_0}, \qquad (1)$$

where $\hbar$ is the Planck constant, k_{B} is the Boltzmann constant, and T_0 is the phonon temperature. We calculated $\lambda\langle\omega^2\rangle$ for $\mathrm{Cu}_{1-x}\mathrm{Ni}_x$ alloys using Quantum Espresso. We assumed a $2\times2\times2$ supercell containing eight atoms, and tuned the Ni concentration x.

Figure 1(a) shows the time-evolution of luminescence intensity of $\mathrm{Cu}_{1-x}\mathrm{Ni}_x$ for various x. The luminescence intensity decreases by an order of magnitude within a few picoseconds. As shown in Fig. 1(b), the decay rate Γ exhibits an anomalous dependence on Ni composition, i.e., it decreased first by adding Ni up to $x = 0.17$ and then started to increase with x. This behavior is well reproduced by the theoretical values of Γ given in Eq. (1). The agreement between experiment and theory indicates that the e-ph coupling strength in $\mathrm{Cu}_{1-x}\mathrm{Ni}_x$ alloys is a nonlinear function of x. A possible origin for this nonlinear behavior is a reduction in the magnitude of the matrix elements and/or a decrease in the available phase space for e-ph scattering in dilute alloys.

We further performed systematic calculations of $\lambda\langle\omega^2\rangle$ for X_7Y_1 alloys with X = Cu, Ag, Au and Y = Ni, Pd, Pt, Cu, Ag, Au. We confirmed that a small inclusion of group 10 elements gives rise to a decrease in $\lambda\langle\omega^2\rangle$. This suggests that alloying can enhance the luminescence lifetime.

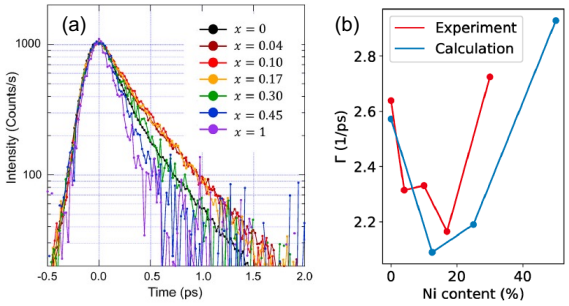


Figure 1: (a) Luminescence decay at 0.6 eV for alloys with various x. Each curve is normalized to 1000 at maxima. (b) The decay rate Γ as a function of Ni content. Data reproduced from Ref. [2].

References

[1] T. Suemoto, S. Ono et al.: Phys. Rev. B **111**, 035150 (2025).

[2] T. Suemoto, H. Morino, S. Ono et al.: Phys. Rev. B **112**, 035138 (2025).

Influence of Laser Excitation on Non-thermal Melting in α-Quartz

Mizuho ONO, Atsuki KOMIYA

Institute of Fluid Science,

Tohoku University, Katahira, Aoba-ku, Sendai, Miyagi 980-8577

When an ultrashort laser pulse is directed at a material, its electrons can become strongly excited, leading to unique properties. Among the resulting phenomena, non-thermal melting, in which the crystal lattice of a solid rapidly collapses, is particularly effective for precision machining [1]. The objective of this work is to clarify the influence of excited electronic states on non-thermal melting through numerical simulations using time-dependent density functional theory (TDDFT). α-quartz was selected as the target material.

Figure 1(a) and 1(b) show the occupied states after laser irradiation at photon energies of 1.55 eV and 3.10 eV, respectively. The results confirm that there is virtually no difference between the two cases in terms of the excited electrons. This is because tunnel ionization dominates, largely eliminating the photon energy dependence. Figure 1(c) displays the occupied electron states and the projected density of states (PDOS) at an electron temperature of 2.5 eV, calculated using finite-temperature DFT. This result shows that electrons near the Fermi level are excited to the conduction band. In the finite-temperature calculations, the conduction band minimum (CBM) is occupied according to the Fermi–Dirac distribution; however, under laser excitation, it is evident that electrons are not present near the CBM but are instead excited to higher energy levels. These differences imply that the interatomic bonding strength after excitation varies depending on the process, suggesting that the atomic behavior during non-thermal melting will also differ.

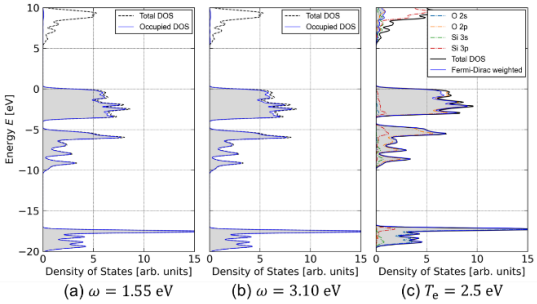


Fig. 1: (a, b) Comparison of the initial DOS and projection of electron orbitals onto the ground state after laser irradiation at $I = 1.00 \times 10^{14}$ W/cm^2 for (a) 1.55 eV and (b) 3.10 eV. (c) PDOS of the ground state overlaid with the occupied states derived from the Fermi–Dirac distribution.

References

[1] M. Boero, A. Oshiyama, P. Luigi Silvestrelli, and K. Murakami, Physica B: Condensed Matter **376-377**, 945 (2006).

First-Principles Study of Optoelectronic Properties of Organic Molecular Aggregates

Takatoshi Fujita
Institute for Quantum Life Science, National Institutes for Quantum Science and Technology
Anagawa, Inage-ku, Chiba 263-8555

We have developed large-scale excited-state methods based on the GW/Bethe-Salpeter equation (GW/BSE) in combination with the fragment molecular orbital (FMO) framework. In parallel, we have established a multi-scale simulation scheme based on quantum dynamics methods using model excited-state Hamiltonians derived from the FMO-GW/BSE. This scheme allows for first-principles simulations of exciton dynamics in realistic molecular aggregates .

As an application of our multi-scale approach [1], we have elucidated the role of charge-transfer (CT) state manifold in the exciton dissociation processes in donor/acceptor (D/A) blends. Understanding the relationship between the driving energy and the charge photogeneration in D/A blends is crucial to improving the power conversion efficiency of organic solar cells. Here, we investigate the exciton dissociation dynamics in P3HT/PCBM blends by employing the FMO-GW/BSE, ensemble-averaged wave packet dynamics, and the Marcus-Levich-Jortner rate formalism. Analysis of the rate constants suggests that direct exciton dissociation into low-energy CT states is inefficient, occurring on timescales longer than ∼1 ns, whereas dissociation into higher-energy CT states can proceed on the ∼1 ps timescale. The thermally-corrected wave packet dynamics simulations for the amorphous structure show that the initial exciton dissociation to high-energy CT state takes place at ∼100 fs after photoexcitation, followed by the thermal relaxation toward low-lying CT. These results demonstrate that higher-energy CT states, often overlooked in conventional models, play a significant role in facilitating exciton dissociation.

As another application [2], we have studied the relationship between the crystal polymorphs and excited states of dipolar azobenzene molecules bearing electron-donating and -accepting units. To gain microscopic insight into the relationship, we have performed FMO-GW/BSE calculations on molecular clusters consisting of 54 dipolar azobenzene molecules extracted from two polymorphs. Our calculations suggest that the low-lying excited states consist of a mixture of intramolecular transitions ($n \rightarrow \pi^*$ and $\pi \rightarrow \pi^*$) and intermolecular CT transitions between the n or π orbital of one molecule to π^* orbital of another. Differences in the degree of mixing among these excitation characters result in distinct spectral features in the two polymorphs.

References

[1] T. Fujita, M. Nozaki, Phys. Chem. Chem. Phys. **38**, 20765 (2025).

[2] M. Yamauchi, E. Machida, M. Nozaki, T. Fujita, H. Sotome, K. Yamamoto, Y. Mizuhata, N. Aratani, H. Yamada, S. Masuo, Adv. Opt. Mater. **14**, e03396 (2026).

Phase transformation and electric state of high entropy alloys

Yoko Yamabe-Mitarai

Frontier Science Graduate School,

The University of Tokyo, Kashiwa-no-ha, Kashiwa, Chiba 277-8561

High-entropy alloys (HEAs) have been attracting attention as new-generation structural and functional materials since this new paradigm was proposed in 2004 [1]. Most HEAs have a single face-centered-cubic (fcc), body-centered-cubic (bcc) structure, or their mixtures. Not many examples of HEAs with the hexagonal-close-packed (hcp) structure have been studied. We are applying to find HEAs with hcp structure experimentally and a few alloys were found to have an hcp structure [2].

Among the hcp-HEAs, CoReRu alloys are of particular interest. By combining Cr, Fe, and V, and by making multiple additions of these elements, the hcp region becomes stable over a wide temperature range between 600 and 1600 ˚C [3]. The equiaxed single-phase hcp phase was observed after heat treatment. The strength of these alloys was around 200 MPa at 1000 ˚C [4].

To investigate whether strong multi-elemental interaction or short-range order formation occurs, Mean Square Atomic Displacement, MSAD and an electron charge of density, Bader Charge, was calculated using DFT [5]. A supercell model with 128 atoms was used to indicate the solid solution phase. Special Quasirandom Structure was used to simulate random atomic positions. The internal coordinate was optimized using Quantum Espresso (QE). The electron charge density was calculated on the optimized coordinates. It is found that atomic displacement of Re and Ru was larger than those of other elements indicating in large lattice distortion by Re and Re. Cr, Fe, and V did not show a specific effect for MSAD and their effect was changed by the combination of elements. The distance between two neighbor atoms calculated from MSAD indicates longer distance of Re-Re, Re-Ru, Ru-Ru compared with the ideal distance indicates large lattice distortion. The strong solid-solution strengthening caused by these three bonds. The Barder charge also indicates the strong bonding between Re-Re, Re-Ru, and Ru-Ru.

References

[1] B. Cantor et. al., A. J. B. Vincent, Mater. Sci. Eng. A, **375-377**, 213 (2004).

[2] Y. Yamabe-Mitarai et. al., JALCOM, **911**, 164849 (2022)

[3] M.C Gao, B. Zhang, et al., Metall. Mater. Trans. A, V47, (2015), p3322-3332.

[4] S. J, Liang, Ph D Thesis, Spt. (2024)

[5] Y. Sakai, Master’s Thesis, Mar. (2026).

Ab initio DFT study of lattice defect electronic structures for emergent polar skyrmions

Takahiro SHIMADA and Susumu MINAMI

Graduate School of Engineering, Kyoto University,

Kyoto daigaku-Katsura, Nishikyo-ku, Kyoto 616-8540

This study proposes a novel strategy to generate atomic-scale ferroelectricity and ultrahigh-density polar skyrmions in a paraelectric perovskite oxide by means of twist grain boundary and/or moiré engineering [1]. Using ISSP supercomputer system B and first-principles density functional theory calculations with the VASP code, we demonstrate that twisting two monolayers of centrosymmetric $SrTiO_3$ induces robust ferroelectric polarization and stabilizes a lattice of polar skyrmions with characteristic sizes on the order of one nanometer. This result overcomes the long-standing critical thickness limitation for ferroelectricity and polarity, which typically suppresses ferroelectric order in ultrathin oxide films.

The twisted $SrTiO_3$ boundaries form moiré superlattices or twist grain boundary in which strong interlayer coupling leads to substantial lattice reconstruction and ion displacement. These structural distortions break local inversion symmetry, giving rise to sizable electric polarization comparable to that of conventional ferroelectrics such as $PbTiO_3$, despite $SrTiO_3$ being intrinsically non-ferroelectric. The polarization vectors curl in the plane and exhibit a continuous reversal in the out-of-plane component from the center to the moiré unit cell. Topological analysis, based on interpolated polarization fields, confirms that these polarization textures correspond to genuine polar skyrmions with a topological charge of approximately ±1.

Notably, polar skyrmions emerge in twist boundaries as thin as a single unit cell and persist across a range of large twist angles. For twist angles of 36.87° and 22.62°, the resulting skyrmion diameters are approximately 0.87 nm and 1.40 nm, respectively, yielding array densities up to $\sim 1.3 \times 10^{18}$ m^{-2}. These values represent the highest polar skyrmion densities reported to date, surpassing those achieved in conventional ferroelectric superlattices and heterostructures by more than an order of magnitude. The absence of a critical thickness and the extreme miniaturization are attributed to the nonlocal strain fields and charge redistribution inherent to moiré superlattices, rather than to geometric confinement alone.

Beyond ferroic topology, the study reveals that twisting engineering also profoundly alters

the electronic structure of $SrTiO_3$. Ultrathin twisted boundaries exhibit remarkably flat valence bands, with bandwidths below 5 meV over a wide range of twist angles, and as small as 0.24 meV at specific angles. Such ultraflat bands, narrower than those in twisted bilayer graphene, suggest strong electronic localization and potential for correlated electronic phenomena.

Overall, this work establishes defect-moiré engineering of perovskite oxides as a powerful platform for creating atomic-scale polar topologies and ferroelectricity in otherwise non-ferroelectric materials. The demonstrated combination of ultrathin ferroelectricity, ultrahigh skyrmion density, and emergent electronic flat bands opens new opportunities for fundamental studies and for the development of ultrahigh-density skyrmion-based memory and nanoelectronic devices.

References

[1] T. Xu, Q. Tao, J. Pang, J. Zhang, S. Li, R. He, J. Wang, T. Shimada, Research. **8**, 0621 (2025).

Density-functional studies on light-element effects in permanent magnets and on metal surfaces

Insung SEO

Graduate School of Natural Science and Technology,

Shimane University, Matsue, Shimane 690-8504

In this project, we conducted first-principles density-functional-theory (DFT) calculations on two subjects, both centered on the role of light elements (B, C, N, O, F): (i) the crystal-field parameters of light-element-doped permanent-magnet compounds $NdFe_{12}X$ under lattice strain, and (ii) the 1s core-level binding energies of light-element atoms on (111) metal substrates. Both studies were carried out on the ISSP system B, ohtaka, using the VASP and OpenMX codes.

Strain response of crystal-field parameters in $NdFe_{12}X$. The $ThMn_{12}$-type RFe_{12} (R = Nd, Sm) compound is a candidate for next-generation permanent magnets, and small light-element doping is widely investigated for stabilizing the structure and tuning the magnetocrystalline anisotropy. Our preliminary calculations on $NdFe_{12}X$ (X = B, C, N, O, F) revealed that the Stevens crystal-field parameter $A_2^0\langle r^2\rangle$, which dominates the single-ion anisotropy of Nd^{3+}, varies significantly and discontinuously across different light elements. To clarify the microscopic origin of this discontinuous variation, in this project we extended the calculations to include lattice strain along the *a*- and *c*-axes from −10% to +10% in 1% increments. Structural relaxation was performed with VASP under the GGA-PBE functional, treating the Nd 4*f* electrons with an open-core pseudopotential, and the crystal-field parameters were extracted from OpenMX electronic-structure calculations through a crystal-field analysis.

For undoped $NdFe_{12}$, $A_2^0\langle r^2\rangle$ remained nearly constant under both *a*- and *c*-axis strain within ±5%, whereas every $NdFe_{12}X$ showed a pronounced and largely monotonic response (Fig. 1). In $NdFe_{12}N$, for example, $A_2^0\langle r^2\rangle$ varies by more than 1300 K across the strain range, with the *a*- and *c*-axis strains giving nearly opposite-sign responses. $NdFe_{12}C$ exhibits a sign change of $A_2^0\langle r^2\rangle$ under sufficiently large *c*-axis compression, suggesting a potential easy-axis switching driven by epitaxial strain. These results indicate that the strain response of the crystal-field environment at the Nd site is qualitatively governed by the chemical bonding of the doped light element.

Core-level binding energies on metal surfaces. In parallel, we evaluated the 1s binding energies of B, C, and N atoms at on-

surface and subsurface sites of Al(111), Cu(111), and Ir(111) substrates using OpenMX with the exact-Coulomb-cutoff method [1]. The (4×4) slab models consisted of four metal layers with a vacuum spacing larger than 15 Å, and seven candidate sites (fcc-/hcp-hollow, ontop, bridge, and three subsurface sites) were considered for each species and substrate.

For B on Ir(111), the hcp-hollow site was found to be the most stable adsorption configuration, and its B 1s binding energy is calculated to be 189.30 eV, which is higher than that reported for the borophene B 1s peak. This identifies a plausible defect origin for the higher-binding-energy shoulder observed in experimental XPS spectra of borophene grown on Ir(111). The site- and substrate-dependent binding-energy table compiled in this study should aid the interpretation of XPS spectra of two-dimensional materials grown on metal surfaces. Part of these results was presented at the 72nd JSAP Spring Meeting (2026) [2].

Outlook. For both studies, further analyses such as internal-coordinate relaxation under strain and an extension to $SmFe_{12}X$ for the magnet study, and an extension to further substrate–adsorbate combinations for the surface XPS study, are envisioned as future work. Manuscripts based on the present results are currently in preparation.

References

[1] T. Ozaki and C.-C. Lee, Phys. Rev. Lett. **118**, 026401 (2017).

[2] I. Seo and H. Kageshima, 72nd JSAP Spring Meeting, 17a-PA3-5 (2026).

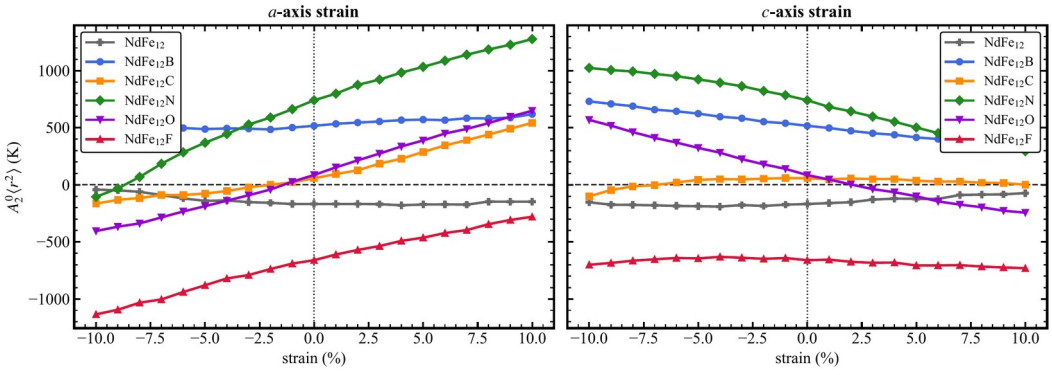


Fig. 1: Crystal-field parameter $A_2^0\langle r^2\rangle$ of $NdFe_{12}X$ (X = none, B, C, N, O, F) under uniaxial lattice strain along the *a*-axis (left) and *c*-axis (right).

Stable Structure of Cu cluster around Fe vacancy

Kazuhito Ohsawa

Institute for Applied Mechanics, Kyushu University,

Kasuga-koen 6-1, Kasuga, Fukuoka 816-8580

Introduction

Iron (Fe) and steel are important structural materials in fusion and fission reactors. Trace amount of cupper (Cu) is included in steel as impurity and precipitates in the irradiation circumstance. Cu clusters cause embrittlement of the steel because they inhibit dislocation motion. Besides, large amount of vacancy type lattice defects are nucleated in the irradiation circumstance by knock-on damage. In the present study, interaction between a Fe vacancy and an impurity Cu in Fe lattice are investigated. Besides, stable structures of Cu clusters nucleated around the Fe vacancy. We expect that vacancy type lattice defects will promote the precipitation of Cu and growth of the Cu cluster.

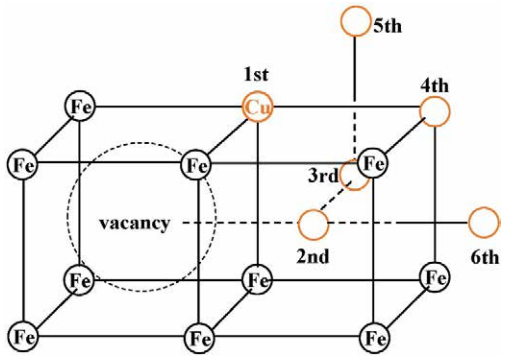


Fig. 1: Schematic view of Fe vacancy and nearest neighbor sites.

Simulation method

First-principle calculations based on density functional theory are performed by Vienna ab-initio simulation package (VASP) with generalized gradient approximation (GGA) and projector augmented wave method (PAW). We used supercell composed of 250 lattice points (5x5x5 bcc lattice) including a vacancy. In the present simulations, Fe atoms are supposed to be ferromagnetic elements.

Binding energy E_b between a Fe vacancy and an impurity Cu is defined, as follows.

$$E_b = E[\mathrm{Fe}_{m-1}\mathrm{V}] + E[\mathrm{Fe}_{m-1}\mathrm{Cu}] - E[\mathrm{Fe}_{m-2}\mathrm{VCu}(k)] - E[\mathrm{Fe}_m], \quad (1)$$

where E is cohesive energy of supercell. For example, supercell $\mathrm{Fe}_{m-1}\mathrm{V}$ is composed of m-1 iron atoms (Fe), one vacancy (V), where m=250. Impurity Cu located at k-th nearest neighbor site from the vacancy is expressed by Cu(k), as shown in Fig. 1.

The most stable structures of Cu clusters around a Fe vacancy are selected among many types of Cu cluster, which is steady work. But first and second nearest neighbor sites would be favorable for Cu atoms. So, the stable structures are able to predict beforehand, to some extent.

Results and discussion

We estimated binding energies of impurity Cu to vacancy in Fe lattice, according to equation (1). As shown in Fig. 2, first and second nearest neighbor sites from the vacancy are energetically favorable for Cu. Therefore, attractive interaction supposed to act between Cu and Fe vacancy, which is good agreement with the fact that Cu does not dissolve in Fe at all. In particular, the first nearest neighbor is the most stable site for Cu. Therefore, we expected that multiple Cu atoms will preferentially occupy the first nearest neighbor sites from Fe vacancy. However, the prediction is not necessarily correct.

Fig. 3 shows the most stable structures of Cu clusters around Fe vacancy. There are 8 first nearest neighbor sites around the Fe vacancy. However, Cu atoms occupy first and second nearest neighbor sites, as shown in Fig. 3 (b)-(e). For example, Fig. 3 (b) exhibits the most stable structure of two Cu atoms. One is at the first nearest neighbor site and the other is at second nearest neighbor site. At the moment, we can not think of a reason why that would happen. But that would be a subject for future research.

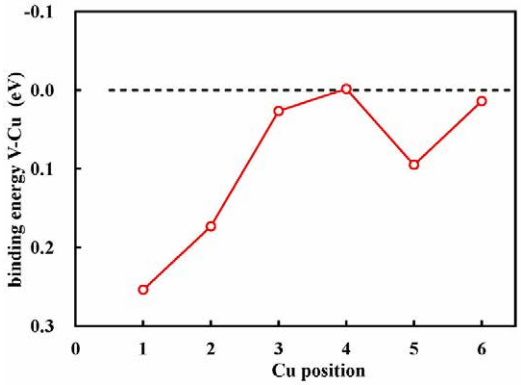


Fig. 2: Binding energy of Cu to Fe vacancy.

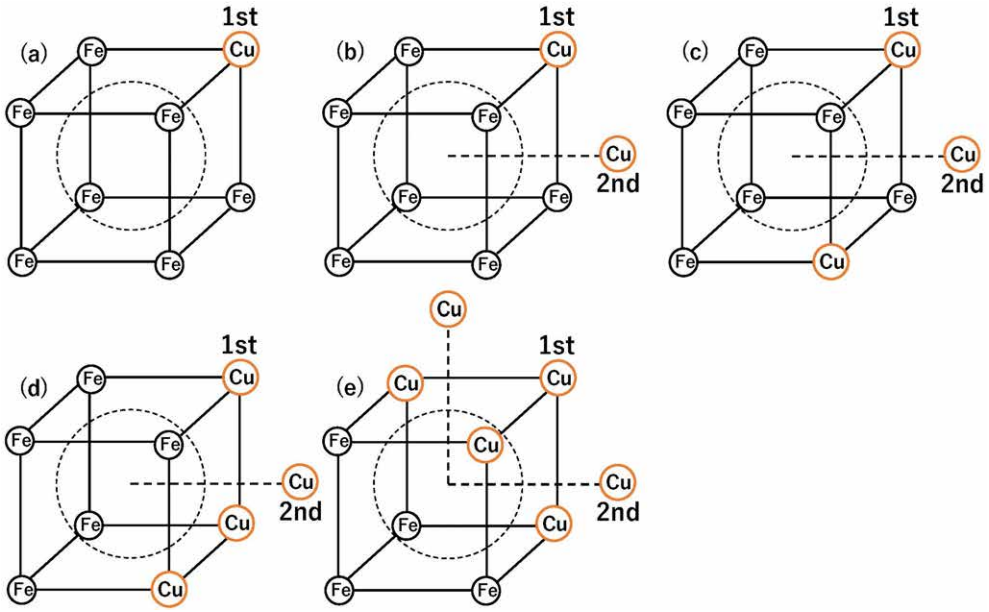


Fig. 3: Schematic view of most stable structures of Cu clusters around Fe vacancy.

First-principles design of magnetic tunnel junctions with an antiferromagnet Mn_3Sn

Katsuhiro Tanaka[1,2] and Yuta Toga[1,3]
[1]*Department of Physics, University of Tokyo, Bunkyo-ku, Tokyo 113-0033, Japan*
[2]*Department of Materials Design and Engineering, University of Toyama, Toyama-shi, Toyama 930-8555, Japan*
[3]*JSR-UTokyo Collaboration Hub, CURIE, JSR Corporation, Minato-ku, Tokyo 105-8640, Japan*

The tunnel magnetoresistance (TMR) effect is one of the prototypical spintronic phenomena, which has been applied to the electric readout. Conventionally, the TMR effect has been discussed in ferromagnetic tunnel junctions since ferromagnets have a net spin polarization and thus give rise to the spin-polarized tunneling current. However, recent studies have revealed that antiferromagnets (AFMs) can also produce a finite spin-polarized tunneling current when the magnetic order of the AFM breaks the macroscopic time-reversal symmetry [1–3], which is owing to the spin splitting in momentum space. This spin-polarized current in such spin-splitting AFMs leads to the realization of a finite TMR effect with antiferromagnets, the TMR ratio of which can be as large as that of ferromagnets.

In this study, we examine the TMR effect from first principles, using the noncollinear antiferromagnet Mn_3Sn as the electrode [4]. Mn_3Sn exhibits an inverse 120° magnetic structure at room temperature, where a finite spin polarization appears in momentum space. For Mn_3Sn, the experimental observation of the TMR effect has been reported as well as theoretical proposals [5–7]. Here, we adopt MgO, one of the representative barrier materials used in the magnetic tunnel junctions (MTJs), as the barrier layer, and investigate the $Mn_3Sn(01\bar{1}0)/MgO(110)/Mn_3Sn$ tunnel junction.

We calculate the TMR effect with the scattering theory formalism [8–11]. We separate the MTJ into the two lead regions and the scattering region in between. The lead and the scattering regions are Mn_3Sn and $Mn_3Sn/MgO/Mn_3Sn$, respectively. When constructing the scattering region, we optimize the interfacial distance between Mn_3Sn and MgO allowing for several percent of the lattice mismatch. After performing the electronic structure calculations for each region, we combine the lead and scattering regions to construct the MTJ, and calculate the transmission. We also calculate the distribution of the spin polarization on the Fermi surface of the bulk Mn_3Sn and the complex band structure of the bulk MgO. The simulations are performed using the Quantum ESPRESSO [12, 13] and Wannier90 [14] packages.

As a result, we obtain a finite TMR effect in the $Mn_3Sn/MgO/Mn_3Sn$ MTJ. The momentum-dependent transmission in the MTJ combined with the spin-split Fermi surfaces of Mn_3Sn and the complex energy bands of MgO reveals that the TMR effect appears due to the spin polarization of Mn_3Sn in the momentum space and the screening effect of MgO. The obtained TMR ratio reaches as high

as $\sim 1000\%$ with a thick barrier, which will be comparable to that in the ferromagnetic MTJs. Our MTJ employs a widely used barrier MgO, and therefore our results will serve as a realistic baseline for the development of the MTJs based on Mn_3Sn.

References

[1] J. Železný *et al.*, Phys. Rev. Lett. **119**, 187204 (2017).

[2] D.-F. Shao *et al.*, Nat. Commun. **12**, 1 (2021).

[3] L. Šmejkal *et al.*, Phys. Rev. X **12**, 011028 (2022).

[4] K. Tanaka, Y. Toga, S. Minami, S. Nakatsuji, T. Nomoto, T. Koretsune, and R. Arita, Phys. Rev. Mater. **10**, 044405 (2026).

[5] X. Chen, T. Higo, K. Tanaka, *et al.*, Nature **613**, 490 (2023).

[6] J. Dong *et al.*, Phys. Rev. Lett. **128**, 197201 (2022).

[7] C.-T. Chou *et al.*, Nat.Commun. **15**, 7840 (2024).

[8] H. Joon Choi and J. Ihm, Phys. Rev. B **59**, 2267 (1999).

[9] A. Smogunov *et al.*, Phys. Rev. B **70**, 045417 (2004).

[10] A. D. Corso and A. M. Conte, Phys. Rev. B **71**, 115106 (2005).

[11] A. Dal Corso *et al.*, Phys. Rev. B **74**, 045429 (2006).

[12] P. Giannozzi *et al.*, J. Phys.: Condens. Matter **21**, 395502 (2009).

[13] P. Giannozzi *et al.*, J. Phys.: Condens. Matter **29**, 465901 (2017).

[14] G. Pizzi *et al.*, J. Phys.: Condens. Matter **32**, 165902 (2020).

Efficient implementation of spin-cluster expansion for general spin models

Tomonori TANAKA
Department of Materials Science and Engineering, Institute of Science Tokyo, Yokohama 226-8501

Evaluating finite-temperature magnetism and spin textures directly from microscopic electronic-structure calculations remains an important challenge in computational materials science. We adopt the spin-cluster expansion [1], which provides a systematic framework for constructing general spin models from first-principles calculations. Within this framework, we determine the model parameters using torque-based regression instead of conventional energy fitting. Because torques encode the local gradient structure of the energy surface, a fixed number of spin configurations carries more information and yields accurate parameters with fewer data—a clear advantage for large systems and models with many interaction channels.

To validate the proposed method, we applied it to B20-type chiral magnetic materials, $Mn_{1-x}Fe_xGe$ and $Fe_{1-y}Co_yGe$. In these compounds, the lack of inversion symmetry in the crystal structure gives rise to the Dzyaloshinskii–Moriya interaction (DMI), which stabilizes twisted spin textures and leads to helical spin structures. Since the quantitative evaluation of the DMI is itself an important challenge in first-principles studies of magnetism, we first assessed the validity and efficiency of the proposed method through its ability to evaluate this interaction accurately.

Figure 1 shows the DMI parameter for first-nearest-neighbor Fe–Fe pairs in FeGe as a function of the number of sampled DFT calculations. Compared with the conventional energy-fitting approach, the torque-fitting method exhibits much faster convergence of the interaction parameters with respect to the number of data points, demonstrating a clear advantage in data efficiency. Moreover, the final values of the obtained interaction parameters were found to be in good agreement with those reported in previous studies, confirming the quantitative reliability of the present approach.

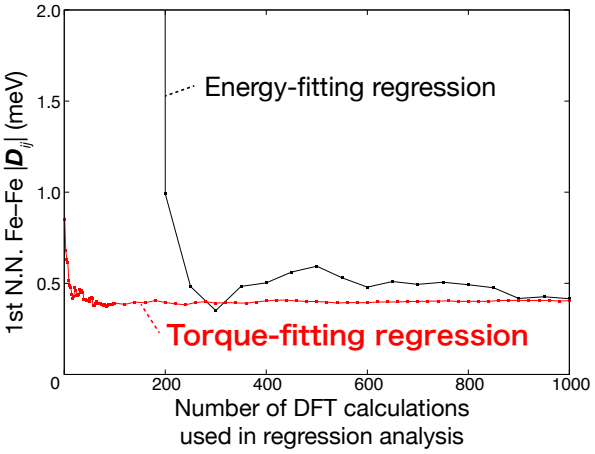


Figure 1: Convergence of the magnitude of the Dzyaloshinskii–Moriya interaction parameter $\boldsymbol{D}_{ij}$ at the first-nearest-neighbor Fe–Fe pairs in FeGe as a function of the number of sampled DFT calculations.

Figure 2 shows the DMI constant D and the helical spin period λ, obtained by mapping the derived spin model onto a micromagnetic model. The divergence of the helical spin period near the composition where $D = 0$,

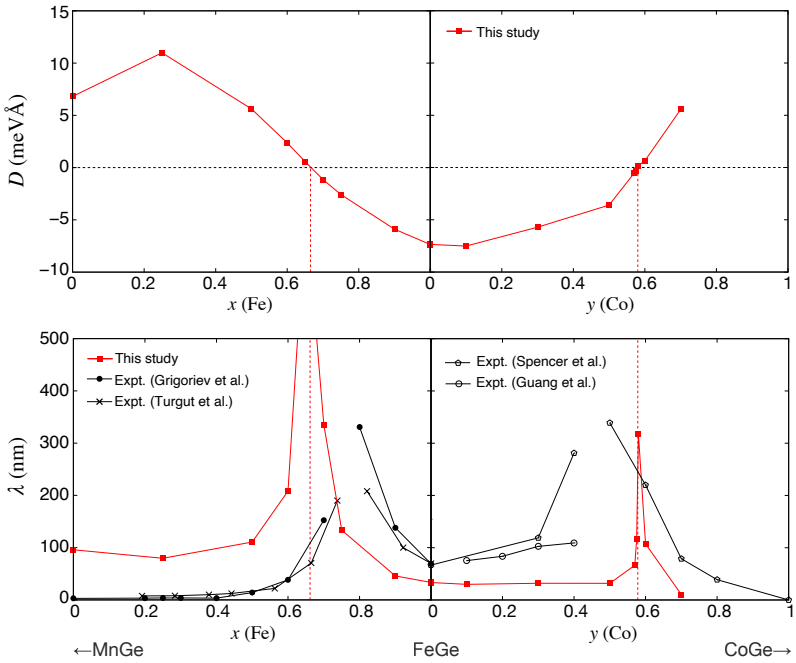


Figure 2: Composition dependence of the micromagnetic D parameter (upper panel) and the helical spin period λ (lower panel) for $Mn_{1-x}Fe_xGe$ and $Fe_{1-y}Co_yGe$. Experimental results are also shown for comparison [4, 5, 6, 7].

which has also been observed experimentally, was successfully reproduced. This result indicates that the present method can correctly capture the composition at which the helical period diverges, and thus that the constructed spin model has sufficient accuracy to describe the magnetic textures of real materials.

These results demonstrate that the spin-cluster expansion combined with torque-based fitting remains accurate when magnetic interactions are anisotropic and mutually competing, while substantially improving efficiency relative to conventional energy fitting. The formulation is anchored in a general multispin Hamiltonian rather than in any specific chemical family, so the same workflow applies broadly across magnetic materials. Wider use of this route should provide a unified first-principles basis for evaluating finite-temperature magnetic behavior over extended temperature windows from a single spin model.

These results have been released on arXiv [2]. In addition, the developed program has been made publicly available on GitHub as the `Magesty.jl` package [3].

References

[1] R. Drautz and M. Fähnle, *Phys. Rev. B* **69**, 104404 (2004).

[2] T. Tanaka and Y. Gohda, arXiv:2512.04458.

[3] https://github.com/Tomonori-Tanaka/Magesty.jl.

[4] S. V. Grigoriev et al., *Phys. Rev. Lett.* **110**, 207201 (2013).

[5] E. Turgut et al., *Phys. Rev. Mater.* **2**, 074404 (2018).

[6] C. S. Spencer et al., *Phys. Rev. B* **97**, 214406 (2018).

[7] Y. Guang et al., *JPhys Mater.* **7**, 025009 (2024).

TDDFT Simulation of Subcycle Reciprocal-Space Electron-Density Dynamics Driven by Intense Laser Fields

Yasushi SHINOHARA[1,2]

[1]*Photon Science Center,*

The University of Tokyo, Hongo, Bunkyo-ku, Tokyo 113-8656

[2]*Basic Research Laboratories,*

NTT Inc. 3-1 Morinosato Wakamiya, Atsugi, Kanagawa 243-0198.

We investigated the behavior of extended materials exposed to strong optical fields by means of time-dependent density functional theory (TDDFT) [1]. When the applied field reaches a magnitude comparable to the internal electric field of the material, highly nonlinear phenomena emerge that are beyond the scope of perturbative approaches. Describing such dynamics therefore requires direct real-time propagation of the time-dependent Kohn–Sham equation. The SALMON-TDDFT code [2] enables real-time simulations of crystalline solids, molecules, and atomic systems based on the Kohn–Sham framework. In the present work, the calculations were carried out using system B at SCC-ISSP.

We carried out TDDFT calculations to investigate subcycle reciprocal-space electron-density images in monolayer hexagonal boron nitride (hBN) and graphene driven by an intense electric field. Real-space electron densities were subsequently obtained through spatial Fourier transformation of the reciprocal-space data. The external field was linearly polarized, with a pulse duration of 14 fs in terms of full width at half maximum (FWHM), a photon energy of 0.4 eV, and a peak intensity of 1 TW/cm^2.

The reciprocal component of the time-dependent density is described by the complex-value amplitudes. Our analysis reveals that the phase (amplitude) time-evolution mainly determines the real-space evolution for monolayer hBN (graphene).

References

[1] Erich Runge and E. K. U. Gross, Phys. Rev. Lett. 52, 997 (1984).

[2] https://salmon-tddft.jp/, M. Noda, S.A. Sato, et al., Computer Physics Communications. 235, 356 (2019).

Ab initio electronic structure analysis for $Ca_5Ir_3O_{12}$

Kazuma NAKAMURA
Quantum Physics Section, Kyushu Institute of Technology
1-1 Sensui-cho, Tobata, Kitakyushu, Fukuoka, 804-8550

Materials with strong spin-orbit interaction (SOI) and their properties are actively studied. In the transition metal oxides, in addition to SOI, crystal field, electronic correlation, Hunds coupling, and frustration are relevant and affect low-energy physics. In the present study, we present *ab initio* calculations for 5*d* transition metal oxide $Ca_5Ir_3O_{12}$.

In $Ca_5Ir_3O_{12}$, there are two phase transitions; the first one is at 107 K, the second one is at 7.8 K [1,2]. Recently, it was clarified that the 107-K transition is the transition to the superlattice structure of $3a \times 3a \times 3c$ [3]. Space group was identified as R_3 with X-ray diffraction analysis [3]. The mechanism is discussed in terms of the order of the electric toroidal moments [3], and the moment configuration in the $3a \times 3a \times 3c$ lattice is proposed. The low-temperature phase transition at 7.8 K is not known apart from the entropy release [1,2].

This report focuses on the origin of the insulating properties of $Ca_5Ir_3O_{12}$. This material is insulating even above 800 K. Although several mechanisms have been proposed, a clear microscopic understanding is still lacking. We show that the insulating behavior of Ca5Ir3O12 originates from a threefold periodic spin structure along the c axis, where the spins rotate in the plane defined by the c axis and the magnetic easy axis. This noncollinear spin structure opens a band gap of approximately 0.2 eV, in good agreement with experiment. We further examine the experimentally observed R_3 structure and find that it can be naturally understood as being based on this threefold periodicity along the c axis. At the

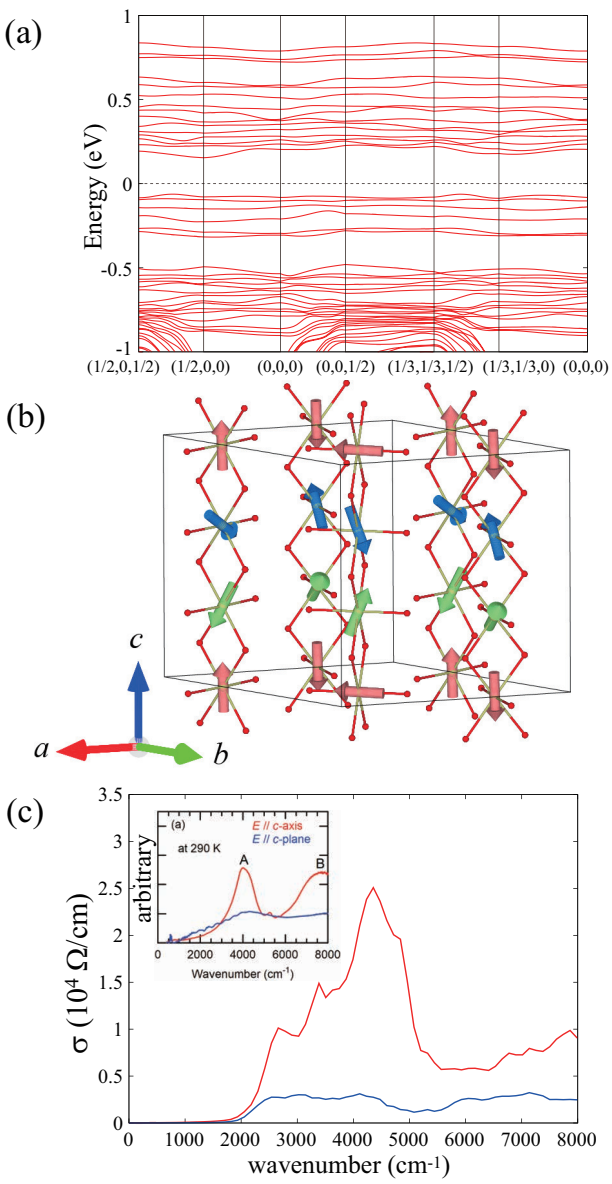


Figure 1: (a) Band structure for the $a \times a \times 3c$ hexagonal supercell, and (b) the corresponding spin configuration. (c) Optical conductivity, where the red and blue curves represent the spectra for $E \parallel c$ and $E \perp c$, respectively. The inset shows the experimental spectrum.

same time, the R_3 structure locally stabilizes a 120-degree spin configuration within the basal plane. As a consequence, local chiral degrees of freedom may emerge, associated with fluctuations of this in-plane 120-degree Neel-like structure.

We performed *ab initio* noncollinear spin density functional calculations using QUANTUM ESPRESSO in which the wave functions were expanded on a plane-wave basis. We employed norm-conserving pseudopotentials, and the generalized-gradient approximation for the exchange-correlation energy. The cutoff energies for the wave function and charge density are 100 Ry and 400 Ry, respectively. The optical spectrum is calculated by using RESPACK, where the energy cutoff for the polarization function was set to 10 Ry, and the total number of bands considered in the polarization calculation was determined to cover unoccupied states up to 10-15 eV above E_F.

Figure 1(a) shows the calculated band structure for the $a \times a \times 3c$ hexagonal supercell, which incorporates the threefold periodicity along the c axis. The system exhibits an insulating band structure with a band gap of approximately 0.2 eV. Panel (b) illustrates the corresponding spin configuration, where spins rotate along the c axis. Panel (c) shows the calculated optical conductivity, together with the experimental spectrum shown in the inset.

Figure 2(a) shows the calculated band structure for the R_3 structure with a rhombohedral lattice. We again obtain an insulating state with a band gap of approximately 0.2 eV. Panel (b) illustrates the corresponding spin configuration. The structure is shown in a $3a \times 3a \times 3c$ hexagonal supercell. We observe a locally stabilized 120-degree Neel-type spin configuration (red vectors) embedded within the antiferromagnetic background. Panel (c) shows the calculated optical conductivity. The agreement with the experimental spectrum is reasonable. This suggests that multiple noncollinear spin configurations can give rise to a similar insulating state.

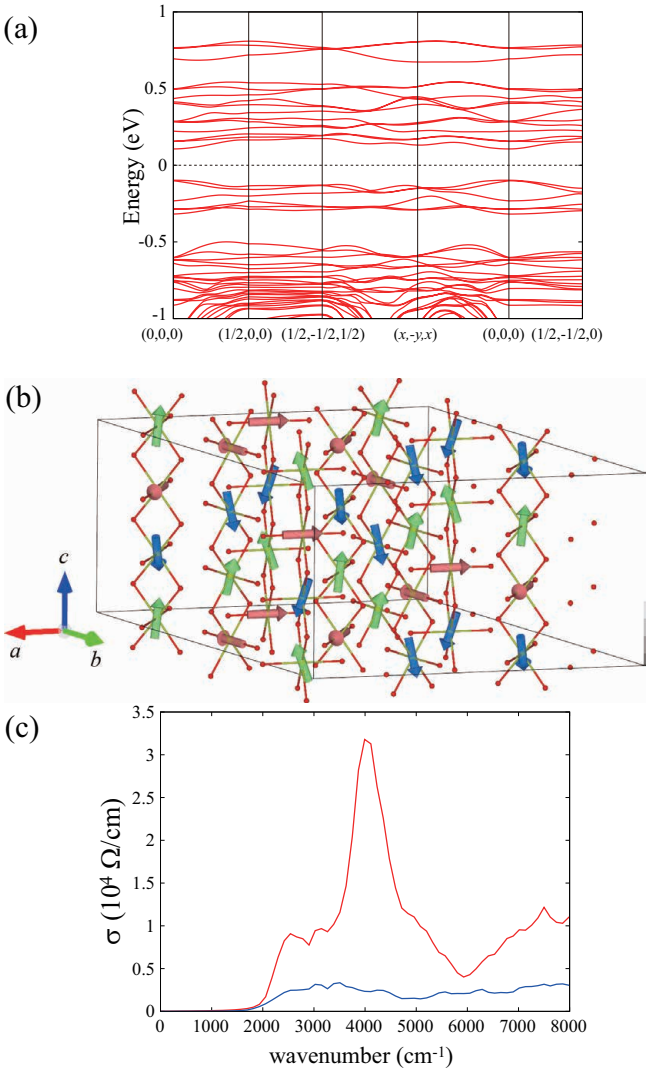


Figure 2: Computational results for the R_3 structure: (a) calculated band structure, (b) corresponding spin configuration, and (c) calculated optical conductivity.

[1] M. Wakeshima, N. Taira, Y. Hinatsu, Y. Ishii, Solid State Commun. **125**, 311 (2003).

[2] K. Matsuhira, K. Nakamura, Y. Yasukuni, Y. Yoshimoto, D. Hirai, Z. Hiroi, J. Phys. Soc. Jpn. **87**, 013703 (2018).

[3] H. Hanate, T. Hasegawa, S. Hayami, S. Tsutsui, S. Kawano, K. Matsuhira, J. Phys. Soc. Jpn. **90**, 063702 (2021).

Ab initio study on static and dynamic properties of light metal alloys

Akihide KOURA

Technical division, Kumamoto University, Kumamoto 860-8555

We have studied static and dynamic properties of light metal alloys, Mg-Zn-Y alloys based on *ab initio* molecular dynamics (AIMD) simulations and MD simulations using machine learning interatomic potentials (MLIPs). In this project, we focused on the concentration of $Mg_{0.8}Zn_{0.08}Y_{0.11}$ alloy to clarify the static structure and dynamic properties. We employed QXMD code for AIMD and MD simulations [1]. We also used the Aenet package to train MLIPs [2].

To develop the robustness of MD simulations using MLIP, we constructed many MLIPs by F4cpu class. Obtained MLIPs were used to make MD simulation robust by the potential averaging method [3]. However, too many MLIPs increase computation time, and the presence of poorly potentials can lead to MD failure. Therefore, it is necessary to carefully select the best MLIPs. In this project, we used four selected MLIPs. Although the calculations were performed without failure, there is room for improvement in the surrounding structure of Zn.

On the other hand, to investigate the concentration dependence of physical properties, we also performed AIMD for liquid $Mg_{0.85}Zn_{0.06}Y_{0.09}$ alloy. As a result of the test run, although average Mulliken charges of Mg and Zn do not depend on the concentration, that of Y at $Mg_{0.85}Zn_{0.06}Y_{0.09}$ alloy is Q = 0.25 in spite of Q = 0.3 at $Mg_{0.8}Zn_{0.08}Y_{0.11}$ alloy. While, the average charge of Zn is approximately $Q = -0.2$. This fact suggests that the Coulombic interaction of Zn and Y atoms contributes the Zn-Y cluster formation ability.

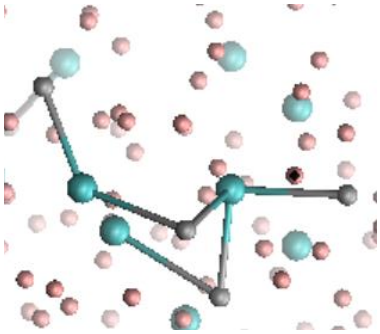


Fig. 1. Fragment of the Zn-Y cluster in liquid $Mg_{0.8}Zn_{0.08}Y_{0.11}$ alloy. Pink, grey, and blue balls correspond to Mg, Zn, and Y atoms, respectively.

References

[1] F. Shimojo, *et al.*, SoftwareX **10**, 100307 (2019).

[2] N. Artrith and A. Urban, Comput. Mater. Sci. **114**, 135 (2016).

[3] D. Wakabayashi, *et al.*, J. Phys. Soc. Jpn. **92**, 074002 (2023).

Machine learning potential for tungsten with defects and hydrogen atoms

Daiji KATO[1], Yuki NOGUCHI[2]

[1]*National Institute for Fusion Science, 322-6 Oroshi-cho, Toki-city, Gifu*

[2]*IGSES, Kyushu University, 6-1 Kasugakoen, Kasuga-city, Fukuoka*

In this project, we performed atomistic simulations to investigate hydrogen–defect interactions in tungsten using system B of the supercomputer facility at ISSP. The primary objective of this study is to develop a novel Machine learning potential to reduce the discrepancy between conventional molecular dynamics simulations based on empirical interatomic potentials and first-principles calculations.

First-principles calculations based on density functional theory (DFT) were carried out using the Vienna ab initio Simulation Package (VASP) [1]. We employed the Perdew–Burke–Ernzerhof (PBE) generalized gradient approximation (GGA) exchange-correlation functional with a plane-wave cutoff energy of 400 eV. To efficiently utilize computational resources, parallel computations were performed using MPI. Each calculation typically used 384 cores, combining k-point parallelization (KPAR = 4) and band parallelization (NCORE = 32). These settings enabled efficient scaling for large supercell calculations containing up to 432 atoms.

To overcome the high computational cost of DFT calculations, a machine learning interatomic potential (MLP) was constructed based on DFT datasets. The MLP was developed using an on-the-fly learning method [2] with the Smooth Overlap of Atomic Positions (SOAP) descriptor and Bayesian linear regression. The training data were generated via high-throughput DFT calculations on the supercomputer, in which a large number of atomic configurations, energies, and forces were computed in parallel. This data generation step required substantial computational resources and was efficiently handled by distributing independent calculations across multiple nodes.

The constructed MLP was applied to structural exploration and cohesive energy calculations. Compared to

first-principles calculations for the same atomic structures, the computational speed was improved by approximately five orders of magnitude. This significant acceleration enabled efficient evaluation of many structures by performing multiple calculations simultaneously, thereby greatly enhancing computational efficiency. Several optimization and tuning techniques were implemented to maximize computational efficiency.

The main results obtained in this study are shown in Fig. 1. It is well known that vacancies in tungsten have positive binding energies for hydrogen atoms, indicating their trapping capability. Figure 1 compares the binding energies of hydrogen atoms to a mono-vacancy in tungsten as a function of the number of hydrogen atoms. For cases with seven or more hydrogen atoms, the results obtained using empirical interatomic potentials exhibit significant uncertainty and deviate from the DFT results. In contrast, the machine learning interatomic potential developed in this study successfully reproduces the DFT results for up to nine hydrogen atoms, thereby improving the reliability and reducing the uncertainty of the predictions [3].

References

[1] G. Kresse and J. Hafner, PRB **47**, 558–561(1993).

[2] R. Jinnouchi et al., PRL 122, 22570 (2019).

[3] Y. Noguchi, and D. Kato, “Machine-learning force fields for hydrogen and vacancy complex in tungsten” Poster presented at: 20th International Conference on Plasma-Facing Materials and Components for Fusion Application (PFMC-20); May 20, 2025; Ljubljana, Slovenia.

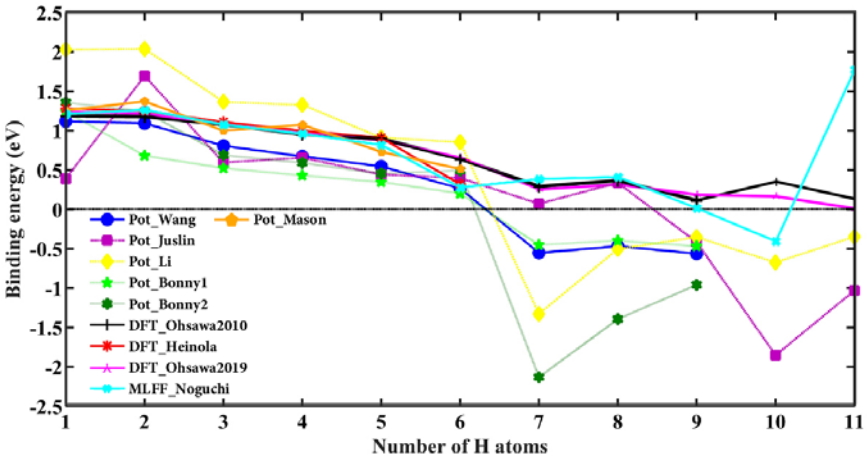


Fig. 1: Binding energy of hydrogen atoms at a mono-vacancy in tungsten. The light blue line (MLFF_Noguchi) is obtained using MLP.

Theoretical study on electronic devices using nitrogen-doped carbon nanotubes

Yoshitaka FUJIMOTO
School of Engineering, Kyushu University, Fukuoka 819-0395

The performance of digital electronic devices has continuously improved through the scaling down of silicon (Si)-based field-effect transistors (FETs) in accordance with Moore's law. However, this downsizing is reaching its physical limits, resulting in the degradation of the device performance. To further enhance the performance of the FETs, novel device structures and new materials with high carrier mobilities for use in the high-speed transport channels have been explored. Among these materials, carbon nanotubes (CNTs) are promising candidates to replace the Si channels due to quasi-one-dimensional structure and high carrier mobility.

The CNTs have been reported to often show p-type conduction property under ambient conditions due to the existence of adsorbates such as oxygen although they originally possess intrinsic semiconducting property. The substitutional doping with nitrogen atoms is expected to be one of the most effective ways to realize the n-type doping property of CNTs. However, the electronic properties of N-doped CNTs and N-doped graphene show p-type doping property under high-temperature growth or high dopant-density conditions of N-doped systems [1].

In this article, we study the electronic transport of the pyridine-type N-doped CNTs and its adsorption effect of an NH_3 molecule based on the first-principles electronic transport theory. We calculate the adsorption energy of NH_3 molecules on the pyridine-type N-doped CNTs. Our calculations suggest that the adsorption of NH_3 molecules induces n-type transport in the system.

We firstly examine the adsorption energy E_a for the adsorption of the NH_3 molecule on the pyridine-type N-doped (10,0) CNTs. Here, the adsorption energy E_a is defined as $E_a = E_{\rm tot} - E_{\rm CNT} - E_{\rm mol}$, where $E_{\rm tot}$, $E_{\rm CNT}$, and $E_{\rm mol}$ are the total energies of the pyridine-type N-doped (10,0) CNTs with and without the adsorption of the NH_3 molecule and the isolated NH_3 molecule, respectively. The adsorption for the NH_3 on the pyridine-type (10,0) CNTs is found to be energetically favorable with $|E_a| = 1.28$ eV for the LDA calculation.

We next examine the electronic transport properties of the pyridine-type N-doped CNTs. The pristine (10,0) CNT shows a semiconducting property with its energy gap of about 0.7 eV. When the pyridine-type N defects are introduced to the nanotubes, they give rise to acceptor-like states near the VBM, rendering the N-doped CNT a p-type semiconductor [2]. We further examine the NH_3 adsorption effects on the electronic transport of the N-doped CNTs. The adsorption of NH_3 molecules can change the electronic transport properties of the pyridine-type N-doped (10,0) CNTs. It is found that the Fermi energy moves towards the CBM from the VBM, and the NH_3 adsorption gives rise to the n-type conduction.

In summary, we have investigated the adsorption effects of NH_3 molecules on the energetics and the electronic transport of pyridine-type N-doped (10,0) CNTs. It is found that the adsorption of the NH_3 molecule on the pyridine-type defects becomes energetically favorable. Our results clarify that the carrier transport (p-type or n-type) is tunable by adsorption of NH_3 molecules on the pyridine-type N-doped CNTs.

References

[1] Y. Fujimoto, Micromachine **15**, 1172 (2024).

[2] Y. Fujimoto, Chem. Phys. **601**, 112933 (2026).

GPU-accelerated QSGW calculations: Application for modulated martensite phases of Ni_2MnGa

Masao OBATA

Institute of Science and Engineering, Kanazawa University, Kanazawa, Ishikawa 920-1192

The quasiparticle self-consistent *GW* (QSGW) method [1] is a powerful first-principles approach that surpasses the G_0W_0 approximation by incorporating off-diagonal elements of the self-energy Σ self-consistently. However, the key steps, evaluation of the screened Coulomb interaction W and the Σ, scale as the fourth power of system size and the square of the number of k-points, restricting QSGW applications to relatively small unit cells. We addressed this limitation by implementing GPU acceleration in the QSGW code ecalj (available on GitHub) using OpenACC and GPU-accelerated math libraries, enabling calculations with 20 or more atoms per unit cell to be practically feasible [2].

Ni_2MnGa exhibits magnetic field-induced strain in its martensite phases, where nanoscale twin boundary modulation plays a central role. Experiments identify modulated martensite structures designated 10M (20 atoms/cell) and 14M (28 atoms/cell) depending on composition and temperature. Standard GGA calculations predict the 10M phase to be metastable, contrary to experimental observations [3], highlighting the importance of beyond-DFT methods. Our previous QSGW studies on the austenite phase suggested that electronic instabilities drive the formation of modulated structures. We extended the QSGW analysis to the 10M and 14M phases, enabled by the GPU acceleration. We find that the minority-spin density of states of Ni near the Fermi level exhibits a characteristic valley structure, with the Fermi level positioned at its minimum in the modulated phases. This suggests that the modulated structures are electronically stabilized by band-energy lowering, a feature absent in GGA calculations, providing a microscopic rationale for GGA's failure to reproduce the stability of the 10M phase.

References

[1] M. van Schilfgaarde et al., Phys. Rev. Lett., 96, 226402 (2006). [2] M. Obata et al., Comp. Mat. Sci, 260, 114190 (2025). [3] M. Zelený et al., Mater. Des. 209, 109917 (2021).

Calculation of adsorption energy of fluorinated molecules on chromate conversion coating layer using DFT+U method

Yuji OHKUBO, Kota YAMAGUCHI, and Kouji INAGAKI
Graduate School of Engineering, The University of Osaka,
2-1 Yamadaoka, Suita, Osaka 565-0871

To realize 6G, which will surpass the performance of current communications systems such as 4G and 5G, high-frequency printed circuit boards capable of high-speed communication with lower dielectric loss than ever before are required. PTFE has significantly lower values of the relative dielectric constant and dielectric loss tangent. Using it as a substrate material enables decreased dielectric loss and increased communication speeds. The substrate material, Cu foil, readily undergoes natural oxidation even in air. Since the formation of this natural oxide layer degrades conductivity and uniformity, industrial applications require corrosion prevention treatment for Cu foil. Among these methods, chrome conversion coating forms an extremely thin layer with high corrosion-resistance properties, making it a suitable treatment for Cu foil used in printed circuit boards. In this study, we calculated the adsorption energies and activation energies for reactions between a chromate conversion coating layer (Cr_2O_3) and fluorinated molecules using DFT calculations, and investigated the functional groups that contribute to improved adhesion.

The calculations were performed using the STATE (Simulation tool for atom technology) code based on density functional theory (DFT) with plane-wave basis and ultra-soft pseudopotentials. In this study, we used the DFT+U method. The generalized gradient approximation exchange-correlation functional based on Perdew-Burke-Ernzerhof (PBE) was used. The wave function and the charge density of cutoff energies were 36 Ry and 400 Ry, respectively. The k-point mesh was 6 × 6 × 2 when calculating bulk Cr_2O_3.

The adsorption energy (E_{ads}) per molecule was calculated using the following equation (1).

$$E_{ads} = (E_{surf} + E_{mol}) - E_{mol/surf} \quad (1)$$

where E_{surf} is the energy of the naked surface slab; E_{mol} is the energy of the isolated fluorinated molecules; $E_{mol/surf}$ is the total energy of the adsorbate–substrate system.

Transition state energies (E_a) were calculated using the CI-NEB method to determine the activation energies of various adsorption reactions. The activation energies (E_{act}) were calculated using the following equation (2).

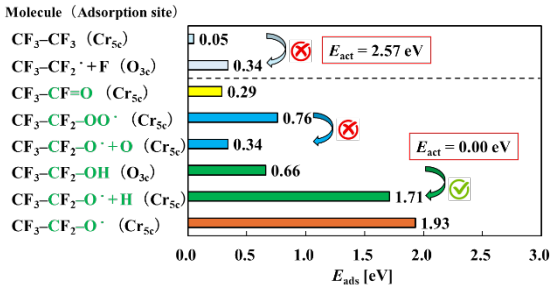


Figure 1 E_{ads} of fluorine-based molecules on the Cr_2O_3 $(10\bar{1}2)$ surface.

$$E_{act} = E_a - E_{ini} \quad (2)$$

Figure 1 shows the calculated adsorption energies of fluorine-based molecules on the Cr_2O_3 $(10\bar{1}2)$ surface. The + in the molecule indicates that atoms from the functional group dissociated and adsorbed separately. CF_3–CF_3 did not adsorb at any site, exhibiting adsorption energies below 0.1 eV. Next, we investigated a system in which F atom is extracted by a surface Cr_{5c} site, undergoing defluorination, and the C atom adsorbs onto a surface O_{3c} site. The E_{act} for this process is extremely high at 2.57 eV, making adsorption onto the Cr_2O_3 surface difficult. On the other hand, fluorinated molecules with oxygen-containing functional groups exhibited higher adsorption energies than CF_3–CF_3, potentially contributing to improved adhesion. Specifically, CF_3–CF_2–OH showed the highest adsorption energy of 1.71 eV after the H atom dissociated during the calculation to form a Cr–O–C bond. The adsorption energy of CF_3–CF_2–O・, lacking the H atom, was exceptionally high

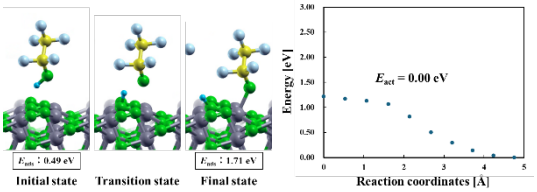


Figure 2 NEB calculation results and model diagram for CF_3–CF_2–OH

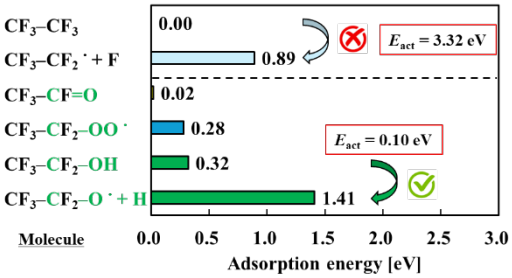


Figure 3 E_{ads} of fluorine-based molecules on the Cr_2O_3 $(10\bar{1}2)$_OH surface.

at 1.93 eV, confirming the strong Cr–O bond. **Figure 2** shows the NEB calculation results and a schematic diagram for the system where H atoms dissociate and adsorb. From **Figure 2**, we found that the E_{act} required for H atom dissociation is 0.00 eV, and the reaction proceeds readily. Therefore, CF_3–CF_2–OH, which has high adsorption energy and sufficiently low E_{act} for the reaction, is considered to be highly effective in contributing to improved adhesion. **Figure 3** shows the calculation results for the surface with OH groups introduced onto the Cr_2O_3 $(10\bar{1}2)$ surface. It was found that even on surfaces with OH groups, CF_3–CF_2–OH contributed most significantly to improving adhesion.

Establishment of guidelines for controlling open-shell nature of molecules by solids

Kohei TADA

Department of Materials Engineering Science, Graduate School of Engineering Science, The University of Osaka, Toyonaka, Osaka 560-8531, Japan

When covalent bonds weaken, the electrons shared in the molecule begin to localise to the atoms, acquiring the properties of unpaired electrons. Such unpaired electrons, originating from covalent bonds, are correlated and cause interesting molecular functions. The unpaired electrons are called open-shell electrons, and molecules possessing the unpaired electrons are called open-shell molecules. The degree of open-shell electrons in molecule, open-shell nature, is utilised in molecular design. However, guidelines for controlling the open-shell nature by solids have yet to be established.

In this project, I analysed the effects of solids on open-shell nature using a proprietary developed method (AP-DFT/plane-wave) [1,2], with the aim of elucidating material functions and designing novel composite materials. I conducted research on catalytic, magnetic, and battery materials, and submitted eight papers (of which five have been accepted) [3–10]. The calculations were performed using Systems B (ohtaka) and C (kugui), and the programme for DFT, VASP, was used. The published papers and concept are summarised in Figure 1. This report provides an overview of (1) surface open-shell nature in Ni_3C catalysts [4], (2) a theoretical proposal for the control of magnetism via solid-molecule interactions [6], and (3) open-shell bands in organic cathodes for batteries [7].

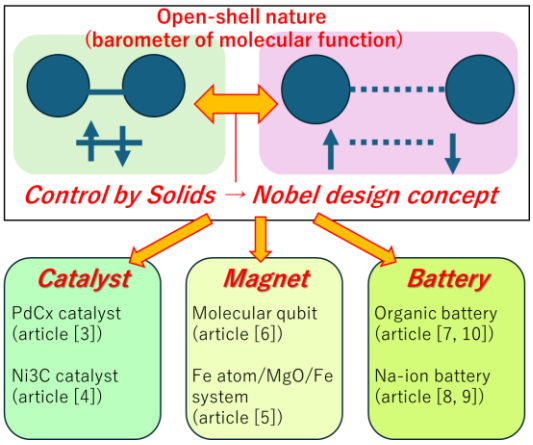


Fig. 1: Concept and Outcome of this study.

In recent years, metal carbides have attracted attention for their unique catalytic activities. However, understanding of their electronic states is insufficient. This study revealed that the surface-exposed carbon atoms in Ni_3C possess intrinsic unpaired electron properties [2]. This is attributed to the covalent nature of the Ni–C, and it will be a factor of different surface reactivity from the metallic or ionic bonds found in metals and oxides.

By controlling the spin of unpaired electrons, open-shell molecules will be applied to high-density memory devices and molecular qubits. Although the integration of the functional molecules into devices requires their incorporation with solids, delocalisation of the unpaired electrons—the source of these functionalities— to the solids has been caused. To propose a solution, I conducted a detailed analysis of the interaction between complexes with radical ligands and metal surfaces, and two approaches were suggested: control of unpaired electron transfer via coverage control, and screening via the insertion of graphene layers [6], which would be verified by experimental study in the future.

Reducing the weight of batteries expands their potential applications. Organic cathodes are attracting attention for the weight reduction. However, redox processes in organic materials often include states with unpaired electrons, which are generally highly reactive. In this study, I investigated a highly durable organic cathode material (trioxotriangulene: TOT) and confirmed the formation of a radical band. To evaluate the stability of this radical band, we quantified the overlap of wave functions between different spins using a developed method. The results demonstrated that the overlap of wave functions in TOT crystals increases with expansion. This implies that intermolecular interactions increase with expansion, suggesting that the radical band will exhibit high robustness against crystal structure changes associated with the insertion of charge carriers such as Li and Na [7].

References

[1] K. Tada, H. Ozaki, K. Fujimaru, Y. Kitagawa, T. Kawakami, and M. Okumura, Phys. Chem. Chem. Phys. **23**, 25024 (2021).

[2] K. Tada, R. Sugimori, R. Kishi, and Y. Kitagawa, Chem. Commun. **61**, 11758.

[3] S. Yamaguchi, M. Sarmiento-Diaz, T. Kawakami, K. Tada, T. Mitsudome, and T. Mizugaki, ACS Appl. Nano Mater. **8**, 13886 (2025)

[4] K. Tada, K. Matsuyama, S. Yamaguchi, R. Kishi, T. Mizugaki, and Y. Kitagawa, Phys. Chem. Chem. Phys. **28**, 1118 (2026)

[5] T.K. Yamada, N.K.M. Nazriq, and K. Tada, Appl. Surf. Sci. Adv. **33**, 100965 (2026)

[6] R. Hirota, K. Tada, K. Ikenaga, K. Katoh, R. Kishi, and Y. Kitagawa, J. Phys. Chem. C, *under review*

[7] Y. Kitano, K. Tada, R. Hirota, T. Kawakami, R. Kishi, and Y. Kitagawa, Bull. Chem. Soc. Jpn. **99**, uoag036 (2026)

[8] R. Kataoka, A. Machida, K. Tada, N. Taguchi, and N. Takeichi, Electrochim. Acta **549**, 148038 (2026)

[9] R. Kataoka, Y. Kitano, K. Tada, Y. Kitagawa, and N. Takeichi, J. Alloy Comp., *under review*

[10] Y. Kitano, K. Tada, T. Kawakami, R. Kishi, and Y. Kitagawa, J. Phys. Chem. C, *under review*

DFT Study of Interfacial Reactions in Plasma-assisted Polishing

Jiayuan Dong and Rongyan Sun

Research Center for Precision Engineering,

The University of Osaka, 2-1 Yamadaoka, Suita, Osaka, 565-0871

Plasma-assisted polishing (PAP) is an advanced technique developed for ultra-precision processing of diamond materials. However, the underlying mechanisms, particularly the interfacial tribochemical reactions, remain unclear at the atomic scale. Therefore, this project employs density functional theory (DFT) calculations to investigate the interfacial chemical processes and clarify the mechanism of material removal in PAP. All calculations were performed using the Quantum ESPRESSO package.

In this study, silicon and diamond surfaces, as well as their friction interface, were constructed to simulate the PAP process. First, the oxidation of the Si(100) surface under oxygen plasma was investigated. The formation of Si–O bonds, replacing Si–Si bonds, indicates a strengthening of the polishing plate due to the higher bond energy of Si–O. Subsequently, the silicon–diamond interface was constructed, as shown in Fig. 1(a), and further oxidized interface, as shown in Fig. 1(b). At the initial interface, Si–C bonds are formed to connect the two surfaces; however, their bond energy is lower than both the C–C back bonds in diamond and the Si–O bonds in the plate,

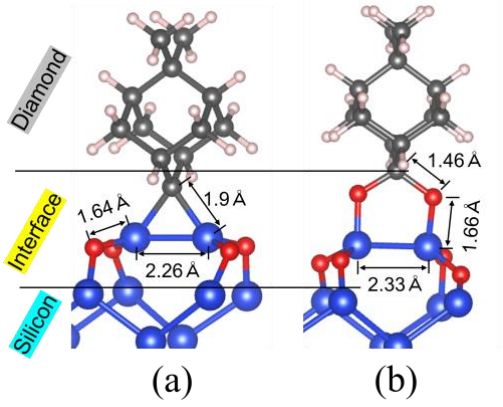


Fig. 1 Frictional interface models. (a) Interface between oxidized Si and diamond surfaces. (b) further oxidized configuration based on (a).

making them insufficient to induce material removal. In contrast, with further oxidation, active oxygen atoms weaken the diamond back bonds and form strong bridging bonds (Si–O–C) across the interface, enabling the breaking of C–C bonds during sliding.

These findings provide theoretical insight into the tribochemical mechanisms governing PAP [1].

References

[1] J. Dong et al., *J. Mater. Process. Technol.*, **348**, 119187 (2026).

Machine Learning-based DFT Calculation of Lignin Adsorption and Oxidative Activity on Co/CeO_2 (111) and Ni/CeO_2 (111)

TEPPEI NUNOURA and ZHIHE ZHAO

Graduate School of Frontier Sciences,

The University of Tokyo, 5-1-5 Kashiwanoha, Kashiwa, Chiba 277-8581

To explore the adsorption behavior of lignin on transition metal cluster-loaded CeO_2 (111) surfaces, we integrated machine learning to the stable adsorption configurations. The machine learning workflow integrates the Atomic Simulation Environment (ASE) with the VASP and the Optuna optimization framework to explore and identify thermodynamically stable adsorption configurations of molecules on solid surfaces. Starting from predefined surface and adsorbate structures, the program systematically varies molecular orientations (Euler angles φ, θ, ψ) and in-plane translation and vertical height (x, y, z) parameters. The adsorption energy is computed as

$$E_{ads} = E_{slab+molecule} - E_{slab} - E_{molecule}$$

Bayesian optimization implemented in Optuna is employed to efficiently sample the high-dimensional configuration space and minimize E_{ads} .

We first identified the thermodynamically stable (111) surface of CeO_2 and modeled Ni and Co cluster loading on this surface. Using a machine learning-assisted workflow, we generated and screened over 500 different lignin adsorption configurations, enabling high-throughput identification of the most stable structures. Among the 500 adsorption configurations, p-Hydroxyphenyl showed the highest adsorption capacity on the Ni/CeO_2 (111) surface than Syringol and Guaiacyl units, and Syringol showed highest adsorption capacity on the Co/CeO_2 (111) surface than p-Hydroxyphenyl and Guaiacyl.

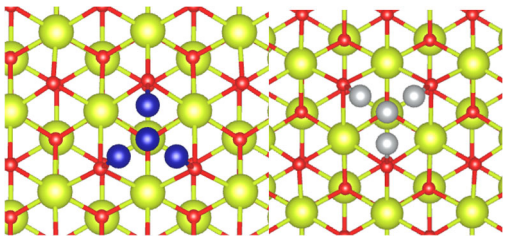


Fig.1 Co/CeO_2 (111) and Ni/CeO_2(111) surfaces.

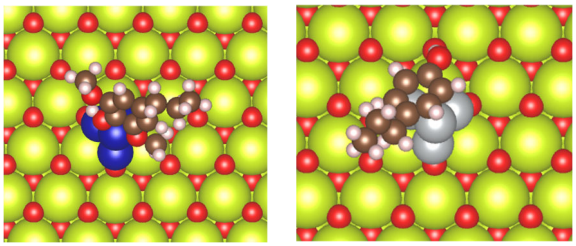


Fig.2 p-Hydroxyphenyl unit adsorbed on Co/CeO_2 (111) and Syringol unit adsorbed on Ni/CeO_2(111) surfaces.

References

[1] Xie, Jin.; et al. *ACS Catal.* **2023**, *13* (14), 9577–958

Surface electronic structure of double perovskite

Kazume NISHIDATE
Graduate School of Science and Engineering, Iwate University
4-3-5 Ueda, Morioka, Iwate, 020-8551

Double-perovskite oxides can be expressed in a general formula $A_2BB'O_6$ and have attracted much attention due to their intriguing physical and chemical properties originating from the mixed valencies of small cations at the B and B' sites. The material is also a potential candidate for the photo-catalysis sensible to the visible light. The energy bandgap separating the valence band and conduction band of semiconductors plays a crucial role in the design of visible-light-driven photocatalysts. It is desirable that the valence and conduction band edges are optimized to effectively facilitate photocatalytic oxidation and reduction processes. Here, the magnitude of the energy bandgap is controlled by the B-site substitution of Sb at Bi ion site.

Higher photocatalytic activities are probably achieved by reducing the rapid recombination of electrons and holes, leading to the photo-excited charge separation, before the progress of the redox reaction at the surface. This fact is related to the presence of multivalent B-site cations. This year, we focused on the double-perovskite oxide $Ba_2Ce(Bi_{1-x},Sb_x)O_6$ We examined the energy band structures and total density of states near the Fermi levels for monoclinic Ba_2CeBiO_6 and cubic Ba_2CeSbO_6 using the density functional theory calculations as implemented in the Quantum ESPRESSO. We applied the Heyd–Scuseria–Ernzerhof hybrid functional (HSE06) formalism for the exchange–correlation in the calculations. Pseudopotentials of the **pslibrary** were used for the relaxation calculations, while in the HSE06 hybrid functional calculations, the norm-conserving pseudopotentials of the **PseudoDojo** were used to accelerate the convergence. We confirmed this transferability by checking the valence band energies at various k-points.

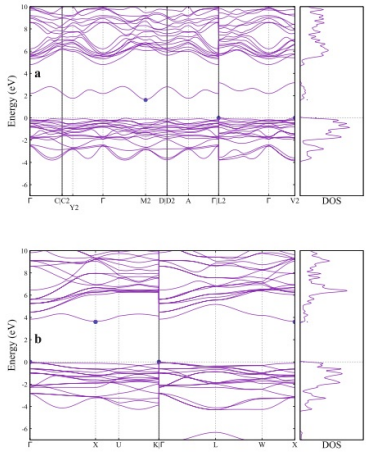


Figure 1: Energy band structures and total density of states near the Fermi levels for **a** monoclinic Ba_2CeBiO_6 and **b** cubic Ba_2CeSbO_6.

We revealed that the band structures, crystalline sizes, and multivalent B-site cations play a significant role in the observed photocatalytic improvements [1].

References

[1] H. Sakou, K. Hata, M. Matsukawa, M. Arakida, K. Nishidate, S. Aisawa, K. Akiba, and D.C. Roy: J Mater Sci: Mater Electron **36**, 1800 (2025)

Density Functional Theory Calculations of CO_2 Adsorption and the Reduction Pathway to CH_4 on Fe (1 1 1) Surface

Masahito Sasaki, Tomoki Oyumi, and Yasuo Izumi

Graduate School of Science

Chiba University, Yayoi 1-33, Inage-ku, Chiba, Japan 263-8522

Photocatalytic CO_2 reduction has attracted considerable attention as a promising approach for establishing a C-neutral cycle to achieve a sustainable society. However, its practical implementation remains challenging because of the high cost of photocatalytic materials and reactor systems. Among the first-row transition metals, Fe is the most abundant and cost-effective element, making it an attractive candidate for CO_2 reduction photocatalysts.

Previously, we demonstrated that Fe–ZrO_2 photocatalysts can reduce CO_2 not only to CO but also to methane, ethane, and propane [1]. It has been suggested that CO_2-derived species activated on the ZrO_2 surface migrate to metallic Fe^0 sites, where sequential hydrogenation proceeds. Furthermore, the product selectivity strongly depended on the irradiated light intensity: CO formation proceeded steadily < 472 mW cm^{-2}, whereas steady CH_4 formation was observed at irradiation intensities > 472 mW cm^{-2}.

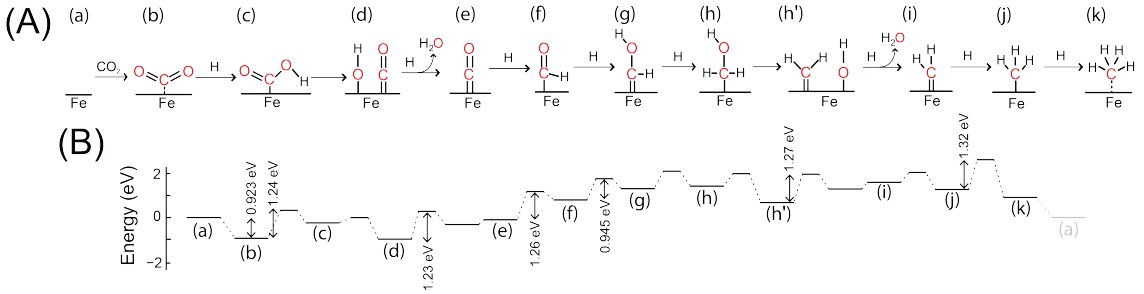
Despite these findings, the origin of the initial catalyst deactivation and the mechanism responsible for the change in product selectivity with irradiation intensity have not yet been sufficiently understood on the atomic level. In particular, the detailed nature of CO_2-derived species adsorbed and the reduction pathway on the metallic Fe^0 surface remain unclear.

In this study, a slab model of the Fe (1 1 1) surface was constructed to investigate the adsorption behavior of CO_2 and the reaction pathway from CO_2 to CH_4 by density functional theory calculations using the Vienna Ab Initio Simulation Package code version 6.4.2 with the generalized gradient approximation in the revised Perdew–Burke–Ernzerhof functional. The reaction pathway was calculated based on the climbing-image nudged elastic band (CI-NEB) method to evaluate the activation energy (E_{act}) barriers of the elementary reaction steps. The memories and processors of supercomputer system at ISSP were indispensable for CI-NEB calculations.

The calculation results showed that the CO_2 molecule adsorbed on the Fe surface in an M-shaped configuration with the adsorption energy = −0.92 eV (Scheme 1b), oxidizing partially the surface Fe atoms by the O atoms of CO_2. This result was consistent with the experimental Fe K-edge shift toward higher energy under CO_2, H_2, and the UV–visible light irradiation. Furthermore, the CO_2 adsorbed on the Fe surface was consistent with the appearance of vibrational peaks in FTIR [1].

The analysis of the reaction pathway from the adsorbed CO_2 to CH_4 revealed relatively large E_{act} values for the three steps: 1.24 eV for CO_2 → OCOH (Scheme 1b and c), 1.26 eV for CO → HCO (e and f), and 1.32 eV for CH_3 → CH_4 (j and k). These steps were comparable energy barriers.

Scheme 1. (A) Proposed reaction pathway for the reduction of CO_2 to CH_4 on the Fe (1 1 1) surface and (B) the corresponding free-energy changes of the reaction.



These results suggested that the intermediate CO, CH_2, and especially CH_3 species competed with H species on Fe^0 surface during the photocatalytic reduction reactions of CO_2. More importantly, this study focused on the catalytic behavior over the Fe (1 1 1) surface assuming sufficient irradiated UV–visible light intensity [2]. In fact, in the preliminary DFT calculation results indicated facilitated reaction pathway to CH_4 than that depicted in Scheme 1 if the three electron reduced relatively unstable COH species from CO_2 transferred from ZrO_2 surface to Fe^0 nanoparticles [3]. The calculations of the step of CO and/or COH from ZrO_2 surface to Fe^0 is underway, and soon reported.

References

[1] T. Oyumi, I. Abe, M. Sasaki, and Y. Izumi, *Chem. Commun.* **61**, 8671–8674 (2025).
[2] M. Sasaki, T. Oyumi, K. Hara, H. Zhang, and Y. Izumi, *J. Am. Chem. Soc.* **148**, 13570–13580 (2026).
[3] K. Hara, M. Nozaki, R. Hirayama, R. Ishii, K. Niki, and Y. Izumi, *J. Phys. Chem. C* **127**, 1776–1788 (2023).

Theoretical exploration of goniopolar high-performance thermoelectric materials

Hidetomo USUI

Department of Engineering Science,

The University of Electro-Communications, Chofugaoka, Chofu, Tokyo 182-8585

Goniopolar materials, in which p-type and n-type transport characteristics appear along different crystallographic directions, are promising for transverse thermoelectric applications [1]. In this work, we theoretically explored goniopolar thermoelectric materials by performing first-principles calculations for approximately 150 compounds selected from the Materials Project [2]. The electronic structures were calculated using the VASP [3] and WIEN2k [4] packages, and the Seebeck coefficients were evaluated using BoltzTraP2 [5] within Boltzmann transport theory.

We found several candidate materials showing large directional dependence of the Seebeck coefficient. Among them, $BaPdS_2$ is a representative example. This compound has a quasi-one-dimensional crystal structure, as shown in Fig. 1. This crystal structure gives rise to different Fermi-surface topologies between the valence and conduction bands. This difference leads to a large anisotropy of the Seebeck coefficient and produces goniopolar thermoelectric behavior.

Our results show that first-principles screening combined with Boltzmann transport calculations is an effective approach for discovering goniopolar thermoelectric materials. The present study also suggests that quasi-one-dimensional crystal structures and orbital-dependent band dispersions are important design principles for realizing large anisotropic thermoelectric responses.

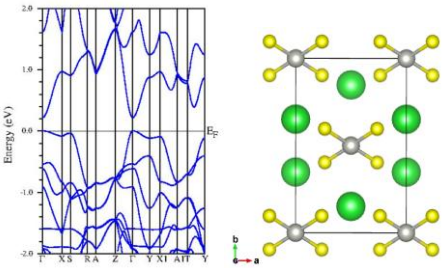


Fig. 1: Electronic and crystal structure of $BaPdS_2$.

References

[1] Y. Tang *et al.*, J. Electron. Mater. **44**, 2095 (2015).

[2] A. Jain *et al.*, APL Mater. **1**, 011002 (2013).

[3] G. Kresse and J. Furthmüller, Comput. Mater. Sci. **6**, 15–50 (1996); G. Kresse and J. Furthmüller, Phys. Rev. B **54**, 11169 (1996).

[4] P. Blaha *et al.*, J. Chem. Phys. 152, 074101 (2020).

[5] G. K. H. Madsen *et al.*, Comput. Phys. Commun. **231**, 140 (2018).

First principles calculation for electron chirality

Shintaro HOSHINO

Department of Physics,

Chiba University, Yayoicho 1-33, Inage-ku, Chiba-shi, Chiba, 263-8522

Recently, chiral materials have attracted significant attention due to characteristic phenomena such as chiral-induced spin selectivity (CISS) and circular dichroism. Quantifying chirality and investigating its relationship with these phenomena are expected to deepen our understanding of their unique properties. This study aims to quantify the chirality of electrons governing material properties, thereby establishing a chirality measure applicable to arbitrary materials.

One candidate for the measure is electron chirality in relativistic quantum theory, which is described by a four-component Dirac spinor at each point in spacetime [1,2]. In condensed matter physics, it is more convenient to use a non-relativistic expression described by the two-component spinor [2-4].

We have studied electron chirality in crystal systems using first-principles calculations and discussed the relationship with the circular dichroism spectrum [5]. Our previous studies have been limited to analyses of semiconductors with simple crystal structures, such as Te. Here, we extended the analysis to other crystal systems. We performed the density functional calculations using Quantum ESPRESSO [6]. After the calculation, we evaluate the electron chirality at each point in space from the obtained Bloch wave function. In this process, we use DiracBilinears.jl, which is a Julia package for computing the electron chirality and other physical quantities in relativistic quantum theory [7].

We employed MPI parallelization in the Quantum ESPRESSO calculations. This enabled efficient computation of the electronic structure, which allowed us to extend our analysis to more complex crystal systems. Furthermore, in the process of calculating electron chirality from the Bloch functions, we also use MPI parallelization over the k-points to achieve additional efficiency improvements.

We apply the present method complex and large-scale material systems. We have computed the electron chirality in organic materials by appropriately employing parallel computations. In addition, to extend our method to the magnetic materials, we examined the computational performance for evaluating Dirac bilinears that characterize the time-reversal symmetry breaking, and confirmed that they can be computed efficiently.

References

[1] J. J. Sakurai, “Advanced quantum mechanics”, Addison-Wesley, (1967).

[2] S. Hoshino, M.-T. Suzuki, and H. Ikeda, Phys. Rev. Lett. **130**, 256801 (2023).

[3] M. Fukuda, K. Soga, M. Senami, A. Tachibana, Int. J. Quantum Chem. **116**, 920 (2016).

[4] S. Hoshino, T. Miki, M.-T. Suzuki, and H. Ikeda, Phys. Rev. B **113**, 115113 (2026).

[5] T. Miki, H. Ikeda, M.-T. Suzuki, and S. Hoshino, Phys. Rev. Lett. **134**, 226401 (2025).

[6] Paolo Giannozzi *et al.*, J. Phys.: Condens. Matter **21**, 395502 (2009).

[7] T. Miki, H.-Y. Chen, T. Koretsune, and Y. Nomura, Comput. Phys. Commun. **317**, 109857 (2025).

Reductive decomposition of fluoroethylene carbonate at electrolyte/electrode interfaces in lithium–sulfur batteries

Yasuhiro UMEBAYASHI

Graduate School of Science and Technology,

Niigata University, 8050 Ikarashi, 2-no-cho, Nishi-ku, Niigata, 950-2181

Fluoroethylene carbonate (FEC) has been widely used as an additive in lithium-ion batteries. More recently, its use as a primary solvent has been reported to suppress polysulfide (PS) dissolution by forming a stable cathode–electrolyte interphase (CEI) on the cathode in lithium–sulfur (Li–S) batteries [1]. However, the detailed mechanisms of CEI formation and PS suppression remain insufficiently understood. In this study, we elucidate the formation of the CEI at the Li metal anode and sulfur cathode, with a focus on the reductive decomposition of solvents and anions.

In the electrolyte/Li anode interface model, a Li (001) slab was constructed by expanding the lattice to a 4 × 4 supercell in the surface plane. The slab initially consisted of four layers with a vacuum region of 15 Å along the c-axis, where each layer contained 16 Li atoms (64 atoms in total). The bottom layer was removed, and the remaining three layers (48 Li atoms) were used as the Li electrode and kept fixed during the simulation. The electrolyte was composed of LiFSA (FSA: $(FSO_2)_2N^-$) and FEC with a molar ratio of 1:12. A cubic simulation cell with a lattice parameter of 11.607 Å ($\alpha = \beta = \gamma = 90°$) was employed.

For the electrolyte/S_8/conductive additive three-phase interface model, a graphene slab was employed as the conductive additive. The slab was constructed by expanding the graphene unit cell to a 3 × 3 supercell in the surface plane, with lattice parameters a = b = 7.392 Å and c = 25.067 Å. The initial four-layer slab was reduced to three layers by removing the bottom layer, and the remaining three layers (54 C atoms in total) were kept fixed during the simulation. The electrolyte composition was set to S_8 : Li : FSA : FEC = 1 : 3 : 12 : 1. The total numbers of atoms and electrons in this model were 358 and 1322, respectively. The initial interface structure was generated by combining the electrode and electrolyte cells. First-principles molecular dynamics simulations were carried out using OpenMX (ver. 3.9.9). The electronic structure was described within the framework of the generalized gradient approximation using the Perdew–Burke–Ernzerhof (GGA-PBE) functional. The basis sets employed were Li8.0-s3p2, N6.0-s2p2d1, S7.0-s2p2d1, O6.0-s2p2d1, F6.0-s2p2d1, C6.0-s2p2d1, and H6.0-s2p1. At the electrolyte/Li interface, FEC solvated to Li^+ was found to undergo reductive decomposition at ~ 1.1 ps, yielding Li_2O and LiF on the Li surface

and CO_2 in the electrolyte. The produced CO_2 may further react to form nonvolatile compounds. No additional reactions were observed even when the simulation was extended beyond 20 ps. During a 23 ps simulation of the electrolyte/S_8/conductive additive three-phase interface, CO_2 formation and FEC dimerization leading to oligomeric species (–HC–O–COO–COO–CH_2CH–) were observed. Sulfur species were also found to decompose into S_5 and S_3 fragments. The LUMO of $Li(FEC)_4$ is significantly lower in energy than that of isolated FEC. The CEI formation is likely facilitated by the presence of chemical species with low-lying LUMO levels that can efficiently accept electrons from polysulfides in the vicinity of the cathode.

References

[1] Y. Torii *et al.*, *J. Phys. Chem. C*, **127**, 15069 (2023)

First-principles studies of magnetic tunnel junctions with noncollinear antiferromagnets

ALPIN N. TATAN

Department of Physics, The University of Tokyo, 7-3-1 Hongo, Bunkyo-ku, Tokyo, 113-0033

Tunneling magnetoresistance (TMR) ratio is an important metric for magnetic tunnel junctions (MTJ). MTJs are commonly made with ferromagnets (FM, e.g. Fe-based compounds) that sandwich an insulating barrier (e.g. MgO). Recently, MTJs made with noncollinear antiferromagnets (AFM) such as Mn_3Sn have been proposed **[1]**. So far, the measured TMR for Mn_3Sn MTJs with MgO barrier is still low (~ few %). This research is thus aimed at exploring new AFM MTJ designs that may achieve a high TMR ratio.

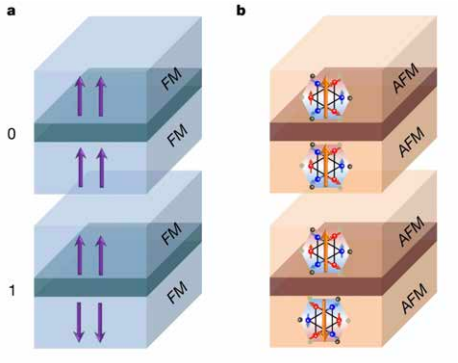


Fig. 1: Illustration of (a) FM- and (b) Mn_3Sn-based AFM MTJs, Figure adapted from **[1]**, which is under Creative Commons Attribution 4.0 International (CC BY 4.0) license.

The open-source first-principles calculation package Quantum Espresso **[2-3]** is used to calculate the electronic structure properties of MTJ models. In particular, the transmission coefficients from solving the quantum scattering problem are connected to the conductance and the TMR, via Landauer-Büttiker formula **[4-5]**:

$$G_{P/AP} = (e^2/h)\sum_{\boldsymbol{k}_\perp} T_{P/AP}\ (\boldsymbol{k}_\perp)$$

$$\mathrm{TMR} = (G_P - G_{AP})/G_{AP}$$

In these first 6 months (Oct 2025~), we screened material databases for barrier candidates and performed interface optimizations by a series of total energy calculations. We then performed TMR calculation on several configurations and obtained mixed results which still require further studies. We believe our preliminary results have promise, and we are collecting more data in the 2026 fiscal year to improve this research comprehensively towards publications.

References

[1] X. Chen et al. Nature **613**, 490 (2023).

[2] P. Giannozzi, et al. J. Phys. Condens. Matter **21**, 395502 (2009); **29**, 465901 (2017)

[3] A. Smogunov, A. Dal Corso, and E. Tosatti. Phys. Rev. B **70**, 045417 (2004)

[4] R. Landauer. IBM J. Res. Dev. **32**, 306 (1988)

[5] M. Büttiker. IBM J. Res. Dev. **32** 317 (1988)

Band tuning of ZnO with varied impurity

Ken-ichi SHUDO

Dep't of Phys, Yokohama National University,

Tokiwadai 79-5, Hodogaya-ku Yokohama, Kanagawa 240-8501

We obtained ultra-violet photoemission spectra (UPS) of nano-particles of ZnO crystals. In the fabrication processes, the purity was varied as the Mg oxide are mixed into the matrix material, and impurity-derived shift of work functions was observed. To elucidates the origin of the shift, we calculated the electronic states for several structures of large-scale crystalline systems (primitive to 5x5x5 unitcell), using a package, the Vienna *Ab initio* Simulation Package (VASP) chiefly.

The band-gap was estimated by means of several methods (LDA, GGA, and +U correction. However, the dependence to the impurity concentration did not reproduce the experimental results, nor apparent tendency to the experimental systematic dose was found. As to size effect, the deeper level electron, chiefly originated from oxygen, was strongly affected by the surface ad-molecules (possible contamination from air) or amorphous peroxide structures.

Thus, the impurity effect is further studied from the view point of calculation methods and re-examination of possible structures. The calculational results suggests requirements for further experimental measurements, in that the surface state in terms of oxidation number should be examined by means of, for example, core shift measurements with X-ray photoemission spectroscopy (XPS) and/or surface local structure using scanning tunneling microscope (STM).

Novel quantum phases in organic Mott insulators based on first-principles calculations

Ryuta IWAZAKI
Department of Physics, Tohoku University
Sendai 980-8578

In a class of materials known as Mott insulators, where electrons are localized at each site due to strong Coulomb repulsion, spin and orbital degrees of freedom become active. As a consequence, Mott insulators provide a platform for rich physical phenomena such as excitonic insulators, in which electrons and holes form bound states called excitons and undergo Bose–Einstein condensation, as well as spin-liquid states [1]. In order to quantitatively elucidate the origin of such phenomena in Mott insulators, analyses based on first-principles calculations are required.

In this study, we aim to explore novel quantum phases using effective models constructed from first-principles calculations for a novel organic Mott insulator λ-(BEST)$_2$GaCl$_4$ (BEST is an abbreviation for the molecule bis(ethylenediseleno)tetrathiafulvalene).
This material exhibits an antiferromagnetic transition at 22 K under ambient pressure. Compared to λ-(BEDT-TTF)$_2$GaCl$_4$, in which the transition temperature is 13 K, the higher magnetic transition temperature suggests that it is located on the negative-pressure side of the temperature–pressure phase diagram, and is considered to be a more strongly correlated system [2]. Furthermore, under applied pressure, it exhibits successive antiferromagnetic–paramagnetic–antiferromagnetic transitions, and the paramagnetic phase realized at intermediate pressure has been suggested to be a spin-liquid state originating from frustration between the magnetic structures of the two antiferromagnetic phases.

We performed density functional theory (DFT) calculations using `Quantum ESPRESSO` [3] for both ambient-pressure and pressurized crystal structures, and constructed a tight-binding model using `Wannier90` [4]. By examining the transfer integrals, we found that the degree of frustration in the triangular-lattice component changes with pressure. Furthermore, based on the constructed Wannier functions, we evaluated Coulomb interactions using `RESPACK` [5]. As a result, we found that the direct integrals differ between molecules. The interface `wan2respack` [6] was used to connect `Wannier90` and `RESPACK`. As a future perspective, we plan to analyze the constructed extended Hubbard model using our developed theoretical framework for localized multi-orbital electron systems [7].

References

[1] As a review, D.I. Khomskii, ECS J. Solid State Sci. Thecnol. **11**, 054004 (2022).

[2] A. Ito *et al.*, Phys. Rev. B **106**, 045164 (2022); N. Yasumura *et al.*, Phys. Rev. B **106**, 245103 (2022).

[3] P. Giannozzi *et al.*, J. Phys.: Condens. Matter **21**, 395502 (2009).

[4] G. Pizzi *et al.*, J. Phys.: Condens. Matter **32**, 165902 (2020).

[5] K. Nakamura *et al.*, Comp. Phys. Commun. **261**, 107781 (2021).

[6] K. Kurita *et al.*, Comp. Phys. Communn. **292**, 107781 (2021).

[7] R.I. and S. Hoshino, Phys. Rev. B **103**, 235145 (2021); R.I. *et al.*, Phys. Rev. B **108**, L241108 (2023); R.I. *et al.*, in preparation.

Decomposition of fluoroethylene carbonate at the electrolyte/Li_2S interface in lithium-sulfur batteries

Jihae HAN

Graduate School of Science and Technology,

Niigata University, 8050 Ikarashi, 2-no-cho, Nishi-ku, Niigata, 950-2181

Dissolution of polysulfides (PS) into the electrolyte during discharge in lithium-sulfur (Li-S) batteries leads to self-discharge and consequently reduces cycle life. The use of fluoroethylene carbonate (FEC) as a primary solvent has been reported to reduce polysulfide (PS) solubility by forming a stable cathode–electrolyte interphase (CEI) on the cathode. [1] However, the formation mechanisms of the cathode–electrolyte interphase (CEI) and the suppression of polysulfide (PS) dissolution in Li-S batteries remain unclear. We have studied to clarify the early-stage formation of the CEI at the electrolyte/cathode active material interface via the reductive decomposition of solvents and anions.

In the electrolyte/Li_2S interface model, Li_2S (fcc, Fm–3m) was constructed as an S-Li-S-terminated slab expanded to a 3 × 3 supercell in the (001) plane, with a vacuum layer of 20 Å along the c-axis. The slab, consisting of 27 Li_2S units, was used to represent the Li_2S active material. The electrolyte was composed of LiFSA (FSA: $(FSO_2)_2N^-$) and FEC with a molar ratio of 1:12. The simulation cell parameters were set to a = b = 12.137 Å and $\alpha = \beta = 90°$, $\gamma = 60°$. The total number of atoms and electrons in the model were 358 and 1322, respectively. The initial structure was constructed by interfacing the two cells. First-principles molecular dynamics simulations were performed using OpenMX ver. 3.9.9. The GGA-PBE functional was used and the basis sets are assigned as follows: Li8.0-s3p2, N6.0-s2p2d1, S7.0-s2p2d1, O6.0-s2p2d1, F6.0-s2p2d1, C6.0-s2p2d1, and H6.0-s2p1.

At the electrolyte/Li_2S interface, FEC solvated to Li^+ was found to undergo ring opening at 0.4-0.5 ps, forming LiF, CH_2CHO, and $LiCO_2$ on the Li_2S surface. No further reactions were observed even when the simulation was extended to 25 ps. The CH_2CHO species is regarded as an intermediate and may subsequently decompose to yield CO_2 and CH_3CH_2OH as final products. This reaction is attributed to the lowering of the LUMO of FEC upon solvation with Li^+, which promotes reductive decomposition. The three-phase interface is crucial for CEI formation, a new electrode model will be developed for further study.

References

[1] Y. Torii *et al.*, *J. Phys. Chem. C*, **127**, 15069 (2023)

Parametric dielectric response and electronic structure analysis of several rare-earth monoxides

Takayuki MAKINO
Research Center for Development of Far-infrared Region, University of Fukui
Bunkyo, Fukui, Fukui 910-8557

1 The Metastable Nature of Rare-Earth Monoxide

Rare-earth sesquioxides are stable wide-gap insulators ($E_g \approx 5.6$ eV), whereas rare-earth monoxides (ReO) form only as metastable phases with an unstable +2 valence. PLD-grown ReO films show a dark brown color, clearly distinct from transparent sesquioxides.

A key difficulty is identifying the origin of low-energy absorption. Earlier work suggested a narrow 0.2 eV gap from linear extrapolation, but this interpretation is limited [1]. Distinguishing a true semiconductor gap from a Drude tail requires a more rigorous multilayer optical model and statistical inference.

The studied heterostructure consists of CaF_2(001), a 180 nm ReO film, a 30 nm sesquioxide reference, and a 10 nm AlO_x cap. Determining the ground state hinges on whether the response is dominated by interband transitions or a semi-metallic Drude contribution.

2 Bayesian Derivation of Dielectric Functions

A three-layer optical model (Substrate / ReO / Effective Layer) with the Denton Fresnel formulation was used to convert R and T into ε_1 and ε_2. To avoid model bias, ε_2 was expanded using 3rd-order B-splines with 40 knots across 0.05–6.5 eV [2], ensuring smoothness and Kramers–Kronig consistency. ε_1 was obtained via KK transformation with a high-energy constant term [3].

Parameter estimation employed STAN's HMC-NUTS algorithm, jointly optimizing film thickness, high-frequency dielectric constant, and spline weights. Computations were performed on a Ryzen 7950X workstation in our lab.

3 Statistical Validation of Free-Electron Response

To identify the physical origin of the optical response, we compared a Drude–Lorentz model (free + bound electrons) with a Lorentz-only model. Model selection used PSIS-LOO cross-validation to estimate ELPD. Calculations were performed on the same Ryzen 7950X system.

Model	ELPD	ΔELPD
Drude-Lorentz	12780.0	—
Lorentz	12734.2	-45.8

The sizable ΔELPD = 45.8 strongly favors the Drude–Lorentz model, indicating a plasma frequency below the measurement window and supporting a semi-metallic ground state.

4 Correlated Electronic Structure Calculations

To validate this interpretation, DFT calculations (Quantum ESPRESSO v7.2) were per-

formed on a Ryzen 7950X system and the ISSP supercomputer. SCF and band calculations used PBE-GGA and PAW potentials. The rock-salt structure was optimized, and a doubled cell with AFM ordering was used to mimic paramagnetic behavior.

Because standard DFT over-delocalizes d-electrons, DFT+U was applied. Linear-response calculations yielded $U = 1.36$ eV for cation-4d and 7.77 eV for anion-2p. Even with U, the band structure retains a semi-metallic overlap, consistent with the Drude–Lorentz optical preference. 4d and 5d monoxides show semi-metallic or metallic ground states, and unlike 3d monoxides, a Hubbard U alone cannot open an insulating gap due to weaker electron localization.

5 Conclusion

Bayesian optical modeling combined with correlated DFT+U calculations establishes ReO as a semi-metallic material. Although earlier absorption extrapolations suggested a narrow-gap insulator, LOOCV strongly supports a Drude contribution, and DFT+U confirms a finite density of states at the Fermi level. This integrated approach resolves the long-standing ambiguity surrounding the electronic ground state of metastable ReO.

References

[1] K. Kaminaga, R. Sei, K. Hayashi, N. Happo, H. Tajiri, D. Oka, T. Fukumura, and T. Hasegawa: Appl. Phys. Lett. **108**, 122102 (2016).

[2] D. Likhachev: Thin Solid Films **636**, 519 (2017).

[3] T. Kurachi, T. Yamaguchi, E. Kobayashi, T. Soma, A. Ohtomo, and T. Makino: Physica B **621**, 413259 (2021).

Theoretical Study on Electronic Properties in New Nanoscale Surfaces and Interfaces

Katsuyoshi KOBAYASHI
Department of Physics, Ochanomizu University
2-1-1 Otsuka, Bunkyo-ku, Tokyo 112-8610

In 2025 we theoretically studied the electronic structure of spiral silicene. In 2024 we had already studied the electronic structure and transmission properties of spiral graphene. The difference between silicene and graphene is the presence or absence of buckling in the atomic structure. The electronic structure is expected to be complex due to the mixing of π and σ states in spiral silicene.

We considered a simple structure for spiral silicene shown in Fig 1. First we calculated

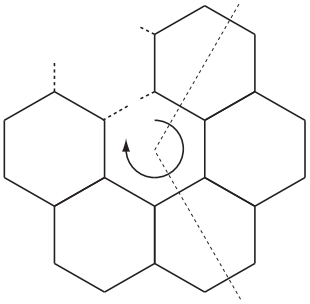


Figure 1: Atomic structure of a spiral silicene. The area enclosed by the thin dotted line is the unit cell of the spiral structure.

the electronic states of a two-dimensional silicene by the density-functional method. The electronic states of a free-standing silicene was calculated. Quantum Espresso was used. Maximally localized Wannier functions were constructed to calculate the electronic states of the spiral silicine. Wannier90 was used. The unit cell of the spiral structure considering the AB sublattice in the bucked structure is shown in Fig 1. The rotational periodic boundary condition was imposed. The calculations took into account that the σ orbitals change direction with a 120° rotation.

Figure 2 shows a band structure calculated as a function of the Bloch phase of the rotational periodic structure. While some bands in the spiral silicene have a shape similar to the π-bands of the spiral graphene, it has been found that the spiral silicene has a complex band structure that is quite different from that of the spiral graphene.

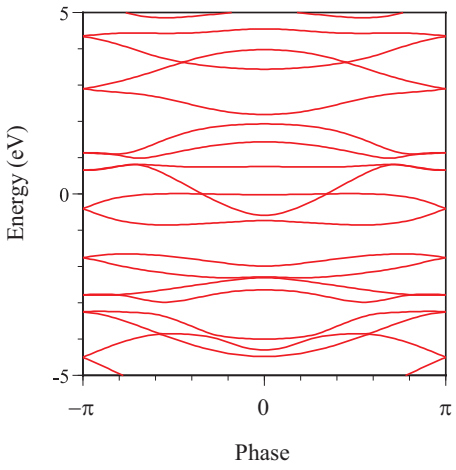


Figure 2: Band structure of a spiral silicene. The origin of energy is the Fermi energy.

Density Functional Tight Binding Calculations of Fullerene Adsorbed on a Tungsten Surface

Hirotaka KITOH-NISHIOKA
Department of Energy and Materials, Faculty of Science and Engineering, Kindai University
3-4-1 Kowakae, Higashiosaka City, Osaka 577-8502

The peculiar field-emission microscope (FEM) images, such as clover-shaped forms, are obtained for the fullerene (C_{60}) adsorbed tungsten (W) nanotip, which is subjected to the strong electric field.[1, 2] Ab initio electronic structure calculations of the C_{60}/W system under strong electric fields are essential to elucidate the mechanisms of the phenomena. However, two primary challenges are remain: (1) the huge computational cost associated with the large system size, and (2) the technical difficulty on performing electonic structure calculations under strong electric-field conditions. This study evaluates the application of the Density Functional-Based Tight-Binding (DFTB) method, which offers computational speeds more than 1,000 times faster than conventional Density Functional Theory (DFT). To focus on the challenge (1) above, all calculations were conducted under zero-electric-field conditions.

A five-layer W slab model with a single adsorbed C_{60} molecule was constructed in a unit cell. For the DFTB calculations, the Slater-Koster parameters for W–W and W–C interactions were adopted from the periodic table-based parameters (PTBP). Dispersion interactions were accounted for using Grimme's DFT-D3(BJ) correction, and all DFTB simulations were performed using the DFTB+ software package. For comparison, reference DFT calculations were performed using the vdW-DF2-B86R functional with the Quantum ESPRESSO package in addition to the calculations using the machine learning potentials with Matlantis.

Figure 1 shows the resultant adsorption energies of C_{60} on the W(100) bridge site as a function of the distance from the surface. The equilibrium distances and adsorption energies at the minima show excellent agreement between the DFTB and DFT methods.

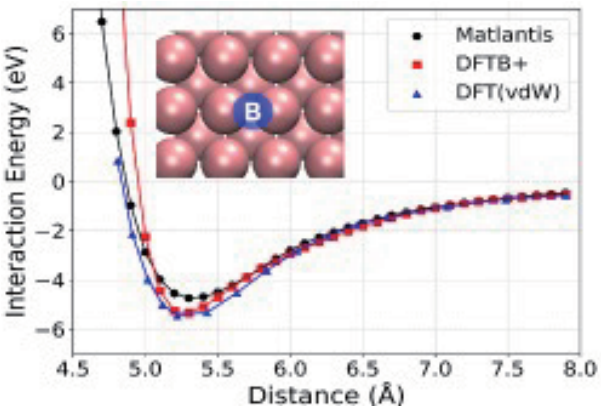


Figure 1: Adsorption Energy Curves for C_{60} on W(100) Bridge Sites, Calculated using DFTB, DFT, and Matlantis(Machine Learning Potential).

References

[1] H. Yanagisawa, M. Bohn, H. Kitoh-Nishioka, F. Goschin, and M. F. Kling: Phys. Rev. Lett. **130**, 106204 (2023).

[2] H. Yanagisawa: Appl. Phys. Lett. **126**, 010501 (2025).

Search and realization of novel electronic properties of surfaces and interfaces and of nanostructures

Takeshi INAOKA
Department of Physics and Earth Sciences, Faculty of Science, University of the Ryukyus, 1 Senbaru, Nishihara, Okinawa 903-0213

We have been performing first principles calculations of the electronic structure of x-form phthalocyanine (x-Pc) crystals [1]. The Pc molecule is a planar π-conjugated macrocyclic molecule which can incorporate an atom of various species at its center position and many kinds of side chains around its molecular plane. The x-Pc crystal is formed by a square-lattice arrangement of molecular chains. In each chain, molecules are stacked with double period and with molecule planes normal to the stacking direction. We can expect effective orbital overlapping between neighboring face-to-face molecule planes. We employed the program package VASP [2-5] mainly on system B.

(I)Pressure-induced metallization of iodine chains in x-LiPcI crystal

The x-LiPcI crystal with Li atoms at molecular centers have iodine (I) atomic chains in open channels between Pc molecule chains. In the stable structure, the I atoms form pentamers as I_5^- in each chain, and this atomic chain is not metallic.

Last year, we reported that, when uniaxial compressive strain is applied to x-SiPcI crystal, trimeric I chains transform into equally spaced metallic atomic chains. In the stable state, the bond length of each trimer is 3.00 Å, and the distance between neighboring trimers is 3.55 Å. With increasing compression in the stacking direction, although the trimer bond length remains unchanged, the intertrimer distance decreases, until it becomes equal to the trimer bond length.

In the case of x-LiPcI, since Pc chains have two-fold periodicity and I atoms are pentamers in each chain, we need to consider a structure with ten-fold periodicity in the stacking direction, in order to track changes in the electronic structure with increasing compression. However, since this primitive unit cell is too large for computational purposes, we calculate that final state in which compressive strain results in equally spaced I atomic chains with the bond length 3.00 Å.

Using the van der Waals density functional theory, we have calculated the electronic structure of the x-LiPcI crystal compressed in the stacking direction to the c-axis lattice constant c_0=6.00 Å (double period). Figure 1 shows the band dispersion on the Γ-Z line in the Brillouin zone. We can identify that rapidly falling band which crosses the Fermi level E_F and which is folded at the Z point because of double period in the stacking direction. Figure 2 exhibits the electron density distribution of the state b193 circled red and that of the state b153 squared red in Fig. 1. As shown clearly in Fig. 2, this

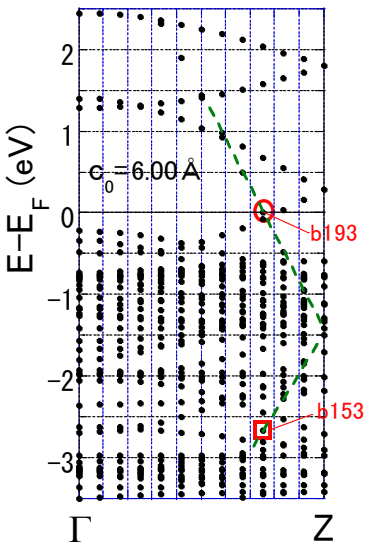


Fig. 1 Band dispersion on the Γ-Z line of x-LiPcI crystal strained compressively in the stacking direction.

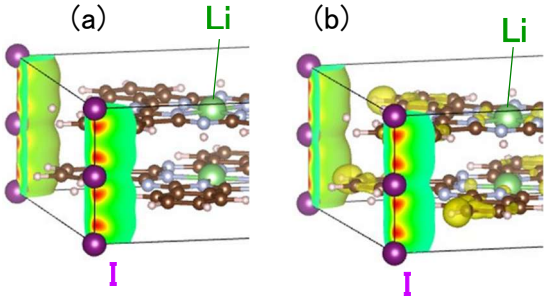


Fig. 2 Electron density distribution of (a) the state b193 circled red and (b) the state b153 squared red in Fig.1.

metallic band is formed by p_z orbital overlapping between adjacent I atoms.

From the gradient of the band energy and the wavenumber at the E_F–crossing point, we can estimate the effective mass ratio and the one–dimensional electron density of the I–derived conduction band to be m^*/m_0=0.09 and n_{1D}=0.83×10^7/cm, respectively. From the strain dependence of the total energy, we found that the uniaxial compressive stress of 1.5 GPa is required to achieve the above compressive strain.

By applying uniaxial compression in the stacking direction, we can transform nonmetallic pentameric I atomic chains into equally spaced metallic ones with high electrical conductivity.

(II) Electronic structure and magnetic properties of x–FePc(CN)$_8$ crystal

In the x–FePc(CN)$_8$ crystal, eight cyano groups are arranged around each molecule plane, and an iron (Fe) atom occupies the center of the molecule plane. We have performed collinear GGA+U calculations and analyzed the electronic structure and magnetic properties of the x–FePc(CN)$_8$ crystal.

Convergent solutions can be obtained in each case of the ferromagnetic (FE) and antiferromagnetic (AF) Fe chains.

Figure 3 (a) displays the total electron density distribution (isosurfaces) of the lower molecule in the unit cell for FE Fe chains. We can observe bonding between the N and H atoms of laterally adjacent molecules, as indicated by red circles. This bonding does not depend on the magnetic state of the Fe atomic chains. From the perspective of avoiding Coulomb repulsion, a stacking angle of 45° is advantageous. However, the staggering angle shifts to 40° to form the N–H bonding.

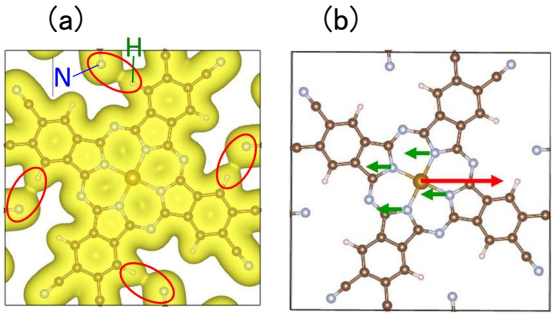


Fig. 3 (a) Total electron density distribution (isosurfaces) of the lower molecule of x–FePc(CN)$_8$ crystal. (b) Magnetic moments of an Fe atom (red) and of its surrounding Ni atoms (green).

Whether the Fe atomic chains are FE or AF, each Fe atom weakly spin–polarizes its surrounding atoms, particularly its nearest N atoms in an AF manner. Figure 3 (b) shows the magnetic moments of an Fe atom and of its surrounding N atoms for the FE Fe chains. The magnetic moment of the Fe atom (red arrow) is 2.1 μ_B (μ_B: Bohr magneton), which is close to the bulk Fe value 2.2 μ_B. The magnetic moments of the N atoms (green arrows) is about 0.035 μ_B, which is two orders of magnitude smaller than that of the Fe atom.

The energy difference between the FE and AF Fe chains is really small, and when using the GGA+U method, we often encounter semistable solutions. After evaluating these magnetic states carefully and accurately, we will conduct a comparative analysis with the comprehensive experimental results [6].

References

[1] T. Inaoka, AIP Advances **14**, 085016 (2024).
[2] G. Kresse and J. Hafner: Phys. Rev. B **47**, 558–561 (1993).
[3] G. Kresse and J. Furthmüller: Comput. Mat. Sci. **6**, 15–50 (1996).
[4] P. E. Blöchl: Phys. Rev. B **50**, 17953 (1994).
[5] J. Klimeš, D. R. Bowler, and A. Michaelides: Phys. Rev. B **83**, 195131 (2011).
[6] M. Isobe et al., ACS Omega **8**, 27264 (2023).

Regional Chemical Potential Analysis for Dimerized Diamond (001) Surface

Masahiro FUKUDA

Institute for Solid State Physics,

The University of Tokyo, Kashiwa-no-ha, Kashiwa, Chiba 277-8581

In this study, we propose the RCP (Regional Chemical Potential) analysis method and demonstrate that it can predict adsorption sites for C dimers and Si atoms on the diamond (001) surface [1]. The RCP on the material surface can be used to evaluate the electron-donating ability of the surface when it tends to form a chemical bond with a probe tip. It can also be used for discussion of where and to what extent atoms or molecules can be selectively adsorbed on the material surface. Specifically, by color-plotting the RCP values within a selected energy range on the zero isosurface of the kinetic energy density of the system, one can visualize regions where covalent bonding is likely to occur, namely sites where atoms or molecules are likely to adsorb.

RCP analysis can be performed by applying post-processing to the density matrix obtained from first-principles electronic structure calculations. As a post-processing code for DFT code, OpenMX [2], we developed a highly parallelized local physical quantity calculation code, FLPQ [3] along with FLPQViewer [4] for visualizing the local RCP.

This analysis enabled visualization of favorable adsorption sites for individual C dimers on the clean diamond (001) surface and allowed prediction of the surface growth process. The results were found to be consistent with AFM experimental observations [5, 6]. We have also applied this approach to the adsorption process of Si atoms on the diamond (001) surface and are exploring the prediction of novel materials ahead of experimental realization.

References

[1] M. Fukuda, M. Senami, Y. Sugimoto, and T. Ozaki, J. Chem. Phys. **164**, 084123 (2026).

[2] T. Ozaki *et al.*, OpenMX package, http://www.openmx-square.org/.

[3] M. Fukuda, FLPQ package, https://github.com/mfukudaQED/FLPQ.

[4] M. Fukuda, FLPQViewer, https://github.com/mfukudaQED/FLPQViewer.

[5] R. Zhang, Y. Yasui, M. Fukuda, T. Ozaki, M. Ogura, T. Makino, D. Takeuchi, and Y. Sugimoto, Nano Letters **25**, 1101 (2025).

[6] R. Zhang, Y. Yasui, M. Fukuda, M. Ogura, T. Makino, D. Takeuchi, T. Ozaki, and Y. Sugimoto, Phys. Rev. Res. **7**, 023036 (2025).

Reexamination of the electron renormalization in conventional superconducting theory

Ryosuke AKASHI
Department of Applied Physics and Physico-Informatics, Keio University
Hiyoshi, Yokohama, Kanagawa 223-0061

The accuracy to theoretically estimate the superconducting transition temperature (T_c) has recently been improved thanks to the development of first-principles electronic and phononic structure calculations. In particular, T_cs of many conventional phonon-mediated superconductors are nowadays calculable from first principles with enough practical accuracy, which are thanks to the development of superconducting density functional theory [1, 2] and Eliashberg theory [3]. There, the screened Coulomb interaction is treated as independent of frequency. The extension to inlude its frequency dependence may enable to treat more significant Coulomb effects but it requires substantially increased computational cost. Practical algorithms are desired.

In this study, we have developed a program to calculate the superconducting properties on the basis of the Eliashberg theory with the frequency dependent screened Coulomb interaction and applied it to a uniform electron gas model with the Einstein-type phonon mode. By linearizing the Eliashberg equations [4] with respect to the anomalous component of the electron self energy, we obtain two set of equations that may be solved sequentially. First one is for the normal state self energy:

$$\Sigma(\mathbf{k}, i\omega_j) = -T\sum_{j'}\sum_{\mathbf{k}'} G(\mathbf{k}', i\omega_{j'})W(\mathbf{k}-\mathbf{k}', i(\omega_j - \omega'_j)) \quad (1)$$

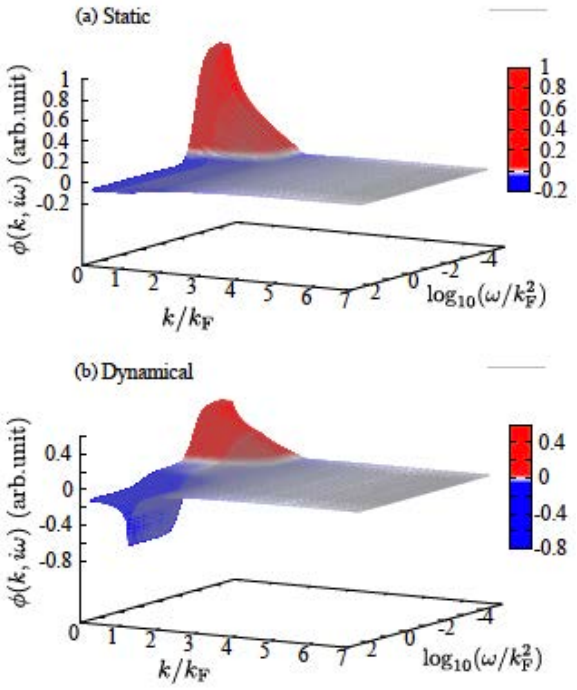


Figure 1: Normalized gap functions at T_c as the eigensolution to Eq. 3. Panels (a) and (b) show the results with the frequency-independent and dependent screened Coulomb interaction, respectively. Taken from Ref. [5].

$$\frac{1}{G(\mathbf{k}, i\omega_j)} = \frac{1}{G_0(\mathbf{k}, i\omega_j)} - \Sigma(\mathbf{k}, i\omega_j). \quad (2)$$

The second one is for the anomalous self-energy component

$$\phi(\mathbf{k}, i\omega_j) = -T\sum_{i'j'} \frac{\phi(\mathbf{k}, i\omega_{j'})W(\mathbf{k}-\mathbf{k}', i(\omega_j-\omega_{j'}))}{\bar{\Theta}(\mathbf{k}, i\omega_j)}, \quad (3)$$

$$\bar{\Theta}(\mathbf{k}, i\omega_j) = \left[\omega_{j'} Z(\mathbf{k}, i\omega_{j'})\right]^2 + \left[\xi(\mathbf{k}) + \chi(\mathbf{k}, i\omega_{j'})\right]^2 . \quad (4)$$

The latter has a nontrivial solution only at the transition temperature. Note that Z and χ in Eq. (3) through $\bar{\Theta}$ are the normal state values related to Σ in Eq. (1) by

$$i\omega_j Z(\mathbf{k}, i\omega_j) = \frac{1}{2}\left[\Sigma(\mathbf{k}, i\omega_j) - \Sigma(\mathbf{k}, -i\omega_j)\right], \quad (5)$$

$$\chi(\mathbf{k}, i\omega_j) = \frac{1}{2}\left[\Sigma(\mathbf{k}, i\omega_j) + \Sigma(\mathbf{k}, -i\omega_j)\right], \quad (6)$$

$W(\mathbf{q}, i\nu)$ is the total interaction between the electrons, that in this case is composed of the Einstein phonon-mediated attraction and the screened Coulomb interaction with the random phase approximation. This model is characterized by four parameters: Wigner-Seitz radius r_s, Debye wavenumber k_D, Einstein frequency ω_E and electron-phonon coupling strength λ: see Ref. [5] for details. We have developed an efficient algorithm to solve those sets using the intermediate representation [6] and continuous Euler transformation [7].

We show in Fig. 1 the calculated gap functions at T_cs with the static and frequency dependent screened Coulomb interactions, respectively. For both cases, the sign changes from low energy ($k \sim k_\mathrm{F}; \omega \sim 0$) to high energy, which indicate the retardation effect. For the dynamical case, we observe a dip at $k \simeq k_\mathrm{F}$ in the intermediate frequency $\omega \gtrsim k_\mathrm{F}^2$. The impact of the dip structure on the resulting T_c is significant, especially in the large r_s regime. We made thorough calculations on the impact for varying model parameters, which should be useful as a reference for the limiting behavior of the first-principles Eliashberg calculations [5].

Also, we have studied the electronic structure of a pressure-induced high-T_c superconductor H_3S [8]. Despite it is formed by compressing the molecular solid phase of H_2S, we have recently found its remarkable uniform-electron like feature of the band structure [9]. To get a deeper insight into this, we calculated the momentum resolved spectral function

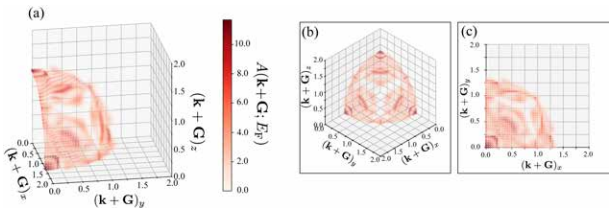


Figure 2: Plane-wave resolved spectral function for the electronic states of H_3S at the Fermi level. Panels (a)–(c) show different views. Taken from Ref. [10].

around the Fermi level

$$A(\mathbf{k}+\mathbf{G}; E_\mathrm{F}) = \sum_n |c_{n\mathbf{k}}(\mathbf{k}+\mathbf{G})|^2 \delta(E_\mathrm{F} - \varepsilon_{n\mathbf{k}}), \quad (7)$$

where $c_{n\mathbf{k}}(\mathbf{k}+\mathbf{G})$ denotes the plane-wave expansion coefficient of the Kohn-Sham eigenstate and $\varepsilon_{n\mathbf{k}}$ is the Kohn-Sham eigenvalue. As clearly shown in Fig. 2, the resulting intensity is concentrated around a spherical region, which indicate that the electronic states around the Fermi level is indeed formed by the uniform-electron-like states. Upon this result we have successfully formulated the nearly uniform electron model for the global band structure with very few parameters [10].

Parts of the model and first principles calculations were executed on System B (Ohtaka). The latter calculations were performed using Quantum Espresso [11] with norm conserving pseudopotentials from Pseudo dojo [12]. See the related publications Refs. [5, 10] for details.

References

[1] M. Lüders *et al.*: Phys. Rev. B **72**, 024545 (2005).

[2] M. A. L. Marques *et al.*: Phys. Rev. B **72**, 024546 (2005).

[3] A. Sanna *et al.*: J. Phys. Soc. Jpn. **87** 041012 (2018).

[4] E. R. Margine and F. Giustino: Phys. Rev. B **87** 024505 (2013).

[5] R. Akashi and H. Shinaoka: Phys. Rev. B **113**, 014507 (2026).

[6] H. Shinaoka, J. Otsuki, M. Ohzeki, and K. Yoshimi: Phys. Rev. B **96**, 035147 (2017).

[7] T. Ooura: J. Comput. Appl. Math. **130**, 259 (2001).

[8] A. P. Drozdov, M. I. Eremets, I. A. Troyan, V. Ksenofontov, and S. I. Shylin: Nature **525**, 73 (2015).

[9] R. Akashi: Phys. Rev. Research **6**, 033012 (2024).

[10] R. Akashi: Ann. Phys. **538**, e00003 (2026).

[11] P. Giannozzi *et al.*: J. Phys. Condens. Matter **29**, 465901 (2017).

[12] G. Pizzi *et al.*: J. Phys. Condens. Matter **32**, 165902 (2020).

Development of a Surface Structure Exploration Program and Supporting Infrastructure

Materials DX Research Center, National Institute of Advanced Industrial Science and Technology (AIST), 1-1-1 Umezono, Tsukuba, Ibaraki 305-8560, Japan

Fumiaki Kuroda

First-principles structure prediction is an important approach for discovering functional materials. By evaluating candidate atomic structures using quantum mechanical calculations, it can identify stable structures without relying only on experimental trial and error. This is especially useful for surfaces, where atomic arrangements strongly affect catalytic activity, electronic properties, and magnetic behavior.

However, surface structure searches are still difficult because many existing methods assume fixed in-plane periodicity and fixed composition. In realistic surface systems, the most stable structure may have a different supercell shape, adsorbate coverage, reconstruction pattern, or alloying composition from those assumed in advance. Therefore, fixing these degrees of freedom can miss important low-energy surface structures.

In this work, we develop a global search framework that treats both two-dimensional superlattice periodicity and stoichiometry as variable degrees of freedom [1]. The method can directly compare surface structures with different supercell shapes and compositions in a unified search. It combines an evolutionary algorithm with surface-specific variation operators and symmetry-enriched initialization, allowing efficient generation of diverse surface candidates.

To reduce computational cost, the framework also uses Bayesian optimization with atomic cluster expansion descriptors. These descriptors represent atomic environments in a form suitable for machine-learning prediction. Bayesian optimization then selects promising structures for further first-principles evaluation, reducing the number of expensive calculations required during the search.

The method is applied to oxygen-induced surface structures on FCC Pt(111) and diamond Ge(100). In both cases, stable structures consistent with experimental observations are obtained. The same framework is also applied to Sn alloying on FCC Au(111), where the predicted alloying motifs agree with reported surface-structure trends.

These results show that the proposed framework can efficiently explore complex surface-structure spaces with variable periodicity and composition. It provides a general route for studying functional materials in heterogeneous catalysis, electronics, and spintronics, where structural and compositional degrees of freedom are strongly coupled.

[1] paper under review.

DFT calculations of the electronic states of guest adsorbates trapped in porous metal-organic thin films

Noriyuki Tsukahara
National Institute of Technology, Gunma College
Maebashi, Gunma 371-0845

I have studied porous two-dimensional metal-organic network (2D-MON) on Cu(111) with guest molecules in the pores of the 2D-MON. The 2D-MON used in this study consists of 1,3,5-tris(pyridyl)benzene (TPyB) molecules and Cu atoms on Cu(111).

DFT calculations were performed using VASP. The slab consists of three layers of Cu(111) substrate, the 2D-MON, and a vacuum layer (about 4 nm thickness), and 405 atoms are included in the slab. In addition, various guest molecules are contained in the pore of the 2D-MON. 2x2x1 k-point sampling was used to perform structural and electronic relaxation, and the adsorption structures and the adsorption energies were calculated.

1. Formation of specific HCOOH oligomer by the 2D-MON

HCOOH molecules aggregate on the Cu(111) surface via hydrogen bonds, forming one-dimensional chain structures. A model was constructed based on the STM results, and structural relaxation was performed on the model. In the pore, a tetramer chain is formed, and its ends are stabilized by electrostatic interactions with the 2D-MON [1].

2. Modulation of adsorption structures of guest 1,3,5-triphenylbenzen (TPhB) and 1,3,5-tris(bromophenyl)benzene (TBB) molecules by the host-guest interaction.

To clarify how the adsorption state of guest molecules in pores is modulated by host-guest interactions, DFT calculations were performed for the host 2D-MON with guest TPhB and TBB molecules. The distance between the TPhB molecule and the Cu substrate is approximately 0.06 Å smaller due to host-guest interactions compared to the TPhB molecule on Cu(111) without the 2D-MON. For guest TBB molecules, the terminal Br interacts attractively with the 2D-MON, causing them to separate from the substrate slightly.

References

[1] N. Tsukahara and J. Yoshinobu, *Small* **21**, e05213 (2025).

Two-dimensional Ag stripe formation on the Ni(110) surface

Tsuneo FUKUDA

Department of Physics and Electronics, Graduate School of Engineering, Osaka Metropolitan University, 1-1 Gakuen-cho, Naka-ku, Sakai, Osaka, 599-8531

The synthesis of materials with novel functionalities is a central goal of materials science. In particular, two-dimensional (2D) metal alloys provide unique opportunities for catalytic and electronic applications that surpass those of their bulk counterparts.

As a model system for such metal-on-metal architectures, we investigate a monolayer of Ag on the Ni(110) surface [1]. Experimentally, Ag deposition on Ni(110) yields a well-defined 2D stripe structure (Fig. 1). Despite its high stability, the mechanism responsible for the formation and stabilization of this Ag stripe phase remains unclear.

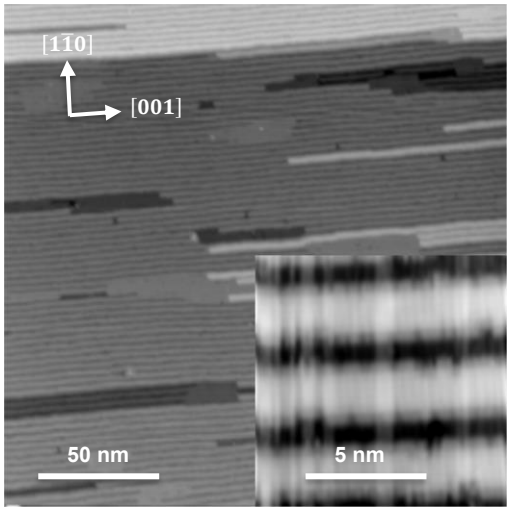


Fig. 1: Typical STM image of Ag-deposited Ni(110) surface showing Ag stripe structure. Inset: Magnified image of the Ag-stripe.

The Ag stripe is composed of one-dimensional (1D) Ag clusters aligned along the [1$\bar{1}$0] direction, which extend in the [001] direction to form a stripe. Our calculations indicate that 1D Ag clusters containing more than seven atoms are unstable, primarily due to the significant lattice mismatch between the Ni substrate and Ag adatoms [2]. This conclusion is based on formation energy comparisons between an n-atom cluster and an (n−1)-atom cluster with an additional Ag atom adsorbed at a neighboring stable site one unit-cell away.

However, such static analyses do not account for kinetic effects, particularly energy barriers associated with atomic motion. To elucidate the dynamics underlying this self-limiting nanocluster formation, we employ the nudged elastic band (NEB) method.

All calculations were performed using VASP with the PBE exchange–correlation functional. To evaluate the stability of 1D Ag clusters, a 12×1 slab model was constructed by extending the Ni(110) surface unit cell along the [1$\bar{1}$0] direction. The slab consists of seven atomic layers and includes vacuum regions of 0.88 nm on both sides, yielding a total of 84 Ni atoms. To allow lattice relaxation along the [001]

Table 1: Calculation Parameters

Parameters	Values
Slab geometry	12×1 or 6×2 units
k- points	4×32 or 8×16
Cutoff energy	384.1 eV
Fermi Energy Smearing	Methfessel–Paxton method σ = 0.12 eV
Vacuum regions	0.88 nm each side
Convergence Condition	Atom position: 0.1 eV/nm Electron energy: <1 μeV
Number of images	Image = 4 (three intermediate states)
Number of cores for each image	256

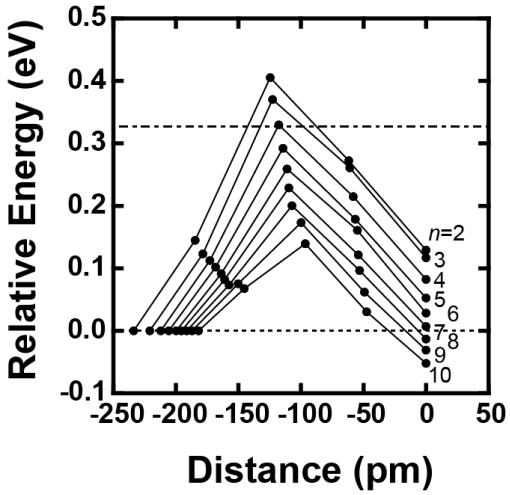


Fig. 2: Potential barrier for the detachment of peripheral Ag atom in the *n*-atom cluster. Number of initial Ag atom (*n*) is indicated nearby each line. Diffusion barrier of single adatom is represented by a dash-dot line.

direction, a 6×2 surface unit cell was also used. Other computational parameters are provided in Table 1.

Transition states for the attachment and detachment of edge Ag atoms were determined using the NEB method. The calculations employed three intermediate states (four images), with convergence criteria identical to those used for adsorption energy calculations.

The results are presented in Fig. 2, where the final state—with the Ag atom at the two-fold hollow site—is taken as a reference position, and the energy barriers are plotted as a function of atomic displacement. For small clusters (n = 2–3), the diffusion barriers are significantly higher than that of a single Ag atom, reflecting the cooperative motion of multiple adatoms. In contrast, for larger clusters (n > 5), the barriers become lower than that of an isolated Ag atom. This reduction arises because edge Ag atoms are subject to lattice mismatch and exhibit weaker adsorption, facilitating their detachment from the cluster.

Thus, edge atoms readily detach (effectively "evaporate") from the 1D clusters, leading to intrinsically self-limiting growth of the Ag stripes. Our results elucidate the origin of stripe formation and the emergence of non-wetting regions between stripes, providing insight into the mechanisms governing this novel nanostructure.

References

[1] A. Mizuhara, T. Fukuda, and K. Umezawa, Surf. Sci. **761**, 122807 (2025).

[2] A. Mizuhara, DaeGwi Kim, and T. Fukuda, e-J. Surf. Sci. Nanotechnol. **24**, 13 (2026).

Structure of Ce-Ti-O honeycomb ultrathin films on Pt(111)

Li Xu and Junji YUHARA

School of Engineering, Nagoya University,

Furo-cho, Chikusa-ku, Nagoya, Aichi 464-8603

Recently, it has been reported that Ba-Ti-O honeycomb structures can be transformed into oxide quasicrystals and approximant structures via Stone-Wales transformations upon oxygen addition [1]. Our group has successfully fabricated Ce-Ti-O ultrathin films on Pt(111) surfaces, featuring both honeycomb and oxide quasicrystal-related structures (Fig. 1) [2]. To gain a deeper understanding of the relationship between honeycomb and quasicrystal structures, it is essential to elucidate the nature of the honeycomb structure itself. The purpose of this study is to characterize the structure of Ce-Ti-O ultrathin films using first-principles calculations.

When 0.5 ML Ce and 2 ML Ti were deposited onto a Pt(111) surface and subjected to annealing in an oxygen atmosphere, followed by vacuum annealing, a Ce-Ti-O-(3×3) honeycomb superstructure was observed (Fig. 1). In the scanning tunneling microscopy (STM) image, the unit cell marked in green corresponds to a (√3 × √3)R30° superstructure; based on the arrangement of bright spots and faint linear features, we interpret this as a honeycomb structure. X-ray photoelectron spectroscopy and resonant photoelectron spectroscopy revealed that Ce corresponds to Ce^{3+}, while Ti corresponds to both Ti^{3+} and Ti^{2+}.

The honeycomb superstructure was modeled based on a Ti_2O_3 honeycomb structure, with Ce atoms decorating the hollow sites of the honeycomb network. Structural optimization was performed using density functional theory with VASP (Fig. 2). The density functional calculations were performed with VASP 5.4.4. The optimized model reveals that the Ti atoms are distributed at different heights. Furthermore, the oxygen atoms in the honeycomb lattice occupied by Ce are found to be positioned closer to the center of the Ce atoms [3].

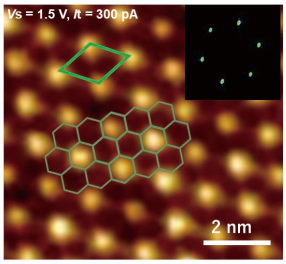


Fig. 1: STM image of the (√3×√3)R30° honeycomb structure

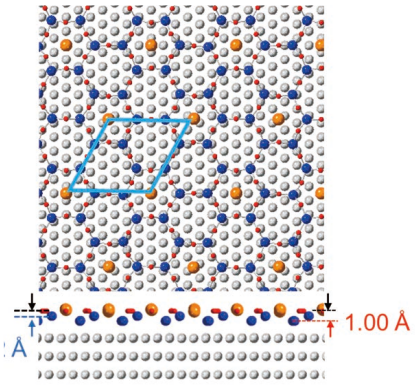


Fig. 2: Computational model of the (√3×√3)R30° honeycomb structure

References

[1] S. Schenk *et al*. Nature Comm. 13, 7542 (2022).

[2] X. Li *et al*., Phys. Chem. Chem. Phys. 25, 26065 (2023).

[3] X. Li *et al*., J. Phys. Chem. C 128, 47, 20238 (2024).

First-principles study of point defects in perovskite photocatalyst $PbTiO_3$

Kazutaka NISHIGUCHI
Graduate School of System Informatics, Kobe University
Rokkodai-Cho, Nada-Ku, Kobe 657-8501

Efficient dopants for perovskite photocatalyst $PbTiO_3$

Perovskite oxide $PbTiO_3$ (PTO) is not only a photocatalyst for overall water splitting but also a ferroelectric material. [1] As in other photocatalysts such as STO:Al, photocatalytic activity is expected to be enhanced through defect control using appropriate dopants. We investigated the electronic structure of doped PTO using first-principles calculations based on density functional theory (DFT). A $3 \times 3 \times 3$ supercell of the primitive PTO cell was used to describe point defects, including oxygen vacancies and substitutional dopants. The DFT calculations were performed within the PBE+U functional using the projector augmented-wave (PAW) method, as implemented in VASP. [2] The Hubbard U parameter was set to 4.75 eV for the Ti-3d orbitals, which reproduces the relative positions of the defect levels with respect to the valence and conduction bands. We also focus on oxygen vacancies V_O and divalent cation D substitution at the nearest Ti site. We consider divalent cations D^{2+} with ionic radii similar to that of Ti^{4+} to introduce hole carriers: D = Mg, Ni, and Zn. Because of the tetragonal crystal structure, the oxygen sites around Ti are distinguished as apical and in-plane oxygens, O_{ap} and O_{in}.

Figure 1 shows the PDOS of PTO:V_{Oap} and PTO:Mg. The presence of V_{Oap} introduces a defect level composed mainly of Ti 3d states below the conduction band. In contrast, Mg substitution at the nearest Ti site (Mg_{Ti}) removes this defect level and restores the band gap. The same trend is observed for V_{Oin}, which is not shown here. Therefore, divalent cation substitution is expected to enhance the photocatalytic activity, similarly to the case of STO. The effects of other divalent cation substitutions, as well as the formation energies of these dopants, will be investigated in future work.

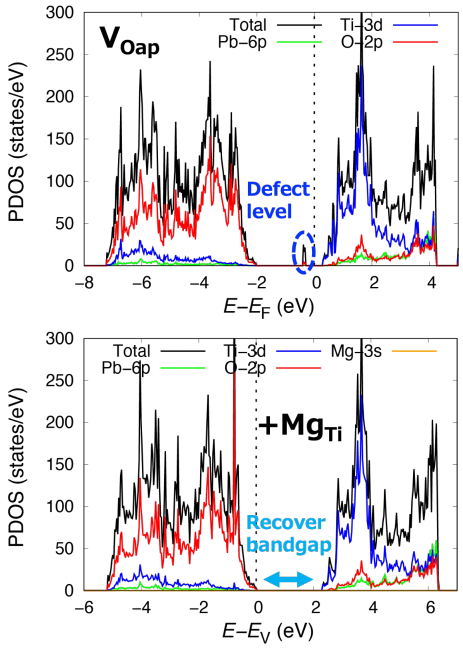


Figure 1: PDOS for PTO:V_{Oap} and PTO:Mg.

Calculation conditions

We have performed hybrid (MPI+OpenMP) parallel computing using, where the parallelization over bands and k-points is used by VASP version 6.4.2.

References

[1] G. Wan *et. al.*: J. Am. Chem. Soc. 2022, 144, 20342–20350.

[2] G. Kresse *et. al.*: Phys. Rev. B **47**, 558 (1993); Phys. Rev. B **49**, 14251 (1994); Computational Materials Science **6** (1996) 15–50; Phys. Rev. B **54**, 11169 (1996).

Development of On-the-fly Machine Learning Potentials in High-Accuracy Phonon Calculations

Takuya NARUSE
Department of Materials Science and Engineering, Kyoto University, Kyoto 606-8501, Japan

Lattice anharmonicity plays an essential role in describing finite-temperature vibrational properties of solids. In particular, temperature-dependent phonon frequencies and finite-temperature thermodynamic properties such as Helmholtz free energy, entropy, specific heat, thermal expansion, and phase stability cannot be fully captured within the conventional harmonic approximation. The stochastic self-consistent harmonic approximation (SSCHA) [1] is a powerful approach for incorporating anharmonic effects at the mean-field level by optimizing an effective harmonic Hamiltonian. However, SSCHA calculations require repeated evaluations of energies and atomic forces for a large number of displaced supercell configurations. Direct application of density functional theory (DFT) to all ensemble structures is therefore computationally prohibitive, especially when wide ranges of temperatures and volumes must be explored.

In this work, we accelerated SSCHA calculations using polynomial machine learning potentials (PolyMLPs) [2] for efficient evaluation of energies and atomic forces. We applied this approach to 33 nonmagnetic elemental metals over wide ranges of temperature and volume to systematically evaluate temperature- and volume-dependent vibrational frequencies and thermodynamic properties. The ISSP supercomputer resources were used primarily for generating DFT reference datasets required for the on-the-fly construction of PolyMLPs and carrying out the SSCHA calculations for these elemental metals.

The PolyMLPs used in this study were constructed through an on-the-fly procedure tailored to SSCHA calculations. For each elemental metal, an initial model was trained from DFT energies and forces of randomly displaced and strained supercells. The model was then used to sample SSCHA ensemble structures at representative temperatures and volumes. When these configurations were not sufficiently described, selected structures were evaluated by DFT and added to the training set. This cycle of SSCHA sampling, DFT data generation, and model retraining was repeated until stable energy and atomic force predictions were obtained, enabling the construction of robust PolyMLPs for 33 non-magnetic elemental metals.

In an SSCHA calculation at a specified temperature and volume, (1) the procedure begins with generating 5,000 configurations based on the density matrix derived from the effective force constants. (2) Next, the energies and atomic forces of these configurations are evaluated using polynomial MLPs. (3) Then, the effective force constants are updated by performing linear regression on the obtained set of displacements and atomic forces. These steps (1)–(3) are repeated starting from the harmonic force constants until the effective force constants converge to a consistent set.

The above SSCHA calculation was performed for 15 volumes with isotropic compression or expansion from the equilibrium volume at 0 K, with temperature increased in 50 K increments. The resulting Helmholtz free energies were fitted to an equation of state to determine the equilibrium volume at each temperature. Subsequently, SSCHA calculations were repeated for the equilibrium volume at each temperature to obtain temperature-dependent frequencies and thermodynamic properties including thermal-expansion effects.

Figure 1 shows the phonon dispersion curves for the body-centered cubic (bcc) phase of Ti. While the dispersion curve obtained from the conventional harmonic approximation exhibits imaginary frequencies, the SSCHA results at 1300 K show no such instabilities and are in good agreement with experimental data. Figure 2 shows the temperature dependence of entropy for both the hexagonal close-packed (hcp) and bcc phases of Ti. The calculated entropies are consistent with experimental values across the

entire temperature range. Similarly, for the other 32 elemental metals, both the calculated phonon dispersion curves and entropies showed good agreement with experiments.

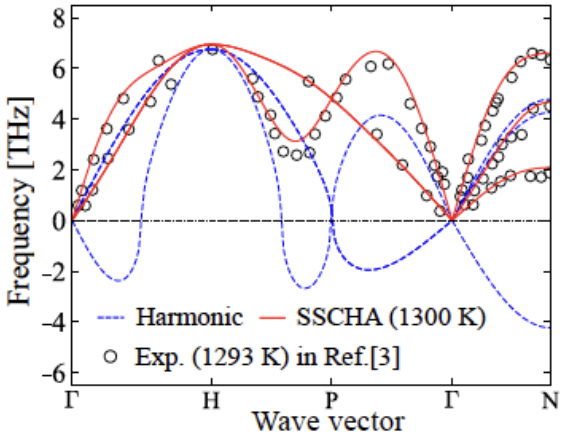


Fig. 1. Phonon dispersion curves from harmonic approximation (dashed line) and SSCHA at 1300 K (solid line) of bcc-Ti. The open symbols are experimental data at 1293 K adapted from Ref. 3.

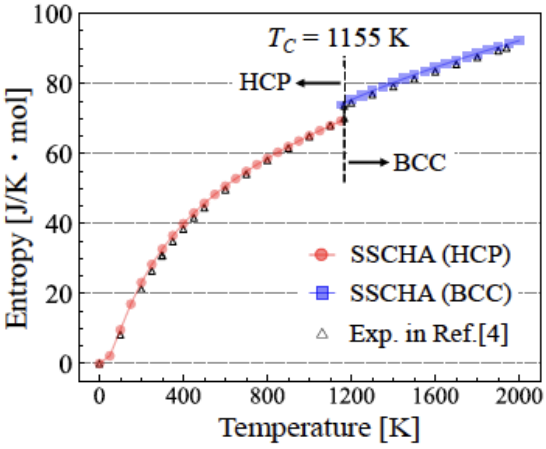


Fig. 2. Entropy as a function of temperature for hcp-Ti (circles) and bcc-Ti (squares). The triangle symbols are experimental values taken from Ref. 4.

Acknowledgment

The computation in this work has been done using the facilities of the Supercomputer Center, the Institute for Solid State Physics, the University of Tokyo (ISSPkyodo-SC-2025-Ba-0028).

References

[1] L. Monacelli, et al., J. Phys.: Condens. Matter 33, 363001 (2021).

[2] A. Seko, J. Appl. Phys. 133, 011101 (2023).

[3] W. Petry, et al., Phys. Rev. B Condens. Matter 43, 10933 (1991).

[4] M. W. Chase, NIST-JANAF Thermochemical Tables (American Institute of Physics, New York, 1998).

Electronic Structure of Rhenium

Takahiro Maehira
Faculty of Science, University of the Ryukyus, Nishihara, Okinawa 903-0213

Rhenium (Re) is a group-VII transition metal with a half-filled d band (electronic configuration $6s^2 5d^5$). The systematics of cohesive energies, bulk moduli, and equilibrium atomic volume for transition metals as the d bands are filled is well understood [1, 2]. The half-filled d band metals are characterized by high cohesive energy, low atomic volume and low compressibility. The early high-pressure work of Bridgman[3] indicated that rhenium is the least compressible of all metals. Re crystallizes in the hexagonal-close-packed (hcp) structure and retains this structure up to its melting temperature of 3180 °C

The compound Re has two phases: a low temperature phase is hexagonal Re. We studied simple cubic Re with a space group of $P6_3mmc$ which contains one molecule in the unit cell. The lattice parameter a and c are 0.2491, 0.402 Å, respectively. The calculation for the energy band structures was carried out by using the OpenMX code(`http://www.openmx-square.org/`). First, we discuss the calculated results for Re as shown in Figure 1, in which we depict the energy band structure along the symmetry axes in the Brillouin zone, which is shown in Figure 1, in the energy region from -10.0 to 10.0 eV. The Fermi level $E_{\rm F}$ is at 0.0 eV. for Re and indicated by dashed lines in Figure 1.

With respect to the energy band structure near $E_{\rm F}$, we emphasize that there is always hybridization between the Re $5d$ and Re $5p$ states in Re. The total number of holes is equal to that of electrons, which represents that Re is a compensated metal. Since the lowest six bands are fully occupied, as shown in Figure 1, the next five bands are partially occupied, while higher bands are empty. This compound is compensated metal because of having two chemical units in the unit cell. We move to discuss the Fermi surface of Re. five bands cross the $E_{\rm F}$, therefore Re has five Fermi surfaces in Figure 2. The color on the Fermi surface illustrates the distribution of the Fermi velocity components. Fermi surfaces for Re centered at the Γ points, respectively. The 10th band has one Cylindrical column-like electron sheet centered at the Γ point. Red-shift indicate the increase of the admixture of Fermi velocity components. The Fermi surfaces were calculated with FermiSurfer [4].

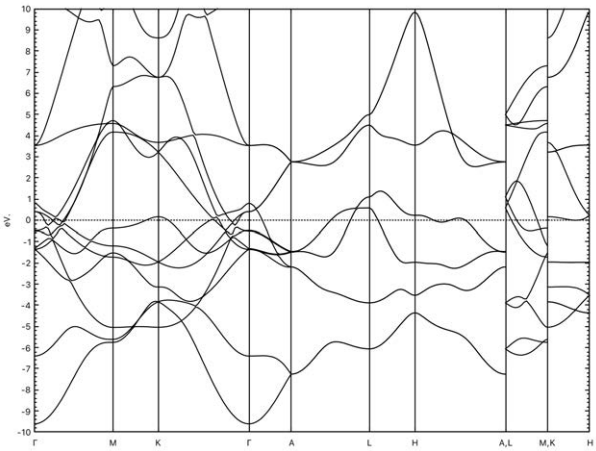


Figure 1: The energy band structure for Re, the symmetry points and axis for the hexagonal structure. $E_{\rm F}$ indicates the position of the Fermi level.

The calculated total density of states (DOS) for Re is shown in Figure 3, in the energy region from -10.0 to 10.0 eV. The total density of states for Re is shown by the solid black line

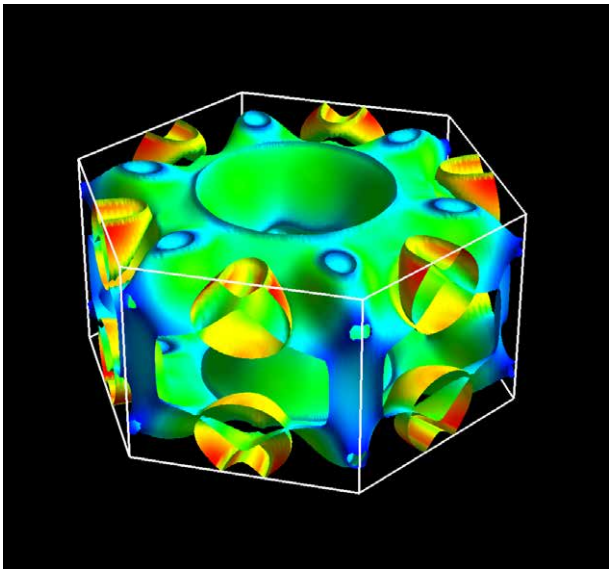


Figure 2: The Fermi surface for Re centered at Γ point. Colors indicate the Fermi velocity components on the Fermi surface.

and the s, p, d and f states are shown by the solid color lines, respectively. This figure tells us that the DOS of the d states is higher than that of the f states at the Fermi level.

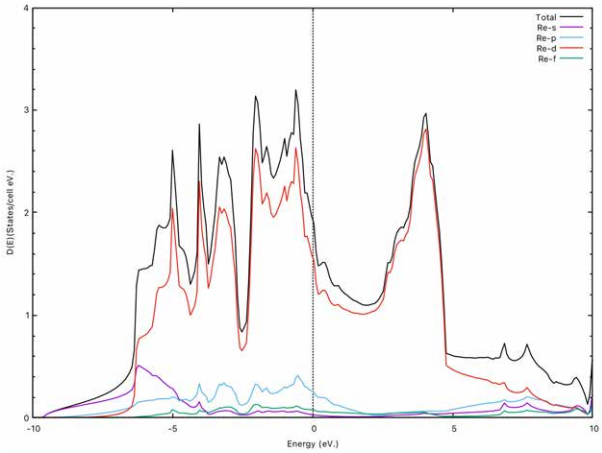


Figure 3: The density of states for Re. E_{F} indicates the position of the Fermi level shown by the dashed line.

References

[1] V. L. Moruzzi, A. R. Williams, and J. F. Janak: Phys. Rev. B 15, 2854 (1977).

[2] C. D. Gelatt, H. Ehrenreich, and R. E. Watson: Phys. Rev. B 15, 1613 (1977).

[3] P. W. Bridgman: Proc. Am. Acad. Arts Sci. 84, 111 (1955).

[4] M. Kawamura: Comp. Phys. Commun 239, 197 (2019).

Analyses of semiconductor surface processes by machine-learning based potentials

Kouji INAGAKI

Graduate School of Engineering, Osaka University

Yamadaoka 2-1, Suita, Osaka 565-087

The mechanochemical processing, a type of ultra-precision surface-flattening and -smoothening technique, utilizes the synergistic effects of mechanical interactions and chemical reactions. The atomic level mechanism, however, remains unclear and its proper understanding is essential for efficient development of the method.

The purpose of this study is to establish and apply a machine learning potential (MLP) based molecular dynamics method to analyze the mechanism. In contrast to previous studies that used MLP trained on structures close to stable (or meta-stable) atomic configurations to explorer new materials with metastable structures, this study aims to realize accurate MLP in the structures near formation and breaking of interatomic bonds to simulate processing phenomena with high accuracy. Nowadays, pretrained potential has widely applied to molecular dynamics. However, because these MLPs incorporate many elements and the total amount of training data is limited, their accuracy is not particularly high, especially for structures in which bond formation occurs. To obtain an accurate MLP, it is necessary to train the model individually by users using a dataset that contains many structures where bond formation occurs, within the range of elements of interest.

Using the diffusion process of hydrogen adsorbed on a Si(001) surface as an example, we implemented an iterative MLP improvement process consisting of training data preparation, MLP generation, MD simulations, and the collection of additional training data. This iterative process enabled the execution of MD simulations. We are currently evaluating the energy barriers associated with the diffusion process. Next, to apply this to mechanochemical processes, we began creating an MLP in Nequip targeting the processes of contact and detachment between two SiO_2 surfaces in water. Furthermore, since SiO_2 in water involves a wide variety of structures, we anticipate that the required training data will be vast; therefore, we have also begun exploring the use of MACE, which can suppress fragmentation even with a small amount of data.

References

[1] K. Inagaki, The 72th JSAP Spring Meeting 2025 14p-K507-9.

Computational study on nanoscale surface/interface structural design based on functional materials

Masaaki MISAWA
Department of Intelligent Mechanical Engineering, Fukuoka Institute of Technology
3-30-1 Wajiro-higashi, Higashi-ku, Fukuoka 811-0295

In this study, we have performed density functional theory (DFT) calculations to investigate structural and electronic properties of (1) in-plane heterostructure of Janus transition metal dichalcogenides (Janus-TMDs), (2) Al (111)/B_4C (001) interfaces, and (3) adsorbed bisphenol-A (BPA) molecule on Al surfaces. All calculations are conducted using the VASP code [1].

Janus-TMDs, which feature different chalcogen atoms on their top and bottom faces, generate an out-of-plane dipole moment due to their structural asymmetry [2]. Based on this property, the new physical phenomena not found in conventional TMDs have been theoretically predicted. This study focuses on the in-plane heterostructure of Janus WSeS/WSeTe, which features a domain wall where the direction of the dipole moment changes. We have performed DFT calculations on the WSeS/WSeTe monolayer and have revealed that it possesses an indirect transition band structure. While the valence states show a mixture of features from both WSeS and WSeTe, the conduction states are primarily derived from WSeTe.

Among lightweight metal-based nanocomposites, Al/B_4C composites have been reported to exhibit excellent mechanical and thermal properties, making them a promising material for advanced structural applications [3]. To clarify the relationship between the Al/B_4C interface structure and its thermal stability, we have performed DFT calculations for the Al (111)/B4C (001) interface with the Al-C stack and the Al-B stack structure, in which C and B atoms are positioned directly below Al atoms, respectively. It is revealed that the Al-B stack model has a greater number of shorter Al-C and Al-B bonds than the Al-B stack model at their interface. On the other hand, the work of adhesion of the Al-C stack model is higher than that of the Al-B stack model, indicating that the Al-C stack model has a more stable Al/B_4C interface.

It has been theoretically and experimentally reported that the adhesion strength of epoxy resins to Al is significantly lower than that to Cu or Fe [4]. To investigate the adsorption properties of epoxy-resin on Al surfaces at atomistic scale, we have performed DFT calculations of the adsorbed BPA molecule, which is a fundamental constituent of epoxy resins, on Al(111), (100), and (110) surfaces. The results showed that a chemical Al-O bond was only formed on the (110) surface, and the vdW interaction plays a dominant role on the other surfaces.

References

[1] G. Kresse and D. Joubert, *Phys. Rev.* **59**, 1758 (1999).
[2] J. Zhang *et al.*, *ACS Nano* **11**, 8192 (2017).
[3] J. Zhou *et al.*, *Nucl. Mater.* **603**, 155465 (2025).
[4] M. Yamazaki *et al.*, *J. Solid Mech. Mater. Eng.* **5**, 54 (2011).

First-principles study of layer-dependent Anomalous Hall Effect in heterostructures

Hana Pratiwi KADARISMAN

Nanomaterials Research Institute (NanoMaRi), Kanazawa University

Kakuma machi, Kanazawa, Ishikawa 920-1192

Anomalous Hall Effect is a Hall effect that occurs in certain magnetic materials where a transverse voltage appears even without an external magnetic field (or with a much smaller role from the external field than in the ordinary Hall effect). The anomalous Hall effect (AHE) arises from two primary mechanisms, namely intrinsic and extrinsic contributions. The intrinsic mechanism originates from the electronic band structure, where spin–orbit coupling (SOC)-induced interband mixing leads to a nonzero Berry curvature.

We performed first-principles calculations of layer-dependent AHE in heterostructures using a local Berry-curvature method on a two-dimensional Brillouin-zone mesh, combined with hybrid Wannier functions localized along a single direction. The electronic structure was investigated through density functional theory (DFT) calculations implemented in the OpenMX code. The results reveal the characteristic features of the anomalous Hall conductivity decomposed by layers, indicating significant contributions from specific layers compared to the other layers [1]. The computational investigation of Fe thin films, Cr thin films, and their combination demands substantial computational resources. For these purposes, we utilized the ISSP Tokyo.

References

[1] H. P. Kadarisman, Y. Morishima, N. Yamaguchi, and F. Ishii: in preparation.

First-principles research on the Catalytic Properties of Quasi-One-Dimensional Boron Chains of CuB/Cu(111)

Takeru Nakashima[1], Yuki Tsujikawa[2], Takahiro Kondo[3], Takanori Koitaya[4], Iwao Matsuda[5], Yasunobu Ando[1]

[1]*Institute of Integrated Research, Institute of Science Tokyo, Yokohama, Kanagawa, 226-8501*

[2]*Department of Chemistry, Keio University, Yokohama, Kanagawa, 223-8522*

[3]*Institute of Pure and Applied Sciences, University of Tsukuba, Tsukuba, Ibaraki, 305-8573*

[4]*Department of Chemistry, Graduate School of Science, Kyoto University, Sakyo-Ku, Kyoto, 606-8502*

[5]*The Institute for Solid State Physics, The University of Tokyo, Kashiwa, Chiba, 277-8581*

We investigated the catalytic properties of the recently reported CuB/Cu(111) surface [1-3], which features unique quasi-one-dimensional boron (B) chains as shown in Fig.1. Using first-principles calculation code based on density functional theory (DFT), we analyzed the adsorption of key intermediates in CO_2 hydrogenation—specifically, hydrogen (H), oxygen (O), and formate (HCOO)—on this surface.

Our calculations revealed that the B chains act as active sites for each step of CO_2 hydrogenation due to significant charge transfer from the Cu atoms to the B atoms. We also identified the stable adsorption configurations of intermediates. Furthermore, we found that H atoms preferentially migrate along these B chains through a three-center two-electron (3c-2e) bonding mechanism at the transition state (see Figs.2 and 3). These findings suggest that the CuB/Cu(111) surface holds great potential as a tunable catalyst for CO_2 conversion.

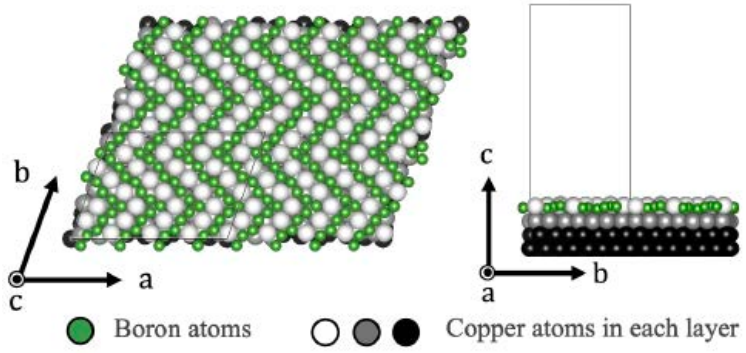


Fig. 1: Slab model of CuB/Cu(111). Spheres, with green and a grayscale gradient from white to black, denote B and Cu atoms, respectively. The reference-slab model has a vacuum layer of 20 Å or more. The system was constructed with monoclinic cell parameters of a=30.0, b=21.8, c=15.9 Å, and α=70.28 degree (a is unique axis). This structure was reported by experimentally by Yue(2021).

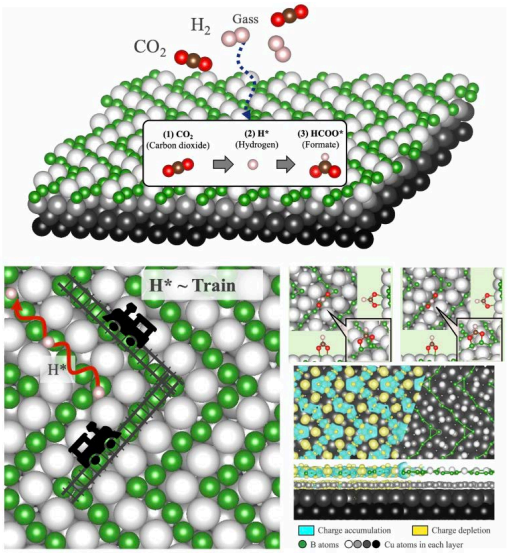


Fig. 2: The concept figure of this research. We focused on the elementary steps relevant to CO_2 hydrogenation—hydrogen, oxygen, and formate adsorption on this surface—by using first-principles calculations (OpenMX), mainly.

The computational resources of the ISSP supercomputer were primarily utilized for large-scale DFT calculations. We employed the OpenMX (Open source package for Materials eXplorer) code (v.3.9) [4], which is based on DFT with norm-conserving pseudopotentials and a local basis of pseudoatomic orbitals (PAOs). The simulations include the structure optimization and charge transfer, and analysis on the nudged elastic band (NEB) calculations from chine-learning potential method (Matlantis)

To manage the high computational cost ociated with these tasks, we utilized the I/OpenMP hybrid parallelization scheme. high-performance computing environment vided by the ISSP enabled us to perform se extensive simulations with high efficiency scalability.

ferences

T. Nakashima, Y. Tsujikawa, T. Kondo *et al.*, J. Phys. Chem. C **130**, 5411 (2026).

[2] Y. Tsujikawa, M. Horio, Z. Zhang *et al.*, Phys. Rev. B **106**, 205406 (2022).

[3] C. Yue, X-J Weng, G. Gao *et al.*, Fundam. Res. **1**, 482 (2021).

[4] T. Ozaki and H. Kino, Phys. Rev. B **72**, 045121 (2005).

[5] S. Takamoto, C. Shinagawa, D. Motoki *et al.*, Nat. Commun. **13**, 2991 (2022).

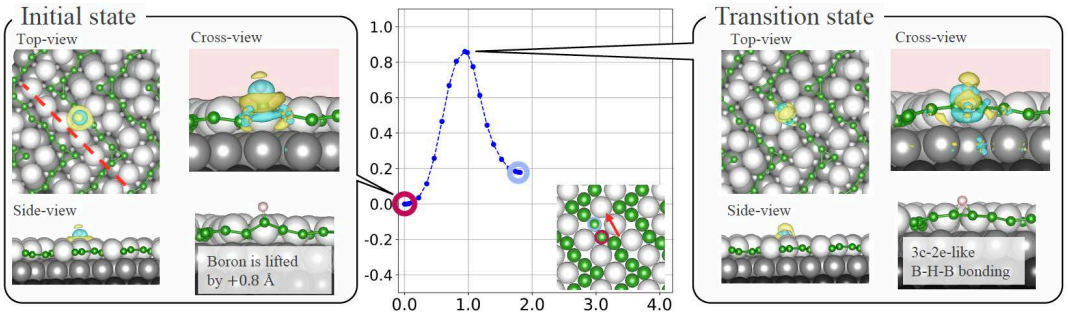


Fig. 3: The charge transfer calculations via OpenMX (transition states are simulated by the Matlantis). We found that H atoms preferentially migrate along these B chains through a three-center two-electron (3c-2e) bonding mechanism at the transition state.

Preliminary Screening of Interfacial Charge Control in Ni/CeO_2 Catalysts for Dry Reforming

Takaya FUJISAKI

Faculty of Materials for Energy, Shimane University,
Matsue, Shimane 690-8504, Japan

Background and objective

Dry reforming of methane (DRM; $CH_4 + CO_2 \rightarrow 2CO + 2H_2$) is an important reaction for the efficient utilization of biogas in solid oxide fuel cells. Biogas typically contains both CH_4 and CO_2, and the direct conversion of these molecules into syngas is therefore attractive for improving the overall efficiency of biomass-derived energy systems. However, DRM proceeds through several elementary reaction steps at the catalyst surface, including CH_4 adsorption and dissociation, CO_2 adsorption and dissociation, oxygen transfer, and the formation and desorption of CO and H_2. The reaction efficiency is strongly affected by the local atomic and electronic structures of the metal–oxide interface. Identifying an appropriate catalyst-design strategy therefore requires an atomistic understanding of how the supported metal cluster, oxide surface, and interfacial charge distribution influence the activation barriers of the elementary reactions.

In our previous DFT and experimental study [1], methane dissociation on $Ni_4/CeO_2(111)$ was investigated using two supported-cluster configurations: a Ni_4-above-Ce configuration and a Ni_4-above-O configuration. Although the exposed Ni atoms directly interacting with methane were similar in the two models, the atomic species located below the supported Ni_4 cluster differed. This difference altered the charge transfer between the CeO_2 support and the Ni cluster. Bader charge analysis showed that the Ni_4 cluster was more positively charged in the Ni_4-above-O configuration (+1.03|e|) than in the Ni_4-above-Ce configuration (+0.78|e|). Correspondingly, the DFT-derived apparent activation barrier for methane dissociation decreased from 0.83 to 0.80 eV. The calculated value was also reasonably consistent with the experimentally estimated activation energy of 0.69 eV obtained using a flower-like Ni-supported CeO_2 catalyst. These results indicated that the reactivity of supported Ni nanoparticles cannot be explained solely by their geometric structures. Instead, the electronic state of the interfacial Ni atoms, which is influenced by the underlying oxide support, is also an important factor in controlling the reaction barrier.

On the basis of this finding, we proposed interfacial charge control as a catalyst-design concept for further improving DRM activity. In particular, substitution of an oxygen atom by a more electronegative fluorine atom near the Ni/CeO_2 interface was examined as a chemically simple approach for modifying the local electronic environment of the supported Ni cluster. During FY2025, we constructed several fluorine-substituted $Ni_4/CeO_2(111)$ interface models and performed structural optimization calculations for the initial and final states of the elementary reactions. We also carried out preliminary screening of CO_2 dissociation pathways because CO_2 activation is another important elementary step in DRM and may become a limiting factor when the methane dissociation barrier is reduced. These calculations were intended to clarify whether fluorine substitution can systematically stabilize favorable reaction states and lower the activation barrier through interfacial electronic modulation. Although a clear low-barrier configuration has not yet been identified, the calculations revealed that the reaction energetics are sensitive to the fluorine-substitution site, the CO_2 adsorption geometry, and the position of the dissociated oxygen atom. The results provide a basis for refining the reaction models and selecting representative pathways for more detailed climbing-image nudged elastic band calculations.

Computational approach

Geometry optimizations and trial climbing-image nudged elastic band (CI-NEB) calculations were conducted with VASP. The computational workflow followed the previous $Ni_4/CeO_2(111)$ model and used PBE-D3 with a GGA+U treatment for Ce 4f states (U = 7 eV). Selected F-substituted interface models were calculated using SCC-ISSP resources, including System B (ohtaka). For each candidate, the initial state (IS) and dissociated final state (FS) were optimized before selected pairs were promoted to more expensive NEB calculations. Because dopant sites, endpoint geometries, and NEB images can be evaluated independently, job-level parallelism was used to screen multiple structures efficiently.

This hierarchical workflow was adopted to avoid spending large computational resources on poorly constructed paths. It is particularly important for supported nanoclusters, where a small change in local geometry can alter the optimized endpoint and the resulting reaction energy.

To examine the effect of fluorine substitution on the local electronic environment of the Ni/CeO_2 interface, an oxygen atom near the supported Ni cluster was replaced by a fluorine atom. Figure 1 shows a representative initial-state structure constructed for the calculation of CH_4 dissociation on the F-substituted $Ni/CeO_2(111)$ interface. A CH_4 molecule was placed near the supported Ni cluster, where the elementary dissociation reaction is expected to occur, and the atomic positions were subsequently optimized by DFT calculations. The fluorine atom was introduced in the vicinity of the Ni cluster to investigate whether local substitution at the oxide surface modifies the interfacial electronic structure and the reaction energetics.

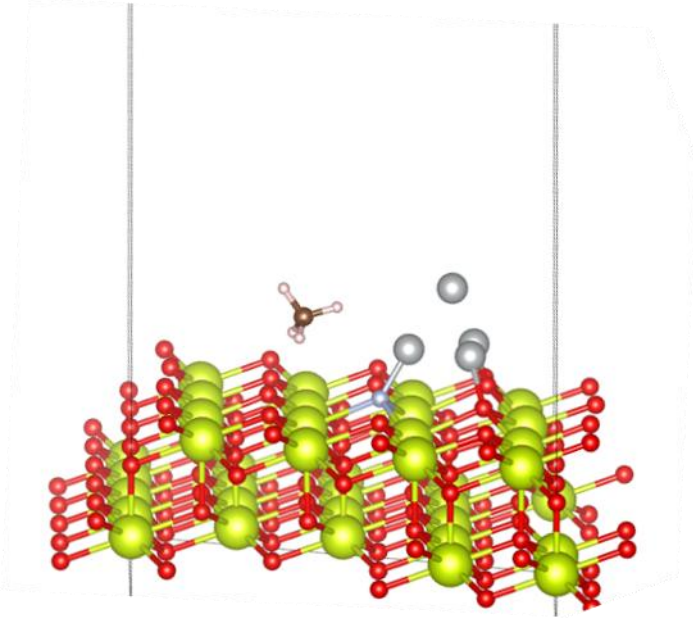


Fig. 1. Representative initial-state structure for CH_4 dissociation on a Ni cluster supported on an F-substituted $CeO_2(111)$ surface. A fluorine atom was introduced near the Ni/CeO_2 interface to modify the local electronic environment of the supported Ni cluster. Gray, pale-colored, red, yellow, brown, and white spheres represent Ni, F, O, Ce, C, and H atoms, respectively.

F-substituted interface models

As a first step, F atoms were placed near the supported Ni_4 cluster and several optimized endpoint structures were compared. The calculated endpoint reaction energies for CH_4 dissociation, ΔEFS-IS, were +0.72, +0.70, +0.21, and -0.19 eV for four representative configurations (Fig. 2). The wide variation demonstrates that the result is sensitive to the dopant position and local geometry. The negative value for Model 4 means that the optimized FS is thermodynamically lower than its IS; however, it does not by itself demonstrate a smaller kinetic barrier.

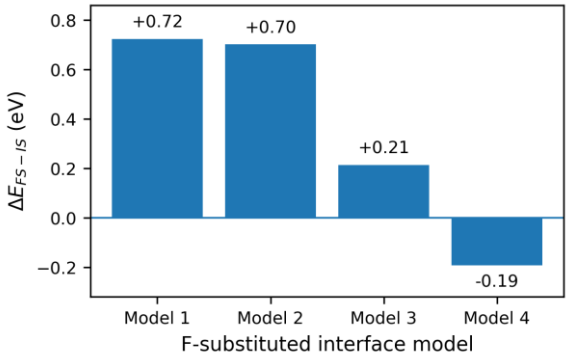


Fig. 2: Endpoint reaction-energy screening for CH_4 dissociation on four F-substituted $Ni_4/CeO_2(111)$ interface models. The values are ΔEFS-IS and should not be interpreted as activation barriers.

Preliminary screening of CO_2 dissociation

Several CO_2 adsorption and dissociation structures were optimized, and a trial NEB pathway was evaluated. A representative profile exhibited a maximum relative energy of approximately 2.60 eV (Fig. 3). This high value is a diagnostic result rather than a final activation barrier: adsorption sites, dissociated-oxygen positions, and IS-FS interpolation require further refinement.

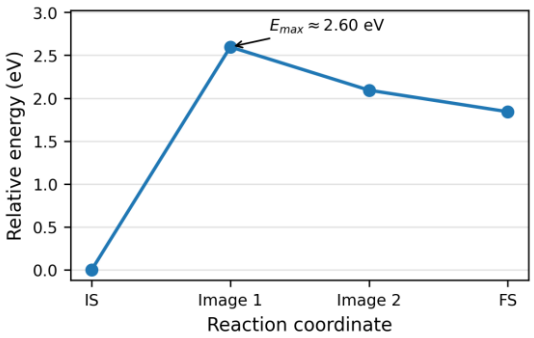


Fig. 3: Representative preliminary CI-NEB profile for CO_2 dissociation on $Ni_4/CeO_2(111)$. The pathway requires further optimization.

Interpretation of the FY2025 calculations

Although a robust low-barrier composition has not yet been identified, the FY2025 calculations yielded a clear intermediate outcome. Simple placement of F close to the Ni cluster does not automatically lower the methane-dissociation barrier. The endpoint results instead show that the interfacial electronic state must be considered together with the detailed local structure. Likewise, the preliminary CO_2 pathway shows that chemically reasonable initial and final structures must be constructed before comparing activation barriers.

Progress relative to the proposed project

The original project aimed to screen $Ce_{1-x}Zr_xO_2$ supports and heteroatom-modified Ni clusters for CO_2 dissociation. The calculations remained at the workflow-establishment stage because both F substitution and CO_2 dissociation exhibited strong configuration sensitivity. This finding changes the order of the screening steps: direct large-scale NEB calculations should be avoided until endpoint structures have been validated. The FY2025 study therefore refined the computational protocol needed for reliable large-scale exploration.

Use of ISSP supercomputer resources

The SCC-ISSP systems were used for multiple VASP geometry optimizations and trial NEB calculations. The resource-intensive component was not a single large job but the parallel evaluation of multiple candidate structures and reaction images. Candidate dopant sites and endpoint pairs were first compared using independent jobs. Only selected pairs were promoted to CI-NEB calculations. This job-level parallel strategy improved throughput and reduced the risk of expending resources on unphysical pathways.

Refined next-stage workflow

The subsequent screening will proceed in four steps (Fig. 4): (i) generate several local configurations for each support and dopant composition, (ii) optimize IS and FS endpoint structures, (iii) retain only physically reasonable endpoint pairs, and (iv) perform CI-NEB calculations followed by Bader-charge and bonding analyses for promising transition states. The refined workflow will be applied to $Ce_{1-x}Zr_xO_2$ supports and heteroatom-modified Ni clusters while retaining multiple local arrangements for each composition.

Summary

During FY2025, SCC-ISSP resources were used to examine interfacial electronic-state control in Ni/CeO_2 catalysts for DRM. Endpoint screening of F-substituted interfaces revealed strong site dependence, and preliminary CO_2-dissociation calculations clarified the need for careful reaction-path optimization. These results provide a practical basis for subsequent systematic exploration of lower-barrier catalyst structures.

References

[1] T. Fujisaki et al., Phys. Chem. Chem. Phys., DOI: 10.1039/d4cp01324g (2024).
[2] H. Jia et al., Curr. Appl. Phys. 43, 9-14 (2022).

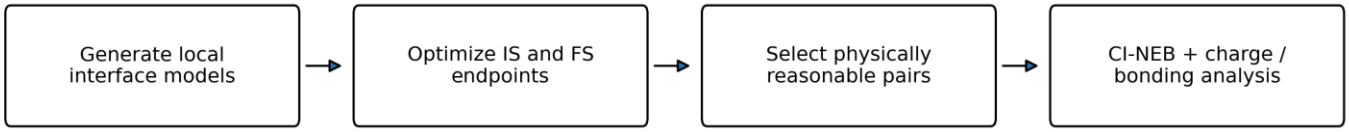


Fig. 4: Refined screening workflow established through the FY2025 SCC-ISSP calculations. Expensive CI-NEB calculations are restricted to physically reasonable endpoint pairs.

3.3 Strongly Correlated Quantum Systems

Development and application of quantum many-body solver

Masatoshi IMADA
Physica Division, Department of Engineering and Applied Sciences, Sophia University, 7-1 Kioi-cho, Chiyoda-ku Tokyo, 102-8554

Accurate description of ground-state wave functions of fermionic many-body systems and applications of the method to strongly correlated electron systems are the target of this project. Neural network combined with the pair-product (Pfaffian) wave function is a promising way for this purpose. Along this line, restricted Boltzmann machine has established an accurate way to approximate ground states of quantum spin systems [1] as well as itinerant fermion systems [2].

The Boltzmann machine introduces hidden variables that are described by classical degrees of freedom. In this project, we are exploring the way mapping of interacting lattice fermions such as the Hubbard model to noninteracting multi-component fermion models in the ground states, from which we have proposed a quantum machine learning algorithm called Fermi machine aiming at an efficient quantum many-body solver [3]. Fermion systems are introduced as the hidden part coupled to the physical system, instead of the classical one such as the Ising spins in the previous Boltzmann machine. This algorithm has been inspired by recent success of fractionalized fermions to describe experimental results of the cuprate superconductors [4–9].

In contrast to the conventional variational Monte Carlo method [10], the present Fermi machine can easily treat the entanglement with the hidden fermion degrees of freedom hybridizing with the physical (visible) fermions, thus allows the formation of the gap structure in the spectra without spontaneous symmetry breaking, generating zeros of the Green's functions as well as poles, which is characteristic of the genuine Mott insulator. Exploration of efficient algorithms for larger systems is under way.

In the application part, the algorithm with neural network combined with the pair-product wave function was recently successfully applied to cuprate superconductors and reproduced the universality and materials dependence [11, 12].

The project was financially supported by MEXT KAKENHI, Transformative Research Area (Grant No. JP22H05111 and No. JP22H05114). and also supported by MEXT under the grant number JPMXP1020230411.

References

[1] G. Carleo and M. Troyer, Science **355**, 602 (2017).

[2] Y. Nomura, *et al.*, Phys. Rev. B **96**, 205152 (2017).

[3] M. Imada. J. Phys. Soc. Jpn. **93**, 104002 (2024).

[4] S. Sakai, M. Civelli, and M. Imada, Phys. Rev. Lett. **116**, 057003 (2016).

[5] Y. Yamaji *et al.*, Phys. Rev. Research **116**, 057003 (2021).

[6] M. Imada: J. Phys. Soc. Jpn. **90**, 111009 (2021).

[7] A. Singh *et al*, Nat. Commun. **13**,7906 (2022).

[8] M. Horio *et al.* PNAS **122**, e2406624122 (2025).

[9] S. Sakai *et al.*, Phys. Rev. X **16** 011018 (2026).

[10] T. Misawa *et al.* Comput. Phys. Commun. **235**, 447 (2019).

[11] M. Schmid *et al.*, Phys. Rev. X **13**, 041036 (2023) .

[12] R. Kaneko snd M. Imada, unpublished.

Exotic superconductivity in the doped Kitaev spin liquid

Takahiro MISAWA
Institute for Solid State Physics, University of Tokyo
Kashiwa-no-ha, Kashiwa, Chiba 277-8581

The Kitaev model on the honeycomb lattice is a rare exactly solvable spin model whose ground state is a quantum spin liquid (QSL) [1]. It has been proposed that Kitaev interactions dominate in Mott insulators with strong spin-orbit coupling, such as α-$RuCl_3$ and iridates [2, 3]. It is expected that carrier doping of such a QSL is a promising route to exotic superconductivity (SC). Mean-field studies of the doped Kitaev model predicted triplet p-wave and singlet $d+id$ pairing [4, 5, 6], but controlled results beyond mean-field theory have been scarce. In this project we studied the hole-doped t-J-type Kitaev model by the many-variable variational Monte Carlo (mVMC) method, focusing on the ferromagnetic (FM) Kitaev interaction.

We consider the Hamiltonian

$$\mathcal{H} = -t \sum_{\langle i,j\rangle,\sigma} \left(c^{\dagger}_{i\sigma} c_{j\sigma} + \text{H.c.} \right) + \sum_{\langle i,j\rangle_{\alpha}} K_{\alpha}\, S^{\alpha}_{i} S^{\alpha}_{j}$$

on the honeycomb lattice, with isotropic coupling $K_x = K_y = K_z \equiv K$ (FM corresponds to $K < 0$, and we set $K/t = -1$) and hole concentration $\delta = 1 - N_e/N_s$. We use a Gutzwiller-projected pair-product (Pfaffian) wave function with a density-density Jastrow factor, optimized by stochastic reconfiguration. Double occupancy is completely excluded by the Gutzwiller projection. In the actual calculations, we use the open-source software mVMC [7]. This wave function exactly reproduces the Kitaev-QSL ground state at half filling, giving a controlled starting point for doping. The calculations were mainly performed on System B ("ohtaka") of the Supercomputer Center, ISSP.

For the FM Kitaev interaction, we find that the triplet p-wave pairing correlations show plateaus at long distances, while singlet correlations remain negligible. The long-range-averaged p-wave correlation forms a dome as a function of hole doping. The correlation peaks around $\delta \simeq 0.2$ and shows essentially no size dependence for $\delta \lesssim 0.2$. This signals robust triplet p-wave superconductivity. For $\delta \gtrsim 0.2$, a saturated ferromagnetic state appears, where the magnetization reaches the fully polarized value $(1-\delta)/2$ and the p-wave correlations are sharply suppressed. This shows that the magnetic background generated by doping controls the pairing.

In summary, using the mVMC method with a pair-product wave function that exactly reproduces the Kitaev QSL at half filling, we have shown that the hole-doped FM Kitaev model hosts robust triplet p-wave superconductivity in a finite doping window, which is suppressed by full ferromagnetic polarization. Investigating the effects of additional interactions, such as Heisenberg and off-diagonal Γ terms, is left for future work.

References

[1] A. Kitaev, Ann. Phys. **321**, 2 (2006).

[2] G. Jackeli and G. Khaliullin, Phys. Rev. Lett. **102**, 017205 (2009).

[3] Y. Motome and J. Nasu, J. Phys. Soc. Jpn. **89**, 012002 (2020).

[4] Y.-Z. You, I. Kimchi, and A. Vishwanath, Phys. Rev. B **86**, 085145 (2012).

[5] T. Hyart, A. R. Wright, G. Khaliullin, and B. Rosenow, Phys. Rev. B **85**, 140510(R) (2012).

[6] S. Okamoto, Phys. Rev. B **87**, 064508 (2013).

[7] T. Misawa *et al.*, Comput. Phys. Commun. **235**, 447 (2019).

Strong-coupling superconductivity in bilayer Hubbard model

Yusuke NOMURA

Institute for Materials Research (IMR), Tohoku University,

2-1-1 Katahira, Aoba-ku, Sendai 980-8577

The quest to understand high-transition temperature (T_c) superconductivity (SC) remains a central issue in condensed matter physics. In this context, the recent discovery of high-T_c SC in $La_3Ni_2O_7$ has generated significant interest [1].

As a canonical model hosting high-T_c SC and as an effective model for $La_3Ni_2O_7$, we investigate the bilayer Hubbard model on a square lattice [2] using state-of-the-art cluster dynamical mean-field theory. Unlike the *d*-wave SC observed in doped Mott insulators such as cuprates, the bilayer model exhibits *s*±-wave SC emerging from a correlated band insulator, where dynamical band repulsion drives the insulating behavior [3]. We uncover kinetic-energy-driven SC in a small doping region and its crossover to conventional potential-energy-driven SC. Above T_c, we observe an unusual metallic state with a striking momentum-space dichotomy in the kinetic-energy-driven regime: one Fermi pocket develops a pseudogap while the other becomes nearly incipient.

Despite differences in pairing symmetry and parent insulating states, we identify the strong momentum-space dichotomy as a remarkable commonality between the *d*-wave SC (antinodal vs. nodal regions) and the *s*±-wave SC (electron vs. hole pockets). The dichotomy in the bilayer system arises from self-energy differences between bonding and antibonding orbitals, further linking it to orbital-selective physics in iron-based superconductors.

Using a novel method for estimating the coherence length in strongly correlated SC [4], we reveal that the coherence length of the *s*±-wave SC is only a few lattice constants, corresponding to ~1 nm in $La_3Ni_2O_7$, which accounts for the exceptionally high critical field (~100 T) observed experimentally. This localized pairing may be driven by an effective pair-hopping term between bonding and antibonding orbitals, analogous to localized Cooper pairing in fullerides, in which the intramolecular pair-hopping term plays a crucial role [5].

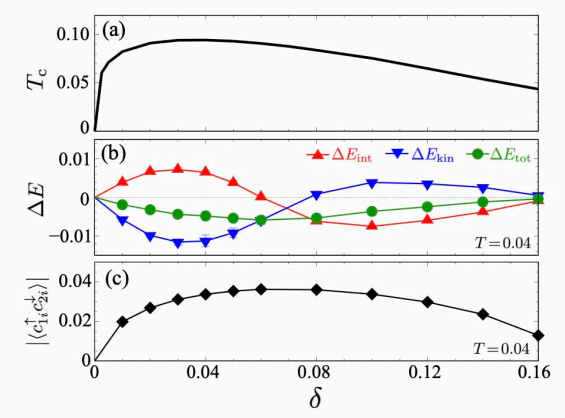


Fig. 1: Doping dependence of (a) T_c, (b) energy difference between SC and normal states at T = 0.04, and (c) the SC order parameter at T=0.04 for the bilayer Hubbard model. The energy unit is set by the intralayer hopping. The interlayer hopping $t_\perp$ and Hubbard U are set to $t_\perp$=2 and U=8, respectively.

References

[1] H. Sun *et al*., Nature **621**, 493 (2023).

[2] Y. Nomura, M. Kitatani, S. Sakai, and R. Arita, Phys. Rev. B **112**, L020504 (2025)

[3] S. S. Kancharla and S. Okamoto, Phys. Rev. B **75**, 193103 (2007).

[4] N. Witt *et al*., npj Quantum Materials **9**, 100 (2024).

[5] Y. Nomura *et al.*, J. Phys.: Condens. Matter **28**, 153001 (2016).

Multilayer effects on the coexistence of antiferromagnetism and superconductivity in cuprate superconductors: a variational Monte Carlo study

Ryui KANEKO
Physics Division, Sophia University
Chiyoda, Tokyo 102-8554, Japan

Clarifying the materials dependence of T_c in cuprate superconductors would provide important clues for the search for materials with even higher T_c. Although the superconducting transition temperature T_c depends strongly on the number of layers, to date, many first-principles studies of cuprate superconductors have focused on compounds with one or two layers. In contrast, the highest T_c among cuprates is found in the trilayer compound $HgBa_2Ca_2Cu_3O_8$ (Hg1223), which exhibits $T_c \sim 138\,\mathrm{K}$ at ambient pressure and even higher $T_c \sim 164\,\mathrm{K}$ under pressure [1, 2].

In this study, we examined the possibility of the coexistence of antiferromagnetism and superconductivity by searching for the ground states of multilayer systems. In multilayer cuprate superconductors, it is often the case that superconductivity is realized in the outermost layers, while superconductivity and antiferromagnetism coexist in the inner layers. We used the three-layer Hg1223 system as a typical example and examined its ground state. We prepared an initial state with the outer layers being superconducting and the inner layers exhibiting the coexistence of superconductivity and antiferromagnetism. We investigated whether such a solution can be stably obtained after optimization over a wide range of doping concentrations.

Effective Hamiltonians for the multilayer system Hg1223, which exhibits the highest T_c among cuprates, were obtained by first-principles calculations at ambient pressure (0 GPa) and under pressure (30 GPa and 60 GPa) [3]. These effective Hamiltonians are given by

$$H = \sum_{i,j,\sigma} t_{ij} c^{\dagger}_{i\sigma} c_{j\sigma} + \sum_{i} U_i n_{i\uparrow} n_{i\downarrow} + \frac{1}{2} \sum_{i \neq j} V_{ij} n_i n_j. \quad (1)$$

Here, for each pressure, the onsite Coulomb repulsion U_i takes layer-dependent values, while the hopping t_{ij} and the further neighbor Coulomb repulsion V_{ij} for intralayers and interlayers are taken up to long-range values satisfying $|\mathbf{r}_i - \mathbf{r}_j| \leq 3\sqrt{2}$. We take the lattice constant as the length unit. For this effective Hamiltonian of Hg1223, we computed the ground state at an average doping concentration of approximately 10% using the many-variable variational Monte Carlo method [4], which enables large-scale parallel computation with MPI and OpenMP. Using a variational wave function constructed from a generalized pairing wave function supplemented by Gutzwiller–Jastrow correlation factors and combined with restricted Boltzmann machine correlation factors, we examined the d-wave superconducting state, as well as that coexisting with antiferromagnetism, as a candidate for the ground state.

By controlling the difference in chemical potential between the outer and inner layers so as to approach the parameter region consis-

tent with experiment, we found a ground-state candidate in which superconductivity is realized in both the outer and inner layers, and another ground-state candidate in which superconductivity is realized in the outer layers, whereas antiferromagnetic and superconducting orders coexist in the inner layer. Since the energies of these two states are highly competing, we further applied the Lanczos procedure and performed variance extrapolation to determine the ground state. As a result, we found a parameter region in which the ground state is a superconducting state in the outer layers and a coexistence of superconductivity and antiferromagnetism in the inner layer. The coexistence of antiferromagnetic and superconducting orders in multilayer cuprates is in agreement with experimental observations [5–7].

These results suggest that the layer-selective coexistence of antiferromagnetic and superconducting orders is not merely a competing instability but can be an essential ingredient of the ground state in multilayer cuprates. Therefore, the present study provides a microscopic perspective on the strong layer dependence of T_c and highlights the importance of interlayer charge imbalance as a key parameter for enhancing superconductivity. Extending this analysis to other multilayer cuprates and systematically examining the pressure- and layer-number-dependent properties will be an important step toward establishing a materials-design principle for realizing even higher T_c.

References

[1] L. Gao, Y. Y. Xue, F. Chen, Q. Xiong, R. L. Meng, D. Ramirez, C. W. Chu, J. H. Eggert and H. K. Mao, Phys. Rev. B **50**, 4260(R) (1994).

[2] A. Yamamoto, N. Takeshita, C. Terakura, and Y. Tokura, Nat. Commun. **6**, 8990 (2015).

[3] J.-B. Morée, Y. Yamaji, and M. Imada, Phys. Rev. Res. **6**, 023163 (2024).

[4] T. Misawa, S. Morita, K. Yoshimi, M. Kawamura, Y. Motoyama, K. Ido, T. Ohgoe, M. Imada, T. Kato, Comp. Phys. Commun., **235**, 447 (2019).

[5] H. Mukuda, S. Shimizu, A. Iyo, and Y. Kitaoka, J. Phys. Soc. Jpn. **81**, 011008 (2012).

[6] K. Kurokawa, S. Isono, Y. Kohama, S. Kunisada, S. Sakai, R. Sekine, M. Okubo, M. D. Watson, T. K. Kim, C. Cacho, S. Shin, T. Tohyama, K. Tokiwa, and T. Kondo, Nat. Commun. **14**, 4064 (2023).

[7] S.-i. Ideta, S. Adachi, T. Noji, S. Yamaguchi, N. Sasaki, S. Ishida, S.-i. Uchida, T. Fujii, T. Watanabe, W. O. Wang, B. Moritz, T. P. Devereaux, M. Arita, C.-Y. Mou, T. Yoshida, K. Tanaka, T.- K. Lee, and A. Fujimori, Nat. Commun. **16**, 9470 (2025).

Topological superconductivity in quantum Hall superconductor hybrids

Koji Kudo

Department of Physics,

Kyushu University, Fukuoka 819-0395, Japan

Creation and manipulation of Abelian and non-Abelian anyons --- emergent particles that are neither bosons nor fermions --- is one of the central goals of modern condensed matter physics. We have studied hybrid systems of quantum Hall states and superconductors as a platform of topological phases hosting anyons.

We discovered a new state, which we call “repulsive-interaction-induced topological superconductivity” [1]. This state emerges in a hybrid system where an interacting electron system at the Landau level filling factor $\nu=1/2$ is proximity-coupled to a type-II *s*-wave superconductor. While the composite Fermi liquid state is realized in the absence of the superconducting proximity effect, we demonstrated that a distinct phase appears upon introducing a finite pairing potential. This state exhibits odd fermion parity, suggesting topological superconductivity. Furthermore, this state disappears as the repulsive interaction is turned off, highlighting its many-body nature. We employed exact diagonalization using the Lanczos algorithm, with a parallel implementation across multiple compute nodes.

As another platform for topological superconductivity, we considered a kagome magnet proximity-coupled to Rashba superconductor. We demonstrated the emergence of scalar-spin-chirality-induced topological superconductivity in this system. We characterized this topological phase by numerically calculating the chiral central charge [2].

We also discussed fractional phases realized in kagome magnets. The exact diagonalization study demonstrated the emergence of the fractional Chern insulating state over a wide region of parameter space [3].

References

[1] K. Kudo, R. Nakai, H. Isobe, J. K. Jain, and K. Nomura, arXiv:2510.04700.

[2] K. Kudo, R. Nakai, H. Isobe, and K. Nomura, arXiv:2602.07383.

[3] S. Tsutsumi, K. Kudo, and. K. Nomura, in preparation.

Theoretical study of strongly correlated quantum properties by mathematical information science

Yukitoshi MOTOME

Department of Applied Physics,

The University of Tokyo, Bunkyo, Tokyo 113-8656

We have conducted theoretical investigations of a wide range of strongly correlated electron systems using advanced numerical approaches, including first-principles calculations, quantum many-body methods, and machine-learning techniques (project numbers: 2025-Ca-0095 and 2025-Cb-0008). We have also established several collaborative efforts with experimental groups. During the last fiscal year, we achieved substantial progress in the following areas.

(i) *Topological spin textures*: By examining the interactions between magnetic hopfions—closed rings formed by twisted skyrmion tubes—we proposed a stable periodic array of magnetic hopfions [1]. Furthermore, we demonstrated that spin–orbit torque induced by a spin current can drive the splitting dynamics of a hopfion with a higher Hopf number into multiple hopfions with lower Hopf numbers [2,3]. In addition, we introduced an efficient method for hopfion creation by applying an electric current to magnetic torons, which consist of a hedgehog–antihedgehog pair connected by a skyrmion tube [4].

(ii) *Spin-orbital coupled physics*: In collaboration with experimental groups, we elucidated that antiferromagnetic olivine compounds exhibit anomalous nonlinear magnetoelectric effects arising from electric-field-induced magnetic toroidal moments [5]. We also worked closely with experimental collaborators to determine the high-magnetic-field phase diagrams of $Pb(TiO)Cu_4(PO_4)_4$, a material characterized by active magnetic quadrupole degrees of freedom [6]. In addition, we conducted collaborative research leading to the discovery of a *p*-wave magnetic material [7] and to the clarification of its exotic physical properties [8].

(iii) *Quantum spin liquids*: We revealed the existence of topological Majorana flat bands in the Kitaev model defined on a periodically depleted honeycomb lattice [9]. We also investigated the competition among different types of quantum-disordered states, including the interplay between quantum spin liquid, spin-glass, and quantum paramagnetic phases in an extended Sachdev–Ye–Kitaev model [10], as well as the competition between the Kitaev spin liquid and the Affleck–Kennedy–Lieb–Tasaki valence-bond-solid state in an S=3/2 spin model on the honeycomb lattice

[11]. In addition, we carried out a series of studies on higher-spin spin-ice models on the pyrochlore lattice [12–14]. We also authored a review paper on α-$RuCl_3$, a prime candidate material for realizing Kitaev spin liquids [15]. Furthermore, we carried out collaborative research on a heterostructure system, which represents a promising platform for realizing a Kitaev spin-liquid state [16].

(iii) *Machine learning related*: In the context of quantum reservoir computing, which employs quantum many-body systems as reservoirs, we demonstrated that computational performance is maximized at the edge of chaos between ordered and chaotic regimes, thereby establishing a fundamental design principle for quantum reservoir computing [17]. We also published two papers proposing a newly developed framework termed *quantum reservoir probing*, which serves as an inverse approach to quantum reservoir computing and enables the extraction of physical information from complex quantum systems [18,19].

References

[1] S. Kasai, K. Shimizu, S. Okumura, Y. Kato, and Y. Motome, Phys. Rev. B **112**, 184424 (2025).

[2] S. Kasai, S. Okumura, and Y. Motome, preprint (arXiv:2511.23027), to appear in APS Open Science.

[3] S. Kasai, S. Okumura, and Y. Motome, preprint (arXiv:2511.23045), to appear in Phys. Rev. B (Editors' Suggestion).

[4] A. Kajihara, S. Okumura, and Y. Motome, preprint (arXiv:2602.05332), to appear in Phys. Rev. B.

[5] Y. Kato, T. Hayashida, K. Matsumoto, T. Kimura, and Y. Motome, Phys. Rev. B. **113**, 094411 (2026).

[6] Y. Ihara *et al.*, Phys. Rev. B **112**, 094405 (2025).

[7] R. Yamada *et al.*, Nature **646**, 837 (2025).

[8] S. Okumura, M. M. Moritz, and Y. Motome, preprint (arXiv:2512.14071).

[9] K. Fukui and Y. Motome, Phys. Rev. B **112**, 14411 (2025).

[10] S. Wadashima and Y. Motome, Phys. Rev. B **112**, 214204 (2025).

[11] S. Ikegami, K. Fukui, R. Pohle, and Y. Motome, preprint (arXiv:2512.06322).

[12] S. Watanabe, Y. Motome, and H. Watanabe, preprint (arXiv:2603.03852).

[13] S. Watanabe, Y. Motome, and H. Watanabe, preprint (arXiv:2603.19620).

[14] S. Watanabe, Y. Motome, and H. Watanabe, preprint (arXiv:2604.04346).

[15] C. Ojeda-Aristizabal *et al.*, preprint (arXiv:2511.13838).

[16] M. Negishi *et al.*, Phys. Rev. Materials **9**, 086202 (2025).

[17] K. Kobayashi and Y. Motome, Phys. Rev. Lett. **136**, 040602 (2026).

[18] K. Kobayashi and Y. Motome, Nat. Commun. **16**, 3871 (2025).

[19] K. Kobayashi and Y. Motome, SciPost Phys. **18**, 198 (2025).

Multipolar fluctuations in $CeRh_2As_2$ studied by DFT+DMFT method

Junya OTSUKI
Research Institute for Interdisciplinary Science, Okayama University, Okayama 700-8530

$CeRh_2As_2$ is a heavy-fermion superconductor that exhibits a nonsuperconducting transition at $T_0 \simeq 0.5$ K above T_{SC} [1]. Its temperature-magnetic field (T–H) phase diagram is strongly anisotropic, with T_0 suppressed for $H \parallel c$ but enhanced for $H \perp c$. The order parameter of this phase has remained controversial between magnetic and quadrupolar scenarios. We apply first-principles approaches taking strong correlations into account to address possible order parameters in $CeRh_2As_2$.

We use density functional theory combined with dynamical mean-field theory (DFT+DMFT), implemented with the open-source software `DCore` [2]. We first derive the low-energy tight-binding model from fully relativistic DFT bands, and then incorporate local Coulomb correlations on Ce $4f$ orbitals within DMFT. We compute the momentum-dependent multipolar susceptibilities using the strong-coupling-limit (SCL) expression for the Bethe-Salpeter equation [3], implemented as `ChiQ` [4]. Both `DCore` and `ChiQ` have been developed with support from the Project for Advancement of Software Usability in Materials Science (PASUMS) [5]. We used the FAT node of System B to handle a sufficiently large system size and obtain reliable $\boldsymbol{q}$ dependence of the susceptibilities.

The calculated momentum-dependent susceptibilities show that the leading fluctuation is the magnetic dipole M_z at $\boldsymbol{q} = (1/2, 1/2, 0)$, corresponding to a two-dimensional checkerboard configuration. The hybridization between the CEF ground-state and first-excited doublets further generates sizable magnetic octupole and electric quadrupole fluctuations. In particular, the fluctuations of $\{Q_{yz}, Q_{zx}\}$-type quadrupoles enhance fluctuations of the magnetic dipole M_z under an in-plane magnetic field, leading to a T–H phase diagram consistent with experiments. We thus proposed an antiferromagnetic M_z order at $\boldsymbol{q} = (1/2, 1/2, 0)$ as the order parameter below T_0 in $CeRh_2As_2$ [6].

References

[1] S. Khim *et al.*, Phys. Rev. Lett. **132**, 076504 (2024).

[2] H. Shinaoka, J. Otsuki, M. Kawamura, N. Takemori, and K. Yoshimi, SciPost Phys. **10**, 117 (2021).

[3] J. Otsuki, K. Yoshimi, H. Shinaoka, and Y. Nomura, Phys. Rev. B **99**, 165134 (2019).

[4] `https://github.com/issp-center-dev/ChiQ`.

[5] K. Yoshimi, Y. Motoyama, T. Aoyama, M. Kawamura, and N. Kawashima, Sci. Technol. Adv. Mater.: Methods **5**, 2564055 (2025).

[6] K. Numa, E. Matsuda, A. Kirikoshi, and J. Otsuki, Phys. Rev. B **113**, 115141 (2026).

Dissipation-induced exotic superfluid phase in non-Hermitian Hubbard model

Akihisa Koga
Department of Physics, Institute of Science Tokyo
Meguro, Tokyo 152-8551

Open quantum systems have attracted significant interest due to their ability to exhibit novel phenomena absent in equilibrium settings. Recent advances in ultracold atom experiments have enabled the realization of dissipative many-body effects. In this context, non-Hermitian (NH) systems provide a useful framework for describing such open-system dynamics. A key feature of dissipation is asymmetric hopping, which leads to the non-Hermitian skin effect—an extreme sensitivity of eigenstates to boundary conditions. This mechanism can strongly modify many-body properties, as demonstrated in interacting systems and dissipation-induced phase transitions.

In non-Hermitian (NH) systems, exceptional points (EPs)—nonequilibrium singularities where eigenvalues and eigenstates coalesce—play a central role and lead to various anomalous phenomena, including enhanced responses and unconventional spectral structures. In many-body settings, EPs are also associated with nonequilibrium phase transitions in systems. However, realizing stable many-body phases hosting EPs remains challenging. In particular, NH fermionic superfluidity (NH-SF) exhibits EP-related reentrant phase transitions, but EPs appear only at phase boundaries where the superfluid becomes unstable [1, 2, 3]. This limitation makes it difficult to experimentally access EPs within the superfluid phase. Establishing mechanisms for stable NH-SF with accessible EPs is therefore crucial for understanding universal physical responses near EPs in NH many-body systems.

In this project, we study the NH attractive Hubbard model and show that spin depairing stabilizes a novel superfluid phase, termed exceptional fermionic superfluidity, characterized by both a finite order parameter and the presence of exceptional points (EPs). Using NH-BCS theory, we reveal that the interplay between EPs and an effective density of states governs its behavior [4, 5]. This phase exhibits distinct stability depending on the lattice geometry and provides a new route to realizing EPs in NH many-body systems.

References

[1] K. Yamamoto, M. Nakagawa, K. Adachi, K. Takasan, M. Ueda, and N. Kawakami, Phys. Rev. Lett. 123, 123601 (2019).

[2] S. Takemori, K. Yamamoto, and A. Koga, Phys. Rev. B 109, L060501 (2024).

[3] S. Takemori, K. Yamamoto, and A. Koga, Phys. Rev. B 110, 184518 (2024).

[4] S. Takemori, K. Yamamoto, and A. Koga, Phys. Rev. Lett. 135, 266002 (2025).

[5] S. Takamori, K. Yamamoto, A. Koga, J. Low Temp. Phys. 222, 37 (2026).

Theoretical study of magnetism in strongly-correlated electron systems: focus on UTe_2

Makoto SHIMIZU
Department of Materials Engineering Science, The University of Osaka
Toyonaka 560-8531, Japan

In strongly correlated systems, the ground state is sensitive to external parameters such as pressure and carrier doping, often leading to multiple competing orders that require a unified treatment of spin, orbital, and sublattice degrees of freedom. To address this problem, we investigate electronic and magnetic structures using density functional theory (DFT) and many-body methods.

Magnetic fluctuations of UTe_2 at ambient and high pressure [1].—UTe_2 is a heavy-fermion paramagnet and a strong candidate for spin-triplet superconductivity. While a close relationship between superconductivity and magnetic fluctuations has been implied, the microscopic mechanism of the magnetic fluctuations has not been clarified. In this study, we construct a 72-orbital model using DFT and investigate magnetic fluctuations at ambient and high pressure applying the random phase approximation (RPA). Large-scale parallel computations using more than one hundred nodes enabled calculations for the huge model. Our results for a 72-orbital effective model constructed from GGA+U (U = 1 eV) show good agreement with experimentally observed magnetic fluctuations and their pressure evolution.

Magnetic fluctuations induced by quantum geometry [2].—Magnetic fluctuations in multiband materials are often discussed in terms of Fermi-surface nesting and orbital (matrix-element) effects. However, their quantitative roles are not always clearly identified. In this study, based on a recently proposed formal decomposition of the static irreducible susceptibility into a dispersion (band) term and a wavefunction-geometry (quantum geometry) term, we implement this framework in first-principles-based tight-binding models. Applying this method to LaFeAsO and $Pb_9Cu(PO_4)_6O$, we analyze the contributions of these terms to magnetic fluctuations. The results indicate that the geometric term significantly affects the leading magnetic correlations: it enhances stripe-type antiferromagnetic correlations in LaFeAsO, while it suppresses antiferromagnetic fluctuations and stabilizes ferromagnetic tendencies in electron-doped $Pb_9Cu(PO_4)_6O$.

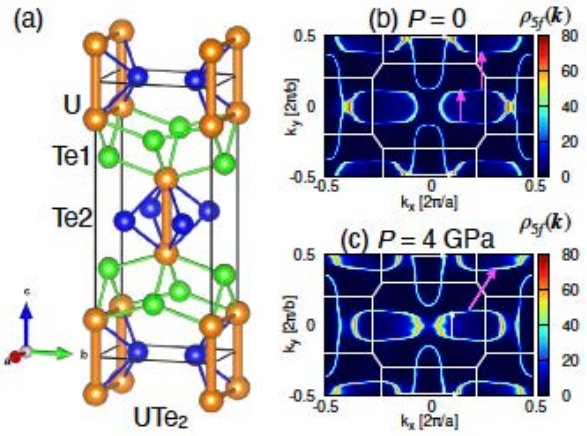


Figure 1: (a) Crystal structure of UTe_2. (b,c) Spectral weights of U-5f states calculated within GGA+U (U = 1 eV). The magenta arrows show effective nestings corresponding to the antiferrmagnetic fluctuations with $\boldsymbol{Q} \parallel \boldsymbol{b}^*$.

Pressure evolution of magnetic structure in nodal-line ferrimagnet $Mn_3Si_2Te_6$ [3].—

$Mn_3Si_2Te_6$ is a layered ferrimagnetic semiconductor with competing exchange interactions and strong magnetic anisotropy. Using DFT combined with Monte Carlo simulations, we investigate how external pressure modifies its electronic structure and magnetic couplings. The results reveal that pressure tunes the balance between ferromagnetic and antiferromagnetic interactions, leading to changes in magnetic order, anisotropy, and structural stability, thereby providing a microscopic understanding of pressure-induced phase transitions. Using ISSP supercomputing resources, we developed and employed Monte Carlo codes.

References

[1] M. Shimizu and Y. Yanase, arXiv:2510.15322 [cond-mat.str-el].
[2] M. Shimizu, C.-g. Oh, and Y. Yanase, arXiv:2602.14511 [cond-mat.str-el].
[3] V. Venkatasubramanian, M. Shimizu, D. Guterding, and H. O. Jeschke, Commun. Mater. **7**, 94 (2026).

Theoretical proposal of superconductivity in a hole-doped reduced bilayer nickelate $La_3Ni_2O_6$: possibility of orbital space bilayer superconductivity

KAZUHIKO KUROKI
Department of Physics, University of University
1-1 Machikaneyama, Toyonaka, Osaka, 560-0043, Japan

The bilayer Hubbard model has been studied as a model where the superconducting T_c can be higher than that of the d-wave superconducting state in the single-orbital Hubbard model [1, 2]. Hence, a realization of the bilayer Hubbard model in actual materials is a promissing path toward finding new high temperature superconductors. Along this path, we previously proposed that a double layer Ruddlesden-Popper compound $La_3Ni_2O_7$ can be a good candidate for realizing the bilayer Hubbard model that satisfies the above-mentioned conditions [3]. Recently, this material $La_3Ni_2O_7$ was found to exhibit high T_c superconductivity with a highest T_c of about 80 K under pressure [4].

On the other hand, our previous studies have shown that the multi-orbital Hubbard model is another example in which superconductivity is enhanced in the presence of an incipient band [5–7]. Although the bilayer Hubbard model involves only a single orbital with intraorbital interactions, the two-orbital Hubbard model comprises two orbitals per site and incorporates interorbital interactions. Despite these differences, in both models, superconductivity is optimized in the incipient-band regime [5]. The two models are mathematically equivalent when $U = U' = J = J'$ as shown in Ref. [8], where onsite interactions U, U', J, and J' are the intraorbital repulsion, interorbital repulsion, Hund's coupling, and pair hopping, respectively, with $2t_\perp$ in the bilayer model corresponding to the orbital level offset ΔE in the two-orbital model (see the middle of Fig. 1). In reality, $U > U' > J \sim J'$ and interorbital hybridization is present; nevertheless, our calculations in the two-orbital Hubbard model for a new type of cuprate $Ba_2CuO_{3+\delta}$ in Ref. [5] indicate that the correspondence between the bilayer and two-orbital models persists to some extent, and that superconductivity is enhanced with increasing ΔE. Furthermore, we have found that the correspondence between the two models persists not only in the two-orbital model but also in the five-orbital model [6, 7]. Our calculations have shown that, even in the five-orbital system, superconductivity is enhanced by increasing the level offset ΔE between one orbital and the remaining four orbitals, and is optimized in the incipient-band regime.

Based on the correspondence between the bilayer and multi-orbital Hubbard models, we refer to the former as the real-space bilayer model (RSBM) and the latter as the orbital-space bilayer model (OSBM). $2t_\perp$ in the RSBM corresponds to ΔE in the OSBM.

Recently, in Ref.[9], we have investigated the possibility of superconductivity based on OSBM in a reduced bilayer nickelate $La_3Ni_2O_6$. We consider two types of structures, T and T', and performed band-structure calculations using three methods: GGA, GGA+U, and QSGW. We have shown that a large orbital level offset ΔE exists between the $d_{x^2-y^2}$ orbital and the other Ni-d orbitals.

By analyzing superconductivity within FLEX calculations, we have found that $s\pm$-wave superconductivity can be enhanced by hole doping due to interorbital interactions in both the T and T' structures. This enhancement originates from the OSBM mechanism, where the Fermi level approaches the lower bands and the incipient-band situation is realized. Furthermore, we demonstrate that superconductivity is not significantly enhanced by the interorbital interaction between the $d_{x^2-y^2}$ and $d_{3z^2-r^2}$ orbitals alone; rather, it is enhanced by the interorbital interactions involving all four orbitals in the lower bands.

We have also shown that the energy difference between the T and T' structures varies under external hydrostatic pressure or internal pressure effects arising from differences in ionic radii, resulting in a shift of the stable structure. In addition, stable phonon dispersions are obtained under pressure in both the T and T' structures as shown in Fig.2. Considering that the insulating behavior at ambient pressure disappears under pressure, we consider the possibility of suppressing the insulating property and realizing OSBM-like superconductivity by applying pressure and hole doping.

[1] K. Kuroki, T. Kimura, and R. Arita, Phys. Rev. B **66**, 184508 (2002).
[2] T. A. Maier and D. J. Scalapino, Phys. Rev. B **84**, 180513(R) (2011).
[3] M. Nakata, D. Ogura, H. Usui, and K. Kuroki, Phys. Rev. B **95**, 214509 (2017).
[4] H. Sun, M. Huo, X. Hu, J. Li, Z. Liu, Y. Han, L. Tang, Z. Mao, P. Yang, B. Wang, J. Cheng, D.-

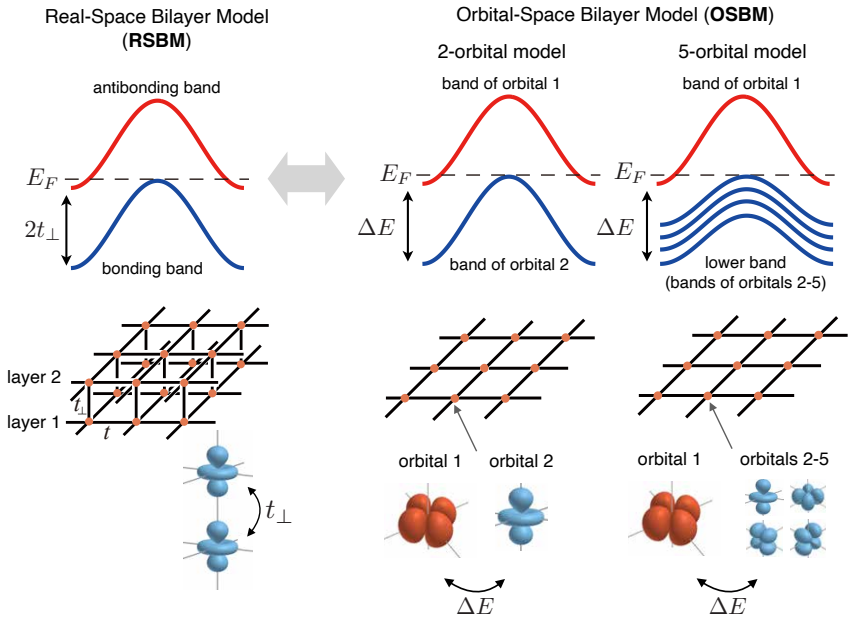


FIG. 1. Schematics of the Real-Space Bilayer Model (RSBM) and the Orbital-Space Bilayer Model (OSBM). The interlayer hopping $t_\perp$ in the RSBM gives rise to bonding and antibonding bands with an energy separation of $2t_\perp$. In the OSBM, orbital-level offsets ΔE between multiple orbitals play an analogous role. In both models, superconductivity is optimized in the incipient-band regime, where one band intersects the Fermi level while the other touches or lies slightly away from it. The correspondence between RSBM and OSBM has been examined also in multi-orbital systems, such as the five-orbital model.

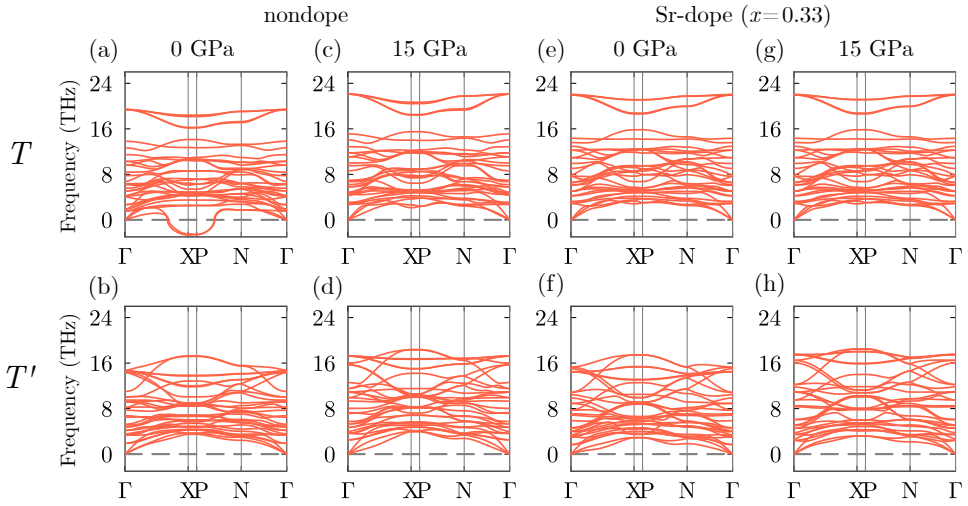


FIG. 2. The phonon dispersions of (a)–(d) non-doped $La_3Ni_2O_6$ and (e)–(h) Sr-doped $(La_{1-x}Sr_x)_3Ni_2O_6$ ($x = 0.33$) for both the T and T' structures under pressures of $P = 0$ and 15 GPa.

X. Yao, G.-M. Zhang, and M. Wang, Nature **621**, 493 (2023).
[5] K. Yamazaki, M. Ochi, D. Ogura, K. Kuroki, H. Eisaki, S. Uchida, and H. Aoki, Phys. Rev. Res. **2**, 033356 (2020).
[6] N. Kitamine, M. Ochi, and K. Kuroki, Phys. Rev. Res. **2**, 042032(R) (2020).
[7] H. Sakakibara, R. Mizuno, M. Ochi, H. Usui, and K. Kuroki, Phys. Rev. B **111**, 224511 (2025).
[8] H. Shinaoka, Y. Nomura, S. Biermann, M. Troyer, and P. Werner, Phys. Rev. B **92**, 195126 (2015).
[9] S. Kamiyama, R. Kohno, Y. Hoshi, K. Ushio, D. Nakaoka, H. Sakakibara, and K. Kuroki, (2026), arXiv:2603.11771.

Control of transverse and longitudinal spin fluctuations in intermediately correlated systems

Hidemaro SUWA
Department of Physics, University of Tokyo, Tokyo 113-0033

Spin fluctuations underpin emergent quantum phenomena from unconventional superconductivity to quantum spin liquids. Their transverse (TSF, orientational) and longitudinal (LSF, amplitude) components are conventionally treated as independent, but whether they are correlated in real materials—particularly in the intermediately correlated regime bridging Slater and Mott limits—had remained an open question. We addressed this both experimentally and theoretically, using bilayer iridate superlattices $[(SrIrO_3)_2/(Sr_{1-x}Ca_xTiO_3)_1]_{20}$ as a tunable $J_{\mathrm{eff}} = 1/2$ platform [1].

The theoretical core is a magnetic phase diagram computed as a function of in-plane and out-of-plane octahedral rotations. Contrary to the long-held view that bilayer iridates host a robust c-axis Ising anisotropy, the calculation shows that a sufficiently strong out-of-plane rotation drives a c- to a-axis antiferromagnetic transition. A symmetry analysis identifies the emergent in-phase rotation about the a-axis as the responsible order parameter: the rotated mirror plane (normal to a) pins the easy axis along a, in close analogy to—yet rotated 45° from—the single-layer iridate case. This furnishes a microscopic, symmetry-based link between octahedral distortion and Néel-vector reorientation. Experimentally, Ca substitution in the spacer continuously tunes the in-phase rotation, realizing the predicted anisotropy competition; TSF is consequently maximized near $x \approx 0.5$.

A second theoretical thread interprets magnetotransport at T_{N} within the intermediately correlated framework, where local moments arise from particle–hole pair formation. LSF then corresponds to thermally excited particle–hole pairs, suppressed by an external field and producing the linear, positive in-plane magnetoresistance (MR) observed in all samples. The strength of this signal tracks the effective correlation, which varies non-monotonically with x and is minimized at $x \approx 0.25$—precisely opposite to TSF. TSF instead drives field-suppressed carrier scattering with a negative, parabolic MR; this hallmark emerges only out-of-plane near $x = 0.25$.

To analyze this material theoretically, we performed large-scale semiclassical calculations of the bilayer iridate system for various octahedral rotation parameters on ISSP System B in the class C project (2025-Ca-0113) using MPI parallelization on up to 10 nodes simultaneously. Our work establishes that TSF and LSF are tied through the effective electronic correlation and modulate in approximately opposite ways across the phase diagram. More broadly, it shows that artificial crystalline engineering can independently target distinct components of the spin-fluctuation spectrum, opening a controllable route to designing complex magnetic states and probing the spin dynamics relevant to unconventional superconductivity.

References

[1] E. Men et al., *Newton* **2**, 100483 (2026).

Photoinduced Nonequilibrium Dynamics in the Charge-Ordered Phase of Doped Mott Insulators

Takami TOHYAMA
Department of Applied Physics, Tokyo University of Science, Katsushika, Tokyo 125-8585

The dynamics of holes doped into a Mott insulator induce both Drude and finite-frequency absorptions within the Mott gap in the optical conductivity. In cuprate superconductors, a broad mid-infrared (mid-IR) absorption around 0.5 eV has been observed. The origin of this mid-IR absorption is generally attributed to a mixture of charge, lattice, and magnetic excitations. Similar broad mid-IR features also appear in two-leg ladder cuprates.

Recent advances in laser technology have enabled ultrashort pump pulses to be tuned to the Drude and mid-IR absorption regions. Indeed, mid-IR pulses have already been applied to cuprate superconductors. In the doped two-leg ladder Mott insulator $Sr_{14-x}Ca_xCu_{24}O_{41}$, which exhibits a tendency toward charge ordering, photo-pumping and pump–probe spectroscopy have been investigated. However, the pump energies used so far lie near the edge of the Mott gap. Thus, it remains an open question how pump pulses tuned directly to the Drude and mid-IR absorptions influence the low-energy charge dynamics in strongly correlated metals with charge order. In particular, theoretical predictions regarding the differences between Drude pumping and mid-IR pumping will be valuable for guiding future experimental studies in these systems.

To address this issue, we investigate the effects of photo-pumping on doped Mott insulators using few-cycle laser pulses with energies corresponding to the Drude and mid-IR absorption regions, and predict how the optical conductivity is modified by the pump [2]. As representative models of strongly correlated metals with a tendency toward charge order (such as charge stripes), we employ a two-leg Hubbard ladder and a four-leg t-J ladder. The optical conductivity after pumping is computed using the time-dependent density matrix renormalization group (tDMRG) implemented with Legendre polynomials [1]. We use two target states at times t and $t+\delta t$ to construct a basis capable of representing wavefunctions in the time-dependent Hilbert space. This two-target tDMRG procedure enables accurate evaluation of time-dependent observables even when the Hamiltonian varies rapidly in time.

We find that a monocycle electric-field pulse tuned to the Drude absorption reduces the Drude weight and slightly enhances the mid-IR spectral weight, although this enhancement diminishes as the pulse intensity increases. In contrast, pumping at the mid-IR absorption leaves the mid-IR weight unchanged and only reduces the Drude weight. This behavior arises because the mid-IR absorption originates from magnetic excitations rather than charge order. These predictions can be tested experimentally by applying ultrashort low-energy pump pulses to cuprate materials.

References

[1] K. Shinjo, S. Sota, and T. Tohyama: Phys. Rev. Res. **4**, L032019 (2022).

[2] S. Chandra, K. Shinjo, S. Sota, S. Yunoki, and T. Tohyama: Phys. Rev. B **113**, 045127 (2026).

First-principles and machine-learning study of pressure-dependent structures and electronic states in organic molecular conductors

Kazuyoshi YOSHIMI
Institute for Solid State Physics, The University of Tokyo
Kashiwa-no-ha, Kashiwa, Chiba 277-8581

Organic molecular conductors are a useful platform for studying pressure-tuned strongly correlated electron systems: charge order, Mott insulating states, Dirac electronic states, and unconventional superconductivity can be controlled by modest changes in lattice geometry. At the same time, their soft van der Waals packing makes first-principles structure prediction demanding, since small errors in the relaxed structure propagate into the bandwidth, Fermi surface, and effective Coulomb interactions. In project 2025-Ca-0011 we used the ISSP supercomputer to address three related topics: (i) the pressure-induced Mott-insulator-to-superconductor crossover in β'-(BEDT-TTF)$_2$ICl$_2$, (ii) the identification of an ambient-pressure organic Dirac electron system, and (iii) a systematic benchmark of dispersion corrections and machine-learning potentials (MLPs) for pressure-dependent molecular crystal structures.

Pressure-induced Fermi-surface change in β'-(BEDT-TTF)$_2$ICl$_2$. β'-(BEDT-TTF)$_2$ICl$_2$ shows the highest reported superconducting transition temperature among molecular organic superconductors, T_c = 14.2 K at 8.2 GPa. To clarify its pressure-induced electronic evolution, we combined synchrotron X-ray crystallography with plane-wave DFT structure relaxation in Quantum ESPRESSO[6] up to 11 GPa, with the systematic parameter sweeps managed by the bulk-job utility Moller[7], as reported in Ref. [1]. Low-energy effective models were then derived by cRPA using RESPACK[3], and their electronic instabilities analysed with the mean-field/RPA solver H-wave[4]. The pressure-induced structural deformation reorganises the Fermi surface in a Lifshitz-type manner, accompanying the crossover from a Mott insulating state to the metallic and superconducting regime[1]. A comparison between dispersion-uncorrected DFT and the experimental structures also revealed a small but systematic change in the BEDT-TTF dimer geometry, which motivated the broader benchmark of dispersion treatments below.

Ambient-pressure Dirac electrons in α-(BETS)$_2$AuCl$_2$. As a chemical-pressure analogue of high-pressure α-(ET)$_2$I$_3$, we identified α-(BETS)$_2$AuCl$_2$ as a quasi-three-dimensional massive Dirac semimetal at ambient pressure[2]. Transport measurements show a large positive in-plane magnetoresistance and an anomalous negative interlayer magnetoresistance. First-principles calculations including spin–orbit coupling, performed on the ISSP system, reproduce the band crossing and residual Fermi pocket and clarify that the Au–Cl anion layer plays an essential role in stabilising the quasi-3D Dirac dispersion. This establishes α-(BETS)$_2$AuCl$_2$ as a clean ambient-pressure platform for spectroscopic and transport studies of organic Dirac fermions.

Benchmarking dispersion corrections and MLPs for pressure-dependent structures. The structural sensitivity found in β'-(BEDT-TTF)$_2$ICl$_2$ prompted a systematic benchmark of structure-relaxation protocols for soft molecular crystals. We compared foundation-model MLPs (ORB, MACE, CHGNet, MatterSim, SevenNet) combined with several dispersion treatments (DFT-D3(BJ) with different damping functions and DFT-D4), against the experimental pressure-dependent crystal structures of three charge-transfer salts: β'-(BEDT-TTF)$_2$ICl$_2$, (TMTTF)$_2$PF$_6$, and (TMTTF)$_2$SbF$_6$, with more than ten pressure points each up to $\sim$ 10 GPa. The equation of state was obtained by fitting the relaxed volumes to a third-order Birch–Murnaghan form. The trends so far indicate that the dispersion-correction protocol, in particular the damping function, affects the predicted equation of state as strongly as, or more strongly than, the MLP architecture, and that the 2D-dimer compound β'-(BEDT-TTF)$_2$ICl$_2$ is systematically softer than experiment for every protocol tested, in contrast to the 1D-stack TMTTF salts. To disentangle MLP-intrinsic errors from those inherited from the underlying DFT functional, reference plane-wave DFT calculations (PBEsol+D3 and PBE without dispersion correction) are now in progress on the ISSP system.

Outlook. Building on our recent ab initio survey of the quasi-one-dimensional (TMTTF)$_2$X family[5], we will convert the relaxed structures into Wannier-based tight-binding models and cRPA effective interactions, and quantify how structural uncertainty from the dispersion treatment propagates into transfer integrals, the Mott U/W ratio, and the resulting phase diagrams of β'-(BEDT-TTF)$_2$ICl$_2$, (TMTTF)$_2$X, and α-(BETS)$_2$AuCl$_2$. The resulting dataset will also serve as a reference for evaluating the next generation of pressure-aware MLPs for soft molecular crystals.

References

[1] T. Kobayashi, K. Yoshimi, H. Ma, S. Sekine, H. Taniguchi, N. Matsunaga, A. Kawamoto, and Y. Uwatoko, Phys. Rev. Materials **9**, L021801 (2025).

[2] T. Kobayashi, K. Yoshimi, A. Nishimoto, S. Michimura, and H. Taniguchi, J. Phys. Soc. Jpn. **95**, 043701 (2026).

[3] K. Nakamura, Y. Yoshimoto, Y. Nomura, T. Tadano, M. Kawamura, T. Kosugi, K. Yoshimi, T. Misawa, and Y. Motoyama, Comput. Phys. Commun. **261**, 107781 (2021).

[4] T. Aoyama, K. Yoshimi, K. Ido, Y. Motoyama, T. Kawamura, T. Misawa, T. Kato, and A. Kobayashi, Comput. Phys. Commun. **298**, 109087 (2024).

[5] K. Yoshimi, T. Misawa, T. Tsumuraya, and H. Seo, Phys. Rev. Lett. **131**, 036401 (2023).

[6] P. Giannozzi, O. Andreussi, T. Brumme *et al.*, J. Phys. Condens. Matter **29**, 465901 (2017).

[7] https://github.com/issp-center-dev/Moller.

Nonequilibrium phenomena in strongly correlated systems

Robert Peters and Tsuneya Yoshida

Kyoto University, Kyoto 606-8501

We have studied nonequilibrium and nonlinear response phenomena in strongly correlated systems using large-scale numerical simulations on the ISSP supercomputer system. In particular, we focused on correlation effects in altermagnetic systems and on the stability of topological phases under generic perturbations.

First, we investigated the nonlinear magnetoelectric effect (NMEE) in a correlated altermagnetic system within a self-consistent dynamical mean-field theory (DMFT) framework. The lattice model was mapped onto an effective quantum impurity problem, which was solved using the numerical renormalization group, allowing us to access real-frequency spectral functions and response functions with high resolution. Based on the interacting Green's functions, we computed the optical conductivity and the frequency-dependent nonlinear magnetoelectric response over a wide range of interaction strengths and temperatures. The calculations reveal that the NMEE is directly controlled by the spin-resolved spectral structure of the correlated system. In particular, the low-frequency response is dominated by electronic states near the Fermi energy, indicating a Fermi-surface origin of the nonlinear response. Furthermore, we find a strong enhancement of the response in the vicinity of an interaction-driven phase transition [see Fig. 1], where coherent quasiparticles and enhanced spin contrast lead to a large nonlinear signal, while thermal fluctuations suppress the response due to increased scattering and reduced spin polarization. These results were obtained through self-consistent DMFT calculations and systematic parameter scans in interaction strength, temperature, and frequency, which required substantial computational resources on the ISSP system. The results are currently under preparation for publication.

In parallel, we performed variational simulations of a quantum spin model using neural-network quantum states (NQS). Specifically, we studied the toric code subject to an isotropic antiferromagnetic Heisenberg perturbation and analyzed the resulting breakdown of topological order. The ground state was obtained using variational Monte Carlo with a symmetry-adapted neural-network ansatz, allowing us to access system sizes beyond exact diagonalization. We identified the quantum phase transition by analyzing the fidelity susceptibility, non-contractible Wilson loop operators, and topological entanglement entropy. In the weak-coupling regime, the numerical results are in excellent agreement with an effective low-energy description derived from a

Schrieffer–Wolff transformation, while at intermediate coupling the topological phase is destroyed and replaced by a magnetically ordered state. These simulations were partially carried out on GPU resources of the ISSP system, enabling efficient optimization of the neural-network wave function.

Overall, the combination of DMFT and neural-network-based approaches provides a complementary framework to investigate correlation-driven phenomena in quantum many-body systems, ranging from nonlinear response in itinerant systems to the stability of topological phases in spin models.

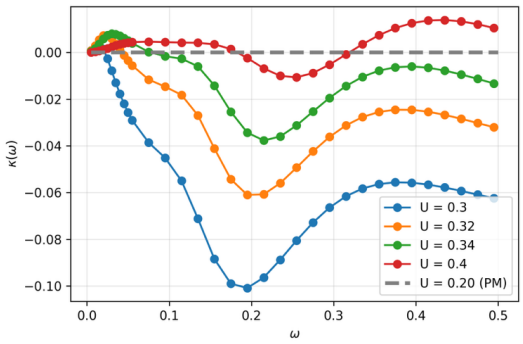


Figure 1: Frequency dependence of the nonlinear magnetoelectric response κ(ω) for different interaction strengths

References

[1] W. Jang, R. Peters, and T. Posske, "*The toric code under antiferromagnetic isotropic Heisenberg interactions*," arXiv:2603.05707.

Numerical calculations of gapped spin orders in low dimensional systems

Yasuhiro Tada

Quantum Matter Program, Graduate School of Advanced Science and Engineering, Hiroshima University, Higashihiroshima, Hiroshima 739-8530

We have studied gapped spin orders in low dimensional quantum systems. The first system is a quantum spin system on a square lattice [1]. In this system, there are two kinds of interactions, the conventional XY interaction and the chirality interaction. We use infinite density matrix renormalization group and consider infinite cylinder geometry. In this setup, the ground state is a gapless Tomonaga-Luttinger liquid for a range of the chiral interaction, while it is a gapped chiral spin liquid when the chiral interaction is large. We demonstrate that both of the gaplessness and the gappedness can be well detected by the polarization amplitude $|z^2|$. Indeed, we find that $|z^2| \sim L^{-\alpha} \to 0$ in the gapless phase in the thermodynamic limit, where α is an exponent which depends on the model parameter. On the other hand, $|z^2| \sim e^{-c/L}$ in the gapped state, where c is a positive constant. This is the first numerical demonstration that the polarization amplitude works for the two dimensional gapped order realized in quasi-one dimensional geometry.

The second system is the S=3/2 Kondo-Heisenberg chain [2]. At half-filling, the system is a Kondo insulator where there exist unscreened spins realizing the topological Haldane state. It was previously argued that, away from half-filling, there is a spin gapped system where the pair-density-wave correlation is enhanced. We show that the pair-density-wave order is indeed the dominant order among several candidate orders. Interestingly, the pair-density-wave correlation shows anomalous behaviors around the edges of the system in sharp contrast to the standard S=1/2 system. Therefore, the charge sector may be regarded as a topological state in this specific sense. On the other hand, the spin correlation exhibits no signature of an edge mode, which implies that the spin sector is not a topological state.

References

[1] T. Yokoyama and Y. Tada, arXiv: 2602.12990.

[2] H. Hirose, S. C. Furuya, and Y. Tada, in preparation.

Microscopic Simulations of Electron-Phonon Dynamics in Mott Insulators

Rico Pohle

Faculty of Science, Shizuoka University, Shizuoka 422-8529

We have developed a computational framework for simulating the nonequilibrium dynamics of strongly correlated Mott insulators, overcoming key limitations of conventional approaches in treating many-body interactions and energy dissipation on equal footing [1].

The method combines concepts from quantum field theory with condensed matter to provide a microscopic description of local electronic degrees of freedom and their coupling to lattice vibrations (phonons) and an external thermal bath.

It enables simulations of energy flow from correlated electrons to phonons and ultimately to the environment, thereby capturing dissipation and relaxation processes within a microscopic framework, in contrast to approaches such as Landau–Lifshitz–Gilbert (LLG) dynamics, where dissipation is introduced phenomenologically.

Numerically, the approach requires solving large sets of coupled stochastic differential equations for electronic and phononic degrees of freedom across extended lattices and long time scales. These simulations are computationally demanding and were carried out using high-performance computing resources.

As a proof of concept, we performed large-scale simulations of a two-orbital spin chain, demonstrating nontrivial hybridization between spin and phonon excitations in the dynamical spectra. The results highlight how electron–phonon coupling qualitatively modifies collective modes and energy transport in strongly correlated systems.

References

[1] R. Pohle, Y. Motome, T. Tadano, and S. Hoshino, preprint (arXiv:2507.19764).

Vison control driven by lattice deformation in Kitaev quantum spin liquids

Joji NASU
Department of Physics, Tohoku University
Sendai 980-8578

Quantum spin liquids (QSLs) host emergent fractionalized excitations and gauge degrees of freedom, providing a unique platform for studying nontrivial quantum phenomena. The Kitaev model is a paradigmatic example of such a system, in which spins are fractionalized into itinerant Majorana fermions and localized Z_2 gauge fluxes (visons) [1]. Although the model is exactly solvable and exhibits rich physics, its highly symmetric structure imposes a fundamental limitation: in the isotropic Kitaev limit, the system lacks an intrinsic directional bias and therefore does not allow controlled manipulation of vison positions along a specific spatial direction.

To establish a mechanism for directional control of visons within the framework of the Kitaev model, we investigate the effects of interaction anisotropy and triaxial lattice strain. In the present study, we calculate the time evolution of the Kitaev QSL in the presence of an excited vison using time-dependent mean-field theory [2, 3]. In the calculations, we use a parallel computing via the intel Math Kernel Library to handle the large system sizes required for accurate simulations of vison dynamics.

To elucidate the role of interaction anisotropy, we first perform a quantitative analysis of vison dynamics under a locally applied magnetic field. Our results demonstrate that increasing the interaction strength along the bond direction corresponding to the desired control direction significantly enhances vison mobility. In particular, a relatively weak magnetic field becomes sufficient to induce the motion of an excited vison when the interaction anisotropy is sufficiently strong. This clearly indicates that vison displacement is strongly governed by the magnitude of the bond-dependent interaction along the direction of motion.

Next, we investigate whether directional control can be achieved solely through lattice deformation, without relying on spatially inhomogeneous magnetic fields. Using triaxial strain introduced in the theoretical model, we perform numerical simulations in which the strain magnitude and orientation are systematically varied. We find that when strain is applied in a direction that breaks translational symmetry along the intended propagation direction, the vison exhibits finite displacement even under a spatially uniform magnetic field. This demonstrates that symmetry breaking induced by strain plays a crucial role in enabling controlled vison dynamics.

References

[1] A. Kitaev, , Ann. Phys. (NY) **303**, 2 (2003).

[2] C. Harada, A. Ono, and J. Nasu, Phys. Rev. B **108**, L241118 (2023).

[3] C. Harada, A. Ono, and J. Nasu, Phys. Rev. B **110**, 214426 (2024).

Computational study on two-particle responses in correlated altermagnets using DFT+DMFT method

Atsushi Hariki

Department of Physics and Electronics,

Osaka Metropolitan University, 1-1 Gakuen-cho, Naka-ku, Sakai, Osaka 599-8531, Japan

We carried out a computational study of resonant inelastic x-ray scattering (RIXS) in candidate altermagnetic materials using DFT+DMFT (density functional theory plus dynamical mean-field theory). Altermagnets have recently revitalized interest in collinear antiferromagnets owing to their unique electronic structure, which breaks time-reversal symmetry despite exhibiting compensated magnetic moments. However, experimentally established altermagnetic materials remain limited, and new experimental techniques capable of detecting the associated symmetry breaking are desirable.

In this project, we explore RIXS as a probe to characterize altermagnetism and to gain insight into two-particle excitations as well as domain structures. At the transition-metal *L*-edge, RIXS involves the resonant excitation of a 2*p* core electron into 3*d* valence states, followed by de-excitation, and is described as a coherent second-order process within the Kramers–Heisenberg formalism. We simulated candidate materials (MnTe and $Fe_2Mo_3O_8$) using our in-house DFT+DMFT and atomic multiplet codes [1]. This is supported by large-scale parallel computations at ISSP, enabling a systematic scan of the incident x-ray energy, which serves as a tuning parameter in the RIXS experiments.

For MnTe, we have shown that altermagnetic domains can be probed by analyzing circular dichroism (CD) in RIXS [2], as demonstrated by direct comparison between recent experimental data and our DFT+DMFT calculations. $Fe_2Mo_3O_8$ is unique among candidate materials in that it hosts two fundamental altermagnetic units, namely octahedral and tetrahedral Fe sites, within its crystal structure. To resolve the altermagnetic symmetry breaking on each unit, our numerical calculations predict distinct CD features at specific energy ranges in the RIXS spectra that can be uniquely attributed to each site. The simulated results are consistent with recent experimental observations for this compound [3].

References

[1] A. Hariki *et al*., Phys. Rev. B **101**, 115130 (2020).

[2] D. Takegami *et al*., Phys. Rev. Lett. **135**, 196502 (2025).

[3] G. Channagowdra *et al*., arXiv: 2512.00737

Computational Study of Magnetic Circular Dichroism in Resonant Inelastic X-ray Scattering Spectra of Strongly Correlated Materials

Atsushi Hariki

Department of Physics and Electronics,

Osaka Metropolitan University, 1-1 Gakuen-cho, Naka-ku, Sakai, Osaka 599-8531, Japan

Altermagnets have recently emerged as a new class of collinear magnets that host time-reversal-symmetry–broken electronic structures while retaining compensated magnetic moments, similar to conventional antiferromagnets in the non-relativistic limit. However, experimentally well-established altermagnetic materials remain limited, mainly because the available probes to identify the symmetry breaking associated with altermagnetism are still scarce.

We conducted computational simulations of circular dichroism (CD) in resonant inelastic X-ray scattering (RIXS) for several candidate altermagnets (MnTe, CrSb, and NiF_2) using our in-house DFT+DMFT (density functional theory plus dynamical mean-field theory) and atomic multiplet codes, together with large-scale parallel computing resources provided by ISSP. RIXS is a complex, coherent second-order optical process, involving core-electron excitation into the valence *d* shell followed by de-excitation, and is described by the Kramers–Heisenberg formalism. We utilized the ISSP facility to efficiently map out the incoming X-ray energies, which serve as a tunable parameter and can be naturally parallelized [1].

We have confirmed strong CD signals in several candidate altermagnets. Notably, these signals appear even in cases where X-ray magnetic circular dichroism (XMCD) is forbidden by symmetry, indicating that RIXS-CD can be used more broadly to probe altermagnetism. Furthermore, we have established selection rules for RIXS-CD, supported by these numerical calculations [2].

In addition, we investigated the electronic structures of UTe_2 [3] using the DFT+DMFT method.

References

[1] A. Hariki *et al*., Phys. Rev. B **101**, 115130 (2020).

[2] M. Furo *et al*., Phys. Rev. B **112**, 214429 (2025).

[3] M. Sundermann *et al*., Phys. Rev. Research **7**, 043195 (2025).

Quantum many-body wave function in strongly correlated electrons

Takashi YANAGISAWA
National Institute of Advanced Industrial Science and Technology (AIST)
1-1-1 Umezono, Tsukuba, Ibaraki 305-8568, Japan

1 On numerical calcualtions

The formulation of many-body wave functions is significantly important in the study of strongly correlated electron systems. In our numerical approach, we proposed an optimized many-body wave function to take account of strong correlation between electrons. The expectation values are evaluated by using the Metropolis Monte Carlo procedure. We carried out parallel computations in Monte Carlo calculations. In order to reduce statistical errors, we performed ~ 500 parallel calculations since parallel computing is very essential to reduce Monte Carlo statistical errors. The parallelization rate of our programs is over 99%.

2 Introduction

The many-body wave function can be written as

$$\psi = e^{-\Delta\tau K} e^{-\Delta\tau V} \cdots e^{-\Delta\tau K} e^{-\Delta\tau V} \psi_0, \quad (1)$$

where K and V are kinetic and interaction part of the Hamiltonian, respectively, and ψ_0 is an initial one-body wave function. We generalize this wave function in the form

$$\psi_M = e^{-\lambda_M K} e^{-\alpha_M V} \cdots e^{-\lambda_1 K} e^{-\alpha_1 V} \psi_0, \quad (2)$$

where λ_j and α_j $(j = 1, \cdots, M)$ are parameters. ψ_M will approach the ground state when M is large enough.

We consider the two-dimensional Hubbard model with the on-site repulsive interaction $V = U \sum_i n_{i\uparrow} n_{i\downarrow}$. $P_G(\alpha) \equiv e^{-\alpha V}$ is identified as the Gutzwiller operator that controls the double occupancy with the variational parameter $g = e^{-\alpha U}$[1]. Let us examine the following wave functions. $\psi^{(1)} \equiv \psi_G = P_G \psi_0$ is the well known Gutzwiller wave function. $\psi^{(2)} \equiv \exp(-\lambda_1 K) P_G \psi_0$ is for $M = 1$, where ψ_0 indicates an initial wave function which is usually taken as the Fermi sea, the BCS wave function or the state with some magnetic (or charge) orders.

We can also consider $\psi^{(3)} \equiv P_G(g_2)\psi^{(2)}$ and $\psi^{(4)} \equiv \exp(-\lambda_2 K) P_G(g_2) \psi^{(2)}$ for different variational parameters λ_2 and g_2. The wave function $\psi^{(4)}$ is a very good many-body wave function because the ground-state energy is lowered greatly and the ground-state energy is lower than those that are evaluated by using any other wave functions. We can further proceed to employ $\psi^{(\ell)}$ with larger ℓ.

3 Pair correlation function and the Gutzwiller effect

We have carried out variational Monte Carlo simulations to examine the ground state of the two-dimensional Hubbard model on a square lattice. We here examine the effect of strong correlation on superconductivity. The BCS wave function $\psi_{BCS}(\Delta_s)$ with the gap function Δ_s clearly shows the long-range correlation. In Fig. 1, we show the d-wave superconducting (SC) correlation function $D_{sc}(\ell) = \langle \Delta^\dagger(i) \Delta(i+\ell) \rangle$ as a function of lattice sites for $N_e = 128$, $U = 18t$ and $t' = 0$ on a 12×12 lattice[6]. Here the pair annihilation operator $\Delta(i)$ at the site i is given by

$$\Delta(i) = \Delta_x(i) + \Delta_{-x}(i) - (\Delta_y(i) + \Delta_{-y}(i)), \quad (3)$$

where $\Delta_{\hat{\alpha}} = c_{i\downarrow} c_{i+\hat{\alpha}\uparrow} - c_{i\uparrow} c_{i+\hat{\alpha}\downarrow}$ for $\alpha = x$ and y. $\hat{\alpha}$ indicates the unit vector in the α-th direction. The pair correlation function $D_{sc}(\ell)$

shows that the long-range order of superconductivity indeed exists in the ground state.

The correlation function $D_{sc}(\ell)$ is, however, reduced by the Gutzwiller operator as shown in Fig. 1 where the Gutzwiller projection operator suppresses the pair correlation considerably. In Fig. 2 we show the expectation value of the superconducting order parameter as a function of the Gutzwiller parameter $1-g$. The strong electron correlation induces the anisotropic pairing and at the same time the pair correlation function is suppressed by the *Gutzwiller effect* caused by P_G. In particular, when g is small, the *Gutzwiller effect* makes the pair correlation function very small. Thus the effect of the Gutzwiller operator might be described as a double-edged sword for superconductivity.

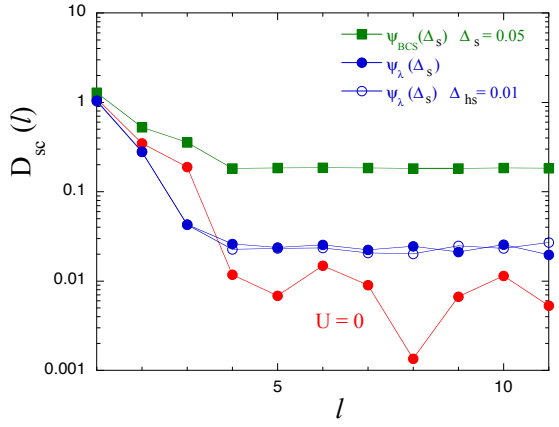


Figure 1: The pair correlation function $D_{sc}(\ell)$ as a function of the lattice site ℓ on a 12×12 lattice with $U = 18t$, $t' = 0$ and $N_e = 128$ for $\psi_\lambda = \psi^{(2)}$. The lattice sites ℓ are ℓ=(1,1), (1,2), (1,3), (1,4), (1,5), (1,6), (2,6), (3,6), (4,6), (5,6) and (6,6) and the site i is chosen as $i = (1,1)$. We show $D_{sc}(\ell)$ for ψ_λ with the SC order parameter $\Delta_s = 0.05$. The figure also includes $D_{sc}(\ell)$ for $U = 0$ (red circles) and that for the non-interacting BCS wave function with $\Delta_s = 0.05$. We also show the result for ψ_λ with an additional variational parameters Δ_{hs} which is the gap parameter introduced in the kinetic term K.

As a summary, we examined the ground state of the two-dimensional Hubbard model by using the optimized many-body wave function ψ_M. We will proceed further for larger M values.

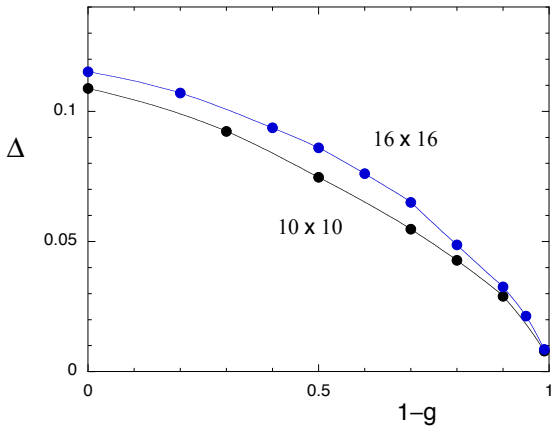


Figure 2: The expectation value of SC order parameter $\Delta \equiv \Delta_s$ as a function of the Gutzwiller parameter $1-g$ for the BCS-Gutzwiller wave function $P_G\psi_{BCS}$ on 10×10 and 16×16 lattices, with $U = 18t$, $t' = 0$ and $N_e = 128$. We set $N_e = 88$ on 10×10 and $N_e = 128$ on 16×16 lattice.

References

[1] T. Yanagisawa et al., J. Phys. Soc. Jpn. 67, 3867 (1998).
T. Yanagisawa, Phys. Rev. B75, 224503 (2007) (arXiv: 0707.1929).

[2] T. Yanagisawa, J. Phys. Soc. Jpn. 85, 114707 (2016).
T. Yanagisawa, J. Phys. Soc. Jpn. 88, 054702 (2019).
T. Yanagisawa, Condensed Matter 4, 57 (2019).

[3] T. Yanagisawa, Phys. Lett. A403, 127382 (2021).
T. Yanagisawa et al., EPL 134, 27004 (2021).

[4] M. Miyazaki, T. Yanagisawa, Phys. Lett. A448, 128276 (2022).

[5] T. Yanagisawa, High Temperature Materials 1, 10004 (2024).

[6] T. Yanagisawa, J. Phys. Soc. Jpn. 94, 074708 (2025).

Computing nonlinear response functions via time evolution

Atsushi Ono
Department of Physics, Graduate School of Science, Tohoku University
Sendai 980-8578

In recent years, there has been growing interest in nonlinear responses in condensed matter systems, and calculating nonlinear response functions is essential for understanding them. Although real-time evolution calculations incorporate response contributions of all orders, a general theory for reconstructing response functions of a specific order from such calculations had not been established.

In Ref. [1], we proposed a general framework for computing nonlinear response functions through real-time simulations. In general, the nth-order frequency response function of a physical quantity Q to an external field f is defined by the functional derivative

$$\bar{\chi}^{(n)}(\omega_1,\ldots,\omega_n) = \frac{(2\pi)^{n-1}}{f(\omega_n)} \frac{\delta^{n-1}\langle Q\rangle^{(n)}(\omega)}{\delta f(\omega_{n-1})\cdots\delta f(\omega_1)}, \quad (1)$$

where $\omega_n = \omega - \sum_{i=1}^{n-1}\omega_i$. In this theory, this functional derivative is numerically evaluated from time-evolution calculations performed under multiple external fields whose phases and amplitudes are appropriately controlled. This framework is, in principle, applicable to a wide variety of methods capable of simulating the real-time dynamics of quantum or classical systems.

As a proof of concept, we calculated the second- and third-order optical response functions in the Rice–Mele model (Fig. 1). The results obtained using this theory, shown by the red solid lines, were confirmed to accurately reproduce those obtained by conventional perturbation theory. We also analyzed a strongly correlated model obtained by adding an on-site Hubbard interaction to the Rice–Mele model using infinite time-evolving block decimation, and identified many-body effects in the second-order response function, including a sign reversal of the optical rectification (photovoltaic) response with increasing interaction strength. This also demonstrates that the present framework is practically applicable to advanced methods such as tensor networks.

In a separate study, we revisited terahertz-field-induced second-harmonic generation (TFISH) in ferroelectrics [2]. By deriving time-domain expressions for the polarization modulation ΔP and the second-harmonic intensity modulation ΔI_{SH} induced by a low-frequency pulsed electric field, we clarified how these quantities are governed by nonlinear dynamical susceptibilities. In particular, we showed that ΔI_{SH} is not necessarily proportional to ΔP, indicating that the commonly assumed relation $\Delta P \propto \Delta I_{\mathrm{SH}}$ should be used with care when interpreting TFISH measurements.

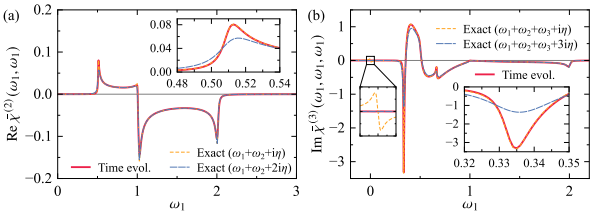


Figure 1: (a) Second- and (b) third-order optical response functions in the Rice–Mele model [1].

References

[1] A. Ono: Phys. Rev. Lett. **135**, 026401 (2025).

[2] A. Ono: Phys. Rev. B **112**, 115146 (2025).

Study on the Novel Mechanism of Superconductivity in Nickel Oxides

Hiroshi WATANABE
Department of Liberal Arts and Basic Sciences, College of Industrial Technology, Nihon University
2-11-1 Shin-ei, Narashino, Chiba 275-8576

The recent discovery of superconductivity in bilayer nickelates [1] has stimulated intensive theoretical efforts to clarify its microscopic pairing mechanism. Although many previous studies have proposed an $s_{\pm}$-type superconducting state, the physical interpretations have often appeared different, because they emphasized different orbitals, bands, or pairing channels. In this project, we addressed this issue by performing large-scale variational Monte Carlo (VMC) calculations for a realistic bilayer nickelate model and clarified the internal structure of the superconducting state [2].

The main purpose of the present study was to determine which superconducting component is primary and which components are induced secondarily by orbital and interlayer hybridization. This distinction is crucial in multiorbital systems, where the optimized gap function may contain several finite components even when only one of them is responsible for the leading pairing instability. We optimized correlated many-body wave functions including superconducting variational parameters and evaluated both the gap structure and equal-time pairing correlations within the same VMC framework.

Our calculations revealed a clear hierarchical structure of superconducting correlations. The primary gap function originates from the bonding–antibonding splitting of the Ni $3d_{z^2}$ orbitals ($\Delta_{zz} \gg \Delta_{xx}$ in Fig. 1), while orbital hybridization redistributes superconducting correlations to the $d_{x^2-y^2}$ channel despite its weak intrinsic pairing interaction. This distinction between the origin of pairing and resulting superconducting correlations explains why the two orbital channels exhibit comparable long-range correlations ($P_{zz} \lesssim P_{xx}$ in Fig. 2). Apparent differences among earlier scenarios can be understood as arising from different representations or projections of the same underlying hierarchical pairing structure.

From the computational point of view, the study required extensive stochastic optimization of many variational parameters and repeated evaluation of correlation functions for large lattice systems, $N = 2\times2\times20\times20 = 1600$ lattice sites in total here. High-performance computing resources were essential for achieving stable convergence, improving statistical accuracy, and systematically exploring the relevant parameter region. The present work demonstrates that large-scale VMC is a powerful method for investigating unconventional superconductivity in strongly correlated multiorbital materials.

In summary, this project established a unified picture of superconductivity in bilayer nickelates by identifying the hierarchical relation between primary and hybridization-induced superconducting correlations. The results resolve an apparent discrepancy among previous theoretical proposals and provide a useful framework for understanding multicomponent superconductivity in correlated layered materials.

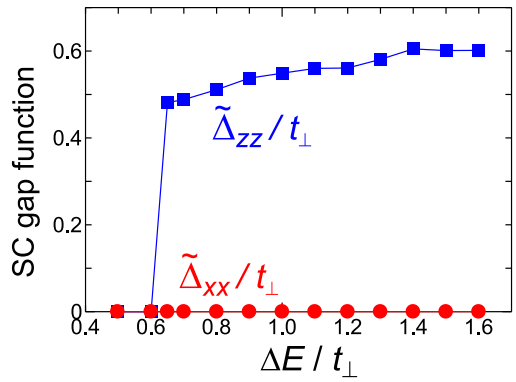


Figure 1: $\Delta E/t_\perp$ dependence of the variational superconducting gap function [2]. ΔE is a level splitting between $d_{x^2-y^2}$ and d_{z^2} orbitals and $t_\perp$ is an interlayer hopping of the d_{z^2} orbital.

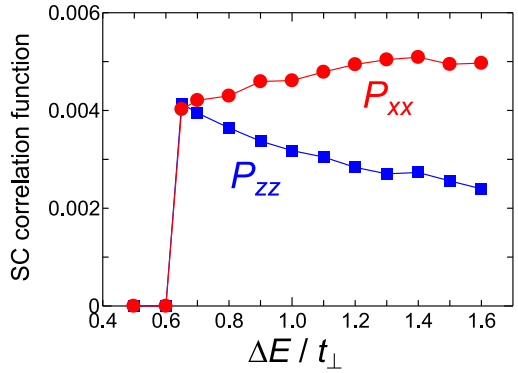


Figure 2: $\Delta E/t_\perp$ dependence of the superconducting correlation function [2].

References

[1] H. Sun *et al.*, Nature **621**, 493 (2023).

[2] H. Watanabe, H. Sakakibara, and K. Kuroki, arXiv:2603.13604.

Tensor-train impurity solvers for dynamical mean-field theory

Naoto TSUJI
Department of Physics, Graduate School of Science, The University of Tokyo
Bunkyo, Tokyo 113-0033, Japan

Strongly correlated electron systems exhibit a wide variety of equilibrium and nonequilibrium phenomena, and dynamical mean-field theory (DMFT) is one of the central theoretical frameworks for their microscopic analysis. In DMFT, a lattice model is mapped onto a quantum impurity model, and the main computational bottleneck lies in solving this impurity problem. In impurity solvers based on perturbative expansions, evaluating higher-order terms requires integration over many internal time variables. As the perturbation order increases, this task becomes a high-dimensional integration problem and quickly becomes computationally demanding. For such problems, the widely used continuous-time quantum Monte Carlo (CT-QMC) method provides a practical approach, but especially for multi-orbital, multi-site, and nonequilibrium impurity models, it suffers from a severe sign problem. In this project, we developed impurity solvers based on tensor-train methods [1, 2] to overcome this difficulty.

To treat these high-dimensional integrals, we employ tensor-train methods, which approximate the integrand in tensor-train format and thereby reduce a multidimensional integration problem to a sequence of one-dimensional integrations. In practice, the tensor-train representation can be constructed using the tensor cross interpolation (TCI) algorithm, which has seen rapid development in recent years. Because this approach is deterministic and does not rely on stochastic sampling, unlike CT-QMC, it is expected to remain effective even for problems in which the sign problem becomes severe in Monte Carlo calculations.

We first combined tensor-train methods with the weak-coupling expansion for equilibrium impurity models [3]. Benchmark calculations for exactly solvable impurity models showed rapid convergence with respect to the tensor-train bond dimension. We then embedded this solver into DMFT for the half-filled Hubbard model on the Bethe lattice and reproduced the metal-to-Mott-insulator transition with an accuracy comparable to that of CT-QMC. An additional advantage of this deterministic tensor-train approach is that the grand potential can also be computed with little extra numerical cost.

We also extended the tensor-train impurity solver to a real-time formulation for nonequilibrium DMFT. Our results show that the integrand of the weak-coupling expansion can be efficiently approximated in tensor-train form even in the real-time formulation. By incorporating this nonequilibrium tensor-train impurity solver into the nonequilibrium DMFT framework, we were able to simulate the dynamics of the Hubbard model after an interaction quench up to times longer than those accessible with CT-QMC in some parameter regimes.

References

[1] Y. Núñez Fernández *et al.*, Phys. Rev. X **12**, 041018 (2022).

[2] Y. Núñez Fernández *et al.*, SciPost Phys. **18**, 104 (2025).

[3] S. Matsuura *et al.*, Phys. Rev. B **111**, 155150 (2025).

Spin Inequivalence Enhanced by Coulomb Interaction in a Compensated Ferrimagnet: A 3/4-Filled Inequivalent Dimer Model Study

Akito Kobayashi[a], Kouki Nunota[a], Kazuyoshi Yoshimi[b], Kenichiro Hashimoto[c], and Takahiro Misawa[b]

[a] *Department of Physics, Nagoya University, Nagoya 464-8602*

[b] *Institute for Solid State Physics, University of Tokyo, Kashiwa, Chiba 277-8581, Japan*

[c] *Department of Advanced Materials Science, University of Tokyo, Kashiwa, Chiba 277-8561, Japan*

Collinear antiferromagnets, characterized by antiparallel spin alignment, have traditionally been regarded as incapable of supporting unconventional transport phenomena, such as spin current generation. Recent theoretical developments, however, have identified a class of antiferromagnetic materials—including altermagnets and compensated ferrimagnets—that exhibit unconventional transport properties, notably the anomalous Hall effect and spin current generation. [1, 2, 3].

We previously proposed the possibility of compensated ferrimagnetism in organic compounds with inequivalent dimer structures [4]. We also formulated a simple design principle whereby compensated ferrimagnetism can be realized when antiferromagnetic order emerges in a system comprising two distinct types of dimers. Based on this mechanism, we highlighted the potential realization of compensated ferrimagnetism in the organic compound $(EDO\text{-}TTF\text{-}I)_2ClO_4$ [4].

In this study, we investigate the effects of the on-site Coulomb interaction U in a three-quarter-filled two-dimensional model with inequivalent dimers using mean-field theory. We find that the spin inequivalence in the compensated ferrimagnetic phase is enhanced by U. When the bare dimer inequivalence is large, the enhancement due to U outweighs the enhancement of the antiferromagnetic (AF) gap, resulting in the emergence of a band-crossing compensated ferrimagnetic insulator (Fig. 1).

References

[1] M. Naka et al., Nat. Commun. **10**, 1, (2019)

[2] H. van Leuken et al., Phys. Rev. Lett. **74**, 1171 (1995)

[3] S. Semboshi et al., Sci. Rep. **12**, 10687 (2022)

[4] T. Kawamura et al., Phys. Rev. Lett. **132**, 156502 (2024)

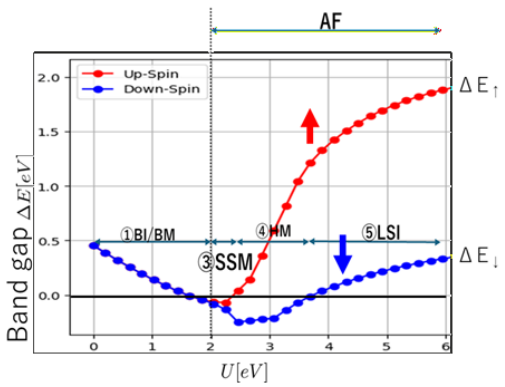


Figure 1: Spin inequivalence enhanced by Coulomb interaction.

Development of the Fermi Machine and Finite-Temperature Tensor Network Algorithms

Wei-Lin Tu

Graduate School of Science and Technology,

Keio University, Yokohama, Kanagawa 223-8522

This year, we established a foundational workflow for applying the Fermi Machine wavefunction to quantum many-body systems and achieved notable results, particularly in numerical simulations of the fermionic Hubbard model. The developed method demonstrated high accuracy in ground-state energy calculations, surpassing existing approaches, thereby strongly suggesting that the Fermi Machine could become a new paradigm in quantum many-body research. In particular, extending the previously proposed Fermi Machine framework [1] by introducing a Pfaffian formulation—well suited for representing pairing phases—constitutes a significant advancement. Because the Hubbard model is widely used in studies of high-temperature superconductivity, adopting a Pfaffian wavefunction that naturally captures the pairing structure of the ground state is physically well-motivated and enables a more reliable and expressive description.

Furthermore, strongly correlated systems often exhibit effects that cannot be captured by a wavefunction ansatz alone, making it essential to incorporate neural networks as projection operators. From this perspective, the present study proposed a new convolutional neural network architecture—Tensor-Augmented CNN (TACNN)—that embeds quantum-state structure into the network design [2]. TACNN replaces conventional convolutional kernels with tensors that can be interpreted as small quantum states, and it has already demonstrated significant accuracy improvements in image-classification tasks. By integrating this architecture with the Fermi Machine, we expect to construct a new framework with exceptionally strong expressive power for quantum many-body systems.

Overall, this research opens a new direction for neural quantum states (NQS) and highlights the importance of “AI for Physics” in an era of rapidly advancing AI technologies. We plan to continue enhancing the methodology and expanding its applications in the coming year.

References

[1] M. Imada, J. Phys. Soc. Jpn. **93**, 104002 (2024).

[2] C.-W. Hsing and W.-L. Tu, arXiv:2604.08072 (2026).

Electronic Structure Engineering in Low Dimensional Systems with Artificial Nanostructures

Toshikaze KARIYADO

Research Center for Materials Nanoarchitectonics,

National Institute for Materials Science, Namiki, Tsukuba, Ibaraki 305-0044

We have worked on artificially stacked 2D materials, mainly focusing on moiré systems in which slight mismatches between adjacent layers induce long-range structural patterns. In moiré systems, modelling plays an important role since number of atoms in a moiré unit cell is typically large. When a moiré length is much larger than original lattice spacing, it is possible to define a “local” structure at each position in a moiré unit cell. A widely adopted modelling method is local approximation, where parameters for an effective model are extracted from electronic structure for each “local” structure [1]. This requires large computational resources since the first-principles calculation should be applied to every “local” structure.

C_{568} is a 2D carbon allotrope featured by a square-like lattice structure and co-existence of 5-membered, 6-membered, and 8-membered carbon rings. This allotrope is predicted to be stable in previous numerical studies [2]. Monolayer C_{568} is a semiconductor with its valence top at the M-point in the Brillouin zone, from which we expect interesting tunability of moiré band structures [1,3].

We have successfully built a model for twisted bilayer C_{568} [4] using Quantum Espresso for the first-principles calculations. Using the derived model, it has been also shown that (1) we have a square lattice Hubbard model as an effective model for twisted bilayer C568 at small twist angles, (2) ratio between nearest-neighbor and next-nearest-neighbor transfer integrals depend crucially on the twist angle, and (3) displacement field can induce anisotropy in the nearest-neighbor transfer integrals [4], all of which indicate that twisted bilayer C_{568} serves as an interesting quantum simulator for a square lattice Hubbard model.

References

[1] T. Kariyado and A. Vishwanath, Phys. Rev. Research **1**, 033076 (2019).

[2] B. Ram and H. Mizuseki, Carbon **158**, 827 (2020).

[3] P. M. Eugenio, Z.-X. Luo, A. Vishwanath, and P. A. Volkov, Phys. Rev. Lett. **134**, 236503 (2025).

[4] T. Kariyado, A. Vishwanath, and Z-X. Luo, Phys. Rev. B 112 125159 (2025).

Development of computational methods for quantum field theories of nonequilibrium systems utilizing information compression techniques and its applications

Ken INAYOSHI
Department of Physics, Saitama University
255 Shimo-Okubo, Sakura-ku, Saitama City, Saitama 338-8570, Japan

April 26, 2026

The nonequilibrium Green's function (NEGF) method [1, 2] is a powerful tool for treating many-body correlations and the time evolution of the system on equal footing. However, in nonequilibrium systems, Green's functions depend on two time variables because time-translational invariance is broken. Therefore, long-time simulations incur high memory and computational costs.

To address this challenge, various memory compression techniques have been developed for the NEGF method. Among them, a recent promising approach is the tensor network technique known as the quantics tensor train (QTT) [3]. In prototype implementations of the NEGF method with QTT (the QTT-NEGF method), benchmarks had been limited to the short-time region [4]. To overcome this, in our recent work we implemented a linear-equation solver for the Dyson equation based on a variational approach and demonstrated that nonequilibrium dynamics in large lattice systems can be simulated up to sufficiently long times [5]. However, the cost of this solver grows rapidly with the length of the simulated time domain, making further extension to longer time regions difficult. A key limitation is that this solver does not exploit the causality of Green's functions and globally updates them over the whole time domain within the self-consistent loop. Therefore, it is desirable to incorporate causality into the QTT-NEGF method.

In this project, we developed a causality-based divide-and-conquer method for the QTT-NEGF method [6]. In this method, the self-energy calculation and the self-consistent loop are performed only in the newly added time domain, exploiting the causality of Green's functions. We applied this method to the quench dynamics of the antiferromagnetic state in the Hubbard model using nonequilibrium dynamical mean-field theory. We found that the data size of the stored Green's function is reduced to 1/1000–1/100 of that required by the conventional method [2]. Moreover, the simulation time domain can be extended without a significant increase in the data size.

Further detailed analyses using other physical quantities, such as magnetic response functions, are ongoing on the ISSP Supercomputer.

References

[1] H. Aoki *et al.*, Rev. Mod. Phys. **86**, 779 (2014).

[2] M. Schüler *et al.*, Comput. Phys. Commun. **257**, 107484 (2020).

[3] H. Shinaoka *et al.*, Phys. Rev. X **13**, 021015 (2023).

[4] M. Murray *et al.*, Phys. Rev. B **109**, 165135 (2024).

[5] M. Środa *et al.*, Phys. Rev. Lett. **135**, 226501 (2025).

[6] K. Inayoshi *et al.*, SciPost Phys. **20**, 077 (2026).

3.4 Cooperative Phenomena in Complex Macroscopic Systems

Molecular Simulation Contributions to Biological Membrane and Energy Materials Research

Wataru SHINODA

Research Institute for Interdisciplinary Science, Okayama University

3-1-1 Tsushima-naka, Kita-ku, Okayama 700-8530

During the last fiscal year, the supercomputing resources allocated to this project supported major advances in the molecular understanding of biological membranes, biomolecular interfaces, and energy materials. By combining coarse-grained and all-atom molecular dynamics simulations with free-energy calculations and enhanced sampling, we published twelve peer-reviewed papers. These results demonstrate the value of large-scale molecular simulation in connecting molecular structure and dynamics with experimentally observed properties and functions.

A central achievement was the development and application of the SPICA coarse-grained force field to complex membrane-related systems. In [1] and [2], we developed nucleic-acid and ionizable lipid nanoparticle models and used them to study lipoplexes and lipid nanoparticles relevant to nucleic acid delivery. These studies reproduced experimentally observed structural features and provided molecular insight into lipid-dependent delivery performance. In [3], simulations clarified the mechanism of transient multilamellar structure formation during ethanol-induced vesicle transformation. In [4], simulation-guided analysis supported the design of a melittin-derived peptide with improved cytosolic delivery efficiency. In [5], we reported the first coarse-grained simulation of the hepatitis B virus envelope–capsid complex, revealing key capsid–envelope interactions and reduced lipid mobility in the viral envelope. In [6], simulations of asymmetric plasma membranes showed marked leaflet-dependent organization, with dynamic nanoscale domains emerging mainly in the inner leaflet.

The project also advanced the study of biomolecular interfaces and membrane proteins. In [7], we extended the SPICA force field to polymeric biomaterial surfaces and showed that surface hydrophobicity is a major factor governing protein adsorption, providing guidelines for the design of biocompatible polymers. In [8], molecular dynamics simulations, together with structural and functional studies, clarified the citrate transport mechanism of the barley membrane transporter HvAACT1, which is important for aluminum tolerance in crops. In [9], we applied the enhanced path-sampling method ∞RETIS to

membrane pore formation and identified the sequence of thinning, defect formation, and pore development.

In parallel, the project produced significant results in electrolyte science for next-generation batteries. In [10], we summarized electrolyte design principles based on ion dynamics and Onsager transport coefficients. In [11], we showed that heterogeneous speciation in lithium electrolytes strongly affects experimentally observed transport properties and can cause discrepancies in lithium transference numbers. In [12], we reported polymer-assisted supercooled lithium salts as a new class of nonflammable single-ion conducting liquid electrolytes with near-unity lithium transference number and promising battery performance.

Overall, the twelve papers published during the reporting period highlight the wide scope of this project, covering force-field development, membrane remodeling, viral and peptide–membrane systems, membrane proteins, biomaterial interfaces, and battery electrolytes. Supercomputing resources were essential for simulating large and complex systems, sampling slow or rare processes, and obtaining quantitative molecular insight. These achievements have strengthened the foundation for both biological membrane research and energy materials design.

References

[1] A. P. Singh, H. Tanaka, Y. Miyazaki, W. Shinoda, J. Phys. Chem. B, **129**, 7939–7950 (2025).

[2] A. P. Singh, H. Tanaka, Y. Miyazaki, S. Nagano, and W. Shinoda, J. Chem. Theory Comput. **21**, 6226-6238 (2025).

[3] K. Shibata, M. Maeki, M. Tokeshi, and W. Shinoda, Langmuir, **41**, 13372-13380 (2025).

[4] Y. Kawaguchi, N. Tamemoto, Y. Uehata, Y. Miyazaki, and W. Shinoda, S. Futaki, Chem. Pharm. Bull. **73**, 896-906 (2025).

[5] R. Urano and W. Shinoda, J. Phys. Chem. Lett. **17**, 77-82 (2026).

[6] T. Yamada and W. Shinoda, Biophys. J. **125**, 387-395 (2026).

[7] H. O. S. Yadav, A. Kuo, S. Urata, K. Funahashi, Y. Imamura, and W. Shinoda, J. Chem. Theory Comput. **21**, 10561-10573 (2025).

[8] T. N. Thao, N. Mitani-Ueno, R. Urano, Y. Saitoh, P. Wang, N. Yamaji, J. -R. Shen, W. Shinoda, J. F. Ma, and M. Suga, Proc. Natl. Acad. Sci. U.S.A. **122**, e2501933122 (2025).

[9] D. T. Zhang, L. Baldauf, G. Lazarski, T. S. van Erp, and W. Shinoda, J. Chem. Theory Comput. **22**, 3072-3083 (2026).

[10] K. Shigenobu, S. Tsuzuki, W. Shinoda, and K. Ueno, BUNSEKI KAGAKU **74**, 427-436 (2025).

[11] F. Philippi, Y. Matsuyama, S. Buyting, T. Sudoh, K. Shigenobu, W. Shinoda, M. Schönhoff, M. Watanabe, K. Ueno, Phys. Chem. Chem. Phys. **27**, 15185-15195 (2025).

[12] T. Sudoh et al., Adv. Energy Mater. **16**, e05229 (2026).

Multiscale Molecular Dynamics Analysis of Cavitation and Chemical Reactions at Sliding Interfaces

Yuta Asano

Faculty of Global Nursing,

Iryo-Sosei University, 1-3-4 Koaota, Kashiwa, Chiba 277-0803

Achieving low friction and high durability in mechanical systems is a critical challenge for a sustainable society, as approximately 23% of global energy consumption is lost to friction [1]. Especially in resource-limited societies, advancing energy and resource conservation through the control of friction and wear is a paramount task. While water lubrication is a key technology, its ultra-low viscosity and limited load-capacity cause inadequate lubrication and cavitation significantly impacts safety and performance; thus, controlling cavitation is essential for the efficient operation of mechanical systems. In this study, we investigate interfacial phenomena across multiple length scales by combining large-scale coarse-grained molecular dynamics (CGMD) simulations and reactive molecular dynamics (RMD) simulations.

First, CGMD simulations were employed to examine whether nanoindentation at experimental scales can be realized. The coarse-grained method described in Ref. [2] was adopted. Simulations with up to several hundred million coarse-grained particles were performed, and indentation responses were successfully obtained using an indenter geometry identical to that used in experiments.

Based on the mechanical and environmental conditions obtained from the CGMD, reactive molecular dynamics simulations were further extended to describe local chemical reactions. To this end, boundary conditions allowing material inflow and outflow were introduced, enabling a pseudo-open system, and the feasibility of maintaining a quasi-steady-state environment was examined. As a representative and well-studied system for water lubrication, hydrogen-terminated diamond-like carbon (DLC) interfaces were selected as a test case. This system has been extensively investigated in previous studies, making it suitable for assessing the validity and limitations of the proposed RMD simulation. This analysis serves as a fundamental validation to reconstruct the localized high-temperature and high-pressure environments typically observed during cavitation bubble collapse.

Observations of hydrogen-terminated DLC surfaces indicated that a quasi-steady atmosphere could be maintained only during the initial stages of sliding. As wear progressed,

a clogging state developed at the fluid interface, which obstructed material inflow and prevented sustained steady-state conditions. In addition, the employed reactive force field led to excessive H_3O^+ generation, indicating that the combined treatment of charge neutrality and molecular insertion/deletion can induce nonphysical reactions in the pseudo-open RMD simulation.

These results clarify that the simultaneous treatment of charge neutrality and molecular insertion/deletion poses a significant challenge in the current RMD simulation. Identifying these factors is a crucial step toward refining the algorithm to suppress such nonphysical reactions. Future work will focus on redesigning boundary conditions to prevent interface clogging and re-optimizing the reactive force field parameters to achieve a sustained quasi-steady state and more accurate reaction analysis.

References

[1] K. Holmberg and A. Erdemir, Friction **5**, 263 (2017).

[2] M. Brownell and A. K. Nair, Phys. Chem. Chem. Phys., **21**, 490 (2019).

String Breaking and Multi-Spinon Complexes near Deconfined Quantum Criticality

Jun TAKAHASHI
Institute for Solid State Physics, University of Tokyo
Kashiwa-no-ha, Kashiwa, Chiba 277-8581

In the valence-bond solid (VBS) phase of a two-dimensional quantum magnet, spinons are elementary topological excitations realized as the nexus of four domain walls. The geometry of the square lattice enforces a parity constraint that neighboring spinons must be located in the opposite sublattice, which can be viewed as analogous to a charge constraint in particle physics. This sublattice constraint was argued to play a role at the Néel-VBS quantum phase transition [1] that is suspected to be generically a *deconfined quantum critical* point (DQCP). In the argument, the spinons form a network interconnected by domain walls giving rise to an effective AFM interaction among the spinons in a two-dimensional geometry, thereby connecting the two seemingly unrelated phases nontrivially. While hadron bound states like protons are the central objects in quantum chromodynamics and their multi-quark extensions (e.g. pentaquarks etc) and their properties are being actively studied, analogous multi-spinon bound states in condensed matter systems, especially under similarly nontrivial geometric and topological constraints, remain much more elusive.

In this work, we study a square-lattice VBS ground state with large-scale quantum Monte Carlo (QMC) simulation to see what type of multi-spinon complexes are stable and explore the constraints they accompany other than the previously argued sublattice constraint. The Hamiltonian is defined to be

$$H = -Q \sum P_{ij} P_{kl}, \qquad (1)$$

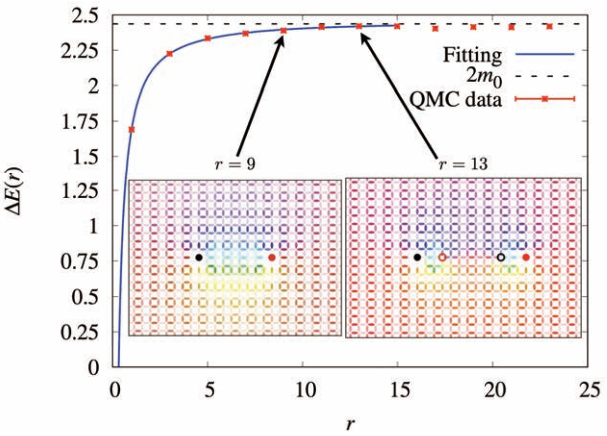


Figure 1: Excitation energy $\Delta E(r)$ as a function of the distance r between the two injected spinons. Two exemplifying configurations are shown for $r = 9$ (spinon dipole) and $r = 13$ (string breaking with emergent spinons).

where $P_{ij} = 1/4 - \mathbf{S}_i \cdot \mathbf{S}_j$ is the singlet projector, and the summation is taken over all parallel pair of bonds (i, j) and (k, l) in a plaquette of the $L \times L$ square lattice with periodic boundary condition. We set the unit $Q = k_{\mathrm{B}} = 1$ and inverse temperature $\beta = L$ to effectively observe the ground state. Note that the Hamiltonian above is in the VBS phase but with a nearby proximate DQCP of the so-called JQ model [2]. We inject spinons by adding infinitely strong magnetic fields $\pm h S_i^z$ with $h \to \infty$ to a specific spin i in the system.

As a first step, we can observe two-spinon bound states forming a "dipole" with four domain walls connecting them (Fig. 1). Upon in-

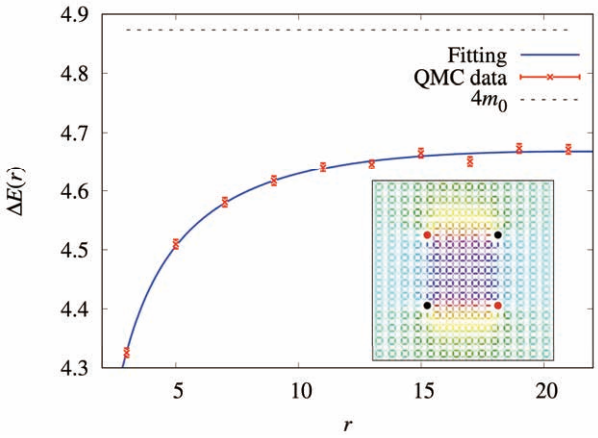


Figure 2: Excitation energy $\Delta E(r)$ as a function of the distance r between the four injected spinons in a square shape. Inset shows an exemplifying configuration.

creasing the distance between the two spinons, the strings break by spontaneously creating two emergent spinons that pair up with the two enforced spinons. This phenomenon is known as string breaking and has been studied in the context of gauge theories realizable with cold atom systems [3]. We can directly observe this using QMC, by visualizing the thermal average of the singlet density $\langle P_{ij} \rangle$ and associating a local two-dimensional VBS order parameter.

Equipped by the two-spinon bound state, we can proceed to create excitations that involve a larger number of spinons. For example, a four-spinon structure as in Fig. 2 can be seen to be far more stable than the two-spinon bound state, since the excitation energy only converges to the $r \to \infty$ limit very slowly. This means that the string breaking only happens at a far larger distance compared to the spinon dipole case.

We further found that the stable pattern with four spinons can form a network of spinons that extends to the system-size as shown in Fig. 3(a). These networks are stable against perturbations, and does not need to be periodic as can be seen from (b) with tilted angles for the four injected spinons and (c)

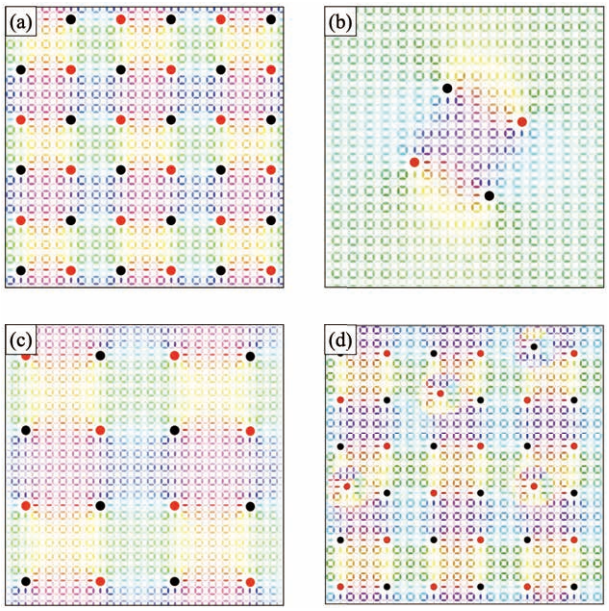


Figure 3: Several QMC configurations showing a domain-wall network.

with larger distance between the spinons. On the other hand, moving the injected spinons by (1,1) lattice spacing destroys the clean domain wall network as shown in (d), although it conserves the sublattice. We find that a *sub*-sublattice structure of the square lattice leads to this destruction because this (1,1) shift adds a π phase in the local VBS ordering. This additional constraint seems to be never addressed before in the field theory of VBS states, and raises questions about what additional considerations are needed to understand the DQCP and its relation to topological excitations.

This work was done in collaboration with Zhiyao Ning, Xuefeng Zhang, and Naoki Kawashima.

References

[1] M. Levin and T. Senthil: Phys. Rev. B **70**, 220403(R) (2004).

[2] A. W. Sandvik: Phys. Rev. Lett. **98**, 227202 (2007).

[3] D. González-Cuadra et al.: Nature **642**, 321 (2025).

Thermal Hall transport in frustrated magnets

Tsuyoshi Okubo
Institute for Physics of Intelligence, University of Tokyo
7-3-1 Hongo, Bunkyo-ku, Tokyo, 113-0033

Frustrated magnets are know to host exotic quantum states, such as quantum spin liquids and complex spin textures. In recent years, thermal Hall transport has attracted considerable attention as a powerful experimental probe of such unconventional magnetic states. In particular, the observation of a half-quantized thermal Hall conductivity in the Kitaev candidate material α-$RuCl_3$ under magnetic fields has stimulated extensive theoretical and experimental studies[1, 2]. Understanding the microscopic origin and finite-temperature behavior of thermal Hall transport in frustrated magnets has therefore become an important issue in condensed matter physics.

In this project, we developed numerical approaches based on finite-temperature tensor network methods to investigate thermal Hall transport phenomena in frustrated quantum magnets. Since thermal Hall transport is intrinsically a finite-temperature dynamical response, reliable numerical calculations require accurate evaluations of finite-temperature equilibrium states in strongly correlated quantum systems. To address this challenge, we employed tensor network simulations based on the exponential tensor renormalization group (XTRG) method [3]. The XTRG method approximates a finite-temperature density matrix as a matrix product operator and optimizes it through imaginary time evolution, allowing us to access finite temperature properties.

First, we investigated the $S = 1/2$ Kitaev model under magnetic fields [4]. We computed finite-temperature density matrices using the XTRG method and evaluated the temperature dependence of the thermal Hall conductivity from equilibrium spin correlations. Our results demonstrated that the thermal Hall conductivity exhibits a characteristic overshoot behavior at finite temperatures, where its value exceeds the half-quantized value expected in the zero-temperature limit. This behavior is qualitatively similar to experimental observations in α-$RuCl_3$, suggesting that a simple Kitaev interaction combined with finite-temperature effects can explain the observed thermal Hall effects. We also clarified the dependence of the thermal Hall response on the direction of the applied magnetic field. In particular, the thermal Hall conductivity vanishes for magnetic fields applied parallel to the b-axis, while its sign is reversed between the a-axis and c-axis field directions. These results provide useful information for understanding the origin of anisotropic thermal transport in Kitaev materials.

In addition, we continued our investigation of the kagome-lattice Heisenberg model under magnetic fields using similar finite-temperature tensor network techniques. By systematically analyzing the magnetic-field and temperature dependence of the thermal Hall conductivity, we found that the sign reversal of the thermal Hall conductivity near the 1/9 magnetization plateau is closely related to the stepwise development of magnetic ordering at finite temperatures [5]. This result suggests a close connection between thermal transport properties and emergent magnetic textures in frustrated systems.

The present study demonstrates that finite-temperature tensor network methods combined with large-scale supercomputing resources provide a powerful framework for investigating thermal transport phenomena in strongly correlated quantum magnets. The developed numerical techniques are expected to be applicable to a broad class of frustrated magnetic systems and to contribute to the microscopic understanding of experimentally observed thermal Hall effects.

References

[1] A. Kitaev, Ann. Phys. **321** (2006) 2.

[2] Y. Motome and J. Nasu, J. Phys. Soc.Jpn. **89** (2020) 012002.

[3] Bin-Bin Chen, Lei Chen, Ziyu Chen, Wei Li, and Andreas Weichselbaum Phys. Rev. X **8** 031082(2018) .

[4] T. Okubo, J. Nasu, T. Misawa, and Y. Motome, arXiv:2507.16558.

[5] Y. Nakanishi, K. Ido, S. Morita, T. Misawa, Y. Yamaji, and T. Okubo, in preparation.

Thermal effects on quantum frustrated magnets

Tokuro Shimokawa
Okinawa Institute of Science and Technology Graduate University, Onna 904-0495, Japan

The properties of quantum frustrated magnets at finite temperatures remain largely unexplored, and there has been a continuous demand for advancements in research based on large-scale numerical calculations. In recent years, with developments in the field of quantum information, experimentally accessible measures of quantum entanglement have attracted considerable attention. In this research project, we focused on the quantum Fisher information (QFI), which can be evaluated from dynamical spin correlations and is closely related to experimentally measurable quantities such as the dynamical spin structure factor.

As a representative example, we studied the $S = 1/2$ J_1-J_2 triangular-lattice Heisenberg antiferromagnet. To evaluate the QFI at finite temperatures, we developed an unbiased numerical code based on the thermal pure quantum state method to calculate the dynamical spin structure factor [1, 2]. We also accelerated our computational code using MPI parallelization techniques. In particular, we were able to evaluate the temperature dependence of the QFI and the finite-temperature dynamical spin structure factor through large-scale parallel computing using the F144cpu partitions.

In this fiscal year, we investigated the quantum critical behavior reported in triangular-lattice magnetic materials such as $KYbSe_2$, $YbZnGaO_4$, and $YbZn_2GaO_5$. To obtain a deeper understanding of the universal nature of this quantum criticality, we studied the finite-temperature spin dynamics and the temperature dependence of the QFI in the $S = 1/2$ J_1-J_2 triangular-lattice Heisenberg model. For this purpose, we treated clusters with up to $N = 30$ sites. In particular, we calculated the temperature dependence of the QFI density near the quantum critical point between the Néel and QSL phases in the $S = 1/2$ J_1-J_2 triangular-lattice Heisenberg model. We found that the experimentally extracted temperature dependence of the QFI for three triangular-lattice materials, $KYbSe_2$, $YbZnGaO_4$, and $YbZn_2GaO_5$, follows the theoretical temperature dependence of the QFI density obtained from our numerical calculations. These results indicate that the temperature dependence of the QFI provides a useful and experimentally relevant probe of universal quantum critical behavior in triangular-lattice quantum magnets.

References

[1] H. Ikeuchi, H. De Raedt, S. Bertaina, and S. Miyashita, Phys. Rev. B **92**, 214431 (2015).

[2] H. Endo, C. Hotta, and A. Shimizu, Phys. Rev. Lett. **121**, 220601 (2018).

[3] T. Shimokawa, S. Sabharwal and N. Shannon, arXiv:2505.11874.

Symmetry-based nonlinear fluctuating hydrodynamics in one dimension

Hiroyoshi NAKANO
Institute for Solid State Physics, University of Tokyo
Kashiwa-no-ha, Kashiwa, Chiba 277-8581

Recently, hydrodynamic theory has emerged as a unifying framework for understanding a broad range of transport phenomena in solids, encompassing both electronic and thermal conduction. In one-dimensional systems, the conventional nonlinear fluctuating hydrodynamics (NFH) proposed as an effective theory for non-integrable many-particle systems was known to exhibit certain theoretical inconsistencies, such as requiring unphysical parameter values. In our recent work, we reconstructed the NFH equations, relying on symmetries and conservation laws without depending on microscopic Hamiltonian details [1]. Furthermore, a dynamic renormalization group (RG) analysis of this model suggested that both the sound and heat modes belong to the Kardar-Parisi-Zhang (KPZ) universality class, characterized by a dynamical exponent $z = 3/2$. In this report, we detail the methodology and results of direct numerical simulations performed on the newly formulated NFH equations to explicitly verify these theoretical predictions.

In our numerical simulations, we solve the NFH equations in the long-wavelength limit, where they are decomposed into three independent normal modes. The fundamental equation is given by:

$$(\partial_t + \alpha c_s \partial_x - D_\alpha \partial_x^2)\phi^\alpha + \sum_{\beta,\gamma} G^\alpha_{\beta\gamma} \partial_x (\phi^\beta \phi^\gamma) = \zeta^\alpha \tag{1}$$

Here, ϕ^α represents each normal mode, with the index $\alpha \in \{+, 0, -\}$ corresponding to the right-moving sound mode, the heat mode, and the left-moving sound mode, respectively. The parameter c_s is the sound velocity, and D_α is the diffusion constant for each mode. Due to symmetry requirements, the diffusion constants of the sound modes satisfy $D_+ = D_- = D_s$. The nonlinear coupling coefficients, $G^\alpha_{\beta\gamma}$, form a parameter matrix determined by symmetry constraints such as thermal equilibrium conditions. The term ζ^α on the right-hand side represents Gaussian white noise satisfying the fluctuation-dissipation relation, with the following spatiotemporal correlation:

$$\langle \zeta^\alpha(x,t)\zeta^\beta(x',t')\rangle = -2D_\alpha \delta_{\alpha\beta}\partial_x^2 \delta(t-t')\delta(x-x') \tag{2}$$

To numerically solve the NFH equations, we adopted a high-precision scheme designed to strictly satisfy conservation laws at the discrete level [1]. For spatial discretization, we utilized a staggered-grid method [2]. By defining the scalar fields at the cell centers and their corresponding fluxes at the cell boundaries, the scheme naturally ensures the conservation of quantities. For time evolution, we employed a third-order stochastic Runge-Kutta (RK3) scheme [3], which provides high accuracy for integrating stochastic terms.

Based on large-scale numerical calculations, we evaluated the spatiotemporal correlation function $\mathbb{S}^\alpha(x,t) = \langle \phi^\alpha(x,t)\phi^\alpha(0,0)\rangle$ and tested the dynamic scaling hypothesis:

$$\mathbb{S}^\alpha(x,t) = t^{-1/z} f_\alpha\left(\frac{x-\alpha c_s t}{t^{1/z}}\right) - \mathcal{C}_\alpha, \tag{3}$$

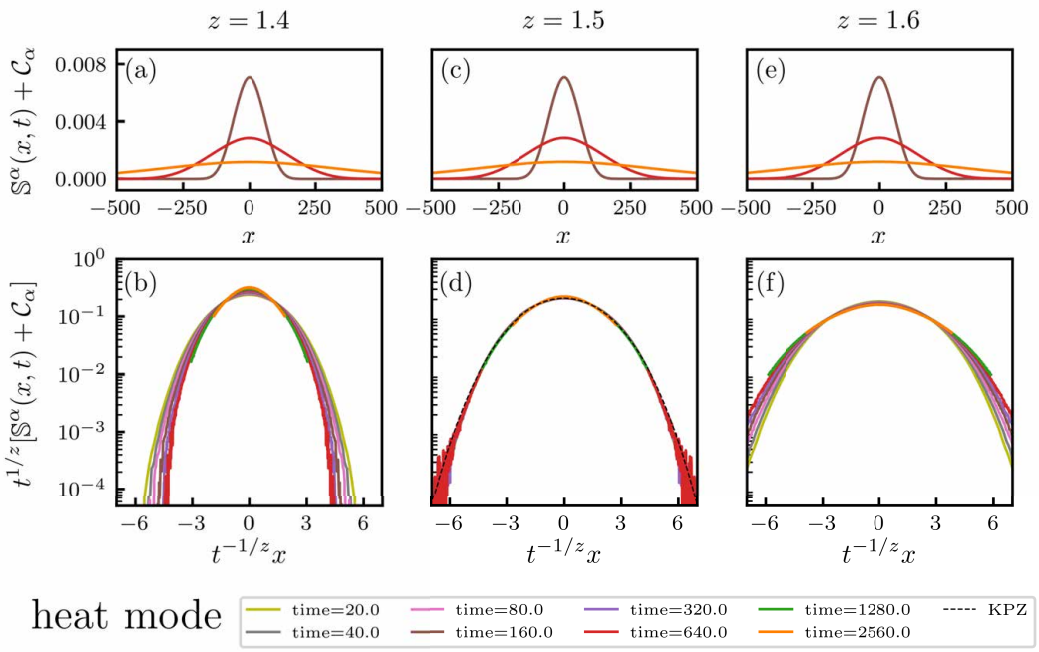


Figure 1: Dynamic scaling analysis of the spatiotemporal correlation function for the heat mode ($\alpha = 0$). Top panel: Raw data of the correlation function $\mathbb{S}^0(x,t)$ at various times. Bottom panel: Data collapse using $z = 3/2$. The horizontal axis is the scaling variable $xt^{-1/z}$ and the vertical axis is the scaled correlation function $t^{1/z}\mathbb{S}^0(x,t)$.

where $\mathcal{C}_\alpha$ is a constant offset accounting for finite-size effects.

Figure 1 shows the results specifically for the heat mode ($\alpha = 0$). By adopting $z = 1.5$, the numerical data for $\mathbb{S}^0(x,t)$ obtained at different times collapse onto a single universal curve. This excellent data collapse confirms that the dynamic scaling exponent is indeed $z = 3/2$. Furthermore, the collapsed scaling function is extremely close to the Prähofer-Spohn function, which is known as the exact scaling function of the KPZ equation.

We verified this result under various parameter settings, revealing that these findings hold robustly across different parameter changes. This demonstrates that the NFH equations, reconstructed solely from symmetry and conservation laws independent of microscopic details, accurately describe the universal KPZ scaling.

References

[1] Y. Minami, H. Nakano, and K. Saito, Phys. Rev. Lett. **136** 187101 (2026)

[2] F. BalboaUsabiaga, J. B. Bell, R. Delgado-Buscalioni, A. Donev, T. G. Fai, B. E. Griffith, and C. S. Peskin, Multiscale modeling & simulation **10,** 1369 (2012).

[3] S. Delong, B. E. Griffith, E. Vanden-Eijnden, and A. Donev, Phys. Rev. E **87**, 033302 (2013).

Molecular Dynamics Study of Rayleigh-Plateau Instability at Liquid-Liquid Interfaces

Shunta Kikuchi and Hiroshi Watanabe
Department of Applied Physics and Physico-Informatics, Keio University, Yokohama 223-8522, Japan

We investigated the Rayleigh-Plateau (RP) instability at liquid-liquid interfaces by molecular dynamics (MD) simulations. Compared with gas-liquid systems, the present setup avoids evaporation and enables a direct comparison with continuum theory for two fluids with identical viscosities [1]. The system consisted of two immiscible Lennard-Jones liquids with the same physical properties inside and outside a cylindrical interface. We examined cylinders with several initial radii under two conditions: one with an imposed single-mode perturbation and one without any imposed perturbation.

For the perturbed initial condition, the growth rate was evaluated from both the breakup time and the time evolution of the imposed mode amplitude. The dispersion relation estimated from breakup times showed strong finite-size effects, especially for small radii. In contrast, when the growth rate was extracted from the early exponential growth of the imposed mode, the agreement with Stone's linear theory became much better [1]. For the largest radius studied, the simulation reproduced the theoretical dispersion relation well, including negative growth rates in the stable region. This shows that continuum theory can remain valid even for a very small liquid cylinder when thermal fluctuations are effectively suppressed by a controlled perturbation.

For the unperturbed initial condition, we analyzed the breakup dynamics induced by thermal fluctuations. The minimum radius $r_{\min}$ followed the power law $r_{\min} \propto (t_c - t)^{\alpha}$, where t_c is the breakup time, following the framework commonly used for singular breakup dynamics [2]. The exponent α increased systematically with the initial cylinder radius, showing that thermal fluctuations become less important as the system size increases. Smaller radii therefore exhibited stronger deviations from macroscopic behavior.

These results show two complementary aspects of microscopic RP instability. With an imposed perturbation, the instability growth follows classical hydrodynamic predictions even for cylinders only several molecular diameters in radius. Without imposed perturbations, the breakup process is strongly affected by thermal fluctuations and finite-size effects. The present study therefore clarifies how continuum-like behavior and fluctuation-dominated dynamics coexist in nanoscale liquid-liquid interfacial instability.

The present liquid-liquid model also provides a useful platform for future studies of microscopic hydrodynamics. Because the physical properties are matched across the interface, deviations from classical theory can be attributed more clearly to thermal fluctuations, finite-size effects, and molecular discreteness. This simplicity should make it possible to quantify the range of validity of continuum descriptions in nanoscale interfacial flows more systematically.

References

[1] H. A. Stone and S. R. Brenner: "Note on the capillary thread instability for fluids of equal viscosities," *J. Colloid Interface Sci.* **145**, 409-411 (1991).

[2] J. Eggers: "Universal pinching of 3D axisymmetric free-surface flow," *Phys. Rev. Lett.* **71**, 3458-3460 (1993).

From Protein Folding Theory to Rational Protein Design

Ryota NISHIKAWA[1], Shinya INOUE[1], Koji OOKA[2], Atsuya WATANABE[1], Shunya OKADA[1], Shunji SUETAKA[1], Yusaku HIRATA[3], Tomohiro NOJI[3], Kaisei NAGAO[1], and Munehito ARAI[1,2,3]

[1]Department of Life Sciences, Graduate School of Arts and Sciences, [2]College of Arts and Sciences, and [3]Department of Physics, Graduate School of Science, The University of Tokyo, Komaba, Meguro, Tokyo 153-8902

Many proteins achieve their biological functions only after folding into well-defined three-dimensional conformations. Accordingly, elucidating protein folding mechanisms remains a central challenge in fundamental life science research. In recent years, deep-learning based approaches to protein structure prediction, most notably AlphaFold [1], have been developed, and its development was honored with the 2024 Nobel Prize in Chemistry. However, despite its remarkable success, AlphaFold cannot predict the actual pathways of protein folding.

To address this limitation, we developed a statistical mechanical framework, the WSME-L model, which enables prediction of folding processes for a broad range of proteins [2]. To assess its general applicability, we applied the model to numerous proteins and analyzed their folding pathways. Inter-residue contact energies were estimated using the MM/PBSA module of the AMBER package [3], while free energy landscapes describing protein folding processes were computed using in-house WSME-L software written in C++ and Python.

Using this approach, we predicted folding pathways for various proteins and validated the results by comparison with experimental data. The WSME-L model successfully distinguished distinct folding behaviors even among structurally similar proteins. We also applied the model to proteins whose folding processes are difficult to investigate experimentally due to highly complex native structures. In particular, we determined the order of structural formation during the folding of laminin and bone morphogenetic protein-2, providing insights relevant to their efficient production for medical applications. Furthermore, we explored extensions of the theory to describe protein-protein interactions, with a particular focus on coupled folding and binding reactions involving intrinsically disordered proteins.

Aldehyde deformylating oxygenase (ADO) synthesizes alkanes equivalent to diesel fuel and is therefore of interest for biofuel production; however, its catalytic activity is very low [5]. We previously showed that ADO

forms a complex with its upstream enzyme, acyl-ACP reductase (AAR), enabling efficient substrate transfer without dissociation [6]. This suggests that strengthening the AAR/ADO interaction could enhance overall alkane production. To test this hypothesis, we rationally designed AAR/ADO mutants with enhanced interactions using the deep learning-based sequence design software ProteinMPNN [7] together with the physics-based protein design platform Rosetta [8]. Experimental validation is currently underway.

Because petroleum-derived products include fuels and plastics, reducing dependence on petroleum requires biological production routes to plastic precursors. Catechol 1,2-dioxygenase (CatA) catalyzes the synthesis of *cis*,*cis*-muconic acid, a precursor of polyethylene terephthalate. To enhance CatA activity using our original strategy for enzyme activity improvement, we performed molecular dynamics simulations with AMBER [3] and GROMACS [9] to characterize the substrate-bound and product-bound conformations of CatA, and used LigandMPNN [10] to rationally design mutants with improved activity. Several mutants with improved Michaelis constants (K_m) were obtained, and the design of mutants with enhanced turnover numbers is ongoing.

Finally, efficient screening of highly active enzymes in directed evolution experiments requires sensor proteins that emit fluorescence proportional to product concentration. To this end, we are developing rational design methodologies for fluorescent sensor proteins that specifically recognize product ligands.

References

[1] J. Jumper, et al.: Nature, **596**, 583-589 (2021).

[2] K, Ooka, and M. Arai: Nat. Commun. **14**, 6338 (2023).

[3] D. A. Case, et al.: AMBER 2024. University of California, San Francisco (2024)

[4] M. Mirdita, K. Schütze, Y. Moriwaki, L. Heo, S. Ovchinnikov, and M. Steinegger: Nat. Methods, **19**, 679-682 (2022).

[5] Y. Hayashi, and M. Arai: Microbial Cell Factories, **21**, 256 (2022).

[6] M. Yoshimura, and M. Arai: Biophys. Physicobiol. **22**, e220003 (2025).

[7] J. Dauparas, et al. Science, **378**, 6615 (2022).

[8] J. K. Leman, et al.: Nat. Methods, **17**, 665 (2020).

[9] S. Pall, C. J. Smith, B. Hess, E. Lindah: SoftwareX, **1–2**, 19-25 (2015).

[10] J. Dauparas, et al.: Nat. Methods, **22**, 717 (2025).

Development of machine-learning force fields to analyze atomic layer processing

Satoshi HAMAGUCHI

R³ Institute of Newly Emerging Science Design (INSD),

The University of Osaka, 1-2 Machikaneyama, Toyonaka, Osaka 560-0043

Recently, machine-learning force fields (ML-FFs) have emerged as accurate surrogate models for density functional theory (DFT) calculations, enabling high-fidelity classical molecular dynamics (MD) simulations in materials science. While various ML-FF models successfully simulate thermodynamic equilibrium systems, they often fail in high-energy ion irradiation environments, such as sputtering and etching. In these simulations, high-energy ion impacts force atoms into extreme proximity, causing standard DFT calculations to diverge and rendering the resulting force fields unstable or inaccurate.

To address this limitation, this study couples Ziegler-Biersack-Littmark (ZBL) potential functions to represent short-range repulsive interactions with ML-FFs for longer-range behaviors. The ML-FFs are constructed using Behler-Parrinello Neural Networks (BPNN) and Graph Neural Networks (GNN), optimized via active learning with "query-by-committee" sampling. Specifically, we use the n2p2, Allegro, and SevenNet trained on reference data computed via Quantum ESPRESSO. We apply this framework to Si and SiO_2 systems to simulate ion beam sputtering and etching. The results demonstrate good agreement with both beam experiments and conventional classical MD simulations. Finally, we also demonstrate the extensibility of this ML-FF framework to chemistry-driven processes, focusing on plasma-enhanced atomic layer etching (ALE) and atomic layer deposition (ALD), including metal oxide and nitride etching using organic precursors,[1] as shown in Fig. 1.

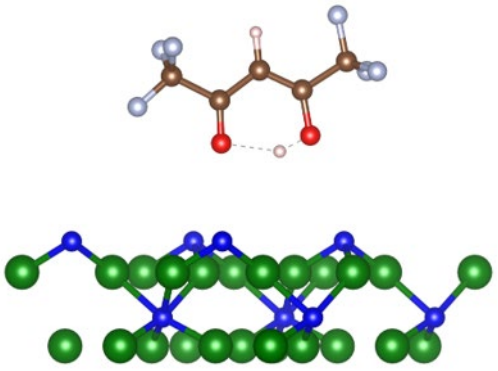


Fig.1 Structure of Hhfac above the Ni3N surface. (Coloring: dark green – Ni, blue – N, white – F, brown – C, red – O, light pink – H)

References

[1] A. H. Basher, et al., J. Vac. Sci. Technol., 38 (2010) 052602.

Record-low thermal boundary resistance at bonded GaN/diamond interface by controlling ultrathin heterogeneous amorphous layer

Xu Bin

Department of Mechanical Engineering,

The University of Tokyo, 7-3-1, Hongo, Bunkyo-ku, Tokyo 113-8656

In semiconductor-on-diamond structures, a non-crystalline buffer layer is required to achieve interfacial bonding due to lattice mismatch, which, however, typically results in high thermal boundary resistance (TBR) and limits device heat dissipation. Interestingly, theoretical studies have suggested that amorphous interfaces can exhibit anomalously low TBR, far below that of their crystalline counterparts. Verifying these predictions and systematically investigating interfacial thermal transport require the fabrication of ultrathin amorphous interfacial layers, yet experimental realization remains highly challenging, thereby limiting related research. Accordingly, this study aims to fabricate ultrathin amorphous interfacial layers and explore their impact on thermal conduction across GaN/diamond interfaces.

We fabricated GaN/diamond samples with varying amorphous interfacial layer thicknesses using a room-temperature bonding method, and measured their TBR via the TDTR technique, as shown in Fig. 1. As the interfacial layer thickness increased from 2.5 nm to 5.3 nm, the TBR rose from 8.3 to 35.0 m^2·K/GW. Notably, the TBR of 8.3 m^2·K/GW represents a record low for directly bonded GaN/diamond interfaces, highlighting its potential significance for efficient thermal management in GaN devices.

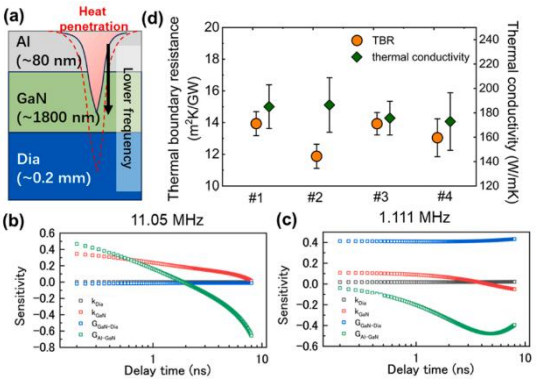


Fig.1 TDTR measurement for GaN-on-diamond system. (a) Schematic of the modulation frequency-control in tunning the penetration depth of TDTR measurement. Sensitivity calculation results for $G_{Al\text{-}GaN}$, $G_{GaN\text{-}Dia}$, $\kappa_{GaN\text{-}Dia}$ under (b) 11.05 MHz, $G_{GaN\text{-}Dia}$=30 MW/m^2K; (c) 1.111 MHz, $G_{GaN\text{-}Dia}$=30 MW/m^2K. (d) Thermal boundary resistance of Al/GaN interface ($R_{Al\text{-}GaN}$) and the thermal conductivity of the GaN layer (κ_{GaN}) measured under a modulation frequency of 11.05 MHz.

Furthermore, we investigated the underlying mechanism for the pronounced sensitivity of the TBR to interfacial thickness using molecular dynamics simulations, as shown in Figs. 2 and 3. Theoretical analysis indicates that the diamond/SiO_x inter-diffusion

layer introduces high-frequency interfacial vibrational modes, whose frequency range extends beyond the primary vibrational spectrum of crystalline diamond, thereby enhancing lattice vibrational mismatch and suppressing phonon transport.

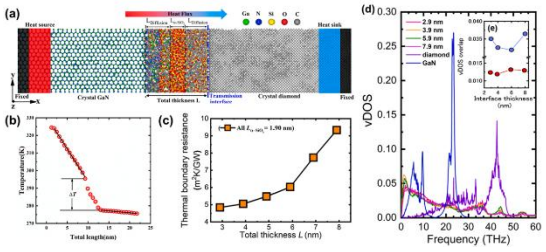


Fig.2 Interfacial heat conduction calculated by MD simulation. (a) Schematic of a typical MD simulations model with a layer-like amorphous interface. (b) Typical temperature profile of the system, where the linear fitting is performed to obtain the difference of temperature at GaN/diamond interface. (c) TBR of GaN/diamond interface with different interfacial thickness; SiO_x layer was fixed to 1.9 nm. (d) vDOS of GaN, diamond, and the entire interfacial layer with a thickness of 2.9, 3.9, 5.9, and 7.9 nm. (e) vDOS overlap between GaN/interfacial layer (blue symbol) and diamond/interfacial layer (red symbol).

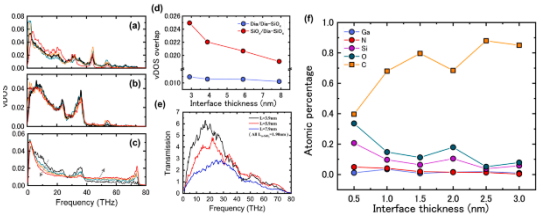


Fig.3 Interfacial vibrational states and heat carrier analysis in MD simulation. vDOS of (a) GaN-SiO_x diffusion region, (b) SiO_x region, and (c) diamond-SiO_x diffusion region; The interfacial layer thicknesses are 2.9 (black), 3.9 (green), 5.9 (orange), and 7.9 nm (red); grey arrow shows the trend in vDOS at individual frequencies ranges. (d) vDOS overlap between SiO_x/diamond-SiO_x diffusion region and diamond/diamond-SiO_x diffusion region, respectively. (e) Heat carrier transmission at interface near the c-diamond (marked in Fig.2(a)) under different interfacial layer thicknesses. (f) Concentration of individual elements in SiO_x/ diamond diffusion layer with different interfacial thickness.

Reference

[1] B. Xu, F. Mu, Y. Liu, R. Guo, S. Hu, J. Shiomi, Record-Low thermal boundary resistance at bonded GaN/diamond interface by controlling ultrathin heterogeneous amorphous layer, Acta Mater., 282 120458 (2025)

Numerical Study on the Magnetization Process of the S=1 Spin Ladder

Tôru SAKAI[1,2], Hiroki NAKANO[1], Tomoki HOUDA[1], Ryoma HASEGAWA[1], Yuki HAMAZAKII[1], Yuuki OHTAKE[1]Kantaro NUNOYA[1], Kiyomi OKAMOTO[1] and Tokuro SHIMOKAWA[3]

[1]*Graduate School of Science, University of Hyogo, Kouto, Kamigori, Hyogo 678-1297, Japan*

[2]*National Institute for Quantum Science and Technology, SPring-8, Kouto, Sayo, Hyogo 679-5148, Japan*

[3]*Theory of Quantum Matter Unit, Okinawa Institute of Science and Technology Graduate University, Onna-son, Okinawa 904-0495, Japan*

The magnetization plateau has attracted a great deal of interest as a macroscopic quantum phenomenon. Oshikawa et al.[1] derived the rigorous necessary condition for the appearance of the magnetization plateau in the one-dimensional quantum spin systems

$$Q(S - m) = n, \tag{1}$$

where S and m are the total spin and the magnetization per unit cell, respectively, Q is the periodicity of the ground sate, and n is a positive integer. The previous magnetization measurement of the organic $S = 1$ spin ladder material[2] 3, 3', 5, 5'-tetrakis(*N-tert*-butylaminoxyl)biphenyl (abbreviated as BIP-TENO), observed a magnetization plateau at 1/4 of the saturation magnetization. According to the rigorous condition Eq.(1), this 1/4 plateau can appear only when the ground state has the two-fold degeneracy due to the spontaneous translational symmetry breakdown. The spin frustration due to the second or third nearest neighbor interaction was proposed[3, 4, 5, 6], but the correct origin of the 1/4 plateau of BIP-TENO has not been clarified[7]. Recently the numerical diagonalization and the density matrix renormalization group analysis indicated the two competing anisotropies can induce the translational symmetry broken magnetization plateau in the $S = 1$ antiferromagnetic chain[8, 9, 10]. Thus it would be interesting to consider the possibility of the translational symmetry broken magnetization plateau based on such competing anisotropies in the $S = 1$ spin ladder system. In the present work we investigated the magnetization process of the $S = 1$ spin ladder with the easy-axis anisotropy at the leg interaction and the easy-plane single-ion one at each site. The numerical diagonalization of finite-size clusters and the level spectroscopy analysis[11, 12, 13, 14, 15] indicated that the translational symmetry broken plateau would appear at 1/4 and 3/4 of the saturation magnetization. In addition the translationally symmetric plateau was revealed to appear at the 1/2 magnetization. The phase diagrams for the two anisotropies at 1/4, 1/2, and 3/4 of the saturation magnetization were obtained[16].

References

[1] M. Oshikawa, M. Yamanaka and I. Affleck, Phys. Rev. Lett. **78**, 1984 (1997).

[2] T. Sakai, N. Okazaki, K. Okamoto, K. Kindo, Y. Narumi, Y. Hosokoshi, K. Kato, K. Inoue and T. Goto, Physica B **329-333**, 1203 (2003).

[3] K. Okamoto, N. Okazaki and T. Sakai, J. Phys. Soc. Jpn. **70**, 636 (2001).

[4] K. Okamoto, N. Okazaki and T. Sakai, J. Phys. Soc. Jpn. **71**, Suppl. 71 (2002).

[5] T. Sakai, K. Okamoto, K. Okunishi, K. Kindo, Y. Narumi, Y. Hosokoshi, K. Katoh, K. Inoue and T. Goto, Physica B **346-347**, 34 (2004).

[6] M. Kikuchi, K. Okamoto, K. Okunishi and T. Sakai J. Phys. Soc. Jpn. **74**, Suppl. 169 (2005).

[7] for recent developments, see H. Kohshiro, R. Kaneko, S. Morita, H. Katsura and N. Kawashima, Phys. Rev. B **104**, 214409 (2021); K. Nomura, Y. H. Matsuda, A. Ikeda, Y. Kohama, H. Tsuda, N. Amaya, T. Ono, and Y. Hosokoshi, Phys. Rev. B **105**, 214430 (2022), and references therein.

[8] T. Sakai, K. Okamoto, K. Okunishi, M. Hashimoto, T. Houda, R. Furuchi, H. Nakano, Phys. Rev. B **108**, 174435 (2023).

[9] T. Kawatsu, H. Suzuki, M. Hashimoto, K. Doi, T. Houda, R. Furuchi, H. Nakano, K. Okamoto and T. Sakai, J. Phsy. Soc. Jpn. **94**, 064701 (2025).

[10] T. Yamada, R. Nakanishi, R. Furuchi, H. Nakano, H. Kaneyasu, K. Okamoto, T. Tonegawa and T. Sakai, JPS Conf. Proc. **38**, 011163 (2023).

[11] K. Okamoto and K. Nomura, Phys. Lett. A **169**, 433 (1992).

[12] K. Nomura and K. Okamoto, J. Phys. A **27**, 5773 (1994).

[13] K. Okamoto, Prog. Theor. Phys. Suppl. 145, 113 (2002).

[14] A. Kitazawa, J. Phys. A **30**, L285 (1997).

[15] K. Nomura and A. Kitazawa, J. Phys. A **31**, 7341 (1998).

[16] Y. Hamazaki, R. Hasegawa, T. Kawatsu, H. Suzuki, T. Houda, H. Nakano, K. Okamoto and T. Sakai, AIP Advances **16**, 025302 (2026).

Magnetization Process of the S=3/2 Antiferromagnetic Chain

Tôru SAKAI[1,2], Hiroki NAKANO[1], Tomoki HOUDA[1], Ryoma HASEGAWA[1], Yuki HAMAZAKII[1], Yuuki OHTAKE[1]Kantaro NUNOYA[1], Kiyomi OKAMOTO[1], Tomohide KAWATSU[1], Haruto SUZUKI[1]and Tokuro SHIMOKAWA[3]

[1]*Graduate School of Science, University of Hyogo, Kouto, Kamigori, Hyogo 678-1297, Japan*

[2]*National Institute for Quantum Science and Technology, SPring-8, Kouto, Sayo, Hyogo 679-5148, Japan*

[3]*Theory of Quantum Matter Unit, Okinawa Institute of Science and Technology Graduate University, Onna-son, Okinawa 904-0495, Japan*

The magnetization plateau is one of interesting topics in the field of the condensed matter physics. It was proposed as the Haldane gap which appears in the magnetization process[1]. Based on the Lieb-Schultz-Mattis theorem[2], the rigorous necessary condition for the appearance of the magnetization plateau in the one-dimensional quantum spin systems was derived as the following form[1]

$$Q(S - m) = \text{integer}, \tag{1}$$

where S and m are the total spin and the magnetization per unit cell, respectively, and Q is the periodicity of the ground sate. Several magnetization plateaux with $Q = 1$ have been theoretically predicted using some numerical analyses[3, 4, 5, 6, 7, 8], and experimentally observed[9]. The translational symmetry broken magnetization plateaux with $Q = 2$ were also theoretically predicted in several systems[10, 11, 12, 13, 14, 15, 16], based on the mechanism caused by the spin frustration.

The recent work[17] using the numerical diagonalization and the density matrix renormalization group calculation revealed that the $S = 1$ antiferromagnetic chain with the single-ion and coupling anisotropies competing each other can exhibit the translational symmetry broken magnetization plateau at half the saturation magnetization. Since the double period structure like $|\cdots 101010\cdots\rangle$ is realized at the plateau, it should be called the Néel plateau. This plateau canno appear, until $Q = 2$ is realised. On the other hand, the Néel plateau like $|\cdots 202020\cdots\rangle$ was also theoretically predicted using the numerical diagonalization at half the saturation magnetization of the $S = 2$ antiferromagnetic chain with the same competing anisotropies, although the necessary condition (1) is satisfied even for $Q = 1$[18]. In the present work, we investigated the $S = 3/2$ antiferromagnetic chain to which the single-ion and coupling anisotropies are introduced in a competing way using the numerical diagonalization of finite-size clusters and the level-spectroscopy analysis. Our purpose is to consider the possibility of the Néel plateau at 1/3 and 2/3 of the saturation magnetization. Several1/3 plateaux for $Q = 1$ had already been theoretically predicted, while no plateau had been revealed to appear at the 2/3 magnetization, because $Q = 2$ is necessary. We obtained an extended phase diagram at the 1/3 magnetization and the initial one at the 2/3

magnetization[19].

References

[1] M. Oshikawa, M. Yamanaka and I. Affleck, Phys. Rev. Lett. **78**, 1984 (1997).

[2] E. H. Lieb, T. Schultz and D. J. Mattis, Ann. Phys. (N.Y.) **16**, 407 (1961).

[3] T. Sakai and M. Takahashi, Phys. Rev. B **57**, R3201 (1998).

[4] A. Kitazawa and K. Okamoto, Phys. Rev. B **62**, 940 (2000).

[5] K. Okamoto, T. Tonegawa and M. Kaburagi, J. Phys.: Condens. Matter **15**, 5979 (2003).

[6] K. Okamoto, M. Sato, K. Okunishi, T. Sakai, and C. Itoi, Physica E **43**, 769 (2011).

[7] T. Sakai and K. Okamoto, Phys. Rev. B **65**, 214403 (2002).

[8] T. Tonegawa, T. Sakai, K. Okamoto and M. Kaburagi, J. Phys. Soc. Jpn. **76**, 124701 (2007).

[9] H. Kikuchi, Y. Fujii, M. Chiba, S. Mitsudo, T. Idehara, T. Tonegawa, K. Okamoto, T. Sakai, T. Kuwai, and H. Ohta, Phys. Rev. Lett. **94**, 227201 (2005).

[10] H. Nakano and M. Takahashi, J. Phys. Soc. Jpn. **67**, 1126 (1998).

[11] N. Okazaki, J. Miyoshi and T. Sakai, J. Phys. Soc. Jpn. **69**, 37 (2000).

[12] N. Okazaki, K. Okamoto and T. Sakai, J. Phys. Soc. Jpn. **69**, 2419 (2000).

[13] A. Nakasu, K. Totsuka, Y. Hasegawa, K. Okamoto and T. Sakai, J. PHys.: Condens. Matter **13**, 7421 (2001).

[14] T. Sakai and Y. Hasegawa, Phys. Rev. B **60**, 48 (1999).

[15] K. Okamoto, N. Okazaki and T. Sakai, J. Phys. Soc. Jpn. **70**, 636 (2001).

[16] K. Okamoto, N. Okazaki and T. Sakai, J. Phsy. Soc. Jpn. **71**, 196 (2002).

[17] T. Sakai, K. Okamoto, K. Okunishi, M. Hashimoto, T. Houda, R. Furuchi and H. Nakano, Phys. Rev. B **108**, 174435 (2023).

[18] T. Yamada, R. Nakanishi, R. Furuchi, H. Nakano, H. Kaneyasu, K. Okamoto, T. Tonegawa and T. Sakai, JPS Conf. Proc. **38**, 011163 (2023).

[19] T. Kawatsu, H. Suzuki, M. Hashimoto, K. Doi, T. Huoda, R. Furuchi, H. Nakano, K. Okamoto and T. Sakai, J. Phys. Soc. Jpn. **94**, 064701 (2025).

Critical behavior of measurement induced transition

TOMI OHTSUKI[1]
TOHRU KAWARABAYASHI[2]
KEITH SLEVIN[3]
1) Dept. Phys., Sophia University, Chiyoda-ku, Tokyo 102-8554, Japan
2) Dept. Phys., Toho University, Miyama 2-2-1, Funabashi 274-8510, Japan
3) Dept. Phys., Osaka University, Toyonaka, Osaka 560-0043, Japan

Our research over the past year centered on the symmetry classification and spectral statistics of random quantum systems, with a particular emphasis on non-Hermitian Hamiltonians and nonunitary quantum dynamics [1,2]. As a principal achievement in 2025, we studied the entropy dynamics of monitored fermion systems, where continuous quantum measurements are performed on free fermions [3]. This problem is motivated by the recent rapid development of measurement-induced phase transitions, in which unitary time evolution tends to scramble quantum information whereas measurements extract information from the system. The competition between these two processes gives rise to purification dynamics that has no direct counterpart in closed quantum systems. Our purpose was to clarify the universal aspects of this dynamics by focusing on the spectral evolution of Gaussian density matrices.

One of the central results is the derivation of universal Rényi entropy fluctuations in the chaotic regime. These fluctuations are independent of microscopic details of the model and are the nonunitary counterpart of the universal conductance fluctuations known in quantum transport in mesoscopic electronic systems. We also clarified how the fluctuations depend on the fundamental symmetry class of the nonunitary dynamics. The analytical predictions were confirmed by extensive numerical simulations, including dynamics generated by Haar-random unitary matrices and by local Hamiltonians.

The above results provide a useful theoretical basis for further studies of measurement-induced transitions and for numerical diagnostics based on Lyapunov exponents of quantum trajectories. As ongoing work, we are extending this research in two directions. First, we are applying time-series analysis based on machine-learning techniques, including LSTM and transformer architectures, to entropy dynamics generated by monitored quantum systems. Second, we are investigating the effect of electron-electron interactions on the entropy dynamics using the tensor network technique, with the aim of clarifying which parts of the free-fermion universality survive in genuinely interacting many-body systems.

References

1. Z. Xiao, K. Kawabata, X. Luo, T. Ohtsuki, R. Shindou, Physical Review Research **4**, 043196 (2022).
2. K. Kawabata, Z. Xiao, T. Ohtsuki, R. Shindou, PRX Quantum **4**, 040312 (2023).
3. Z. Xiao, T. Ohtsuki, K. Kawabata, Phys. Rev. Lett. **134**, 140401 (2025).

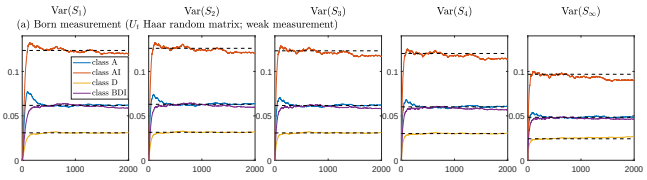


Figure 1: Variance Var(S_α) of Rényi entropy in the presence of weak measurement with the Haar random unitary dynamics in various symmetry classes. Taken from Ref. [3].

Crystal structure prediction of quaternary oxides based on mathematical crystal chemistry

Ryotaro KOSHOJI
Institute for Solid State Physics, University of Tokyo
Kashiwa-no-ha, Kashiwa, Chiba 277-8581

Mixed-integer nonlinear programming (MINLP), which has been widely used in process systems engineering, is the optimization problem involving both the continous and discrete variables. Generalized disjunctive programming (GDP) represented by continuous and Boolean variables is the special case of MINLP, where Boolean variables is just utilized to enforce the constraint on continous variables. GDP models can be reformulated as MINLP problems using the Big-M or Hull Reformulation [F. Trespalacios *et al.*, Chemie Ingenieur Technik **86**, 991 (2014)]. Mathematical crystal chemistry formulates the empirical rules of inorganic structural chemistry as GDP [R. Koshoji, in preparation]. The formalization is based on the concept that crystal structures can be discovered very efficiently if we successfully assume the atomic environment of each atom. The algorithm to solve this problem makes use of two subproblems as done in the Outer-approximation or Generalized Bender Decomposition. For the former subproblem, the Boolean variables are fixed, and accordingly, the continous optimization problem can be regarded as the dense packing problem of atomic spheres with several radii under the constraints on such as coordination polyhedra and interatomic distances. For the latter subproblem, the continous variables are fixed, and the Boolean variables are optimized to maximize the number of chemical bonds with satisfying all the constraints on interatomic distances, feasible compositions of coordination polyhedra, and feasible linking of polyhedra.

The algorithm demands tiny data such as atomic position and Boolean variables designating the type of interatomic-distance constraints, and besides, the algorithm itself is very simple. Therefore, it spends tiny computational time to design crystal structure prototypes. For example, the laptop computer will discover the quaternary oxides of $BaDyFe_4O_7$ and VMo_2CsO_8 in one second. The software **MARICI** implementing the algorithm is distributed under the MIT License [3], so you can freely check the computational efficiency on your laptop computer.

The previous studies clarifies that at least most of oxides registered in database can be regarded as optimal solution of GDP, and besides, the algorithm can discover a wide variety of ionic crystal structures such as spinel, pyrochlore (α and β), pyroxene, quadruple perovskite, $YBa_2Cu_3O_7$, and LaFeAsO [1-2]. Note that some of them can be designed as unique optimal solution.

An exhaustive search for crystal structures of quaternary oxides $\mathrm{A}_k\mathrm{B}_l\mathrm{C}_m\mathrm{O}_n$ and $\mathrm{A}_k\mathrm{B}_l\mathrm{D}_m\mathrm{O}_n$ discovers a wide variety of structural prototypes. The constraints for each cation is listed below.

- Cation A: $r^{(I)} = 0.32$, $R^{(I)} = 0.32$, $R^{(R_I)} = 1.4$, $c_i^{(I,O)} = 4$, $C_i^{(I,O)} = 4$
- Cation B: $r^{(I)} = 0.60$, $R^{(I)} = 0.60$, $R^{(R_I)} = 1.4$, $c_i^{(I,O)} = 6$, $C_i^{(I,O)} = 6$
- Cation C: $r^{(I)} = 1.40$, $R^{(I)} = 1.40$, $R^{(R_I)} = 1.8$, $c_i^{(I,O)} = 9$, $C_i^{(I,O)} = 12$
- Cation D: $r^{(I)} = 0.80$, $R^{(I)} = 1.30$, $R^{(R_I)} = 1.8$, $c_i^{(I,O)} = 8$, $C_i^{(I,O)} = 8$

The number of chemical composition is 3055 if k, l, m, n are constrained as

$$1 \leq k + l + m + n \leq 25$$
$$\frac{1}{7} \leq \frac{l}{k}, \frac{k}{l}, \frac{m}{k}, \frac{k}{m}, \frac{m}{l}, \frac{l}{m} \leq 7.$$

Among them, the optimal solutions are discovered in about 350 kinds of chemical composition. Although the number of optimal solutions for each chemical composition obtained by mathematical crystal chemistry tends to be very small, it is difficult to execute *ab-initio* simulation for all the optimal structures for evaluating structural stability due to too many chemical compositions. Therefore, I must pick up primising crystal structures from them to predict synthesizable materials. At first, I select crystal structures consisting of the smaller number of wyckoff positions, and I evaluated the formation enthalpies of them. Accordingly, I found several materials whose formation enthalpies per atom are less than 0.1 eV/atom compared to the several experimentally known decomposition mixtures.

I should note that the software **MARICI** also implements the algorithm to create chemical bonds based on Voronoi polyhedra, which is also formulated by GDP. Accordingly, I confirmed that only one type of crystal structure (e.g. $CeP_2Al_3O_{14}$) makes the kagome lattice of octahedra via edge or face sharings among the $A_kB_lC_mO_n$ and $A_kB_lD_mO_n$ crystal structures. Since I successfully discovered new crystal prototypes with kagome lattice, we can expect that mathematical crystal chemistry will find many unknown crystal structures with exotic quantum phenomena.

Furthermore, the algorithm to calculate Eward Sum is also implemented in the software **MARICI**. To remove most of unpromising crystal structures from all the optimal solutions, at first I calculate the Löwdin charge of each cation in the simple binary compounds by the software **LOBSTER** [Peter C. Müller *et al.*, J. Phys. Chem. C **125**, 7959 (2021)]. Next, the atomic charges are assigned to all the cations to calculate Madelung energies to estimate the structural stability. Accordingly, I found that some of the crystal structures have negative Madelung energy compared to the convex hull consisting of the Madelung energies of experimentally known materials. The "promising" structures do not necessarily have high symmetry or consist of small number of wyckoff positions. The result shows that the estimation of structural stability by the classical model is effective. The AI techniques are considered to be more robust and effective to select promising structures, but I plan to make finishing mathematical crystal chemistry as the extension of inorganic structural chemistry without AI techniques.

Finally, we can suggest the new coputational scheme to predict unknown materials. First, the feasible atomic environments of each atom is assumed. Second, crystal structure prototypes are dicovered by solving GDP. Third, atomic charges of atoms are evaluated to calculate Madelung energy. Fourth, we remove most of unstable structures with respect to Madelung energy. Fifth, we execute *ab-initio* simulation to confirm the structural stability. We will show that this scheme is very effective by succeeding in synthesizing new oxides with experimentalists based on mathematical crystal chemistry.

Now I collect many data of crystal structure prototypes. I will continue to use the supercomputer of ISSP, and I plan to write a few papers in the academic year of 2026.

References

[1] R. Koshoji and T. Ozaki, Phys. Rev. Mater. **8**, 113801 (2024).

[2] R. Koshoji, Physical Review Research **7**, 033078 (2025).

[3] https://marici.mathematical-crystal-chemistry.solutions

Study on structure-properties relationship in uniform/dynamic polymer networks via precise graph structure analysis.

Yusuke Yasuda

The Graduate School of Frontier Sciences, the University of Tokyo, Kashiwa-no-ha, Kashiwa, Chiba 277-8561

Introduction

Polymer gels and cross-linked rubbers are widely used materials that exhibit both flexibility and toughness. However, their network structures are heterogeneous, making it difficult to quantitatively describe their mechanical properties based on structure. In particular, the quantitative impact of cross-links and structural defects on elasticity remain poorly understood. Recent approaches to improving mechanical performance include the homogenization of strand lengths and the introduction of dynamic cross-links. Nevertheless, clear molecular design principles have not yet been established.

In our previous work, we developed a graph-based structural analysis algorithm for tetra-/tri-PEG like networks (SPNs) enabling the extraction of elastically effective cross-links and strands and the quantitative prediction of elastic modulus [1]. However, the general applicability of this method to other networks remains unclear.

In this study, we apply coarse-grained molecular dynamics simulations and graph-based structural analysis to TPNs (Fig. 1.) to elucidate the effective network for elasticity.

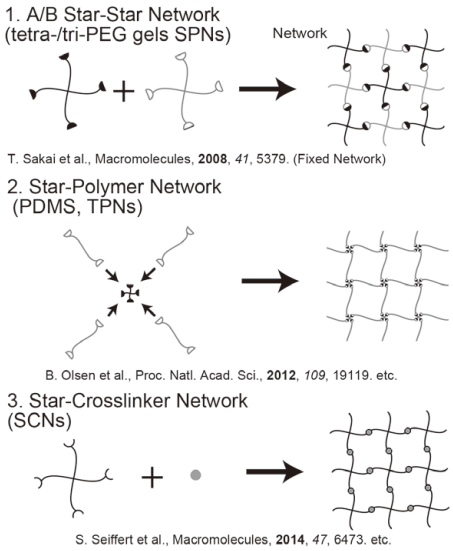


Fig.1. Schematics of TPNs, SPNs, SCNs

Computational Methods

Uniformly cross-linked PDMS-like networks (Telechelic Polymer Networks, TPNs) with tri- and tetra-functional junctions were constructed, and their mechanical properties were systematically evaluated. The developed graph-based analysis method was applied to extract effective network structures.

For comparison, tetra-PEG/tri-PEG networks (Star Polymer Networks, SPNs) and networks formed via star-shaped macromers and crosslinker molecule (Star Crosslinker Networks, SCNs) were also constructed.

Each system consisted of approximately

100,000 particles. After sufficient equilibration and cross-linking reactions, uniaxial stretching simulations were performed along three directions at a constant strain rate (10^{-6} τ^{-1}), and stress–strain curves were obtained. Excluded-volume interactions were introduced in all simulations.

Results and Discussions

(1) Comparison between SPNs and TPNs

The elastic modulus calculated from the density of effective strands and junctions using the phantom network model was compared with simulation results. Both SPNs and TPNs exhibited a scaling relationship with a slope of approximately 2 [3].

TPNs showed lower modulus values than SPNs. This difference originates from the formation of primary loop structures, which remain as elastically inactive defects in TPNs, whereas in SPNs such structures can be transformed into effective strands during network formation [3].

Consistently, simulations of dynamic cross-linked elastomers revealed that the elastic modulus initially increases and subsequently decreases over time, accompanied by a conversion of intermolecular cross-links into intramolecular ones [4]. This transition leads to an increase in loop-like, elastically inactive structures, supporting the interpretation that loop formation governs the reduction in elasticity.

However, TPNs showed lower modulus values than SPNs. This difference originates from the formation of primary loop structures, which remain as elastically inactive defects in TPNs, whereas in SPNs such structures can be transformed into effective strands during network formation [3].

(2) Comparison between TPNs and SCNs

Stress–strain curves were compared by varying strand length, functionality, and cross-linking density. For identical strand length and functionality, TPNs and SCNs exhibited nearly identical mechanical responses. (Fig. 2. as an example) This suggests that when network strand length is equivalent, effective network structure does not depend on relative size of multifunctional/bifunctional precursors.

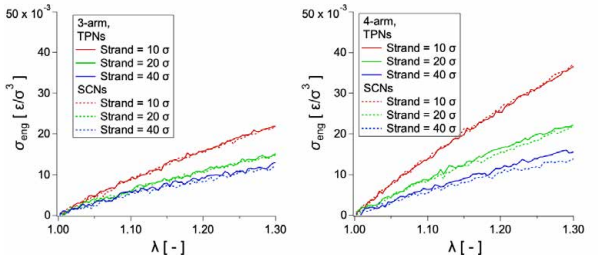


Fig. 2. Stress-elongation curves of TPNs and SCNs with conversion = 0.96 at various network strand lengths and number of branches.

References [1] Y. Yasuda and H. Morita, Macromolecules **57**, 4804 (2024).

[2] N. Sakumichi, Y. Yoshikawa, and T. Sakai, Polym J **53**, 1293 (2021).

[3] Y. Akagi, K. Fujimoto, and Y. Yasuda, Polym J **57**, 1183 (2025).

[4] Y. Yasuda *et al.*, Polym J **57**, 467 (2024).

MD Simulations on Single-Molecule Reactors based on Bottlebrush Polymers

Yusuke Yasuda

The Graduate School of Frontier Sciences, the University of Tokyo, Kashiwa-no-ha, Kashiwa, Chiba 277-8561

Introduction

Bottlebrush polymer reactors (BBPRs), recently developed by Nakagawa et al., , are nanoscale reactors for polymerization constructed by grafting substrate monomers and long side chains onto a polymer backbone[1]. Owing to the excluded-volume effect of the side chains, intermolecular polymerization is suppressed, while catalyst molecules can freely penetrate the brush region and react with substrate monomers. As a result, substrates are locally concentrated within the brush, enabling precise intramolecular polymerization within a single molecule [1]. However, the molecular mechanism underlying this process remains unclear, so computational investigation is required.

In this study, we constructed a coarse-grained model of BBPRs, then analyzed static property and reaction kinetics using coarse-grained molecular dynamics simulations using various brush and main chain lengths. The resulting structures and reaction efficiencies were systematically evaluated.

Calculation Methods

Polymer backbones and grafted chains were modeled using the Kremer–Grest bead–spring model, where approximately five to six carbon atoms were coarse-grained into a single bead. Nine systems were prepared with backbone lengths of 50, 100, and 200 beads and side-chain lengths of 10, 20, and 40 beads. The ratio of monomer to brush segments in the side chains was set to approximately 1:1. The number of initiator beads are set as 1/5 of monomer beads.

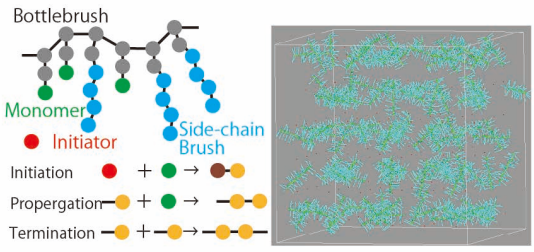


Fig.1. Reaction protocols of BBPRs and snapshot of a system.

First, equilibrium simulations were conducted in the dilute regime to evaluate the radius of gyration R_g, from which the overlap concentration φ^* was estimated. Subsequently, 23–266 molecules were introduced into the simulation box to maintain a total particle number of approximately 100,000. Reaction conditions were implemented via kinetic Monte

Carlo simulations (Fig.1.). The molecular weight distributions after reaction were analyzed to elucidate the shielding effect of the brush architecture.

Results and Discussion

After sufficient equilibration in the dilute regime ($\varphi=0.0085\sigma^{-3}$) the mean-square radius of gyration $<R_g^2>$ was evaluated, and the overlap concentration was defined as:

$$\varphi^* = \frac{3N_{\mathrm{br}}}{4\pi < R_{\mathrm{g}}^2 >^{\frac{3}{2}}}$$

Where N_{br} is the total number of beads per bottlebrush molecule. The resulting φ^* values ranged from 0.04 to 0.15 across all systems. Based on this, reaction simulations were performed in the semidilute ($\varphi=0.085\sigma^{-3}$) and melt ($\varphi=0.85\sigma^{-3}$)) regimes, and reaction kinetics were analyzed over $10^4\tau$

In the concentrated regime, intermolecular polymerization dominated, leading to gelation of the entire system into a single macromolecule. In contrast, in the semidilute regime, polymerization behavior depended strongly on the side-chain length.

The average degree of polymerization of brushes was defined as N_w/N_{br}, where N_w is the weight-average molecular weight. As shown in Figure 2, the average degree of polymerization decreased with increasing side-chain length, while it was less sensitive to backbone length. This indicates that longer side chains effectively shield intermolecular reactions and promote intramolecular polymerization, consistent with experimental observations.

Conclusion

In this study, bottlebrush polymer reactors (BBPRs) were investigated using coarse-grained molecular dynamics simulations. By systematically varying brush length and concentration, we demonstrated that the excluded-volume effect of the brush suppresses intermolecular reactions and promotes intramolecular polymerization, resulting in narrower molecular weight distributions.

Although free-radical polymerization was considered in this work, extending the analysis to living radical and condensation polymerizations is expected to further establish the general applicability of this reactor concept.

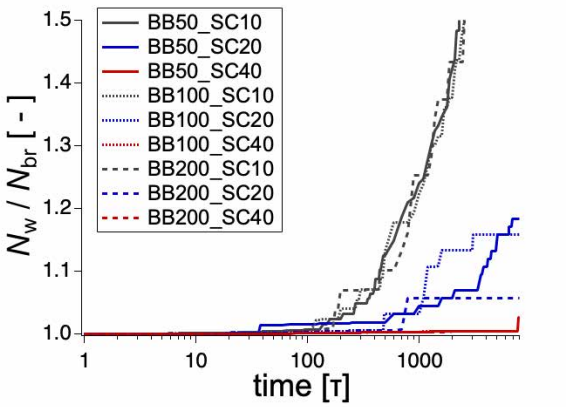


Fig. 2., Reaction time dependence of the average degree of polymerization, bottlebrushes with main chain length = x, side-chain length = y is labeled as BBx_SCy

References [1] X. Guo et al., J. Am. Chem. Soc. 147, 23910 (2025)

Molecular dynamics simulation of disease-causing protein aggregates

Hisashi Okumura

Exploratory Research Center on Life and Living Systems,

Institute for Molecular Science, Okazaki, Aichi 444-8585

Protein aggregates such as oligomers and amyloid fibrils cause more than 40 diseases. For example, Alzheimer's disease is caused by aggregated amyloid-β (Aβ) peptides. We have performed molecular dynamics (MD) simulations to understand the aggregation and disaggregation mechanisms of Aβ peptides.

Recent studies have revealed that the aggregation propensity of Aβ peptides depends on the curvature of the cell surface. Specifically, Aβ peptides tend to aggregate more readily as the radius of curvature decreases. However, the underlying mechanism remains unclear. Since Prof. Noguchi at ISSP is an expert in membrane simulations, we initiated a collaborative study with him to elucidate how membrane curvature influences Aβ peptide aggregation.

First, a lipid bilayer and an aqueous NaCl solution were placed in a simulation box, and molecular dynamics simulations were performed. During the simulation, when the system was gradually compressed laterally while maintaining a constant volume, the membrane suddenly bent at a certain point, and buckling behavior was observed. We generated highly curved membranes in this way. We then placed Aβ peptides on them, and are currently continuing molecular dynamics simulations (Figure 1). In parallel, we are also performing simulations of Aβ peptides on flat lipid bilayers without buckling.

We plan to analyze structural changes in Aβ peptides induced by membrane interactions and to elucidate the mechanism by which membrane curvature affects the aggregation propensity of Aβ peptides.

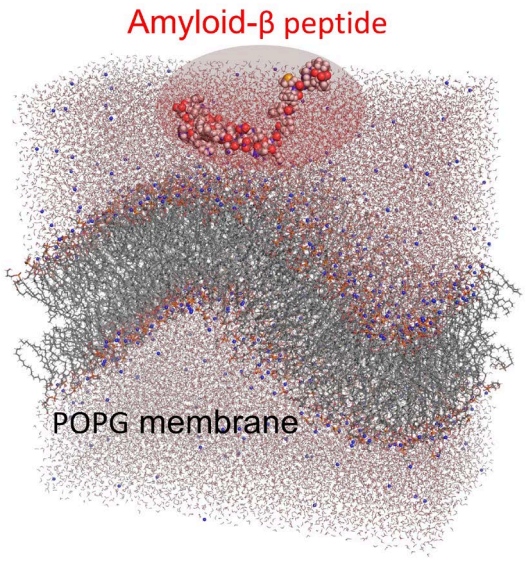


Fig. 1: Molecular dynamics simulation of amyloid-β on POPG membrane.

Dynamics of active Potts models with factorizable numbers of states

Hiroshi NOGUCHI
Institute for Solid State Physics, University of Tokyo

We simulated the nonequilibrium dynamics of q-state active Potts models in square and hexagonal lattices [1–4]. A cyclic flip consumes energy (state $s = 0 \to 1 \to 2 \to 0$ in the three-state Potts model). At low and high flipping energy, the homogeneous cycling and wave modes occur, respectively, for $q \in \{3, 8\}$ at cyclically symmetric conditions. We found that several modes with factorized symmetry additionally emerge when q is factorizable [1]. For example, the modes shown in Fig. 1 are obtained at $q = 6$. In particular, three even- or odd-numbered states ($s = 0, 2, 4$ or $s = 1, 3, 5$) can form domains of spiral waves with two different parameter regions [Fig. 1(c) and (d)]. They rotate forward ($s = 1 \to 3 \to 5 \to 1$) and backward ($s = 1 \to 5 \to 3 \to 1$) directions owing to the stability of the minor three states at the domain boundaries (green domains are inside of red domains in Fig. 1(c) but outside in Fig. 1(d)) [4]. Nucleation and growth at the domain boundary play an essential role in these three-state spiral waves.

When the diagonal states (e.g, $s = 0$ and 3) have attractions, the diagonal states are mixed. The three mixed domains can form spiral waves as shown in Fig. 1(e). When mixed states cover the entire lattices, the dominant two states cyclically change [Fig. 1(f)].

We revealed that the transition between three-state wave and six-state mixing modes is second-order, and its scaling exponents are modified from the equilibrium values [1]. In contrast, the transition between the homogeneous cycling and mixing modes of three states is also second-order, but no change is detected in the exponents. Moreover, a first-order transition is obtained between the waves of three even- or odd-numbered states under asymmetric contact energies, as in the Ising model under a magnetic field [4].

During coarsening from a random mixture to a uniform equilibrium phase in Potts models, the domain length grows proportionally to $t^{1/2}$, following the Lifshitz–Allen–Cahn law. We found that the growth exponent transiently increases slightly before the saturation to spiral waves in the active Potts models [3]. The transient increase is greater at higher q. The coarsening to the three-state waves at $q = 6$ exhibits similar domain growth to that in the three-state active Potts model. We also confirmed that the choice of lattice type (square or hexagonal) and update scheme (Metropolis or Glauber) does not alter the dynamic behavior.

References

[1] H. Noguchi, Phys. Rev. Res. 7, 033243 (2025).

[2] H. Noguchi, Phys. Rev. E 113, 034210 (2026).

[3] H. Noguchi, Phys. Rev. E 113, 054108 (2026).

[4] H. Noguchi, arXiv:2604.22353 (2026).

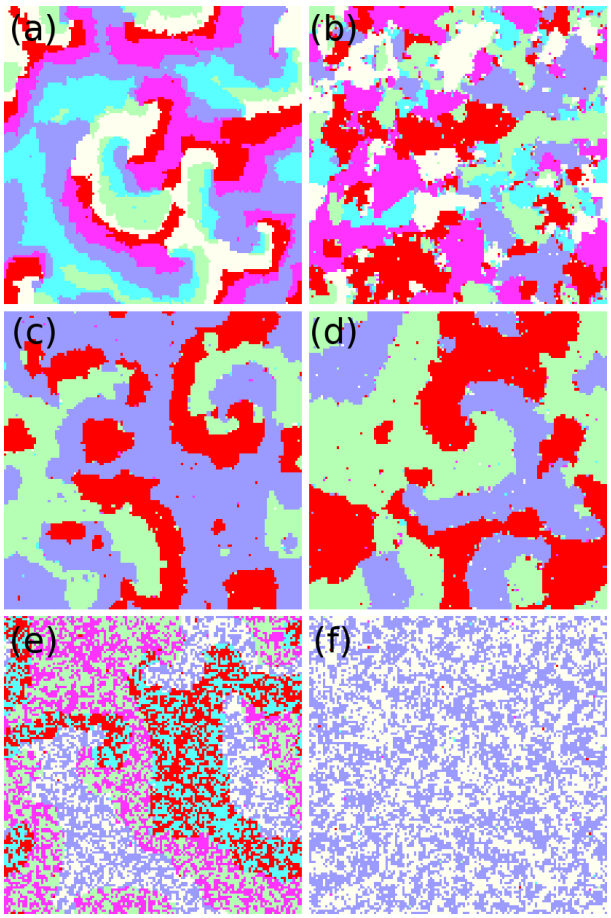


Figure 1: Snapshots of the active six-state Potts model [1]. (a) Spiral waves. (b) Disordered waves. (c) Forward waves of three states. (d) Backward waves of three states. (e) Waves of three domains comprising two diagonal states. (f) Homogeneous cycling of mixed diagonal states. The light yellow, light green, cyan, blue, magenta, and red sites (light to dark in grayscale) represent $s = 0$, 1, 2, 3, 4, and 5, respectively.

Efficient sampling simulation of the soft modes significantly that contributes to protein properties

Duy Tran, Zhen Bai, Soichiro Kijima, Wenbo Lu, Toan Vi Lam, Yoshito Hasegawa, Reiya Hayashi, Yoshie Iijima, Kazuki Tanaka, Eisuke Tamura

School of Life Science and Technology,

Institute of Science Tokyo, Ookayama, Meguro-ku, Tokyo 152-8550

Lysine acetylation is a critical, reversible post-translational modification that modulates protein functions by altering local charge and conformation. Among the enzymes regulating this process are sirtuins, such as the NAD+-dependent deacetylase Sir2, which play essential roles in stress resistance, energy metabolism, and aging. A major target for Sir2 is the tumor suppressor protein p53, particularly its C-terminal domain where acetylation at residue K382 regulates transcriptional activity and stability. Although the binding of p53 to Sir2 has been structurally characterized, the precise regulatory role of the conserved cofactor-binding loop in facilitating NAD+ entry remained poorly understood.

To investigate the loop dynamics, we employed a combination of conventional molecular dynamics and parallel cascade selection molecular dynamics simulations [1] to capture rare conformational transitions. These advanced techniques allowed for the characterization of the conformational space occupied by apo Sir2 as well as complexes bound to either acetylated or nonacetylated p53 [2]. By defining specific surface areas at the entrance of the NAD+-binding pocket as shown in Fig. 1, the study was able to quantitatively distinguish between various open and closed states of the enzyme. The simulations revealed that the cofactor-binding loop acts as a flexible ceiling for the binding pocket, directly influencing the accessibility of NAD+.

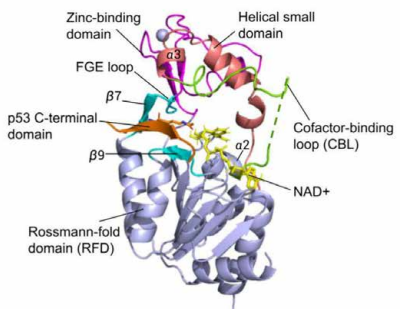


Fig. 1: The structure of the Sir2-Af2 complex with acetylated p53.

The findings suggest that the acetylation status of p53 exerts a profound allosteric influence on the structural state of Sir2. Specifically, the binding of acetylated p53 was found to drive the cofactor-binding loop into an open conformation, which significantly expands the entrance to the NAD+-binding

pocket and facilitates the deacetylation reaction. Conversely, when Sir2 is bound to nonacetylated p53 or exists in its apo form, it predominantly adopts closed conformations that naturally impede the entry of NAD+. This indicates that the presence of the acetyl group on the substrate is the key signal that triggers the enzyme's transition into a catalytically receptive state.

This sequential regulation is characterized as a tandem allosteric effect, where both the reactant and the product contribute to the efficiency of the catalytic cycle. Initially, the forward allosteric effect of the reactant promotes cofactor binding by opening the pocket to allow NAD+ entry. Following the deacetylation of p53, the resulting product exerts a reverse allosteric effect that drives the pocket toward a closed state. This closure likely prevents the rebinding of inhibitors like nicotinamide and facilitates the release of reaction products, thereby preventing the reverse reaction and accelerating the overall cycle.

Analysis of entropy transfer pathways identified how the allosteric signal from residue K382 of p53 travels through the Sir2 structure to reach the distant cofactor-binding loop as shown in Fig 2. The communication involves multiple interconnected routes passing through the Rossmann-fold domain, the helical small domain, and the zinc-binding domain. Many of the residues involved in these signaling pathways, as well as those stabilizing the open and closed states, are highly conserved across species ranging from archaea to humans. This conservation suggests that the tandem allosteric mechanism is a universal feature of the Sir2 family, providing a fundamental framework for their biological functions.

These insights into the molecular mechanisms of Sir2 opening and closure have significant implications for drug discovery and disease intervention. Understanding how to specifically target the closure mechanisms of the NAD+-binding pocket could lead to new classes of inhibitors that obstruct NAD+ binding, offering alternatives to traditional pocket-occupying drugs.

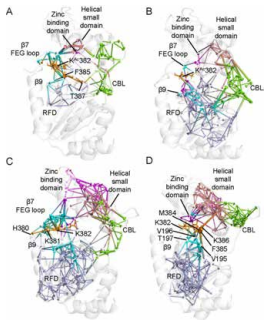


Fig. 2: Allosteric communication pathways from $K^{Ac}382$/K382 to the CBL during the opening and closure processes of the NAD+-binding pocket. (A) S1 opening. (B) S2 opening for Sir2/$K^{Ac}382$-p53. (C) S1 closure. (D) S2 closure for Sir2/p53.

References

[1] R Harada, A. Kitao, J. Chem. Phys. 139, 035103 (2013).

[2] Z. Bai, D.P. Duy, A. Kitao, J. Chem. Inform. Modeling 65, 11326 (2025).

Nonlinear particle-continuum switching in multiscale Smoothed-Particle Hydrodynamics (SPH) method

Yohei MORII[1,2] and Toshihiro KAWAKATSU[1,2]

1) *Department of Physics, Tohoku University, Sendai, Miyagi 980-8578*

2) *Admissions Center, Tohoku University, Sendai, Miyagi 980-8576*

There are two regions in a complex polymeric flow around an obstacle, i.e. the bulk flow region and the boundary layer region near the obstacle surface. We have been developing an "embedding-type multiscale simulation" where the macroscopic flow is simulated using smoothed particle hydrodynamics (SPH) simulation where the local constitutive relation is determined by microscopic simulator (MicS) embedded in each of the SPH particles. For an accurate evaluation of the local stress field, we usually embed a molecular dynamics (MD) simulator as MicS. As the use of such molecular dynamics simulators requires a large amount of computational resources, it is desired to accelerate the simulation by switching the MD simulator with a much faster simulator such as an analytic constitutive model when the local stress is less than a threshold value. In Ref.[1], we applied such a switching technique between MD simulator and a linear viscoelastic constitutive model in the boundary layer near the obstacle.

In highly nonlinear and non-Markovian complex viscoelastic and elastoplastic flows, however, the use of the linear constitutive model is not enough to realize a high efficiency of the switching technique. Therefore, we developed a switching technique using nonlinear constitutive model and applied it to a MicS composed of nonlinear dumbbell molecules bonded with an FENE (finite extensible nonlinear elastic) spring [2]. Figure 1 shows a comparison between a switching technique using linear constitutive model (Fig.1(a)) and that using nonlinear constitutive model (Fig.1(b)). Shown are the time evolution of the local normal stress of a system under an external oscillatory elongation and compression deformation, where the red data were calculated with constitutive model and the green data with MD simulations. While linear constitutive model shows discontinuity at the switching time, the nonlinear constitutive model can be smoothly connected to the MD simulation. It is also confirmed that the linear

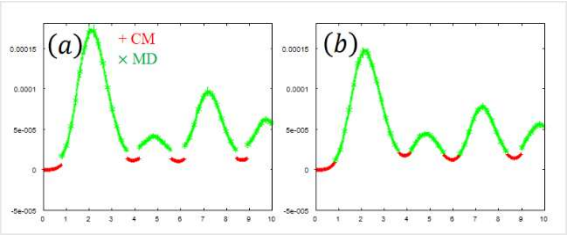


Figure 1: Time evolution of the normal stress under a periodic elongation and compression deformation simulated with a switching technique using (a) linear constitutive model and (b) nonlinear constitutive model, respectively.

constitutive model overestimates stress while the nonlinear one does not.

Figure 2 shows a snapshot of a flow near a surface of a cylindrical obstacle (bottom right) simulated with the nonlinear switching technique, where the parameters of the nonlinear dumbbell molecules in the MD simulation are chosen so that the dumbbell corresponds to a DNA. In this figure, white SPH particles are those with nonlinear constitutive model and non-white SPH particles are those with embedded MD simulators. The color legend shows the trace of the deviation of the bond orientation tensor from its equiribrium value, i.e. unit tensor. This figure shows that the nonlinear switching can successfully simulate the polymeric flow near the obstacle.

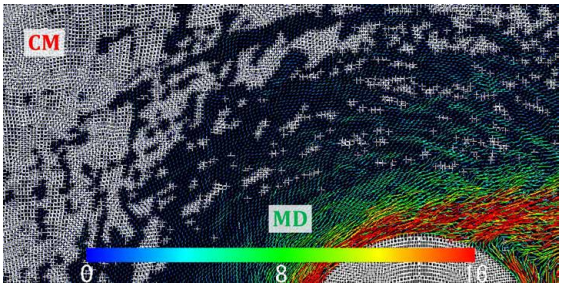


Figure 2: A snapshot of a flow near a cylindrical obstacle.

Acknowledgement

The computation in this work has been done using the facilities of the Supercomputer Center, the Institute for Solid State Physics, the University of Tokyo.

References

[1] Y.Morii and T.Kawakatsu, Phys. Fluids, **33**, 093106 (2021).

[2] Y.Morii and T.Kawakatsu, *in preparation.*

[3] Y.Morii and T.Kawakatsu, “Multiscale simulations using particle-field hybrid model”, International Conference on Principles of Soft Matter Science, Wenzhou, China (11 May, 2025).

[4] T.Kawakatsu, “Coarse-grained and multiscale simulations of polymers”, International Workshop on Computational Soft-Matter, Sendai, Japan (6 March, 2026)

Molecular dynamics simulation studies of soft matters

Takahiro MURASHIMA

Department of Physics,

Tohoku University, 6-3, Aramaki-Aza-Aoba, Aoba-ku, Sendai, Miyagi 980-8578

We systematically investigated the nonlinear rheology of equi-weight blends of ring and linear polymers under uniaxial elongational flow by coarse-grained molecular dynamics simulations, and identified for the first time the threshold chain length for the emergence of stress overshoot [1]. Using flexible Kremer‐Grest chains (Ne ≈ 80, Ntot ≈ 600,000), we varied the number of entanglements Z = N/Ne = 1, 2, and 4. The shorter chains (Z ≤ 2) exhibited only monotonic stress growth, whereas a clear stress overshoot emerged at Z ≈ 4. Stress decomposition, a topological analysis based on the Gauss linking number, and a conformational analysis revealed that at the threshold chain length each ring is penetrated on average by three to four linear chains, and that this "multiple threading" state excessively stretches the rings, giving rise to the stress peak via subsequent unthreading. Previously, stress overshoots in ring-linear blends had been reported only for highly entangled systems (Z ≈ 14), which are difficult to synthesize and purify. Our finding that the phenomenon already appears at Z ≈ 4 lowers the experimental hurdle substantially, since moderately entangled rings are much more accessible via liquid chromatography at the critical condition (LCCC). We also predicted two-dimensional SANS patterns as a direct structural signature of the thread-to-unthread transition, providing a concrete route for experimental validation. These results were available on arXiv [1].

In NEMD simulations of elongational flow, the simulation box deforms with the flow and the minimum image distance eventually vanishes. For planar elongation, the Kraynik‐Reinelt (KR) boundary conditions [3] give a time-periodic lattice, but no such time-periodic lattice exists for uniaxial or biaxial elongation with real-eigenvalue automorphisms [3]. Dobson [4] proposed the generalized KR (g-KR) boundary conditions using two commuting automorphisms to keep the lattice deformation bounded; our existing code UEFEX [2] is based on this framework. More recently, Dobson and Geraldo [5] proposed the Rotating KR (R-KR) boundary conditions, which use a single automorphism with complex conjugate eigenvalues, are time-periodic up to a rotation for uniaxial and biaxial flows, and analytically give a larger minimum image distance than g-KR. However, Ref. [5] presented only the concept and algorithm; no actual MD

implementation had been reported. In this work, as the first implementation of the R-KR method in an MD code, we developed a new LAMMPS plugin that supports R-KR for uniaxial/biaxial elongation and KR for planar elongation (Figs. 1 and 2).

To validate the implementation, we compared the LAMMPS + KR/R-KR results with those of UEFEX [2] for Kremer‐Grest polymer melts under identical conditions. As shown in Fig. 3, the stress-strain curves from the two codes agree within statistical error for uniaxial, biaxial, and planar elongations, providing the first numerical demonstration that R-KR works correctly in actual NEMD simulations. Combined with the extensive potentials and parallelization of LAMMPS, the plugin now enables large-scale NEMD simulations of all three elongational flow geometries. The larger minimum image distance of R-KR is especially beneficial for ring-linear blends with extended rings, which we plan to exploit for higher-Z systems and various mixing ratios beyond Ref. [1]. The packages (KR and R-KR) will be released on GitHub [6].

References

[1] T. Murashima, K. Hagita, and T. Kawakatsu, arXiv:2603.25505 (2026).

[2] T. Murashima, K. Hagita, and T. Kawakatsu, Nihon Reoroji Gakkaishi, **46**, 207 (2018).

[3] A. Kraynik and D. Reinelt, Int. J. Multiphase Flow, **18**, 1045 (1992).

[4] M. Dobson, J. Chem. Phys., **141**, 184103 (2014).

[5] M. Dobson and A. K. A. Geraldo, J. Comp. Phys., **473**, 111740 (2023).

[6] https://github.com/t-murash

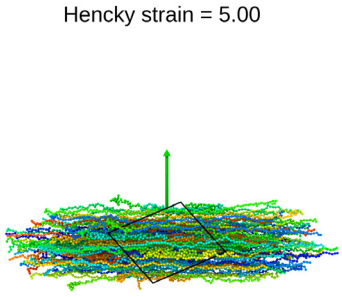


Fig. 1: KR boundary condition for planar elongation

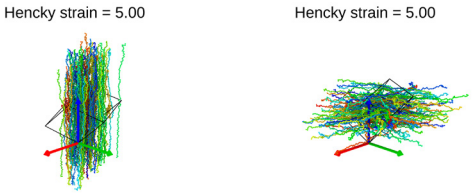


Fig. 2: R-KR boundary condition for uniaxial elongation (left) and biaxial elongation (right).

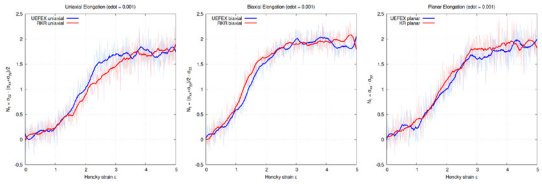


Fig. 3: Comparison of stress-strain curves between UEFEX and R-KR for uniaxial (left) and biaxial (center) elongations and between UEFEX and KR for planar (right) elongation.

Creating a quantum computing database for sensor materials

Wataru Mizukami

Center for Quantum Information and Quantum Biology, Osaka University, Osaka 560-0043, Japan

Over the past decade, quantum-computing hardware has advanced substantially. Although noise remains a major challenge, the field is entering a regime in which classical emulation is becoming increasingly difficult. There is also growing interest in tackling difficult real-world problems through hybrid quantum-classical approaches that combine quantum computers with high-performance computing (HPC). In such a context, our research focuses on developing hybrid quantum-classical methods for materials simulation, particularly for sensor materials. This includes machine-learning approaches that use results from quantum computers, as well as the development of sampling-based algorithms.

In the past year, we applied the framework of Sakka et al. [arXiv:2504.07396], which uses large language models to automatically generate, evaluate, and refine quantum feature maps for quantum machine learning, to materials systems. Using a quantum kernel method, we designed quantum feature maps that enable efficient and accurate modeling of real-world chemical data, such as NMR chemical shifts.

Another line of our work concerns QSCI (Quantum-Selected Configuration Interaction), a representative sampling-based algorithm that we previously developed. QSCI uses samples obtained from a quantum computer to identify important electron configurations and then diagonalizes the electronic-structure Hamiltonian in the resulting subspace on classical computers. The method is well suited to quantum-HPC workflows, and its applications have been expanding both in Japan and internationally. For example, IBM provides the QSCI functionality through its Qiskit addon as the sample-based quantum diagonalization (SQD) package. We have recently developed a method that effectively doubles the number of spatial orbitals accessible to QSCI by restricting the space sampled on the quantum computer to the seniority-zero space, in which spatial orbitals are either doubly occupied or empty [arXiv:2602.07912]. This approach was then combined with the QSCI-AFQMC method that we reported last year, yielding a DOCI-QSCI-AFQMC workflow. The resulting workflow was evaluated on the H_6 chain, N_2 dissociation, and the addition of singlet oxygen to a BODIPY dye. Calculations were also carried out on actual quantum hardware, yielding quantitatively meaningful results. Together, these developments provide methodological foundations for building a quantum-computing database for sensor-materials research.

Investigation of Unknown Ice Phases Using Large-Scale Metadynamics Simulations with Unsupervised Machine Learning

Hiroki NADA

Faculty of Engineering, Tottori University, 4-101 Koyama-Minami, Tottori 680-8552

Ice polymorphism is an important research subject, because it plays important roles in the Earth's environment, our daily life, and industry. Recently, a new amorphous ice phase, which has an intermediate density between high- and low-density amorphous ice phases, was discovered experimentally [1], implying the existence of many other unknown ice phases.

In this project, a molecular dynamics (MD) simulation was conducted to search for unknown ice phases. To determine whether amorphous ice phases, which are detected with the MD simulation, correspond to unknown ones, the structure of those phases were analyzed with a method of unsupervised machine learning [2]. To check whether those phases correspond to local minimum ones, an MD simulation combined with the metadynamics (MTD) method (MTD simulation) [3] was also carried out.

The MD simulation was performed for an amorphous ice phase, which was created by quenching a liquid water phase at 1 atm and every 100 atm in the pressure range of 0–3000 atm. The interaction between pairs of water molecules was calculated using the TIP4P/Ice model. The simulation was carried out with DL_POLY 2.20 [4], in which PLUMED 1.3 [5] was implemented, using System C of ISSP Supercomputer Center.

Results of the analysis with the unsupervised machine learning method indicated that the structure of amorphous ice phase changed around 1500 atm. The density of amorphous ice as a function of pressure also showed a discontinuous change around 1500 atm. A free energy surface obtained with the MTD simulation showed a few shallow minima, implying the existence of a few different amorphous ice phases.

References

[1] A. Rosu-Finsen at al.: Science **379** (2023) 474.

[2] H. Nada: Sci. Rep. **10** (2020) 15465.

[3] A. Laio and M. Parrinello: Proc. Natl. Acad. Sci. U. S. A. **99** (2002) 12562.

[4] W. Smith and T. R. Forester: J. Mol. Graph. **14** (1996) 136.

[5] M. Bonomi et al.: Comput. Phys. Commun. **180** (2009) 1961.

A Metadynamics Simulation Study on the Mechanism of Ice VI Formation

Hiroki NADA

Faculty of Engineering, Tottori University, 4-101 Koyama-Minami, Tottori 680-8552

According to a phase diagram of water, ice VI is stable at pressures higher than 0.96 GPa at 298 K. However, Lee et al. observed the formation of ice VII in the stability region of ice VI [1]. The reason for it remains elusive. Therefore, in this project, a molecular dynamics (MD) simulation based on the metadynamics (MTD) method (hereafter, MTD simulation [2]) was conducted to resolve this reason.

The MTD simulation was performed for a rectangular-parallelepiped system consisting of 2880 water molecules. The interaction between pairs of water molecules was calculated using the TIP4P/Ice model. The volume of the system was maintained to reproduce the equilibrium density of liquid water at 298 K and 2.12 GPa in the TIP4P/Ice model. Following a previous study [3], two discrete oxygen-oxygen radial distribution functions represented by Gaussian window functions were used as collective variables. The MTD simulation was carried out with DL_POLY 2.20 [4], in which PLUMED 1.3 [5] was implemented to permit combination with the MTD method, using System C of ISSP Supercomputer Center.

Simulation results indicated the formation of a liquid water phase that had a different structure from that of the equilibrium liquid water at 298 K. A free energy surface obtained with the MTD simulation indicated a shallow local minimum at the position of this phase, suggesting the detected phase was a metastable one. Pair-distribution functions and angular distribution functions were analyzed for this detected phase. Results of the analysis indicated that the arrangement of water molecular oxygen atoms was in a highly ordered state like ice VII. We speculate that this detected phase is related to the formation of ice VII in the stability region of ice VI.

References

[1] G. W. Lee et al.: Phys. Rev. B **74** (2006) 134112.

[2] A. Laio and M. Parrinello: Proc. Natl. Acad. Sci. U. S. A. **99** (2002) 12562.

[3] H. Nada, Sci. Rep. **10** (2020) 4708.

[4] W. Smith and T. R. Forester: J. Mol. Graph. **14** (1996) 136.

[5] M. Bonomi et al.: Comput. Phys. Commun. **180** (2009) 1961.

Machine Learning and Molecular Dynamics Simulation-Assisted Structural Optimization of Carbon Nanotube Yarns

Go Yamamoto and Redha A. Ramadhan

Department of Aerospace Engineering,

Tohoku University, 6-6-01 Aramaki-Aza Aoba, Aoba-ku, Sendai 980-8579

In this study, molecular dynamics (MD) simulations were used to model carbon nanotube yarns (CNTYs) under tensile loading. The nominal strength — defined as the strength of a CNTY accounting for its hollow core — was used as the optimization objective. Approximately 100 models with varying structural parameters were simulated across multiple supercomputers, including ISSP at the University of Tokyo. Each model was simulated three times, yielding around 300 data points comprising structural parameters and nominal tensile strength values. Based on these results, machine learning optimizations were conducted to identify the combination of structural parameters that yields the highest nominal tensile strength. A parametric study was also carried out to understand the relationships between various parameters and their impact on CNTY strength.

The MD simulations were conducted primarily using Python-based input scripts[1] and run on Supercomputer System B (Ohtaka) at ISSP. For each model, the base files were first prepared on a local computer. Once the model build was complete, the base files were uploaded to ISSP, where LAMMPS was executed using those files as input. Each model typically required 512 nodes with a 100-hour wall time, using the L4cpu partition. Upon completion of the MD simulations, post-processing was performed on a local computer to conserve the computational quota at ISSP. The post-processing stage extracted the relevant data from each simulated model, including the nominal tensile strength and the simulated twist angle. The simulations yielded nominal tensile strength data for CNTYs with different structural parameters, which served as the training dataset for subsequent machine learning-based structural optimization.

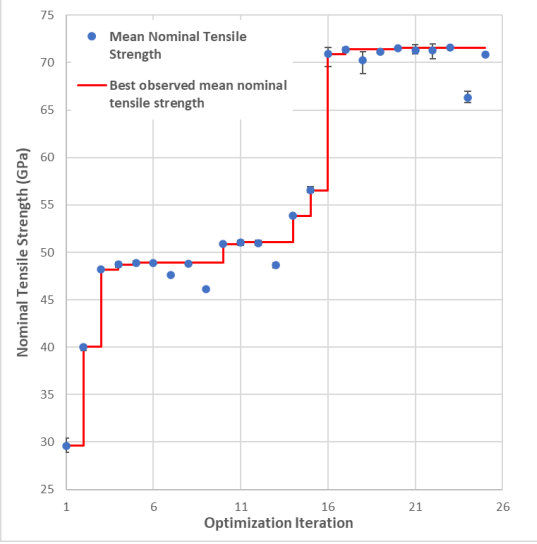


Figure 1. Plot of the main optimization generation vs the nominal strength of CNTY

The main optimization revealed that the optimal CNTY structure is characterized by an

armchair configuration, a small inner tube diameter, a low wall count, near-zero crosslink density between walls, and a low twist angle. Compared to our previous parametric study[1], the optimization favored a wall count of 2 with no interwall crosslinks. This is attributed to the fact that crosslinks introduce defects in the CNTY wall, thereby reducing nominal tensile strength. The progression of nominal tensile strength across the main optimization generations is shown in Figure 1.

To further investigate the relationship between crosslink density and nominal tensile strength, a separate machine learning optimization was conducted on a 5-wall CNTY group, following the same procedure but with the wall count fixed at 5. The crosslink densities between walls were varied from 0.00% to 1.90%. This optimization retained the preference for a small inner wall diameter and a low twist angle. However, in the 5-wall case, models with interwall crosslink densities above 1.00% tended to yield higher tensile strength. From these findings, it was concluded that in multi-wall CNTYs with a high wall count and large inner wall diameter, a high crosslink density is preferable to facilitate interwall load transfer. When the outer wall fails, the load is transferred to the next inner wall via crosslinks acting as anchors. Figure 2 shows the trade-off between outer wall diameter (determined by inner wall diameter) and the presence of crosslinks. At low outer wall diameters, the no-crosslink scenario is preferable for achieving high tensile strength. However, beyond a certain outer wall diameter, the presence of crosslinks becomes increasingly beneficial for load transfer, ultimately yielding higher nominal tensile strength than the no-crosslink case.

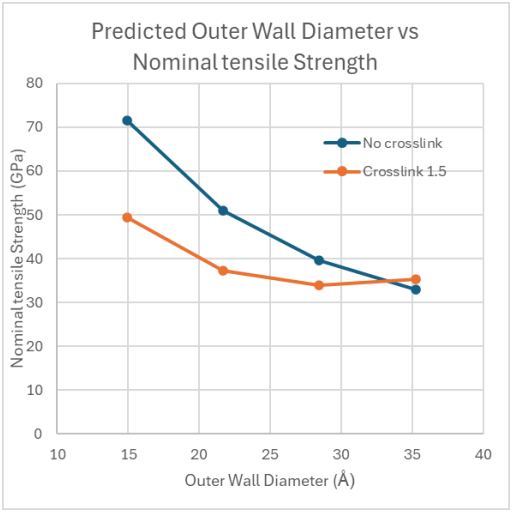


Figure 2. Trade-off graph between the no-crosslink CNTY and CNTY with 1.50% crosslink density, considering the outer wall diameter.

The results of this study will be reported in a manuscript following the completion of the next optimization for 10-degree twist angle CNTYs. The manuscript is currently in progress alongside the ongoing study on twisted CNTYs.

References

[1] Ramadhan RA, Yu C, Kunitomo A, Shigemitsu N, Shindo T, Yamamoto G. Structure-Mechanical Property Relationships in Carbon Nanotube Yarns. SSP 2024;364:3–9. https://doi.org/10.4028/p-gWe5Gw.

Development of Tensor-Network-based Monte Carlo Methods

Koji HUKUSHIMA
Department of Basic Science, University of Tokyo
3-8-1 Komaba, Meguro-ku, Tokyo 153-8902

Recently, tensor-network (TN)-based sampling has emerged as a promising alternative to conventional local-update Monte Carlo (MC) methods for frustrated and disordered systems. Whereas earlier TN methods were primarily used as deterministic tools to evaluate partition functions, free energies, and related thermodynamic quantities, more recent work has explored their use for sampling itself, either through conditional-probability-based generation or through collective MC proposals corrected by Metropolis sampling. This approach has already shown promise for random-bond Ising models and has even been extended to three-dimensional spin glasses. At the same time, it has become clear that direct TN-based sampling faces a central limitation: in strongly frustrated systems at low temperatures, the underlying TN contraction can become numerically unstable. Our collaborative work addresses this situation in two complementary directions: one study demonstrates that TN-based sampling can resolve subtle phase-transition structures in a modified spin-glass model [1], while the other proposes a new hybrid framework, tensor-network population annealing (TNPA) [2], specifically designed to overcome to the low-temperature instability of existing TN-based samplers.

First, we applied a TN-based hierarchical sampling scheme to a modified Nishimori model on the two-dimensional square lattice [1]. Because the bond variables in this model are correlated, direct sampling is computationally demanding. Our framework enables hierarchical, independent generation of both bond and spin variables, enabling high-precision calculations at large sizes. Using these data, we obtained clear numerical evidence that the ferromagnetic and spin-glass transitions on the Nishimori line are separated, supporting the existence of an intermediate Mattis-like spin-glass phase.

Second, we proposed a new low-temperature sampling method, TNPA [2]. The motivation is the complementary weakness of direct TN-based sampling and conventional population annealing (PA): the former becomes unstable at low temperatures, while the latter requires a long annealing schedule when initialized from the high-temperature limit. TNPA uses TN only for initialization within a reliable temperature range, then uses PA for subsequent low-temperature equilibration, assigning distinct roles to the two methods. The method also introduces an effective-sample-size-based diagnostic that adaptively selects the initialization temperature for each disorder instance. In this sense, TNPA is not just a hybrid of two existing algorithms, but a principled division of work designed to overcome the low-temperature bottleneck of previous TN-based samplers.

Overall, these studies establish TN-based sampling as a practical and promising framework for the numerical study of disordered frustrated systems.

[1] arXiv:2603.18486, [2] arXiv:2604.11155

Generation of spin model with higher-order spin interactions based on machine learning

Satoru Hayami
Graduate School of Science, Hokkaido University, Sapporo 060-0810, Japan

Spin textures exhibiting properties fundamentally distinct from conventional ferromagnetic and antiferromagnetic states have attracted significant attention in condensed matter physics. In particular, magnetic skyrmions—topologically nontrivial spin configurations with swirling structures—have emerged as central objects in the study of topological magnetism since their experimental discovery in 2009. While skyrmion crystal phases, characterized by periodic arrangements of such topological objects, have been observed in a wide range of materials, a comprehensive understanding of the microscopic conditions that stabilize these phases—especially the roles of lattice geometry and complex magnetic interactions—remains incomplete. In this context, recent developments in machine learning provide a powerful framework for systematically constructing effective spin models beyond conventional pairwise interactions. In the project 2025-Ca-0003, we have employed machine-learning-based approaches to generate spin Hamiltonians incorporating higher-order spin interactions, aiming to uncover the essential ingredients for stabilizing skyrmion crystal phases under diverse physical conditions. Through extensive numerical simulations, we have identified key mechanisms by which higher-order interactions promote nontrivial spin textures and stabilize skyrmion crystals across different lattice structures. We have also gained key insights into the stabilization mechanisms of topological spin textures through large-scale Monte Carlo simulations. The main results obtained this year are summarized below.

(i) Stabilization of skyrmion crystals via higher-order spin interactions and inverse model design: We have investigated the stabilization mechanisms of topological spin textures by focusing on higher-order spin interactions, particularly four-spin couplings, in frustrated magnetic systems [1]. By developing a theoretical framework that connects real-space four-spin interactions to their effective momentum-space representations, we established an inverse design approach for constructing spin Hamiltonians that realize target multiple-Q states. Using this approach, we successfully designed a minimal model incorporating nearest-neighbor four-spin interactions that stabilizes a skyrmion crystal with a topological number of two per magnetic unit cell even in the absence of an external magnetic field. Large-scale Monte Carlo simulations revealed that such higher-order interactions induce an instability from single-Q spiral states toward multiple-Q superpositions, thereby stabilizing complex spin textures. Furthermore, we demonstrated that the physically relevant ring-exchange interaction naturally generates effective interaction channels favorable for skyrmion formation, leading to the emergence of skyrmion crystal phases and their field-induced transitions. These results provide a unified understanding of how higher-order interactions promote topological magnetic order and offer a systematic pathway for designing spin models hosting complex spin

textures.

(ii) Finite-temperature stabilization of skyrmion crystals based on momentum-space analysis: We have investigated the finite-temperature stability of skyrmion crystal phases in frustrated magnetic systems by analyzing the momentum-space exchange interactions of a triangular-lattice Heisenberg model [2]. Through large-scale Monte Carlo simulations, we demonstrated that skyrmion crystals emerge as thermally stabilized multiple-Q states, even when the ground state is a single-Q spiral state. We identified two key factors governing their stability: the sixfold anisotropy of the momentum-space interaction, which acts as a locking potential selecting triple-Q ordering, and the energy of the uniform spin mode, which correlates with the appearance of the skyrmion phase. A larger sixfold anisotropy enhances the stability region of the skyrmion crystal in the temperature–magnetic-field phase diagram, while a sufficiently large uniform-mode contribution is required for its emergence. These results reveal that the stabilization of skyrmion crystals at finite temperatures is driven by an interplay between energetic competition and entropic effects encoded in the momentum-space interaction landscape. Our findings provide a systematic understanding of thermal stabilization mechanisms and offer guiding principles for designing frustrated magnetic systems hosting robust skyrmion phases.

(iii) Square skyrmion lattice in multiorbital f-electron systems: We have theoretically investigated the emergence of square skyrmion lattices (S-SkLs) in centrosymmetric tetragonal f-electron systems by incorporating multiorbital effects originating from spin–orbit coupling and crystalline electric fields [3]. Using a mean-field analysis of an effective localized model with two Kramers doublets, we revealed that an S-SkL with skyrmion number of one is stabilized in an intermediate magnetic-field region when the crystal-field splitting between the doublets is moderate. The phase diagram shows that the S-SkL appears only when multiorbital degrees of freedom are active, while it disappears in the large-splitting limit where the system effectively reduces to a single-orbital model. The S-SkL is characterized by a double-Q magnetic structure with fourfold symmetry and finite scalar chirality, as confirmed by the structure factor and real-space spin configurations. We further identify another multiorbital-induced double-Q state with nonzero scalar chirality at low fields, as well as a variety of competing multiple-Q phases, highlighting the richness of magnetic textures in multiorbital systems. These results demonstrate that multiorbital effects provide a new mechanism for stabilizing skyrmion crystals in centrosymmetric systems, offering a pathway toward realizing S-SkLs in f-electron materials such as Ce-based compounds.

References

[1] K. Okigami and S. Hayami, Phys. Rev. B **113**, 064442 (2026).

[2] K. Okigami and S. Hayami, J. Phys. Soc. Jpn. **95**, 044702 (2026).

[3] Y. Zha and S. Hayami, Phys. Rev. B **111**, 165155 (2025).

Dynamical scaling study of three-dimensional $SU(2)$ gauge glass model

Y. Ozeki and Y. Takada

Graduate School of Informatics and Engineering, The University of Electro-Communications

The $SU(2)$ gauge glass (GG) model is a random model that exhibits a ferromagnetic (FM) phase and a spin glass (SG) phase at low temperatures. The Hamiltonian is expressed as

$$\mathcal{H} = -J \sum_{\langle ij \rangle} \mathrm{Tr} \left(\phi_i \omega_{ij} \phi_j^\dagger \right),$$

where a spin variable ϕ_i and a quenched random variable ω_{ij} are $SU(2)$ matrices. The distribution of ω_{ij} is

$$P(\omega_{ij}) \propto \exp(D \mathrm{Tr} \omega_{ij}),$$

where $D = 0$ means the uniform distribution and $D = \infty$ corresponds to the regular case. We apply the dynamical scaling analysis to this model in three dimensions and obtain some locations of critical points and corresponding critical exponents, in order to discuss the critical universality classes of FM and SG transitions.

Like the $\pm J$ Ising model, it possesses gauge symmetry and features the Nishimori line [1]. On the Nishimori line, the exact energy and the upper bound of the specific heat can be obtained analytically, and the relation between FM and SG order parameters, $m = q$, holds. It is also derived that this line passes through a multicritical point (MCP), and the phase boundary at low temperatures is either vertical or reentrant. While such models with gauge symmetry exist for single-component Ising systems and two-component XY systems, they have not yet been identified for three-component Heisenberg systems (though they do exist for Potts systems).

By introducing four real numbers σ_i and $\boldsymbol{\pi}_i = (\pi_{i1}, \pi_{i2}, \pi_{i3})$, the spin variable ϕ_i can be parametrized as

$$\phi_i = \sigma_i I + \mathrm{i} \boldsymbol{\tau}_i \cdot \boldsymbol{\pi}_i,$$

where I is the identity matrix and $\boldsymbol{\tau} = (\tau_1, \tau_2, \tau_3)$ are the Pauri matirices. The $SU(2)$ GG model corresponds to a four-component $O(4)$ model in its regular limit

$$\mathcal{H}_0 = -J \sum_{\langle ij \rangle} \mathrm{Tr} \left(\phi_i \phi_j^\dagger \right) = -J \sum_{\langle ij \rangle} \mathbf{S_i} \cdot \mathbf{S}_j,$$

where

$$\mathbf{S}_i = (\sigma_i, \pi_{i1}, \pi_{i2}, \pi_{i3})$$

is a unit $O(4)$ vector with $\sigma_i^2 + \pi_{i1}^2 + \pi_{i2}^2 + \pi_{i3}^2 = 1$. Thus the $SU(2)$ GG model can be regarded as an $O(4)$ random system with gauge symmetry [1]. Evaluating the phase diagrams and critical exponents of models with these properties—and understanding the trends in the critical universality of gauge glass models in general—is highly beneficial for gaining a comprehensive overview of random systems as a whole.

At the paramagnetic (PM)-FM boundary, we measured the magnetization relaxation $m(t)$ for $1/D = 0$ (the $O(4)$ model), $1/D = 0.2, 0.5$, and on the Nishimori line ($1/D = T$). Calculations were carried out on a $L = 151$ cubic lattice with the skew boundary condition. We then precisely evaluated the transition temperatures through dynamical scaling analysis using Gaussian process regression (GPR) [2]. At these transition temperatures, the relaxation functions of $m(t)$, the magnetic susceptibility $\chi(t)$, and the temperature derivative of magnetization $\partial m(t)$ were measured with high precision. Calculations were carried out on a $L = 81$ cubic lattice up to 2000 MCS with 10^6 samples. By evaluating the logarithmic derivatives via GPR [3], we determined the thermodynamic critical exponents in the $t \to \infty$ limit. The results are summarized in Table 1.

Table 1: Results for the FM transition

$1/D$	T_c	ν	z
0	2.137247(3)	0.7465(14)	1.982(1)
0.2	1.78676(7)	0.7476(20)	2.041(1)
0.5	1.26776(4)	0.7482(9)	2.112(1)
T	0.7284(2)	0.987(1)	2.767(1)

Regarding the PM-SG boundary, we measured the relaxation of the SG susceptibility

$$\chi_{\mathrm{SG}}(t) = \frac{1}{N} \Big[\sum_{ij} \langle \mathbf{S}_i \cdot \mathbf{S}_j \rangle^2 \Big]$$

for $1/D = \infty$ and $1/D = 2.0$. Calculations were carried out on a $L = 151$ cubic lattice with the skew

boundary condition. Through dynamical scaling analysis using GPR, we estimated the transition temperatures with high accuracy and simultaneously obtained the critical exponents $\gamma_{\rm SG}/z_{\rm SG}\nu_{\rm SG}$ and $z_{\rm SG}\nu_{\rm SG}$ [4, 5]. At the determined transition temperatures, we measured the SG correlation function

$$f_{\rm SG}(r,t) = \frac{1}{N}\Big[\sum_i \langle \mathbf{S}_i \cdot \mathbf{S}_{i+r}\rangle^2\Big]$$

and derived the dynamical correlation length $\xi_{\rm SG}(t)$ at each time step from its dynamical scaling [6, 7]. Calculations were carried out on a $L = 251$ cubic lattice up to 1000 MCS. From the asymptotic behavior of $\xi_{\rm SG}(t)$, we evaluated the thermodynamic critical exponent $z_{\rm SG}$. The results are presented in Table 2.

Table 2: Results for the SG transition

$1/D$	$T_{\rm SG}$	$\nu_{\rm SG}$	$z_{\rm SG}$
2.0	0.450(2)	1.81(4))	2.93(6)
∞	0.440(1)	1.84(1)	3.01(1)

For the regular case ($1/D = 0$), the transition temperature and critical exponents for the $O(4)$ model are consistent much with those obtained previously [8, 9]. The results in Table 1 suggest that the FM boundary belongs to the same universality class as the regular system, except at the MCP. Since the specific heat exponent α of the regular system is negative, this indicates that the Harris criterion is satisfied. On the other hand, Table 2 shows results that are consistent with the hypothesis that universality also holds for the SG boundary, excluding the MCP. The dynamic critical exponent is shown to increase with increasing randomness, a trend that has also been observed in other gauge glass systems (such as the Ising spin glass). Furthermore, it is evident that the MCP forms its own independent critical universality class.

References

[1] Y. Ozeki and H. Nishimori, J. Phys. A: Math. Gen. **26** 3399 (1993).

[2] Y. Echinaka and Y. Ozeki, Phys. Rev. E**94** 043312 (2016).

[3] Y. Osada and Y. Ozeki, J. Phys. Soc. Jpn. **93** 114001 (2024).

[4] T. Nakamura, unpublished.

[5] Y. Terasawa and Y. Ozeki, J. Phys. Soc. Jpn. **92** 074003 (2023)

[6] T. Nakamura, *Phys. Rev.*E**93** 011301 (2016); **99** 023301 (2019).

[7] Y. Terasawa and Y. Ozeki, arXiv:2603.06008 (2026).

[8] K. Kanaya and S. Kaya, Phys. Rev. D**51** 2404 (1995).

[9] M. Hasenbusch, Phys. Rev. B**105** 054428 (2022).

Evaluation of Self-Healing Performance and Microscopic Damage in Vitrimers via Molecular Simulations

Yutaka OYA

Department of Mechanical Systems Engineering,

Tokyo Metropolitan University, Asahigaoka, Hino-shi, Tokyo 191-0065

We have studied covalent bond healing and microscopic damage accumulation in epoxy vitrimer systems using massive parallel molecular dynamics (MD) simulations. Vitrimers exhibit dynamic covalent bonding associated with disulfide bond (S-S) which enables network rearrangement and self-healing behavior. However, conventional studies have mainly focused on bond exchange reactions, and the direct recombination of broken covalent bonds has not been fully clarified [1].

In this study, we focus on post-scission recombination processes of disulfide bonds and their contribution to network repair. A multi-scale computational framework combining quantum chemical calculations and molecular dynamics (MD) simulations have been employed to elucidate the molecular mechanisms and their impact on macroscopic mechanical properties.

First, quantum chemical calculations based on the GRRM method are performed to explore energetically accessible recombination pathways of sulfur-centered radicals generated by disulfide bond cleavage. As shown in Fig. 1, multiple bonding configurations were identified along the recombination pathway, including

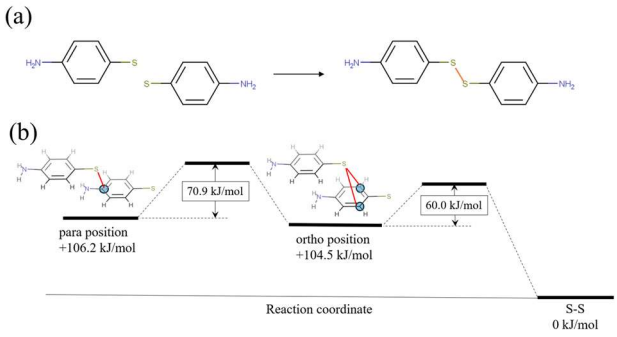


Fig. 1: (a) Recombination reaction of disulfide bonds considered in this study, and (b) Recombination reaction pathway identified by quantum chemical calculations.

transient sulfur–carbon interactions at the ortho and para positions of the benzene ring. These configurations are higher in energy than the fully recombined disulfide bond but remain energetically accessible after bond scission.

Importantly, these intermediate states are not conventional stable bonds but metastable configurations with partial covalent character, which facilitate migration of radicals prior to recombination. This result indicates that bond healing proceeds not only through direct S–S recombination but also through intermediate states involving aromatic interactions. This finding provides a new perspective on vitrimer healing mechanisms, highlighting the importance of post-scission pathways distinct from conventional bond exchange reactions.

Second, large-scale MD simulations are

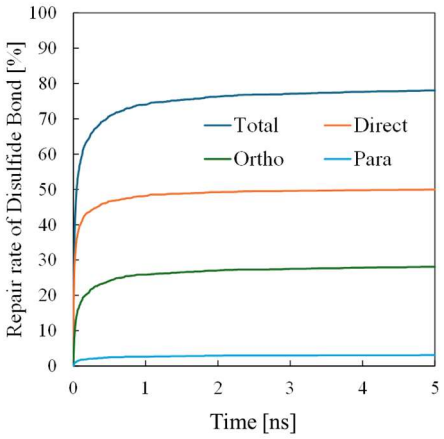


Fig. 2: Time evolutions of the repair rate of disulfide bonds during the damage recovery simulation.

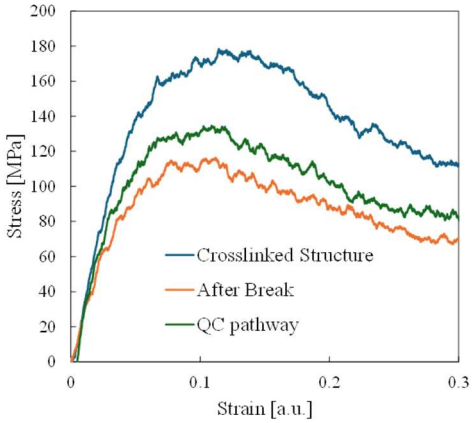


Fig. 3: Stress–strain curves obtained from uniaxial tensile deformation of three different network.

conducted to evaluate the deformation behavior and healing processes of a cross-linked epoxy vitrimer network (~27,000atoms). The simulation workflow consists of:

1. Construction of a cross-linked network
2. Tensile deformation with bond scission
3. Damage recovery via bond recombination
4. Re-evaluation of mechanical properties

During deformation, disulfide bonds are found to preferentially break compared with other covalent bonds. This selective bond scission suppresses catastrophic failure and distributes damage throughout the network.

The self-healing process for the crosslinked network is simulated by introducing our finding recombination reactions based on quantum chemical results. As shown in Fig. 2, approximately 78% of broken disulfide bonds were recovered within several nanoseconds. The healing process consists of two main pathways, direct sulfur–sulfur recombination (~64%) and Ortho-mediated recombination via transient S–C bonding (~36%). This clearly demonstrates that the quantum chemically identified recombination pathway significantly contributes to network repair.

The effect of bond healing on macroscopic mechanical properties is evaluated by tensile simulations. As shown in Fig. 3, the stress–strain responses reveal healed network shows partial recovery. Both Young's modulus and tensile strength are restored to an intermediate level after healing, demonstrating that microscopic bond recombination directly contributes to macroscopic property recovery.

In conclusion, we have investigated covalent bond healing in epoxy vitrimer systems using QM calculations and MD simulations. The results showed that disulfide bonds preferentially break and are partially reformed, leading to recovery of mechanical properties.

References

[1] A. V. Karatrantos, Polymers. **16**, 1373 (2024).

Coherent current generation in graphene driven by structured light fields

Tomohiro Tamaya

Department of Nuclear Engineering and Management, Graduate School of Engineering, The University of Tokyo, 7-3-1 Hongo, Bunkyo-ku, Tokyo 113-8656, Japan

We have studied coherent electronic and spin-related responses in crystalline solids driven by intense light fields using large-scale time-dependent simulations. The original motivation of this project was to clarify the microscopic mechanism of THz-induced spin magnetization accumulation in semiconductors, where coherent interband polarization and spin-orbit coupling play essential roles. During this year, we focused on developing and testing a computational framework for light-induced coherent currents and magnetic responses in a prototype two-dimensional material. In particular, we investigated graphene driven by spatially structured Laguerre-Gaussian beams, whose intensity and phase vary in real space and whose polarization state can be controlled.

The time-dependent electronic dynamics were calculated in momentum space by propagating the quantum states under pulsed optical fields [1–4]. The photoinduced current was then evaluated from the time-evolved states, and its angular dependence was decomposed into winding-number components. This analysis enabled us to identify how the orbital angular momentum and polarization helicity of light select different dc current channels. Since the calculations require dense sampling of the Brillouin zone, time propagation for many optical parameters, and repeated simulations for different angular positions and beam profiles, the ISSP supercomputer system was essential for carrying out this study.

The numerical code was parallelized mainly over momentum-space grid points and optical/angular parameters using MPI. We further optimized the calculations by precomputing field-dependent and geometrical factors, reducing redundant evaluations inside the time-evolution loop, and organizing the output files so that the winding-number analysis could be performed without repeating the computationally expensive real-time propagation. These improvements enabled systematic parameter scans over the optical angular momentum, polarization helicity, field strength, pulse duration, and radial position of the structured light field.

As a result, we obtained winding-number-resolved spectra of the dc current induced by structured light in graphene, with separate analysis of local and gradient-induced current components. Figure 1 shows representative spectra for optical angular momenta $l = 1$ and $l = 2$. The dominant winding channels are switched by changing the polarization helicity

and optical angular momentum. In addition, the selected channels differ between the local and gradient-induced current components, indicating that the spatial structure of the light field provides a way to distinguish different microscopic current-generation mechanisms. In particular, the selective appearance of the $m = 0$ component is important because it is directly connected to circulating photocurrents and the resulting magnetic response. These results provide a basis for evaluating light-induced magnetic responses, thereby connecting the present calculations to the original goal of controlling spin and magnetic responses in solids. Although the full three-dimensional simulation of spin magnetization accumulation in GaAs remains a challenging next step, the present calculations established an important numerical and physical foundation for future studies.

References

[1] T. Tamaya, A. Ishikawa, T. Ogawa, and K. Tanaka, Phys. Rev. Lett. 116, 016601 (2016).

[2] T. Tamaya and T. Kato, Phys. Rev. B 100, 081203(R) (2019).

[3] T. Tamaya and T. Kato, Phys. Rev. B 103, 205202 (2021).

[4] T. Tamaya, A. Akiyama, and T. Kato, Phys. Rev. B 107, L081405 (2023).

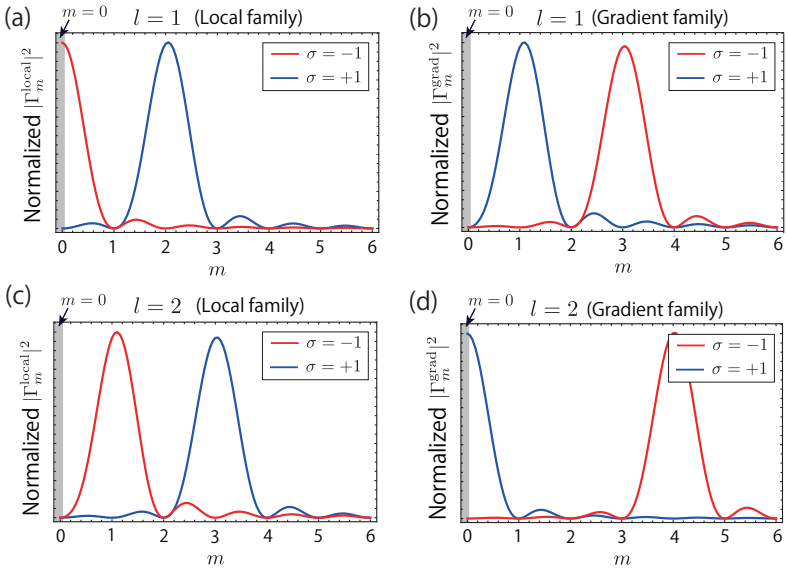


Fig. 1: Winding-number-resolved spectra of dc currents induced in graphene by Laguerre-Gaussian beams. Panels (a,b) and (c,d) show the results for optical angular momenta $l = 1$ and $l = 2$, respectively. Local and gradient-induced current components are shown separately. Red and blue curves represent opposite polarization helicities, $\sigma = -1$ and $\sigma = +1$. The helicity-dependent peak positions demonstrate selective activation of different winding-number channels. The arrows indicate the $m = 0$ channel, which is related to circulating photocurrents and magnetic responses.

Simulated tempering simulations of model silica glasses

Yoshihiko NISHIKAWA
Department of Physics, Nagoya University
Nagoya 464-8602, Aichi, Japan

Both experiments and computer simulations of glass-forming liquids experience a drastic growth of the relaxation time at low temperatures. Only a few percent change in temperature of glasses can result in decades slower dynamics, whereas its static structures remain disordered. Understanding the physical origin of the slow glassy dynamics has been a central problem of the glass physics, and accessing equilibrium glassy states at low temperature is challenging.

In the last decade, the Swap Monte Carlo algorithm has revolutionized the computer simulations of glasses [1, 2]. The algorithm simply attempts to swap particle diameters of randomly chosen pairs of particles. Despite its simplicity, this algorithm can reduce the timescale of tailored polydisperese models at low temperatures by many orders of magnitude, thereby allowing us to access very stable glassy states and to study their thermodynamic and mechanical properties in detail. However, when applied to binary systems, such as silica glasses, it cannot accelerate the dynamics much, as swapping different types of particles is barely accepted at low temperature. Different strategies are thus needed to sample stable glass configurations of such systems.

Here, we apply simulated tempering (ST) [4] to a model silica glass in three dimensions [3] and test if it can efficiently equilibrate the system at very low temperatures. In ST simulations, we dynamically change temperature (or any other intensive control parameters) of the system with maintaining equilibrium at any time, in addition to updating the microscopic degrees of freedom as usual. The range of temperature needs to be set so that the system in the high-temperature regime can decorrelate rapidly, and that particle configurations at low temperatures are statistically independent after each round trip in the temperature space. Unlike the exchange Monte Carlo (also known as parallel tempering) [5], unfortunately, ST needs careful tuning of parameters to have the algorithm reach the whole temperature space. We have iteratively adjusted the parameters with extensive parallelization of preliminary ST simulations on the ISSP Supercomputer System B, which has accelerated the process by a factor of ≈ 50.

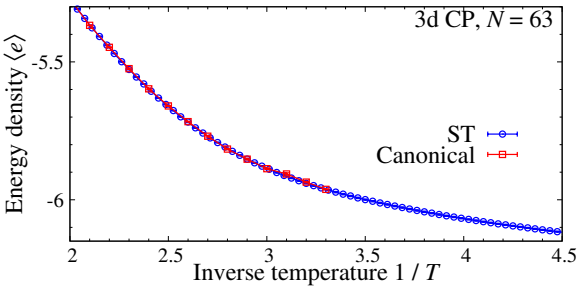


Figure 1: Mean energy density $\langle e \rangle$ obtained with canonical and ST simulations, represented by red square and blue circular points, respectively.

We show the energy density $\langle e \rangle$ of the model with the number of particles $N = 63$. Canonical simulations (i.e., local Monte Carlo simula-

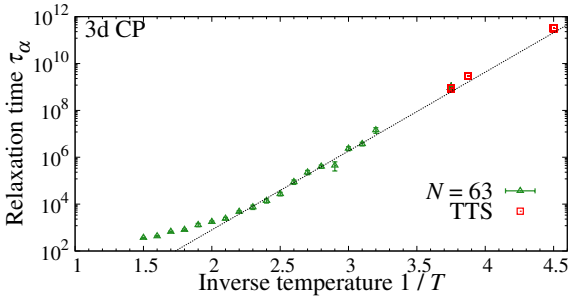


Figure 2: Structural relaxation time τ_α as a function of inverse temperature β of the model with $N = 63$. Green triangular and red square points represent τ_α measured with initial configurations generated by the local Monte Carlo dynamics and ST simulations, respectively. For the latter case, τ_α is estimated using the time-temperature superposition (TTS) assumption.

tions without the tempering process) and ST ones yield results consistent with each other, confirming the correctness of the ST algorithm. The local Monte Carlo as well as molecular dynamics can reach up to $\beta \approx 3.3$ for this model [3], as the dynamics in this temperature regime is so slow – the structural relaxation time τ_α, which is defined as the timescale of the time correlation of particle positions, grows exponentially with β and exceeds 10^8 at $\beta \approx 3.5$, see Fig. 2. On the other hand, ST can reach equilibrium states at much lower temperatures, e.g., $\beta = 4.5$, within 10^8 Monte Carlo sweeps per particle, therefore accelerating the dynamics by several orders of magnitude. To verify configurations from ST runs at that low temperature are compatible with other equilibrium data, we study the dynamics of the local Monte Carlo dynamics starting from configurations obtained by ST runs. Since the dynamics there is so slow that the time correlation does not decay to a small value within simulation times, we estimate τ_α with the time-temperature superposition assumption [6]. We find τ_α measured in this protocol is indeed consistent with an Arrhenius curve for τ_α at higher temperatures (see Fig. 2). In future work, we will apply the algorithm to larger system sizes and more realistic models to establish ST as a efficient tool to access stable glassy states.

References

[1] T. S. Grigera and G. Parisi, Phys. Rev. E **63**, 045102 (2001).

[2] A. Ninarello, L. Berthier, and D. Coslovich, Phys. Rev. X **7**, 021039 (2017).

[3] D. Coslovich and G. Pastore, J. Phys. Condens. Matter **21**, 285107 (2009).

[4] E. Marinari and G. Parisi, EPL **19**, 451 (1992).

[5] K. Hukushima and K. Nemoto, J. Phys. Soc. Jpn. **65**, 1604 (1996).

[6] W. Kob and H. C. Andersen, Phys. Rev. E **51**, 4626 (1995).

Defect structures and their transport properties in thermoelectric chalcogenides

Susumu FUJII
Department of Materials, Faculty of Engineering, Kyushu University
Motooka, Fukuoka 819-0395
Nanostructures Research Laboratory, Japan Fine Ceramics Center
Mutsuno, Atsuta, Nagoya 456-8587

In this project, we investigated nanoscale thermal transport at grain boundaries (GBs) in PbTe, a representative thermoelectric material, by combining machine-learning interatomic potentials with large-scale perturbed molecular dynamics (MD) simulations. The main objective was to clarify how GB atomic structures affect lattice thermal conductivity and to establish a basis for improving the thermoelectric performance through defect engineering.

The most intensive use of the ISSP supercomputer resources was devoted to large-scale atomistic simulations based on a neural-network potential (NNP). Direct evaluation of thermal transport for GBs by DFT is prohibitively expensive, because both structural optimization and finite-temperature transport calculations require large supercells and long simulation times. To overcome this difficulty, we employed an NNP trained on DFT data for bulk, point defects, surfaces, and GB structures [1]. This strategy retained high accuracy for GB energetics and atomic forces while reducing the computational cost by several orders of magnitude compared with direct DFT calculations. As a result, it became possible to perform systematic simulations for 24 symmetric tilt GBs in PbTe, including both [001] and $[1\bar{1}0]$ rotation-axis systems [2].

The largest share of the supercomputer time was spent on perturbed MD calculations of lattice thermal conductivity. For each lowest-energy GB structure with different misorientations, we constructed supercells containing two equivalent GBs, with lengths of approximately 100 Å along the GB-normal direction and more than 45 Å along the in-plane directions. Lattice thermal conductivity was evaluated not only normal to the GB plane but also along the two GB-parallel directions. Because each conductivity calculation requires long-time averaging under finite perturbation within the linear-response regime, and because this procedure was repeated for many GB models and multiple heat-flux directions, the total computational demand was substantial. In addition, atom-resolved and wave-decomposed analyses were carried out from the same PMD framework to identify the microscopic origin of the anisotropic thermal transport.

Using this computational framework, we showed that the GB thermal resistance in PbTe varies by as much as a factor of seven depending on GB structure (Fig. 1). Along the direction normal to the GB plane, the thermal conductivity tends to decrease as the coordination-number change at the GB increases. In contrast, along the GB-parallel directions, the thermal conductivity is influenced more strongly by bond-length distortion and crystallographic orientation. We further found that the influence of GBs on heat transport parallel to the boundary extends over

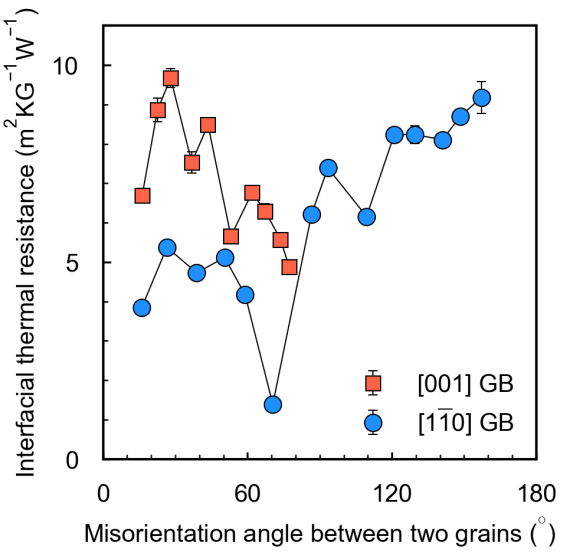


Figure 1: Interfacial thermal resistance of PbTe GBs as a function of GB misorientation angle. The results for GBs with [001] and [1$\bar{1}$0] rotation axes are shown. Adapted from Ref. [2] under CC BY 3.0.

roughly 10 nm from the GB plane, indicating that in-plane transport suppression is also non-negligible in nanocrystalline PbTe.

Overall, this project demonstrated that NNP-based atomistic simulation is a powerful approach for quantitatively analyzing defect-dependent thermal transport in thermoelectric materials. The ISSP supercomputer played a central role by enabling extensive NNP-MD sampling, systematic GB-structure searches, and repeated PMD calculations over many large supercells. These computations yielded a microscopic and quantitative picture of how structurally diverse GBs control lattice thermal conduction in PbTe.

In addition to these results, several tens of further calculations of GB thermal conductivity and electronic transport have been carried out. These large-scale simulations are steadily providing new insights toward elucidating the structure–property relationships in GBs and providing a basis for future microstructure design of high-performance thermoelectric materials.

References

[1] T. Yokoi, S. Fujii, Y. Ogura, K. Matsunaga, Phys. Rev. B **112**, 024111 (2025).

[2] S. Fujii, T. Yokoi, K. Matsunaga, J. Mater. Chem. A, published online (2026).

Molecular Analysis of Surface Tension Changes in Mixed Ionic Liquids via Large-Scale MD Simulation on ISSP Supercomputer System

Yuiko TOMITA, Wataru SATO, and Ikuya KINEFUCHI

Department of Mechanical Engineering,

The University of Tokyo, Hongo, Bunkyo-ku, Tokyo 113-8656

Ionic liquids (ILs) are promising materials for CO_2 separation membranes owing to their negligible volatility and high gas solubility [1]. Precise control of surface tension is critical for stable IL retention within support membranes. Although mixing multiple ILs is an effective strategy to tune physicochemical properties [2], the surface tension of mixed ILs deviates from ideal mixing [3], and the underlying molecular mechanism remains poorly understood. In this study, large-scale MD simulations were performed on the ISSP supercomputer (ohtaka) to reproduce the gas–liquid interface of mixed imidazolium-based ILs ([$C_n$mim][NTf_2], n = 2, 4) and to elucidate the molecular origin of the nonlinear surface tension change upon mixing.

A total of 4096 ion pairs (~57,000 atoms) were placed in a simulation box (~200 × 120 × 120 Å^3) to construct a slab model. MD simulations were performed using LAMMPS [4] with the OPLS-AA-based force field [5–7], with MPI parallelization across 128 cores per job on ohtaka (~2,000 CPU-core hours per system). Surface tension was evaluated via the Kirkwood–Buff mechanical route [8], and local stress distributions were analyzed using the volume averaging method (VAM) [9] at 1 Å resolution.

Number density profiles (Fig. 1) show that the outermost layer is enriched in nonpolar moieties (alkyl chains) in all systems. In the equimolar mixture, C_4mim is markedly enriched in the outermost layer, reflecting selective surface adsorption of the longer alkyl chain. The polar layer in the mixture (12.0 Å) is thicker than in single-component systems (7.5 Å), due to a sublayer structure from the coexistence of two cation species.

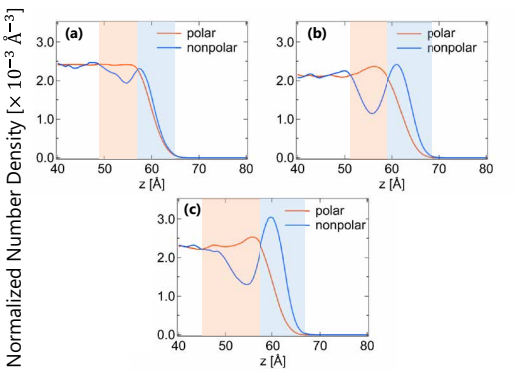


Fig. 1: Normalized number densities of polar (red) and non-polar (blue) moieties across the interface for (a) [C_2mim][NTf_2], (b) [C_4mim][NTf_2], and (c) the mixture.

Decomposition of the local stress tensor anisotropy by interaction type (Fig. 2) revealed that the majority of net surface tension originates in the polar layer in all systems; intermolecular interactions (Coulomb and LJ) produce large positive peaks near the interface, while intramolecular interactions (bond, angle) provide partially canceling contributions. The calculated surface tensions were 44.8 mN/m (C_2mim), 31.4 mN/m (C_4mim), and 35.0 mN/m (mixture), with a deviation of −3.1 mN/m from ideal mixing (Fig. 3). This deviation is dominated by the Coulomb term (−23.9 mN/m), indicating that coexistence of two cation species in the polar layer alters the local electrostatic environment, a finding enabled by high-resolution local stress analysis on the ISSP supercomputer.

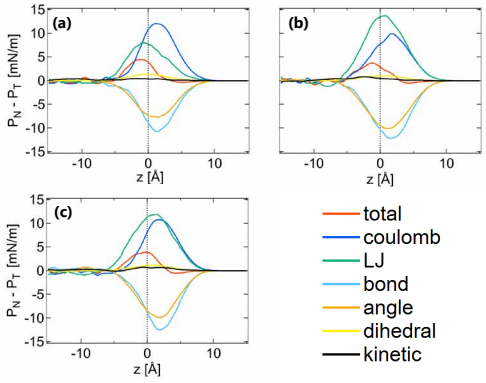


Fig. 2: Surface tension contributions decomposed by interaction type for (a) [C_2mim][NTf_2], (b) [C_4mim][NTf_2], and (c) the mixture.

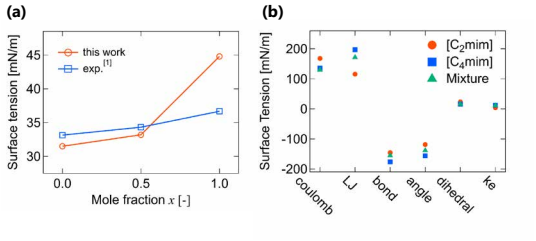


Fig. 3: (a) Composition dependence of surface tension. (b) Decomposition into interaction components for [C_2mim][NTf_2] (red), [C_4mim][NTf_2] (blue), and the mixture (green).

References

[1] R. D. Rogers and K. R. Seddon, *Science*, **302**, 792 (2003).

[2] Y. Kohno *et al., ACS Omega,* **7**, 42155 (2022).

[3] M. B. Oliveira *et al.*, *J. Phys. Chem. B*, **116**, 12133 (2012).

[4] A. P. Thompson et al., *Comp. Phys. Comm.*, **271**, 108171 (2022).

[5] W. L. Jorgensen et al., *J. Am. Chem. Soc.*, **118**, 11225 (1996).

[6] J. N. Canongia Lopes et al., *J. Phys. Chem. B*, **108**, 2038 (2004).

[7] J. N. Canongia Lopes et al., *J. Phys. Chem. B*, **108**, 11250 (2004).

[8] J. G. Kirkwood et al., *J. Chem. Phys.*, **17**, 338 (1949).

[9] J. H. Irving and J. G. Kirkwood, *J. Chem. Phys.*, **18**, 817 (1950).

[10] B. D. Todd et al., *Phys. Rev. E*, **52**, 1627 (1995).

Quantum emulator using GPU toward fault-tolerant quantum computing for reacting flow analysis

Takaki AKIBA

Department of Mechanical Engineering, School of Engineering,

The University of Tokyo, 7-3-1, Hongo, Bunkyo-ku, Tokyo 113-8656

This study presents a GPU-based emulator for Quantum Phase Estimation (QPE) designed for practical quantum applications in science and engineering. As shown in Figure 1, the QPE circuit is built from measurement qubits, controlled powers of the target unitary, and an inverse quantum Fourier transform, providing the basic structure used throughout the implementation. The emulator was developed with NVIDIA cuQuantum and CUDA, with HDF5-based input and output to make preprocessing and postprocessing straightforward. It was designed to exploit GPU resources aggressively, especially VRAM, so that larger and faster simulations could be achieved.

The implementation was validated using both analytically constructed test cases and random unitary matrices. Benchmark results showed that computational cost rises rapidly with total qubit count, while higher-end GPUs provide clear speed advantages. At the same time, the error in estimated eigenphases decreased exponentially as the number of measurement qubits increased. This trend is clearly illustrated in Figure 2, which confirms that adding measurement qubits systematically improves numerical precision. Overall, the work establishes a practical platform for mid-scale quantum emulation and provides a useful computational basis for future applications of quantum algorithms such as QPE and HHL

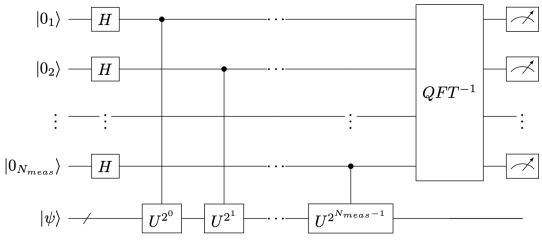


Figure 2 Quantum circuit of quantum phase estimation.

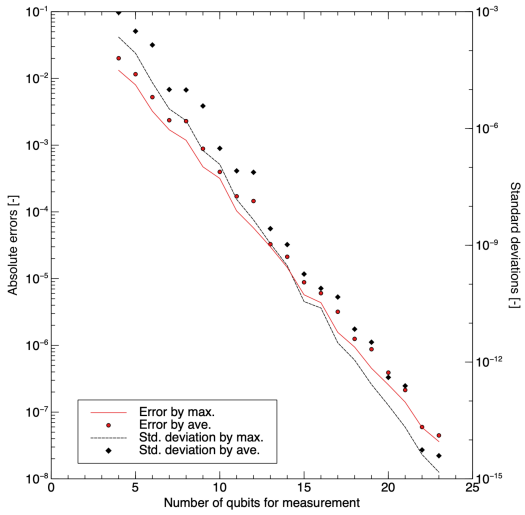


Figure 1 Numerical precision vs the number of qubits for measurement bit.

Theoretical and Experimental Study on Ambipolar Transport and Conduction Path Control in Nickel Dithiolene Complexes

Tomoko FUJINO

Graduate School of Engineering Science, Faculty of Engineering,
Yokohama National University, Tokiwadai, Hodogaya-ku, Yokohama, Kanagawa 240-8501

Molecular organic semiconductors are a class of materials characterized by their flexibility, high structural designability, and the solution-processability inherent to molecular systems. While p-type and n-type unipolar semiconductors with high mobility have already been commercialized, ambipolar semiconductors—which switch between p-type and n-type operation via the application of a gate potential—remain in the developmental stage. The realization of ambipolar behavior requires not only high solubility and highly ordered crystallinity on substrates but also high-dimensional electronic structures that stabilize conduction paths, alongside meeting stringent requirements for the electronic state in the stacked arrangement.

Focusing on these electronic requirements, we investigated nickel dithiolene complexes as d/π-conjugated molecules, which offer high structural designability via side chains and fine-tunability of solubility. These complexes functioned as exceptionally well-balanced ambipolar semiconductors, exhibiting solution-processability, high crystallinity, a two-dimensional (2D) electronic structure derived from their stacked morphology, and high atmospheric stability [1].

Carrier transport in these materials is governed by HOMO-derived bands for holes and LUMO-derived bands for electrons, originating from their respective molecular orbital interactions. Electronic structure analysis performed using theoretical calculations predicted that within the 2D plane, the HOMO-derived band is anisotropic, whereas the LUMO-derived band is isotropic. This finding implies that the conduction paths for holes and electrons are distinct; more specifically, the direction of carrier flow can be switched depending on the applied potential.

In this study, aiming to manifest this unique functionality, we optimized the solution-processing methods and successfully fabricated single-crystal thin films with large domain sizes of 500 μm². This achievement allowed us to experimentally validate the theoretical predictions. The experimental results showed excellent agreement with the simulations, demonstrating for the first time that carrier-dependent transport paths can be switched by the gate potential [2]. Furthermore, we have

expanded this research to the observation of magnetic anisotropy in aqueous environments [3] and the development of pure π-conjugated systems [4].

This research was conducted during my appointment as an Assistant Professor at the University of Tokyo. The work was performed in collaboration with Professor Mori, members of the Mori Laboratory, and numerous other partners. I would like to express my sincere gratitude for their invaluable support and contributions.

References

[1] M. Ito, T. Fujino*, L. Zhang, S. Yokomori, T. Higashino, R. Makiura, K. J. Takeno, T. Ozaki, and H. Mori*, J. Am. Chem. Soc. 145 (4), 2127–2134 (2023).

[2] M. Ito, T. Fujino*, T. Higashino, M. Hishida, and H. Mori*, Angew. Chem. Int. Ed. e202512609 (2025).

[3] T. Fujino,* M. Hishida,* M. Ito, T. Nakamura, M. Asada, N. Kurahashi, H. Kiuchi, Y. Harada, K. Harano, R. Makiura, K. J. Takeno, S. Yokomori, H. Oike, H. Mori, Adv. Sci. 12 (29), 71029 (2025).

[4] H. Nishimoto, T. Fujino*, T. Higashino, and H. Mori*, J. Mater. Chem. C, 13 (33), 16067–16077 (2025).

Numerical study on low-energy states of quantum spin systems

Hiroki NAKANO
Graduate School of Science, University of Hyogo
Kouto, Kamigori, Hyogo 678-1297, Japan

It is well known that researchers encounter many-body problems in condensed matter physics that make it difficult to accurately estimate physical quantities. The problem of quantum spin systems is a typical one. Numerical approaches have been widely and effectively utilised in the study of quantum spin systems. Computational studies have provided valuable information about the target systems.

Three methods have been successfully employed in the computational studies of quantum spin systems. The numerical diagonalisation method is the standard, traditional approach. The second approach is based on a quantum Monte Carlo (QMC) simulation. The third approach is the density matrix renormalization group (DMRG) method. Each of these methods has its own advantages and disadvantages. Regardless of their spatial dimensions, QMC simulations can handle significantly larger systems. However, this approach encounters the negative sign problem when attempting to accurately evaluate physical quantities in frustrated systems. The DMRG method is useful when its spatial dimension is one, regardless of whether or not the target system has frustration. This method is still being developed for cases where the spatial dimension is more than one. The numerical diagonalization method can be used in various systems, no matter what the spatial dimension is or if there are any frustrations. However, this method is only effective for very small systems. To overcome the numerical diagonalization method's drawback, we developed a parallel code based on the Lanczos diagonalization method[1]. Using this code, we can treat various large systems that have not yet been treated. In this project, we primarily use this method to analyze various quantum spin systems.

In 2025, this project reported our achievement concerning the spin-S Heisenberg antiferromagnet on the orthogonal dimer lattice for $S = 2$[2] in addition to our previous studies of spin-1/2, 1, and 3/2 cases[4, 3]. In this study, we successfully carried out Lanczos diagonalizations of this system 16 and 20 sites for $S = 2$ case. It is for the first time that within Lanczos-diagonalization studies, numerical results of this model had been presented for $S = 2$ case to the best of our knowledge. We clarified the change of the behavior of this model when the ratio of two interaction amplitudes denoted by $r = J_2/J_1$, where J_1 denotes the amplitude of the Heisenberg interaction at the orthgonal dimer and J_2 denotes the amplitude of interaction forming the square lattice. Consequently, we successfully captured the edge of the exact-dimer phase. At the same time, we also detected the edge of the Néel-ordered phase at a different r from the edge of the exact-dimer phase. We confirmed that differences between systems of the 16 and 20 sites are small in our results with respect to the values of r corresponding each of the edges. Our results strongly suggest that the existence of an intermediate phase between both the edges

irrespective of spin-S up to $S = 2$. Combining the results with previous ones, we succuessfully clarify the systematic S-dependence of the edges of the two phases. The project also investigated the Haldane gap issue in the case of $S = 7$[5] and successfully provide a numerical estimate for the gap. Our studies contribute greatly to our deeper understanding of quantum magnetism. Further investigations would shed light on the nontrivial quantum effects in these systems.

References

[1] H. Nakano and A. Terai: J. Phys. Soc. Jpn. **78**, 014003 (2009).

[2] H. Nakano and T. Sakai: J. Phys. Soc. Jpn. **95**, 033704 (2026).

[3] H. Nakano and T. Sakai: J. Phys.: Condens. Matter **36**, 455805 (2024).

[4] H. Nakano and T. Sakai: JPS Conf. Proc. **38**, 011166 (2023).

[5] H. Nakano and T. Sakai: J. Low Temp. Phys. **222**, 69 (2026).

The physical picture of Johari-Goldstein relaxation in metallic glasses

TAKEAKI ARAKI and UJJWAL KUMAR NANDI

Department of Physics, Kyoto University, Sakyo-ku, Kyoto 606-8502

Johari–Goldstein (JG) relaxation, often referred to as slow ß relaxation, is a ubiquitous feature of supercooled liquids and glasses and plays a key role in determining material properties such as impact strength, particularly below the glass transition temperature. Despite its importance, the microscopic origin of JG relaxation remains poorly understood, largely due to the difficulty of probing this process experimentally and capturing it accurately in simulations.

In this study, we investigate the relaxation dynamics and mechanical response of a ZrCuAl metallic glass using molecular dynamics simulations with LAMMPS. Cyclic shear deformation is applied, and the loss modulus is evaluated as a function of temperature for systems with different structural stability. We find that, at low temperatures, the loss modulus becomes negligible as the glass becomes more stable. Consequently, the Johari–Goldstein secondary relaxation is suppressed in highly stable glasses, suggesting that the localized atomic rearrangements responsible for this process are hindered by enhanced stability. We further examine the stress–strain response at zero temperature under applied strain. Two structures are considered: glassy and crystalline configurations of the same ZrCuAl composition, both initially equilibrated at 300 K. The stress–strain curves exhibit clear differences. The glassy system shows a pronounced stress peak, indicative of brittle behavior, whereas the crystalline system exhibits a smoother deformation response. These results highlight the correlation between structural stability, relaxation dynamics, and mechanical properties in metallic glasses.

References

[1] M. Saito, et al, Acta Materialia **284**, 120536 (2025)

Stress propagation in colloidal gels

TAKEAKI ARAKI and KOICHI HIRATA

Department of Physics,

Kyoto University, Kitashirakawa-oiwake-cho, Sakyo-ku, Kyoto 606-8502

This study investigates the mechanical response and yielding behavior of aerogels under isotropic expansion using coarse-grained simulations. Aerogels exhibit linear elastic behavior at small strains, followed by sudden yielding at a critical strain ($\varepsilon \approx 0.18$), accompanied by bond rupture and plastic deformation.

The deformation is highly heterogeneous and hierarchical. At small length scales, particles move cooperatively within structurally defined regions, while at larger scales, deformation is dominated by transverse, vortex-like nonaffine displacements. A characteristic length scale separates these regimes and reflects the underlying structural heterogeneity of the gel network.

Mechanical properties are strongly controlled by the bond-creation probability p_{bond}, which determines the network structure. Lower p_{bond} leads to more branched and locally dense structures with higher stiffness but reduced durability, whereas higher p_{bond} results in softer yet more robust networks. This establishes a clear trade-off between bulk modulus and yielding strain.

To understand stress transmission, the study introduces the concept of stretched and directed paths (strDPs), which represent locally stiff regions that carry stress across the system. During deformation, these paths elongate through bond alignment and eventually form system-spanning structures. Yielding occurs when the extension of these paths reaches a limit, leading to mechanical saturation beyond which further deformation induces bond breakage rather than additional structural rearrangement.

Overall, the results provide a unified framework linking microscopic structural organization, cooperative dynamics, and macroscopic mechanical response, offering insights for designing aerogels with tailored stiffness, flexibility, and durability.

References

[1] L. D. Gelb, J. Phys. Chem. C **111**, 15792 (2007).

[2] K. Hirata and T. Araki, J. Chem. Phys. **160**, 234901 (2024).

[3] K. Hirata and T. Araki, submitted.

Ground state phase diagram and finite-T Study of Sr_2IrO_4

Matthias GOHLKE, Jiahui BAO
Theory of Quantum Matter Unit, Okinawa Institute of Science and Technology
1919-1 Tancha, Onna-son, Okinawa 904-0495

Competing interactions in quantum magnets can suppress conventional dipolar magnetic order and stabilize phases characterized by higher-rank spin correlations. A paradigmatic example is a quantum spin nematic (QSN), the quantum magnetic analogue of a liquid crystal, in which spin-rotational symmetry is broken while time-reversal symmetry remains intact. Because QSN order does not carry a static magnetic dipole moment, it is difficult to detect with standard linear-response probes and, thus, can be classified as *hidden order*. In spin-1/2 systems, these higher-rank spin correlations can only emerge from an intricate interplay of the individual spins forming quadrupoles (n-type nematic) [1] or vector-chiral moments (p-type nematic) [2] on bonds.

This makes the recent observation of quadrupolar signatures in the $J_{\text{eff}} = 1/2$ spin-orbit-coupled Mott insulator Sr_2IrO_4 particularly striking [3]. Sr_2IrO_4 is a square-lattice antiferromagnet with well-established canted Néel order, where spin-orbit coupling-induced Dzyaloshinskii-Moriya interactions (DMI) naturally generate vector-chiral bond correlations, yet do not by themselves explain symmetric bond-quadrupolar order. The reported coexistence of dipolar magnetism and QSN-like quadrupolar order therefore poses a question: *why should a spin nematic appear in an antiferromagnetic* $J_{\text{eff}} = 1/2$ *material, far from the conventional spin-1 or frustrated-ferromagnet settings?*

We have identified a possible resolution based on the algebra of spin-1/2 bond operators [5]. The key point is that antisymmetric vector-chiral bilinears and symmetric quadrupolar bilinears are not independent: the anticommutator of two distinct vector-chiral components on the same bond generates an off-diagonal bond quadrupole. Using a minimal model of Sr_2IrO_4 [4],

$$\begin{aligned}\mathcal{H} = \sum_{\langle ij\rangle_1} \big[& J_1\, \mathbf{S}_i \cdot \mathbf{S}_j + D^z \left(S_i^x S_j^y - S_i^y S_j^x\right) \\ & + \Gamma_2 \left(S_i^x S_j^x - S_i^y S_j^y\right)\big] + \sum_{\langle ij\rangle_2} J_2\, \mathbf{S}_i \cdot \mathbf{S}_j \\ & + \sum_{\langle ijkl\rangle} J_c \big[(\mathbf{S}_i \cdot \mathbf{S}_j)(\mathbf{S}_k \cdot \mathbf{S}_l) \\ & + (\mathbf{S}_j \cdot \mathbf{S}_k)(\mathbf{S}_l \cdot \mathbf{S}_i) - (\mathbf{S}_i \cdot \mathbf{S}_k)(\mathbf{S}_j \cdot \mathbf{S}_l)\big] ,\end{aligned} \tag{1}$$

incorporating out-of-plane DMI D^z, Γ_2 due to orthorhombic distortions, and cyclic ring exchange J_c around a square, we identify a spin-nematic phase *VC+AFQ* illustrating this mechanism [5].

We map out the ground-state phase diagram as a function of the second-neighbor exchange J_2 and cyclic ring exchange J_c at fixed $D_z/J_1 = 0.25$ and $\Gamma_2/J_1 = 0.1$. Besides conventional dipolar phases, including canted Néel, stripe, and four-sublattice antiferromagnetic order, we find an extended VC+AFQ region with finite vector-chiral and antiferro-quadrupolar bond moments but no dipolar long-range order. Most importantly in the context of Sr_2IrO_4, this spin-nematic phase borders the canted Néel phase through a narrow

coexistence regime in which dipolar, vector-chiral, and quadrupolar moments are simultaneously present. This provides a natural route to the experimentally observed coexistence of canted antiferromagnetism and quadrupolar order.

We further investigate the thermodynamics of these orders using TPQ-MPS simulations. The specific heat shows a broad high-temperature feature associated with the buildup of short-range antiferromagnetic correlations and DMI-induced vector chirality. At lower temperature, the vector-chiral and quadrupolar structure factors grow strongly, followed closely by the onset of canted Néel correlations. This sequence suggests a narrow temperature window in which spin-nematic correlations develop before dipolar magnetic order becomes dominant, consistent with the experimental indication of quadrupolar order appearing above or together with the magnetic transition in Sr_2IrO_4.

This work has relied heavily on the open source MPS and DMRG package *TenPy* [8] providing parallelization of matrix operations within a single node through optimized LAPACK and BLAS packages.

References

[1] A. F. Andreev and I. A. Grishchuk, Sov. Phys. JETP **60** 267 (1984).

[2] A. Läuchli, J. C. Domenge, C. Lhuillier, P. Sindzingre, and M. Troyer, PRL **95** 137206 (2005).

[3] H. Kim et al., Nature **625** 264 (2024).

[4] J. Bao, M. Gohlke, K. Penc and N. Shannon, (in preparation).

[5] J. Bao, K. Penc, N. Shannon and M. Gohlke (in preparation).

[6] A. Iwaki, A. Shimizu, and C. Hotta, PRR **3** L022015 (2021).

[7] M. Gohlke, A. Iwaki, and C. Hotta, SciPost Phys. **15** 206 (2023).

[8] J. Hauschild, and F. Pollmann, SciPost Phys. Lect. Notes 5 (2018).

Realistic finite-temperature simulations and application to giant magnetocaloric effects with charge–spin–lattice coupling

Hung Ba TRAN
Advanced Institute for Materials Research (WPI-AIMR), Tohoku University,
Email: *tran.ba.hung.a6@tohoku.ac.jp*,

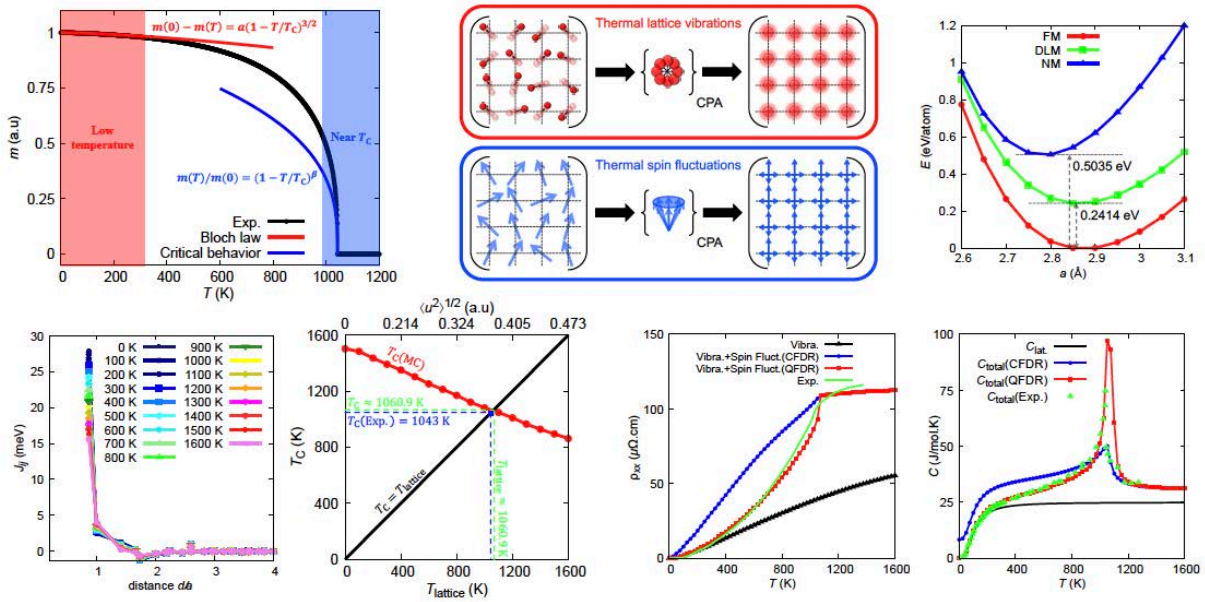


Figure 1: Realistic finite-temperature simulations for magnetic properties of bcc Fe.

Accurate prediction of magnetic properties at finite temperatures is essential for designing functional materials. Conventional simulations based on the classical Heisenberg model fail to reproduce experimental spontaneous magnetization, particularly at low and intermediate temperatures, due to the neglect of the quantization effect of spin. In this work, we developed a realistic finite-temperature simulation framework by combining first-principles calculations with Monte Carlo simulations, including both thermal lattice vibration and spin fluctuation effects[1], as shown in Fig. 1. The magnetic exchange coupling constants J_{ij} are evaluated at finite temperatures with lattice vibration effect. A quantum fluctuation–dissipation relations (QFDR) are introduced to describe thermal energy as magnon excitations using Bose–Einstein statistics.

The developed method significantly improves the temperature dependence of spontaneous magnetization and Curie temperature compared to conventional approaches. The inclusion of thermal lattice vibration reduces the exchange interactions, while quantum spin fluctuations

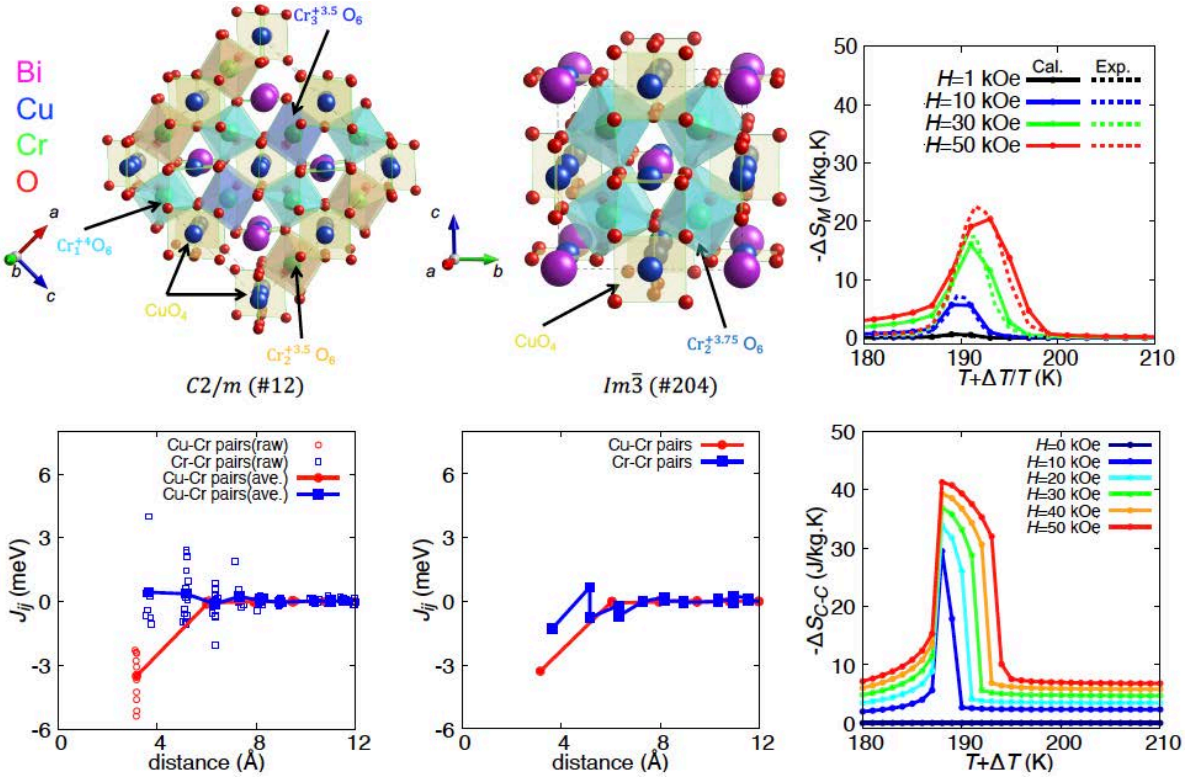


Figure 2: Giant magnetocaloric effect in $BiCu_3Cr_4O_{12}$ with charge–spin–lattice coupling.

correct the low-temperature behavior. This framework enables accurate prediction of magnetic and transport properties at finite temperatures[1].

Based on this method, we further investigated the giant magnetocaloric effect (MCE) in $BiCu_3Cr_4O_{12}$, where strong charge–spin–lattice coupling plays a key role[2]. This material exhibits a first-order magnetostructural transition between $C2/m$ and $Im\bar{3}$ phases, accompanied by charge disproportionation, as shown in Fig. 2. To describe this behavior, we employed a mixed-phase model combining magnetic and lattice contributions, and evaluated the entropy change using both Maxwell relations and the Clausius–Clapeyron equation.

The giant MCE originates from the strong interplay between charge, spin, and lattice degrees of freedom. In contrast to conventional systems, the entropy change includes significant lattice and electronic contributions in addition to the magnetic component. This coupling enhances the total entropy change through a first-order phase transition, providing a new mechanism for large MCE.

In summary, we developed a realistic finite-temperature simulation framework and demonstrated its application to magnetocaloric materials. The results reveal that multi-physics coupling is essential for accurately describing and enhancing magnetocaloric effects, providing a guideline for designing next-generation energy-efficient cooling materials.

References

[1] H. B. Tran and H. Li, J. Mater. Chem. C **13**, 11393–11401 (2025).

[2] H. B. Tran, H. Li, M. Goto, K. Sato, and Y. Shimakawa, J. Mater. Chem. A **13**, 34286–34296 (2025).

Multiphase-Reactive Simulations of Aluminum Particle Combustion with Detailed Kinetics and Interfacial Phase Change

Hangpeng JIANG, Yuji SUZUKI, and Minhyeok LEE
Department of Mechanical Engineering, School of Engineering,
The University of Tokyo, 7-3-1 Hongo, Bunkyo-ku, Tokyo 113-8656

In recent years, aluminum (Al) has attracted considerable attention as a potential carbon-free fuel for thermal energy systems [1]. Recently, extensive efforts have been made to develop Al combustion models. Most research has incorporated detailed chemical kinetics for Al oxidation, while treating the complex phase-change process with analytic approaches and relying on restrictive assumptions. These simplifications significantly limit their applicability to practical combustion environments.

To address these limitations, we developed an interface-resolved multiphase CFD model for Al particle combustion based on the Volume-of-Fluid (VOF) method, to fully resolve mass and heat transfer processes at the liquid-gas interface, to capture droplet deformation and the complex physicochemical phenomena that arise during combustion, and to reveal both species consumption/generation behavior and global combustion characteristics.

The model is validated by comparing the predicted particle/droplet diameter evolution under pure evaporation conditions with experimental data. Here, we simulate the microgravity evaporation of isolated *n*-heptane droplets in nitrogen and compare the numerical results with experimental data by Nomura et al. [2]. As shown in Fig. 1, the squared droplet diameter exhibits an approximately linear decay, consistent with the classical d^2-law. Comparisons between our numerical predictions and experimental data show good agreement, especially at higher temperatures. As the droplet diameter decreases, the discrepancy between predictions and measurements becomes non-negligible, which can be attributed to the neglect of gravity effects.

The combustion of a 93 μm Al particle under the conditions $X_{O2} = 0.21$, $X_{N2} = 0.79$, $T = 300$ K is simulated. To initiate ignition, an external volumetric heat source term $\boldsymbol{q}_{\mathrm{ext}} = 100$ MW/m^3/K is applied uniformly within the Al particle. This source remains active until the average particle temperature reaches $T_0 = 2327$ K. Under this configuration, ignition is achieved within approximately 0.013 ms.

Figure 2 shows the evolution of the radial temperature profiles. After ignition, the

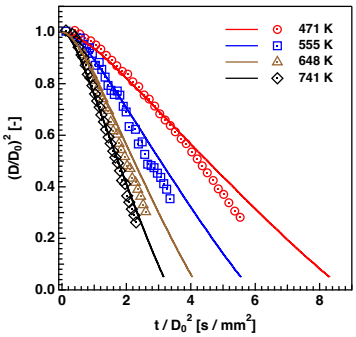


Fig. 1: Comparison of $(D/D_0)^2$ at different temperatures for the evaporation of *n*-heptane. Markers and solid lines indicate the experimental data [2] and numerical results, respectively.

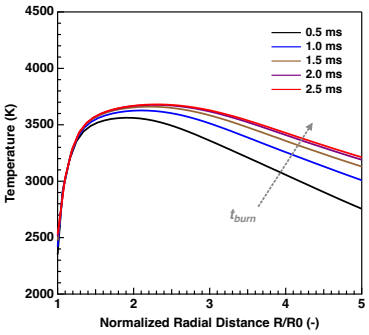


Fig. 2: Evolution of temperature distribution along radial distance.

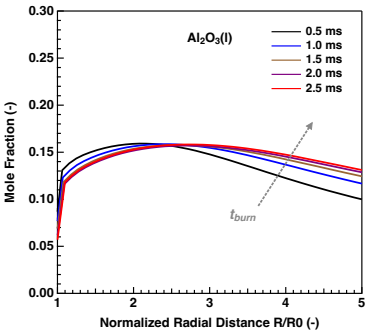


Fig. 3: Evolution of $Al_2O_3(l)$ distribution along radial distance.

interfacial temperature rapidly rises to about 2350 K at 0.5 ms and approaches a quasi-steady value of about 2500 K at around 2.5 ms. Under the interfacial thermal-equilibriu m assumption, evaporation and combustion are diffusion-limited. Vaporized Al is transported outward by diffusion, and its oxidation with O_2 releases heat and raises the flame temperature until a quasi-steady state is established. The predicted quasi-steady flame temperature reaches about 3650 K, in good agreement with recent measurements [3], whereas the interfacial temperature is about 150 K lower, likely because heterogeneous reactions and radiative feedback from Al_2O_3 smoke are neglected.

Figure 3 shows the temporal distribution of the major product $Al_2O_3(l)$. The peak mole fraction of $Al_2O_3(l)$ remains nearly constant at about 0.15 during the first 2.5 ms, while its peak position shifts outward from about 2 to 2.8 particle radii, consistent with the temperature peak. Similar outward shifts in both the temperature and $Al_2O_3(l)$ reflect the dominant heat release associated with $Al_2O_3(g)$ condensation, which is modeled through $Al_2O_3(g) \rightarrow Al_2O_3(l)$ reaction.

References

[1] K.A. Trowell, S. Goroshin, D.L. Frost, J.M. Bergthorson, Appl. Energy **275,** 115112 (2020).

[2] H. Nomura, Y. Ujiie, H.J. Rath, J. Sato, M. Kono, Symp. Combust. Proc. **26**, 1267–1273 (1996).

[3] H. Keck, C. Chauveau, G. Legros, S. Gallier, F. Halter, Combust. Flame **268**, 113616 (2024).

Theoretical study of static and dynamic spin structure factors in 3D antiferromagnets

Harald JESCHKE
Research Institute for Interdisciplinary Science, Okayama University
3-1-1 Tsushima-naka, Kita-ku, Okayama 700-8530

Precise evaluation of magnetic Hamiltonians is the first step in the study of complex magnetic materials. For 3*d* materials, DFT+U methods give a very good description, and an energy mapping approach with statistical evaluation of energies of many spin configurations yields excellent results. The mineral nabokoite ($KCu_7TeO_4(SO_4)_5Cl$) which realizes a square kagome network of Cu^{2+} spins has an intricate hierarchy of exchange interactions that realizes complex spin dynamics on pyramids [1]; theoretical results are in excellent agreement with experiment. By analyzing the spin structure factors for 2D and 3D systems and for different sublattices, we can identify distinct degeneracies and tendencies to form a spin liquid. We also studied $(CsCl)Cu_5As_2O_{10}$ [2] and $Mn_3Si_2Te_6$ [3] using DFT energy mapping and classical Monte Carlo simulations. For $Mn_3Si_2Te_6$, our calculations allow us to precisely capture and explain a dome in the pressure dependence of the ferrimagnetic ordering temperature.

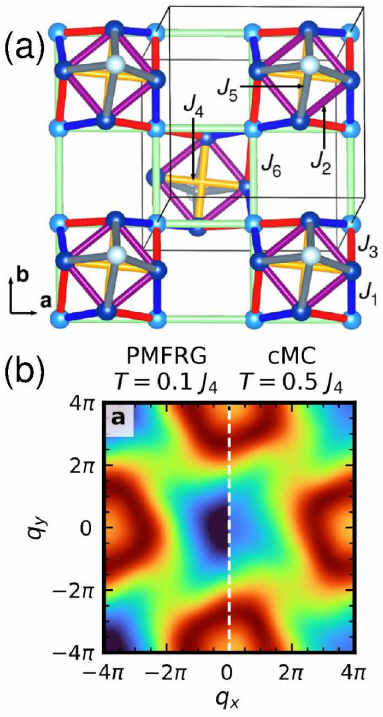


Figure 1: (a) Exchange paths of nabokoite. (b) Quantum and classical spin structure factor.

References

[1] M. G. Gonzalez, Y. Iqbal, J. Reuther, H. O. Jeschke, Field-induced spin liquid in the decorated square-kagome antiferromagnet nabokoite $KCu_7TeO_4(SO_4)_5Cl$, Comm. Mater. **6**, 96 (2025).

[2] I. V. Kornyakov, M. V. Likholetova, I. E. Lezova, S. V. Krivovichev, H. O. Jeschke, Y. Iqbal, A. V. Tkachev, S. V. Zhurenko, A. Gippius, L. V. Shvanskaya, A. Vasiliev, Crystal structure, magnetic and resonant properties of decorated spin kagome system $(CsCl)Cu_5As_2O_{10}$, J. Mater. Chem. C **14**, 3749 (2026).

[3] V. Venkatasubramanian, M. Shimizu, D. Guterding, H. O. Jeschke, Origin of pressure-induced anomalies in the nodal-line ferrimagnet $Mn_3Si_2Te_6$, Comm. Mater. **7**, 94 (2026).

Development of tensor network algorithms

Kenji HARADA
Graduate School of Informatics, Kyoto University
Kyoto 606-8501, Japan

We studied information-theoretic aspects of stochastic time-evolution models using tensor network representations. As a representative nonequilibrium system, we considered the one-dimensional Fredrickson–Andersen (FA) model[1], a kinetically constrained model in which a local spin can flip only when a neighboring site is excited. Although the equilibrium distribution of this model is simple, its dynamical behavior is highly nontrivial. In particular, in the s-ensemble of trajectories, where histories are biased by the dynamical activity, kinetically constrained models exhibit a first-order dynamical phase transition between active and inactive dynamical phases[2].

Our main target was the finite-time transition observed on the $s > 0$ side of the one-dimensional FA model. We analyzed this process with a tensor network simulation of the biased time evolution[3]. Starting from a finite-density state, the system first remains in an active state for a long time and then rapidly approaches an inactive state. The time-dependent density distribution shows a clear bimodal structure for weak bias, such as $s = 0.05$, while it remains essentially single-peaked for stronger bias, such as $s = 0.5$. This contrast indicates that the finite-time transition at weak positive bias can be interpreted as an escape process from a metastable active state in trajectory space.

We then evaluated the second Rényi entropy density of the probability distribution,

$$h_2 = -\frac{1}{N} \log \sum_x P(x)^2,$$

together with the contribution from the zero-density state. The Rényi entropy starts to decrease well before the average density begins to drop at $s = 0.05$. Moreover, its decay is almost dominated by the contribution of the zero-density state. This result shows that the Rényi entropy is sensitive to a structural change in the full probability distribution, even when conventional observables such as the average density still appear to remain in the metastable regime.

These results demonstrate that tensor network methods provide a useful framework for directly evaluating information measures of probability distributions generated by stochastic time-evolution models. The present analysis clarifies the role of the inactive state in the metastable escape process of the s-ensemble and is consistent with the scenario of a first-order dynamical phase transition in kinetically constrained models. As a future direction, we plan to extend the Rényi-entropic analysis to dynamical quantities and to investigate its relation to entropy production and other measures of nonequilibrium irreversibility.

References

[1] G. H. Fredrickson and H. C. Andersen, "Kinetic Ising Model of the Glass Transition," Phys. Rev. Lett. **53**, 1244 (1984).

[2] J. P. Garrahan, *et al.*, "First-order dynamical phase transition in models of glasses: an approach based on ensembles of histories," J. Phys. A: Math. Theor. **42**, 075007 (2009).

[3] K. Harada and N. Kawashima, "Entropy Governed by the Absorbing State of Directed Percolation," Phys. Rev. Lett. **123**, 090601 (2019).

Partially Entangled Typical Thermal State for Variational Quantum Monte Carlo Calculation

Toshiaki IITAKA

Discrete Event Simulation Research Team

RIKEN Center for Computational Science (R-CCS),

2-1 Hirosawa, Wako, Saitama, 351-0198, Japan.

Random state methods, also known as typical thermal state methods [1-3] , have been successfully applied to finite-temperature calculations of quantum many-body systems in the full Hilbert space. The key idea is that the trace of an operator can be approximated by the statistical average of its expectation values over random states,

$$\mathrm{tr}[X] \approx \mathbb{E}[\langle\Phi|X|\Phi\rangle]. \quad (1)$$

The random state method has been extended to *variational wavefunctions* by replacing some of the variational parameters with random variables [4-6]. However, since the number of random parameters is significantly smaller than in the full Hilbert space, the statistical convergence deteriorates, requiring averages over a large number of random states [7, 8].

To address this issue, we propose the *Partially Entangled Typical Thermal State* (PETTS) as a class of random states suitable for finite-temperature Variational Quantum Monte Carlo (VQMC) calculations. PETTS, $|\Phi_{PETTS}\rangle$, is defined as a tensor product of random states in non-overlapping plaquette subspaces that cover the entire system. It satisfies the trace formula. (1).

Compared to both fully entangled states in the full Hilbert space and simple product states, PETTS has an intermediate number of random parameters and an intermediate degree of entanglement. As a result, it improves statistical convergence while introducing only a modest increase in computational cost compared to product-state calculations. Examples of plaquette configurations for a 4×4 square lattice are shown in Fig. 1.

For finite-temperature calculations, we consider an extended variational wavefunction defined as the product of a PETTS and a physical ansatz.

$$\Phi(x;\sigma) = \Phi_{\mathrm{PETTS}}(\xi;\sigma)\,\Phi_{\mathrm{ansatz}}(w;\sigma)$$

where x stands for the combination of ξ and w. The state evolves in imaginary time and thermal expectation values are computed in the same manner as in the full Hilbert space formulation [6]. The most time-consuming part of the calculation, inverting large quantum metric matrices, is efficiently computed using NetKet[9] and JAX[10] on the GPU nodes of System C.

Fig. 2 shows the energy, $E(\beta)$ for each random state in the AFM Heisenberg model on a 4×4 square lattice with J=1. A Restricted Boltzmann Machine with $6N_{spin}$ hidden units is used as the physical ansatz. The results demonstrate that stochastic fluctuations are significantly reduced when using PETTS (2×4), compared to the product-state approach.

References

[1] T. Iitaka, and T. Ebisuzaki, Phys. Rev. Lett. **90**, 047203 (2003).

[2] T. Iitaka, and T. Ebisuzaki, Phys. Rev. E **69**, 057701 (2004).

[3] S. Sugiura, and A. Shimizu, Phys. Rev. Lett. **111**, 010401 (2013).

[4] K. Takai *et al.*, J Phys Soc Jpn **85**, 034601 (2016).

[5] T. Iitaka, arXiv:2006.14459 (2020).

[6] D. Hendry, H. Chen, and A. Feiguin, Phys. Rev. B **106**, 165111 (2022).

[7] A. Iwaki, A. Shimizu, and C. Hotta, Phys. Rev. Res. **3**, L022015 (2021).

[8] S. Goto, R. Kaneko, and I. Danshita, Phys. Rev. B **104**, 045133 (2021).

[9] https://www.netket.org/

[10] https://docs.jax.dev/en/latest/

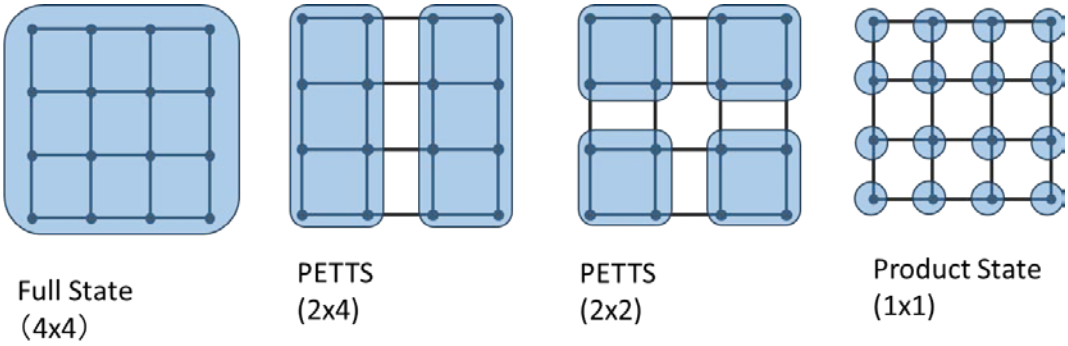


Fig. 1: Examples of plaquette configurations for 4x4 square lattice

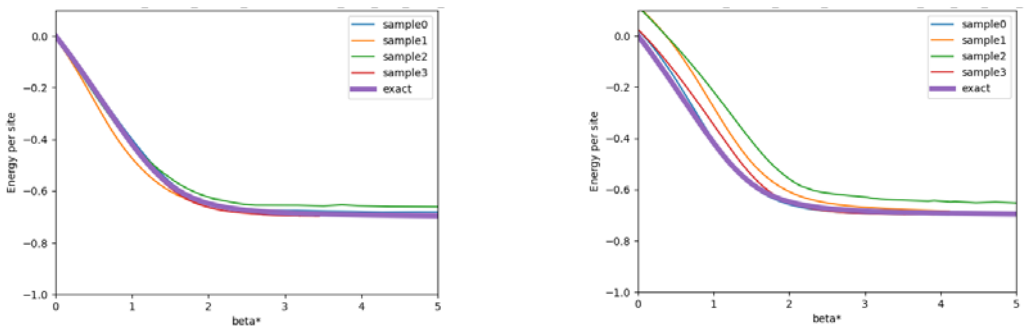


Fig. 2 : Energy, $E(\beta)$ of AFM Heisenberg model on 4x4 square lattice
(a) PETTS(2x4) (b)Product State

Physical properties of crosslinked polymer networks through network topology analysis

Katsumi HAGITA,[1] and Takahiro MURASHIMA[2]

[1]*Department of Applied Physics, National Defense Academy, Yokosuka 239-8686*

[2]*Department of Physics, Tohoku University, Sendai 980-8578*

To investigate the physical/mechanical properties of the crosslinked polymer networks, we studied mainly two types of coarse-grained MD models. (1) Bead-spring type Kremer-Grest (KG) model with bond breakage [1] and (2) Martini force field.

Regarding KG model with bond breakage [1], we studied abnormal butterfly patterns (ABPs) in small angle two-dimensional scattering patterns (2DSPs) of stretched inhomogeneous networks and finalized as a published paper [2]. The product run was performed on FUGAKU on the basis of the preparation study using the ISSP supercomputer. Here, uniaxial stretching was performed under the constant volume condition. Figure 1 (left) shows the ABPs in 2DSPs for stretching ratios λ = 4.0, 4.2, 4.4, and 4.6 for a diamond lattice network with bimodal strand lengths ($N_s - N_b$, $N_s + N_b$) = (10, 40). In the large λ regions, a small number of bond breaks occur, gradually increasing the non-uniformity. Reflecting this, the 2DSPs change. Furthermore, in Figure 1 (right), the ABP peak position was evaluated as a function of q_x and it was revealed that it shifts according to the stretching.

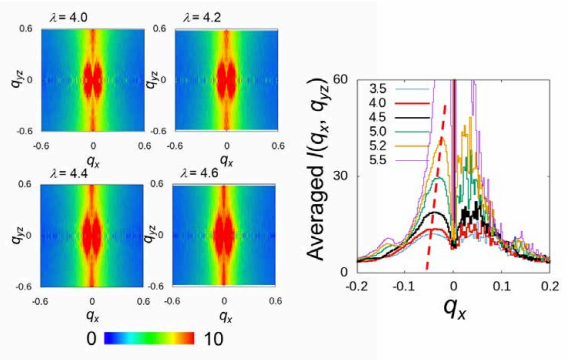


Fig. 1: (Left) ABPs in 2DSPs for stretching ratios of 4.0, 4.2, 4.4, and 4.6, and (right) evaluation of ABP peak shift.

Regarding the Martini force field, we simulated Tetra-PEG gels at eight (2x2x2) times the system size of all-atom (AA) models [3]. Despite evaluating stress values across various temperatures and shear strains over 2000 ns, significant noise has hindered systematic results, requiring improved methods to address long-wavelength fluctuations.

References

[1] K. Hagita, T. Murashima, Macromolecules, **57**, 10903–10911 (2024).

[2] K. Hagita, T. Murashima, Macromolecules, 58, 10, 5368–5376 (2025).

[3] K. Hagita, et al. Macromolecules, 56, 8095–8105 (2023).

Research of superconductivity induced by multipole fuctuations in the bi-layer orbital degenerate Hubbard model

Takashi HOTTA
Department of Physics, Tokyo Metropolitan University
1-1 Minami-Osawa, Hachioji, Tokyo 192-0397

In 2023, $La_3Ni_2O_7$ superconductor has been discovered [1], and it was the first bulk superconductor other than cuprates to exhibit a transition temperature T_c higher than the boiling temperature 77K of liquid nitrogen. This material possesses a bilayer Ruddlesden-Popper-type perovskite structure, and the formal valence of nickel ion is $Ni^{2.5+}$ ($3d^{7/5}$). This is described as a mixed-valence state of Ni^{2+} ($3d^8$) and Ni^{3+} ($3d^7$), corresponding to a configuration in which both the $d_{3z^2-r^2}$ and $d_{x^2-y^2}$ orbitals are half-filled, and a configuration in which only the $d_{3z^2-r^2}$ orbital is singly occupied, respectively.

At ambient pressure, $La_3Ni_2O_7$ does not become superconducting, but when a pressure of 14.0-43.5 GPa is applied, it becomes a superconductor with a maximum T_c of 80 K. According to synchrotron X-ray diffraction (XRD) measurements, $La_3Ni_2O_7$ belongs to the orthorhombic *Amam* space group under low pressures of 1.6-10.0 GPa, while a structural transition is observed around 10.0 GPa, and at pressures above 15 GPa, it is known to adopt the orthorhombic *Fmmm* space group. This transition corresponds to a change in the Ni-O-Ni bond angle along the c-axis from 168 to 180 degrees. Accompanying this structural change, the σ-bonding between the Ni $d_{3z^2-r^2}$ orbital and the apical oxygen $2p$ orbital is strengthened. Unlike in cuprate high-temperature superconductors, the $d_{3z^2-r^2}$ orbital is believed to play a crucial role, which is considered one of the characteristic features of nickelate superconductors.

A large number of theoretical studies have been conducted to clarify the symmetry of the gap function in $La_3Ni_2O_7$ [2–10]. Previous works have shown that the most stable solution is an $s^{\pm}$-wave state, originating from interlayer pairing of the $d_{3z^2-r^2}$ orbitals. On the other hand, $d_{x^2-y^2}$-wave and d_{xy}-wave states are energetically competitive with the $s^{\pm}$-wave state, suggesting that the symmetry may change with slight variations in pressure or crystal-field splitting. Experimentally, it remains difficult to precisely determine the gap structure under high pressure, and no definitive conclusion has been obtained. However, point-contact spectroscopy (PCS) measurements have observed a V-shaped spectrum, indicating the possible presence of nodes and suggesting the d-wave gap symmetry [11].

In this research, we analyze the following bi-layer two-orbital Hubbard model for the e_g electron system.

$$\begin{aligned} H &= \sum_{\boldsymbol{k},\sigma}\sum_{\ell\ell',\mu\mu'} \varepsilon_{\boldsymbol{k}\ell\ell'\mu\mu'} c^{\dagger}_{\boldsymbol{k}\sigma\ell\mu} c_{\boldsymbol{k}\sigma\ell'\mu'} \\ &+ U\sum_{\boldsymbol{i},\ell,\mu} n_{\boldsymbol{i}\uparrow\ell\mu} n_{\boldsymbol{i}\downarrow\ell\mu} + U'\sum_{\boldsymbol{i},\ell} n_{\boldsymbol{i}\ell a} n_{\boldsymbol{i}\ell b} \\ &+ J\sum_{\boldsymbol{i},\ell,\sigma\sigma'} c^{\dagger}_{\boldsymbol{i}\sigma\ell a} c^{\dagger}_{\boldsymbol{i}\sigma'\ell b} c_{\boldsymbol{i}\sigma'\ell a} c_{\boldsymbol{i}\sigma\ell b} \\ &+ J'\sum_{\boldsymbol{i},\ell} (c^{\dagger}_{\boldsymbol{i}\uparrow\ell a} c^{\dagger}_{\boldsymbol{i}\downarrow\ell a} c_{\boldsymbol{i}\downarrow\ell b} c_{\boldsymbol{i}\uparrow\ell b} + \text{h.c.}) \\ &+ U_{\perp}\sum_{\boldsymbol{i}} n_{\boldsymbol{i}Ab} n_{\boldsymbol{i}Bb}, \end{aligned}$$

where $c_{\boldsymbol{k}\sigma\ell\mu}$ indicates the annihilation operator of an electron wave vector $\boldsymbol{k}$ of the layer ℓ

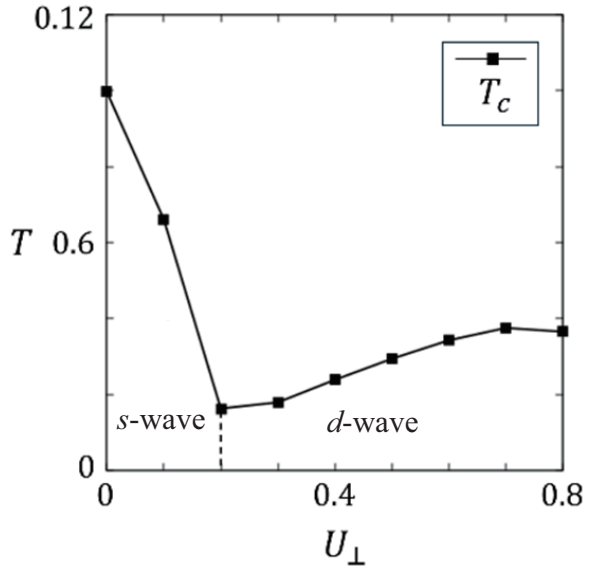


Figure 1: Superconducting phase diagram. With the increase of $U_\perp$, the symmetry of the gap function is changed from s- to d-wave.

(=A and B) and the orbital μ (=a and b), a and b denote $d_{x^2-y^2}$ and $d_{3z^2-r^2}$ orbitals, respectively, $\varepsilon_{\boldsymbol{k}\ell\ell'\mu\mu'}$ denotes one-electron energy among layers and orbitals, $\boldsymbol{i}$ indicates the Ni site, $n_{\boldsymbol{i}\sigma\ell\mu} = c^\dagger_{\boldsymbol{i}\sigma\ell\mu}c_{\boldsymbol{i}\sigma\ell\mu}$, $n_{\boldsymbol{i}\ell\mu} = \sum_\sigma n_{\boldsymbol{i}\sigma\ell\mu}$, U is an intra-orbital Coulomb interaction, U' is an inter-orbital Coulomb interaction, J is an exchange interaction, J' is a pair-hopping interaction, and $U_\perp$ denotes an interlayer Coulomb interaction between b orbitals.

In this research, we clarify the effect of $U_\perp$ on the superconducting states of $La_3Ni_2O_7$. For the purpose, we solve the gap equation with the effective interaction obtained by a random phase approximation in terms of the Coulomb interactions. As for the details of $\varepsilon_{\boldsymbol{k}\ell\ell'\mu\mu'}$ and hopping parameters, readers can consult with Ref. [12]. The values of the on-site Coulomb interactions are set as $U = 1.2$, $U' = 0.8$, $J = 0.2$, and $J' = 0.2$ in the unit of eV. The electron number per Ni ion is set as 1.5 throughout the numerical calculations.

A typical results is shown in Fig. 1, in which T_c is depicted as a function of $U_\perp$. For $U_\perp = 0$, the gap function is dominated by interlayer pairing of the $d_{3z^2-r^2}$ orbitals, and an isotropic s-wave symmetry is obtained in the orbital representation. This result is consistent with previous studies. For $U_\perp \geq 0.2$, the gap function is likewise dominated by interlayer $d_{3z^2-r^2}$-orbital pairing. Note, however, that the symmetry is found to change to a d-wave state. These results demonstrate that the increase of the interlayer Coulomb interaction $U_\perp$ drives a transition in the gap symmetry from an s-wave to a d-wave state.

References

[1] H. Sun *et al.*, Nature **621**, 493 (2023).

[2] Q. Yang and Q. Wang, Phys. Rev. B **108**, L140505 (2023).

[3] Y. Gu *et al.*, Phys. Rev. B **108**, 165141 (2023).

[4] Y. Gu *et al.*, Phys. Rev. B **111**, 174506 (2024).

[5] C. Lu *et al.*, Phys. Rev. B **110**, 094509 (2024).

[6] Z. Luo *et al.*, npj Quantum Materials **9**, 61 (2024).

[7] Y. Liu *et al.*, Phys. Rev. Lett. **131**, 236002 (2023).

[8] L. Braz, G. Martins, and L. Silva, Phys. Rev. Research **7**, 033023 (2025).

[9] Y. Zhang *et al.*, Nat. Commun. **15**, 2470 (2024).

[10] C. Xia *et al.*, Nat. Commun. **16**, 1054 (2025).

[11] Z. Cao *et al.*, arXiv: 2509.12606.

[12] Z. Luo *et al.*, Phys. Rev. Lett. **131**, 126001 (2023).

Temperature dependence of specific heat in an extended Kitaev model on a honeycomb lattice

Takafumi SUZUKI
Graduate School of Engineering,
University of Hyogo, Shosha 2167, Himeji, Hyogo 671-2280

In 2025, we studied the following two projects.

(1) Temperature dependence of specific heat in an extended Kitaev model on a honeycomb lattice

The S=1/2 Kitaev- Γ model on a honeycomb lattice is considered as an effective model of $RuCl_3$. Numerous efforts have also been devoted to realize materials described by the spin-S Kitaev model and the related model. In this project, we investigated the temperature dependence of the specific heat in S=1 Kitaev-Γ model on a honeycomb lattice. In this model, anisotropy exists in the nearest neighbor interaction on each bond as shown in figure 1. In previous project, we clarified the ground state phase diagram and found that the C_3 symmetric phase is lacked in the N=18 cluster. Since the C_3 symmetric phase only appears in the S=1/2 case under a regular-hexagonal periodic-boundary condition [2], we tried the computation for N=24 cluster for the S=1 case. However, because the computational cost for N=24 cluster is huge, we have not obtained yet enough results to conclude the existence of the C_3 symmetric phase in the S=1 case. However, we continue this project to clarify it.

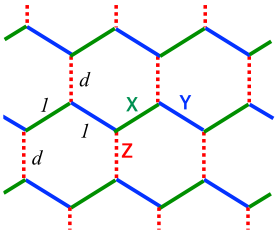


Fig. 1: Anisotropically interacting Kitaev-Γ model. The coupling strength on the X/Y bond is unity, and *d* is the ratio of the coupling strength on the Z bond against that on the X/Y bond.

Next, we investigated the temperature dependence of the specific heat for the same model in the S=1 case by using a thermal pure quantum state [3]. In the S=1 case, the two-peak structure is only confirmed near isotopically interacting case ($d \sim 1$) and the two-peak structure disappears as anisotropy of the interaction exists. We find that the single peak in the spin chain limit corresponds to the high-temperature peak. The obtained results are quite similar to those in the S=1/2 case [3].

(2) Temperature classification by machine learning assisted method

In recent condensed matter physics, Machine learning (ML) techniques have been applied to condensed matter physics: ML is applicable to classify phases from a given magnetization distribution [4]. On the other hand, it is known that estimation of temperature from a given magnetization distribution is difficult. This is because similar magnetization distribution appears at different temperatures due to thermal fluctuation. In this project, we focused on the classification of temperatures from given magnetization distribution. First, we prepared data sets of magnetization distribution for several temperatures by classical Monte Carlo calculations for two-dimensional (2d) three-state Potts model on a square lattice. Next, we trained a convolutional neural network by the prepared magnetization distribution, where we adopted a supervised ML method for training. We found that the accuracy of temperature classification is improved when the system size increases and the temperatures are located near the phase transition temperature. In addition, the accuracy of temperature classification shows data collapse with critical exponent for the 2d three-state Potts model, when we perform finite-size scaling analysis.

References

[1] G. Jackeli and G. Khaliullin, Phys. Rev. Lett. **102**, 017205 (2009). [2] M. Gohlke, J. C. Pelayo, and T. Suzuki, Phys. Rev. B **109**, L220410. [3] S. Sugiura, and A. Shimizu, Phys. Rev. Lett. **108**, 240401 (2012). [4] J. Carrasquilla and R. G. Melko, Nat. Phys. **13**, 431-434 (2017). [5] W. -C. Guo and L. He, New J. Phys. **25**, 083037 (2023).

Kinetics of phase transition and polyamorphism

Kazuhiro FUCHIZAKI
Department of Physics, Ehime University, Matsuyama 790-8577

FY2025 was the year in which the author retired. As part of this retirement, he had to shut down his lab during the latter half of FY2025. The author could not substantially access the supercomputer. Therefore, the outcome obtained during the first half, which was reported at the international conference DGK2026, held in Lübeck, Germany, in February 2026, was summarized in this report.

The author has reconsidered polyamorphism, especially a liquid–liquid transition, since 2023. Polyamorphism, by definition, restricts a separation or transition between two states that must consist of a single chemical component. He started the investigation by taking a phosphorus system as an example because it has been established as one that undergoes a transition between thermodynamically stable liquid phases [1]. As reported last year, quantum chemical calculations using GAUSSIAN 19 [2] indicated that approximately 4 eV of activation energy is required to break a single bond in a P_4 molecule to form a radically polymerizable state. That is, the reaction between n P_4 molecules and a $(P_4)_n$ molecule is not physical but indeed chemical. Therefore, the liquid–liquid transition (LLT) in phosphorus could be a monotectic phase transition between two phases composed of different chemical species.

The author examined a similar possibility for SnI_4, for which he has claimed the presence of the water-type LLT [3] for more than 10 years based on his group's experimental and theoretical studies, including molecular dynamics simulations. As noted, SnI_4 molecules undergo pressure-induced local symmetry breaking prior to the LLT [4]. The author speculated that this symmetry-lowering, which naturally introduces two length scales [4] assumed by the Jagla model [5] used to explain water's LLT [6], is due to a change in the molecular electronic configuration. GAUSSIAN 19 was again used to find the stable configuration and energy of two SnI_4 molecules approaching each other in a given orientation as a function of the distance between their central tin atoms. (The author performed similar computations already in 2023 without fixing the distance between two molecules. The relaxation finished to push molecules away from a starting distance.) When two molecules approach in an edge-to-edge orientation, the computation allowed the author to calculate the energy until the Sn-Sn distance reached ~ 1 Å, at which point the molecular symmetry lowered from T_d to C_{2v}. The energy increases up to ~ 6 eV at the closest approach. The calculation ended when the molecular distance became 5 Å in a face-to-face orientation. The final energy was slightly less than 1 eV, resulting in squashed C_{3v} molecular deformation. A similar energy–distance relation resulted when two molecules approached in a face-to-vertex (F2V) orientation. The computation was again not converged in this case when the distance decreased below 5 Å. The F2V orientation caused a pair of molecules to deform into squashed, elongated tetrahedra. Experimental measurements confirmed the deformation observed in the computations.

Physical molecular interactions were assessed as follows. First, it was decomposed into three contributions: the dispersion, the

octupole–octupole interaction, and the induced one. The first one was implemented using the four-center Lennard-Jones potential [7], whereas the formula from Ref. [8] was used for the second interaction, leaving the magnitude of the maximum octupole moment as a free parameter. The third interaction was ignored. To the author's surprise, this assessment based on classical mechanics quantitatively reproduced the quantum-chemical energy–distance relationships obtained under the specified mutual molecular orientations within the distances over which the computations converged. It should be noted that the classical assessment in the F2V orientation showed a peculiar energy–distance behavior at distances beyond the range of quantum assessment; an energy barrier amounting to 30 eV appeared when the intermolecular iodine–iodine separation takes the minimum distance of 2.51 Å. We may conclude the formation of a metallic I_2 bond when two intermolecular iodine atoms approach close within a distance of ~ 3 Å. Therefore, the LLT in SnI_4 may also be a transition associated with a change in chemical components.

References

[1] Y. Katayama *et al.*: Nature **403**, 170 (2000).

[2] M. J. Frisch *et al.*: GAUSSIAN 09 Revision E.01, Gaussian, Inc., Wallingford, CT, 2009.

[3] K. Fuchizaki *et al.*: J. Chem. Phys. **135**, 091101 (2011).

[4] K. Fuchizaki *et al.*: J. Chem. Phys. **150**, 114501 (2019).

[5] E. A. Jagla: J. Chem. Phys. **111**, 8980 (1999).

[6] G. Franzese: Nature **409**, 692 (2001).

[7] K. Fuchizaki *et al.*: J. Chem. Phys. **112**, 10379 (2000).

[8] K. Fuchizaki and K. Nagai: Solid State Commun. **132**, 305 (2004).

Application of sine-square deformation to calculate thermodynamic properties in frustrated quantum magnets

Chisa HOTTA

Department of Basic Science,

The University of Tokyo, Meguro-ku Komaba, Tokyo 153-8902

We studied finite temperature prooerties of a quantum spin-1/2 antiferromagnets on two-dimensional lattices. To access bulk behavior with limited system sizes, we employ the sine-square deformation (SSD) technique, where a smooth real-space envelope function continuously suppresses the local energy scale toward the system boundaries. The resulting SSD Hamiltonian yields quantum eigenstates whose central region reproduces bulk-like properties, enabling accurate evaluation of thermodynamic quantities close to the thermodynamic limit even for relatively small finite clusters [1]. Using these effective bulk states, we calculate the temperature dependence of the energy density, specific heat, and magnetic susceptibility [2]. The 1D and square lattice results show agreement with the exact solutions typically within the accucary of 10^{-3} of the data plotted in Fig. 1. Both the triangular- and kagome-lattice antiferromagnets exhibit characteristic low-temperature anomalies in the specific heat, including shoulder-like features and pronounced double-peak structures. In contrast, the kagome lattice shows a particularly strong enhancement of magnetic susceptibility extending down to the lowest accessible temperature regime. By comparing these frustrated systems with the square-lattice and one-dimensional antiferromagnets, we clarify the distinct nature of their low-energy excitations. Although both the triangular and kagome lattices retain substantial residual entropy at low temperatures, the excitations below approximately $0.5J$ in the kagome lattice are dominated by magnetic excited states, whereas such magnetic contributions remain much less significant in the triangular-lattice .

References

[1] C. Hotta, K. Asano, Phys.Rev. B. **98**, 140405 (2018).

[2] C. Hotta, to appear in Zeitschrift für Naturforschung A, DOI:10.1515/ZNA-2025-0392 (2026).

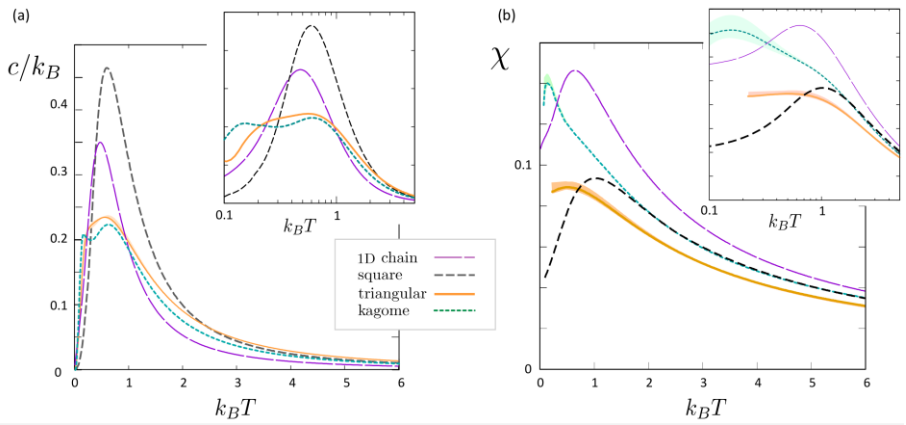


Fig.1: Specific heat and susceptibility of the S=1/2 Heisenberg model on four different lattices.

Stabilization of borophene by step edges on Ni(111)

Takeshi NAKAGAWA

Interdisciplinary Graduate School of Engineering Sciences,

Kyushu university, 6-1 Kasuga koen, Kasuga, Fukuoka 816-8580

We have investigated the formation of borophene on the Ni(111) surface. Experimental scanning tunneling microscopy (STM) and low-energy electron diffraction (LEED) results indicate that B_{13} borophene is formed, which is supported by corresponding theoretical simulations. However, density functional theory (DFT) calculations using VASP, combined with structural searches based on particle swarm optimization (CALYPSO) [1], suggest that B_{13}, B_{14}, and B_{15} borophene structures are energetically competitive, as shown in Fig. 1(a).

To reconcile these experimental and theoretical results, we further examined the formation energies of borophene at step edges. Figure 2 shows the structural models for B_n (n = 12–17) with Ni [-110] steps. The angles between the step edges and the borophene frameworks are also indicated. The adsorption energy per boron atom is lowest for the B_{13} structure, as shown in Fig. 1(b). The formation energies, including the effect of step edges, further support the stability of the B_{13} structure.

These results demonstrate that borophene is stabilized at Ni step edges, which broadens the structural diversity of two-dimensional borophene sheets and provides new insights into the controlled synthesis of complex borophene architectures at step edges [2].

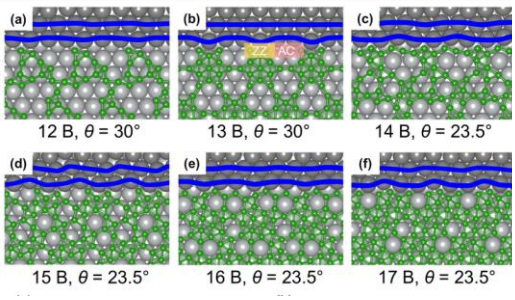


Fig. 1. Structural models for B_n (n = 12–17) with Ni [-110] steps. The angles between the step edges and the borophene frameworks are also indicated.

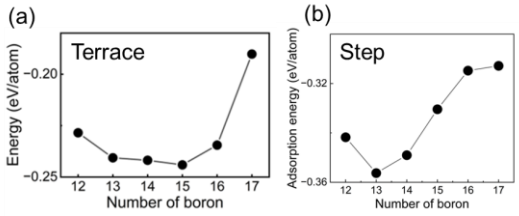


Fig. 2. Adsorption energy for B_n (n = 12–17) borophene models (a) on terrace and (b) terrace a with Ni [-110] steps. The angles between the step edges and the borophene frameworks are also indicated.

References

[1] Y. Wang, J. Lv, L. Zhu, Y. Ma, Phys. Rev. B **82**, 094116 (2010).

[2] X. Chen, I. Yamamoto, K. Takahashi, and T. Nakagawa, submitted.

Enhancement of correlation functions due to deficit in quantum spin systems

Chitoshi YASUDA
Department of Physics and Earth Sciences, Faculty of Science, University of the Ryukyus, Okinawa 903-0213, Japan

In a square-lattice antiferromagnetic Heisenberg model consisting of coupled bond-alternating chains of spin size $S = 1/2$, the ground state becomes an antiferromagnetic long-range ordered state and a dimerized state depending on the strengths of the bond alternation and interchain interaction. Dilution effects on the systems have been investigated using a quantum Monte Carlo method [1,2]. In the antiferromagnetic long-range ordered phase of the system without bond alternation, the finite staggered magnetization decreases monotonically with increasing the concentration of site dilution, and reaches zero at the percolation threshold. On the other hand, in the dimer phase, the finite staggered magnetization is induced by dilution. Interestingly, near the parameter where a quantum phase transition is driven in the pure system, it has been reported that the staggered magnetization does not decrease due to site dilution but increases once, even though the phase is antiferromagnetic long-ordered phase [1].

In this project, we calculated spin correlation functions of the ground state in the bond-diluted antiferromagnetic Heisenberg model consisting of bond-alternated chains on a square lattice using the quantum Monte Carlo method with the continuous-imaginary-time loop algorithm. In the loop algorithm, spin correlation functions between two spins can be calculated efficiently by an improved estimator. In order to investigate relations between the staggered magnetization and the spin correlation function, we examined the change in the distribution of the correlation functions with dilution in a randomly diluted bond system. At the concentration of dilution where the staggered magnetization is increased, the distribution of the nearest-neighbor correlation functions changed significantly compared to those of other correlation functions. However, no significant change was observed in the distribution due to the bond alternation and interchain interaction. Further investigation is needed.

In the process of this research, we found that all nearest-neighbor spin correlation functions are enhanced in a 1/8-depleted lattice system. The system is obtained by periodic site dilution in a square-lattice antiferromagnetic Heisenberg system and is composed of bipartite sublattices. Since the numbers of spins on the A and B sublattices are different due to the 1/8 depletion, the 1/8-depleted lattice system exhibits ferrimagnetic properties. We investigated the phase-transition temperatures in quasi-two-dimensional systems with 1/8-depleted lattices as the two-dimensional plane using the quantum Monte Carlo method. Our results establish a universal relation between the phase-transition temperatures and the interplane interactions [3].

References

[1] C. Yasuda, S. Todo, M. Matsumoto, and H. Takayama, Phys. Rev. B **64**, 092405 (2001).

[2] C. Yasuda, S. Todo and H. Takayama, J. Phys. Soc. Jpn. **75**, 124704 (2006).

[3] C. Yasuda *et. al*, Phys. Rev. Lett. **94**, 217201 (2005).

Analyses on the dynamics of metal ion solutes in ionic liquid-based electrolytes at the interfaces

Ken-ichi FUKUI

Department of Materials Engineering Science, Graduate School of Engineering Science, Osaka University, Machikaneyama, Toyonaka, Osaka 560-8531

Ionic liquids (ILs) are promising electrolytes for electrochemical devices such as secondary battery, capacitor, etc., due to their high chemical stability with negligible vaporization. Structuring and dynamics of the interfacial IL faced to charged graphite electrodes have been analyzed by molecular dynamics (MD) calculations [1], but the transport of Li^+ ion inside EDL formed at negatively charged electrode is not apparent because Li^+ coordinated with anions has negative charge in total. Recent our interface-selective spectroscopic study (EC-ATR-FUV) revealed such ion dynamics at the electrified interface [2], but molecular view is still insufficient. In the present study, we have analyzed the transport of Li^+ ion inside EDL of a BMIM-TFSI ionic liquid electrolyte at the negatively charged graphite electrode by MD calculations, which is closely related to charging process of Li-ion battery composed of these components.

All MD simulations were conducted by classical MD package of LAMMPS. A simulation cell contains 650 ion pairs of BMIM-TFSI with randomly distributed 150 pairs of Li-TFSI ($9\times8\times11$ nm^3) sandwiched with 5-layer graphite electrodes from top and bottom separated with vacuum layer. The same amounts of positive and negative charges were assigned to the top and bottom electrodes, respectively at the graphene layer faced to the electrolyte reproducing the electrified interfaces. In Fig. 1, interface structure obtained by following two different applied potential sequences; (i) firstly stabilized the interface structure by annealing the cell at the surface charge equivalent to ±1.8 V and then the surface charge equivalent to ±3.5 V was applied (lower case in Fig. 1) and (ii) the surface charge equivalent to ±3.5 V was directly applied (upper case in Fig. 1). MD trajectories for 10 ns at 350 K were analyzed.

Apparent difference was found for the interface structure at the electrode potential of –3.5 V depending on the applied potential sequences (Fig. 1). By the sequence (ii), no Li^+ was present close to the electrode. By analyzing the MD trajectories, it was due to the dense BMIM cation layers already formed by equilibrium at –1.8 V, which prevent the exchange of Li^+ at least during 10 ns. In the sequence (i), the interface is rather randomized and provided the chance for some Li^+ to be attached to the electrode by deforming the coordination with TFSI anions in 10 ns.

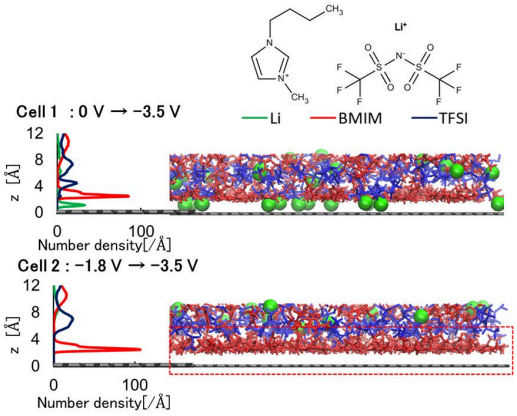


Fig. 1 Applied-potential-sequence dependent interfacial structure of a Li^+ containing BMIM-TFSI electrolyte at -3.5 V vs. PZC by MD calculation.

Reference

[1] H. Miyamoto, Y. Yokota, A. Imanishi, K. Inagaki, Y. Morikawa, K. Fukui, *Phys. Chem. Chem. Phys.* **20**, 1940 (2018).

[2] T. Kakinoki, A. Imanishi, S. Kondou, I. Tanabe, K. Fukui, *Phys. Chem. Chem. Phys.* **27**, 6056 (2025).

Self-organization and dynamics in dendrimer polyelectrolytes

Takamichi TERAO

Department of Electrical, Electronic and Computer Engineering,

Gifu University, Yanagido 1-1, Gifu, 501-1193

Dendrimers are macromolecules characterized by molecular chains that extend radially from the center of the molecule through repeated branching [1]. Due to their unique tree-like architecture, they possess precisely controlled shapes and functions at the molecular level. Molecular dynamics simulations of charged dendrimer systems have been conducted to investigate their structural formation. Karatasos [2] performed such simulations on charged dendrimer solutions with varying surface charge densities. The study reported that systematic variations in the Bjerrum length induce a mechanism related to the spatial correlation of counterions, driving the system from an amorphous, liquid-like arrangement to an ordered state with cubic phase symmetry.

However, this previous research was performed on a very small system consisting of only 30 molecules. Since order formation in soft matter is significantly affected by finite-size effects, it is of great interest to perform large-scale computer simulations using parallel supercomputers to better study this phenomenon in dendrimers.

In this study, the structure formation of charged dendrimer systems was investigated through parallel molecular dynamics simulations using LAMMPS. The simulated system contained 1,600 molecules. Evaluation of the generalized local order parameter [3] and the structure factor revealed that the system did not undergo crystallization even at high densities, instead remaining in a random configuration (Fig. 1). The identification of a crystalline phase remains an important subject for future investigation.

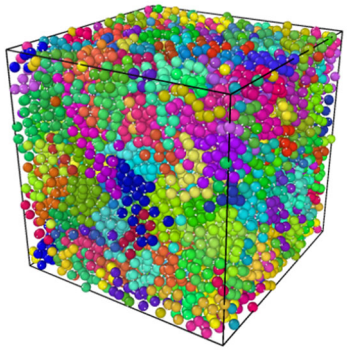


Fig. 1: Snapshot of the dendrimers with $\rho\sigma^3 = 1.25$.

References

[1] D. A. Tomalia, Prog. Polym. Sci., **30**, 294 (2005).

[2] K. Karatasos, Macromolecules **41**, 1025 (2008).

[3] R. Mizuno, K. Okumura, J. Oguri, and T. Terao, Mol. Sim. 45, 743 (2019).

Shape dependence of dynamic friction in viscoelastic materials

Michio OTSUKI

Institute of Science and Engineering,

Shimane University, Nishikawatsu-cho, Matsue, Shimane 690-8504

In this project, we investigate dynamic sliding friction in viscoelastic solids by finite element simulations. Frictional behavior of viscoelastic materials is computed over a wide range of viscosity coefficients and for sliding velocities from low speeds up to the elastic wave speed scale.

The simulations are executed on System C kugui using MPI-based domain decomposition of the finite element mesh. A typical run uses 16 compute nodes (2,000 cores) for 24 hours, solving a problem with 10 million finite-element nodes and 100 million time steps using our in-house code compiled with the Intel Fortran compiler.

As shown in Fig. 1, we show that the friction coefficient μ varies depending on the material viscosity $\tilde{\eta}$, and that the critical velocity where μ reaches a peak changes systematically. In particular, for low viscosity, the singular deformations occur at sliding velocities near the sound speed, resulting in rapid increases around the Rayleigh wave speed $\tilde{c}_{\mathrm{R}}$ and rapid decreases around the longitudinal wave speed $\tilde{c}_{\mathrm{L}}$ in the friction coefficient that cannot be explained solely by viscous effects. Based on the findings obtained in this study, we are further investigating the effect of geometric factors, such as contact shape, on frictional behavior.

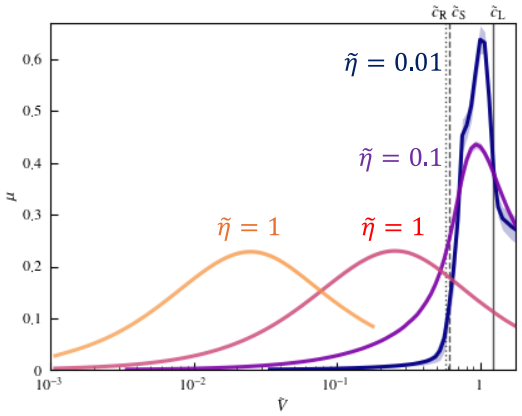


Fig. 1: Dependence of friction coefficient μ on sliding velocity $\tilde{V}$ for different viscosity coefficients $\tilde{\eta}$. The vertical lines represent the Rayleigh wave speed $\tilde{c}_{\mathrm{R}}$, shear wave speed $\tilde{c}_{\mathrm{S}}$, and longitudinal wave speed $\tilde{c}_{\mathrm{L}}$.

References

[1] W. Iwashita and M. Otsuki, Tribology Conference 2026 Spring Tokyo, F12 (2026).

Numerical Study of Dynamics in Spin Systems

Yasuyuki KATO
Department of Applied Physics, University of Fukui
Bunkyo, Fukui 910-8507

In this project, we continued numerical studies related to Kitaev spin systems from several complementary directions. As a recent outcome along this line, we studied the spin Seebeck effect in Kitaev spin liquids and clarified characteristic spin-current responses associated with fractional Majorana excitations [1]. This study also highlighted the importance of investigating dynamical and transport properties in a broader class of spin systems beyond the Kitaev limit, and provided useful background and motivation for the present project.

A main subject of the present project is a model interpolating between the AKLT state and the Kitaev spin liquid. Since the original honeycomb-lattice problem is computationally demanding, we started from a two-leg ladder geometry and developed a finite-system DMRG code for this purpose. The implementation was based on the ITensor library [2]. During this project period, the main emphasis was placed on establishing the numerical framework, carrying out benchmark calculations against exact diagonalization for small systems, and performing preliminary calculations for larger ladder systems. We also initiated a basic survey of the evolution between the AKLT and Kitaev limits for both ferro- and antiferromagnetic Kitaev couplings, as a step toward a more systematic analysis in future work.

Another important direction of the present project was international collaborative studies of spin systems using quantum Monte Carlo and related analytical approaches, including coupled-dimer antiferromagnets [3]. In particular, these studies clarified characteristic dynamical responses and field-induced features in such systems, providing a useful point of comparison for the spin-dynamical aspects of the present project. They also helped refine our perspective on spin dynamics and on the interpretation of numerical results obtained in the present study.

Further related results were presented at the 2025 Hokuriku Branch Meeting of the Physical Society of Japan. These included real-time simulations of current response in a classical Kondo lattice model with a helical spin structure and a study of the stability of vortex-antivortex crystals in a two-dimensional XY model with variable interaction range and magnetic field. Based on these results and ongoing collaborative work, we identified a concrete direction for extending the present project toward dynamical phenomena in both insulating and metallic magnetic systems.

References

[1] Y. Kato, J. Nasu, M. Sato, T. Okubo, T. Misawa, and Y. Motome: Phys. Rev. X **15**, 011050 (2025).

[2] M. Fishman, S. R. White, and E. M. Stoudenmire: SciPost Phys. Codebases **4** (2022).

[3] S.-S. Zhang, Y. Kato, E. A. Ghioldi, L. O. Manuel, A. E. Trumper, and C. D. Batista: Phys. Rev. B **112**, 024410 (2025).

Theoretical study on cooperative phenomena between magnetism and superconductivity in electron systems with multiple degrees of freedom

Shuntaro SUMITA
Department of Basic Science, The University of Tokyo, Meguro, Tokyo 153-8902

We have theoretically studied the interplay between superconductivity and magnetism in strongly correlated electron systems, by using numerical methods of microscopic models with multiple degrees of freedom including quantum many-body calculations as well as phenomenological analyses (project number: 2025-Ba-0006). During the last fiscal year, we have achieved some progress on the following topics.

(1) Phase-modulated superconductivity coexisting with altermagnetism

We conducted a study on spatially nonuniform superconducting states coexisting with altermagnetism [1], which induces anisotropic spin splitting in the energy bands despite a collinear antiferromagnetic structure. We performed many-body calculations of a Hubbard model on a two-sublattice tetragonal lattice, which incorporates a molecular field of the altermagnetic order and describes the anisotropic spin splitting. To discuss superconductivity mediated by magnetic fluctuations, we analyzed the linearized Eliashberg equation based on the random phase approximation. In this analysis, we employed the Matsubara Green's function method and utilized the `SparseIR.jl` package [2], which is based on the intermediate representation [3] and the sparse sampling [4], to reduce memory usage and computation time. As a result, we demonstrated that Fulde–Ferrell–Larkin–Ovchinnikov (FFLO) superconductivity, a spatially nonuniform state characterized by a finite center-of-mass momentum, is stabilized in the presence of altermagnetism.

Next, we microscopically constructed the phenomenological Ginzburg–Landau (GL) theory for superconductivity in altermagnets. The GL free energy density in tetragonal systems is represented by

$$f = \alpha|\eta|^2 + \beta|\eta|^4 + \kappa|\nabla|^2 + \delta|\nabla^2\eta|^2 + \delta'|\partial_X\partial_Y\eta|^2,$$

up to the fourth order of the superconducting order parameter η and spatial derivatives ∂_i. We numerically determined the coefficients α, β, and κ of the GL free energy, and revealed that κ (the second-order gradient term) changes its sign from positive to negative as the molecular field of altermagnetism increases, while β (the fourth-order uniform term) remains positive. Consequently, the FF state, in which only the *phase* of the order parameter is spatially modulated, is induced by altermagnetism. This is in contrast to the well-known result that the *amplitude*-modulated LO state is stabilized under a uniform Zeeman field, where both κ and β almost simultaneously change their sign. Thus, we conclude that the altermagnetism-induced FF state manifests itself as a novel type of exotic superconductivity that had not been previously identified.

(2) Magnetic excitations in heavy-fermion spin-triplet superconductors

We studied magnetic excitation spectrum, which can be observed by inelastic neutron scattering experiments, in the heavy-fermion multiband superconductor UTe_2 [5]. We numerically calculated the dynamical spin susceptibility, within the random phase approximation, of a mixed-dimensional periodic Anderson model [6] that reproduces the antiferromagnetic fluctuations observed near $\boldsymbol{Q}_{\mathrm{AFM}} = (0, \pi, 0)$ in UTe_2. In the normal state, we showed

that the hybridization between the conduction and localized f electrons gives rise to a magnetic resonance at $\boldsymbol{Q}_{\mathrm{AFM}}$, which is enhanced by the quasi-one-dimensional structure of the conduction bands. Furthermore, we demonstrated the resonance in the dynamical spin response due to the superconducting feedback effect when the order parameter belongs to the B_{2u} representation, which changes its sign upon momentum transfer of $\boldsymbol{Q}_{\mathrm{AFM}}$. The enhancement of the spin response is shaped by the orbital-dependent coherence factor, and the sign reversal of the order parameter determines whether the dynamical spin susceptibility is reinforced or suppressed.

References

[1] S. Sumita, M. Naka, and H. Seo, Phys. Rev. B **112**, 144510 (2025).

[2] M. Wallerberger, *et al.*, SoftwareX **21**, 101266 (2023); T. Wang *et al.*, Phys. Rev. B **102**, 134503 (2020).

[3] H. Shinaoka *et al.*, Phys. Rev. B **96**, 035147 (2017).

[4] J. Li *et al.*, Phys. Rev. B **101**, 035144 (2020).

[5] K. Shimura, S. Sumita, and Y. Kato, in preparation.

[6] R. Hakuno *et al.*, Phys. Rev. B **109**, 104509 (2024).

Hyperuniformity in generalized Aubry-André model

Shiro SAKAI
Physics Division, Sophia University, Chiyoda-ku, Tokyo 102-8554, Japan

We have studied a generalized Aubry-André (GAA) model [1] in terms of hyperuniformity (HU) [2], extending our previous study [3] on the genuine Aubry-André (AA) model [4]. The HU is a framework originally proposed to quantify and classify point distributions in a space. It provides a measure for a uniformity of the point distributions, and classify them into several distinct classes, such as nonhyperuniform, and hyperuniform class I, II and III, characterized by a large-scale behavior of the point-density fluctuation. The framework has been generalized to a scalar field, which allows us to characterize the inhomogeneous electron distributions in quasiperiodic systems.

The GAA Hamiltonian reads

$$\hat{H} = t\sum_i \left(\hat{c}_{i+1}^\dagger \hat{c}_i + \text{H.c.}\right) + \sum_i V_i \hat{c}_i^\dagger \hat{c}_i. \quad (1)$$

where $\hat{c}_i^\dagger$ ($\hat{c}_i$) is the creation (annihilation) operator of a spinless fermion (electron) at site i. The parameter t denotes the nearest-neighbor hopping amplitude, and

$$V_i = \lambda \frac{\cos(2\pi i/\tau)}{1-\alpha\cos(2\pi i/\tau)} \quad (2)$$

with $\tau = \frac{1+\sqrt{5}}{2}$ (golden mean) is the onsite potential, where the overall scale is set by λ while an additional modulation is introduced by $\alpha \in (-1, 1)$.

In Ref. [3], we have shown that inhomogeneous charge distributions in the AA model, which corresponds to $\alpha = 0$ in the GAA model, are hyperuniform: For $\lambda < 2|t|$, the electron states are extended and the charge distribution is class-I hyperuniform, whereas for $\lambda > 2|t|$ the electron states are localized and the charge distribution is class-I or class-II hyperuniform, depending on whether the Fermi level lies inside a gap or not. We examined this notion in the GAA model.

By using the ISSP Supercomputer System B, we explored various sets of parameters (λ, α). We diagonalized the Hamiltonian Eq. (1) of 46368 sites, which is the 23rd Fibonacci number, calculated the charge distribution and its HU class. We find that the HU class is I (II) when the Fermi level is in the gapless region and the electron state at the Fermi level is extended (localized); In the gapped region the HU class is always I. These are true even when the Fermi level is above the mobility edge, which exists in the GAA model unlike the AA model, where both extended and localized states contribute to the charge distribution.

These results clarifies a close relationship between the extended/localized nature of the electron states and the HU class of the charge distribution in quasiperiodic systems.

References

[1] S. Ganeshan, J. H. Pixley, and S. Das Sarma : Phys. Rev. Lett. **114**, 146601 (2015).

[2] S. Torquato and F. H. Stillinger: Phys. Rev. E. **68**, 041113 (2003).

[3] S. Sakai, R. Arita, and T. Ohtsuki: Phys. Rev. Res. **4**, 033241 (2022).

[4] S. Aubry and G. André: Ann. Israel Phys. Soc. **3**, 18 (1980).

Physical properties of Ising machines

Shu Tanaka

Department of Applied Physics and Physico-Informatics, Keio University

Hiyoshi, Yokohama, Kanagawa, 223-8522

We have continued our studies on the physical properties and computational performance of Ising machines, with a particular focus on quantum annealing (QA). QA is a metaheuristic for solving combinatorial optimization problems by searching for the ground state of an Ising-type problem Hamiltonian, and elucidating its physical mechanisms and limitations is essential for the practical use of current and future quantum hardware. This year, we addressed three complementary aspects: (i) a quantitative analysis of the effectiveness of mid-anneal measurement (MAM) in constrained combinatorial optimization [1], (ii) the application of MAM to multi-objective optimization (MOO) on a physical quantum annealer [2], and (iii) the acceleration of QA in small-energy-gap instances by introducing controlled diagonal catalysts [3].

In the first study [1], we introduced a quantitative metric Q_d to evaluate the effectiveness of MAM. Numerical simulations of the graph bipartitioning problem and the quadratic knapsack problem, formulated using the augmented Lagrangian function, revealed that MAM is most effective when the energy difference between the desired (feasible/optimal) solutions and the ground state of the problem Hamiltonian is small. Through additional analysis on fully connected Ising models exploiting their permutation symmetry, we further demonstrated that this effectiveness persists as the system size increases, indicating the scalability of MAM toward large-scale quantum annealing.

In the second study [2], we extended this idea to multi-objective optimization, where the conventional linear weighted-sum method inherently fails to reach solutions located in non-convex regions of the Pareto front. We validated the proposed MAM-based scheme through complementary approaches: physical experiments on a D-Wave Advantage2 quantum annealer using quench-based readout, and numerical simulations of closed quantum systems assuming ideal MAM. Both consistently exhibited a clear trade-off in which earlier measurement timing enhances solution diversity, whereas later timing ensures convergence to non-dominated solutions, with a practical compromise timing balancing both metrics.

In the third study [3], we proposed a method

that introduces additional longitudinal magnetic fields as controlled diagonal catalysts to mitigate the small energy gaps that arise from perturbative crossings. By variationally optimizing only the schedule of these linear catalyst terms via optimal-control theory, we demonstrated an approximate quadratic speedup of the exponential scaling exponent of the time-to-solution for the maximum weighted independent set problem on complete bipartite graphs, by actively exploiting diabatic transitions in the small-gap region. We further confirmed that the optimized catalyst schedules are transferable across instances sharing a similar energy-gap structure, suggesting a route to eliminate per-instance optimization overhead.

In all three studies, the time-dependent Schrödinger equation was integrated using QuTiP, and the large-scale numerical simulations were carried out on the System B supercomputer at SCC-ISSP.

References

[1] K. Takahashi and S. Tanaka, J. Phys. Soc. Jpn. 95, 034002 (2026).

[2] K. Takahashi and S. Tanaka, J. Phys. Soc. Jpn. 95, 053001 (2026).

[3] T. Hattori and S. Tanaka, Phys. Rev. A 113, 022433 (2026).

Tensor Renormalization Group Calculation of Universal Values of Partition-Function Ratios

Satoshi MORITA
Graduate School of Science and Technology, Keio University
Yokohama, Kanagawa 223-8522

The tensor renormalization group (TRG) method is a numerical method for approximating the contraction of tensor networks by performing coarse-graining corresponding to the real-space renormalization group [1]. Since the tensor network representation of the partition function can be obtained relatively easily even for complex systems, it is expected to be able to handle systems and physical quantities that are difficult to calculate by conventional methods such as Monte Carlo methods. Recently, a method called bond-weighted tensor renormalization group (BWTRG) was proposed, which significantly improves the calculation accuracy without increasing the computational cost by leaving a diagonal matrix called bond weight on the bond connecting the tensors [2].

In the numerical analysis of phase transitions and critical phenomena, the critical temperature and critical exponent can be calculated with high accuracy by using dimensionless quantities such as the Binder ratio. Since the partition function can be calculated directly by TRG, a dimensionless quantity defined from the ratio of partition functions,

$$X_1 = \frac{Z(L,L)^2}{Z(2L,L)}$$

is useful [3]. This dimensionless quantity proposed by Gu and Wen can extract the information of the tensor corresponding to the fixed point of the renormalization group by canceling out redundant correlations on loops in the numerator and denominator. Therefore, it can detect phase transitions by jumping in value before and after the transition point in the thermodynamic limit.

In this study, we investigate the behavior of the partition-function ratio near the critical point and find that it follows a scaling law of the same form as the Binder ratio, and that the universal value at criticality is expected from the modular invariant partition function in conformal field theory [4]. We perform numerical calculations using BWTRG in three two-dimensional models belonging to different universality classes: the Ising model, the three-state Potts model, and the four-state Potts model. We verify their behavior near the transition point and clarify the bond-dimension dependence of the calculation accuracy. In particular, in the 4-state Potts model, logarithmic corrections to finite-size effects can be directly observed, which is an example showing the usefulness of tensor renormalization group. We also consider anisotropic systems and show that the correlation length ratio can be estimated from the universal value of the partition function ratio.

References

[1] M. Levin and C. P. Nave, Phys. Rev. Lett. **99**, 120601 (2007).

[2] D. Adachi, T. Okubo, and S. Todo, Phys. Rev. B **105**, L060402 (2022).

[3] Z. C. Gu and X. G. W, Phys. Rev. B **80**, 155131 (2009).

[4] S. Morita and N. Kawashima, J. Phys. Soc. Jpn. **95**, 044001 (2026)

Phase structure and rheology in polymer blends: A molecular dynamics simulation study

Takeshi SATO
Advanced Manufacturing Technology Institute, Kanazawa University
Kanazawa, Ishikawa 920-1192

Polymer blends are typically immiscible and exhibit phase-separated structures. Such blends are widely used in polymer products, such as multilayer films. To design sophisticated products, it is necessary to understand the fundamental phenomena associated with phase-separated structures under an external field. Regarding this point, Macosko and coworkers measured the shear viscosity (η) of a laminated system of two immiscible polymers.[1] They reported that η decreased with increasing layer number, attributing this decrease to slip at the interface. To investigate interfacial phenomena at the microscopic scale, this study examined the shear rheological properties of immiscible polymer multilayer systems using coarse-grained molecular dynamics (CGMD) simulations.

This study used the Kremer-Grest (KG) model, a standard CGMD model for polymers.[2] The KG model represents polymer chains by a series of beads connected by finitely extensible nonlinear elastic springs. We introduced a Lennard-Jones (LJ) potential with interaction strength ϵ_{ij} $(i, j \in \{1, 2\})$ for all bead pairs of polymers 1 and 2. To systematically adjust polymer compatibility, we varied the LJ parameter (ϵ_{12}) across polymers. To apply shear flow, solid walls were placed at the top and bottom of the computational domain in the z-direction. Different types of polymers were stacked in the z-direction with 2 or 4 layers. For the equilibrated system, we applied shear flow by moving the walls at a constant velocity in the x-direction. Then, the mechanical responses, such as η, were investigated. We conducted all KG simulations using LAMMPS.

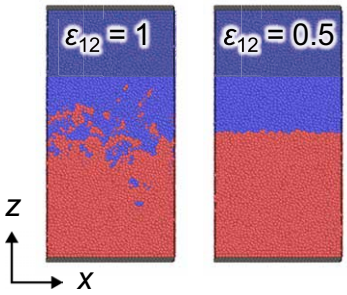


Figure 1: Snapshots of KG simulations for different ϵ_{12} values as indicated.

We constructed a system consisting of 400 polymer chains, each with $N = 100$, in each layer. By decreasing ϵ_{12} from its standard value of 1, we reproduced a clear phase-separated state in equilibrium, as shown in Fig. 1. From the phase-separated profile, we estimated the Flory-Huggins interaction parameter (i.e., χ parameter). When we applied shear flow to these equilibrium structures, the steady-state viscosity η decreased over a wide range of shear rates as ϵ_{12} decreased (i.e., as the χ parameter increased). This observation qualitatively agrees with the experimental results by Macosko and coworkers.[1]

References

[1] R. Zhao and C. W. Macosko, J. Rheol., **46**, 145 (2002).

[2] K. Kremer and G. S. Grest, J. Chem. Phys. **92**, 5057 (1990).

Tensor-network approach to phase transition of quantum chiral spin model

Yusuke MASAKI
Department of Applied Physics, Tohoku University
Sendai, Miyagi 980-8579

Classical spin models of monoaxial chiral magnets exhibit a continuous phase transition (CPT), known as the Dzyaloshinskii transition, driven by chiral solitons under magnetic fields perpendicular to the helical axis. Below the saturation field, chiral solitons form a periodic array, and the inter-soliton distance, determined by their repulsive interactions, diverges logarithmically. In tilted magnetic fields, two multicritical points appear, leading to discontinuous phase transitions (DPTs) in intermediate angular regions due to attractive soliton interactions.

In quantum monoaxial chiral magnets, several quantum effects have been identified, such as spin parity effects in small systems with periodic boundary conditions and quantum tunneling across surface barriers. Concerning the phase transitions under tilted magnetic fields, quantum fluctuations strongly modify the classical behavior: the discontinuous region disappears for $S = 1/2$, while it remains for $S = 1$ and $S = 3/2$, although it is significantly reduced. Nevertheless, the critical behavior of the Dzyaloshinskii transition in the quantum regime has remained unclear.

In this project, we investigate magnetization processes and phase transitions in quantum monoaxial chiral magnets under tilted magnetic fields using tensor network methods, focusing on the higher-order tensor renormalization group (HOTRG). This year, we have improved the HOTRG implementation, including a more accurate evaluation of excitation energies and a refined method for extracting excitation gaps. These developments enable a highly precise determination of critical points from gap-closing behavior.

Based on this improved approach, we have successfully determined the critical behavior of the Dzyaloshinskii transition in the quantum $S = 1/2$ case. Although the magnetization curves exhibit a sharp increase just below the transition point, similar to the classical case, the criticality is qualitatively different. Instead of the logarithmic singularity characteristic of the chiral soliton lattice in classical systems, the magnetization approaches saturation in a power-law manner. We further confirm that the quantum $S = 1$ case exhibits the same power-law critical behavior with an identical critical exponent.

Furthermore, we find that this power-law critical behavior is universal across all field angles, indicating that the critical exponent is independent of the tilt angle.

Numerical Simulation of Microwave Responce for Fractional Quantum Hall droplet

Takeo Kato
Institute for Solid State Physics, University of Tokyo
Kashiwa-no-ha, Kashiwa, Chiba 277-8581

The fractional quantum Hall effect (FQHE) has had a profound impact on condensed matter physics. Thanks to significant advances in nanofabrication and measurement technology, this fractional statistics has recently been directly verified through Fabry–Pérot interferometry and nonequilibrium noise measurements [1, 2]. Previous studies have focused on transport properties such as current and nonequilibrium noise in devices where a quantum point contact (QPC) or an interferometer is fabricated in the edge channel. Against this background, probing edge excitations via microwave absorption in an isolated quantum Hall droplet is expected to provide a fundamentally new experimental window distinct from conventional transport measurements.

We numerically evaluated the microwave response of edge states in a system composed of a droplet in the fractional quantum Hall state (Laughlin state) coupled to a microwave waveguide [3]. The system considered in this study was theoretically proposed in a previous work [4] as a setup capable of observing the anyonic statistics of excitations in the edge states. Our numerical results are expected to enable detailed comparisons with future experimental results.

We formulated the effective action of the system by assuming a circular droplet and employing bosonization. The response function to be calculated involves the correlation function of the bosonic field describing the edge states. Since this correlation function cannot be obtained analytically, we performed numerical calculations using the path-integral quantum Monte Carlo method using large-scale parallel computations on ISSP supercomputer. We numerically evaluated the response functions for two cases: a fractional quantum Hall droplet with Landau level filling factor $\nu = 1/3$, $\nu = 1/5$, and an integer quantum Hall droplet with $\nu = 1$, for which analytical theoretical construction is possible. In the numerical simulations, we performed 30,000 Monte Carlo steps for thermalization, followed from 1×10^6 to 1.2×10^6 steps for measuring the correlation functions.

The results of our numerical calculations are presented below. Figure 1 and 2 show the coupling dependence of the response function for the case of Landau level filling factor $\nu = 1/3$, $\nu = 1/5$ and $\nu = 1$. These results show that the peak position depends on the coupling strength, and that this dependence becomes increasingly pronounced as the filling factor decreases, indicating that higher-order contributions become more significant at smaller filling factors. This leads to an enhanced peak shift. This behavior has not been reported in previous studies, including Ref. [4], and thus represents a novel finding.

In the future, we plan to extend our analysis from simple droplet geometries to annular systems with a nontrivial topology. By evaluating the microwave response in such geometries, we aim to clarify how the unique properties of anyons manifest in the optical response of sys-

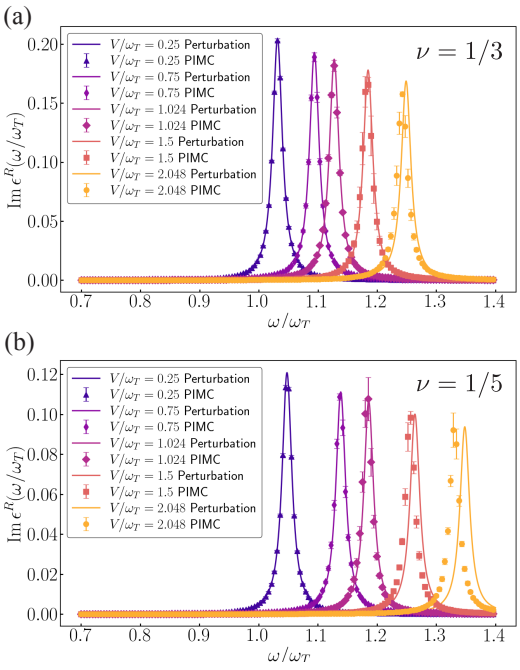


Figure 1: Imaginary part of the dielectric function for FQH droplets with (a) $\nu = 1/3$ and (b) $\nu = 1/5$ at temperature $T/\omega_T = 0.1$. Solid lines show results from second-order perturbation theory, whereas symbols with error bars represent data obtained using PIMC. Coupling strengths are $V/\omega_T = 0.25, 0.75, 1.024, 1.5$, and 2.048. A finite broadening $\delta = \omega_T/100$ is used.

tems with non-contractible topology.

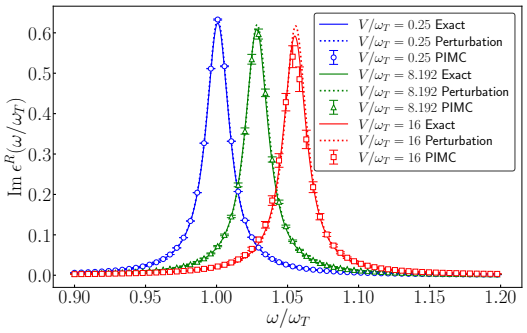


Figure 2: Imaginary part of the dielectric function for the $\nu = 1$ IQH droplet, shown in units of L^2/ω_T. The temperature is set to $T/\omega_T = 0.1$. Solid and dashed lines show the results of scattering theory and second-order perturbation theory, respectively, while symbols with error bars represent numerical data obtained using the PIMC method. Dimensionless coupling strengths are $V/\omega_T = 0.25$, 8.192, and 16. For visual clarity, delta functions are broadened into Lorentzians with linewidth $\delta = \omega_T/100$.

References

[1] J. Nakamura, S. Liang, G. C. Gardner, and M. J. Manfra, Nat. Phys. **16**, 931 (2020).

[2] H. Bartolomei, M. Kumar, R. Bisognin, A. Marguerite, J.-M. Berroir, E. Bocquillon, B. Plaçais, A. Cavanna, Q. Dong, U. Gennser, Y. Jin, and G. Féve, Science **368**, 173 (2020).

[3] F. Murabayashi, R. Sano, F. Ronetti, J. Rech, T. Martin, T. Jonckheere, and T. Kato, preprint (arXiv:2602.24116).

[4] J. Cano, A. Doherty, C. Nayak, D. Reilly, Phys. Rev. B **88**, 165305 (2013).

Non-reciprocal neighbor interaction and non-equilibrium phase transition in self-propelled hard polygon systems

Masaharu ISOBE
Nagoya Institute of Technology
Gokiso-cho, Showa-ku, Nagoya, 466-8555

Hard disk and sphere systems are among the most fundamental models in statistical mechanics, with a long history of molecular simulation studies spanning equilibrium and non-equilibrium phenomena [1]. In this project, we explore equilibration dynamics and non-equilibrium phase transitions in self-propelled hard particle systems using advanced computational methods: Event-Chain Monte Carlo (ECMC) [2, 3], Newtonian Event-Chain Monte Carlo (NECMC) [4], and Event-Driven Molecular Dynamics (EDMD) [5].

Crystallization and Motility-Induced Phase Separation in the Flow of Active Brownian Particles Around an Obstacle [6]: Fluid-obstacle interactions are central to fluid dynamics, from the Kármán vortex street to Reynolds number-dependent instabilities. While well characterized via Navier-Stokes simulations and classical molecular dynamics, the behavior of active matter under analogous conditions remains largely unexplored. Through large-scale simulations of active Brownian particles (ABPs) flowing past a fixed obstacle, we discover novel emergent patterns including unexpected crystallization. These phenomena are governed by both Reynolds number and self-propulsion velocity, with crystallization arising from two distinct mechanisms: compression-induced ordering upstream and motility-induced phase separation in specific flow regions.

Self-organized spatial inhomogeneity in self-propelled quasi-elastic hard disk systems [7]: Freely cooling inelastic hard sphere systems serve as a primal model for granular gases. Using large-scale molecular dynamics simulations, we explore the emergence of self-organized spatial structures in quasielastic hard disk systems. Across high-density regimes near the Alder transition, we uncover previously unreported dynamical behaviors and striking spatial patterns. We further assess the influence of different velocity scaling schemes on the observed dynamics. These results offer fresh perspectives on self-organization phenomena in dense quasielastic hard disk systems.

Cooperative phenomena in active matter systems with alternative interaction of neighbors [8]: We examine how nearest neighbor (NN) determination methods affect flocking phase transitions in the Vicsek model. Beyond conventional approaches (Cutoff, Voronoi, k-NN), we introduce 2D SANNex [9], a novel method. While metric-free Voronoi maintains a constant transition point across densities, both k-NN and 2D SANNex exhibit density-dependent shifts despite also being metric-free. This reveals that the metric-free property alone does not govern density dependence; rather, the non-reciprocal characteristics inherent to k-NN and 2D SANNex play a crucial role in modulating transition behavior.

Quantitative analysis of pedestrian counter-flow in crowded condition using floor field

model [10]: Building upon the model by S. Nowak and A. Schadschneider (Phys. Rev. E, 85, 066128 (2012)), which analyzed lane formation and gridlock in pedestrian counter-flows using the floor field model, we extended the framework from a square lattice (4-directional) to a triangular lattice (6-directional) and compared the phase diagrams of both systems. We further applied these models to pedestrian crossing flows at T-junctions, examining differences in crowd formation using two static floor fields.

Flyer-Target simulation of shock waves in crystal-fluid impact in hard disk systems: Shock waves from supersonic impacts induce phase changes in crystalline materials under extreme compression, but conventional Navier-Stokes simulations cannot resolve particle-level phenomena such as phase transitions. Using EDMD with stripe-shaped biphasic (SSBP) initial configurations and the Flyer-Target method, we analyze shock-induced effects near the crystal–fluid transition point. Packing fractions in the shocked region exceed the Alder transition point, with pressure overshoot due to compression-induced crystallization. Wavefront velocity increases with packing fraction in fluid and crystalline phases, but propagation delays occur in the coexistence regime. Cluster analysis reveals that crystal growth aligns with pre-existing cluster orientations and that initial positional disorder promotes multinuclear crystallization.

Diffusional characteristics and non-equilibrium phase transitions of active glass model in dense binary hard disk systems: The emerging field of "active glasses" explores the interplay between self-propulsion and glassy dynamics. We introduce Vicsek interactions into a binary hard disk glass-forming system and investigate diffusion and phase transitions via EDMD. A flocking transition is confirmed even at high densities. Near the transition, structural relaxation is enhanced, whereas in the ordered phase, diffusion slows despite fluidization. The non-Gaussian parameter and four-point correlations exhibit two distinct peaks, suggesting a novel dynamic heterogeneity induced by Vicsek interactions.

References

[1] M. Isobe: Mol. Sim. **42** (2016) 1317.

[2] E. P. Bernard, W. Krauth, and D. B. Wilson: Phys. Rev. E **80** (2009) 056704.

[3] W. Krauth: Front. Phys. **9** (2021) 229.

[4] M. Klement and M. Engel: J. Chem. Phys. **150** (2019) 174108.

[5] M. Isobe: Int. J. Mod. Phys. C **10** (1999) 1281.

[6] K. Iwase and M. Isobe: EPJ Web of Conferences **334** (2025) 01004.

[7] D. Mugita, R. Kitagawa, N. Murase, and M. Isobe: EPJ Web of Conferences **334** (2025) 01005.

[8] T. Nakamura, N. Murase, and M. Isobe: EPJ Web of Conferences **334** (2025) 02001.

[9] D. Mugita, K. Souno, H. Koyama, T. Nakamura, and M. Isobe: J. Chem. Phys. **160** (2024) 174104.

[10] Y. Nakai and M. Isobe: Proceedings of the 31th Symposium on Traffic Flow and Self-driven Particles, **31** (2025) 13. (in Japanese)

Generalizing bulk-edge correspondence to monitored quantum systems

Yohei FUJI
Department of Applied Physics, University of Tokyo, Tokyo 113-8656

Quantum many-body systems subject to repeated measurements of local observables exhibit measurement-induced phase transitions (MIPTs) [1, 2]. A prominent example is the entanglement transition, where the steady-state entanglement entropy changes from a volume-law to an area-law scaling. Beyond these, MIPTs can also occur between distinct area-law phases characterized by the underlying topology of many-body states. In Ref. [3], we generalized the concept of bulk-edge correspondence, which has been established in equilibrium topological phases, to such monitored systems. This generalization is achieved by introducing an effective Hamiltonian derived from a quantum-trajectory evolution operator, which allows for the definition of an energy spectrum and a bulk topological invariant as a response to a symmetry twist. While this protocol was initially demonstrated for a monitored Kitaev-Majorana chain, it possesses the potential for application across diverse classes of measurement-induced topological phases.

In this project, we numerically investigated this protocol for two additional types of measurement-induced topological phases using the supercomputing facilities at ISSP (System B).

First, we considered a monitored version of the one-dimensional cluster state, which represents a symmetry-protected topological (SPT) phase protected by $\mathbb{Z}_2 \times \mathbb{Z}_2$ symmetry. Our results show that the effective Hamiltonian exhibits a four-fold degeneracy in its energy spectrum under open boundary conditions. Furthermore, we identified a quantized topological invariant by measuring a $\mathbb{Z}_2$ charge conditioned on the postselection of twisted measurement outcomes for the other $\mathbb{Z}_2$ charge. Numerical simulations confirmed that these signatures effectively identify phase transitions into either a trivial area-law phase or a volume-law entangled phase induced by unitary evolution.

Second, we examined a monitored version of the Su-Schrieffer-Heeger chain, an SPT phase protected by $U(1)$ and chiral symmetries. Similar to the monitored cluster state, we observed symmetry-protected zero modes within the bulk gap under open boundary conditions. We also computed a quantized topological invariant by generalizing the Zak phase to this monitored framework.

We are currently investigating the further extension of this protocol to a broader range of monitored SPT phases.

References

[1] A. C. Potter and R. Vasseur, *Entanglement Dynamics in Hybrid Quantum Circuits*, in Entanglement in Spin Chains: From Theory to Quantum Technology Applications, edited by A. Bayat, S. Bose, and H. Johannesson (Springer International Publishing, Cham, 2022) pp. 211-249.

[2] M. P. A. Fisher, V. Khemani, A. Nahum, and S. Vijay, *Random Quantum Circuits*, Ann. Rev. Condens. Matter Phys. **14**, 335 (2023).

[3] H. Oshima, K. Mochizuki, R. Hamazaki, and Y. Fuji, *Topology and Spectrum in Measurement-Induced Phase Transitions*, Phys. Rev. Lett. **134**, 240401 (2025).

A Microscopic Theory for Charge Imbalance in Nonequilibrium Superconductors

Taira KAWAMURA
Department of Physics, College of Science and Technology, Nihon University
Tokyo 101-8308, Japan

In nonequilibrium electron systems, electron distributions generally deviate from the Fermi–Dirac function. However, a unified description of nonequilibrium electron distributions across different scattering regimes has remained challenging. To address this issue, we formulate a systematic approach based on the Keldysh Green's function technique, in which scattering processes are incorporated self-consistently via self-energies [1]. We apply this framework to voltage-biased nanowires and demonstrate that it provides a unified description of nonequilibrium electron distributions over a wide range of transport regimes.

Using this framework, we further clarify the microscopic origin of charge imbalance in nonequilibrium superconductors [2]. Charge imbalance refers to a nonequilibrium state in which quasiparticles and Cooper pairs acquire distinct effective chemical potentials, and has traditionally been understood phenomenologically in terms of the branch-imbalance picture introduced by Tinkham. In the present work, we explicitly compute nonequilibrium electron distributions and show that voltage-induced asymmetric distributions naturally generate particle–hole imbalance, leading to charge imbalance. In this way, Tinkham's branch-imbalance picture is microscopically justified in terms of the underlying nonequilibrium distribution function.

In these studies, the numerical calculations require self-consistent evaluation of Green's functions with both frequency and internal degrees of freedom, including iterative determination of scattering self-energies. Moreover, systematic exploration of parameter space, such as bias voltage and scattering strength, necessitates large-scale parallel computations. Therefore, the use of high-performance computing resources is essential to achieve tractable computation times.

The present study provides a unified understanding of nonequilibrium electron distributions and establishes a microscopic foundation for charge imbalance in superconductors. As a future direction, the framework developed here can be extended to time-dependent and periodically driven systems, opening the way to studies of the dynamical control of superconducting properties.

References

[1] T. Kawamura and Y. Kato, J. Phys. Soc. Jpn. **95**, 034702 (2026).

[2] T. Kawamura and Y. Ohashi, arXiv:2603.00435.

Numerical study of the dynamical structure factor on the triangular-lattice Heisenberg antiferromagnet

Yoshiyuki Fukumoto
Department of Physics and Astronomy, Faculty of Science and Technology, Tokyo University of Science, 2641 Yamazaki, Noda, Chiba 278-8510

The coexistence of magnon excitations and spinon continuum in neutron scattering of magnetic materials has become an important topic in quantum spin system research [1], as evidenced by recent experiments with $Ba_3CoSb_2O_9$ and $Cs_2Cu_3SnF_{12}$ [2,3]. In this study, starting with the RPA approximation framework based on spinon operators (fermions) by Zhang and Li [4], we systematically investigated its validity and limitations through comparison with variational Monte Carlo methods and exact diagonalization that strictly incorporate constraints.

First, variational Monte Carlo calculations were performed for large-scale systems up to 900 sites using variational states derived from the spinon operator representation of the ground state of the triangular-lattice Heisenberg model. As a result, energy per site of $-0.5408(1)$ was obtained. Although this value is higher than $-0.5502(4)$ obtained by series expansion [5], it is lower than -0.538 obtained by spin wave calculations, confirming that it exhibits accuracy at or above that of conventional methods. On the other hand, in the calculation of the dynamic structure factor for a 36-site system, the result showed that the intensity of the continuity band was weak around point K and strong around point M, showing a trend opposite to that of the $Ba_3CoSb_2O_9$ experiment [2], similar to the RPA approximation [4].

To clarify the origin of this discrepancy, we compared in detail the variational states and exact diagonalization ground states for 36-site systems of square [1] and triangular lattices using spinon operators. The mean-field Hamiltonian H_{MF} includes only nearest-neighbor spinon hopping, and the states constructed from it correspond to nearest-neighbor RVB states. Furthermore, by introducing a staggered magnetic field H_{st} and constructing energy-optimized magnetic ordered states, we found that while the energy and static structure factors were reproduced relatively well, the overlap between the variational states and the exact ground state decreased rapidly with increasing system size. This result indicates that the nearest-neighbor valence bond alone cannot adequately represent long-range order, and that the introduction of long-range spinon hopping, i.e., long-range valence bonds, extending between different sublattices is essential.

Based on the above, we concluded that the construction of an extended H_{MF} including long-range hopping, and the systematic comparison of dynamic structure factors based on it using variational Monte Carlo and Lanczos methods, are critically important for improving the variational state that simultaneously describes RVB-like properties and magnetic order. This study provides a new perspective on understanding spinon continuum in two-dimensional quantum spin systems.

[1] B. D. Piazza *et al.*, Nat. Phys. 11, 62, 2015.
[2] S. Ito *et al.*, Nat. Commun. 8, 235, 2017.
[3] M. Saito *et al.*, PRB 105 064424, 2022.
[4] C. Zheng *et al.*, PRB 102, 075108, 2020.
[5] W. Zheng *et al.*, PRB 74, 224420, 2006.

Numerical study of magnon crystal states in a spin-1/2 distorted kagome antiferromagnet

Yoshiyuki Fukumoto
Department of Physics and Astronomy, Faculty of Science and Technology, Tokyo University of Science, 2641 Yamazaki, Noda, Chiba 278-8510

The magnetization plateaus $M/M_{\rm sat} = 1/3$, 5/9, and 7/9 that appear in the magnetization process of kagome-lattice Heisenberg antiferromagnets have been thought to originate from the magnon crystal state (MCS), a triple degenerate state accompanied by spontaneous breaking of translational symmetry [1]. Using a model with a distortion corresponding to $Y_3Cu_9(OH)_{19}Cl_8$, Bodaiji *et al.* studied a phase diagram on the distortion-magnetic field plane using the exact diagonalization method and identified six types of magnetization plateau phases [2]. Of these phases, the spin correlation function shows the same arrangement pattern as a single MCS, while the remaining three phases located on opposite sides of the distortion-zero line show a characteristic correlation pattern that extends throughout the entire lattice. However, the microscopic origin of this "lattice-extended" correlation has not been clear until now.

This study aims to provide a picture of this problem as a "quantum superposition of multiple degenerate MCSs." Specifically, it focuses on the $M/M_{\rm sat} = 7/9$ plateau, performs exact diagonalization on a 63-site system suitable for handling degeneracy [1], and constructs a variational framework by extracting a subspace spanned by only three MCSs as a low-energy effective space and solving the generalized eigenvalue problem within it. Under this setting, the wave function is expressed as a linear combination of the three MCSs, and by determining the optimal way in which each MCS component is superimposed, it becomes possible to directly track "what kind of MCS interference is producing the observed correlation pattern."

This analysis revealed that, when the distortion vanishes, the phase switches via a first-order transition from a phase based on a single MCS to a phase based on a superposition state of two MCSs. Furthermore, in the limit of decreasing the distortion, we confirmed that the overlap between this variational state and the lowest energy state of exact diagonalization rapidly approaches 1, demonstrating that the essential physics near the 7/9 plateau can be described solely by projection onto the MCS subspace and quantum hybridization within it. The spin correlation function calculated from the variational wavefunction and the exact ground state is quantitatively consistent, and in particular, it became clear that the correlation pattern extending across the entire lattice, as pointed out by Bodaiji *et al.*, can be naturally understood as an interference effect originating from the superposition of two MCSs. This study introduces a new theoretical framework for describing the magnetization plateau phase, shifting from a"single magnon crysta" to"quantum interference between multiple MCSs", and represents an important step towards a unified understanding of the magnetism of strained kagome lattice systems.

[1] S. Capponi *et al.*, PRB 88, 144416, 2013.
[2] K. Bodaiji *et al.*, PRB 110, 104431, 2024.

Vibration of Granular System: Relation Between Viscoelastic Relaxation and Particle Dynamics

Fumiaki Nakai
Department of Earth and Space Science, The University of Osaka
1-1 Machikaneyama, Toyonaka 560-0043, Japan

Understanding the rheological response of granular materials to mechanical perturbations is of broad importance across disciplines ranging from earth science to chemical engineering. This study concerns the rheology of granular materials under external perturbations. In the course of this research, an unexpected but significant finding was obtained regarding the mechanical response of granular materials to small-amplitude perturbations [1]. In addition, related results were obtained on the rheological behavior of structured granular materials [2, 3].

The main part of this study was carried out theoretically. Numerical simulations using the discrete element method (DEM) implemented in LAMMPS were performed to support the theoretical analysis, including preliminary explorations of parameter space and numerical checks of the stress–strain relation up to yielding. These simulations were performed on the i8cpu and F1cpu partitions of the System B supercomputer (Ohtaka), typically on a single node.

As a model system, we considered a granular assembly arranged in a two-dimensional triangular crystalline configuration under uniform shear. The theoretical analysis focused on the stress–strain relation near yielding, the dispersion relation $\omega(k)$, and the vibrational density of states (vDOS), which characterizes the vibrational spectrum of the system. The DEM calculations were used to examine the consistency of the predicted yield stress and yield strain.

A central result is that, near the yielding strain, many k-points within a single vibrational branch soften simultaneously, forming a cross-shaped soft region in wave vector space. This softening over an extended region of wave vector space contrasts sharply with the behavior of amorphous solids, where only spatially localized vibrational modes become unstable near yielding. This multimode softening in our system is directly reflected in the vibrational spectrum: at small shear strains, the system exhibits a linear dispersion relation $\omega \sim k$, consistent with the continuum wave equation, whereas near the yielding strain a large number of low-frequency modes are excited and the dispersion relation crosses over to a quadratic form $\omega \sim k^2$. Correspondingly, the vDOS crosses over from the Debye law $D(\omega) \sim \omega$ to an anomalous scaling $D(\omega) \sim \omega^{1/2}$. These scalings were also derived explicitly and reveal an essential difference in the yielding mechanism between crystalline and amorphous granular systems. We validated the theoretical framework by comparing the theoretically predicted yield stress and yield strain against the DEM simulation results.

References

[1] F. Nakai, M. Otsuki, K. Saitoh, H. Katsuragi, arXiv:2603.26825 (2026).

[2] F. Nakai, T. Uneyama, Y. Sasaki, K. Yoshii, and H. Katsuragi, Phys. Rev. Lett.

135, 048202 (2025).

[3] F. Nakai, T. Uneyama, Y. Sasaki, K. Yoshii, and H. Katsuragi, EPJ Web Conf. **340**, 04008 (2025).

Role of counterions in the ion-mediated permeation of hydrophobic ions into lipid bilayers

Tomoko MIZUGUCHI and Souma SHIMADA

Faculty of Materials Science and Engineering, Kyoto Institute of Technology
Matsugasaki, Sakyo-ku, Kyoto 606-8585

The lipid bilayer, which constitutes the basic structure of the cell membrane, exhibits selective permeability. For example, sodium ions are transported across the membrane through specific ion channels. In general, because ions carry electric charges, they cannot pass through the hydrophobic core of the lipid bilayer, and therefore mechanisms such as ion channels are considered necessary for their transmembrane transport.

However, there are ionic species that are capable of directly permeating lipid membranes, although the mechanisms underlying this process remain poorly understood. For example, it is known that direct membrane permeation of ionic compounds is promoted when their counterions are more hydrophobic [1]; however, this phenomenon cannot be explained by classical partitioning models.

In this study, we aim to perform free-energy calculations of the membrane permeation of hydrophobic ions using an all-atom model to elucidate the role of counterions. Clarifying the mechanisms of ionic compound permeation across lipid membranes is essential for the advancement of applied research, such as the transport of ionic drugs using phospholipid vesicles.

To elucidate the effect of counterions on the membrane permeation of the hydrophobic ion $R6G^+$, we calculate the free energy profile of $R6G^+$ using the hydrophilic chloride ion and the hydrophobic perchlorate ion as counterions. We employed the umbrella sampling, and approximately 20 independent simulations were performed from within the membrane to the aqueous phase.

After 50 ns of equilibration for each window, a 50 ns production run was carried out. The CHARMM36 force field was used for DOPC lipids [2, 3] and TIP3P-CHARMM [4] was applied for water. The force fields for $R6G^+$ and the perchlorate ion were derived from Refs. [5] and [6], respectively. Molecular dynamics (MD) simulations were performed with NAMD and the free-energy profile was calculated using the Grossfield's WHAM code [7].

The calculated free energy profiles are shown in Figure 1. For both counterions, chloride and perchlorate, $R6G^+$ is most stabilized near the membrane interface. The system containing chloride ions exhibits a smaller energy barrier for entering the membrane and higher stability within the membrane, suggesting that $R6G^+$ can more readily permeate the membrane in the presence of chloride ions.

However, this result is contrary to experimental observations. Electrochemical measurements using DOPC vesicles indicate that $R6G^+$ permeates the membrane more easily when perchlorate ions are present as counterions [1]. The origin of this discrepancy will be investigated in future studies.

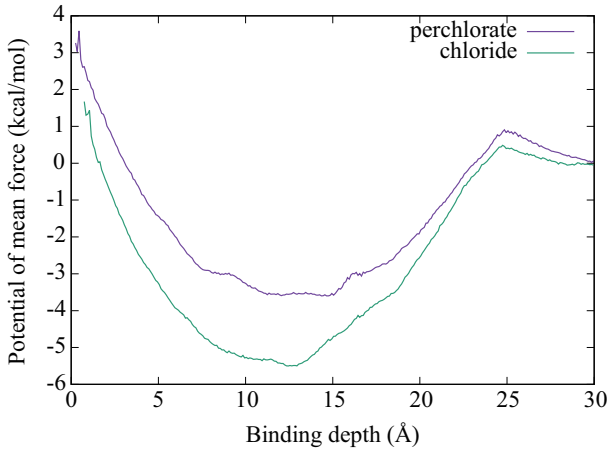


Figure 1: Free energy profiles of $R6G^+$ in the presence of chloride or perchlorate ions.

References

[1] K. Murakami, K. Hori, K. Maeda, M. Fukuyama, Y. Yoshida: Langmuir **32** (2016) 10678.

[2] J. B. Klauda, R. M. Venable, J. A. Freites, J. W. O'Connor, D. J. Tobias, C. Mondragon-Ramirez, I. Vorobyov, A. D. MacKerell, Jr., R. W. Pastor: J. Phys. Chem. B **114** (2010) 7830.

[3] J. B. Klauda, V. Monje, T. Kim, W. Im: J. Phys. Chem. B **116** (2012) 9424.

[4] A. D. MacKerell Jr, M. Feig, C. L. Brooks 3rd: J. Comput. Chem. **25** (2004) 1400.

[5] A. C. Vaiana, A. Schulz, J. Wolfrum, M. Sauer, J. C. Smith: J. Comput. Chem. **24** (2003) 632.

[6] S. Das, B. Mukherjee, R. Biswas: J. Chem. Sci. **129** (2017) 939.

[7] A. Grossfield: Wham: the weighted histogram analysis method, version 2.1.0.

Numerical Study of Pipe Flow and Clogging of Cells

Katsuyoshi MATSUSHITA
Graduate School of Integrated Science for Life , Hiroshima University
Higashi-Hiroshima, Hiroshima 739-0046

Collective cell migration is a phenomenon, which spontaneously delivers cells to proper positions, where the cells function. Collective migration helps our understanding of active matter by providing a typical example of its collective behavior. In contrast to simple active matter, the mechanism that stabilizes collective cell migration remains elusive in many physical aspects owing to its complexity. To overcome the complexity, the virtual experiment, using numerical simulations based on theoretical models, has been a standard method for clarifying the stabilization mechanism, in order to support its experimental clarification, which often encounters difficulties in the necessary controls over cell features.

In this work, we apply a theoretical model to examine guiding scaffolds of cell migration. Guiding scaffolds are well known as a stabilizing origin for the migration of neurons, both in artificial experiments and in physiological environments [1, 2]. The scaffold chemically guides migration along the shortest path to the appropriate positions. The physical mechanism of this stabilization is not well understood from a physics point of view, and its clarification may provide fundamental insights that help us develop a treatment for neuron dysfunction. Based on numerical simulations using a theoretical model, we investigate the effect of scaffold-guided collective cell migration in tissues and examine it as a treatment for dysfunction in collective migration.

Migration dysfunction results from various mechanisms, including disorders of intercellular interactions. One significant interaction contributing to the disorder is overstrengthened cell-cell adhesion, which promotes cell aggregation in certain cases [3]. This cell aggregation inhibits collective cell migration. The guiding scaffold may lead to a transition from cell aggregation without migration. We model this type of cell aggregation and examine the effect of guiding scaffolds on cell aggregation to stabilize collective cell migration [4].

Our results show that the guiding scaffold can induce a transition from cell aggregation to collective migration as follows. The collective migration is absent under low-strength scaffold guidance. At a certain strength of guidance, the collective velocity of cells starts to increase linearly. With a further increase in guidance strength, the collective velocity disappears. Therefore, collective migration occurs in an optimal range of guidance strength.

References

[1] M. Sawada and K. Sawamoto: Keio J. Med. **62**, 13 (2013).

[2] K. Matsushita: Phys. Rev. E **101**, 052410 (2020).

[3] M Matsumoto, *et al.*: EMBO molecular medicine **16**, 1228 (2024).

[4] K Matsushita, M Matsumoto, K Sawamoto, K Fujimoto: Proc. Sympo. Traffic Flow and Self-driven Part., **31**, 9 (2026).

Phonon-mediated Chirality Control in Molecular Triangles by Photoirradiation

Kunio ISHIDA

School of Engineering, Utsunomiya University

Yoto 7-1-2, Utsunomiya, Tochigi 321-8585

We have studied the ultrafast quantum dynamics of a triangular molecular system in which Frenkel excitons are coupled to local optical phonons [1]. The purpose of this project was to clarify how phonon degrees of freedom mediate the control of exciton chirality under photoirradiation. Numerical calculations were performed using the facilities of the Supercomputer Center, Institute for Solid State Physics, The University of Tokyo.

We considered a minimal three-site exciton–phonon model. Each molecular site was described as a two-level excitonic system represented by a pseudospin, and each exciton was locally coupled to an Einstein phonon. The exciton chirality was defined by the scalar spin chirality of the pseudospin variables. By introducing a symmetry-adapted phonon basis for the threefold rotational symmetry of the triangle, we separated the phonon modes into a totally symmetric mode and two nontrivial symmetry modes. The latter modes form composite exciton–phonon states that directly control the expectation value of the chirality operator.

Using numerical diagonalization, we first analyzed the eigenstates of the exciton–phonon Hamiltonian. The results show that the chirality is strongly correlated with the occupation of the symmetry-adapted phonon modes. In particular, phonon excitations in the nontrivial symmetry sector give rise to discrete changes in the chirality expectation value. This provides a microscopic mechanism by which phonons can act as active quantum degrees of freedom for controlling molecular chirality, rather than merely as an environment causing decoherence.

We then investigated real-time dynamics under semiclassical photoirradiation by solving the time-dependent Schrödinger equation. Starting from the ground state of the exciton–phonon system, we examined how the chirality evolves after optical excitation. We found that photoirradiation can induce a sign change of the exciton chirality when the excitation frequency is tuned to an appropriate absorption peak. This chirality inversion is caused by the competition between electronic transitions and phonon generation driven by exciton–phonon coupling. The light intensity plays an important role: moderate intensity allows phonon-assisted chirality inversion, whereas excessively strong

fields lead to rapid Rabi oscillations that suppress the phonon adjustment required for efficient control.

We also calculated the circular dichroism response of the triangular exciton–phonon system. The results indicate that the sign of the circular dichroism signal reflects the sign of the exciton chirality, suggesting that the chirality inversion may be detected through polarization-dependent optical measurements.

These results demonstrate that coherent phonon dynamics can provide a route to controlling chiral excitonic states in triangular molecular systems. The present study gives a theoretical basis for phonon-mediated chirality control and may be extended to more general light–matter systems, including cavity-coupled exciton–phonon–photon states.

References

[1] N. Aoyagi, H. Matsueda, and K. Ishida, J. Phys. Soc. Jpn. **95**, 014702 (2026).

Numerical Study of One Dimensional Frustrated Quantum Spin Systems

Kazuo HIDA
Professor Emeritus, Division of Material Science,
Graduate School of Science and Engineering,
Saitama University, Saitama, Saitama 338-8570

1 Model

We investigate the ground-state phases of $(1/2, 1/2, 1)$ mixed diamond chains with single-site anisotropy described by the following Hamiltonian:[1]

$$\mathcal{H} = \sum_{l=1}^{L} \Big[(1+\delta)\boldsymbol{S}_l(\boldsymbol{\tau}_l^{(1)} + \boldsymbol{\tau}_{l-1}^{(1)}) + (1-\delta)\boldsymbol{S}_l(\boldsymbol{\tau}_l^{(2)} + \boldsymbol{\tau}_{l-1}^{(2)}) + \lambda \boldsymbol{\tau}_l^{(1)}\boldsymbol{\tau}_l^{(2)} + D\tau_l^{(2)z2} \Big], \quad (1)$$

where $\boldsymbol{S}_l, \boldsymbol{\tau}_l^{(1)}$ and $\boldsymbol{\tau}_l^{(2)}$ are spin operators with magnitudes $S_l = \tau_l^{(1)} = 1/2$ and $\tau_l^{(2)} = 1$, respectively. The number of unit cells is denoted by L. The spontaneous magnetization $M_{\rm sp}^z$ in the ground state is defined by

$$M_{\rm sp}^z = \left\langle \sum_{l=1}^{L} \left[S_l^z + \tau_l^{(1)z} + \tau_l^{(2)z} \right] \right\rangle, \quad (2)$$

where $\langle\rangle$ denotes the expectation value in the ground state.

The lattice structure is depicted in Fig.1. We consider the region $\lambda \geq 0$ and $1 \geq \delta \geq -1$. The isotropic case ($D = 0$) is investigated in [2, 3].

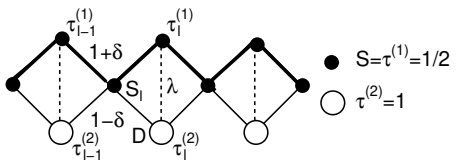


Figure 1: Structure of the diamond chain investigated in this work.

2 Numerical Results

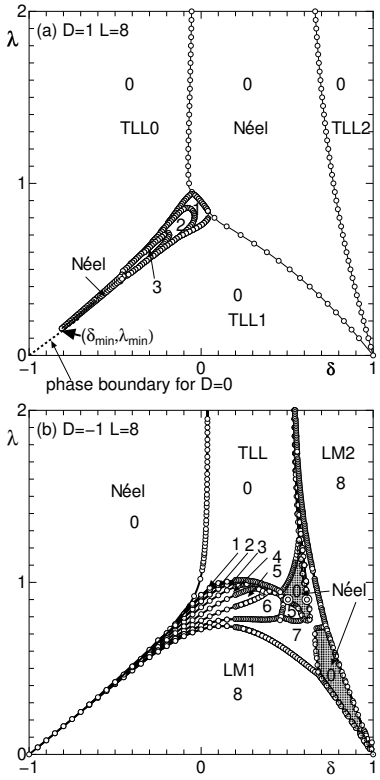


Figure 2: Ground-state phase diagrams based on the NED data with $L = 8$ for (a) $D = 1$ and (b) $D = -1$. The number indicated for each phase is $M_{\rm sp}^z$. The double circles (◎) in (b) are the phase boundaries obtained by DMRG with $L = 48$.

We have carried out the numerical exact diagonalization (NED) calculation for $L = 4, 6$, and 8. The phase diagrams for $L = 8$ are shown in Fig.2 for (a) $D = 1$ and (b) $D = -1$.

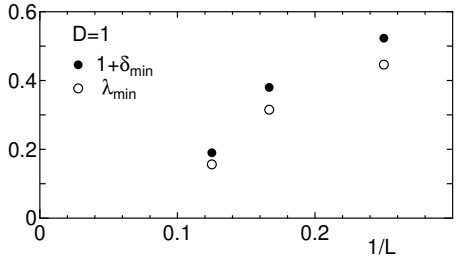


Figure 3: Minimum value of $1+\delta$ and λ plotted against $1/L$ in the narrow Néel phase for $D = 1$.

The number indicated for each phase is $M^z_{\rm sp}$ of the ground state. For $D = 1$, three kinds of Tomonaga-Luttinger liquid phases (TLL0, TLL1, TLL2) are found in addition to the Néel phase, and partial ferrimagnetic (PF) phases. The end point $(\delta_{\rm min}, \lambda_{\rm min})$ of the narrow Néel phase between TLL0 and TLL1 phases tends to $(\delta_{\rm min}, \lambda_{\rm min}) = (-1, 0)$ in the thermodynamic limt as shown Fig.3 confirming that TLL0 and TLL2 phases are different phases. The phase boundary between the TLL0 and TLL1 phases is close to the TLL-LM1 phase boundary for $D = 0$ shown by the dotted line in Fig.2(a). Hence, this phase boundary is insensitive to the value of D. It should be remarked that the Néel phase is present even in the case of easy-plane anisotropy $D > 0$. This is an example of the anisotropy inversion phenomena previously reported in frustrated spin-1/2 chains with trimer structure[5]. For $D = -1$, two kinds of Lieb-Mattis type ferrimagnetic phases[4] (LM1, LM2) appear in addition to the Néel, TLL and PF phases. According to the DMRG calculation for $L = 48$ shown by ◎ in Fig.2(b), the upper shaded part of the Néel phase remains in the thermodynamic limit, while the lower shaded part vanishes in the thermodynamic limit. We expect that the latter region will be replaced by the PF phase with $0 < m_{\rm sp} < 1$ as in the isotropic case.[3] The anisotropy inversion phenomenon is also observed for large λ region where the TLL phase remains even in the presence of easy-axis anisotropy $D < 0$.

The numerical diagonalization program is based on the TITPACK ver.2 coded by H. Nishimori.

References

[1] K. Hida, to be published in J. Phys. Soc. Jpn.; arXiv:2601.20328 (2026).
[2] K. Hida, J. Phys. Soc. Jpn. **90**, 054701 (2021).
[3] K. Hida, J. Phys. Soc. Jpn. **93**, 044703 (2024).
[4] E. Lieb and D. Mattis, J. Math. Phys. **3**, 749 (1962).
[5] K. Okamoto, *Proceedings of the 12th Asia Pacific Physics Conference (APPC12)*, JPS Conf. Proc. 012031 (2014) and references therein.

Scrambling in long-range interacting quantum systems

Tatsuhiko Shirai
Waseda Institute for Advanced Study, Waseda University
Nishi Waseda, Shinjuku-ku, Tokyo 169-0051

Out-of-time-order correlator (OTOC) has attracted attention in non-equilibrium statistical mechanics, quantum information, and quantum gravity. The time evolution of the OTOC estimates the scrambling time t_* when local perturbation propagates to the entire system. Estimating the scrambling time in long-range interacting quantum spin systems, where the interaction decays as a power law $J \sim r^{-\alpha}$ with distance r, is still challenging on both theoretical and numerical sides.

Here, we propose a discrete truncated Wigner approximation (DTWA) based method for computing temporal correlation functions including OTOCs. The DTWA method needs a computational cost of the order of N^2, where N is the system size, whereas exact methods generally require exponentially growing computational costs. Thus, DTWA offers a promising approach for exploring dynamical features of large-sized systems even when $\alpha > 0$. The method is applied to calculate an auto-correlation function, a squared commutator of local operators, and its higher-order extensions, and compared between systems with varying values of α. Our numerical results reproduce the exact dynamics for the average spreading of quantum information (i.e., squared commutators) across all time regimes for $\alpha \leq d$. Furthermore, we identify the limitations of the DTWA method when simulating scrambling dynamics for $\alpha > d$ and the fastest spreading of quantum information. Finally, we apply the DTWA method to investigate N dependence of t_* for $\alpha \leq 1$ on a one-dimensional lattice and compare the numerical result with a theoretical lower bound. Figure 1 reveals that the scaling behavior of t_* for large systems changes depending on the value of α.

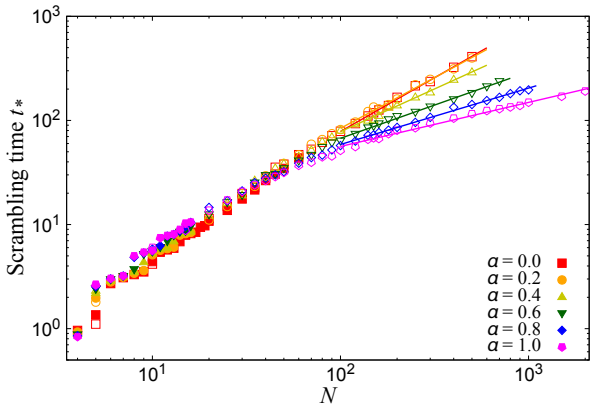


Figure 1: System-size dependence of the scrambling time t_* for different values of α. Open symbols and filled symbols indicate the DTWA results and the exact results, respectively. The bold lines are fitting using data of $N \geq 100$.

References

[1] T. Shirai, T. Mori: Phys. Rev. B **112**, 014309 (2025).

Theoretical study for excited states of firefly bioluminescence emitters

Miyabi HIYAMA
Gunma University
Tenjin-cho, Kiryu, Gunma 376-8515

Analogs of firefly bioluminescent substrates are attracting attention as next-generation luminescent probes for *in vivo* imaging techniques for animal tissues and cells, and their development is currently underway [1]. As such substrate analogues, not only AkaLumine, of which bioluminescence color is red (675 nm), but also more water-soluble analog seMpai producing similar bioluminescence color have been reported [2]. To investigate the differences in the electronic states of these analogues, we performed optimization of structure and vibrational analysis of the ground states for their oxy-form using the density functional theory (DFT) method. We also determined the structures of the excited states using the time-dependent (TD) DFT method.

Since the chemical species studied in this research consist of approximately 30 atoms, the computational time for preliminary calculations using a small number of basis sets, as well as for structural optimization and vibrational analysis in the ground state, was less than 24 hours. Therefore, we primarily used the F1cpu on System B for these calculations. On the other hand, since computational jobs involving structural optimization of excited states take more than one day to complete, we primarily used the L1cpu on System B.

Based on preliminary calculation results for the oxy-form of AkaLumine, we performed the quantum chemical calculations using Conductor-like Polarizable Continuum Model (CPCM) and Solvation Model based on Density (SMD) for the solvent effects. We found that, in the case of oxy-AkaLumine, structural optimization calculations using SMD failed to converge. Since the same problem occurred even in calculations with improved integration accuracy, this would be due to noise in the SMD method in Gaussian16, rather than an issue with the installation process or system B of Super Computer Center in ISSP.

According to the results of structural optimization, absorption calculations, and relative concentration analyses in 2024 for the conjugate acids and bases of seMpai, which were presumed to exist in aqueous solution, it was found that the chemical form of seMpai at pH 8, at which bioluminescence spectra is measured, is a carboxylate anion structure like that of AkaLumine [3, 4]. Following these results, the structures of oxy-AkaLumine and oxy-seMpai were determined. The results revealed that the charge distributions of the Highest Occupied Molecular Orbital (HOMO) for oxy-AkaLumine and oxy-seMpai are very similar to each other. Those of the Lowest Unoccupied Molecular Orbital (LUMO) are also similar to each other. The main configuration of the first excited states for all chemical species was the excitation from HOMO to LUMO.

References

[1] S. Iwano, M. Sugiyama, H. Hama, A. Watakabe, N. Hasegawa, T. Kuchimaru,

K. Z. Tanaka, M. Takahashi, Y. Ishida, J. Hata, S. Shimozono, K. Namiki, T. Fukano, M. Kiyama, H. Okano, S. Kizaka-Kondoh, T. J. Mchugh, T. Yamamori, H. Hioki, S. Maki and A. Miyawaki: Single-cell bioluminescence imaging of deep tissue in freely moving animals. Science. **359**, 935-939 (2018).

[2] R. Saito, T. Kuchimaru, S. Higashi, S. W. Lu, M. Kiyama, S. Iwano, R. Obata, T. Hirano, S. Kizaka-Kondoh, and S. A. Maki: Bull. Chem. Soc. Jpn.. **92**, 608 (2019).

[3] H. Ogawa, R. Ono, Y. Noguchi, N. Kitada, R. Saito-Moriya, S. A. Maki, H. Akiyama, H. Itabashi, and M. Hiyama: Photochem. Photobiol. **97**, 1016-1022 (2021).

[4] M. Harada, T. Nakano, R. Ono, T. Uchiyama, Y. Noguchi, R. Saito-Moriya, N. Kitada, S. A. Maki, T. Hirano, H.i Aoyama, M. Kobayashi, H. Akiyama, K. Kanno, H. Itabashi, and M. Hiyama: Photochem. Photobiol. **102**, 237-247 (2026).

Vortex structures and superconducting properties in quasicrystals

Nayuta Takemori
Department of Physics,
The University of Osaka
1-1 Machikaneyama,Toyonaka,Osaka 560-0043

We have investigated superconducting properties of quasiperiodic systems using large-scale numerical simulations based on the Bogoliubov–de Gennes (BdG) mean-field theory. In particular, we studied vortex states and the orbital upper critical field $B_{c2}(T)$ in an s-wave superconductor defined on the Ammann–Beenker tiling with octagonal symmetry.

Although previous studies have addressed intrinsic pinning of a single vortex [1] and spatially inhomogeneous superconducting states [2], the collective organization of vortices under strong magnetic fields and its impact on $B_{c2}(T)$ remain unclear. In quasiperiodic systems, intrinsic spatial inhomogeneity of the order parameter suggests that vortices preferentially penetrate weakly superconducting regions, which can significantly modify vortex configurations and field responses. Clarifying these effects is particularly relevant in light of recent experimental studies on magnetic-field responses in quasicrystalline superconductors [3].

Due to the absence of translational symmetry, the BdG equations must be solved in real space for large system sizes, leading to a substantial computational cost. The supercomputer system enabled us to perform calculations for systems with sizes up to $\mathcal{O}(10^3)$ sites, including diagonalization of large sparse matrices and extensive parameter sweeps over temperature and magnetic field.

We find that vortex configurations in quasiperiodic systems differ qualitatively from the Abrikosov triangular lattice observed in periodic superconductors. Near half filling, vortices form patterns reflecting the underlying eightfold symmetry. Furthermore, vortices preferentially occupy weak-pairing regions, resulting in vortex clustering and the formation of giant vortex states. This effect effectively protects strongly superconducting regions from orbital pair breaking.

As a consequence, the orbital upper critical field $B_{c2}(T)$ is significantly enhanced compared to periodic systems. In addition, $B_{c2}(T)$ exhibits anomalous low-temperature behavior, showing an approximately linear increase down to low temperatures without clear saturation.

A manuscript based on these results is currently under preparation [4].

References

[1] Y. Nagai, Phys. Rev. B 106, 064506 (2022).

[2] S. Sakai *et al.*, Phys. Rev. Res. 1, 022002 (2019).

[3] Y. Tokumoto *et al.*, Nat. Phys. **20**, 123 (2024).

[4] T. Fukushima, Y. Yamamoto, N. Takemori, S. Sakai. M. Ichioka and A, Jagannathan *et al.*, in preparation.

Spontaneous formation of multiple-Q orders in two-dimensional Hubbard models

Takashi UCHIDA
Hokkaido University of Science
4-1, 7-15, Maeda, Teine-ku, Sapporo 006-8585

In recent years, the multiple-Q orders in magnetic systems have attracted attention because they sometimes reveal nontrivial magnetic structures such as magnetic skyrmions. These structures are realized in both noncentrosymmetric and centrosymmetric systems. In noncentrosymmetric systems, the competition among the Dzyaloshinskii-Moriya (DM) and ferromagnetic interactions causes the multiple-Q orders. In the case of centrosymmetric systems, the formation mechanism of nontrivial multiple-Q orders is not unique and still under investigation [1, 2].

The purpose of the present research is to investigate the multiple-Q orders in the centrosymmetric systems, starting from the itinerant electron model where the electronic structures play an important role in forming the multiple-Q orders. Specifically, we investigate the multiple-Q orders in the centrosymmetric triangular-lattice single-band Hubbard model by means of the molecular spin dynamics (MSD) method [3]. The present formulation of the MSD adopts the static approximation to the functional integral method and the isothermal molecular dynamics technique, and reduces to the generalized Hartree-Fock approximation at the ground state.

Starting from a random distribution of local magnetic moments, the MSD scheme can automatically determine the stable magnetic structure. In this scheme, the most time-consuming process is the magnetic force calculation at each time step, where the local electronic structures are calculated in real space by means of the recursion method. We have adopted the MPI parallel calculation scheme in the recursion calculation and found it effective in saving both computing time and CPU resources.

In the present work, we have included the 1st, 2nd and 3rd neighbor transfer integrals t_i ($i = 1, 2, 3$) in the Hubbard model. We have performed magnetic structure calculations on a hexagonal supercell with 972 lattice points, which is embedded in a large cluster consisting of 6 such supercells, each of which are connected by the periodic boundary condition. Under zero magnetic field and the fixed value of the temperature $T/t = 0.0005$, we have explored the magnetic structures changing the Coulomb interaction strength U/t_1, transfer integral ratios t_2/t_1, t_3/t_1 and the electron number n.

In the case of $t_2 = 0$, $t_3/t_1 = -0.42 \sim -0.40$, 3Q + 1Q order is stabilized for $U/t_1 = 7.0$ and $n = 1.20 \sim 1.22$, where the magnetic structure shows phase separation. The electronic density of states becomes zero in the vicinity of the Fermi energy E_{F}, opening a gap at E_{F}.

References

[1] T. Okubo, S. Chung, and H. Kawamura: Phys. Rev. Lett. **108** (2012) 017206

[2] Y. Kakehashi: J. Phys. Soc. Jpn. **89** (2020) 094710.

[3] Y. Kakehashi, S. Akbar, and N. Kimura: Phys. Rev. B**57** (1998) 8354.

Understanding the characteristics of sentence production based on differences in language acquisition methods

Takehito SUZUKI
Department of Human Science, Takachiho University
2-19-1, Omiya, Suginami-ku, Tokyo 168-8508

Language has been attracted the interests of researchers in the field of physics (e.g., [1, 2, 3]). However, grammar for natural language has not been considered there. We employ the combinatory categorial grammar (CCG) to deal with natural languages mathematically. The definition of CCG is as follows. First, we define noun (N), noun phrase (NP), and sentence (S) as ground category. We then employ operators / and \. These operators represent the grammar. Let us consider two categories A and B. The category A/B indicates that if the category B emerges after this category, the categories are merged into the category A. The category A\B indicates that if the category B emerges before this category, the categories are merged into the category A. If we write the sequence of the categories A and B as A+B, these rules are described with the equations

$$\mathrm{A/B} + \mathrm{B} \to \mathrm{A}, \tag{1}$$

$$\mathrm{B} + \mathrm{A\backslash B} \to \mathrm{A}. \tag{2}$$

Equations (1) and (2) are called forward and backward functional application rules, respectively. For example, let us write intransitive verb with CCG for English. If the noun phrase comes before the intransitive verb, the sentence is generated. We therefore conclude that the intransitive verb is a category S\NP. An additional example is the adjective. In languages like English where modifiers precede the modified word, it can be written as N/N with CCG. Notably, the operators can be utilized recursively. With this framework, all categories are represented by the combinations of N, NP, S, /, and \. The categories other than the ground categories such as intransitive verb S\NP are called syntactic categories.

We regard the sentence as the sequence of the categories, and apply the metropolis method to CCG. As an initial condition, the first step is to arrange the categories randomly. We then select one of the categories and change it into another category (i.e., upgrade). If the sequence from the beginning of the sentence to the selected category is grammatical, we accept the upgrade. On the other hand, if the sequence is not grammatical, we accept it with probability $\exp(-\Delta E/k_B T)$, where ΔE is the measure of instability of the sequence, k_B is the Boltzmann constant, and T is temperature. We assume the scale unit where $\Delta E/k_B$ is normalized to be unity. Temperature can be interpreted as the disturbance for the grammar, and describes how the learner is familiar with the grammar.

We consider the generating mechanism of the sentence with N_W words. We fix $N_W = 40$ in the current study. Though we initially arrange categories randomly, as mentioned above, note that the first category is fixed to be an article. We then apply the metropolis method. We repeat the calculation 10000 times for each temperature. We inves-

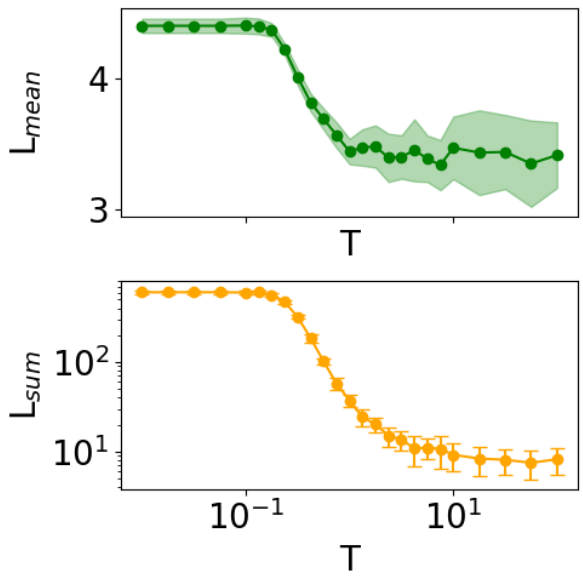


Figure 1: Dependences of L_{mean} and L_{sum} on T [4].

tigate the probability that the grammatically correct sentences are generated. Using the probability, we calculate the expected value of the sentence length L, L_{mean}. We also investigate numbers of the grammatically-finished sentences, L_{sum}, for each temperature.

The upper panell in Fig. 1 describes the relationship between T and L_{mean}. Discontinuous behavior of dependence of L_{mean} on temperature is observed; above a certain temperature, correct sentences are hardly generated anymore. The boundary is $T \sim 0.1$. We can observe that L_{sum} also shows phase-transition-like behavior (lower panel in Fig. 1). The probability generating grammatically correct sentence is almost $5-6\%$ for $T < 0.1$, whereas it is almost 0.05% for $T > 1$.

High temperature represents the children who do not understand the grammar completely. The language acquisition may be a phase-transition process.

References

[1] E. De Giuli: J. Phs. A: Math. Theor. **52**, 504001 (2019).

[2] T. Yamamoto, S. Yamada, and T. Mizuguchi: Eir. Phys. J. B **94**:200 (2021).

[3] K. Nakaishi, and K. Hukushima: Phys. Rev. Res. **4**, 023156 (2022).

[4] T. Suzuki, and T. Mizuguchi: JPS Annual Meeting (2025).

Molecular dynamics simulation of graphene-nanosapcer stacking heterostructure properties

Mingda Ding, Taiki Inoue, Yoshihiro Kobayashi

Department of Applied Physics, The University of Osaka,

Yamadaoka, Suita, Osaka 565-0871

In our previous studies, we investigated graphene (Gr) stacking structures containing nanodiamond (ND) nanospacers and carbon nanotube (CNT) spacers. These studies showed that the insertion of nanospacers between Gr layers effectively modulates the interlayer distance and interlayer interaction of multilayer Gr [1,2]. Building on these studies, this year we investigated the loading–unloading behavior of graphene–carbon nanotube (Gr–CNT) hybrid systems using molecular dynamics (MD) simulations and nanoindentation experiments.

MD simulations were conducted using the open-source software LAMMPS. The AIREBO potential was used to describe short-range carbon–carbon interactions, while the LJ potential was employed for interlayer van der Waals interactions. Dynamic relaxation was performed using the velocity-Verlet algorithm to obtain energy-minimized structures.

The MD simulations focused on stacked Gr–CNT structures, in which CNTs were confined between two graphene layers. By applying periodic boundary conditions, we examined systems with different intertube spacings, CNT diameters, and wall numbers. Representative snapshots of the MD simulations under different structural conditions are shown in Figure 1.

Under certain conditions, the Gr–CNT structures exhibited mechanical bistability with two stable configurations: adhesion and separation of the graphene layers. This bistability originates from the competition between interlayer van der Waals attraction and elastic deformation of the graphene layers and CNTs. The simulated loading–unloading curves showed clear hysteresis, indicating energy dissipation associated with structural transitions between stable configurations.

To experimentally verify the mechanical behavior predicted by the simulations, reduced graphene oxide–carbon nanotube (rGO–CNT) hybrid films were fabricated as macroscopic assemblies corresponding to the unit structures modeled in the MD simulations. Atomic force microscopy-based nanoindentation measurements were performed on the rGO–CNT films. The obtained force–displacement curves exhibited pronounced hysteresis and larger dissipation energy compared with pure rGO films, in good agreement with the

simulation results.

These results show that the mechanical response of Gr–CNT hybrid systems is governed by the balance between van der Waals interactions and elastic deformation. The combined MD simulation and nanoindentation approach provides fundamental insight into the design of graphene-based hybrid microstructures with tunable mechanical stability, hysteresis, and energy dissipation properties. The outcomes of this study have been compiled into a manuscript and submitted for publication [3].

References

[1] M. Ding, T. Inoue, J. I. Enriquez, H. Handoko Halim, Y. Ogawa, Y. Taniyasu, Y. Hamamoto, Y. Morikawa, and Y. Kobayashi, *J. Phys. Chem. C* **127**, 23768 (2023).

[2] M. Ding, T. Inoue, J. I. Enriquez, H. H. Handoko, Y. Ogawa, Y. Taniyasu, Y. Hamamoto, Y. Morikawa, Y. Kobayashi, Carbon **229**, 119464 (2024).

[3] M. Ding, N. Sakurai, M. Shen, T. Inoue, T. Matsuzaki, T. Mizuno, K. Suzuki, J. I. Enriquez, H. H. Halim, Y. Hamamoto, Y. Nishina, H.Y. Yoshikawa, Y. Morikawa, Y. Kobayashi, Submitted.

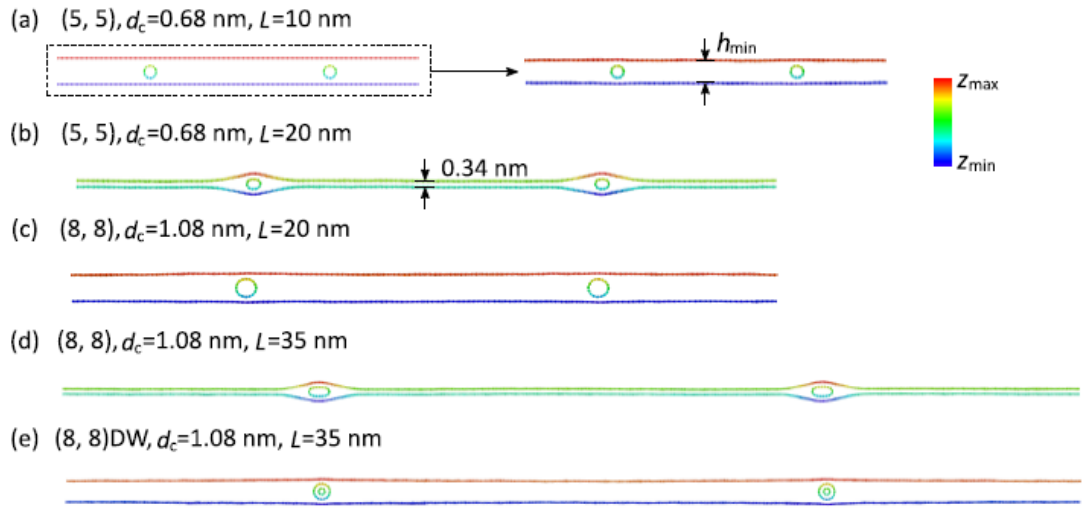


Fig. 1 (a) Relaxed configurations obtained from MD simulations of the Gr–CNT stacked structure with different intertube distances L, CNT diameters d_c, and wall numbers.

3.5 SCCMS Projects

Data Generation for Magnetic Properties at Finite Temperature

Tetsuya FUKUSHIMA
National Institute of Advanced Industrial Science and Technology (AIST)
1-1-1 Umezono, Tsukuba, Ibaraki 305-8568, Japan

The purpose of Data Creation and Utilization-Type Material Research and Development Project (Digital Transformation Initiative Center for Magnetic Materials) is to find new functional magnetic materials by data-driven approaches.

In this year, we developed the the all-electron full-potential Korringa–Kohn–Rostoker (FPKKR) Green's function method which can treat finite temperature effects [1], and systematically investigated how Pr substitution affects the magnetocrystalline anisotropy of $(Nd_{1-x}Pr_x)_2Fe_{14}B$. We present our results on the latter topic in this report. Motivated by experimental observations indicating that local lattice distortions near grain boundaries modify the magnetocrystalline anisotropy, our objective was to clarify the responses of the anisotropy constant K_u and the magnetization J_S to the Pr concentration x and to changes in the lattice constants (the biaxial strain δa and the c-axis strain δc).

For the calculations, we employed the FPKKR method, adopting the local density approximation for the exchange–correlation functional. Spin–orbit coupling was included self-consistently in the total-energy calculations, and the magnetocrystalline anisotropy constant was evaluated from the total-energy difference between the quantization axes along [001] and [100] as

$$K_u = \frac{E_{100} - E_{001}}{V},$$

where V is the unit-cell volume. Substitutional disorder on the rare-earth sublattice was treated within the coherent potential approximation (CPA), and $(Nd_{1-x}Pr_x)_2Fe_{14}B$ was evaluated in steps of $x = 0.1$. The $4f$ orbitals of Nd and Pr were treated as open-core, assuming the trivalent states $Nd^{3+}(4f^3)$ and $Pr^{3+}(4f^2)$. As an initial magnetic configuration, the Fe $3d$ spins and the rare-earth $5d$ spins were set antiparallel, and self-consistent calculations were performed to obtain converged solutions.

Lattice distortions were introduced by varying only the lattice constants a and c while preserving tetragonal symmetry. Assuming tetragonal symmetry, the biaxial strain was defined as

$$\delta a := \delta d_{[110]} = \frac{d_{[110]} - d^{\mathrm{bulk}}_{[110]}}{d^{\mathrm{bulk}}_{[110]}},$$

where $d_{[hkl]}$ denotes the lattice spacing along the $[hkl]$ direction and $d^{\mathrm{bulk}}_{[hkl]}$ is its bulk value. In the Pr-dependence analysis, we mainly compared the x and δa dependences of K_u and J_S under the conditions $\delta c = 0, \pm 3\%$ (Fig. 1).

In the following, we summarize the results obtained as the Pr-substitution effect. First, in the strain-free condition ($\delta c = 0$), the FPKKR calculations estimate $K_u = 6.0$ MJ/m^3 for $Pr_2Fe_{14}B$, which is larger than $K_u = 4.2$ MJ/m^3 for $Nd_2Fe_{14}B$. Moreover, at $\delta c = 0$, K_u increases almost linearly with the Pr concentration x, indicating that Pr addition enhances the anisotropy in the low-temperature regime. In contrast, J_S is slightly smaller on the Pr-rich side, consistent with the smaller

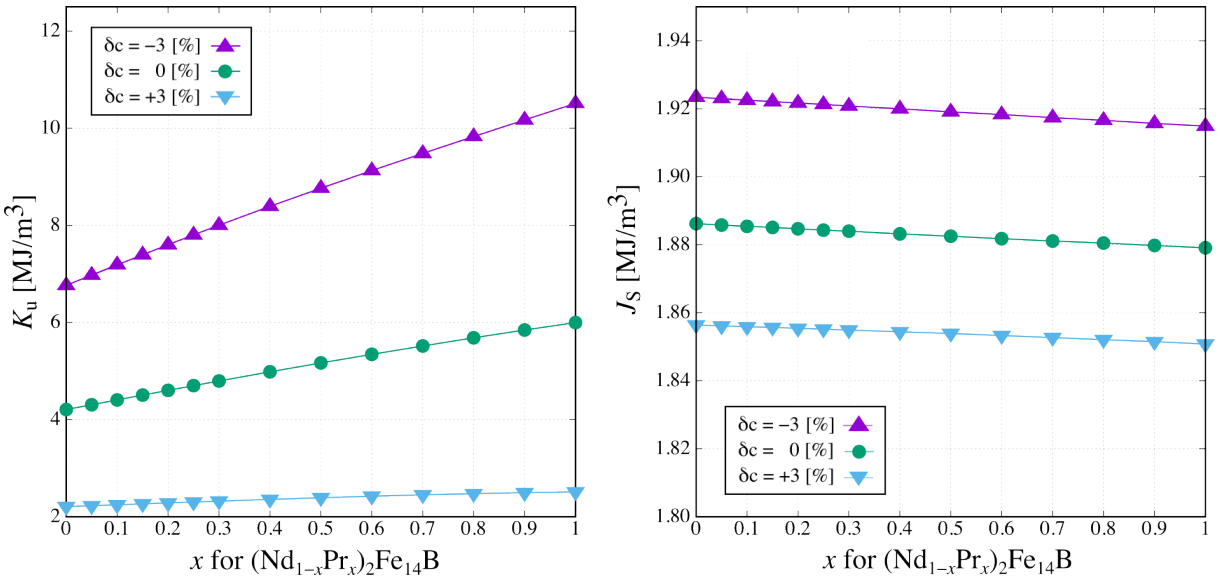


Figure 1: Schematic overview of the Pr-concentration (x) dependence of (a) K_u and (b) J_S in $(Nd_{1-x}Pr_x)_2Fe_{14}B$, and of the changes in K_u and J_S under [110] compression (δa).

effective magnetic moment of Pr^{3+} (3.20 μ_B) compared with Nd^{3+} (3.27 μ_B). Notably, the magnetization (or total magnetic moment) excluding the $4f$ contribution is identical for $Nd_2Fe_{14}B$ and $Pr_2Fe_{14}B$, amounting to 1.57 T (31.9 μ_B/f.u.), confirming that J_S is predominantly governed by Fe.

Next, we compare the response of K_u to uniform biaxial compression ($\delta a < 0$). At $\delta c = 0$, K_u in $Pr_2Fe_{14}B$ decreases with increasing compression, similarly to $Nd_2Fe_{14}B$. The reduction of K_u is more pronounced for Pr-richer compositions: the K_u values of $Pr_2Fe_{14}B$ and $Nd_2Fe_{14}B$ become equal around $\delta a \simeq -4\%$, and under stronger compression the Pr-rich side exhibits smaller K_u. From the viewpoint of crystal-field theory, this difference is attributed to the difference in the Stevens factor α_J (Pr^{3+} : −0.02, Nd^{3+} : −0.006): both have $\alpha_J < 0$ (oblate), but the larger magnitude for Pr^{3+} implies stronger nonsphericity of the $4f$ charge distribution, making K_u more sensitive to lattice distortions. For $\delta c = +3\%$, the decrease in K_u for the Pr-based compound is even stronger: K_u of $Pr_2Fe_{14}B$ becomes negative at approximately $\delta a \simeq -3.5\%$. By contrast, for $\delta c = -3\%$, the reduction of K_u under biaxial compression is partially suppressed, and at least up to $\delta a = -5\%$ the K_u of $Pr_2Fe_{14}B$ remains larger than that of $Nd_2Fe_{14}B$. These results suggest that Pr substitution enhances K_u in strain-free bulk, whereas it can markedly accelerate the reduction of K_u under biaxial compression, especially under conditions with a larger c/a ratio.

Finally, to examine the influence of local site preference, we compared three occupation models in which Pr selectively occupies the $4f$ site, selectively occupies the $4g$ site, or is uniformly distributed over both sites. In all models, K_u increases with increasing Pr concentration, indicating that the trend is robust. For example, at $x = 0.50$, K_u is 5.59, 5.16, and 4.75 MJ/m^3 for the $4f$-selective, uniform, and $4g$-selective models, respectively; although the absolute values differ due to site preference, the qualitative conclusion that Pr substitution enhances K_u in the strain-free case remains unchanged.

References

[1] M. Ogura and H. Akai, *J. Phys. Condens. Matter.* **17**, 5741 (2005).

Finite-Temperature Magnetism of Transition-Metal Alloys Using KKR Green's Function Method

Takashi MIYAKE
Materials DX Research Center, AIST
Umezono, Tsukuba, Ibaraki 305-8568

We have studied finite-temperature magnetism of binary alloys of 3d transition metals using first-principles calculation. This year, we focused on the dependence of the magnetization on the lattice parameters.

The calculation is based on density functional theory. The generalized gradient approximation (GGA) of the Perdew-Burke-Ernzerhof (PBE) type functional is employed for the exchange and correlation energies We assume that the potential of the system is represented as a collection of spherically symmetric mffin-tin potentials. The relativistic effect is considered within the scalar relativistic approximation. We use the AkaiKKR program package. Chemical disorder is treated in the coherent potential approximation (CPA) combined with the Korringa-Kohn-Rostoker (KKR) Green's function method. Finite-temperature effects are included by considering scattering by phonons and magnons in CPA, where lattice displacements and ratio of majority spins to minority spins are adjusted at each temperature. Target material space is selected from the combinations of V, Cr, Mn, Fe, Co, Ni and Cu in the body-centered tetragonal structure with changing c/a and volume. We perform structure optimization for pure Cr, Mn, Fe, Co, Ni, and Cu by using the QUANTUM ESPRESSO package. Then, the lattice parameters of the alloys are determined by the Vegard ' s law.

Figure 1 shows the magnetic moment of binary alloys as a function of the average electron number. At 0 K and $a/a_0 = 1$, the magnetic moment increases with increasing the electron number, then turns to decreases, as is know as the Slater-Pauling curve. The average electron number at which the magnetic moment is maximized decreases (increases) as a/a_0 increases (decreases). Similar trend is observed at finite temperatures. With increasing temperature, the magnetic moment decreases and the peak position is shifted to larger electron number.

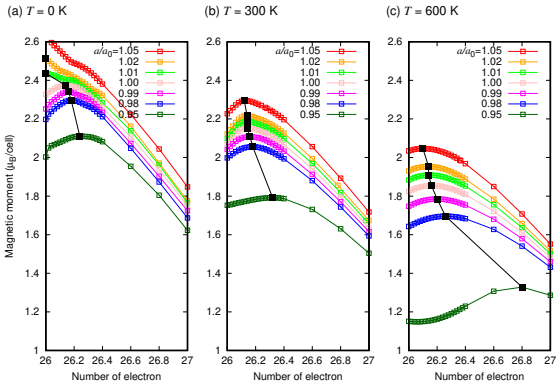


Figure 1: Calculated Slater-Pauling curve at 0 K, 300 K, 600 K. The lattice constant is varied to see volume dependence of the Slater-Pauling curve.

References

[1] Reo Kita, Taro Fukazawa, Takashi Miyake, and Tetsuya Fukushima: Materials Research Meeting 2025.

Chiral Effects on Aqueous Solubility of Polypeptides Explored by Molecular Simulations

Kazuo Yamada and Nobuyuki Matubayasi

Division of Chemical Engineering Science, Graduate School of Engineering Science, The University of Osaka, Toyonaka, Osaka 560-8531, Japan

Background

Partial substitution of L-amino-acid residues by their mirror-image D counterparts is a promising strategy for improving the proteolytic stability of peptide drugs. In contrast, the effect of such stereochemical modification on water solubility remains poorly understood. In particular, it is still unclear whether the solubility change is governed simply by the number of D residues or by the detailed L/D substitution pattern along the chain. Here we address this issue for Ala homopolypeptides by combining all-atom molecular dynamics (MD) simulations of the aqueous and peptide-solid phases with free-energy calculations. The present report focuses on the results for the tetrapeptides, while calculations for 8- and 12-residue systems are in progress.

Methods

Ala homotetrapeptides with several L/D substitution patterns were constructed by molecular modeling. For each pattern, all-atom MD simulations were carried out in liquid water and in the peptide solid phase. GROMACS (ver. 2022.4) was used for MD sampling, and ERmod (ver. 1.0.4) was used for free-energy analysis. As a thermodynamic proxy for water solubility, we evaluated the transfer free energy $\Delta G^{\mathrm{tr}} = \mu_{\mathrm{liq}}^{\mathrm{solv}} - \mu_{\mathrm{solid}}^{\mathrm{solv}}$; a more negative value indicates higher water solubility. To identify the physical origin of the pattern dependence, the solvation free energy was decomposed within the ERmod framework as

$$\mu^{\mathrm{solv}} = \langle v \rangle + \mu^{\mathrm{excl}} + \mu^{\mathrm{re-org}},$$

where $\langle v \rangle$ is the direct solute-solvent interaction term, μ^{excl} is the excluded-volume term, and $\mu^{\mathrm{re-org}}$ is the solvent-reorganization term in the low-energy region.

Results and Discussion

Figure 1 shows the L/D-pattern dependence of the calculated solubility proxy for Ala homotetrapeptides. The LLLL, DLLL, and DLLD patterns exhibit similar values of ΔG^{tr}, indicating only a slight change in water solubility. In contrast, the alternating LDLD pattern gives a distinctly more negative ΔG^{tr} and therefore a marked enhancement of water solubility. These results show that the stereochemical arrangement along the chain, rather than the mere presence of D residues, is the decisive factor. We also performed the ERmod free-energy decomposition. The dominant contribution to the LDLD enhancement is the reduction in the solvent-reorganization term $\mu^{\mathrm{re-org}}$ between the liquid and solid phases. By contrast, the difference in μ^{excl} is small, showing that the improvement does not originate from a substantial change in molecular size. The direct interaction term $\langle v \rangle$ also contributes, but less significantly than $\mu^{\mathrm{re-org}}$.

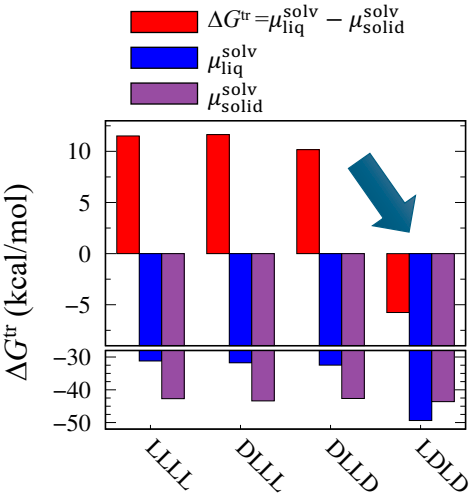


Figure 1: Pattern dependence of $\mu_{\mathrm{liq}}^{\mathrm{solv}}$, $\mu_{\mathrm{solid}}^{\mathrm{solv}}$, and ΔG^{tr} for Ala homotetrapeptides.

These results suggest that the LDLD pattern induces a solution structure that lowers the solvent-reorganization penalty without greatly changing the effective peptide size. For Ala homotetrapeptides, the alternating L/D pattern is therefore a favorable motif for water solubility. Ongoing calculations for longer Ala homopolypeptides will test how general this mechanism is.

Passivation in Sn-Based Perovskites and Interpretable Machine Learning Approaches

Tomomi Shimazaki

Graduate School of Nanobioscience,

Yokohama City University, 22-2 Seto, Kanazawa, Yokohama 236-0027

In this study, we investigated the passivation of surface tin-vacancy defects in Sn-based mixed-halide perovskites, focusing on materials with different bromine concentrations.[1-2] These wide-bandgap perovskites are promising for tandem solar cell applications. We found that Lewis base molecules effectively suppress deep p-type defect states on perovskite surfaces. These defects were attributed to halide dimer structures, indicating that strong interactions between passivating molecules and surface halide dimers are required for effective passivation. The results are consistent with previous studies on related Sn-based perovskite systems. Overall, this work provides guidance for molecular surface passivation strategies and supports the rational design of perovskite materials for photovoltaic applications, although further microscopic studies on bromine-containing films are needed.

In addition, we developed a modified convex clustering (regression) method in which representative points are selected directly from the training dataset.[3] By varying the number of representative points, the method enables control over both data representation and model complexity. Applying this approach to acrylate (ACR) and methyl acrylate (MA) radical reaction datasets, we constructed machine learning models for predicting reaction energy barriers and observed improved prediction accuracy with more representative points. Because these points are real data samples used directly in the prediction process, the models are highly interpretable. This framework offers a promising approach for analyzing chemical reaction data and other complex scientific datasets.

References

[1] E. Kino, M. Takagi, M. Tachikawa, K. Yamashita, and T. Shimazaki, *J. Chem. Phys.,* 163, 104703 (2025).

[2] E. Kino, M. Takagi, M. Tachikawa, K. Yamashita, and T. Shimazaki, *Phys. Chem. Chem. Phys*., 27, 7429 (2025).

[3] T. Shimazaki and M. Tachikawa, *Phys. Chem. Chem. Phys.* 28, 2499 (2026).

Numerical Spectroscopy for Cuprate Superconductors

Youhei YAMAJI
Research Center for Materials Nanoarchitectonics (MANA), National Institute for Materials Science (NIMS), Namiki, Tsukuba-shi, Ibaraki 305-0044

To elucidate properties of correlated quantum materials, numerical methods have evolved alongside advances in computing facilities with machine learning [1]. In particular, neural quantum states, such as resonating-valence-bond wavefunctions augmented by neural networks [2], have enabled access to accurate ground state properties of the quantum materials.

Building on this progress, the researchers extend the generator-coordinate method [3, 4, 5] within a flexible variational Monte Carlo framework by incorporating artificial neural networks [2]. This dynamical variational scheme [6, 7] allows unified simulations of a wide range of spectra, including electron energy loss spectroscopy, neutron scattering, (inverse) photoemission, and resonant inelastic neutron scattering.

Applying the method to cuprate superconductors, we show that the characteristic spin-excitation energy extracted from simulated neutron spectra does not correlate with the optimal critical temperature. Figure 1 shows examples of dynamical spin and charge structure factors of $Bi_2Sr_2CuO_6$ (Bi2201) at half filling, which are proportional to the inelastic neutron scattering and electron energy loss spectroscopy spectra, respectively.

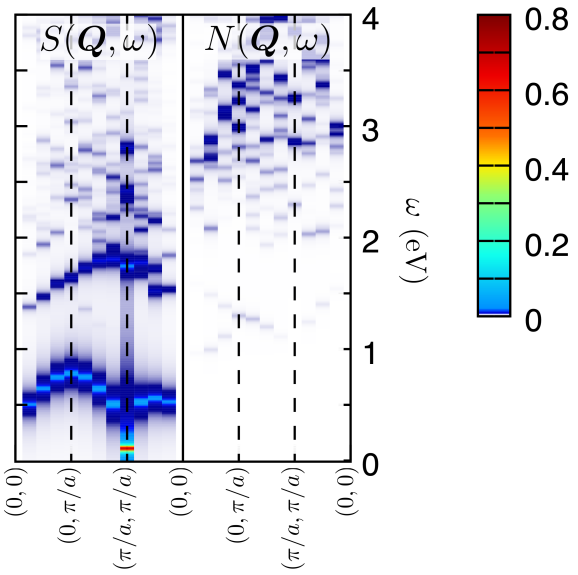


Figure 1: Dynamical spin (charge) structure factors for Bi2201 at half filling shown in the left (right) panel.

References

[1] As a review, H. Lange, *et al.*: Quantum Sci. Technol. **9**, 040501 (2024).

[2] Y. Nomura, *et al.*: Phys. Rev. B **96**, 205152 (2017).

[3] D. L. Hill and J. A. Wheeler: Phys. Rev. **89**, 1102 (1953).

[4] J. J. Griffin and J. A. Wheeler: Phys. Rev. **108**, 311 (1957).

[5] T. Li and F. Yang: Phys. Rev. B **81**, 214509 (2010).

[6] K. Ido, M. Imada, and T. Misawa: Phys. Rev. B **101**, 075124 (2020).

[7] M. Charlebois and M. Imada: Phys. Rev. X **10**, 041023 (2020).

3.6 Software Advancement Projects and Workshop Support

Advancement of Bayesian Optimization Package PHYSBO

Ryo TAMURA
Center for Basic Research on Materials, National Institute for Materials Science
1-1 Namiki, Tsukuba, Ibaraki 305-0044

Bayesian optimization is an experimental design method that leverages machine-learning-based predictions to identify better conditions with as few trials as possible. In FY2020, under the project for advancement of software usability in materials science(PASUMS) at the Institute for Solid State Physics, the University of Tokyo, we developed PHYSBO, a Bayesian optimization package targeted at physics and materials science [1,2]. In FY2025, we carried out a major update aimed at improving ease of installation and portability across diverse computational environments [3]. The core of this update lies not in changes to the optimization algorithms themselves, but in reducing the burden of practical deployment and operation. In PHYSBO version 2, we changed the license from GPL to MPL in order to enhance compatibility with a wider range of research and software ecosystems. This change provides greater flexibility in how code is handled when the PHYSBO module is imported. In the subsequent version 3, we carried out a fundamental redesign of the implementation, achieving the following functional enhancements and improvements:

- Strengthened support for multi-objective optimization
- Introduction of a range-based policy for continuous-variable optimization
- Elimination of environment dependencies through a Cython-free implementation
- Support for the latest libraries, including NumPy 2

These improvements lower both technical and organizational barriers to adoption and facilitate integration into a wide variety of computational environments and research workflows.

As a result, practical applications using PHYSBO are also accelerating, and the original PHYSBO paper [1] has been cited in numerous influential research articles. Furthermore, PHYSBO has been implemented as the standard engine of NIMO [4], a software package for autonomous materials exploration, and its use is expanding not only within Japan but also internationally.

References

[1] Y. Motoyama, R. Tamura, K. Yoshimi, K. Terayama, T. Ueno, and K. Tsuda, Comput. Phys. Commun. **278**, 108405 (2022).

[2] https://www.pasums.issp.u-tokyo.ac.jp/physbo/

[3] Y. Motoyama, K. Yoshimi, T. Aoyama, K. Terayama, K. Tsuda, R. Tamura, arXiv:2603.01349.

[4] https://www.nims.go.jp/nimo/

Development and Maintenance of Tutorials and Documentation for the First-Principles Quantum Monte Carlo Package TurboRVB

Kosuke NAKANO
Center for Basic Research on Materials (CBRM), National Institute for Materials Science (NIMS)
1-2-1 Sengen, Tsukuba, Ibaraki 305-0047, Japan

The goal of this project is to improve the usability and accessibility of the first-principles quantum Monte Carlo (QMC) package TurboRVB [1, 2] and its associated Python tools, TurboGenius [3, 4] and TurboWorkflows [5], within the framework of the FY2025 Project for advancement of software usability in materials science(PASUMS) [6], by developing comprehensive tutorials, manuals, and documentation.

During FY2025, we established a unified documentation portal (Fig. 1) that consolidates the manuals for TurboRVB, TurboGenius, and TurboWorkflows into a single, user-friendly website [7]. The portal guides users to the appropriate manual depending on whether they want to run QMC calculations directly via the core TurboRVB executables, use the higher-level Python interface provided by TurboGenius, or automate multi-step workflows with TurboWorkflows. This development addressed the problem that the relevant information had previously been scattered across separate resources, making it difficult for users to identify the appropriate starting point and understand how these tools should be used in combination.

For TurboRVB, we carried out a comprehensive survey of input variable names for each program in the package. Previously, no systematic list of input parameters existed, making it difficult for new users to set up calculations. The newly compiled input-variable reference covers all major executables and is now included in the TurboRVB manual, thereby resolving this bottleneck significantly lowering the barrier to entry.

For TurboGenius, we prepared tutorials that demonstrate the higher-level Python and command-line interface for common TurboRVB workflows, including geometry optimization, energy calculations, and high-throughput screening setups. These tutorials were developed in response to the problem that, despite the availability of a higher-level interface, practical guidance for standard research use cases had been insufficient. For TurboWorkflows, we documented the remote-execution capabilities, dependency handling, and multi-step workflow orchestration features, thereby addressing the difficulty of routinely using these functions without adequate documentation, enabling users to automate chained QMC jobs across computing resources.

All documentation is publicly available at the TurboTutorials website [7] and is maintained alongside the source code repositories to ensure long-term consistency and updates. Thus, through PASUMS, we improved not only the availability of documentation itself but also the research software support environment by identifying concrete usability issues and providing corresponding solutions.

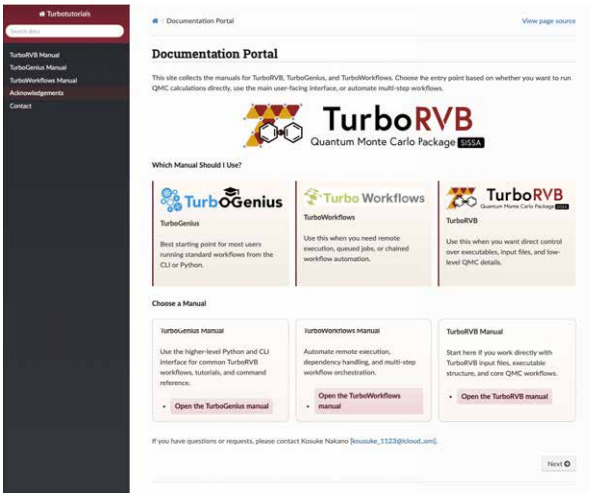


Figure 1: Top page of the TurboTutorials documentation portal, providing unified access to the manuals for TurboRVB, TurboGenius, and TurboWorkflows.

References

[1] TurboRVB, `https://github.com/sissaschool/turborvb`.

[2] K. Nakano, C. Attaccalite, M. Barborini, L. Capriotti, M. Casula, E. Coccia, M. Dagrada, Y. Luo, G. Mazzola, A. Zen, and S. Sorella, J. Chem. Phys. **152**, 204121 (2020).

[3] TurboGenius, `https://github.com/kousuke-nakano/turbogenius`.

[4] K. Nakano, A. Raghav, and S. Sorella, J. Chem. Phys. **159**, 224801 (2023).

[5] TurboWorkflows, `https://github.com/kousuke-nakano/turboworkflows`.

[6] K. Yoshimi, Y. Motoyama, T. Aoyama, T. Kawamura amd N. Kawashima, Science and Technology of Advanced Materials: Methods, **5**,1 (2025).

[7] TurboTutorials, `https://kousuke-nakano.github.io/turbotutorials/`.

Report of CCMS hands-on sessions in the 2025 fiscal year

Masahiro FUKUDA

Institute for Solid State Physics,

The University of Tokyo, Kashiwa-no-ha, Kashiwa, Chiba 277-8581

In the 2025 fiscal year, Center for Computational Materials Science (CCMS) in the Institute for Solid State Physics (ISSP) held 3 hands-on sessions where the ISSP supercomputer was used [1-3]. In this report, we briefly summarize them.

Table 1 shows the list of the hands-on sessions in the 2025 fiscal year. There are 3 hands-on sessions were held. Development of the software except for CrySPY was supported by “Project for advancement of software usability in materials science” (PASUMS) [4].

Features of each software are as follows. DCore [5] is open-source software for performing dynamical mean-field theory (DMFT) calculations for strongly correlated electron systems. ChiQ [6] is a tool for calculating susceptibilities and related response functions based on electronic structure data. CrySPY [7] is open-source software for crystal structure prediction using evolutionary algorithms and other global optimization techniques. ODAT-SE [8] is a framework for managing and automating high-throughput simulations and data analysis workflows in computational materials science.

In all of the hands-on sessions, lecturers explained the basics of each software and gave its tutorial. Materials of some hands-on sessions are available on each official page.

References

[1] https://ccms.issp.u-tokyo.ac.jp/event/7137

[2] https://ccms.issp.u-tokyo.ac.jp/event/7527

[3] https://mdcl.issp.u-tokyo.ac.jp/scc/news/7779

[4] https://www.pasums.issp.u-tokyo.ac.jp/en/

[5] https://www.pasums.issp.u-tokyo.ac.jp/dcore/en/

[6] https://www.pasums.issp.u-tokyo.ac.jp/chiq/en/

[7] https://tomoki-yamashita.github.io/CrySPY_doc/

[8] https://www.pasums.issp.u-tokyo.ac.jp/odat-se/en/

Table 1: List of CCMS hands-on sessions where the ISSP supercomputer was used in the 2025 fiscal year.

Date	Lecturer	Software	# of applicants
May. 13	J. Otsuki *et al.*	DCore, ChiQ	20
Oct. 15	T. Yamashita *et al.*	CrySPY	40
May. 27	T. Hoshi *et al.*	ODAT-SE	16

Supercomputer course of Computational Materials Design (CMD®) workshop

Masaaki GESHI[1], Yoshitada MORIKAWA[2], Tomoya ONO[3]

[1]*R^3 Institute for Newly-Emerging Science Design,*
The University of Osaka, Machikaneyama, Toyonaka, Osaka 560-0043

[2] *Department of Precision Engineering, Graduate School of Engineering,*
The University of Osaka, Yamada-oka, Suita, Osaka 565-0871

[3]*Graduate School of Engineering,*
Kobe University, Rokkodai-cho, Nada, Kobe 657-8501

The 47th Computational Materials Design (CMD®) workshop (CMD47) was held from September 1st to September 5th, and the 48th CMD® workshop (CMD48) took place from February 23rd to February 27th. Both were held online. In this workshop, we offer the supercomputer course to train human resources for advancing research using the System B supercomputer at the Institute for Solid State Physics (ISSP), the University of Tokyo.

In CMD47, four participants took the supercomputer course and followed a tutorial on STATE-Senri developed by Y. Morikawa. After an introductory lecture on large-scale computing and an explanation of how to use the supercomputer of ISSP by M. Geshi, the participants started constructing computational models for their own research subjects with the help of the lecturers. Then they carried out calculations using supercomputers. Specific themes including molecular adsorption and reactions on solid surfaces, atom doping in bulk Si, and formation of amorphous SiO2 were investigated. The participants performed calculations and examined their results.

In CMD48, two participants took the supercomputer course and used the supercomputer of ISSP. They got a tutorial on RSPACE developed by T. Ono. After giving the introductory lecture of large-scale computing by M. Geshi and introducing the calculation method of electronic structures and electron-transport property using RSPACE by T. Ono, Y. Egami, and M. Uemoto, the exercises instructed in the textbook were carried out. Then, electronic structure calculations were carried out for various molecules, and the optimized atomic structures and electronic density distributions were visualized. The attendees also performed massively parallel calculations to confirm the efficiency for parallel computing. Finally, the electronic structures of SiC bulk and/or electronic transport property of molecular junctions were investigated using large scale models.

4 PUBLICATION LIST

Example:

LASTNAME, Firstname [project class; # points (B), # points (C)] (Page #)

— *Project title*

1. First paper
   Names of Authors, etc.
2. Second paper
   ...

□ ISSP Joint Research Projects

○ B–E classes

AKASHI, Ryosuke [B class; 400 (B), 70 (C)] (195)

— *Reexamination of the electron renormalization in conventional superconducting theory*

1. Uniform electron benchmark for the first-principles GW0-Eliashberg theory
   R. Akashi, and H. Shinaoka Phys. Rev. B **113**, 014507 (2026).
   DOI:10.1103/fkvr-t2n8

2. Electronic Structure Theory of H3S: Plane-Wave-Like Valence States, Density-of-States Peak and Its Guaranteed Proximity to the Fermi Level
   R. Akashi Annalen der Physik **538**, e00003 (2026).
   DOI:10.1002/andp.202600003

AKIBA, Takaki [BC class; 2850 (B), 400 (C)] (315)

— *Development of reactive system for interactions of gas phase kinetics and solid surface*

— *Transformation technology of non-linear dynamics to Hamiltonian system*

1. GPU Benchmark through QPE Emulator with cuQuantum for Practical Quantum Applications
   Takaki Akiba and Youhi Morii arXiv:2507.17175 (2025).
   DOI:10.48550/arXiv.2507.17175

ANDO, Yasunobu [B class; 400 (B), 70 (C)] ()

— *First-principles calculation for building boron-compounds library*

AOYAMA, Kazushi [B class; 250 (B), 70 (C)] ()

— *Ordering of localized spins in a charge-density-wave (CDW) state*

ARAI, Munehito [C class; 7800 (B), 450 (C)] (270)

— *Accurate prediction of protein dynamics by statistical mechanical models*

— *Development of novel protein design methods for medical and industrial applications*

ARAKI, Takeaki [BC class; 2650 (B), 330 (C)] (320, 321)

— *Stress propagation in colloidal gels*

— *The physical picture of Johari-Goldstein relaxation in metallic glasses*

1. Mechanical properties and cooperative motion of aerogels under isotropic expansion

K. Hirata and T. Araki Soft Matter (submitted)

2. Topological-Defect-Mediated Glass-Like Viscoelasticity in a Quasi-Two-Dimensional Crystal
Ryoga Moroboshi, Masashi Kobayashi, Tetsuya Abe, Nobumoto Nagasawa, Yoshitaka Yoda, Yusuke Wakabayashi, Takeaki Araki, Makina Saito Communications Physics (submitted)

3. Hydrodynamics substantially affects induced structure formation in magnetic fluids
Henning Reinken, Markus Heiber, Takeaki Araki and Andreas M. Menzel Physical Review Letters (submitted)

ASANO, Yuta [E class; 14500 (B), 1500 (C)] (260)
— *Molecular dynamics simulation of bubble-ring cavitation*
— *Molecular dynamics simulations of cavitation erosion in hydrodynamic lubrication*
1. 100-Billion-Atom Molecular Dynamics Simulation of Acoustic Cavitation in a Simple Liquid
Y. Asano J. Phys. Soc. Jpn., in press.

BAE, Soungmin [C class; 5000 (B), 400 (C)] (72)
— *First-Principles Design of Chemical Doping of Two-Dimensional Transition Metal Dichalcogenides*

BIN, Xu [C class; 6000 (B), 650 (C)] (273)
— *Machine-Learning-Assisted Thermal Transport Analysis in Twisted van der Waals Interfaces*
— *Numerical evaluation of the effect of twist angle on phonon hydrodynamics in twisted 2D materials*

COSTA-AMARAL, Rafael [C class; 2200 (B), 250 (C)] (122)
— *Investigating the role of oxidation in amorphous TeO2 properties from first principles*
1. Oxygen-deficiency-driven phase segregation enables enhanced hole transport in amorphous tellurium oxides
R. Costa-Amaral and Y. Kumagai submitted to Chemistry of Materials; arXiv:2510.00473.

EGAMI, Yoshiyuki [C class; 6800 (B), 0 (C)] (64)
— *First-principles study of molecular adsorption properties on low-dimensional material surfaces and their electronic properties*
— *First-principles study on the control of valley transport properties in two-dimensional honeycomb structured materials*
1. Wide regime of Efros-Shklovskii variable-range-hopping in $La_{1-x}Ce_xNiO_2$
M. Kouda, K. Osame, S. Koura, H. Nobukane, S. Shimoda, K. Takahama, Y. Egami, and M. Sakoda Journal of Physics: Condensed Matter, resubmitted.

FUCHIZAKI, Kazuhiro [C class; 1600 (B), 0 (C)] (336)
— *Kinetics of phase transition and polyamorphism*

FUJI, Yohei [B class; 450 (B), 0 (C)] (357)
— *Symmetry and universality in measurement-induced phase transitions*

FUJII, Susumu [C class; 3000 (B), 400 (C)] (311)
— *Effect of PbTe grain boundary structures on thermoelectric properties*
1. Proton Conduction Mechanisms in Spinel Compounds: A First-Principles Study of Structural and Elemental Effects
S. Yoshida, S. Fujii, M. Yoshiya J. Phys. Chem. C, 129, 17, 8030-8037 (2025).
DOI:10.1021/acs.jpcc.5c01341

2. Lattice Dynamics and Ionic Transport in Antiperovskites M3XCh (M = Li, Na; X = H, F; Ch = S, Se, Te): A First-Principles Study Incorporating Anharmonicity and Vacancy Effects
Y. Kim, S. Fujii, W. Sekimoto, C. Kim, T. Tran, M. Yoshiya, H. Kageyama J. Phys. Chem. C, 129, 20, 9282-9290 (2025).
DOI:10.1021/acs.jpcc.5c01371

3. Origin of reduced thermal conduction by native point defects in PbTe: Perturbed molecular dynamics with neural network potential
T. Yokoi, S. Fujii, Y. Ogura, K. Matsunaga Phys. Rev. B, 112, 2, 024111 (2025).
DOI:10.1103/1175-sd2m

4. Nanoscale thermal transport at PbTe grain boundaries: a neural-network-potential molecular dynamics study
S. Fujii, T. Yokoi, K. Matsunaga J. Mater. Chem. A, published online (2026).
DOI:10.1039/D5TA09725H

FUJIMOTO, Yoshitaka [C class; 1000 (B), 0 (C)] (166)
— *Study on electronic devices using doped carbon nanotubes*
— *Theoretical study on electronic devices using nitrogen-doped carbon nanotubes*

1. Theoretical study on detection of harmful molecules for designing carbon-nanotube-based sensors
Y. Fujimoto Chemical Physics **601**, 112933 (2026).

2. Enhanced Hydrogen Release from Hydrogen Boride Nanosheets via Carbon Doping
R. Kawamura, R. Kawamura, A. Varadwaj, K. Kisu, R. Tanaka, A. Yamamoto, R. Ishibiki, S. Ito, T. Fujita, T. Tokunaga, O. Oki, Y. Fujimoto et al. Small Structures, e202500578 (2025).

FUJINO, Tomoko [C class; 2800 (B), 350 (C)] (316)
— *Investigation of Unique Charge Density Gradient Variations in Electron Correlation-Controlled Oligomer Conductors*

1. Distinct Hole and Electron Transport Anisotropy in Ambipolar Nickel Dithiolene-based Semiconductor
M. Ito, T. Fujino, T. Higashino, M. Hishida, H. Mori Angew. Chem. Int. Ed. **64**, e202512609 (2025).
DOI:10.1002/anie.202512609

FUJISAKI, Takaya [C class; 4400 (B), 450 (C)] (214)
— *Design of hetero-doped CeO2 catalysts for high efficiency fuel cells with direct biogas supply*

FUJISHIRO, Hiroki [C class; 3800 (B), 0 (C)] ()
— *Strained Band-Structure Engineering for Antimonide-Based Terahertz Transistors and Diodes*

FUJITA, Takatoshi [C class; 1400 (B), 0 (C)] (148)
— *Exciton Properties of Functional Supramolecules Using First-Principles Calculations*

1. Exciton dissociation pathways in donor/acceptor blends studied by the wave packet dynamics approach
T. Fujita, M. Nozaki Phys. Chem. Chem. Phys. **38**, 20765 (2025).
DOI:10.1002/adom.202503396

2. Dipole-Driven Polymorphism in Azobenzene: A Supramolecular Strategy for Photoresponsive Microresonators
M. Yamauchi, E. Machida, M. Nozaki, T. Fujita, H. Sotome, K. Yamamoto, Y. Mizuhata, N. Aratani, H. Yamada, S. Masuo Adv. Opt. Mater. **14**, e03396 (2026).

DOI:10.1039/D5CP01637A

FUKUDA, Jun-Ichi [B class; 750 (B), 150 (C)] ()
— *Calculation of ordered structures, dynamics and optical properties of soft materials*

FUKUDA, Masahiro [B class; 400 (B), 70 (C)] (194)
— *Analysis of electronic chirality density in material surfaces*

1. Regional chemical potential analysis for material surfaces
M. Fukuda, M. Senami, Y. Sugimoto, and T. Ozaki J. Chem. Phys. **164**, 084123 (2026).
DOI:10.1063/5.0288934

Data Repository
Regional Chemical Potential Analysis for Material Surfaces
https://isspns-gitlab.issp.u-tokyo.ac.jp/masahiro.fukuda/RCP_Analysis_for_Material_Surfaces
DOI:10.1063/5.0288934

FUKUDA, Tuneo [B class; 400 (B), 0 (C)] (200)
— *First-principles study of thin Ag films formed on Ni(110) surfaces*

1. Initial stage of silver overlayer formation on the Ni(110) surface
A. Mizuhara, T. Fukuda, and K. Umezawa Surf. Sci. 761, 122807 (2025).
DOI:10.1016/j.susc.2025.122807

2. First-principles study of Ag stripe formation on the Ni(110) surface
Aoi Mizuhara, DaeGwi Kim, and Tsuneo Fukuda e-J. Surf. Sci. Nanotechnol. 24, 13 (2026).
DOI:10.1380/ejssnt.2026-003

FUKUI, Ken-Ichi [C class; 1800 (B), 100 (C)] (341)
— *Analyses on the dynamics of metal ion solutes in ionic liquid based electrolyte at the interfaces*

FUKUMOTO, Yoshiyuki [B class; 400 (B), 20 (C)] (360, 361)
— *Numerical study of magnon crystal states in a spin-1/2 distorted kagome antiferromagnet*
— *Numerical study of the dynamical structure factor on the triangular-lattice Heisenberg antiferromagnet*

1. Numerical Calculation of the Quantum Phase Transition due to the DzyaloshinskiiMoriya Interaction in the Kagome Lattice Antiferromagnet Using the Linked-Cluster Expansion Method
Tomoki Kobayashi, and Yoshiyuki Fukumoto: J. Phys. Soc. Jpn. 95, 025003 (2026).

GOHDA, Yoshihiro [C class; 3800 (B), 350 (C)] (92)
— *First-principles electron theory of strain-induced magnetic switching*

1. Orbital magnetic moment controlled converse magnetoelectric eect in bcc-Co3Mn/Fe/V/PMN-PT multiferroic heterostructures
T. Usami, Y. Murakami, R. Watarai , Y. Shiratsuchi, Y. Gohda, and K. Hamaya Adv. Sci. **2026**, e22581 (2026).
DOI:10.1002/advs.202522581

2. Electric Field Modulation of Interlayer Coupling via Piezostrain in a Synthetic Antiferromagnet
Y. Hisada, S. Komori, K. Imura, C. Shen, Y. Gohda, C.C.I. Ang, W.S. Lew, and T. Taniyama Adv. Sci. **13**, e17798 (2026).
DOI:10.1002/advs.202517798

3. Strain-induced magnetocrystalline anisotropy in L21 Co2FeSi: first-principles study
R. Watarai and Y. Gohda npj Spintronics **3**, 50 (2025).
DOI:10.1038/s44306-025-00116-w

4. Tunable Magnetic Coupling of Monolayer CrI2 by Strain Engineering
H. Y. Widyandaru and Y. Gohda npj Spintronics **3**, 34 (2025).
DOI:10.1038/s44306-025-00100-4

5. Efficient first-principles approach to Gibbs free energy with thermal expansion
K. Hashimoto, T. Tanaka, and Y. Gohda Phys. Rev. B **111**, 224309 (2025).
DOI:10.1103/6qsr-xzgb

6. First-Principles Exploration of NdFe Magnetic Compounds Assisted by Transfer Learning and Genetic Algorithm
S. Ito, I. Seo, S. Tanaka, M. Endo, Y. Tsutsui, T. Tanaka, and Y. Gohda J. Phys. Soc. Jpn., in press.

7. Physically Interpretable Force Constants Based on Spherical Tensor Expansion: Ecient Parameter Reduction for Low-Symmetry Systems
D. Ito, K. Hashimoto, T. Tanaka, and Y. Gohda J. Phys. Soc. Jpn., in press.

GOHLKE, Matthias [C class; 2600 (B), 350 (C)] (322)
— *Tensor network study of an effective spin model for square-lattice antiferromagnets*

GONOME, Hiroki [C class; 1600 (B), 250 (C)] (138)
— *Study of the principle of photothermal conversion by ab initio calculations*

HAGITA, Katsumi [C class; 1600 (B), 300 (C)] (332)
— *Physical properties of crosslinked polymer networks through network topology analysis*

1. Butterfly Patterns for Stretched Inhomogeneous Gel Networks Using Large-Scale Molecular Dynamics Simulations
K. Hagita and T. Murashima Macromolecules **58**, 53685376 (2025).
DOI:10.1021/acs.macromol.5c00207

2. Nano-structuring for strengthening semi-crystalline polymers
K. Hagita and T. Murashima NPG Asia Materials **17**, 44 (2025).
DOI:10.1038/s41427-025-00625-4

HAGIWARA, Satoshi [C class; 2000 (B), 0 (C)] (135)
— *Adsorption reactions at the solid electrode/aqueous solution interfaces*

1. Anion Adsorption-induced Charge Separation at the Alumina/Aluminum Interface
S. Hagiwara, T. Murata, and M. Otani Corrosion Sci. **256**, 113150 (2025).
DOI:10.1016/j.corsci.2025.113150

2. An Efficient Implementation of the ESM-RISM Method for Simulating Electrode/Electrolyte Interfaces
S. Hagiwara, and M. Otani J. Chem. Theory Comput. **22**, 3633 (2026).
DOI:10.1021/acs.jctc.5c01920

HALIM, Harry Handoko [C class; 2000 (B), 250 (C)] (127)
— *Machine Learning Accelerated Path Sampling for Exploration of Rate and Mechanisms of Rare Events on Heterogenous Catalysis*

1. Bridging the Pressure Gap in Hydrogenation of CO_2 to Formate on Cu(100) by Machine Learning Molecular Dynamics and First-Principles Microkinetic Modeling
W. O. N. F. Rajaelo, H. H. Halim, M. F. Anshor, Y. Yamada, S. Ramadhani, F. A. Mubarok, S.

E. M. Putra, A. L. Ivansyah, T. D. K. Wungu, Suprijadi, Y. Morikawa, and F. Muttaqien ACS Catalysis **16**, 5068–5079 (2026).
DOI:10.1021/acscatal.5c09279

2. CO Coadsorption Effects on Water–Gas Shift Reaction over Cu Clusters on Cu(111): Insights from Machine Learning Force Field and Microkinetic Modeling
M. F. Anshor, H. H. Halim, and Y. Morikawa Phys. Chem. Chem. Phys. (2026), in press.
DOI:10.1039/D5CP05031F

HAMADA, Ikutaro [C class; 9600 (B), 850 (C)] (48)

— *Density functional theory study of adsorption and reaction of molecules on solid surfaces*

1. Interlayer Hydrogen–Hydrogen Spacing Regulates the Formation of Molecular Hydrogen from Hydrogen Boride Nanosheets
Y. Yasuda, O. Ok, K. Goto, N. Noguchi, S. Ito, M. Hikichi, R. Tsuji, Y. Nakahira, R. Utsumi, H. Saitoh, S. Nakano, S. Naka, I. Hamada, S. Orimo, and T. Kondo ACS Nano **20**, 9951 (2026).
DOI:10.1021/acsnano.5c20691

2. Interlayer Hydrogen–Hydrogen Spacing Regulates the Formation of Molecular Hydrogen from Hydrogen Boride Nanosheets
Y. Yasuda, O. Ok, K. Goto, N. Noguchi, S. Ito, M. Hikichi, R. Tsuji, Y. Nakahira, R. Utsumi, H. Saitoh, S. Nakano, S. Naka, I. Hamada, S. Orimo, and T. Kondo ACS Nano **20**, 9951 (2026).
DOI:10.1021/acsnano.5c20691

3. Predicting Reactive Graphene Edge-Adsorbed Pt Single-Atom Catalyst Structures for Oxygen Reduction via Machine Learning-Enhanced Calculations
B. A. C. Tan, N. A. Sofi, T. N. Pham, K. I. M. Rojas, S. E. P. Masan, Y. Hamamoto, I. Hamada, and Y. Morikawa Philos. Trans. R. Soc. A **384**, 20240555 (2026).
DOI:10.1098/rsta.2024.0555

4. Assessing the Accuracy of Exchange–Correlation Functionals in Density Functional Theory for Hydrogen–Benzene and Hydrogen–Hydrogen Interactions
Y. Kataoka and I. Hamada Phys. Rev. B **113**, 085143 (2026).
DOI:10.1103/PhysRevB.113.085143

5. Electronic States of Ag and Au Atoms on Graphene/Rh(111)
H. Okuyama, H. Ogawa, K. Kusumoto, S. Hatta, K. Hirashima, and I. Hamada J. Phys. Chem. C **129**, 19396 (2025).
DOI:10.1021/acs.jpcc.5c05109

6. Density Functional Theory Study on the Structure and Hydrogen Storage Performance of Hydrogen Boride Sheet
S. Naka, K. I. M. Rojas, and I. Hamada e-J. Surf. Sci. Nanotechnol. **23**, 339 (2025).
DOI:10.1380/ejssnt.2025-048

7. Submolecular-Resolution Probing of Vibrational Anharmonicity Using Tip-Enhanced Raman Spectroscopy
Y. Park, I. Hamada, M. Wolf, and A. Shiotari Angew. Chem. Int. Ed. e202514215 (2025).
DOI:10.1002/anie.202514215

8. Vibrational Recognition of Local Structures in Hydrogen Boride Sheets
K. I. M. Rojas, L. T. Ta, S. Naka, Y. Morikawa, and I. Hamada J. Chem. Phys. **163**, 124702 (2025).
DOI:10.1063/5.0280856

HAMAGUCHI, Satoshi [C class; 6600 (B), 700 (C)] (272)
— *Development of machine-learning force fields to analyze atomic layer processing II*
— *Development of machine-learning force fields to analyze atomic layer processing*

HAMAMOTO, Yuji [CD class; 2600 (B), 0 (C)] (120, 121)
— *First principles study of germanene superstructures on Ag(111)*
— *Structure search for planar silicene on Au(111) thin films based on Gaussian regression*
— *Band structure calculation of germanene superstructures on Ag(111)*

HAN, Jihae [AB class; 500 (B), 130 (C)] (187)
— *First-principles investigation of reaction mechanisms at the electrode/electrolyte interface in Li-S batteries*
— *Reductive decomposition mechanism of electrolyte at electrode/electrolyte interface by first-principles calculations*

HARADA, Kenji [C class; 1800 (B), 300 (C)] (329)
— *Development of tensor network algorithms*
1. Plastic tensor networks for interpretable generative modeling
   Katsuya O Akamatsu, Kenji Harada, Tsuyoshi Okubo, Naoki Kawashima Machine Learning: Science and Technology **7**, (2026) 015014.
   DOI:10.1088/2632-2153/ae3048

HARASHIMA, Yosuke [C class; 1800 (B), 0 (C)] (141)
— *Prediction of materials properties and exploration of materials with materials informatics.*
1. Data-Driven Approach Considering Imbalance in Data Sets and Experimental Conditions for Exploration of Photocatalysts
   W. Takahara, R. Baba, Y. Harashima, T. Takayama, S. Takasuka, Y. Yamaguchi, A. Kudo, M. Fujii ACS Omega, **10**, 14626-14639 (2025).
   DOI:10.1021/acsomega.4c06997

2. Covariance Linkage Assimilation method for Unobserved Data Exploration
   Y. Harashima, T. Miyake, R. Baba, T. Takayama, S. Takasuka, Y. Shigeta, Y. Yamaguchi, A. Kudo, and M. Fujii Phys. Rev. Materials **9**, 093803 (2025).
   DOI:10.1103/8tjv-wtx5

3. Materials Dual-Source Knowledge Retrieval-Augmented Generation for Local Large Language Models in Photocatalysts
   W. Takahara, Y. Yamaguchi, M. Ogano, F. Kakami, Y. Harashima, T. Takayama, S. Takasuka, A. Kudo, and M. Fujii J. Chem. Inf. Model. **65**, 13098 (2025).
   DOI:10.1021/acs.jcim.5c01941

HARIKI, Atsushi [B class; 1100 (B), 0 (C)] (243, 244)
— *Computational Study of Magnetic Circular Dichroism in Resonant Inelastic X-ray Scattering Spectra of Strongly Correlated Materials*
— *Computational study on two-particle responses in correlated altermagnets using DFT+DMFT method*
1. Circular Dichroism in Resonant Inelastic X-Ray Scattering: Probing Altermagnetic Domains in MnTe
   D Takegami, Takuya Aoyama, T Okauchi, T Yamaguchi, S Tippireddy, S Agrestini, M Garca-Fernndez, T Mizokawa, K Ohgushi, Ke-Jin Zhou, J Chaloupka, J Kune, A Hariki, Hakuto Suzuki Phys. Rev. Lett. **135**, 196502 (2025).
   DOI:10.1103/512v-n5f9

2. Fingerprints of Mott and Slater gaps in the core-level photoemission spectra of antiferromagnetic iridates
K Nakagawa, A Hariki, T Okauchi, H Fujiwara, K-H Ahn, Y Murakami, S Hamamoto, Y Kanai-Nakata, T Kadono, A Higashiya, K Tamasaku, M Yabashi, T Ishikawa, A Sekiyama, S Imada, J Kune, K Takase, A Yamasaki Phys. Rev. B **111**, 195114 (2025).
DOI:10.1103/PhysRevB.111.195114

3. Theory of circular dichroism in resonant inelastic x-ray scattering
M. Furo, A. Hariki, J. Kunes Phys. Rev. B **112**, 214429 (2025).
DOI:10.1103/x96x-znr8

4. UTe2: A narrow-band superconductor
Martin Sundermann, Takaki Okauchi, Naoki Ito, Denise S Christovam, Andrea Marino, Daisuke Takegami, Andrei Gloskovskii, Priscila FS Rosa, Jan Kune, Shin-ichi Fujimori, Liu Hao Tjeng, Andrea Severing, Atsushi Hariki Phys. Rev. Research **7**, 043195 (2025).
DOI:10.1103/t6hm-q647

HARUYAMA, Jun [C class; 3600 (B), 400 (C)] (93)
— *Electrochemical reaction analysis using density functional calculation + implicit solvation model 7*

1. Benchmarking of Oxygen Adsorption Using TPD Spectroscopy for Accurate DFT Prediction of ORR on Anatase Titanium Dioxide(101)
S. Muhammady, J. Haruyama, S. Kasamatsu, and O. Sugino J. Phys. Chem. C **129**, 20079 (2025).
DOI:10.1021/acs.jpcc.5c04600

2. Elucidation of superionic conduction in K2NiF4-type BaLi oxyhydrides from a first-principles molecular dynamics study
J. Haruyama, F. Takeiri, G. Kobayashi, and O. Sugino J. Mater. Chem. A **14**, 8332 (2026).
DOI:10.1039/d5ta08063k

Data Repository
BLHO_DFT-MD
https://isspns-gitlab.issp.u-tokyo.ac.jp/j-haruyama/BLHO_DFT-MD
DOI:10.1039/d5ta08063k

HAYAMI, Satoru [C class; 3600 (B), 350 (C)] (301)
— *Generation of spin model with higher-order spin interactions based on machine learning*

1. Square skyrmion lattice in multi-orbital f -electron systems
Y. Zha and S. Hayami Physical Review B **111**, 165155 (2025).
DOI:10.1103/PhysRevB.111.165155

2. Bimeron Crystals by a Linearly Polarized AC Electric Field in Frustrated Magnets
T. Shirato, R. Yambe, and S. Hayami J. Phys. Soc. Jpn. **94**, 063601 (2025).
DOI:10.7566/JPSJ.94.063601

3. Finite-q antiferrotoroidal and ferritoroidal order in a distorted kagome structure
A. Kirikoshi and S. Hayami Physical Review B **111**, L201112 (2025).
DOI:10.1103/PhysRevB.111.L201112

4. Symmetry Rules on Multipole Interactions under Crystallographic Point Groups and Application to Multiple-Q Multipole States
R. Yambe and S. Hayami J. Phys. Soc. Jpn. **94**, 074704 (2025).
DOI:10.7566/JPSJ.94.074704

5. Multiple-Q spin textures induced by spiralstaggered interference in one-dimensional itinerant magnets
S. Hayami and K. Okigami J. Phys. Soc. Jpn. **95**, 034706 (2026).
DOI:10.7566/JPSJ.95.034706

6. Four-spin interactions as a route to multiple-Q topological magnetic order
K. Okigami and S. Hayami Phys. Rev. B **113**, 064442 (2025).
DOI:10.1103/3njw-f1jt

7. Finite-Temperature Stability of Skyrmion Crystals in Frustrated Magnets: Role of Sixfold Anisotropy and Uniform Spin Mode in Momentum Space
K. Okigami and S. Hayami J. Phys. Soc. Jpn. **95**, 044702 (2026).
DOI:10.7566/JPSJ.95.044702

HIDA, Kazuo [B class; 300 (B), 60 (C)] (369)
— *Numerical Study of One Dimensional Frustrated Quantum Spin Systems*

1. Ground-State Phase Diagram of (1/2,1/2,1) Mixed Diamond Chains with Single-Site Anisotropy
Kazuo Hida to be published in J. Phys. Soc. Jpn.; arXiv:2601.20328
DOI:10.48550/arXiv.2601.20328

HIGUCHI, Yuji [C class; 9200 (B), 850 (C)] (32)
— *Deformation Process of Crystalline Polymer and Filler*
— *Interfacial Delamination between Crystalline Polymer and Filler*

1. Influences of secondary and tertiary amines in epoxy resins on water dynamics by all-atomic molecular dynamics simulations
Yuji Higuchi, Yasuyuki Nakamura, Masanobu Naito, and Yoshihisa Fujii Chem. Phys. **597**, 112766 (2025).
DOI:10.1016/j.chemphys.2025.1

2. Interfacial delamination between semicrystalline polymers and filler materials by coarse-grained molecular dynamics simulations
Yuji Higuchi, Yuta Hikima, Naoto Kamiuchi, Erica Uehara, Yutaka Oya, Go Yamamoto, and Keita Sakakibara Polymer **333**, 128539 (2025).
DOI:10.1016/j.polymer.2025.128

3. Effect of zwitterionic monomer polymerization on water dynamics: a molecular dynamics simulation study supported by differential scanning calorimetry and terahertz spectroscopy
Md Abu Saleh, Yuji Higuchi, Shohei Shiomoto, Takahisa Anada, Mafumi Hishida, and Masaru Tanaka Polym. J. **57**, 1127 (2025).
DOI:10.1038/s41428-025-01066-0

4. Ion distribution in the vicinity of phase-separated membrane
Yuji Higuchi, Hiroaki Ito, Naofumi Shimokawa, Jurij Reščič, Stefano Maset, Klemen Bohinc J. Mol. Liq. **444**, 129168 (2025).
DOI:10.1016/j.molliq.2025.1291

HIRAMATSU, Ryoya [C class; 4600 (B), 0 (C)] (79)
— *Ab Initio Study of Finite-Temperature Magnetic Properties in Transition Metal Systems*

1. First-Principles Calculations of Magnetization Curves and Spin Susceptibility in the High-Anisotropy Alloy $L1_0$-FePt
R. Hiramatsu, A. Sakuma, T. Miyake, and T. Fukushima submitted to Phys. Rev. B.

HIYAMA, Miyabi [B class; 350 (B), 0 (C)] (372)
— *Theoretical study for excited states of firefly bioluminescence emitters*

1. Absorption and fluorescence properties and assignments of firefly bioluminescence substrate analog: seMpai
   M. Harada, T. Nakano, R. Ono, T. Uchiyama, Y. Noguchi, R. Saito-Moriya, N. Kitada, S. A. Maki, T. Hirano, H.i Aoyama, M. Kobayashi, H. Akiyama, K. Kanno, H. Itabashi, and M. Hiyama Photochem. Photobiol. **102**, 237-247 (2026).
   DOI:10.1111/php.14121

HO, Ngoc Nam [C class; 1200 (B), 250 (C)] ()
— *Computational design of high-entropy alloy catalysts for direct methanol fuel cells*

HOSHI, Takeo [C class; 3200 (B), 300 (C)] (102)
— *HPC-based fusion of simulation, experiment analysis and datadriven science*

1. Monte Carlo simulation method for incoherent Thomson scattering spectra from arbitrary electron distribution functions
   Kentaro Sakai, Kentaro Tomita, Takeo Hoshi, Ryo Yasuhara Journal of Instrumentation 21, C01002 (2025).
   DOI:10.1088/1748-0221/21/01/c01002

Data Repository
2DMAT Gallery
https://isspns-gitlab.issp.u-tokyo.ac.jp/2dmat-dev/2dmat-gallery

ODAT-SE Gallery
https://isspns-gitlab.issp.utokyo.ac.jp/takeohoshi/odat-se-gallery

HOSHINO, Shintaro [B class; 450 (B), 80 (C)] (179)
— *First principles calculation for electron chirality*

HOTTA, Chisa [C class; 1400 (B), 0 (C)] (338)
— *Disorder and glassy dynamics of strongly correlated multi-orbital electric systems*
— *Effect of quenched disorder in the triangular lattice Heisenberg magnet*

1. Specific heat and susceptibility of S=1/2 antiferromagnets on square, triangular, and kagome lattices
   C. Hotta Zeitschrift für Naturforschung A ,in press (arXiv:2605.17420).
   DOI:10.1515/ZNA-2025-0392

HOTTA, Takashi [C class; 1800 (B), 0 (C)] (333)
— *Research of superconductivity induced by multipole fluctuations in the bi-layer orbital degenerate Hubbard model*

1. Effect of Γ_7 and Γ_8 Hybridizations on Three-Channel Kondo Phase Emerging from Ho Ions
   T. Hotta J. Phys. Soc. Jpn. **94**, 114702 (2025).
   DOI:10.7566/JPSJ.94.114702

HUKUSHIMA, Koji [C class; 4000 (B), 0 (C)] (300)
— *Development of Tensor-Network-based Monte Carlo Methods*

1. High-dimensional asymptotics of VAEs: threshold of posterior collapse and dataset-size dependence of rate-distortion curve

Yuma Ichikawa, and Koji Hukushima J. Stat. Mech. 073402 (2025).
DOI:10.1088/1742-5468/adde3e

2. Ratio divergence learning using target energy in restricted Boltzmann machines: Beyond Kullback-Leibler divergence learning
Yuichi Ishida, Yuma Ichikawa, Aki Dote, Toshiyuki Miyazawa, and Koji Hukushima Phys. Rev. E 112, 045306 (2025).
DOI:10.1103/fxnm-y5pd

IDO, Kota [E class; 6000 (B), 600 (C)] (23)
— *Stability of many-body topological states in strongly correlated quantum systems*

IIMURA, Soshi [D class; 7000 (B), 500 (C)] (63)
— *Hydrogen Ion Doping on Solid Acid and Base Sites and the Exploration of New Functions*

IITAKA, Toshiaki [C class; 1800 (B), 250 (C)] (330)
— *Calculation of quantum spin systems at finite temperature using random quantum states of Plaquette variational wave functions*

IKEDA, Hiroaki [B class; 450 (B), 90 (C)] ()
— *Electron chirality and spin current in chiral materials*

IMADA, Masatoshi [DE class; 35000 (B), 2550 (C)] (217)
— *Development and application of Fermi machine*
— *Development and application of quantum many-body solver*
— *Development of Fermi Machine for Quantum Many-Body Solver*

1. Unified description of cuprate superconductors by fractionalized electrons emerging from integrated analyses of photoemission spectra and quasiparticle interference
Sakai, Shiro and Yamaji, Youhei and Imoto, Fumihiro and Tamegai, Tsuyoshi and Kaminski, Adam and Kondo, Takeshi and Kohsaka, Yuhki and Hanaguri, Tetsuo and Imada, Masatoshi Phys. Rev. X **16** (2026) 011018
DOI:10.1103/mww7-32gn

2. Quantum Many-Body Solver Using Artificial Neural Networks and its Applications to Strongly Correlated Electron Systems
Yusuke Nomura, asatoshi Imada J. Phys. Soc. Jpn., **94** (2025) 031001
DOI:10.7566/JPSJ.94.031001

INAGAKI, Kouji [B class; 300 (B), 60 (C)] (209)
— *Analyses of semiconductor surface processes by machine-learning based potentials*

INAOKA, Takeshi [B class; 400 (B), 70 (C)] (192)
— *Search and realization of novel electronic properties of surfaces and interfaces and of nanostructures*

INAYOSHI, Ken [B class; 350 (B), 0 (C)] (255)
— *Development of computational methods for quantum field theories of nonequilibrium systems utilizing information compression techniques and its applications*

1. A causality-based divide-and-conquer algorithm for nonequilibrium Green's function calculations with quantics tensor trains
Ken Inayoshi, Maksymilian Sroda, Anna Kauch, Philipp Werner, and Hiroshi Shinaoka SciPost Phys.
DOI:10.21468/SciPostPhys.20.3.077

INOUE, Kazutoshi [C class; 4000 (B), 200 (C)] (90)
— *Exploring stable atomic structures and segregation behavior at ceramics interfaces*
— *Investigation of stable atomic structure in twist grain boundaries and their segregation behavior by theoretical calculations*

1. Structural transition and the effect of Ca impurities in MgO Σ5(210) grain boundary
   Q. Chen, M. Saito, K. Kawahara, A. Nakamura, K. Inoue, Y. Ikuhara J. Euro. Ceram. Soc. **46**, 118068 (2026)
   DOI:10.1016/j.jeurceramsoc.2025.118068

ISHIBASHI, Shoji [C class; 2200 (B), 0 (C)] (131)
— *Prediction of properties of organic ferroelectrics and piezoelectrics by first-principles calculations*

1. Field-Effect Crystal Engineering in Proton-π-Electron Correlated Systems
   S. Horiuchi, H. Minemawari, J. Tsutsumi, and S. Ishibashi Crystals **15**, 736 (2025).
   DOI:10.3390/cryst15080736

ISHIDA, Kunio [B class; 300 (B), 60 (C)] (367)
— *Coherent dynamics of strongly coupled electron-phonon-photon systems*

1. Phonon-mediated Chirality Control in Molecular Triangles by Photoirradiation
   Noriyuki Aoyagi, Hiroaki Matsueda, and Kunio Ishida Journal of the Physical Society of Japan 95, 014702 (2026).
   DOI:10.7566/JPSJ.95.014702

ISHII, Fumiyuki [C class; 8400 (B), 800 (C)] (52)
— *Development and Application of First-Principles Methods for Spin Conversion Materials*
— *Development and application of first-principles computational methods for real-space analysis of transport coefficients*

1. First-principles study of interface states in diamond(111)/Al2O3 with different terminations
   Y. Zhang, N. Yamaguchi, X. Zhang, M. Saito, N. Tokuda, and F. Ishii Surfaces and Interfaces **72**, 107147 (2025).
   DOI:10.1016/j.surfin.2025.107147

2. First-principles study of electric-dipole-induced Rashba spin-splitting in Janus WSSe
   S. A. Putri, M. A. U. Absor, N. Yamaguchi, and F. Ishii Japanese Journal of Applied Physics **64**, 10SP21 (2025).
   DOI:10.35848/1347-4065/ae00cf

3. Direct determination of layer anomalous Hall conductivity using uniaxial Wannier functions
   Y. Morishima, F. Ishii, and N. Yamaguchi arXiv:2506.01160 (2025).

4. Real-Space Imaging and Topological Indices of Finite Skyrmion Systems
   J. Yang, N. Yamaguchi, and F. Ishii submitted.

5. Capacitance profile of graphene via effective screening medium method: first-principles study
   A. Sohib, N. Yamaguchi, and F. Ishii Japanese Journal of Applied Physics **64**, 11SP11 (2025).
   DOI:10.35848/1347-4065/ae0cd3

6. First-principles study of thickness-dependent vertical polarization in multilayer hexagonal boron nitride
   N. M. Chadiza, H. P. Kadarisman, N. Yamaguchi, and F. Ishii Japanese Journal of Applied Physics **64**, 11SP09 (2025).
   DOI:10.35848/1347-4065/ae0e2b

7. The effect of interlayer coupling on thermoelectricity in atomically thin CaGe2: a first-principles study
A. A. Ghiffari, R. Syariati, Y. Morishima, N. Yamaguchi, and F. Ishii Japanese Journal of Applied Physics **64**, 11SP31 (2025).
DOI:10.35848/1347-4065/ae11bf

8. Tunable visible-light shift current in strain-engineered ferroelectric perovskite CsPbI3
Y. Y. S. Teweng, N. Yamaguchi, and F. Ishii Applied Physics Express **18**, 121001 (2025).
DOI:10.35848/1882-0786/ae241f

9. Band Unfolding in Finite Nanostructures: Visualizing Dirac, Spin-Valley, and Rashba Features
N. Yamaguchi, S. Yunitasari, W. Amalia, C.-C. Lee, T. Ozaki, and F. Ishii Nano Letters **25**, 17725–17732 (2025).
DOI:10.1021/acs.nanolett.5c04721

10. First-principles calculations of the effect of X-site halogen composition ratio on the stability of vacuum deposited CsPbIxBr3-x-based perovskite films
S. Miura, N. Yamaguchi, Md. Shahiduzzaman, Md. Akhtaruzzaman, M. Nakano, M. Karakawa, J. M. Nunzi, F. Ishii, and T. Taima Japanese Journal of Applied Physics **65**, 04SP02 (2026).
DOI:10.35848/1347-4065/ae37b5

11. Ab initio prediction of large thermoelectric effect in distorted Heusler alloy Ti-Fe-Sb compound
R. Syariati, A. Vora-ud, F. Ishii, and T. Seetawan Journal of Materials Science **61**, 3909–3918 (2026).
DOI:10.1007/s10853-025-12100-0

12. Fe-doping enhances the thermoelectric properties of Bi2Te3 thin films within a balance of oxidation states and magnetism
A. T. T. Pham, A. Vora-ud, C. Chananonnawathorn, P. Muthitamongkol, S. Ruamruk, S. Limwichean, M. Horprathum, R. Syariati, S. Park, F. Ishii, T. Seetawan, G. J. Snyder, and T. B. Phan Vacuum **244**, 114879 (2026).
DOI:10.1016/j.vacuum.2025.114879

ISHII, Kohei [B class; 400 (B), 80 (C)] ()
— *First-principles calculation of electronic structure considering electron-2-phonon interactions*

ISHIKAWA, Takahiro [C class; 2000 (B), 200 (C)] (130)
— *Exploration of hydride superconductors*

1. Evolutionary search for superconducting hydrides in the La-Pt-H ternary system under compression
T. Ishikawa, Y. Tanaka, and S. Tsuneyuki Phys. Scr. **101**, 105903 (2026).
DOI:10.1088/1402-4896/ae49c3

ISOBE, Masaharu [B class; 400 (B), 70 (C)] (355)
— *Non-reciprocal neighbor interaction and non-equilibrium phase transition in self-propelled hard polygon systems*

1. Crystallization and Motility-Induced Phase Separation in the Flow of Active Brownian Particles Around an Obstacle
K. Iwase and M. Isobe EPJ Web of Conferences **334** 01004 (2025).
DOI:10.1051/epjconf/202533401004

2. Self-organized spatial inhomogeneity in self-propelled quasi-elastic hard disk systems

D. Mugita, R. Kitagawa, N. Murase, and M. Isobe EPJ Web of Conferences **334** 01005 (2025).
DOI:10.1051/epjconf/202533401005

3. Cooperative phenomena in active matter systems with alternative interaction of neighbors
T. Nakamura, N. Murase, and M. Isobe EPJ Web of Conferences **334** 02001 (2025).
DOI:10.1051/epjconf/202533402001

4. Quantitative analysis of pedestrian counter-flow under congested conditions using floor field model
Y. Nakai and M. Isobe Proceedings of the 31th Symposium on Traffic Flow and Self-driven Particles, **31**, 13 (2025).

IWAZAKI, Ryuta [B class; 400 (B), 80 (C)] (185)
— *Novel quantum phases in organic Mott insulators based on first-principles calculations*

IZUMI, Yasuo [B class; 450 (B), 90 (C)] (176)
— *Theoretical Monitoring of the Behavior of Surface Intermediate Species on Semiconductor-Based Photocatalysts to Realize Highly-Selective CO_2 Photoreduction*

1. Charge Separation and/or Hot Spots: Clarification of Efficient CO2 Reduction over Ru-Ni Nanoparticles Compared to Photocatalysis on Ru- Ni-ZrO2 Composites
Masahito Sasaki, Tomoki Oyumi, Keisuke Hara, Hongwei Zhang, and Yasuo Izumi J. Am. Chem. Soc. 148, 13, 13570 (2026).
DOI:10.1021/jacs.5c17533

JANG, Seonghoon [C class; 2600 (B), 0 (C)] ()
— *Material Design for Mg-ion Cathode Materials with High Ion Conductivity*

JESCHKE, Harald [C class; 2200 (B), 0 (C)] (328)
— *Theoretical study of static and dynamic spin structure factors in 3D antiferromagnets*

1. Field-induced spin liquid in the decorated square-kagome antiferromagnet nabokoite $KCu_7TeO_4(SO_4)_5Cl$
M. G. Gonzalez, Y. Iqbal, J. Reuther, H. O. Jeschke Comm. Mater. **6**, 96 (2025).
DOI:10.1038/s43246-025-00806-2

2. The crystal structure, and magnetic and resonant properties of decorated spin kagome system $(CsCl)Cu_5As_2O_{10}$
I. V. Kornyakov, M. V. Likholetova, I. E. Lezova, S. V. Krivovichev, H. O. Jeschke, Y. Iqbal, A. V. Tkachev, S. V. Zhurenko, A. Gippius, L. V. Shvanskaya, A. Vasiliev J. Mater. Chem. C **14**, 3749 (2026).
DOI:10.1039/D5TC03217B

3. Origin of pressure-induced anomalies in the nodal-line ferrimagnet $Mn_3Si_2Te_6$
V. Venkatasubramanian, M. Shimizu, D. Guterding, H. O. Jeschke Comm. Mater. **7**, 94 (2026).
DOI:10.1038/s43246-026-01132-x

JIA, Xue [C class; 1400 (B), 300 (C)] (143)
— *Discover High-Performance Metal Carbide/Nitride Electrocatalysts Based on Catalysis Theory and Machine Learning*

1. Closed-Loop Framework for Discovering Stable and Low-Cost Bifunctional Metal Oxide Catalysts for Efficient Electrocatalytic Water Splitting in Acid
X. Jia, Z. Zhou, F. Liu, T. Wang, Y. Wang, D. Zhang, H. Liu, Y. Wang, S. Ye, K. Amezawa, L. Wei, and H. Li Journal of the American Chemical Society **147**, 22642 (2025).
DOI:10.1021/jacs.5c04079

JIE, Sun [C class; 2400 (B), 250 (C)] ()
— *Machine Learning for Screening Layered Materials with Ultrallow Thermal Conductivity*

JOSHI, Ashish [B class; 150 (B), 80 (C)] ()
— *Investigation of quantum skyrmions via neural quantum states*

KADARISMAN, Hana [B class; 300 (B), 0 (C)] (211)
— *First-principles study of nanodiamonds*

KAGESHIMA, Hiroyuki [C class; 3000 (B), 350 (C)] (104)
— *Study on physical properties of structural elementary excitations at solid surfaces and interfaces*

1. First-principles Study of Interstitial-Related Defects in Quartz
   H. Kageshima, T. Akiyama, K. Shiraishi J. Phys. Soc. Jpn. 94 (2025) 074707 (4 pages).
   DOI:10.7566/JPSJ.94.074707

2. Atomic Scale Insights into Si Transport Pathway in Si-oxide Film Based on Theoretical Investigation of Medium Density Eects
   H. Kageshima, T. Akiyama, K. Shiraishi e-J. Surf. Sci. Nanotechnol. 23 (2025) 306 (8 pages).
   DOI:10.1380/ejssnt.2025-043

3. First-principles study of excess Si transport in Si oxide on Si substrate using two-layer-oxide model for thermally oxidized interface
   H. Kageshima, I. Seo, T. Akiyama, K. Shiraishi Jpn. J. Appl. Phys. 65 (2026) 03SP18 (10 pages).
   DOI:10.35848/1347-4065/ae3d40

4. First-principles study on network effects of medium on excess Si transport in Si oxide films
   H. Kageshima, I. Seo, T. Akiyama, K. Shiraishi Mater. Sci. Semicond. Process. 209 (2026) 110582 (8 pages).
   DOI:10.7566/JPSJ.94.074707

KAIJU, Hideo [C class; 6000 (B), 650 (C)] (65)
— *Calculation of electronic structures and estimation of interfacial spin polarization in molecular spintronic devices*
— *Electronic structure analysis of molecular spintronic devices using first-principles calculation*

1. Observation of magnetoresistance effect in $Ni_{78}Fe_{22}$/tris-(8-hydroxyquinoline) erbium (Erq_3)/FeCo organic spin valves
   Mizuki Matsuzaka, Ryunosuke Miyamoto, Chika Hashimoto, Mari Taniguchi, Kotaro Kashima, Shun Dekura, Takumi Ueda, Yusuke Nomura, Tomoyuki Akutagawa, Kazuya Ando, Hideo Kaiju
   Journal of Magnetism and Magnetic Materials
   DOI:10.1016/j.jmmm.2025.173465

KANEKO, Ryui [DE class; 12500 (B), 1100 (C)] (223)
— *Variational Monte Carlo Study of the Impact of Multilayer Effects on Antiferromagnetism and Superconductivity*
— *Variational Monte Carlo study of ground states of a multilayer superconductor under pressure*

1. Seeding neural network quantum states with tensor network states
   R. Kaneko and S. Goto Phys. Rev. B **112**, 155163 (2025).
   DOI:10.1103/3rq4-2m5k

2. Adaptive interpolating quantum transform: A quantum-native framework for efficient transform learning
   G. Budiutama, S. Daimon, H. Nishi, R. Kaneko, T. Ohtsuki, and Y.-i. Matsushita Phys. Rev. A

112, 062410 (2025).
DOI:10.1103/vyr3-h9hq

KARIYADO, Toshikaze [B class; 350 (B), 0 (C)] (254)
— *Electronic structure engineering in low dimensional systems with artificial nanostructures*

1. Single-band square-lattice Hubbard model from twisted bilayer C568
T. Kariyado, A. Vishwanath, and Z.-X. Luo Phys. Rev. B **112**, 125159 (2025).
DOI:10.1103/73rf-cw9d

2. Spin States of Trioxotriangulene Controlled by SiO Bond Formation and Dissociation on $AuSi_x$ Surfaces
Z. Yuan, T. Kariyado, T. Murata, K. Sun, D. Li, O. Custance, Y. Morita, S. Kawai Nano Letters **25** 13040-13046 (2025).
DOI:10.1021/acs.nanolett.5c03477

KASAMATSU, Shusuke [C class; 3400 (B), 300 (C)] (100)
— *Thermodynamics of disordered crystalline systems considering phonons and charge ordering*

1. Mitigating proton trapping in cubic perovskite oxides via ScO_6 octahedral networks
Kota Tsujikawa, Junji Hyodo, Susumu Fujii, Kazuki Takahashi, Yuto Tomita, Nai Shi, Yasukazu Murakami, Shusuke Kasamatsu, and Yoshihiro Yamazaki Nature Mater. **24**, 1949 (2025).
DOI:10.1038/s41563-025-02311-w

KATAOKA, Yuta [C class; 2200 (B), 250 (C)] ()
— *Development of analytical method for hydrogen state by ab initio path integral molecular dynamics and machine learning*

KATO, Daiji [C class; 800 (B), 200 (C)] (164)
— *Scaling Up First-Principles Simulations of Plasma-Facing Material Damage Behavior Using Machine Learning*

KATO, Takeo [B class; 400 (B), 70 (C)] (353)
— *Numerical calculation of microwave response in a fractional quantum Hall droplet*

Data Repository
https://zenodo.org/records/18933586
DOI:10.5281/zenodo.18933586

KATO, Yasuyuki [B class; 500 (B), 90 (C)] (344)
— *Numerical study on transition between quantum spin liquids*

1. Large-N SU(4) Schwinger boson theory for coupled-dimer antiferromagnets
Shang-Shun Zhang, Yasuyuki Kato, E. A. Ghioldi, L. O. Manuel, A. E. Trumper, and Cristian D. Batista Phys. Rev. B **112**, 024410 (2025).
DOI:10.1103/qfmw-whbp

KAWAGUCHI, Kaishu [AB class; 600 (B), 50 (C)] ()
— *Investigation of Substrate Effects on Topological-Insulator Bi_2Te_3 Thin Films*
— *Spin-Polarized Band-Structure Analysis of Bi_2Te_3 Topological-Insulator Thin Films under Optical Excitation*

KAWAKATSU, Toshihiro [C class; 5000 (B), 0 (C)] (291)
— *Nonlinear particle-continuum switching in multiscale Smoothed-Particle Hydrodynamics (SPH) method*

KAWAMURA, Hikaru [C class; 1200 (B), 400 (C)] ()
— *Novel order in frustrated magnets*

KAWAMURA, Taira [B class; 400 (B), 40 (C)] (359)
— *A microscopic theory for charge imbalance in nonequilibrium superconductors*

1. Nonequilibrium electron distribution function in a voltage-biased metal wire: A nonequilibrium Green ' s function approach
   T. Kawamura, and Y. Kato J. Phys. Soc. Jpn. 95, 034702 (2026).
   DOI:10.7566/JPSJ.95.034702

2. Emergence of Charge-Imbalanced BCS State and Suppression of Nonequilibrium FFLO State in Asymmetric NSN Junctions
   T. Kawamura, and Y. Ohashi arXiv:2603.00435
   DOI:10.48550/arXiv.2603.00435

KINEFUCHI, Ikuya [C class; 3000 (B), 300 (C)] (313)
— *Study on gas separation mechanisms in facilitated transport membranes*

KITAO, Akio [C class; 4600 (B), 400 (C)] (289)
— *Efficient sampling simulation of the soft modes significantly contribute to protein properties*

1. Tandem Allosteric Effects of Reactant and Product that Promote Deacetylation Cycles in Sir2
   Z. Bai, D. P. Tran, A. Kitao Journal of Chemical Information and Modeling **65**, 11326 (2025).
   DOI:10.1021/acs.jcim.5c01755

2. Protein domain movement involved in binding of belinostat and HPOB as inhibitors of histone deacetylase 6 (HDAC6): a hybrid automated-interactive docking study
   G. Iakovou, L. Palmer, A. Ganesan, A. Kitao, S. D. Laycock, and S. Hayward Journal of Computer-Aided Molecular Design **39**, 52 (2025).
   DOI:10.1007/s10822-025-00636-x

3. RNA Binding Mechanism of the FUS Zinc Finger in Concert with Its Flanking Intrinsically Disordered Region
   S. Kijima and A. Kitao Journal of Chemical Information and Modeling **65**, 8262 (2025).
   DOI:10.1021/acs.jcim.5c01059

4. Interactive docking workshop: Docking the anticancer drug Belinostat to its cellular histone deacetylase (HDAC) target
   G. Iakovou, L. Palmer, A. Ganesan, A. Kitao, S. D. Laycock, and S. Hayward Journal of Chemical Education **102**, 2514 (2025).
   DOI:10.1021/acs.jchemed.4c01347

5. The strategy used by nave anti-PEG antibodies to capture flexible and featureless PEG chains
   Y. Liu, T. Mori, Y. Ito, K. Kuroki, S. Hayashi, D. Kohda, T. Shimizu, T. Ishida, S. R. Roffler, M. K. Kaneko, Y. Kato, T. Arimori, T. Teramoto, K. Takemura, K. Ishibashi, Y. Katayama, K. Maenaka, Y. Kakuta, A. Kitao, and T. Mori Journal of Controlled Release **380**, 396 (2025).
   DOI:10.1016/j.jconrel.2025.02.001

KITOH, Hirotaka [B class; 400 (B), 70 (C)] (191)
— *Electronic structure calculations and molecular dynamics simulations for fullerenes on a tungsten surface*

KOBAYASHI, Akito [B class; 450 (B), 80 (C)] (252)
— *Compensated Ferrimagnets with Spin Splitting based on inequivalent dimers in organic compounds*

KOBAYASHI, Katsuyoshi [B class; 400 (B), 70 (C)] (190)
— *Theoretical study on electronic properties of new nanoscale surfaces and interfaces*

KOBAYASHI, Nobuhiko [C class; 3400 (B), 350 (C)] (97)
— *Quantum transport theory by large scale first-principles electron transport calculations*

1. Evolution of electronic correlation in highly doped organic two-dimensional hole gas
   N. Kasuya, T. Furukawa, H. Ishii, N. Kobayashi, K. Hirose, H. Takayanagi, T. Okamoto, S. Watanabe, and J. Takeya Nat. Commun.16, 3214 (2025).
   DOI:10.1038/s41467-025-58215-5

2. Field emission from vertically aligned graphene edges at the apex of the pencil lead
   T. Igari, R. Tsuruta, Y. Nishiyama, M. Adachi, T. Myojin, K. Asanagi, M. Sasaki, N. Kobayashi, and Y. Yamada Sci. Rep. 15, 27456 (2025).
   DOI:10.1038/s41598-025-11895-x

KOBAYASHI, Yoshihiro [B class; 100 (B), 30 (C)] (378)
— *Molecular dynamics simulation of graphene-nanospacer stacking heterostructure properties*

1. Mechanical bistability and hysteresis in graphene-CNT hybrid systems: from atomistic simulations to macroscale structural responses
   M. Ding, N. Sakurai, M. Shen, T. Inoue, T. Matsuzaki, T. Mizuno, K. Suzuki, J. I. Enriquez, H. H. Halim, Y. Hamamoto, Y. Nishina, H.Y. Yoshikawa, Y. Morikawa, and Y. Kobayashi Submitted

KOGA, Akihisa [CD class; 6900 (B), 650 (C)] (229)
— *Analyzing ferromagnetic order in a particle doped SU(N) Fermi-Hubbard model using DMFT*
— *Numerical analysis of fermionic superfluidity with an interplay between dissipation and external fields in non-Hermitian SU(N) Hubbard models*
— *Magnetic phases near commensurate fillings in the SU(N) Fermi-Hubbard model*

1. Generalized Nagaoka ferromagnetism accompanied by flavor-selective Mott states in an SU(N) Fermi-Hubbard model
   J. Fujii, K. Yamamoto, and A. Koga Phys. Rev. B 113, 115132 (2026).
   DOI:10.1103/kx3p-phyq

2. Elliptical-rod geometries enhance photonic band gaps in disordered stealthy hyperuniform photonic crystals
   K. Asakura, K. Yamamoto, and A. Koga J. Phys. Soc. Jpn. 95, 024711 (2026).
   DOI:10.7566/JPSJ.95.024711

3. Itinerant ferromagnetism in an SU(3) Fermi-Hubbard model at finite temperature: A DMFT study
   J. Fujii, K. Yamamoto, and A. Koga Phys. Rev. B 112, 115136 (2025).
   DOI:10.1103/vpb4-4d54

4. Measurement-induced phase transitions for free fermions in a quasiperiodic potential
   T. Matsubara, K. Yamamoto and A. Koga Phys. Rev. B 112, 054309 (2025).
   DOI:10.1103/3zfd-3hqt

5. Quasiperiodically modulated honeycomb lattices and their magnetic properties
   A. Koga and T. Matsubara Phys. Rev. B 111, 214422 (2025).
   DOI:10.1103/7hsy-sct6

KOMIYA, Atsuki [C class; 1200 (B), 250 (C)] (147)

— *Numerical simulations of electron-lattice interactions under laser irradiation using time-dependent density-functional theory*

1. First-principles investigation of the relationship between laser irradiation intensity and non-thermal melting of α-quartz
   Mizuho Ono, Hiroki Gonome, Atsuki Komiya J. Appl. Phys. 138, 105103 (2025).
   DOI:10.1063/5.0279804

KOSHOJI, Ryotaro [C class; 5000 (B), 600 (C)] (280)

— *Ionic crystal structure search based on mathematical crystal chemistry*

— *Materials synthesis based on mathematical crystal chemistry*

Data Repository
Website for mathematical crystal chemistry
https://marici.mathematical-crystal-chemistry.solutions/optimal-solutions

KOURA, Akihide [C class; 1000 (B), 0 (C)] (163)

— *Ab initio study on static and dynamic properties of light metal alloys*

1. 機械学習ポテンシャルを用いたSiO¡sub¿2¡/sub¿メルトおよびガラスの大規模分子動力学シミュレーション
   若林大佑, 島村孝平, 下條冬樹, 高良明英日本結晶学会誌 **67**,121 (2025).
   DOI:10.5940/jcrsj.67.121

2. Structural Insights into Liquid Malic and Lactic Acids from First-Principles Simulations and X-ray Diffraction
   W. Sugimoto, K. Ito, H. Shimakura, S. Tahara, K. Ohara, A. Koura, K. Shimamura, and F. Shimojo J. Phys. Soc. Jpn. **95**, 014602 (2026).
   DOI:10.7566/JPSJ.95.014602

KUDO, Koji [CD class; 10200 (B), 0 (C)] (225)

— *Numerical study on a quantum anomalous Hall-superconductor hybrid*

— *Numerical study on a quantum anomalous Hall-superconductor hybrid: Creation of non-Abelian anyons*

— *Quantum anomalous Hall-superconductor hybrid: topological superconductivity*

1. Repulsive-Interaction-Driven Topological Superconductivity in a Landau Level Coupled to an s-Wave Superconductor
   K. Kudo, R. Nakai, H. Isobe, J. K. Jain, and K. Nomura arXiv:2510.04700
   DOI:10.48550/arXiv.2510.04700

KUNISADA, Yuji [C class; 6000 (B), 0 (C)] (69)

— *Designing of Ceramic Protective Coating and Grain Boundary to suppress hydrogen embrittlement of metallic materials*

— *Development of Ceramic Protective Coating for High Corrosion Resistance of Metallic Materials*

KURODA, Fumiaki [B class; 350 (B), 90 (C)] (198)

— *Development of a Surface Structure Exploration Program and Supporting Infrastructure*

KUROKI, Kazuhiko [C class; 4800 (B), 0 (C)] (232)

— *Theoretical designing of high T_c superconductivity at ambient pressure in multilayer nickelates and related materials*

1. TImprovement of the simplification method for the local two-particle full-vertex towards precise

frequency behavior
Myota Mizuno, Kazuhiko Kuroki, Masayuki Ochi Phys. Rev. B **111**, 205136 (2025)
DOI:10.1103/PhysRevB.111.205136

2. t-J model for strongly correlated two-orbital systems: Application to bilayer nickelate superconductors
Tatsuya Kaneko, Masataka Kakoi, Kazuhiko Kuroki Phys. Rev. B **112**, 075143 (2025)
DOI:10.1103/bsgt-sg2s

3. Doublon-Holon Pairing State in Photodoped Mott Insulators
Ryota Ueda, Madhumita Sarkar, Zala Lenarčič, Denis Golež, Kazuhiko Kuroki, Tatsuya Kaneko Phys. Rev. B **113**, L161109 (2026).
DOI:10.1103/dc6n-hrzj

4. Possible high thermoelectric power factor in alkali-metal-intercalated BC: anisotropic multiple valleys originating from the van Hove singularity of graphene
Ryutaro Enami, Kazuhiko Kuroki, Masayuki Ochi Phys. Rev. Mater. **9**, 084001 (2025).
DOI:10.1103/rqrv-7hqt

5. Optical control of the crystal structure in the bilayer nickelate superconductor $La_3Ni_2O_7$ via nonlinear phononics
Shu Kamiyama, Tatsuya Kaneko, Kazuhiko Kuroki, Masayuki Ochi Phys. Rev. B **112**, 094115 (2025).
DOI:10.1103/h6vj-fd4n

6. Theoretical study on the possibility of high s-wave superconductivity in the heavily hole-doped infinite layer nickelates
Hirofumi Sakakibara, Ryota Mizuno, Masayuki Ochi, Hidetomo Usui, Kazuhiko Kuroki Phys. Rev. B **111**, 224511 (2025).
DOI:10.1103/nl4m-n5dx

KUSAKABE, Koichi [C class; 3400 (B), 0 (C)] (103)
— *Electron excitation induced phase transformation of quantum materials*

1. Modulated Dirac bands and integer hopping ratios in a honeycomb lattice of phenalenyl-tessellation molecules
N. Morishita, K. Komatsu, M. Kitatani, and K. Kusakabe Physical Review B 111, 235117 (2025).
DOI:10.1103/PhysRevB.111.235117

2. Computational study of conformational interconversion of an amyloid β double layer system
Y. Oishi, M. Kitatani, K. Nakajima, H. Ogi, and K. Kusakabe RSC Advances, 15, 42395-42401, (2025).
DOI:10.1039/D5RA08004E

3. Real-space imaging of thermally and photo induced phase transition in quasi one dimensional organic complexes
K. Fukumoto, K. Onda, T. Tanaka, K. Kusakabe, E. Pyatenko, H. Yamochi, S. Adachi, S. Koshihara submitted to Phys. Rev. Res.

LEE, Minhyeok [C class; 2400 (B), 0 (C)] (326)
— *Multiphase-reactive simulations of aluminum particle combustion with detailed kinetics and interfacial phase change*

LI, Hao [E class; 2400 (B), 250 (C)] (115)

— Computational Screening of Magnetic Properties for Enhanced CO_2 Reduction Reaction (CO_2RR) Catalysts

1. HERO (Hessian-Engineered Relaxation Optimizer): Suppressing "Hessian pollution" for accelerated first-principles structural relaxation
   M. Li, P. Ma, L. Li, W. Yang*, and H. Li* CMC-Comput. Mater. Con. 2026, In Press.

2. Spin Effect Regulation as A Design Principle for M-N-C Catalysts for Oxygen Electrocatalysis
   H. Li, Z. Fu, Y. Yuan, D. Zhang, Y. Chen, H. Li*, and A. Cao* Chemical Science, 2026, In Press.

3. Unveiling the correlation between high-entropy alloy element systems and electrocatalytic activity
   X. Shan, F. Cai, Y. Tu, D. Zhang, Y. Pan, L. Chen, J. Liang, H. Gao, J. Xu, H. Li*, J. Li, E. Wang*. and M. Zhou* National Science Review, 2026, nwag161.
   DOI:10.1093/nsr/nwag161

4. Revealing Zn and Ga as effective promoters for Cu-catalyzed CO2 hydrogenation to methanol
   M. Ma, H. Li, A. Cao*, and J. Yan Journal of Energy Chemistry, 2026, In Press.

5. Data-Driven Paradigms for Advancing Alkali-Metal-Ion Battery Technologies
   H. Shao, N. Kumar, W.-H. Lai, H. Li, X. Jia, H.-K. Liu, and Y. Wang* Energy Storage Materials, 2026, 105044.

6. AI Agents: Opportunity, Hype, and the Way Through
   C. Zhao* and H. Li* AI Agent, 2026, 2, 3.
   DOI:10.20517/aiagent.2026.07

7. StableOx-Cat Agent: An AI Agent for Exploring Stable Metal Oxide Electrocatalysts
   X. Jia, D. Zhang, Y. Lu, Q. Wang, and H. Li* AI Agent, 2026, 2, 1.
   DOI:10.20517/aiagent.2026.03

8. Digital Materials Ecosystem: From Databases to AI Agents for Autonomous Discovery
   D. Zhang, X. Jia, Y. Wang, H. Liu, Q. Wang, S. H. Jang, D. Shah, S. Ye, H. B. Tran, and H. Li* Chemical Science, 2026, 17, 5782 (Invited Perspective; Front Cover Article).

9. Ligand-Intercalated MOFs Enable Reaction-Pathway Engineering in Biomass Electrooxidation via Steric and π- Electronic Microenvironment Control
   J. Chen, Z. Guo, J. Xie, L. Tang, S. Li, Y. Bu, C. Peng, M. Zhao, L. Zhang, J. Zhou, H. Liu*, H. Li*, and M. Li* Angewandte Chemie International Edition, 2026, e4762494.

10. Catalytic Strategies and Mechanisms for Enhancing MgH2 Solid-State Hydrogen Storage
    Z. Gao, X. Yang, Z. Zhuang, Y. Zhang, J. Cai, Y. Li, W. Fu, H. Li*, and W. Yang* Chem Catalysis, 2026, 6, 101692 (Invited Perspective).

11. Recent Development in Designing Electrocatalysts for Efficient and Selective Ammonia Oxidation Reaction
    Y. Deng, Z. Bao, Y. Huang, M. Cui, Y. Chen, H. Li*, and L. Wei* Advanced Energy and Sustainability Research, 2026, 7, e202600002 (Invited Review).

12. Accelerating Catalyst Materials Discovery with Large Artificial Intelligence Models
    D. Zhang, Y. Chen*, C. Liu, Y. Liu, H. Xin, J. Peng*, P. Ou*, and H. Li* Angewandte Chemie International Edition, 2026, e26150 (Invited Review; Cover Article).

13. Catalysis AI Agent Guides Discovering the Universal Design Principle of Cu-based Single-atom Alloy Catalysts for CO2 Electroreduction
    X. Wang, Z. Li, D. Zhang, H. Li*, H. Xu* and D. Cheng* Angewandte Chemie International

Edition, 2026, e24612.

14. Interface-Mediated Jahn–Teller Effect in a Structure-Reinforced $LiMnO_2$ Cathode
H. Liu, T. Shen, X. Zhu, M. Yang*, Y. Yao, J. Cheng, Y. Zhao, H. Li*, S. Li*, L. Gu, and H. Xia* J. Am. Chem. Soc. 2026, 148, 7388.
DOI:10.1021/jacs.5c20036

15. Coordination-Dependent Oxygen Reduction Reaction Activity of Single Atom Co-Nx-C Electrocatalysts
C. Liu, D. Zhang, J. Chen, F. She, F. Liu, Z. Yu, Z. Zhi, M. S. Levine, J. L. Sessler, Y. Chen, H. Li*, and L. Wei* J. Am. Chem. Soc. 2026, 148, 6569.
DOI:10.1021/jacs.5c20980

16. Boosting ammonia decomposition for hydrogen production over Co/CeO2 catalysts via Sr doping
L. Su, F. Zeng, J. Wang, Q. Qasim, X. Liu, J. Li, H. Li*, and W. Cen* Catal. Sci. Technol. 2026, In Press.

17. Strategically Advancing Semiconducting Phthalocyanines as High-Performance Electrocatalysts for Electrochemical CO2 Reduction
T. Liu*, X. Hou, D. Zhang, Y.Hirai, K. Ishibashi, Y. Matsuo, S. Ono, H. Li*, and H. Yabu* ACS Applied Electronic Materials, 2026, 8, 2187 (Invited Spotlight Review; Cover Article).

18. Enhancement of Methanol Yield in CO2 Hydrogenation by Promoting CO_2 Activation and Unlocking the RWGS + CO-Hydrogenation Pathway over Cu-La/ZrO_X Catalysts
J Yang, T. Gao, J. Yang, F. Xiao, S. Liu, N. Zhao* , D. Cao*, H. Li* ACS Catal. 2026, 16, 4773.
DOI:10.1021/acscatal.5c08427

19. Materials Databases: Foundations of Modern Digital Materials
Y. Zhuang, X. Yang, C. Zhang, X. Jia, D. Zhang, M. Li, T. Yao, J. Peng, Z. Gao, W. Yang*, and H. Li* Precision Chemistry, 2026, In Press (Invited Perspective).

20. Y-Induced Oxygen Vacancy Engineering and Local Electronic Reconstruction for Enhanced Ammonia Decomposition over $Ni_1Ce_{1-x}Y_xO_\alpha$
Z. Bao, H. Liu, Y. Zhang, Z. Wang, H. Li*, and H. Hu* Journal of Catalysis, 2026, 455, 116718
DOI:10.1016/j.jcat.2026.116718

21. AI-Driven Multi-Agent Collaborations for Accelerating Catalyst Design
H. Li* National Science Review, 2026, 13, nwag067 (Invited).
DOI:10.1093/nsr/nwag067

22. "DIVE" into Hydrogen Storage Materials Discovery with AI Agents
D. Zhang*, X. Jia, T. B. Hung, S. H. Jang, L. Zhang, R. Sato, Y. Hashimoto, T. Sato, K. Konno, S. Orimo*, and H. Li* Chemical Science, 2026, 17, 3031-3042 (Cover Article).

23. Atomic Eu-Mediated Acetonitrile Adsorption Configuration Switch Drives Long-Term, Ampere-Level Electrosynthesis of Ethylamine via Eu-Mediated Acetonitrile Adsorption Configuration Switching
H. Du, X. Wang, M. Li*, R. Lv, C. Wang, W. Xue, L. Li, D. Sun, Y. Tang, H. Li*, and G. Fu* Advanced Materials, 2026, 38, e21105.
DOI:10.1002/adma.202521105

24. Stepwise Acceleration of Water Dissociation and Hydrogen Spillover for Enhanced Overall Alkaline Hydrogen Evolution
T. Lu, J. Li, C. Wang, H. Liu, S. Ye, X. Jia, L. Zhang, D. Zhang, D. Sun, Y. Gu*, Q. Wang, B. Da, L. Wei, Y. Zhang*, H. Li*, and Y. Tang* ACS Catalysis, 2026, 16, 2827.

25. Tuning Stability of AB3-Type Alloys by Suppressing Magnetism
H. B. Tran*, T. Sato, R. Sato, H. Saitoh, S. Orimo*, and H. Li* Chemistry of Materials, 2026, 38, 497.

26. The Influence of Anion Effects on the Morphology of Copper-Based Hydroxides and Their Electrocatalytic Performance in Reduction of Nitrite to Ammonia
C. Sun, T. Wu*, X. Xing, L. Ding*,W. Xiong*, and H. Li* Ind. Eng. Chem. Res., 2026, 65, 4361.

27. Artificial Intelligence - Driven Discovery and Design of Solid-State Hydrogen Storage Materials
Y. Chu, Y. Li, Y. Lyu, D. Zhang, H. Li*, W. Yang*, J. Li, and L. Zhang* Green Energy Environ. 2026, In Press (Invited Review).

28. Recent Advances in the Application of Transition Metal-Based Catalysts in Electrocatalytic Ammonia Synthesis and C-N Bond Formation
S. Tu , J. Li , T. Wu* , X. Xing, W. Xiong*, and H. Li* Journal of Materials Chemistry A, 2026, 14, 1383.

29. Making Reactivity General for Machine-Learning Potentials
H. Li* Chem Catalysis, 2026, 6, 101572 (Invited).

30. Non-Directly Bonded Single-Atom Pairs Towards H2/CO Electrooxidation
T. Yang, H. Liu, H. Liu, W. Zhao, J. Ge, W. Wang, S. Yang, M. Tang, K. Wei, K. Wang, Z. Qi, X. Wang*, H. Li*, and J. Ge* Science Bulletin, 2026, 71, 399.

31. Roadmap for Transforming Heterogeneous Catalysis with Artificial Intelligence
H. Xin*, J. R. Kitchin*, N. Lpez*, N. M. Schweitzer*, N. Artrith, F. Che, L. C. Grabow, G. Gunasooriya, H. J. Kulik, T. Laino, H. Li, S. Linic, A. Medford, R. Meyer, J. Peng, C. Phillips, J. Qian, L. Qi, W. Shaw, Z. W. Ulissi, S. Wang, and X. Wang Nature Catalysis, 2026, 9, 102.

32. Universal Catalyst Design Framework for Electrochemical Hydrogen Peroxide Synthesis Facilitated by Local Atomic Environment Descriptors
Z. Liu, Y. Liu, Y. Zhang, Y. Deng, Z. Zheng, R. Knibbe, T. Gao, M. Li, Z. Wang, B. Zhang, X. Jia, D. Zhang, H. Liu, X. Shao, Z. Gao, L Wei*, H. Li*, and W. Yang* Angewandte Chemie International Edition, 2026, 65, e18027 (Cover Article).

33. Covalent Bridges Enabling Layered C60 as an Exceptionally Stable Anode in Lithium-Ion Batteries
S. Wang, H. Liu, Y. Lei, D. Li, Y. Fan, L. Hong, X. Guo, M. Wang, Z. Huang, Y. Cheng, X. Yang, J. Zhang, H. Li*, and G. Wang* J. Am. Chem. Soc. 2025, 147, 47663.

34. 2D Topological Electrocatalysts with SpinOrbit Coupling: Interplay Between The “Electrochemical” and “Topological” Surface States
H. Liu*, T. B. Hung, Y. Wang, D. Zhang, Y. Lu, and H. Li* Journal of Physical Chemistry Letters, 2025, 16, 12892.

35. Atomic Eu Substitution in Cu2O Tailors C1 and C2+ Product Selectivity by Frustrated Deep Hydrogenation in Electrochemical CO2 Reduction
Y. Liu, X. Wang, Z. Mao, J. Zhang, M. Li, D. Sun, Y. Tang, H. Li*, and G. Fu* Journal of the American Chemical Society, 2025, 147, 45808.

36. Selective Electrocatalytic Reduction of Nitrate for the Synthesis of Hydroxylamine with Cu-ZnO/N-C Catalyst
J. Li, Y. Wang, T. Wu, X. Xing, L. Li, W. Xiong*, and H. Li* Chemical Engineering Science, 2025, 323, 123204.

37. Machine Learning-Driven Advances in Environmental Pollutant Management
Z. Qiu, Z. Zhuang, X. Jia, H. Li, C. Chen, and B. Yu* Journal of Environmental Chemical Engineering, 2025, 13, 120441.

38. Physically Interpretable Descriptors Drive the Materials Design of Metal Hydrides for Hydrogen Storage
S.-H. Jang*, D. Zhang, H. B. Tran, X. Jia, K. Konno, R. Sato, S. Orimo*, and H. Li* Chemical Science, 2025, 16, 23111- 23120

39. Atomically Ordered RuGa Intermetallic Electrocatalyst Enables High-Efficiency Nitrate-to-Ammonia Conversion
Y.-Z. Yu, Q.-L. Jiang, Y. Cheng, S. Li, T. Li, K.-Z. Xue, Y. Xu, S. Cheng, H. J. Sun, T. Wang, J. Xu,* X. Su, Y. Chen, B. Da, H. Li*, and Z.-Y. Wu* Advanced Functional Materials, 2025, e24120.

40. Synergistic MultiPhysics Catalysis Enabled by LotusRootInspired Flow Fields in Proton Exchange Membrane Fuel Cells
Y. Zhou, Z. Miao*, H. Li*, K. Meng, B. Chen, M. Chen, H. Luo, Y. Guan, Y. Duan, Q. Ding, D. Wu, J. Li, and X. Tian* Journal of Materials Chemistry A, 2025, 13, 40821.

41. Theory-Guided Design of Non-Precious Single-Atom Catalyst for Electrocatalytic Chlorine Evolution
K. Ma, L. Yang, X. Yang, C. Zhang, D. Zhang, L. Zhang, L. Wei, C. Ye*, H. Li*, and W. Yang* Advanced Functional Materials, 2025, 36, e25210.

42. Design of Metal-Supported MgO Catalysts for Electrochemical CO2 Reduction to Formic Acid via the MottSchottky Effect
S. Zhao, Y. Wang, H. Liu, X. Jia, Y. Zhang, L. Zhang, B. Da, Q. Wang, H. Zheng*, H. Li*, and W. Li* Journal of Catalysis, 2025, 453, 116502.

43. Simultaneous Electrocatalytic Oxidation and Hydrogenation of Biomass-Derived Aldehydes on Single- Atom Ru Catalysts
Y. Wang, B. Liu, Y. Duan, B. Da, Z. Hu, H. Wen, W. Bu, H. Luo, S. Zhang, H. F. Garces, C. Wang, T. Mu, H. Li*, and K. Yan* Advanced Energy Materials, 2025, 15, e04502.

44. Cloud Synthesis: A Global Closed-Loop Feedback Powered by Autonomous AI-Driven Catalyst Design Agent
D. Zhang, X. Jia, H. Liu, Y. Wang, S. Ye, Q. Jiang, Y. Wang, Z. Guo, L. Zhang, L. Wei, W. Yang, H. Liu, S. Zhao, H. Xu, D. Cheng, Y. Hashimoto, T. Tomai, and H. Li* AI Agent, 2025, 1, 2.
DOI:10.20517/aiagent.2025.02

45. Probing the Reactivity of In-Situ Formed Oxygen Vacancies of Non-Noble Lead Oxides for Anodic Propylene Oxidation
J. Ge, T. Wang, X.-L. Zhang, H. Sun, R. Wang, P.-C. Yu, X. Sun, S.-P. Sun, H. Liu, Y. Liu, C.-L. Zhang, B. Da, Y.- R. Zheng,* M.-R. Gao,* and H. Li* Catal. Sci. Technol. 2025, 15, 7228.

46. Decoding pH- Dependent Electrocatalysis through Electric Field Models and Microkinetic Volcanoes
S. Ye, Y. Wang, H. Liu, D. Zhang, X. Jia, L. Zhang, Y. Zhang, A. Kumatani, H. Shiku*, and H. Li* Journal of Materials Chemistry A, 2025, 13, 37821 (Invited Perspective; Front Cover Article)

47. Ampere-Level Electrosynthesis of CO via Well-Defined Pyridinic-N Incorporated Cobalt Phthalocyanine
T. Liu*, X. Hou, D. Zhang, Y. Hirai, K. Ito, K. Ishibashi, Y. Matsuo, J. Yoshida, S. Ono, H. Li*,

and H. Yabu* Small, 2025, e07824.

48. Designing Interfacial Edge Microenvironments of Cobalt Phosphide Quantum Dots/Graphitic Carbon Nitride to Modulate Electron Delocalization for Ultrafast Photocatalytic Hydrogen Evolution
X. Hu, Y. Zeng*, H. Liu*, B. D, H. Li, B. Hong, X. Peng, and X. Wang Chemical Engineering Journal, 2025, 523, 168790.

49. Artificial Intelligence Technology in Environmental Research and Health: Development and Prospects
Z. Guo, L. Huang*, J. Yan, H. Zhang*, X. Jia*, M. Li, and H. Li* Environmental International, 2025, 23, 109788.

50. Temperature Dependent Mechanism Evolution Effect Enables Stabilized RhRu3Ox for Water Oxidation in Proton Exchange Membrane Electrolyzer
M.-R. Qu, H. Liu, S.-H. Feng, X.-Z. Su, J. Xu, H.-L. Duan, R.-Q. Liu, Y.-Y. Qin, W.-S. Yan, S. Zhu*, R. Wu*, H. Li*, and S.-H. Yu* Nature Communications, 2025, 16, 9261.

51. High-Density W Single Atoms in Two-Dimensional Spinel Break the Structural Integrity for Enhanced Oxygen Evolution Catalysis
Y. Wang, B. Jia*, W. Qin, Y. Wang, S. Liu, Y. Qin, Y. Zhao, L. Liu, D. Zhang, H. Liu, H. Zhong, J. Liu, J. Tu, Y. Liu, H. Wu, D. Zhang, J. Fan, X. Qu, H. Li*, and M. Qin* J. Am. Chem. Soc. 2025, 147, 32249.

52. Selective Epitaxial Growth of MOF-on-MOF-derived Core-shell $Fe_2O_3/CoFe_2O_4$ Nanocomposites for Efficient Electrochemical Detection of Multiple Heavy Metal Ions
J. Guo, S. Tu, L. Li, X. Xing, W. Xiong*, and H. Li* Ind. Eng. Chem. Res., 2025, 64, 19075.
DOI:10.1021/acs.iecr.5c02521

53. Modulating Surface-Active Hydrogen for Facilitating Nitrate-to-Ammonia Electroreduction on Layered Double Hydroxides Nanosheets
B. Liu, Y. Wang, H. Wen, Y. Wang, H. Liu, B. Da, K. Li, H. Luo, H. Li*, and K. Yan* Advanced Functional Materials, 2025, e19238.

54. Unveiling Multilayer Cobalt Phthalocyanine/Carbon Core-Shell Structures as Efficient Catalytic Units for CO2-to-CO Electroreduction
T. Liu*, D. Zhang, Y. Chu, K. Ohashi, Y. Hirai, K. Ito, K. Ishibashi, Y. Matsuo, J. Yoshida, S. Ono, K. Kamiya, H. Li*, and H. Yabu* Applied Catalysis B: Environment and Energy, 2025, 381, 125852.

55. AI Agent-Defining the Next Era of Intelligent Agents
H. Li* AI Agent, 2025, 1, 1.
DOI:10.20517/aiagent.2025.01

56. Application of An Explainable Machine Learning to CO2 Methanation for Optimal Design Nickel-Based Catalysts
J. Zhang, X. Jia*, H. Li, F. Xiao, Q. Wang*, and N. Zhao* ACS Sustainable Chem. Eng. 2025, 13, 14278.

57. Hydrophobically Modified Cu_2O Nanocube for Selective CO_2 Electroreduction to C_{2+} Products
C. Li, Z. Guo, X. Mao, Y. Shen, S. Yang, Y. Jiang, P. Tang, H. Li*, H. Li*, C. Li* AIChE Journal, 2025, 71, e70049.
DOI:10.1002/aic.70049

58. Insights Into Giant Magnetocaloric Effect in $BiCu_3Cr_4O_{12}$ with Charge-Spin-Lattice Coupling
H. B Tran*, H. Li*, M. Goto, K. Sato, and Y. Shimakawa J. Mater. Chem. A, 2025, 13, 34286.
DOI:10.1039/D5TA03354C

59. C60 Fullerene as the Active Site for CO2 Electroreduction
S.-W. Ying, Y. Wang, P. Du, Q. Wang*, C. Yue, D. Zhang, Z.-C. Chen, J.-W. Zheng*, S.-Y. Xie*, and H. Li* Angewandte Chemie International Edition, 2025, 64, e202511924 (Editor's Choice; Cover Article).

60. Reinforcing the Chemical Bonding in Pt3Ni Catalysts via Metallic Interface-Directed Activation for Durable Fuel Cells
M. Chen, C. Wu, Z. Miao*, H. Li, H. Zhang, Q. Liu, J. He, Y. Zhou, D. Wu*, J. Li, R. Li, and X. Tian* Advanced Functional Materials, 2025, e12164.

61. The Key Steps and Distinct Performance Trends of Pyrrolic vs. Pyridinic M-N-C Catalysts in Electrocatalytic Nitrate Reduction
Q. Jiang, M. Gu, S. Pei, T. Wang, F. Liu, X. Yang, D. Zhang, Z. Wu, Y. Wang*, L. Wei*, and H. Li* J. Am. Chem. Soc. 2025, 147, 26029.

62. Unraveling the Potential-Dependent Selectivity of Propylene Electrooxidation: The Role of Electrochemistry-Induced Reconstruction
D. Li , P. Sun, D. Zhang, H. Li*, H. Xu*, and D. Cao* J. Am. Chem. Soc. 2025, 147, 24900.

63. Closed-Loop Framework for Discovering Stable and Low-Cost Bifunctional Metal Oxide Catalysts for Efficient Electrocatalytic Water Splitting in Acid
X. Jia, Z. Zhou, F. Liu, T. Wang, Y. Wang, D. Zhang, H. Liu, Y. Wang, S. Ye, K. Amezawa*, L. Wei*, and H. Li* J. Am. Chem. Soc. 2025, 147, 22642 (Cover Article).

64. Rare Earths Evoked Gradient Orbital Coupling in Electrocatalysis: Recent Advances and Future Perspectives
X. Wang, M. Li, Y. Tang, H. Li*, and G. Fu* Progress in Materials Science, 2025, 155, 101539.

65. Furfural Electrovalorisation to Hydrofuroin with Near-Unity Faradaic Efficiency on a Single-Atom Zinc Catalyst
J. Chen, S. Ye, F. She, X. Yang, F. Liu, Z. Yu, Z. Zheng, M. Hong, Q. Wang, Y. Chen, H. Li*, and L. Wei* EES Catalysis, 2025, 3, 1062.

66. The Hidden Engine of AI in Electrocatalysis: Databases and Knowledge Graphs at Work
D. Zhang and H. Li* Mol. Chem. Eng. 2025, 1, 100003 (Invited Editorial; Cover Article).

67. Preview: Polymer Solubility Dictates the Fate of Polymer Chains
H. Li* Newton, 2025, 100191 (Invited Preview).

68. Bridging Theory and Experiment: Machine Learning Potential-Driven Insights into pH-Dependent CO2 Reduction on Sn-Based Catalysts
Y. Wang, Z. Wu, Y. Jiang, D. Zhang, Q. Wang*, C. Wang, H. Li*, X. Jia, J. Fan*, and H. Li* Advanced Functional Materials, 2025, e06314 (Cover Article).

69. Advancing Electrochemical Nitrate Reduction: Overcoming Rate-Limiting Bottlenecks with Copper/Cobalt Catalysts
J. Li, Y. Wang, X. Xing, Y. Wang, W. Xiong*, and H. Li* Advanced Functional Materials, 2025, 35, e13717.

70. Dynamic Evolution of Self-Renewal Fe- N-C Catalysts for Acidic Oxygen Reduction Reaction
F. Liu, L. Lai, Z. Guo, F. She, J. Prabowo, H. Li*, L. Wei*, and Y Chen* EES Catalysis, 2025, 3, 1358.

71. A Materials Map Integrating Experimental and Computational Data via Graph-Based Machine

Learning for Enhanced Materials Discovery
Y. Hashimoto*, X. Jia, H. Li, and T. Tomai APL Machine Learning, 2025, 3, 036104.

72. Chlorine-Dopant Dynamically Stabilizes Cu0/Cu+ Active Sites for Selective CO2 Electroreduction to Multicarbon Products
C. Li, Z. Guo, J. Cui, T. Zhang, Z. Liu, X. Mao, Y. Shen, S. Yang, Y. Jiang, P. Tang, H. Li*, H. Li*, and C. Li* AIChE Journal, 2025, 71, e18934.

73. Data-Driven Strategies for Designing Multicomponent Molten Catalysts to Accelerate Industrialization of Methane Pyrolysis
Y. Chen*, X. Huang, Y. He, Q. Liu, J. Du, W. Yang, W. Wang, D. Zhang, X. Jia, H. Wang, Y. Tang*, Q. Yu, S. K. Kim*, and H. Li* ACS Catalysis, 2025, 15, 11003.

74. Phosphorus-Mediated Oxygen Vacancy Engineering in Cu2O for Highly Selective CO2 Electroreduction to Multi-carbon Products
X. Mao, Z. Guo, S. Yang, Y. Shen, L. Wei, C. Li, H. Li*, H. Li*, and C. Li* ACS Nano, 2025, 19, 23, 21669.

LIU, Heng [E class; 2500 (B), 600 (C)] ()
— *Explore the pH-dependent surface state and oxygen evolution reaction performance for transition metal nitrides*

MAEHIRA, Takahiro [B class; 300 (B), 60 (C)] (207)
— *Electronic Structure of Rhenium*

MAKINO, Takayuki [B class; 400 (B), 70 (C)] (188)
— *Optical properties of transition-metal monoxides based on coherent potential approximation*

1. Hubbard energy dependence of electronic structures in rare-earth monoxides
M. Tago, T. Kurachi, and T/ Makino Jpn. J. Appl. Phys. 64 09SP18 (2025).
DOI:10.35848/1347-4065/adfee3

2. Sensitivity enhancement of surface plasmon resonance sensor employing 2D black phosphorus: an analytical insight
A. Saha, B. Dey, Md. Sherajul Islam, M. Tago, and T. Makino Jpn. J. Appl. Phys. 64 11SP13 (2025).
DOI:10.35848/1347-4065/ae1143

MASAKI, Yusuke [B class; 400 (B), 70 (C)] (352)
— *Tensor-network approach to phase transition of quantum chiral spin model*

MATSUSHITA, Katsuyoshi [C class; 400 (B), 0 (C)] (366)
— *Study of Self-transport and Clogging of Cells in Tissue Pipeline*

MATSUSHITA, Yu-Ichiro [E class; 13000 (B), 1800 (C)] (44)
— *Development of an HPC/Quantum Hybrid Platform for High-Precision Defect Analysis to Accelerate Materials Innovation*
— *High-precision calculation of semiconductor defects using an HPC/quantum hybrid computer*

1. Tensor-decomposition technique for qubit encoding of maximal-fidelity Lorentzian orbitals in real-space quantum chemistry
T. Kosugi, X. Huang, H. Nishi, and Y. Matsushita Phys. Rev. A **5**, 052615 (2025).
DOI:10.1103/PhysRevA.111.052615

2. Practical rule for trimming the DFT-1/2 self-interaction: Band gap, absolute band alignment,

and defect properties of semiconductors
C. Homma, R. Akashi, Y. Nishiya, S. Tsuneyuki, and Y. Matsushita Phys. Rev. B **112**, 115111 (2025).
DOI:10.1103/mp93-55g3

3. Towards improved quantum machine learning for molecular force fields
Y. Couzini, S. Daimon, H. Nishi, N. Ito, Y. Harazono, and Y. Matsushita Phys. Rev. A **112**, 062442 (2025).
DOI:10.1103/5s9m-h7yb

4. Adaptive interpolating quantum transform: A quantum-native framework for efficient transform learning
G. Budiutama, S. Daimon, H. Nishi, R. Kaneko, T. Ohtsuki, and Y. Matsushita Phys. Rev. A **112**, 062410 (2025).
DOI:10.1103/vyr3-h9hq

5. Advancing N-type doping in semiconductors through hydrogen-defect interactions
A. Kiyoi, Y. Nishiya, Y. Matsushita, and T. Umeda Comm. Materials **7**, 8 (2026).
DOI:10.1038/s43246-025-00955-4

6. Logical quantum phase estimation for x-ray absorption spectra
H. Nishi, T. Kosugi, S. Hirose, T. Okayama, and Y. Matsushita Phys. Rev. Applied **25**, 034026 (2026).
DOI:10.1103/cwj3-xmsg

MINAMI, Susumu [B class; 950 (B), 180 (C)] ()
— *First-principles study for mechanical control of magnetic thermoelectric properties in topological magnets*
— *High-throughput study of strain-induced anomalous Nernst effect*

MISAWA, Masaaki [B class; 350 (B), 0 (C)] (210)
— *Computational study on nanoscale surface/interface structural design based on functional materials*

1. Dendritic WS2 Nanoribbon Networks Grown in Interfacial Confinement Space: Edge-Rich Architectures for Enhanced Hydrogen Evolution
H. Suzuki, K. Hirata, Y. Takahashi, S. Fujii, M. Misawa, T. Tokunaga, I. Nakaya, Y. Senda, Y. Hayashi, Y. Takahashi Small Structures **7**, e202500542 (2025)
DOI:10.1002/sstr.202500542

MISAWA, Takahiro [E class; 18500 (B), 1700 (C)] (219)
— *Analysis of the mechanism of pressure-induced superconductivity in molecular solids*Exotic superconductivity in the doped Kitaev spin liquid

MITARAI, Yoko [C class; 1000 (B), 300 (C)] (149)
— *Phase transformation and electric state of high entropy alloys*

MIURA, Yoshio [C class; 1200 (B), 0 (C)] ()
— *Theoretical study on spin related phenomenon at interfaces of ferromagnetic materials*

MIZUGUCHI, Tomoko [C class; 400 (B), 0 (C)] (364)
— *Role of counterions in ion-mediated permeation of hydrophobic ions into lipid bilayers*

MIZUKAMI, Wataru [C class; 4400 (B), 0 (C)] (295)
— *Creating a quantum computing database for sensor materials*

1. Enhancing quantum computations with the synergy of auxiliary field quantum Monte Carlo and computational basis tomography
   Viktor Khinevich, Wataru Mizukami Phys. Rev. Research **7**, 043344 (2025).
   DOI:10.1103/rbhc-dkh1

2. Integrating Classical and Quantum Software for Enhanced Simulation of Realistic Chemical Systems
   Tomoya Shiota, Klaas Gunst, Toshio Mori, Toru Shiozaki, Wataru Mizukami arXiv:2506.18877
   DOI:10.48550/arXiv.2506.18877

3. Symmetry-Adapted State Preparation for Quantum Chemistry on Fault-Tolerant Quantum Computers
   Viktor Khinevich, Wataru Mizukami arXiv:2601.08533
   DOI:10.48550/arXiv.2601.08533

4. Doubling the size of quantum selected configuration interaction based on seniority-zero space and its application to QC-QSCI-AFQMC
   Yuichiro Yoshida, Takuma Murokoshi, Rika Nakagawa, Chihiro Mori, Naoya Kuroda, Shigeki Furukawa, Hanae Tagami, Wataru Mizukami arXiv:2602.07912
   DOI:10.48550/arXiv.2602.07912

5. Expanding Universal Machine Learning Interatomic Potentials to 97 Elements Towards Nuclear Applications
   Naoya Kuroda, Kenji Ishihara, Tomoya Shiota, Wataru Mizukami arXiv:2603.03223
   DOI:10.48550/arXiv.2603.03223

MOCHIZUKI, Yasuhide [C class; 2400 (B), 250 (C)] (113)
— *Theoretical prediction of negative thermal expansion behavior from molecular dynamics calculations using machine learning potential and experimental verification*

1. Discovery of Biaxial Negative Thermal Expansion in KNbSi2O7 from Computations and Experiments
   H. Koiso, S. Kawasoe, J. Zhang, T. Isobe, A. Nakajima, and Y. Mochizuki* J. Phys. Chem. C 129, 9509 (2025).
   DOI:10.1021/acs.jpcc.5c01247

2. Reply to Comment on “Thermal expansion and phase stability of BF3 (B = Sc, Y, La, Al, Ga, In) from first principles”
   H. Koiso, S. Yoshida, T. Nagai, T. Isobe, A. Nakajima, and Y. Mochizuki Phys. Rev. B 112, 226102 (2025).
   DOI:10.1103/njgh-v8dh

MOID, Mohammad [B class; 200 (B), 50 (C)] ()
— *Impact of Electrostatic Forces on the Crystallization Process of Water Droplets*

MORI, Hatsumi [D class; 2500 (B), 0 (C)] ()
— *First-principles NEB calculations of proton tautomeric conduction pathways based on Neutron diffraction*

MORIKAWA, Yoshitada [E class; 17000 (B), 2450 (C)] (42)
— *Theoretical study on chemical reaction processes at surfaces and interfaces using density functional theory and machine learning methods*

1. O Coadsorption Effects on Water-Gas Shift Reaction over Cu Clusters on Cu(111): Insights from Machine Learning Force Field and Microkinetic Modeling
   M. F. Anshor, H. H. Halim, and Y. Morikawa Phys. Chem. Chem. Phys. in press.
   DOI:10.1039/d5cp05031f

2. Predicting reactive graphene edge-adsorbed Pt single-atom catalyst structures for oxygen reduction via machine learning-enhanced DFT calculations
   B. A. C. Tan, N. A. Sofi, P. N. Thanh, K. I. M. Rojas, S. E. P. P. Masan, Y. Hamamoto, I. Hamada, and Y. Morikawa Phil. Trans. R. Soc. A, **384**, 20240555 (2026).
   DOI:10.1098/rsta.2024.0555

3. Clarifying Photodetachment in Al_{13}^- Anions and Photoionization in Al13 Neutrals Using Diffusion Monte Carlo
   M. R. Chiong III, A. Nakajima, and Y. Morikawa J. Phys. Chem. A **130**, 1851 (2026).
   DOI:10.1021/acs.jpca.6c00226

4. Bridging the Pressure Gap in Hydrogenation of CO2 to Formate on Cu(100) by Machine-learning Molecular Dynamics and First-Principles Microkinetic Modeling
   W. O. N. F. Rajaelo †, H. H. Halim †, M. F. Anshor, Y. Yamada, S. Ramadhani, F. A. Mubarok, S. E. M. Putra, A. L. Ivansyah, T. D. K. Wungu, Suprijadi, Y. Morikawa*, and F. Muttaqien*, † These authors contributed equally ACS Catal., **16**, 5068 (2026).
   DOI:10.1021/acscatal.5c09279

5. Enhancing Atomic Structure Exploration: The Scaled-LCB and Similarity-based Structure Sharing
   S. E. P. P. Masan, T. N. Pham, K. I. M. Rojas, B. A. C. Tan, F. Rusydi, Y. Hamamoto, and Y. Morikawa, J. Ceram. Soc. Jpn. **133**, 602 (2025).
   DOI:10.2109/jcersj2.25083

MORITA, Satoshi [B class; 450 (B), 80 (C)] (350)
— *Development of tensor renormalization group method for random spin systems*

1. TeNeS-v2: Enhancement for Real-Time and Finite Temperature Simulations of Quantum Many-Body Systems
   Y. Motoyama, T. Okubo, K. Yoshimi, S. Morita, T. Aoyama, T. Kato, and N. Kawashima Comput. Phys. Commun. **315**, 109692 (2025).
   DOI:10.1016/j.cpc.2025.109692

2. Tensor renormalization group calculations of partition-function ratios
   S. Morita and N. Kawashima J. Phys. Soc. Jpn. **95**, 044001 (2026).
   DOI:10.7566/JPSJ.95.044001

Data Repository

Tensor Renormalization Group Calculations of Partition-Function Ratios
https://datarepo.mdcl.issp.u-tokyo.ac.jp/repo/63

MOTOME, Yukitoshi [C class; 9200 (B), 800 (C)] (226)
— *Theoretical study of strongly correlated quantum properties by mathematical information science*

1. Quantum reservoir probing of quantum phase transitions
   K. Kobayashi and Y. Motome Nature Communications **16**, 3871 (2025).
   DOI:10.1038/s41467-025-58751-0

2. Topological Majorana flat bands in the Kitaev model on a Bishamon-kikko lattice

K. Fukui and Y. Motome Physical Review B **112**, 14411 (2025).
DOI:10.1103/ztny-z9yb

3. Three-dimensional topological superstructure of magnetic hopfions threaded by meron strings in easy-plane magnets
S. Kasai, K. Shimizu, S. Okumura, Y. Kato, and Y. Motome Physical Review B **112**, 184424 (2025).
DOI:10.1103/l11y-9gnq

4. Spin-liquid and spin-glass behavior in quantum spin models with all-to-all p-spin interactions
S. Wadashima and Y. Motome Physical Review B **112**, 214204 (2025).
DOI:10.1103/r5d6-2cby

5. Edge of Many-Body Quantum Chaos in Quantum Reservoir Computing
K. Kobayashi and Y. Motome Physical Review Letters **136**, 040602 (2026).
DOI:10.1103/j2qj-vwcl

6. Controlling Knot Topology in Magnetic Hopfions via Spin-orbit Torque
S. Kasai, S. Okumura, and Y. Motome, accepted for publication in APS Open Science

7. Nonequilibrium dynamics of magnetic hopfions driven by spin-orbit torque
S. Kasai, S. Okumura, and Y. Motome, accepted for publication in Physical Review B

8. Kitaev Meets AKLT: Competing Quantum Disorder in Spin-3/2 Honeycomb Systems
S. Ikegami, K. Fukui, R. Pohle, and Y. Motome submitted to Physical Review B

MURAMATSU, Mayu [B class; 500 (B), 0 (C)] ()
— *Development of a FEM-MD Coupling Analysis Method*
— *Development of a MD-FEM Coupling Analysis Method*

MURAOKA, Azusa [C class; 2800 (B), 0 (C)] (110)
— *Theoretical Study Aiming at Novel Renewable Energy Materials Using First-Principles Calculations*

MURASHIMA, Takahiro [C class; 4200 (B), 350 (C)] (293)
— *Molecular dynamics simulation studies of soft matters*

1. Identifying the Threshold Chain Length for Stress Overshoot in Ring-Linear Polymer Blends under Uniaxial Elongation: The Role of Multiple Threading
T. Murashima, K. Hagita and T. Kawakatsu arXiv:2603.25505 (2026).
DOI:10.48550/arXiv.2603.25505

NADA, Hiroki [BC class; 4250 (B), 0 (C)] (296, 297)
— *A Metadynamics Simulation Study on the Mechanism of Ice VI Formation*
— *Investigation of Unknown Ice Phases Using Large-Scale Metadynamics Simulations With Unsupervised Machine Learning*

1. Multiple freezing-melting pathways of high-density ice at room temperature
Y.-H Lee, J. K. Kim, Y.-J. Kim, M. Kim, Y. C. Cho, R. J. Husband, E. Ehrenreich-Petersen, R. Bauer, F. Lehmkuhler, H.-P. Liermann, C. Strohm, K. Appel, M. Tang, Z. Konopkova, T. Eklund, K. Amann-Winkel, E. F. O ' Bannon, Z. Jenei, C.-. Yoo, H. Marquardt, H. Nada, and G. W. Lee Nat. Mater. **25**, 302 (2026).
DOI:10.1038/s41563-025-02364-x

NAKAGAWA, Naoko [C class; 4600 (B), 200 (C)] ()
— *Thermodynamics of phase separation and molecular association*

NAKAGAWA, Takeshi [B class; 900 (B), 170 (C)] (339)
— *Structural analysis of two dimensional boride using electron diffraction and DFT*
— *Surface structural analysis of single layer thin films using TensorLEED and DFT*

1. Structural investigation of pristine and Mn-intercalated flat-honeycomb bismuthene on Ag(111)
   Ziyong Zhang , Xiaobin Chen, and Takeshi Nakagawa Phys. Rev. B 113, 035436
   DOI:10.1103/nflc-z372

2. Large Hole Borophene Formation on Ni surface via Edge-Orientation Control
   X. Chen, I. Yamamoto, K. Takahashi, and T. Nakagawa, submitted

NAKAI, Fumiaki [B class; 400 (B), 0 (C)] (362)
— *Vibrated Granular System: Relation Between Viscoelastic Relaxation and Particle Dynamics*

1. Dislocation Glides in Granular Media
   F. Nakai, T. Uneyama, Y. Sasaki, K. Yoshii, and H. Katsuragi Phys. Rev. Lett. 135, 048202 (2025).
   DOI:10.1103/7g7s-c157

2. Dislocation glides in monolayered granular media: Effect of lattice constant
   F. Nakai, T. Uneyama, Y. Sasaki, K. Yoshii, and H. Katsuragi EPJ Web Conf. 340, 04008 (2025).
   DOI:10.1051/epjconf/202534004008

3. Anomalous phonon dispersion near yielding in athermal crystals
   F. Nakai, M. Otsuki, K. Saitoh, H. Katsuragi EPJ Web of Conferences
   DOI:10.48550/arXiv.2603.26825

Data Repository
Dataset for "Anomalous phonon dispersion near yielding in athermal crystals"
https://zenodo.org/records/19244125
DOI:https://doi.org/10.5281/zenodo.19244125

Dataset for "Dislocation Glides in Granular Media"
https://zenodo.org/records/14942701
DOI:https://doi.org/10.5281/zenodo.14942701

NAKAMURA, Kazuma [C class; 1000 (B), 0 (C)] (161)
— *Ab initio electronic structure analysis for Ca5Ir3O12*
— *Ab initio electronic structure calculation for grain boundary in transition metal oxides*

1. Hidden Markov model analysis of fluorescence blinking in fluorescently labeled DNA
   T. Furuta, S. Fan, T. Takada, Y. Kondo, M. Fujitsuka, A. Maruyama, K. Kawai, K. Nakamura Sci. Rep. **16**, 11306 (2026).
   DOI:10.1038/s41598-026-40876-x

2. Reflectance spectral studies of spark plasma sintered tungsten carbide pellet
   T. Chono, H. Tokutomi, K. Nakamura, K. Miyazaki Jpn. J. Appl. Phys. **64**, 010905 (2025).
   DOI:10.35848/1347-4065/ad9a43

NAKAMURA, Kohji [C class; 2800 (B), 0 (C)] (109)
— *Material search and functional creation for interfacial spin-orbitronics*

1. Interface Design for Concurrent Realization of High Perpendicular Magnetic Anisotropy and Low

Magnetic Damping in Fe/MgO
Y. N. Apriati, M. Tsuchida, M. Arifin, K. Nakamura IEEE Transactions on Magnetics **62**, 4400107 (2025).
DOI:10.1109/TMAG.2025.3620412

2. Tensor representation of four-magnon interactions Hamiltonian and magnon decay rates suppression by magnetic dipolar interactions in antiferromagnetic insulator NiO
A. Gumarilang, K. Nawa, K. Nakamura Physical Review B **113**, 024411 (2026).
DOI:10.1103/kfmn-wfkg

3. Role of Rashba spinorbit coupling for voltage-controlled magnetic anisotropy at magnetic tunnel junction interface Fe/MgO
Y.-N. Apriati, M. Tsuchida, K. Nawa, K. Nakamura Applied Physics Letters **128**, 042401 (2026).
DOI:10.1063/5.0304651

4. Tailoring Spin-Exchange Interactions and Topological Magnons in 2D Ferromagnetic van der Waals CrI_3/As via Multiple Stacking Orders
A. Gumarilang, K. Nakamura Physical Review Materials **10**, 024407 (2026).
DOI:10.1103/kd5v-grhn

NAKANO, Hiroki [C class; 2800 (B), 300 (C)] (318)
— *Numerical study on low-energy states of quantum spin systems*

1. Numerical Diagonalization Study of the Phase Boundaries of the S=2 Heisenberg Antiferromagnet on the Orthogonal Dimer Lattice
H. Nakano, T. Sakai, and Y. Hosokoshi J. Phys. Soc. Jpn. 95, 033704 (2026).
DOI:10.7566/JPSJ.95.033704

2. The Haldane Gap of the $S = 7$ Antiferromagnetic Chain
H. Nakano and T. Sakai J. Low Temp. Phys. 222, 69 (2026).
DOI:10.1007/s10909-026-03406-7

NAKANO, Hiroyoshi [C class; 8000 (B), 800 (C)] (267)
— *Development of a numerical solver for three-dimensional fluctuating hydrodynamics*
— *Numerical study of the upper critical dimension of nonequlibrium critical phenomena*

1. Symmetry-based nonlinear fluctuating hydrodynamics in one dimension
Y. Minami, H. Nakano, and K. Saito Phys. Rev. Lett. **136** 187101 (2026).
DOI:10.1103/2z9s-5d7w

2. Dissipation anomaly in gradient-driven nonequilibrium steady states
H. Nakano, and Y. Minami arXiv:2511.17851
DOI:10.48550/arXiv.2511.17851

3. Looking at bare transport coefficients in fluctuating hydrodynamics
H. Nakano, Y. Minami, and K. Saito arXiv:2502.15241
DOI:10.48550/arXiv.2502.15241

NAKASHIMA, Takeru [B class; 250 (B), 0 (C)] (212)
— *Development of the real-space topology of crystals: Fundamental research for materials discovery based on homotopy of real-space crystals.*

NAKAYAMA, Akira [C class; 2400 (B), 250 (C)] (112)
— *Multiscale simulation for liquid/oxide interface based on first-principles calculations*

NARUSE, Takuya [B class; 300 (B), 60 (C)] (205)
— *Development of On-the-fly Machine Learning Potentials in High-Accuracy Phonon Calculations*

NASU, Joji [C class; 1800 (B), 150 (C)] (242)
— *Numerical analysis of excitation spectra and thermal responses arising from quasiparticles in insulating magnets*

1. Formulation of the spin Nernst effect for spin-nonconserving insulating magnets
   S. Koyama and J. Nasu Phys. Rev. B **112**, 014447 (2025).
   DOI:10.1103/8xgc-d9ch

2. Controlling discrete time crystals via single-site operations in zero-field diamond quantum simulators
   N. Egawa, K. Mizuta, and J. Nasu Phys. Rev. B **111**, 144311 (2025).
   DOI:10.1103/PhysRevB.111.144311

3. Magnetic-Field Effect on Excitonic Condensation Emergent in Extended Falicov-Kimball Model
   N. Ohta and J. Nasu J. Phys. Soc. Jpn. **94**, 054702 (2025).
   DOI:10.7566/JPSJ.94.054702

NIKI, Kaori [C class; 1400 (B), 400 (C)] (139)
— *Electronic state calculations under photoinduced reactions*

1. Femtosecound concerted rotation of molecules on a 2D material interface
   K. Baumgrtner, M. Nozaki, M. Reuner, N. Wind, M. Haniuda, C. Metzger, M. Heber, D. Kutnyakhov, F. Pressacco, L. Wenthaus, K. Hara, K. Chordiya, C.-H. Min, M. Beye, F. Reinert, F. Roth, S. Kr Mahatha, A. Madsen, T. Wehling, K. Niki, D.P. Gorelova, K. Rossnagel, M. Scholz
   Nat. Commun C, 17, 2110 (2026).
   DOI:10.1038/s41467-026-69801-6

NISHIDATE, Kazume [C class; 600 (B), 0 (C)] (175)
— *Surface electronic structure of double perovskite*

1. Electrophoretic deposition films and photocatalytic activities for doubleperovskite oxide $Ba_2Ce(Bi,Sb)O_6$
   H. Sakou, K. Hata, M. Matsukawa, M. Arakida, K. Nishidate, S. Aisawa, K. Akiba, and D.C. Roy
   J Mater Sci: Mater Electron **36**, 1800 (2025).
   DOI:10.1007/s10854-025-15846-0

Data Repository
Computer simulation with C
http://web.cc.iwate-u.ac.jp/ñisidate/main.pdf

NISHIGUCHI, Kazutaka [B class; 300 (B), 60 (C)] (203)
— *First-principles study of point defects in perovskite photocatalyst $PbTiO_3$*

NISHIKAWA, Yoshihiko [C class; 3400 (B), 0 (C)] (309)
— *Numerical study on finite-time non-equilibrium phase transitions*

NOGUCHI, Hiroshi [C class; 4800 (B), 400 (C)] (287)
— *structure formation of biomembrane*

1. Dynamic modes of active Potts models with factorizable numbers of states
   H. Noguchi Phys. Rev. Res. 7, 033243 (2025).
   DOI:10.1103/w1fg-6qmv

2. Coarsening dynamics for spiral and disordered waves in active Potts models
H. Noguchi Phys. Rev. E 113, 054108 (2026).
DOI:10.1103/sc5g-rpvs

3. Spiral, target, stripe, and disordered waves in active six-state Potts models
H. Noguchi arXiv:2604.22353
DOI:10.48550/arXiv.2604.22353

Data Repository
Data of Monte Carlo Simulations of Active Potts Models
https://isspns-gitlab.issp.u-tokyo.ac.jp/hiroshi.noguchi/activePotts

NOGUCHI, Yoshifumi [C class; 7800 (B), 750 (C)] (57)
— *Development of full-frequency electron-hole interaction kernel*
— *Development of self-interaction-corrected GWΓ method*

1. Significance of self-interaction corrections in the GWΓ method
T. Isago, Y. Noguchi, and K. Ohno Phys. Rev. B, **111**, 195146 (2025).
DOI:10.1103/PhysRevB.111.195146

NOMURA, Yusuke [E class; 13000 (B), 1000 (C)] (221)
— *Study on nickelate superconductors using transformer-based wave functions*

1. Strong-coupling high- superconductivity in doped correlated band insulators
Yusuke Nomura, Motoharu Kitatani, Shiro Sakai, and Ryotaro Arita Phys. Rev. B **112**, L020504 (2025).
DOI:10.1103/dygc-94fq

NOZAWA, Kazuki [C class; 1600 (B), 500 (C)] (133)
— *First-principles study of surface atomic structure and chemical properties of intermetallic compounds*

1. Creation of novel Pd single-atom catalysts using complex intermetallic compound $Al_{13}Fe_4$
M. Hanaoka, S. Iwado, K. Nozawa, M. Aoyama, S. Ohhashi, N. Fujita, and S. Kameoka Applied Materials Today, ¥bf 46, 102878 (2025).
DOI:10.1016/j.apmt.2025.102878

2. Toward Accurate Modeling of Aperiodic Surfaces: Cluster-Based DFT Analysis of Pentacene on Cu(111) Surface
M. Sato and K. Nozawa Materials Transactions, in press

NUNOURA, Teppei [B class; 600 (B), 0 (C)] (174)
— *Interface characterization and performance optimization of Ni/CeO_2-Al_2O_3 catalysts: A combined DFT and experimental study*
— *Theoretical study on catalytic hydrogenolysis mechanism of lignin structural units over Ni/CeO_2-Al_2O_3 based on first-principle calculations*

OBATA, Masao [B class; 750 (B), 180 (C)] (168)
— *Development of quasiparticle self-consistent GW calculation code and its application to interfacial materials*
— *Development of quasiparticle self-consistent GW calculation code and its application to metals and magnetic materials*

1. Efficient implementation of the quasiparticle self-consistent GW method on GPU
Masao Obata, Takao Kotani, Tatsuki Oda Comp. Mat. Sci. 260, 114190 (2025).
DOI:10.1016/j.commatsci.2025.114190

OCHI, Masayuki [C class; 5000 (B), 0 (C)] (76)
— *Development of the optimization method for the long-range correlation factor in the first-principles wave-function theory*

1. Theoretical study on the possibility of high T_c $s\pm$-wave superconductivity in heavily hole-doped infinite layer nickelates
   H. Sakakibara, R. Mizuno, M. Ochi, H. Usui, and K. Kuroki Phys. Rev. B **111**, 224511 (2025).
   DOI:10.1103/nl4m-n5dx

2. Possible high thermoelectric power factor in alkali-metal-intercalated BC_3: Anisotropic multiple valleys originating from the van Hove singularity of graphene
   R. Enami, K. Kuroki, and M. Ochi Phys. Rev. Mater. **9**, 084001 (2025).
   DOI:10.1103/rqrv-7hqt

ODA, Masato [B class; 400 (B), 0 (C)] ()
— *Diffusion reactions of large defects in GaN and GaN/AlN*

ODA, Tatsuki [C class; 7000 (B), 750 (C)] (60, 61)
— *Analyses on electronic structure and magnetic anisotropy in high-performance spintronics magnetic materials and development/application in quasi-particle self-consistent GW code*
— *Development/application in quasi-particle self-consistent GW and analyses on magnetic anisotropy in spintronics magnetic materials*

1. Layer-resolved Rashba spin-orbit coupling of ferromagnetic interface from a first-principles study
   I. Pardede, M. Obata, D. Yoshikawa, T. Kanagawa, N. Ikhsan, and T. Oda Key Engineering Materials, **1015**, 23 (2025).
   DOI:10.4028/p-3gsPr4

2. Efficient implementation of the quasiparticle self-consistent GW method on GPU
   M. Obata, T. Kotani, and T. Oda Computational Materials Science, **260**, 114190 (2025).
   DOI:10.1016/j.commatsci.2025.114190

3. Role of magnetic ordering on transformation properties of Heusler Ni_2MnGa magnetic shape memory alloy
   J. Lutinec, M. Obata, P. Sedlk, J. Hamrle, H. Seiner, O. Heczko, and T. Oda J. Phys.: Condens. Matter, **38**, 015502 (2026).
   DOI:10.1088/1361-648X/ae2a9a

4. Machine learning band gap predictions: linking quasiparticle self-consistent GW and LDA-derived partial density of states
   S. Takano, T. Kotani, M. Obata, K. Sato, H. Saito, and T. Oda Jpn. J. Appl. Phys., **65**, 031002 (2026).
   DOI:10.35848/1347-4065/ae3bc0

5. Optical and electronic spectra in a transparent transition-metal oxide $LiTi_2O_4$ from first-principles quasiparticle self-consistent GW calculations
   H. Niwa, M. Obata, T. Kotani, and T. Oda Phys. Rev. B, **113**, 155114 (2026).
   DOI:10.1103/hsmv-pgd7

OHKUBO, Yuji [B class; 850 (B), 0 (C)] (169)
— *Calculation of adsorption energy of fluorinated molecules on chromate conversion coating layer containing hydroxyl groups using DFT+U method*
— *Calculation of adsorption energy of fluorinated molecules on chromate conversion coating layer using*

DFT+U method

OHMURA, Satoshi [C class; 3600 (B), 100 (C)] (98, 99)
— *Ab Initio Molecular Dynamics Study of the Structural Instability of Ettringite under Dehydration and Rehydration Conditions*
— *Ab initio molecular-dynamics study on self-healing in cement-based hydrated minerals*

1. Local structure and mechanical properties of 1.1 nm tobermorite under compression and recompression using ab initio molecular dynamics simulations
   I. KANEMASU, and S. OHMURA High Pressure Reserch, 1-9 (2026).
   DOI:10.1080/08957959.2026.2660933

OHNISHI, Masato [E class; 21500 (B), 1900 (C)] (40)
— *Construction of anharmonic phonon property database using first-principles calculations*
— *Data creation for higher-order anharmonic phonon properties*

1. Database and deep-learning scalability of anharmonic phonon properties by automated brute-force first-principles calculations
   Masato Ohnishi, Tianqi Deng, Pol Torres, Zhihao Xu, Terumasa Tadano, Haoming Zhang, Wei Nong, Masatoshi Hanai, Zhiting Tian, Ming Hu, Xiulin Ruan, Ryo Yoshida, Toyotaro Suzumura, Lucas Lindsay, Alan J. H. McGaughey, Tengfei Luo, Kedar Hippalgaonkar, and Junichiro Shiomi npj Computational Materials
   DOI:10.1038/s41524-026-02033-w

Data Repository
Phonix
https://huggingface.co/phonix-db
DOI:10.57967/hf/8233

OHNO, Kaoru [C class; 4400 (B), 400 (C)] (78)
— *Improvement and application of all-electron mixed basis program*

1. Significance of Self-Interaction Corrections in GWΓ Method
   Tamao Isago, Yoshifumi Noguchi, and Kaoru Ohno Phys. Rev. B **111**, 195146 (2025).
   DOI:10.1103/PhysRevB.111.195146

2. First-Principles Self-Interaction Free GWΓ Simulations for First Ionization Potentials and Electron Affinities
   Tamao Isago, Yoshifumi Noguchi, and Kaoru Ohno J. Chem. Phys. **164**, 144110 (2026).
   DOI:10.1063/5.0317103

3. Temperature-dependent electron-capture decay rate of ^{7}Be in a Nb crystal
   Riichi Kuwahara, Tsutomu Ohtsuki, Hidetoshi Yamaguchi, Takashi Hashimoto, Yasuo Wakabayashi, Seiya Hayakawa, Daid Kahl, Shigeru Kubono, Kentaro Hirose, and Kaoru Ohno Phys. Rev. C **113**, 113, 044617 (2026).
   DOI:10.1103/kgsv-fgs4

OHSAWA, Kazuhito [C class; 1200 (B), 0 (C)] (154)
— *Study of interaction between radiation damage and lattice defect*

OHTSUKI, Tomi [C class; 5200 (B), 450 (C)] (279)
— *Critical behavior of measurement induced transition*

1. Universal Stochastic Equations of Monitored Quantum Dynamics
   Z. Xiao, T. Ohtsuki, K. Kawabata Phys. Rev. Lett. **134**, 140401 (2025).
   DOI:10.1103/PhysRevLett.134.140401

2. Predicting unmeasured asymmetry time spectra in μSR experiments using Random Forest
K.F. Chin, M.R. Omar, T.L. Yoon, Y. Komiyama, D.P. Sari, W.N. Zaharim, T. Ohtsuki, T. Adachi, T. Goto, I. Watanabe J. Magn. Magn. Mat. **629**, 173320 (2025).
DOI:10.1016/j.jmmm.2025.173320

3. Adaptive interpolating quantum transform: A quantum-native framework for efficient transform learning
G Budiutama, S Daimon, H Nishi, R Kaneko, T Ohtsuki, Y Matsushita Phys. Rev. A **112**, 062410 (2025).
DOI:10.1103/vyr3-h9hq

OKUBO, Tsuyoshi [C class; 9600 (B), 850 (C)] (264)
— *Novel phenomena in frustrated magnets*

1. Tensor tree learns hidden relational structures in data to construct generative models
K. Harada, T. Okubo, and N. Kawashima Machine Learning: Science and Technology **6**, 025002 (2025).
DOI:10.1088/2632-2153/adc2c7

2. TeNeS-v2: Enhancement for Real-Time and Finite Temperature Simulations of Quantum Many-Body Systems
Y. Motoyama, T. Okubo, K. Yoshimi, S. Morita, T. Aoyama, T. Kato, and N. Kawashima Computer Physics Communications **315**, 109692 (2025).
DOI:10.1016/j.cpc.2025.109692

3. Thermal Hall transport in Kitaev spin liquids
T. Okubo, J. Nasu, T. Misawa, and Y. Motome arXiv:2507.16558
DOI:10.48550/arXiv.2507.16558

4. Plastic tensor networks for interpretable generative modeling
K. O. Akamatsu, K. Harada, T. Okubo, and N. Kawashima Machine Learning: Science and Technology **7**, 015014 (2026).
DOI:10.1088/2632-2153/ae3048

OKUMURA, Hisashi [C class; 5000 (B), 400 (C)] (286)
— *Molecular dynamics simulation of disease-causing protein aggregates*

ONO, Atsushi [B class; 600 (B), 100 (C)] (247)
— *Analysis of nonlinear response functions through real-time evolution*

1. Extracting Nonlinear Dynamical Response Functions from Time Evolution
A. Ono Phys. Rev. Lett. **135**, 026401 (2025).
DOI:10.1103/qsxr-c2pq

2. Temporal modulation of second harmonic generation in ferroelectrics by a pulsed electric field
A. Ono Phys. Rev. B **112**, 115146 (2025).
DOI:10.1103/xsrf-t1hj

ONO, Shota [B class; 1300 (B), 240 (C)] (145, 146)
— *A novel framework for predicting non-van der Waals 2D materials*
— *Prediction of quasi-2D materials in non-layered materials based on stacking fault and cleavage energy calculations*
— *What can be mixed with noble metals to enhance their brightness?*

1. Composition-dependent ultrafast luminescence in Cu-Ni alloys: Combined experimental and ab initio study
   T. Suemoto, H. Morino, S. Ono, T. Okuno, T. Suzuki, K. Okazaki, S. Tani, and Y. Kobayashi Phys. Rev. B **112**, 035138 (2025).
   DOI:10.1103/xn1s-28z3

2. Framework for identifying nonvan der Waals two-dimensional materials
   S. Ono Phys. Rev. B **112**, 075403 (2025).
   DOI:10.1103/crw6-zvpx

Data Repository
Crystal structure and thin film energy for non-van der Waals 2D materials
https://zenodo.org/records/16187681
DOI:doi.org/10.5281/zenodo.16187681

ONO, Tomoya [C class; 11000 (B), 950 (C)] (46)
— *First-principles study on functionality of electronic devices*

1. Theoretical investigation of interface atomic structure of graphene on NiFe alloy substrate
   N. Matsumoto, R. Endo, M. Uemoto, and T. Ono J. Appl. Phys. **138**, 104305 (2025).
   DOI:10.1063/5.0283881

2. Effects of inserted methylene groups on structure and flexibility of molecule junction system
   M. Furushima, T. Tahara, M. Uemoto, Y. Majima, and T. Ono Jpn. J. Appl. Phys. submitted.

OSHIKAWA, Masaki [B class; 450 (B), 80 (C)] ()
— *Elucidation of conformal field theory on closed manifolds by tensor network*

OSHIYAMA, Atsushi [C class; 4000 (B), 350 (C)] ()
— *Clarification of Microscopic Mechanisms of Semiconductor Epitaxial Growth and Device-Interface Formation by Large-Scale Quantum-Theory-Based Computations*

OTSUKI, Junya [C class; 8000 (B), 300 (C)] (228)
— *Dynamical mean-field calculation of non-linear electric conductivity under magnetic toroidal ordering*
— *Study of multipolar fluctuations and cross-correlated responses by dynamical mean-field theory*

1. From localized $4f$ electrons to anisotropic exchange interactions in ferromagnetic $CeRh_6Ge_4$
   S. Itokazu, A. Kirikoshi, H. O. Jeschke, and J. Otsuki Commun. Mater. **6**, 269 (2025).
   DOI:10.1038/s43246-025-00998-7

2. Multipolar fluctuations from localized $4f$ electrons in $CeRh_2As_2$
   K. Numa, E. Matsuda, A. Kirikoshi, and J. Otsuki Phys. Rev. B **113**, 115141 (2026).
   DOI:10.1103/nw88-plgx

OTSUKI, Michio [B class; 550 (B), 90 (C)] (343)
— *Shape dependence of dynamic friction in viscoelastic materials*

OYA, Yutaka [C class; 3600 (B), 200 (C)] (305)
— *Evaluation of Self-Healing Performance and Microscopic Damage in Vitrimers via Molecular Simulations*

1. Molecular Mechanism of Disulfide Bond Healing and Network Repair in Epoxy Vitrimers Revealed by Quantum Chemical and Molecular Dynamics Simulations
   T. Uyama, N. Kishimoto, Y. Oya, T. Murashima and J. Koyanagi Polymers **18**, 861 (2026).
   DOI:10.3390/polym18070861

OZEKI, Yukiyasu [C class; 3400 (B), 500 (C)] (303)
— *Deepening studies for critical universality with high precision dynamical scaling analysis*
— *High precision study on critical phenomena by relaxation analysis of fluctuations using machine learning*

PETERS, Robert [C class; 2200 (B), 350 (C)] (238)
— *Nonequilibrium phenomena in strongly correlated systems*
1. The toric code under antiferromagnetic isotropic Heisenberg interactions
W. Jang, R. Peters, T. Posske arXiv:2603.05707 (under review).

PHUNG, Manh Quan [C class; 600 (B), 0 (C)] ()
— *Density Functional Theory Investigation of Sodium Intercalation and Ion Migration Mechanisms in Next-Generation Battery Electrode Materials*

POHLE, Rico [C class; 2200 (B), 250 (C)] (241)
— *Dynamical properties of spin nematic phases*
1. Electron-phonon coupled Langevin dynamics for Mott insulators
R. Pohle, Y. Motome, T. Tadano, and S. Hoshino preprint (arXiv:2507.19764)
DOI:10.48550/arXiv.2507.19764

RAEBIGER, Hannes [C class; 4000 (B), 350 (C)] (85)
— *High-entropy MXenes and MAX-phase materials*
1. Prediction of superconductivity in haeckelite compounds using first-principles calculations
K. Hamidi, M. Keivanloo, M. Sandoghchi, M. R. Mohammadizadeh, H. Raebiger, K. Hongo, R. Maezono, K. Ohno, and M. Khazaei iScience **28**, 113219 (2025).
DOI:10.1016/j.isci.2025.113219

2. Diverse surface reconstructions in MAX phases
M. Khazaei, M. Bagheri, A. Ranjbar, S. Bae, R. Khaledialidusti, Y. Mochizuki, T. D. Kühne, K. Shudo, H. Raebiger, H.-P. Komsa, and H. Hosono Nanoscale **17**, 24184 (2025).
DOI:10.1039/D5NR02421H

SAKAGUCHI, Norihito [C class; 7600 (B), 0 (C)] (62)
— *Reduction of Rare Metals in Fuel Cell and Formic Acid Decomposition Catalysts*
1. Real-Space Observation of Spin-Induced Lattice Distortion of O_2 Monolayers Revealed by Atomic Force Microscopy
M. Kimura, Y. Kunisada, and Y. Sugimoto ACS Nano **20**, 2633 (2026).
DOI:10.1021/acsnano.5c11357

2. Tailoring Catalytic Properties via Light-Element Doping into Graphene Supports
Y. Kunisada, K. Sato, and N. Sakaguchi Vacuum and Surface Science **69**, 135 (2026).
DOI:10.1380/vss.69.135

SAKAI, Shiro [B class; 450 (B), 90 (C)] (347)
— *Numerical simulation of disordered hyperuniform electron systems*

SAKAI, Toru [C class; 5600 (B), 300 (C)] (275, 277)
— *Magnetization Process of the S=3/2 Antiferromagnetic Chain*
— *Numerical Study on the Magnetization Process of the S=1 Spin Ladder*

1. Translational-Symmetry-Broken Magnetization Plateaux of the $S = 3/2$ Anisotropic Antiferromagnetic Chain
T. Kawatsu, H. Suzuki, M. Hashimoto, K. Doi, T. Houda, R. Furuchi, H. Nakano, K. Okamoto, T. Sakai Journal of the Physical Society of Japan, 94, 064701 (2025).
DOI:10.7566/JPSJ.94.064701-1-7

2. Possible Spin Gap Transition of ESR at the Magnetization Plateau of the Distorted Diamond Spin Chain
T. Sakai Applied Magnetic Resonance, 56, 1499 (2025).
DOI:10.1007/s00723-025-01788-7

3. Translational Symmetry Broken Magnetization Plateau of the S=1/2 Anisotropic Spin Ladder with Ferromagnetic Rung Interaction
T. Sakai, K. Doi, K. Okamoto, K. Okunishi, M. Hashimoto, T. Houda, R. Furuchi, and H. Nakano Journal of Physics: Conference Series, 3161, 012004 (2026).
DOI:10.1088/1742-6596/3161/1/012004

4. Magnetization Plateau of the S=1/2 Distorted Diamond Spin Chain with Ferromagnetic Interaction
M. Hashimoto, K. Doi, T. Houda, R. Furuchi, H. Nakano, K. Okamoto, T. Sakai Journal of Physics: Conference Series, 3161, 012006 (2026).
DOI:10.1088/1742-6596/3161/1/012006

5. Field-Induced Spin Nematic Liquid of the S=1/2 Kondo Necklace Spin Chain
R. Hasegawa, Y. Hamazaki, T. Kawatsu, H. Suzuki, T. Houda, H. Nakano, K. Okamoto and T. Sakai AIP Advances 16, 025102 (2026).
DOI:10.1063/9.0000960

6. Magnetization plateau of the S = 1 spin ladder with anisotropies
Y. Hamazaki, R. Hasegawa, T. Kawatsu, H. Suzuki, T. Houda, H. Nakano, K. Okamoto and T. Sakai AIP Advances 16, 025302 (2026).
DOI:10.1063/9.0000956

7. Spin nematic phase of the ferromagnetic dimer system on the Shastry-Sutherland lattice
T. Sakai AIP Advances 16, 025006 (2026).
DOI:10.1063/9.0000952

8. Magnetization Plateaus of the Antiferromagnetic Chain with Competing Anisotropies
T. Sakai, T. Houda, T. Kawatsu, H. Suzuki, R. Hasegawa, Y. Hamazaki, H. Nakano, K. OKamoto Journal of Low Temperature Physice. 222, 1 (2026).
DOI:10.1007/s10909-025-03333-z

9. The Haldane Gap of the S = 7 Antiferromagnetic Chain
H. Nakano and T. Sakai Journal of Low Temperature Physics. 222, 69 (2026).
DOI:10.1007/s10909-026-03406-7

10. Spin excitation of the Heisenberg antiferromagnet with frustration: from the bounce-lattice antiferromagnet through the maple-leaf-lattice antiferromagnet to the exact-dimer system
H. Nakano and T. Sakai to appear in Zeitschrift für Naturforschung A

SAKAKIBARA, Hirofumi [CD class; 7700 (B), 730 (C)] (58)
— Study of unconventional multi-orbital and -layer superconductors in first-principles
— Theoretical exploration of ambient pressure superconducting materials based on multilayer mixed anion nickel oxide systems

1. Theoretical study on the possibility of high T_c $s\pm$-wave superconductivity in heavily hole-doped infinite layer nickelates
H. Sakakibara, R. Mizuno, M. Ochi, H. Usui, K. Kuroki Phys. Rev. B 111, 224511 (2025).
DOI:10.1103/PhysRevB.109.L201124

SAKASHITA, Tatsuya [B class; 150 (B), 140 (C)] ()
— *Development of integrated interface of eigensolvers Rokko and application to quantum spin systems*

SASAKI, Takehiko [C class; 3600 (B), 600 (C)] (87, 88)
— *Study on poisoning of Pt nanoparticles with sulfur by first principles calculations*
— *Study on surface diffusion of adsorbed hydrogen atoms on Ru(001)*
1. Cyclic Voltammetry − Synchronized Operando HERFD-XANES and RIXS Analyses of Adsorbed Structures and Bonding States of Active Oxygen Species on Pt Nanoparticle Electrocatalysts in PEFC
H. Ariga-Miwa, T. Sasaki, T. Sakata, K. Higashi, T. Yoshida, O. Sekizawa, T. Kaneko, T. Uruga, and Y. Iwasawa ACS Catal. **15**, 9856 (2025).
DOI:10.1021/acscatal.5c01160

SATO, Naoki [AC class; 3300 (B), 50 (C)] (106)
— *Complementary analysis of chemical pressure and lattice dynamics in complex crystal structures*
— *Effects of anomalous chemical bonding and local structures on thermal transport and thermoelectric properties*

SATO, Ryuhei [C class; 2400 (B), 0 (C)] (124)
— *Understanding the super high-pressure synthesis of superhydride by machine-learning MD simulation*
1. Surface melting–driven hydrogen absorption for high-pressure polyhydride synthesis
Ryuhei Sato, Lewis J. Conway, Di Zhang, Chris J. Pickard, Kazuto Akagi, Kartik Sau, Hao Li, and Shin-ichi Orimo Proceedings of the National Academy of Sciences USA 122, e2413480122 (2025).
DOI:10.1073/pnas.2413480122

2. Visualizing Concerted Ion Migration of Superionic Conductors via Directed Graphs
Ryuhei Sato, Yasunobu Ando, Kartik Sau, and Yasushi Shibuta Chemistry of Materials 38, 287 (2026)..
DOI:10.1021/acs.chemmater.5c02374

3. Competing Hydrogenation Pathways to Metastable CaH_6 Revealed by Machine-Learning-Potential Molecular Dynamics
Ryuhei Sato, Peter I. C. Cooke, Maelie Causse, Hung Ba Tran, Seong Hoon Jang, Di Zhang, Hao Li, Shin-ichi Orimo, Yasushi Shibuta, Chris J. Pickard arXiv:2603.08950
DOI:10.48550/arXiv.2603.08950

SATO, Shunsuke [C class; 3600 (B), 0 (C)] (15)
— *Microscopic investigation on light-induced nonlinear and ultrafast phenomena in semiconductors*
1. Polarized Houston State Framework for Nonequilibrium Driven Open Quantum Systems
Shunsuke A. Sato, Hannes Hübener, Umberto De Giovannini, Angel Rubio arXiv:2507.20160
DOI:10.48550/arXiv.2507.20160

SATO, Takeshi [B class; 400 (B), 70 (C)] (351)
— *Phase structure and rheology in polymer blends: A molecular dynamics simulation study*

SAU, Kartik [C class; 2200 (B), 0 (C)] (129)
— *Designing Advanced Hydride Materials Toward Next-Generation Battery, Hydrogen Storage and Heat Management Systems using Computer Simulation*

SEINO, Kaori [C class; 3600 (B), 550 (C)] (91)
— *First-principles study of surface and defect systems for power-electronics materials II*

1. Atomic and electronic structures of point defects related to vacancy-mediated mechanism of Mg diffusion in GaN
   K. Seino , K. Shiraishi, and A. Oshiyama Jpn. J. Appl. Phys. **64**, 121004 (2025).
   DOI:10.35848/1347-4065/ae2174

2. Diffusion mechanisms via vacancies of a magnesium acceptor in gallium nitride
   K. Seino, K. Shiraishi, and A. Oshiyama Phys. Rev. B **113**, 045201 (2026).
   DOI:10.1103/ybl9-fqwz

SEKI, Yuya [B class; 350 (B), 60 (C)] ()
— *Analysis of Ising model in statistical-mechanical informatics*

SEO, Insung [C class; 1200 (B), 0 (C)] (152)
— *First-principles study on magnetocrystalline anisotropy of $RFe_{12}X$*

1. Lithiation of Epitaxial Monolayer Borophene
   Kamal, Sherif ; Seo, Insung; Cojocariu, Iulia; Jugovac, Matteo; Locatelli, Andrea; Gohda, Yoshihiro; Kralj, Marko; Mente, Tevfik; Petrovi, Marin In revision

SHIMADA, Takahiro [B class; 1050 (B), 190 (C)] (150)
— *Ab initio DFT study of lattice defect electronic structures for emergent polar skyrmions*
— *First-principles lattice defects engineering for polar skyrmions and their lattices*

SHIMAMURA, Kohei [C class; 2000 (B), 250 (C)] (126)
— *Improving Stability of Molecular Dynamics Simulation using Machine-Learning Interatomic Potentials II*

SHIMIZU, Koji [C class; 8000 (B), 800 (C)] (56)
— *Analysis of Atomic and Ionic Behavior in Complex Structures Using First-Principles Calculations and Machine Learning*
— *Atomic and Ionic Behavior Analysis in Complex Structures via First-Principles Calculations and Machine Learning*

1. Construction of machine learning potentials toward the exploration of alloy cluster catalysts
   K. Miyamoto, K. Shimizu, A.K.A. Lu, and S. Watanabe e-J. Surf. Sci. Nanotechnol. **23**, 188 (2025).
   DOI:10.1380/ejssnt.2025-028

2. Charge States of Ions around Σ 5(310)/[001] Grain Boundary in Cubic-ZrO2 Revealed by First-Principles Calculations
   S. Arai, K. Shimizu, A.K.A. Lu, H. Masuda, H. Yoshida, S. Watanabe e-J. Surf. Sci. Nanotechnol. **23**, 323 (2025).
   DOI:10.1380/ejssnt.2025-044

3. Reactivity of high-entropy alloy CoCuFeMnNi surface toward CO adsorption and CO2 conversion processes: A combined density functional theory and machine learning study
   E.R. Beronio, M. Palmero, H.O. Tubalinal, A.N. Hipolito, T. Chookajorn, K. Shimizu, A.A. Padama Surf. Interfaces **82**, 108457 (2026).
   DOI:10.1016/j.surfin.2026.108457

4. Study of the ion mobility in defect-laden ZrO2 under an electric field using neural network with predictions for Born effective charges
   A.K.A. Lu, N. Maekawa, A. Ikeda, K. Shimizu, H. Masuda, H. Yoshida, S. Watanabe Phys. Rev. Mater. under review.

5. Exploring the low-temperature synthesis pathway of lithium ionic conductor garnet-type solid electrolytes
   K. Onoue, A. Nasu, Y. Douchi, S. Mori, H. Kobayashi, K. Shimizu, M. Matsui ACS Appl. Energy Mater. under review.

6. Distance-Insensitive Graph Neural Networks and Multi-Task Learning for Accurate Prediction of Adsorption Energies on Alloy Nanoclusters
   K. Otsuka, A.K.A. Lu, K. Shimizu, S. Watanabe Computer. Mater. Sci. under review.

SHIMIZU, Makoto [C class; 5200 (B), 0 (C)] (230)
— *Spin fluctuations and superconductivity in UTe2 under pressure*
— *Spin fluctuations and superconductivity in heavy-fermion systems*

SHIMOJO, Fuyuki [C class; 3200 (B), 300 (C)] (101)
— *First-Principles Molecular-Dynamics Study of Structural and Electronic Properties of Disordered Materials under Extreme Conditions*

1. Bonding nature of Cu^{2+} in distorted tetragonal pyramidal coordination in clinoclase and callaghanite
   Masaaki Misawa, Akira Yoshiasa, Fuyuki Shimojo, Makoto Tokuda, Satoko Ishimaru, Kazumasa Sugiyama J. Mineral. Petrol. Sci. **120**, 240925 (2025).
   DOI:10.2465/jmps.240925

2. Intermolecular Correlations in Liquid Racemic Lactic Acid: A Comparison with Liquid L-Lactic Acid
   K. Ito, H. Shimakura, S. Tahara, K. Ohara, A. Koura, K. Shimamura, and, and F. Shimojo J. Phys. Soc. Jpn. **94**, 044604 (2025).
   DOI:10.7566/JPSJ.94.044604

3. Structural Insights into Liquid Malic and Lactic Acids from First-Principles Simulations and X-ray Diffraction
   Wataru Sugimoto, Kai Ito, Hironori Shimakura, Shuta Tahara, Koji Ohara, Akihide Koura, Kohei Shimamura, and Fuyuki Shimojo J. Phys. Soc. Jpn. **95**, 014602 (2026).
   DOI:10.7566/JPSJ.95.014602

SHIMOKAWA, Tokuro [C class; 9400 (B), 850 (C)] (266)
— *Multipartite entanglement in quantum frustrated magnets*

SHINAOKA, Hiroshi [B class; 500 (B), 90 (C)] ()
— *Parallelizing quantics tensor cross interpolation*

SHINODA, Wataru [E class; 28000 (B), 2200 (C)] (258)
— *Large-Scale Molecular Simulations of Soft Matter Using All-Atom and Coarse-Grained Models*
— *Large-scale Molecular Simulation of Soft Materials using All-Atom and Coarse-Grained Model*

1. SPICA Force Field for Nucleic Acids and Its Application to Lipid Nanoparticles
   Akhil Pratap Singh, Hiroki Tanaka, Yusuke Miyazaki, Wataru Shinoda J. Phys. Chem. B **129**, 7939 (2025).
   DOI:10.1021/acs.jpcb.5c01729

2. In Silico Study of Ionizable Lipid Nanoparticles Using the SPICA Force Field
Akhil Pratap Singh, Hiroki Tanaka, Yusuke Miyazaki, Shusaku Nagano, Wataru Shinoda J. Chem. Theory Comput. **21**, 6226 (2025).
DOI:10.1021/acs.jctc.5c00498

3. Unraveling the Molecular Mechanism of Transient Multilamellar Formation in Ethanol-Modified Vesicle Solutions
Kana Shibata, Masatoshi Maeki, Manabu Tokeshi, Wataru Shinoda Langmuir **41**, 13372 (2025).
DOI:10.1021/acs.langmuir.5c01139

4. A Melittin-Derived Peptide with Improved Cytosolic Delivery Efficiency through Caveolae-and Actin-Mediated Endocytosis
Yoshimasa Kawaguchi, Naoki Tamemoto, Yusuke Uehata, Yusuke Miyazaki, Wataru Shinoda, Shiroh Futaki Chem. Pharm. Bull. **73**, 896 (2025).
DOI:10.1248/cpb.c25-00479

5. Molecular Insight into the Hepatitis B Virus: Coarse-Grained Simulations of the EnvelopeCapsid Complex
Ryo Urano, Wataru Shinoda J. Phys. Chem. Lett. **17**, 77 (2026).
DOI:10.1021/acs.jpclett.5c03156

6. Asymmetry and Heterogeneity in the Plasma Membrane
Teppei Yamada, Wataru Shinoda Biophys. J. **125**, 387 (2026).
DOI:10.1016/j.bpj.2025.06.026

7. Hydrophobicity-Governed Protein Adsorption on Poly (ω-methoxyalkyl acrylate) Surfaces: A Coarse-Grained Molecular Dynamics Study
Hari OS Yadav, An-Tsung Kuo, Shingo Urata, Kosuke Funahashi, Yutaka Imamura, Wataru Shinoda J. Chem. Theory Comput. **21**, 10561 (2025).
DOI:10.1021/acs.jctc.5c01218

8. Structural insights into a citrate transporter that mediates aluminum tolerance in barley
Tran Nguyen Thao, Namiki Mitani-Ueno, Ryo Urano, Yasunori Saitoh, Peitong Wang, Naoki Yamaji, Jian-Ren Shen, Wataru Shinoda, Jian Feng Ma, Michihiro Suga Proc. Natl. Acad. Sci. U.S.A. **122**, e2501933122 (2025).
DOI:10.1073/pnas.2501933122

9. Membrane Pore Formation Unveiled by ∞ RETIS Path Sampling: From Thinning to Flip-Flop
Daniel Tianhou Zhang, Lukas Baldauf, Grzegorz Lazarski, Titus S van Erp, Wataru Shinoda J. Chem. Theory Comput. **22**, 3072 (2026).
DOI:10.1021/acs.jctc.5c01814

10. Design of Liquid Electrolytes for Next-Generation Batteries Based on Analysis of Ion Dynamics
Keisuke Shigenobu, Seiji Tsuzuki, Wataru Shinoda, Kazuhide Ueno BUNSEKI KAGAKU **74**, 427 (2025).
DOI:10.2116/bunsekikagaku.74.427

11. Discrepant lithium transference numbers due to heterogeneous speciation
Frederik Philippi, Yuna Matsuyama, Simon Buyting, Taku Sudoh, Keisuke Shigenobu, Wataru Shinoda, Monika Schnhoff, Masayoshi Watanabe, Kazuhide Ueno Phys. Chem. Chem. Phys. **27**, 15185 (2025).
DOI:10.1039/D5CP00222B

12. Polymer‐Assisted Supercooled Lithium Salts: Nonflammable Single‐Ion Conducting Liquid Elec-

trolytes for Next - Generation Batteries
Taku Sudoh, Keisuke Shigenobu, Frederik Philippi, Choji Niwamura, Yosuke Ugata, Yuna Matsuyama, Shinji Kondou, Seiji Tsuzuki, Saki Sawayama, Kenta Fujii, Wataru Shinoda, Kazuhide Ueno Adv. Energy Mater. **16**, e05229 (2026).
DOI:10.1002/aenm.202505229

SHINOHARA, Yasushi [C class; 1000 (B), 0 (C)] (160)
— *First-principles simulations for time-resolved diffraction imaging of crystalline solids*

SHIOMI, Junichiro [E class; 21000 (B), 1600 (C)] ()
— *Analysis of phonon transport properties in surface modified systems*
— *Disorder-Driven Phonon Engineering for Advanced Thermal Management in Twisted and Amorphous Materials*

SHIRAI, Tatsuhiko [B class; 350 (B), 0 (C)] (371)
— *Scrambling in long-range interacting quantum systems*

1. Out-of-time-order correlator computation based on a discrete truncated Wigner approximation
   T. Shirai, and T. Mori Phys. Rev. B **112**, 014309 (2025).
   DOI:10.1103/lxwb-ql9q

SHIRAISHI, Kenji [C class; 10300 (B), 0 (C)] (50, 51)
— *Clarification of Atomic Level Operation Mechanism of New Vibration-Powered Generator Using Si/SiO2 Interfaces*
— *Theoretical Studies on the Electron Traps in a-SiN for Flash Memory Application*

1. Space-induced floating electronic states in non-stoichiometric amorphous silicon nitride for memory devices applications
   M. Boero, K. Shiraishi, T. Nagahashi, F. Nanataki, and A. Oshiyama Phys. Rev. Materials **9**, 084601(2025).
   DOI:10.1103/mc16-76ck

SHUDO, Ken-Ichi [B class; 400 (B), 80 (C)] (184)
— *Band tuning of ZnO with varied impurity*

SUGINO, Osamu [C class; 2400 (B), 200 (C)] (119)
— *Mechanism of fast ion conductivity*

1. Elucidation of superionic conduction in K2NiF4-type BaLi oxyhydride from a first-principles molecular dynamics study
   J. Haruyama, F. Takeiri, G. Kobayashi, and O. Sugino J. Mater. Chem. A, 14, 8332 (2026).
   DOI:10.1039/D5TA08063K

SUMITA, Shuntaro [B class; 550 (B), 0 (C)] (345)
— *Theoretical study on cooperative phenomena between magnetism and superconductivity in electron systems with multiple degrees of freedom*

1. Phase-modulated superconductivity via altermagnetism
   S. Sumita, M. Naka, and H. Seo Phys. Rev. B **112**, 144510 (2025).
   DOI:10.1103/3k12-2467

SUMIYA, Yosuke [B class; 1000 (B), 180 (C)] ()
— *Elucidation of principles for the polymer adhesion based on first-principle calculations*
— *Theoretical elucidation of adhesion principle in polymers based on first-principle calculations*

SUN, Rongyan [B class; 650 (B), 0 (C)] (173)
Elucidation of Chemical Reaction Mechanisms at the Frictional Interface in Plasma-assisted Polishing via First-Principles Calculations
— *Elucidation of Interfacial Chemistry in Plasma-Assisted Polishing Using First-Principles Calculations*

1. Plasma-assisted polishing with silicon and silica plates: Comparison of interaction mechanism and achievement of atomically flat surfaces on single- and polycrystalline diamond
   J. Dong, S. Sugihara, K. Fujiwara, R. Sun, Y. Ohkubo, J. Wang, T. Suga, and K. Yamamura
   Journal of Materials Processing Technology, 348, 119187 (2025).
   DOI:10.1016/j.jmatprotec.2025.119187

SUWA, Hidemaro [C class; 3400 (B), 350 (C)] (234)
— *Novel magnetic order induced by spin-charge coupling in bilayer systems*

1. Thermally quenched metastable phase in the Ising model with competing interactions
   H. Oike, H. Suwa, Y. Takahashi, and F. Kagawa Phys. Rev. B 112, 064409 (2025).
   DOI:10.1103/ydc4-cfrm

2. Contrasting magnetic behavior in MnSc2X4 (X=S,Se) spinel compounds investigated by magnetoelastic studies
   J. Grumbach, J. Sourd, M. Deeb, A. Miyata, H. Suwa, T. Gottschall, A. Hauspurg, S. Chattopadhyay, M. Rotter, S. Granovsky, L. Prodan, V. Tsurkan, S. Zherlitsyn, M. Doerr, and J. Wosnitza
   Phys. Rev. B 112, 214415 (2025).
   DOI:10.1103/479d-4jvy

3. Unified Description of Spin-Lattice Coupling and Thermodynamics in the Pyrochlore Heisenberg Antiferromagnet
   M. Gen, H. Suwa, S. Imajo, C. Dong, H. Ueda, M. Tachibana, A. Ikeda, K. Kindo, and Y. Kohama
   Phys. Rev. Lett. 136, 116702 (2026).
   DOI:10.1103/8c73-l4nk

SUZUKI, Takafumi [C class; 1400 (B), 250 (C)] (335)
— *Temperature dependence of specific heat in an extended Kitaev model on a honeycomb lattice*

SUZUKI, Takehito [B class; 100 (B), 30 (C)] (376)
— *Analysis of phase transition in complexity of sentences based on combinatory categorial grammar*
— *Understanding the characteristics of sentence production based on differences in language acquisition methods*

SUZUKI, Yuji [C class; 5800 (B), 650 (C)] (67)
— *Simulation of Metal Nitriding by Ammonia Flame*

1. Molecular dynamics simulation of nitrogen diffusion in iron and iron nitrides using ab initio data trained machine learning potentials
   Peijie Feng, Aditya Dilip Lele, Minhyeok Lee, Yiguang Ju, Yuji Suzuki Physical Chemistry Chemical Physics **28**, 9341 (2026).
   DOI:10.1039/D6CP00172F

2. Prediction of Nitrogen Diffusion into Iron-Based Materials under High Temperature
   Peijie Feng, Minhyeok Lee, Yuji Suzuki 62nd NHTS/HTSJ Int. Heat Transf. Symp., Okinawa, Japan, IGS15-2-01, (2025).

TADA, Kohei [C class; 400 (B), 300 (C)] (171)
— *Establishment of guidelines for controlling open-shell nature of molecules by solids*

1. Efficient Hydrogenation of Nitrobenzene to Aniline over a Palladium Carbide Nanocube Catalyst
   S. Yamaguchi, M. Sarmiento-Diaz, T. Kawakami, K. Tada, T. Mitsudome, and T. Mizugaki ACS Appl. Nano Mater. **8**, 13886 (2025).
   DOI:10.1021/acsanm.5c02582

2. Toward a deeper understanding of HNi3C interactions: rule-based insights
   K. Tada, K. Matsuyama, S. Yamaguchi, R. Kishi, T. Mizugaki, and Y. Kitagawa Phys. Chem. Chem. Phys. **28**, 1118 (2026).
   DOI:10.1039/d5cp02869h

3. Local structural evolutions of the Na23(Mn23Ni13)O2 with two different crystallinities during Na extraction/insertion using in situ PDF analysis
   R. Kataoka, A. Machida, K. Tada, N. Taguchi, and N. Takeichi Electrochim. Acta **549**, 148038 (2026).
   DOI:10.1016/j.electacta.2025.148038

4. A theoretical study of singly occupied molecular bands and their magnetic character in one-dimensional trioxotriangulene chains
   Y. Kitano, K. Tada, R. Hirota, T. Kawakami, R. Kishi, and Y. Kitagawa Bull. Chem. Soc. Jpn. **99**, uoag036 (2026).
   DOI:10.1093/bulcsj/uoag036

5. Stabilization of isolated Fe atoms on a 1-nm-thick MgO/Fe(001) insulating surface via critical tunneling for a robust quantum spin platform
   T.K. Yamada, N.K.M. Nazriq, and K. Tada Appl. Surf. Sci. Adv. **33**, 100965 (2026).
   DOI:10.1016/j.apsadv.2026.100965

6. Impact of the surface energy of the layered Na2/3(Mn2/3Ni1/3)O2 on the structural change at higher state of charge
   R. Kataoka, Y. Kitano, K. Tada, Y. Kitagawa, and N. Takeichi J. Alloy Comp., under review

7. Controlling the Ligand Spin of Surface-Adsorbed Double-Decker Phthalocyaninato Complexes: Suggestions Based on Theoretical Calculations
   R. Hirota, K. Tada, K. Ikenaga, K. Katoh, R. Kishi, and Y. Kitagawa J. Phys. Chem. C, under review

8. Rechargeable battery reaction mechanisms of tribromotrioxotriangulene crystal investigated by density functional theory calculations
   Y. Kitano, K. Tada, T. Kawakami, R. Kishi, and Y. Kitagawa J. Phys. Chem. C, under review

TADA, Yasuhiro [C class; 2200 (B), 250 (C)] (240)
— *Study of quantum many-body systems under external fields*

1. Diagnosing energy gap in quantum spin liquids via polarization amplitude
   T. Yokoyama and Y. Tada arXiv:2602.12990

TAHARA, Shuta [B class; 300 (B), 60 (C)] ()
— *Structure and ionic diffusion of liquid AgI-RbI system*

TAKAHASHI, Jun [E class; 13000 (B), 1000 (C)] (262)
— *Physical and Computational Phase Diagrams for Quantum and Classical Spin Models*

1. Plastic tensor networks for interpretable generative modeling

Katsuya O Akamatsu*, Kenji Harada, Tsuyoshi Okubo, and Naoki Kawashima Mach. Learn.: Sci. Technol. 7 015014 (2026).
DOI:10.1088/2632-2153/ae3048

TAKAYAMA, Akari [B class; 400 (B), 0 (C)] ()
— *Structure analysis of atomic layer alloy with Rashba-type superconductor studied by TRHEPD*

TAKEMORI, Nayuta [C class; 200 (B), 100 (C)] (374)
— *Superconductivity properties in 12-fold symmetrical quasicrystals*

1. Photonic band gap properties of two-dimensional quasiperiodic tiling approximants
   Nayuta Takemori and Akiji Yamamoto J. Phys.: Condens. Matter **37**, 355701 (2025).
   DOI:10.1088/1361-648X/adfbb9

TAMAYA, Tomohiro [C class; 3200 (B), 350 (C)] (307)
— *Polarized Spin Magnetization Accumulation on Semiconductor Surfaces Under Intense Light Irradiation*

TANAKA, Katsuhiro [B class; 900 (B), 170 (C)] (156)
— *First-principles calculation of tunnel magnetoresistance effect with antiferromagnetic materials*
— *Study on control of magnetic and transport properties of antiferromagnets from first-principles*

1. *Ab initio* study of magnetoresistance effect in $Mn_3Sn/MgO/Mn_3Sn$ antiferromagnetic tunnel junction
   K. Tanaka, Y. Toga, S. Minami, S. Nakatsuji, T. Nomoto, T. Koretsune, and R. Arita Phys. Rev. Materials **10**, 044405 (2026).
   DOI:10.1103/xt7z-sf3x

TANAKA, Shu [B class; 450 (B), 80 (C)] (348)
— *Physical properties of Ising machines*

1. Machine Learning Supported Annealing for Prediction of Grand Canonical Crystal Structures
   Y. Couzini, Y. Seki, Y. Nishiya, H. Nishi, T. Kosugi, S. Tanaka, Y. Matsushita J. Phys. Soc. Jpn. **94**, 044802 (2025).
   DOI:10.7566/JPSJ.94.044802

2. Improving the efficiency of quantum annealing with controlled diagonal catalysts
   T. Hattori and S. Tanaka Phys. Rev. A **113**, 022433 (2026).
   DOI:10.1103/vff6-cf7c

3. Quantitative analysis of the effectiveness of mid-anneal measurement in quantum annealing
   K. Takahashi and S. Tanaka J. Phys. Soc. Jpn. **95**, 034002 (2026).
   DOI:10.7566/JPSJ.95.034002

4. Utilizing intermediate states in quantum annealing for multi-objective optimization
   K. Takahashi and S. Tanaka J. Phys. Soc. Jpn. **95**, 053001 (2026).
   DOI:10.7566/JPSJ.95.053001

TANAKA, Tomonori [B class; 850 (B), 160 (C)] (158)
— *Application of the Magnetic Interaction Parameter Calculation Program to Skyrmion Systems*
— *Development of a non-perturbative calculation tool for magnetic coupling parameters*

1. General spin models from noncollinear spin density functional theory and spin-cluster expansion
   T. Tanaka and Y. Gohda arXiv:2512.04458
   DOI:10.48550/arXiv.2512.04458

TATAN, Alpin [AB class; 500 (B), 130 (C)] (183)
— *First-principles studies of magnetic tunnel junctions with non-collinear antiferromagnets*
— *Foundational first-principles studies of magnetic tunnel junctions*

TATETSU, Yasutomi [C class; 2600 (B), 300 (C)] (108)
— *Computational study on the stability of magnetic ordered alloy nanoparticles*

TEN-NO, Seiichiro [C class; 4000 (B), 350 (C)] (83)
— *Material design of in perovskite photocatalysts using first-principles calculations*

TERAO, Takamichi [B class; 600 (B), 130 (C)] (342)
— *Self-organization and dynamics in dendrimer polyelectrolytes*

1. Repulsive interactions between oppositely charged macroions in asymmetric multivalent salt solutions: Ion-valence and many-body effects
   M. Eguchi, and T. Terao J. Mol. Liq. 437 128377 (2025).
   DOI:10.1016/j.molliq.2025.1283

TEZUKA, Masaki [C class; 4000 (B), 350 (C)] ()
— *Scrambling in Sachdev-Ye-Kitaev-like strongly correlated models*

TODO, Synge [C class; 4800 (B), 400 (C)] ()
— *Simulation of quantum many-body systems by tensor network and sampling*

TOHYAMA, Takami [C class; 3000 (B), 0 (C)] (235)
— *Photoinduced nonequilibrium dynamics in the charge-ordered phase of doped Mott insulators*

1. Easy-axis Heisenberg model on the triangular lattice: From a supersolid to a gapped solid
   M. Ulaga, J. Kokalj, T. Tohyama, and P. Prelovsek Phys. Rev. B **111**, 174442 (2025).
   DOI:10.1103/PhysRevB.111.174442

2. Optical absorption activated by an ultrashort half-cycle pulse in metallic and superconducting states of the Hubbard model
   K. Shinjo, S. Sota, S. Yunoki, and T. Tohyama Phys. Rev. B **111**, 235125 (2025).
   DOI:10.1103/q1fw-tdk1

3. Low-energy photoexcitations inside the Mott gap in doped Hubbard and t-J ladders
   S. Chandra, K. Shinjo, S. Sota, S. Yunoki, and T. Tohyama Phys. Rev. B **113**, 045127 (2026).
   DOI:10.1103/pt16-43yd

TRAN BA, Hung [E class; 2600 (B), 300 (C)] (324)
— *Quantum Corrections to Classical Heisenberg Model for Giant Magnetocaloric Hydrogen Liquefaction*

1. Realistic finite temperature simulations for magnetic and transport properties of ferromagnets
   H. B. Tran and H. Li J. Mater. Chem. C **13**, 11393 (2025).
   DOI:10.1039/d5tc01141h

2. Insights into giant magnetocaloric effects in $BiCu_3Cr_4O_{12}$ with charge–spin–lattice coupling
   H. B. Tran, H. Li, M. Goto, K. Sato, and Y. Shimakawa J. Mater. Chem. A **13**, 34286 (2025).
   DOI:10.1039/d5ta03354c

3. 2D topological electrocatalysts with spin–orbit coupling: interplay between electrochemical and topological surface states
   H. Liu, H. B. Tran, Y. Wang, D. Zhang, Y. Lu, and H. Li J. Phys. Chem. Lett. **16**, 12892 (2025).

DOI:10.1021/acs.jpclett.5c03589

TSUJI, Naoto [B class; 500 (B), 80 (C)] (250)
— *Development of the nonequilibrium dynamical mean-field theory with tensor train methods*

TSUJI, Yuta [C class; 3200 (B), 600 (C)] (96)
— *Exploration of High-Entropy Oxide Catalysts Using First-Principles Calculations and Machine Learning*First-Principles Computational Approach to the Oxygen Evolution Reaction

1. Understanding the transition from reversed to conventional conductance decay in single-molecule wires from the effective Hamiltonian and frontier orbital perspective
K. Okazawa, Y. Tsuji, and K. Yoshizawa Bull. Chem. Soc. **98**, uoaf040(2025).
DOI:10.1093/bulcsj/uoaf040

2. A ferroelectric proton conductor with colossal polarization induced by in-plane symmetry breaking in a two-dimensional coordination polymer
Y. Song, Y. Tsuji, K. Sugimoto, T. Kikuchi, Y. Shi, Y. Murakami, K. Hiramatsu, B.L. Ouay, M. Ohba, and R. Ohtani Chem. Sci. **16**, 13413 (2025).
DOI:10.1039/d4sc08700c

3. First-Principles Calculation on the Adsorption of Ethylene-Acrylic Acid Molecules on Chromium Oxide Surfaces
H. Iwai,and Y. Tsuji ACS Omega **10**, 29578 (2025).
DOI:10.1021/acsomega.5c03021

4. Identifying Active Sites of IrOx Catalysts for OER: A Combined Operando XAS, SEIRAS, and Theoretical Study
N. Thakur, Y. Ren, M. Kumar, T. Uchiyama, M. Fujita, I. Arima, M. ishida, Y. Wu, Y. Tsuji, H. Imai, M. Matsumoto, Y. Zhuang, K. Yamamoto, T. Matsunaga, K. Ohara, M. Matsumoto, Y. Orikasa, Y. Kuroda, S. Mitsushima, and Y. Uchimoto J. Am. Chem. Soc. **147**, 30613 (2025).
DOI:10.1021/jacs.4c18510

5. Reversible and Massive Structural Transformation in MeltableCyanido-bridged Coordination Polymer Crystals
Y. Iwai, S. Kimura, M. Nakaya, T. Nakane, A. Kawamoto, G. Kurisu, Y. Tsuji, K. Hirai, K. Kimoto, O.Cretu, F.Takeiri, K. Sugimoto, B.L. Ouay, M. Ohba, and R. Ohtani Chem. Eur. J. **31**, e02640 (2025).
DOI:10.1002/chem.202502640

6. Discovery of Stable Short-Range Order in High-Entropy Oxides Assisted with Bayesian Optimization
T. Ueno, and Y. Tsuji J. Chem. Theory Comput. **21**, 11697 (2025).
DOI:10.1021/acs.jctc.5c01284

7. Co3O4-FeOOH as a heterojunction electrocatalyst for highly-efficient hydrazine-assisted water electrolysis and pollutant degradation
L. Dai, Y. Tsuji, H. Iwai, Q. Quan, D. Song, X. Liu, J. Liu, T. Yanagida, J.C. Ho and S. Yip Appl. Surf. Sci. **721**, 165458 (2026).
DOI:10.1016/j.apsusc.2025.165458

8. Navigating the Bio-Inspired Structure-Function Landscape: Spectroscopy Driven Finding of Hidden Radical Oxidation in Co-porphyrinic Porous Organic Polymer
B. Boro, C. Biswas, T.H. Vuong, S. Nandy, A. Shrotri, Y. Tsuji, J. Rabeah and J. Mondal Small Methods **10**, e01981 (2026).
DOI:10.1002/smtd.202501981

9. Facet-Selective Electrostatic Assembling of 2D MXene ontoAnisotropic Single-Crystal Metal Oxides for EnhancedPhotocatalysis
S. Kashiwaya, S.N. Myakala , S. Nekita, Y. Tsuji, Y. Niu, X. Liu, L. Qin, M. Sharma, A. Zakharov, L. Hultman, D. Eder, H. Saito, A. Cherevan and J. Rosen Adv. Mater. **38**, e19087 (2026).
DOI:10.1002/adma.202519087

TSUKAHARA, Noriyuki [B class; 350 (B), 80 (C)] (199)
— *The trapping mechanism of guest adsorbed molecules by porous metal-organic films on metal surfaces*

1. Microscopic Observation of the Oligomerization Process of HCOOH Molecules Confined by a 2D Metal-Organic Network on Cu(111)
Noriyuki Tsukahara and Jun Yoshinobu Small **21**, e05213 (2025).
DOI:10.1002/smll.202505213

TSUNEYUKI, Shinji [C class; 5800 (B), 0 (C)] (70)
— *Advancement and application of methods for predicting dielectric properties and structure exploration of materials*

1. Transferability of the chemical-bond-based machine learning model for dipole moment: The GHz to THz dielectric properties of liquid propylene glycol and polypropylene glycol
T. Amano, T. Yamazaki, N. Matsumura, Y. Yoshimoto and S. Tsuneyuki Phys. Rev. B ¥bf 111, 165149 (2025).
DOI:10.1103/PhysRevB.111.165149

2. Assessing the possible superconductivity in the doped perovskite hydride $KMgH_3$: Effects of lattice anharmonicity and spin fluctuations
S. Lu, R. Akashi, M. Kawamura and S. Tsuneyuki Phys. Rev. B ¥bf 111, 134516 (2025).
DOI:10.1103/PhysRevB.111.134516

3. Practical rule for trimming the DFT-1/2 self-interaction: Band gap, absolute band alignment, and defect properties of semiconductors
C Homma, R Akashi, Y Nishiya, S Tsuneyuki, Y Matsushita Phys. Rev. B ¥bf 112, 115111 (2025).
DOI:10.1103/mp93-55g3

4. Evolutionary search for superconducting hydrides in the La-Pt-H ternary system under compression
T. Ishikawa, Y. Tanaka, and S. Tsuneyuki Physica Scripta ¥bf 101, 105903 (2026).
DOI:10.1088/1402-4896/ae49c3

5. Search for high-pressure phases of yttrium via a data assimilation approach
Y. Kubo, T. Ishikawa, Y. Tanaka, Y. Nakamoto, M. Sakata and S. Tsuneyuki submitted

TU, Wei-Lin [B class; 400 (B), 70 (C)] (253)
— *Development of Fermi machine and finite temperature tensor network algorithm*

1. Probing the Dynamical Structure Factor of Quantum Spin Chains via Low-Temperature Gibbs States with Matrix Product State Subspace Expansion
T. Takahashi, W.-L. Tu, J.-Y. Chen, and Y. Nomura arXiv:2601.09326 (2026).
DOI:10.48550/arXiv.2601.09326

Data Repository

Dataset for "Probing the Dynamical Structure Factor of Quantum Spin Chains via Low-Temperature Gibbs States with Matrix Product State Subspace Expansion"

https://zenodo.org/records/18408712
DOI:10.5281/zenodo.18408711

UCHIDA, Takashi [B class; 200 (B), 60 (C)] (375)
— *Spontaneous formation of multiple-Q orders in two-dimensional Hubbard models*

UEMURA, Naoki [C class; 4600 (B), 550 (C)] (75)
— *The effect of added elements on the slip system of magnesium*

1. Density Functional Theory Study of the Role of Molybdenum in Weakening Hydrogen Effect on bcc Iron: A Comparison with Carbon and Nitrogen Effects
   S. Kato, N. Uemura, M. Vijendran, and R. Matsumoto ISIJ Int. **66**, 702 (2026).
   DOI:10.2355/isijinternational.ISIJINT-2025-390

UMEBAYASHI, Yasuhiro [AB class; 500 (B), 140 (C)] (181)
— *Interaction between Electrodes and Electrolytes in Li-S Batteries Studied by Classical Molecular Dynamics and First-Principles Calculations*
— *Molecular Dynamics and First-Principles Study of Cathode-Electrolyte Interfaces in Lithium-Sulfur Batteries*

USUI, Hidetomo [B class; 450 (B), 80 (C)] (178)
— *Theoretical exploration of goniopolar high-performance thermoelectric materials*

1. $Rb(Cd,Zn)_4As_3$ as a new n-type Zintl phase thermoelectric compound
   K. Ono, Y. Goto, H. Usui, M. Murata, S. Tsutsui, K. Kuroki, Y. Kamihara, and C.-H. Lee Acta Mater. **307**, 121968 (2026).
   DOI:10.1016/j.actamat.2026.121968

VENGAYIL KRISHNAN, Vishnu [B class; 500 (B), 60 (C)] ()
— *Yielding and aging of colloidal gels*

WANG, Tianyi [C class; 2200 (B), 250 (C)] ()
— *Exploring Transition Metal Oxide Catalysts for Nitrogen Reduction Reactions*

WANG, Yinqiao [C class; 800 (B), 150 (C)] ()
— *Exploring the Phase Behavior and Glassy Dynamics of Sticky Spheres*

WATANABE, Hiroshi [C class; 8200 (B), 300 (C)] (269)
— *Molecular dynamics study on analysis and control of Rayleigh-Plateau instability*
— *Molecular dynamics study on the interface instability with perturbations*

1. Molecular dynamics study of Rayleigh-Plateau instability at liquid-liquid interfaces
   S. Kikuchi and H. Watanabe Phys. Rev. Fluids **11**, 023901 (2026).
   DOI:10.7566/JPSJ.93.114601

Data Repository
Simulation data of the Rayleigh-Taylor instability
https://isspns-gitlab.issp.u-tokyo.ac.jp/kaityo256/rt-instability-data

WATANABE, Hiroshi [B class; 500 (B), 80 (C)] (248)
— *Study on the Novel Mechanism of Superconductivity in Nickel Oxides*

1. Hierarchical structure of primary and hybridization-induced superconducting correlations in bilayer nickelates
   H. Watanabe, H. Sakakibara, and K. Kuroki arXiv:2603.13604

WATANABE, Satoshi [C class; 8200 (B), 800 (C)] (54)
— *Analyses on correlation between material properties and atomic structures in complex structures via ab-initio-based methods*

1. Construction of Machine Learning Potentials toward the Exploration of Alloy Cluster Catalysts
   K. Miyamoto, K. Shimizu, A. K. A. Lu, S. Watanabe e-Journal of Surface Science and Nanotechnology **23**, 188 (2025).
   DOI:10.1380/ejssnt.2025-028

2. Charge States of Ions around Σ 5 (310)/[001] Grain Boundary in Cubic-ZrO2 Revealed by First-principles Calculations
   S. Arai, K. Shimizu, A. K. A. Lu, H. Masuda, H. Yoshida, S. Watanabe e-Journal of Surface Science and Nanotechnology **23**, 323-327 (2025).
   DOI:10.1380/ejssnt.2025-044

3. Study of the ion mobility in defect-laden ZrO_2 under an electric field using neural network with predictions for Born effective charges
   A. K. A. Lu, N. Maekawa, A. Ikeda, K. Shimizu, H. Masuda, H. Yoshida, S. Watanabe Phys. Rev. Mater., submitted.

YAMADA, Atsuo [C class; 3600 (B), 350 (C)] (95)
— *Exploration of novel rechargeable battery materials using first-principles calculations and machine learning*

1. Kinetic Suppression of Anion Intercalation into Cathode Conductive Carbon in High-Voltage Lithium Batteries
   K. Nakamura, N. Takenaka, S. Hagiwara, M. Otani, A. Yamada ACS Appl. Mater. Interfaces. **17**, 61439 (2025).
   DOI:10.1021/acsami.5c14007

2. Prerequisite of Oxygen Local Environment for Facile Proton Intercalation into Transition-Metal Oxides
   S. Park, S. Nishimura, J. Li, A. Kitada, S. Lee, W.-S. Yoon, A. Yamada J. Am. Chem. Soc. **148**, 7931 (2026).
   DOI:10.1021/jacs.5c22803

YAMADA, Atsushi [C class; 1000 (B), 200 (C)] ()
— *Analyses of the superconductivity in Hubbard models and their applications to strongly correlated electron systems.*

YAMAGUCHI, Naoya [C class; 1200 (B), 350 (C)] (144)
— *Development of First-principles Berry Phase Calculation codes for Application to Large Systems*

1. First-principles study of interface states in diamond(111)/Al2O3 with different terminations
   Y. Zhang, N. Yamaguchi, X. Zhang, M. Saito and N. Tokuda, and F. Ishii Surf. Interfaces **72**, 107147
   DOI:10.1016/j.surfin.2025.107147

2. First-principles study of electric-dipole-induced Rashba spin-splitting in Janus WSSe
   S. A. Putri, M. A. U. Absor, N. Yamaguchi, and F. Ishii Jpn. J. Appl. Phys. **64**, 10SP21
   DOI:10.35848/1347-4065/ae00cf

3. First-principles study of thickness-dependent vertical polarization in multilayer hexagonal boron nitride

N. M. Chadiza, H. P. Kadarisman, N. Yamaguchi, and F. Ishii Jpn. J. Appl. Phys. **64**, 11SP09
DOI:10.35848/1347-4065/ae0e2b

4. Capacitance profile of graphene via effective screening medium method: first-principles study
A. Sohib, N. Yamaguchi, and F. Ishii Jpn. J. Appl. Phys. **64**, 11SP11
DOI:10.35848/1347-4065/ae0cd3

5. The effect of interlayer coupling on thermoelectricity in atomically thin CaGe2: a first-principles study
A. A. Ghiffari, R. Syariati, Y. Morishima, N. Yamaguchi, and F. Ishii Jpn. J. Appl. Phys. **64**, 11SP31
DOI:10.35848/1347-4065/ae11bf

6. Band Unfolding in Finite Nanostructures: Visualizing Dirac, SpinValley, and Rashba Features
N. Yamaguchi, S. Yunitasari, W. Amalia, C.-C. Lee, T. Ozaki, and F. Ishii Nano Lett. **25**, 17725
DOI:10.35848/1882-0786/ae241f

Data Repository
layerAHC
https://isspns-gitlab.issp.u-tokyo.ac.jp/n-yamaguchi/layerAHC

GMBU.jl
https://isspns-gitlab.issp.u-tokyo.ac.jp/n-yamaguchi/GMBU.jl

Code for the Giant Molecule Band Unfolding
https://zenodo.org/records/17815785
DOI:10.5281/zenodo.17815785

YAMAMOTO, Go [C class; 3800 (B), 400 (C)] (298)
— *Machine Learning and Molecular Dynamics-Based Prediction of Optimal Structures for High-Strength MWCNT Yarns*

YAMASHITA, Tomoki [C class; 4000 (B), 350 (C)] (82)
— *Material Design Using Crystal Structure Prediction and First-Principles Calculations*

YAMAUCHI, Kunihiko [C class; 2600 (B), 0 (C)] (118)
— *Spintronics applications based on spin-splitting phenomena in altermagnets*

1. Spin-degenerate bulk bands and topological surface states associated with Dirac nodal lines in RuO2
T. Osumi, K. Yamauchi, S. Souma, S. Paul, A. Honma, K. Nakayama, K. Ozawa, M. Kitamura, K. Horiba, H. Kumigashira, C. Bigi, F. Bertran, T. Oguchi, T. Takahashi, Y. Maeno, and T. Sato Physical Review B **113**, 085116 (2026).
DOI:10.1103/wvs6-hqfv

YANAGISAWA, Susumu [BC class; 4450 (B), 0 (C)] (81)
— *First-principles investigation in search for organic materials in two-dimensional perovskite photovoltaics*
— *First-principles investigation of organic materials as candidates for materials of two-dimensional perovskite solar cells*
— *First-principles investigation on the electron-phonon coupling in organic semiconductor crystals*First-principles study on the mechanism of charge transfer at organic-electrode interfaces

1. Fingerprinting weak electronic interaction at a van derWaals interface: Fano signatures in a pentacene monolayer on graphite

Y. Hasegawa, T. Yamaguchi, M. Meissner, T. Ueba, F. Bussolotti, S. Ideta, K. Tanaka, S. Yanagisawa and S. Kera Phys. Rev. B **112**, 085301 (2025).
DOI:10.1103/2k7h-h8jm

YANAGISAWA, Takashi [B class; 700 (B), 140 (C)] (245)
— *Study of optimized many-body wave functions in strongly correlated electron systems*

1. Superconductivity and Inhomogeneous charge-ordered state in the two-dimensional Hubbard model – Off-Diagonal Wave Function Monte Carlo Studies of Hubbard Model IV–
T. Yanagisawa J. Phys. Soc. Jpn. 94, 074708 (2025).
DOI:10.7566/JPSJ.94.074708

YASUDA, Chitoshi [C class; 1000 (B), 0 (C)] (340)
— *Enhancement of correlation functions due to deficit in quantum spin systems*

1. Classical Ground-State Phase Diagram of the Multiple-Spin Exchange Model on a Honeycomb Lattice
C. Yasuda and Y. Chibana J. Phys. Soc. Jpn. **94**, 084704 (2025).
DOI:10.7566/JPSJ.94.084704

YASUDA, Yusuke [BC class; 5000 (B), 470 (C)] (282, 284)
— *MD Simulations on Single-Molecule Reactors based on Bottlebrush Polymers*
— *Study on structure-properties relationship in uniform/dynamic polymer networks via precise graph structure analysis*

1. Coarse-grained molecular dynamics simulations of slide-ring gels under finite deformation: influence of sliding ring rearrangement on softness and extensibility
Y. Yasuda, K. Mayumi, M. Toda, H. Yokoyama, H. Morita, and K. Ito Soft Matter **21**, 4573 (2025).
DOI:10.1039/D5SM00003C

YASUHARA, Sou [C class; 2600 (B), 0 (C)] (117)
— *Investigation of polarization switching in Li2GeO3*

1. Ferroelectric behavior of divalent cation-doped LiGaO2 with a distorted wurtzite-type structure
Sou Yasuhara, Yuto Tomizawa, Kazuki Okamoto, Masaki Tozuka, Ayato Nakagawa, Shintaro Yasui, Hiroshi Funakubo and Takuya Hoshina Jpn. J. Appl. Phys. 64 08SP02 (2025),
DOI:10.35848/1347-4065/adefe9

YOKO, Akira [C class; 4200 (B), 250 (C)] ()
— *Adsorption effects on electronic states of ultrasmall metal oxides*
— *Electronic state and new properties of ultrasmall metal oxides*

YOSHIDA, Tsuneya [C class; 3400 (B), 0 (C)] ()
— *Topology of strongly correlated electrons with dissipation*

YOSHIMI, Kazuyoshi [C class; 2600 (B), 100 (C)] (236)
— *Verification of the Effects of van der Waals interactions in Organic Materials by First-Principles Calculations toward Materials Design*

1. Pressure-induced topological changes in Fermi surface of two-dimensional molecular conductor
T. Kobayashi, K. Yoshimi, H. Ma, S. Sekine, H. Taniguchi, N. Matsunaga, A. Kawamoto, and Y. Uwatoko Phys. Rev. Materials **9**, L021801 (2025).
DOI:10.1103/PhysRevMaterials.9.L021801

2. Ambient-Pressure Organic Dirac Electron State in α-$(BETS)_2AuCl_2$
T. Kobayashi, K. Yoshimi, A. Nishimoto, S. Michimura, and H. Taniguchi J. Phys. Soc. Jpn. **95**, 043701 (2026).
DOI:10.7566/JPSJ.95.043701

Data Repository
Data for "Pressure-induced topological changes in Fermi surface of two-dimensional molecular conductor β'-$(BEDT\text{-}TTF)_2ICl_2$"
https://isspns-gitlab.issp.u-tokyo.ac.jp/k-yoshimi/betap-ET2ICl2

Data for "Ambient-Pressure Organic Dirac Electron State in α-$(BETS)_2AuCl_2$"
https://isspns-gitlab.issp.u-tokyo.ac.jp/k-yoshimi/alpha-bets2-aucl2

YUHARA, Junji [B class; 300 (B), 60 (C)] (202)
— *Structural analysis of metal oxide quasicrystal thin films*

ZHANG, Di [C class; 1600 (B), 300 (C)] (136)
— *Exploring high Ionic Conductivity Solid-State Electrolytes using Machine-Learning Driven Genetic Algorithms and Metadynamic Simulations*

1. 2D Topological Electrocatalysts with Spin–Orbit Coupling: Interplay between the "Electrochemical" and "Topological" Surface States
H. Liu, H. B. Tran, Y. Wang, D. Zhang, Y. Lu, and H. Li J. Phys. Chem. Lett. **16**, 12892 (2025).
DOI:10.1021/acs.jpclett.5c03589

2. Ampere-Level Electrosynthesis of CO via Well-Defined Pyridinic-N Incorporated Cobalt Phthalocyanine
T. Liu, X. Hou, D. Zhang, Y. Hirai, K. Ishibashi, Y. Matsuo, J. Yoshida, S. Ono, H. Li, and H. Yabu Small **21**, e202507824 (2025).
DOI:10.1002/smll.202507824

3. C60 Fullerene as the Active Site for CO2 Electroreduction
S.-W. Ying, Y. Wang, P. Du, Q. Wang, C. Yue, D. Zhang, Z.-C. Chen, J.-W. Zheng, S.-Y. Xie, and H. Li Angew. Chem. Int. Ed. **64**, e202511924 (2025).
DOI:10.1002/anie.202511924

4. High-Density W Single Atoms in Two-Dimensional Spinel Oxide Break the Structural Integrity for Enhanced Oxygen Evolution Catalysis
Y. Wang, B. Jia, W. Qin, Y. Wang, S. Liu, Y. Qin, Y. Zhao, L. Liu, D. Zhang, H. Liu, H. Zhong, J. Liu, J. Tu, Y. Liu, H. Wu, D. Zhang, J. Fan, X. Qu, H. Li, and M. Qin J. Am. Chem. Soc. **147**, 32249 (2025).
DOI:10.1021/jacs.5c12122

5. Stepwise Acceleration of Water Dissociation and Hydrogen Spillover for Enhanced Overall Alkaline Hydrogen Evolution
T. Lu, J. Li, C. Wang, H. Liu, S. Ye, X. Jia, L. Zhang, D. Zhang, D. Sun, Y. Gu, Q. Wang, B. Da, L. Wei, Y. Zhang, H. Li, and Y. Tang ACS Catal. **16**, 2827 (2026).
DOI:10.1021/acscatal.5c08576

6. Universal Catalyst Design Framework for Electrochemical Hydrogen Peroxide Synthesis Facilitated by Local Atomic Environment Descriptors
Z. Liu, Y. Liu, Y. Zhang, Y. Deng, Z. Zheng, R. Knibbe, T. Gao, M. Li, Z. Wang, B. Zhang, X. Jia, D. Zhang, H. Liu, X. Shao, Z. Gao, L. Wei, H. Li, and W. Yang Angew. Chem. Int. Ed. **65**, e202518027 (2026).
DOI:10.1002/anie.202518027

○ A class

Since this class is for trial use, research reports are not required.
When other classes are also used, their publications are shown in the list of B–E classes.
Then, the pages of their reports and publications are given in ( ).

AKIYAMA, Ryota [A class; 100 (B), 50 (C)] ()
— *Exploration of topological properties in natural minerals in Japanese mines*

AONISHI, Toru [A class; 100 (B), 50 (C)] ()
— *Image Analysis and Feature Extraction for Fusion Reactor Materials*

DEKURA, Shun [A class; 100 (B), 50 (C)] ()
— *Calculation of the electronic states of vapochromic HOF involving structural modulation*

HAN, Jihae [A class; 100 (B), 50 (C)] (187, 400)
— *Reductive decomposition mechanism of electrolyte at electrode/electrolyte interface by first-principles*

HATANO, Naomichi [A class; 100 (B), 50 (C)] ()
— *Dynamics of quantum walkers interacting with a localized spin*

HAZE, Masahiro [A class; 100 (B), 50 (C)] ()
— *Role of atomic steps in the transport properties of monolayer films*

KAMEYAMA, Ryohei [A class; 100 (B), 50 (C)] ()
— *Electronic-Structure Design and Mechanism Discovery in Molecular Crystals and Interfaces*

KAWAGUCHI, Kaishu [A class; 100 (B), 50 (C)] (409)
— *Investigation of Substrate Effects on Topological-Insulator Bi_2Te_3 Thin Films*

KAWAI, Kosuke [A class; 100 (B), 50 (C)] ()
— *Exploring anionic redox reactions induced by zinc-ion insertion/extraction*

KISHIDA, Ippei [A class; 100 (B), 50 (C)] ()
— *First-principles calculations of ionics in Li-gradient compounds and their application to battery materials*

KONISHI, Yusuke [A class; 100 (B), 50 (C)] ()
— *Computational Materials Exploration of High-Entropy REBCO Compounds*

KUSANO, Akane [A class; 100 (B), 50 (C)] ()
— *Theoretical study on molecular adsorption on metal catalyst surface*

MASUDA, Go [A class; 100 (B), 50 (C)] ()
— *Molecular Simulation of Polymer-Carbon Fiber Interfaces for Advanced Matrix Design*

MATSUNAGA, Noriaki [A class; 100 (B), 50 (C)] ()
— *Study of Electronic States in Low-Dimensional Organic Conductors*

MATSUURA, Keisuke [A class; 100 (B), 50 (C)] ()
— *Investigation of the origin of low-temperature hysteresis broadening in the antiferromagnetic-ferromagnetic phase transition*

MORITA, Katsuhiro [A class; 100 (B), 50 (C)] ()
— *MPI parallelization for finite-temperature quantum calculations*

1. Chemically tunable quantum magnetism on the anisotropic triangular lattice in rhenium oxyhalides
   M. Gen, D. Hirai, K. Morita, K. Nawa, S. Kogane, N. Matsuyama, T. Yajima, M. Kawamura, K. Deguchi, A. Koda, M. Kofu, S. Ohira-Kawamura, T. J. Sato, A. Matsuo, K. Kindo, Y. Kohama, and Z. Hiroi Nat Commun 16, 9938 (2025).
   DOI:10.1038/s41467-025-65913-7

OHKOSHI, Shin-Ichi [A class; 100 (B), 50 (C)] ()
— *Theoretical studies on the physical properties of novel functional phase transition materials*

OSADA, Wataru [A class; 100 (B), 50 (C)] ()
— *The effect of electronic states of the Pd/Cu(111) single atom alloy catalyst on its catalytic activity*

OSADA, Wataru [A class; 100 (B), 50 (C)] ()
— *The effect of electronic states of the Pd/Cu(111) single atom alloy catalyst on its catalytic activity 2*

ROY, Tufan [A class; 100 (B), 50 (C)] ()
— *First-principles and machine-learning study of magneto-transport phenomena in Kagome magnets and Heusler alloys for spintronics applications*

SATO, Naoki [A class; 100 (B), 50 (C)] (106, 435)
— *Complementary analysis of chemical pressure and lattice dynamics in complex crystal structures*

SEKI, Shinichiro [A class; 100 (B), 50 (C)] ()
— *Search of antiferromagnets hosting non-relativistic splitting based on DFT calculation*

SHIMADA, Toshihiro [A class; 100 (B), 50 (C)] ()
— *Electronic structure calculation of organic crystals with polarity*

TATAN, Alpin [A class; 100 (B), 50 (C)] (183, 443)
— *Foundational first-principles studies of magnetic tunnel junctions*

UDAGAWA, Masafumi [A class; 100 (B), 50 (C)] ()
— *Conserved charge and critical phenomena in geometrically frustrated systems*

UMEBAYASHI, Yasuhiro [A class; 100 (B), 50 (C)] (181, 446)
— *Molecular Dynamics and First-Principles Study of Cathode-Electrolyte Interfaces in Lithium-Sulfur Batteries*

UMEYAMA, Daiki [A class; 100 (B), 50 (C)] ()
— *Research on the band structure design and semiconductor properties of hybrid materials*

WANG, Jinxin [A class; 100 (B), 50 (C)] ()
— *Development of an MP-PIC-based solver for 3D circulating fluidized bed full-loop analyses*

1. Development of a virtual CFD model for regulating temperature in a liquid tank
   uthorJ. Wang, F. Xu, Y. Sakai, H. Takahashi, R. Zhang, H. Kanayama, D. Satou, and Y. Kansha
   The 35th European Symposium on Computer Aided Process Engineering (ESCAPE—35), July 6-9, 2025, Ghent, Belgium

WAIZUMI, Hiroki [A class; 100 (B), 50 (C)] ()
— *First-principles study on surface structure and electronic states of layered chalcogenides under molecular adsorption*

ZUSHO, Yu [A class; 100 (B), 50 (C)] ()
— *Molecular dynamics modeling of repair behavior in self-healing composite materials*

□ SCCMS Projects

FUKUSHIMA, Tetsuya [4000 (B), 400 (C)] (381)
— *Data Generation for Magnetic Properties at Finite Temperature*

1. Impact of Lattice Distortions on Magnetocrystalline Anisotropy and Magnetization in $(Nd_{1-x}Pr_x)_2Fe_14B$ Alloys
   H. Okumura, T. Miyake, T. Fukazawa, N. Sakuma, Y. Suzuki, T. Shoji, H. Akai, M. Ogura, and T. Fukushima arXiv:2512.07285
   DOI:10.48550/arXiv.2512.07285

MATUBAYASI, Nobuyuki [2000 (B), 200 (C)] (384)
— *Chiral Effects on Aqueous Solubility of Polypeptides Explored by Molecular Simulations*

MISAWA, Takahiro [4000 (B), 400 (C)] (219)
— *Estimation of the Hamiltonians of quantum spin liquid candidate material using Bayesian optimization*

MIYAKE, Takashi [2000 (B), 0 (C)] (383)
— *First-principles study of magnetic materials using KKR Green's function method*

1. Covariance Linkage Assimilation method for Unobserved Data Exploration
   Yosuke Harashima, Takashi Miyake, Ryuto Baba, Tomoaki Takayama, Shogo Takasuka, Yasuteru Shigeta, Yuichi Yamaguchi, Akihiko Kudo, and Mikiya Fujii Phys. Rev. Materials **9**, 093803 (2025).
   DOI:10.1103/8tjv-wtx5

2. Liquid structure of SmFe12-based alloys
   Kengo Nishio, Takehide Miyazaki, Taro Fukazawa, Tetsuya Fukushima and Takashi Miyake Computational Materials Science **256**, 113947 (2025).
   DOI:10.1016/j.commatsci.2025.113947

SHIMAZAKI, Tomomi [2000 (B), 100 (C)] (385)
— *Theoretical study on proton behavior in fuel cell material based on first-principles method*

1. Theoretical study of Lewis base passivation of p-type surface defects in IBr mixed-halide tin perovskites
   Emi Kino, Makito Takagi, Takumi Naito, Masanori Tachikawa, Koichi Yamashita, Tomomi Shimazaki J. Chem. Phys, **163**, 104703 (2025).
   DOI:10.1063/5.0285545

2. Theoretical study on the analyzability of modified convex regression for radical reaction
   Tomomi Shimazaki, Masanori Tachikawa Phys. Chem. Chem. Phys., **28**, 2499 (2026).
   DOI:10.1039/d5cp03946k

3. Rolling two-dimensional covalent organic framework (COF) sheets into one-dimensional electronic and proton-conductive nanotubes
   Zhuowei Li, Rajendra Prasad Paitandi, Yusuke Tsutsui, Wakana Matsuda, Masaki Nobuoka, Bin Chen, Samrat Ghosh, Takayuki Tanaka, Masayuki Suda, Tong Zhu, Hiroshi Kageyama, Yoshihiro Miyake, Hiroshi Shinokubo, Makito Takagi, Tomomi Shimazaki, Masanori Tachikawa, Katsuaki Suzuki, Hironori Kaji, Yasunobu Ando, Takahiro Ezaki, Shu Seki Proceedings of the National Academy of Sciences, **122**, e2424314122 (2025).
   DOI:10.1073/pnas.2424314122

YAMAJI, Youhei [5000 (B), 500 (C)] (386)

— *AI numerical spectroscopy for analyzing emergent structures of quantum entanglement in correlated quantum materials*

1. Photoemission microscope tomography for polycrystalline metals
   Y. Yamaji, S. Tsuda, and K. Yaji Science and Technology of Advanced Materials: Methods **6** 2611609 (2026).
   DOI:10.1080/27660400.2025.2611609

2. Unified Description of Cuprate Superconductors by Fractionalized Electrons Emerging from Integrated Analyses of Photoemission Spectra and Quasiparticle Interference
   S. Sakai, Y. Yamaji, F. Imoto, T. Tamegai, A. Kaminski, T. Kondo, Y. Kohsaka, T. Hanaguri, and M. Imada Phys. Rev. X **16** 011018 (2026).
   DOI:10.1103/mww7-32gn

5 THESES

□ Doctor Theses

1. **AKAMATSU, Katsuya**
   Adaptive tensor trees for generative modeling
   The University of Tokyo, 2025-10

2. **BAO, Jiahui**
   Theory of Nel and Hidden Orders in Perovskite Magnets
   Okinawa Institute of Science and Technology, 2026-03

3. **FUJII, Akihiro**
   Development of a materials design framework utilizing property-prediction models and their gradients
   The University of Tokyo, 2026-03

4. **FENG, Peijie**
   Nitrogen Diffusion into Iron-Based Materials under High Temperature
   The University of Tokyo, 2026-01

5. **KHINEVICH, Viktor**
   Developing Efficient Quantum Algorithms for State Preparation and Post-Processing in Quantum Chemistry
   The University of Osaka, 2026-03

6. **LU, Shaocong**
   Spin-Fluctuations in Hydride Superconductors from First Principles
   The University of Tokyo, 2025-09

7. **MAHMUD Rabiatul Aliah Binti**
   Theoretical and Experimental Investigations of the Enhancement of ZnO Semiconductor as a Photocatalyst: Insights into the Reduction of CO2
   The University of Osaka, 2026-04

8. **MASUDA, Shuya**
   Development of metal-oxide photoelectrodes using computational materials science
   Nara Institute of Science and Technology, 2026-03

9. **MATSUKIYO, Hiroki**
   Numerical and theoretical study on active fluids under spatial confinements
   Kyushu University, 2026-03

10. **MATSUZAKA, Mizuki**
    A Study on Organic Spin Valves Using Functional Molecules
    Keio University, 2026-03

11. **MIURA, Shohei**
    Verification of the durability of halide perovskite materials using first-principles calculations
    Kanazawa University, 2026-03

12. **MIZUHARA, Aoi**
    Atomistic study of the initial stages of metal heteroepitaxial growth
    Osaka Metropolitan University, 2026-03

13. **OISHI, Yasuhiro**
Computational study of conformational changes in a PASE molecule and an amyloid-β (20-34) peptide
University of Hyogo, 2026-03

14. **ONO, Mizuho**
First-Principles Study of Energy Conversion Pathway in Ultrafast Light-Matter Interaction
Tohoku University, 2026-03

15. **OSHIMA, Hisanori**
Symmetry and Topology for Measurement-Induced Phase Transitions
The University of Tokyo, 2026-03

16. **PUTRI, Salsabila Amanda**
First-Principles Study of Spin-Splitting in Janus Transition Metal Dichalcogenides
Kanazawa University, 2026-03

17. **ROJAs, Kurt Irvin Medina**
First-Principles Exploration of the Chemical and Spectral Properties of Hydrogen Boride Sheets
The University of Osaka, 2025-09

18. **SALEH, Md Abu**
Water Dynamics around Osmolytes and Polymers Using Molecular Dynamics Simulations: Insights for the Design of Effective Protein Stabilizers
Kyushu University, 2025-09

19. **SATO, Masanori**
First-principles study of Pentacene adsorption on the surfaces of the Tsai-type Ag-In-Yb quasicrystal
Kagoshima University, 2026-03

20. **SHIOTA, Tomoya**
Developing Quantum-Classical Hybrid Interfaces for Solving Realistic Atomic Scale Chemical Problems
The University of Osaka, 2025-09

21. **TAKAHARA, Wataru**
Development of a Data-Driven Approach for the Discovery of Novel Photocatalysts
Nara Institute of Science and Technology, 2026-03

22. **TEWENG, Yedija Yusua Sibuea**
First-Principles Study of the Shift Current in Perovskite CsPbI3
Kanazawa University, 2026-03

□ Master Theses

1. **ARAI, Atsuro**
   Theoretical Study on Magnetism and Superconductivity in the Kitaev-Heisenberg Ladder Model
   The University of Tokyo, 2026-03

2. **ASAKURA, Yuto**
   Influence of molecular torsion on the Soret effect
   Kyoto University, 2026-03

3. **BANDHASO, David**
   First-principles study of BaTiO3/BaRuO3
   Kanazawa University, 2025-09

4. **CHADIZA, Nadia Maharani**
   First-principles study of dielectric properties of BN multilayers
   Kanazawa University, 2025-09

5. **FENG, Fan**
   Electronic structures of lanthanum copper oxide using quasi-particle self-consistent GW method
   Kanazawa University, 2025-09

6. **FUJII, Akio**
   Defect calculation of ZnM_2O_4 (M=Co,Rh,Ir) spinel by SCAN
   Yokohama National University, 2025-03

7. **FUJIMORI, Shota**
   Molecular Dynamics study of the electrical double layer and solvent molecules in electrolyte solutions
   Gifu University, 2026-03

8. **HAMURO, Shinasaku**
   Theoretical study of p-n coexisting thermoelectric materials based on first-principles calculations
   Shimane University, 2026-03

9. **HARADA, Masahiro**
   Experimental and Theoretical Study of the Physical Properties of a Firefly Bioluminescence Substrate Analog: seMpai
   Gunma University, 2024-03

10. **HASHIMOTO, Chika**
    Fabrication of molecular nanojunctions utilizing magnetic thin-film edges and first-principles calculations
    Keio University, 2026-03

11. **HATTORI, Kazuki**
    Systematic First-Principles Study of Structural and Elemental Dependence of Lattice Thermal Transport in Zintl-Based Thermoelectric Materials
    Keio University, 2025-03

12. **HAYASHI, Eisuke**
    Diffusional characteristics and non-equilibrium phase transitions of active glass model in dense binary hard disk systems
    Nagoya Institute of Technology, 2026-03

13. **HIDA, Ichika**
Research on Hydrogen Isotope Effects in Water Electrolysis/Fuel Cells Using Fe-Based Catalysts
Hokkaido University, 2026-03

14. **HIDAKA, Kotaro**
Statistical machine learning analysis of the blinking phenomenon of fluorescent molecules: Development of Poisson-emission type hidden Markov model
Kyushu Institute of Technology, 2026-03

15. **HIRATA, Yusaku**
Predicting the folding process of a structurally complex protein using statistical mechanical models
The University of Tokyo, 2026-03

16. **HOSHI, Yuto**
Theoretical analysis and material design of high-T_c superconductors by performing fluctuation exchange approximation
Tottori University, 2025-03

17. **HOSODA, Masakage**
Molecular dynamics study of scaling law for droplet growth
Keio University, 2026-03

18. **HWANG, Youngseok**
Theoretical study on the stability of hydrogen impurities at the α-Al_2O_3/Fe interface
Hokkaido University, 2026-03

19. **IKEGAMI, Sogen**
Quantum phenomena arising from competition between distinct topological phases in two-dimensional systems
The University of Tokyo, 2026-03

20. **IRIE, Yusuke**
Electrode potential in ionic liquid
The University of Tokyo, 2026-03

21. **ITO, Daigo**
First-principles method to calculate force constants using spherical tensors
Institute of Science Tokyo, 2026-03

22. **ITO, Sayaka**
Exploration of magnetic compounds by first-principles calculations and machine learning
Institute of Science Tokyo, 2026-03

23. **KADOWAKI, Reo**
Molecular dynamics simulations of photoresponsive membrane modulator molecules that enhance the membrane permeation of drugs with low cell-membrane permeability.
Okayama University, 2026-03

24. **KAJIHARA, Aoi**
Theoretical study on spin current generation via topological spin textures
The University of Tokyo, 2026-03

25. **KASAI, Yuki**
Cluster-expansion method refined by Bayes compressing sensing

Institute of Science Tokyo, 2026-03

26. **KATO, Shinya**
Density Functional Theory Study of Influence of Molybdenum in Suppressing Hydrogen Embrittlement in bec Iron
Kyoto University of Advanced Science, 2026-03

27. **KATSUTA, Takumi**
High-precision magnetic anisotropy analysis and its application to spintronics materials based on first-principles calculations
Kanazawa University, 2026-03

28. **KAWATSU, Tomohide**
Magnetization Plateau of the S=3/2 Antiferromagnetic Chain with the Biquadratic Interaction
University of Hyogo, 2026-03

29. **KIMURA, Kanta**
Verification of the accuracy of spinon variational wave-functions in the antiferromagnetic Heisenberg model -comparison with the exact diagonalization method-
Tokyo University of Science, 2026-03

30. **KOBAYASHI, Koki**
Investigation of Water Quality in Firefly Habitats and the Effects of Metal Ions on Bioluminescent Substrates for Biosensors
Gunma University, 2026-03

31. **KOBAYASHI, Mutsumi**
Analyzing the internal structure of restricted Boltzmann machines trained on classical music
Keio University, 2026-03

32. **KOBAYASHI, Tomoki**
Numerical calculation of quantum phase transition under Dzyaloshinsky-Moriya interaction in Kagome-lattice antiferromagnets using the linked cluster expansion method
Tokyo University of Science, 2026-03

33. **KONDO, Yuki**
Flyer-Target simulation of shock waves in crystal-fluid impact in hard disk systems
Nagoya Institute of Technology, 2026-03

34. **KOSUGI Kaito**
Li-ion Diffusion Mechanisms in $Li_{2-2x}Mg_{1+x}Cl_4$ Studied by Molecular Dynamics Simulations
Nagaoka University of Technology, 2026-03

35. **KUBO, Mahiro**
Theoretical study on work function of multilayer graphene on SiC and its origin
Shimane University, 2026-03

36. **KUMANO, Shinsuke**
Multi-orbital extended Hubbard model for $GaBa_2CuO_4F$ with stacked CuO_2 and buffer layers
University of Hyogo, 2026-03

37. **KUWABARA, Shuta**
Theoretical Analysis of Electronic Properties in Transition Metal Alloys using Coherent Potential Approximation Based on Wannier Functions
Keio University, 2025-03

38. **MASUMI, Sao**
Evaluation of the complex dielectric function of YbO thin films and investigation of optical transitions based on the electronic band structure.
University of Fukui, 2025-03

39. **MASTSUDA, Kotaro**
Hydrogen Diffusion on Stepped Ru Surface
The University of Tokyo, 2026-03

40. **MATSUMOTO, Naohiro**
First-principles study on stability and electronic structure of NiFe/2D material interface
Kobe University, 2026-03

41. **MATSUMOTO, Sora**
Theoretical material design of new superconductor with malleability and ductility
Tottori University, 2025-03

42. **MATSUURA, Shuta**
Dynamical mean-field theory with the tensor-train method and the analysis of the strongly correlated electron systems
The University of Tokyo, 2026-03

43. **MIKI, Ryotaro**
confidential
Nara Institute of Science and Technology, 2026-03

44. **MIZUKAMI, Masatake**
Process Informatics for Photocatalysts Integrating Experiments, Simulations, and Machine Learning
Nara Institute of Science and Technology, 2026-03

45. **MORIKAWA, Misaki**
Theoretical study on the magnon crystal state of the distorted Kagome system $Y_3Cu_9(OH)_{19}Cl_8$
Tokyo University of Science, 2026-03

46. **MORITA Asahi**
Molecular Dynamics Simulations on the Surface Segregation of CuZn Surfaces in Methanol Synthesis by using Machine-Learning Interatomic Potential
The University of Osaka, 2026-03

47. **MURAKAMI, Ryosuke**
Evaluation of the complex dielectric function of YO thin films and investigation of optical transitions based on the electronic band structure
University of Fukui, 2025-03

48. **NAKAI, Yura**
Quantitative analysis of pedestrian counter-flow under congested conditions using a floor field model
Nagoya Institute of Technology, 2026-03

49. **NAKAOKA, Daiki**
Theoretical material design of new high-T_c compounds based on the orbital space bilayer model
Tottori University, 2025-03

50. **NAKAYAMA, Takahiro**
First-principles calculations of acetylene hydrogenation on the $Al_{13}Fe_4(010)$ surface with the addition of trace amounts of Pd
Kagoshima University, 2026-03

51. **NIWA, Haruya**
Analysis on electronic properties of spinel transition-metal oxides by first-principles GW method
Kanazawa University, 2026-03

52. **OKADA, Shunya**
Computational design of cyanobacterial enzymes to improve alkane biosynthesis efficiency
The University of Tokyo, 2026-03

53. **OKADA, Yuki**
First-Principles Study of NO Detection Based on Fe-doped (6,4) Single-Walled Carbon Nanotubes
Hokkaido University, 2026-03

54. **Oshima, Takumi**
Tensor-network sampling and its application to spin glasses
The University of Tokyo, 2026-03

55. **OTAKE, Mai**
Theoretical study on the defect structure of Sn-based double perovskite solar cell materials
Japan Women's University, 2026-03

56. **OTSUKA, Koki**
Composition optimization of high-entropy nanoparticle catalysts using machine learning
The University of Tokyo, 2026-03

57. **REZA, Selim**
First-principles computational study on electronic structures and optical properties in the zinc pyrovanadates
Kanazawa University, 2025-09

58. **RIDHO, Muhammad Rosyid**
First-principles study of tensile test for carbon nanotubes
Kanazawa University, 2025-09

59. **ROWLAND, Noelle**
Effect of polymers on multi-bubble nucleation
Keio University, 2026-03

60. **SAKAI, Akihiro**
Mechanism of dwave superconductivity induced by interlayer Coulomb interaction in bilayer nickelates
Tokyo Metropolitan University, 2026-03

61. **SAKANOUE, Ryuji**
Development of a magnetic EXAFS analysis method for Co2FeSi
Chiba University, 2026-03

62. **SASAOKA, Tomohiro**
First-Principles Molecular Dynamics Analysis of Structural Changes in Ettringite upon Heating
Hiroshima Institute of Technology, 2026-03

63. **SATO, Kazuma**
Applicability of metal single-atom catalysts supported on light-element-doped graphene for formic acid decomposition
Hokkaido University, 2026-03

64. **SEKI, Yuji**
Magnon Dispersion Analysis in Layered Nickelates Using the Frozen Magnon Method
Keio University, 2025-03

65. **SHIMIZU, Ken**
Curie Temperature of α''-$Fe_{16}N$ predicted considering spin-phonon couplings
Institute of Science Tokyo, 2026-03

66. **SHIMIZU, Yushiro**
Evaluation of Surface Activation Methods for the Development of MoS_2-based Oxygen Reduction Reaction Catalysts Using First-Principles Calculations
Hokkaido University, 2026-03

67. **SHIMOJI, Rikuto**
Quantum Monte Carlo Study on Phase Transition Temperatures in Quasi-Two-Dimensional Ferrimagnets
University of the Ryukyus, 2026-03

68. **SHINOZAKI, Hiyori**
First-principles calculations on carrier transport properties of semiconductors: Temperature dependence of relaxation time
Kyushu Institute of Technology, 2026-03

69. **SHOGAN, Rikuto**
Mechanical Property of High-Entropy MXene
Yokohama National University, 2025-03

70. **SUGIYAMA, Kosei**
First-principles study on electronic structure and conduction property of 4H-SiC/SiO_2 interface after NO annealing
Kobe University, 2026-03

71. **SUGIYONO, Vani**
First-principles study of ferroelectricity in BaTiO3 thin-film
Kanazawa University, 2025-09

72. **SUZUKI, Haruto**
Theoretical Study on the Ground State of the Heisenberg Antiferromagnet on the Distorted Shastry-Sutherland Lattice
University of Hyogo, 2026-03

73. **SYAWLY, Adzky Mathla**
First-principles crystal structure prediction for SnSe
Kanazawa University, 2025-09

74. **TAKAHASHI, Tomoya**
Numerical calculations of dynamical spin structure factor using tensor networks and their application to a quasi-one-dimensional antiferromagnet $YbAlO_3$
Keio University, 2025-03

75. **TANAKA, Naotaka**
Construction of the quantum many-body calculation system of the high-T_c materials and its benchmark
Tottori University, 2025-03

76. **TSUGAWA, Tomoya**
Temperature estimation from magnetiation distribution by machine-learning assisted method
University of Hyogo, 2026-03

77. **USHIO, Kensei**
Theoretical study on the bilayer high-T_c superconductors performing first principles
Tottori University, 2026-03

78. **WATANABE, Atsuya**
Development of a rational design strategy for enhancing the activity of a bioplastic precursor-synthesizing enzyme
The University of Tokyo, 2026-03

79. **WATANEBE, Ryo**
Electronic Theory of Spin Dynamics Induced by Circularly Polarized Light in Solids
The University of Tokyo, 2026-03

80. **XU, Yang**
Persistent Homology Analysis of Li Ion Diffusion in Partially Crystallized Lithium Thiophosphate
The University of Tokyo, 2025-09

81. **YAMAGUCHI, Hikaru**
Electronic states and optical properties of perovskite solar cell materials analyzed by quasi-particle self-consistent GW method
Kanazawa University, 2026-03

82. **YAMAMOTO, Kazuki**
Electronic Properties of Titanium Oxide Surfaces Doped with Heterogeneous Atoms
Iwate University, 2026-03

83. **YAMATE, Sota**
Development of a First-Principles Method for Computing Spin Hall Conductivity
Kanazawa University, 2026-03

84. **YANASE, Shigetomo**
Machine Learning Potential for Twisted Bilayer Graphene
Kanazawa University, 2026-03

85. **YASHIMA, Givenname**
Evaluation of the complex dielectric function of LuO thin films and investigation of optical transitions based on the electronic band structure
University of Fukui, 2025-03

86. **YIPING, Chen**
Quantum diffusion process of hydrogen atoms on Ru(001)
The University of Tokyo, 2026-03

87. **ZHANG Ziyong**
Structural investigation of flat honeycomb bismuthen grown on Ag(111)
Kyushu university, 2026-03